

Copper Bond Wire Corrosion Induced by Sulfur-Containing Adhesion Promoters:

Kinetic and Diffusive Aspects of Copper Sulfide Facilitated Degradation



Dissertation

ZUR ERLANGUNG DES DOKTORGRADES
DER NATURWISSENSCHAFTEN (DR. RER. NAT.)
DER FAKULTÄT FÜR CHEMIE UND PHARMAZIE
DER UNIVERSITÄT REGENSBURG

VORGELEGT VON

MAXIMILIAN SEHR

AUS SULZBACH-ROSENBERG

OKTOBER 2021

Die vorliegende Dissertation wurde im Zeitraum von November 2017 bis Februar 2021 am Institut für Anorganische Chemie I der Universität Regensburg unter der Leitung von Herrn Prof. Dr. Arno Pfitzner angefertigt.

Diese Arbeit wurde von Herrn Prof. Dr. Arno Pfitzner angeleitet.

Einreichung des Promotionsgesuchs:

Tag der mündlichen Prüfung:

Prüfungsausschuss:

Vorsitzender: Herr Prof. Dr. A. Slenczka

1. Gutachter: Herr Prof. Dr. A. Pfitzner
2. Gutachter: Herr Prof. Dr. R. Weihrich

Weiterer Prüfer: Herr Prof. Dr. F.-M. Matysik

Meinen Eltern gewidmet

Danksagung

Das Zustandekommen der vorliegenden Arbeit wäre ohne die Unterstützung vieler Menschen nicht möglich gewesen. Deshalb möchte ich mich bei den folgenden Personen ganz herzlich bedanken:

Mein besonderer Dank gilt meinem Doktorvater Herrn Prof. Dr. Arno Pfitzner für die Möglichkeit zur Durchführung dieser Arbeit, den großen wissenschaftlichen Freiraum, den er mir für die Anfertigung gewährt hat, die wertvollen Ratschläge sowie fachlichen und freundschaftlichen Gespräche während der letzten Jahre.

Zudem gilt mein Dank Herrn Dr. Steffen Jordan für die stetige Unterstützung und Beratung, die zahlreichen fachlichen und freundschaftlichen Diskussionen in Meetings und Workshops und die gute Zusammenarbeit, die erheblich zum Gelingen dieser Arbeit beigetragen haben.

Der Infineon Technologies AG, die diese kooperative Zusammenarbeit durch ihre finanzielle Unterstützung sowie die spannende wissenschaftliche Themenstellung und die Teilnahme an zahlreichen Workshops, Seminaren und Konferenzen ermöglicht hat.

Dem Fraunhofer IMWS, im speziellen Frau Sandy Klengel, Herrn Jan Schischka und Herrn Robert Klengel für die Unterstützung bei der Präparation und Durchführung der Elektronenmikroskopischen Aufnahmen sowie die fachliche Diskussion bei zahlreichen Workshops.

Herrn Prof. Dr. Richard Weihrich für die Bereitschaft diese Arbeit zu begutachten.

Herrn Dr. Marc Schlosser für die gute Zusammenarbeit bezüglich der Praktikumsbetreuung, die Unterstützung in allen Angelegenheiten und den hilfreichen fachlichen Diskussionen rund um die Pulverdiffraktometrie, sowie das Aufhellen des Unialltags durch seine humorvolle Art.

Herrn Dr. Florian Pielnhöfer für seine Unterstützung zu theoretischen Fragestellungen, dem hilfreichen wissenschaftlichen Austausch und den freundschaftlichen Gesprächen.

Frau Bianca Frömel und Katharina Trögl für ihre Hilfe bei allen organisatorischen Angelegenheiten und den vielen freundschaftlichen Gesprächen während der Kaffeepausen.

Herrn Florian Truksa für seine große Hilfsbereitschaft und seine kreative Unterstützung bei den verschiedensten Problemstellungen. Frau Heidi Paulus für die Unterstützung der präparativen Arbeiten.

Frau Ulrike Schießl für die Durchführung der thermischen Analysen, der Unterstützung bei der Rasterelektronenmikroskopie und den vielen freundschaftlichen Unterhaltungen.

Frau Dr. Claudia de Giorgi, Herrn Dr. Thomas Buchecker, Herrn Dr. Christoph Vitzthumecker, Herrn Dr. Daniel Fiedler, Herrn Dr. Max Vilsmeier, Herrn Dr. Daniel Friedrich, Herrn Dr. Dominik Gigl, Herrn Dr. Thomas Rothenaiger und Herrn Severin Bauer für ihre großartige Unterstützung während meiner Masterzeit, die Einweisung in die Gerätschaften und den vielen freundschaftlichen und fachlichen Diskussionen.

Herrn Christoph Meier für die gemeinsamen Ausflüge zu Tagungen, die vielen Unterhaltungen und Unternehmungen außerhalb der Uni, die großartige Zusammenarbeit während der Praktika und die unterhaltsamen Gespräche im Laboralltag.

Herrn Philipp Schmid für die zahlreichen Whiteboard-Sessions während der gemeinsamen, angenehmen Bürozeit und den fachlichen und freundschaftlichen Unterhaltungen während der Kaffeepausen.

Herrn Dr. Christian Klimas und Herrn Florian Wegner für die vielen unterhaltsamen Gespräche, ihre Hilfsbereitschaft und die hervorragende Zusammenarbeit.

Herrn Serkan Damnali, Herrn Martin Schmauser, Herrn Bastian Höfler, Herrn Sven Schedlowski, Frau Susan Rank und Herrn Rafal Samp, deren von mir betreute Bachelor- und Forschungsarbeiten erheblich zum Gelingen dieser Arbeit beigetragen haben, für die präparative Unterstützung.

Allen Beteiligten der mittäglichen Schafkopfrunden.

Allen anderen aktuellen und ehemaligen Mitgliedern des Lehrstuhls von Prof. Dr. Arno Pfitzner für die tolle Stimmung, die unterhaltsamen Kafferunden, die großartigen Lehrstuhlfeiern und den angenehmen Arbeitsalltag: Herrn Ferdinand Gigl, Herrn Sebastian Fäth, Herrn Sebastian Haumann, Frau Ria Mandal, Herrn Salil Bal, Herrn Amadeus-Samuel Tragl, Frau Daniel Garcia, Herrn Maximilian Röhl, Frau Franziska Kamm, Herrn Gasper Jost, Herrn Simon Stemplinger, Herrn Martin Schmid, Herrn Dr. Florian Wisser, Herrn Michael Földi, Frau Elisabeth Bauer.

Danken möchte ich besonders meiner Familie und meiner Freundin, Lydia Simmann, die mich immer auf meinem Weg bestärkt und in allen Lebenslagen Geduld und Unterstützung während meiner Studien- und Promotionszeit entgegengebracht haben. Ohne euch wäre diese Arbeit nicht möglich gewesen.

Continuous improvement is better than delayed perfection

Mark Twain

Eidesstattliche Erklärung

- (1) Ich erkläre hiermit an Eides statt, dass ich die vorliegende Arbeit ohne unzulässige Hilfe Dritter und ohne Benutzung anderer als der angegebenen Hilfsmittel angefertigt habe; die aus anderen Quellen direkt oder indirekt übernommenen Daten und Konzepte sind unter Angabe des Literaturzitats gekennzeichnet
- (2) Bei der Auswahl und Auswertung folgenden Materials haben mir die nachstehend aufgeführten Personen in der jeweils beschriebenen Weise unentgeltlich geholfen:

(siehe „Danksagung“)

- (3) Weitere Personen waren an der inhaltlich-materiellen Herstellung der vorliegenden Arbeit nicht beteiligt. Insbesondere habe ich hierfür nicht die entgeltliche Hilfe eines Promotionsberaters oder anderer Personen in Anspruch genommen. Niemand hat von mir weder unmittelbar noch mittelbar geldwerte Leistungen für Arbeiten erhalten, die im Zusammenhang mit dem Inhalt der vorgelegten Dissertation stehen.
- (4) Die Arbeit wurde bisher weder im In- noch im Ausland in gleicher oder ähnlicher Form einer anderen Prüfungsbehörde vorgelegt.

Regensburg, den 18. Oktober 2021

.....(Maximilian Sehr)

ABSTRACT

The application of integrated circuits in the automotive sector involves quality, reliability, durability, and safety (QRD+S) issues over a period of 10 - 15 years. Consequently, huge efforts have been made to ensure the reliability and safety of the chips over a long period of time. This caused the introduction of new qualification standards such as the automotive electronics council (AEC) Q100 Grade 0 stress test standard for integrated circuits. Thereby, copper (Cu) bond wires proved to be a critical component in high temperature storage life (HTSL) tests above 150 °C. Therein, sulfur-containing adhesion promoters are found to induce Cu bond wire corrosion, which may lead to device failure. Also, various prevention strategies are applied to avoid Cu corrosion, such as coating the Cu wire. However, the utilized Pd-coating can act as a corrosion accelerator by Cu-Pd galvanic coupling with Cu_xS as solid electrolyte. To date, the detailed mechanisms of different protective coatings, as well as the reactivity and temperature stability of various sulfur-containing adhesion promoters within the mold compound have not been clarified.

This thesis identifies the underlying sulfur induced corrosion mechanisms as this understanding is crucial to support further package and bond wire development. To achieve this, different problems which arise from sulfur-containing adhesion promoters and their sulfur induced corrosion are considered.

For this purpose, powder X-ray diffraction (PXRD) is established in this thesis, which allows us to identify corrosion products, gain structural information, and study quantitative conversions. After identifying the main corrosion products, the focus shifts on electrochemical properties, as these are key parameters in corrosion processes. Here, electrochemical impedance spectroscopy (EIS) and polarization measurement techniques were used.

The electrochemical properties are especially important for the Pd-coated bond wires which may form Cu/Pd galvanic couples and thus lead to galvanic corrosion. To clarify the role of the Pd-coating during sulfur corrosion, various coated bond wires are investigated with corrosive S-compounds. High temperature in situ powder X-ray diffraction (HT-in situ-PXRD) and scanning electron microscopy (SEM) are applied to gain further insight into the underlying corrosion mechanisms. Moreover, HT-in situ-PXRD is successfully used to screen a wide range of different organic S-compounds and to classify specific S-moieties for their corrosive capabilities.

Since adhesion promoters decompose at elevated temperatures, the risk for sulfidation reaction with Cu bond wire rises. The decomposition of adhesion promoters is known to strongly increase at temperatures above 150 °C which may not be a realistic temperature profile for real semiconductor applications. Hence, the question arises whether different failure mechanisms emerge if higher temperatures than 150 °C are applied to accelerated stress tests. Therefore, HT-in situ PXRD is established to resolve this question by identifying the respective corrosion mechanisms and kinetics. Accordingly, the temperature dependant kinetic parameters are obtained and discussed.

KURZZUSAMMENFASSUNG

Die Anwendung von integrierten Schaltkreisen im Automobilbereich beinhaltet Qualitäts-, Zuverlässigkeits-, Haltbarkeits- und Sicherheitsfragen (QRD+S) über einen Zeitraum von 10 - 15 Jahren. Folglich wurden große Anstrengungen unternommen, um die Zuverlässigkeit und Sicherheit der Chips über einen langen Zeitraum zu gewährleisten. Dies führte zur Einführung neuer Qualifizierungsstandards wie dem Stressteststandard AEC Q100 Grade 0 für integrierte Schaltkreise. Dabei erwiesen sich Kupferbonddrähte als kritische Komponente in HTSL-Tests über 150 °C. Darin wurde festgestellt, dass schwefelhaltige Haftvermittler eine Korrosion des Kupferbonddrahts induzieren, die zum Versagen des Bauteils führen können. Zudem werden verschiedene Präventionsstrategien wie das Beschichten des Kupferdrahts verwendet, um Kupferkorrosion zu vermeiden. Die verwendete Pd-Beschichtung könnte jedoch durch galvanische Cu-Pd-Kopplung mit Kupfersulfid als Festelektrolyt als Korrosionsbeschleuniger wirken. Bis heute sind die detaillierten Mechanismen verschiedener Beschichtungen sowie die Reaktivität und Temperaturstabilität verschiedener schwefelhaltiger Haftvermittler innerhalb der Mold Compound nicht aufgeklärt.

Diese Arbeit identifiziert die zugrunde liegenden schwefelinduzierten Korrosionsmechanismen, da dieses Verständnis entscheidend für die weitere Entwicklung der Mold Compound und Bonddrähte ist. Um dies zu erreichen, werden verschiedene Probleme betrachtet, die sich aus schwefelhaltigen Haftvermittlern und deren schwefelinduzierter Korrosion ergeben.

Dazu wird in dieser Arbeit die Röntgenpulverdiffraktometrie (PXRD) verwendet, die eine detaillierte Korrosionsstudie durch die Identifizierung von Korrosionsprodukten, Strukturinformationen und quantitativen Umwandlungen ermöglicht. Anschließend wurden die Korrosionsprodukte identifiziert und die elektrochemischen Eigenschaften durch elektrochemische Impedanzspektroskopie (EIS) und Polarisationsmessungen gemessen, da die elektrochemischen Eigenschaften Schlüsselparameter in Korrosionsprozessen sind.

Um die Rolle der Pd-Beschichtung in Bezug auf die Schwefelkorrosion aufzuklären, werden verschieden beschichtete Bonddrähte mit korrosiven Schwefelverbindungen untersucht. Dazu werden Hochtemperatur-in-situ-Röntgenpulverdiffraktometrie und Rasterelektronenmikroskopie (REM) eingesetzt und ein grundlegendes Verständnis über die zugrunde liegenden Korrosionsmechanismen erlangt. Darüber hinaus wird diese Methode erfolgreich verwendet, um eine Vielzahl verschiedener organischer Schwefelverbindungen zu screenen und funktionelle Schwefelgruppen auf ihre korrosiven Fähigkeiten zu klassifizieren.

Da sich Haftvermittler bei erhöhten Temperaturen zersetzen, steigt die Korrosionsgefahr. Es ist bekannt, dass die Zersetzung von Haftvermittlern bei Temperaturen über 150 °C stark zunimmt, was für reale Halbleiteranwendungen möglicherweise kein realistisches Temperaturprofil ist. Es stellt sich daher die Frage, ob unterschiedliche Korrosionsmechanismen zum Tragen kommen, wenn bei beschleunigten Stresstests höhere Temperaturen als 150 °C angewendet werden. Um diese Frage zu lösen, wird Hochtemperatur-in-situ-Röntgenpulverdiffraktometrie etabliert und damit die Korrosionsmechanismen und Korrosionskinetiken identifiziert. Anschließend werden die temperaturabhängigen kinetischen Parameter erhalten und diskutiert.

Table of Contents

1	Introduction.....	1
2	Motivation and Goals of this PhD Thesis	11
2.1	Part 1: Literature Review and Electrochemical Measurements on Cu_xS	11
2.2	Part 2: General Reactivity of Cu Mixtures with Bifunctional Thiols.....	12
2.3	Part 3: Corrosion Susceptibility of Cu Bond Wire versus Organic Sulfur Compounds	12
2.4	Part 4: A Corrosion Comparison of Coated Cu Bond Wires with Thiols	12
2.5	Part 5: Solvent Mediated Corrosion Effects	13
2.6	Part 6: Temperature Induced Acceleration of Sulfur-Compound Facilitated Corrosion....	13
3	General theory.....	14
3.1	Mass and Charge Transport in Solids	14
3.2	Cell Arrangements and Electrodes.....	17
3.3	Polarization / EMF / Coulometric titration.....	19
3.4	Electrochemical Impedance Spectroscopy (EIS)	21
3.5	Quantitative Phase Analysis (QPA) via PXRD	28
3.6	Lotgering Factor – Preferred Orientation	33
3.7	Solid State Kinetic Analysis.....	33
4	General Experimental	47
4.1	Methods	47
4.2	Materials	51
5	Literature Review of the Cu-S System.....	56
5.1	Abstract.....	56
5.2	Introduction	56
5.3	Results & Discussion	57
5.4	Conclusion.....	67
6	Polarization and EIS on Cu_{2-x}S	68
6.1	Abstract.....	68
6.2	Introduction	68
6.3	Experimental	69

Table of Contents

6.4	Results & Discussion	71
6.5	Conclusion.....	85
7	General Reactivity of Cu and Pd Mixtures with Bifunctional Thiols	86
7.1	Abstract.....	86
7.2	Introduction	86
7.3	Experimental	87
7.4	Results and Discussion.....	89
7.5	Conclusion.....	105
8	Corrosion Susceptibility of Bare Cu bond Wire versus Various Organic Sulfur Compounds	106
8.1	Abstract.....	106
8.2	Introduction	106
8.3	Experimental	107
8.4	Results and Discussion.....	109
8.5	Conclusion.....	122
9	Corrosion of Coated Cu Bond Wires – A Comparison	123
9.1	Abstract.....	123
9.2	Introduction	123
9.3	Experimental	124
9.4	Results and Discussion.....	126
9.5	Conclusion.....	154
10	Solvent Mediated Corrosion Effects	157
10.1	Abstract.....	157
10.2	Introduction	157
10.3	Experimental	158
10.4	Results and Discussion.....	159
10.5	Conclusion.....	164
11	Grain Growth and Reorientation in APC Bond Wire	166
11.1	Abstract.....	166
11.2	Introduction	166

Table of Contents

11.3	Experimental	167
11.4	Results and Discussion.....	168
11.5	Conclusion.....	171
12	Temperature Induced Acceleration of Sulfur Facilitated Corrosion.....	173
12.1	Abstract.....	173
12.2	Introduction	173
12.3	Experimental	174
12.4	Results and Discussion.....	175
12.5	Conclusion.....	197
13	Conclusive Discussion on Adhesion Promoter Experiments	200
14	Summary and Outlook.....	203
15	Bibliography.....	207
A	Appendix	215

Abbreviations

AEC	Automotive electronics council
APC	Gold-palladium coated copper
APCX	Gold-palladium coated copper with doped X core
CAGR	Compound annual growth rate
CD	Counterdiffusion
COF	Covalent organic framework
CT	Coulometric titration
DCM	Direct comparison method
DMSO	Dimethyl sulfoxide
EBE	Electron blocking electrode
EIS	Electrochemical impedance spectroscopy
EMF	Electromotive force
ESM	External standard method
FD	Finite-Diffusion
GB	Grain boundary
GBE	Grain boundary engineering
HAST	Highly accelerated temperature and humidity stress test
HTS	High temperature storage
HTSL	High temperature storage life
IC	Integrated circuit
IGC	Intergranular corrosion
IMC	Intermetallic compound
JMAEK	Johnson-Mehl-Avrami-Erofe'ev-Kolmogorow
KE	Kirkendall effect

MC	Molding compound
MIEC	Mixed ionic-electronic conductor
ND	Nernst-Diffusion
PC	Propylene carbonate
PCB	Printed circuit board
PCC	Palladium-coated copper
PT	Potentiostatic titration
PXRD	Powder X-ray diffraction
QPA	Quantitative phase analysis
RCM	Relative calibration method
RIR	Reference intensity ratio
SC	Shrinking core
SH-plot	Sharp-Hancock plot
TC	Temperature cycling

1 Introduction

Modern life is unimaginable without smart devices such as smartphones, smartwatches, tablets, notebooks and many more. These little electrical helpers surround us in our everyday lives and enable infinite possibilities. An ever-growing demand of these electrical devices led to rapid technological innovation and is accompanied by a growth of related industry sectors such as the semiconductor industry. It is one of the main beneficiaries as all electrical devices contain semiconductor components within the devices. Due to the thriving digitalization and the rising market share of electric and hybrid cars, the semiconductor industry is expected to grow further. Therein, the fastest growth is expected for the automotive market with a compound annual growth rate (CAGR) of 11.9%, see **Figure 1.1**.¹ One reason for this predicted development is the two- to fivefold need of semiconductor components in electric cars and the strong market potential for autonomous driving and associated driver-assistance systems.

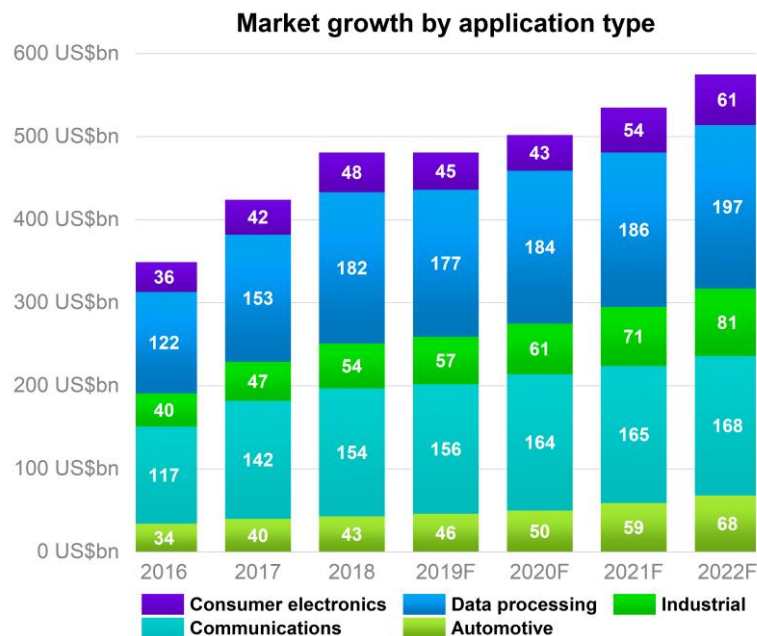


Figure 1.1: Expected market growth by application type. Note that the data processing and automotive sectors are the markets that develop the fastest. Data taken from PwC research.¹

However, the application in the automotive sector involves quality, reliability, durability, and safety (QRD+S) issues over a period of 10 - 15 years. Imagine, an autonomous car or a driver-assistance system fails due to a defective semiconductor chip. Such a case happened in 2014, which was recorded as “A Record Year for Auto Recalls” because of a faulty ignition switch for airbags.² This led to almost 64 million vehicle recalls as the lives of people depend on the reliability of these chips.² As a consequence, huge efforts have been made to ensure the reliability and safety of the chips over a long period of time. This caused the introduction of new qualification standards such as the automotive electronics council (AEC) Q100 Grade 0 (operating temperature: -40 °C – +150 °C) stress

test standard for integrated circuits, as well as the zero-defect production approach in automotive applications. For example, the stress test for AEC Q100 Grade 0 is, among others, comprised of high temperature testing at 150 °C/175 °C for 2000 h/1000 h. Despite these high qualification standards, constantly increasing requirements regarding conductivity, longevity, and thermostability in harsh environments must be fulfilled.³⁻⁵ A typical mission profile for a microcontroller in vehicles in 2006 was a lifetime of 10 years with operating times of 8 000 h, non-operating times of 80 000 h, and 36 000 on/off switching cycles.⁵ Though these are already high demands, they are ever-expanding due to new appearances like car-sharing or fully autonomous driving with 24/7 operation time. These demands go along with cost management in the extremely competitive automotive market. Hence, the need for cost reduction has driven the transition from well-known gold (Au) to copper (Cu) wire-bonding in integrated circuits (IC) due to the exploding gold prices, starting from 2005 up to date.^{6, 7} Though Cu is an alternative to Au wire to save material cost, it requires an elaborate bonding procedure and several equipment modifications.⁸⁻¹⁰ Thus, the lowest cost packaging choice is no longer obvious and a thorough cost analysis must be made (see e.g. **Figure 1.2**).^{7, 11}

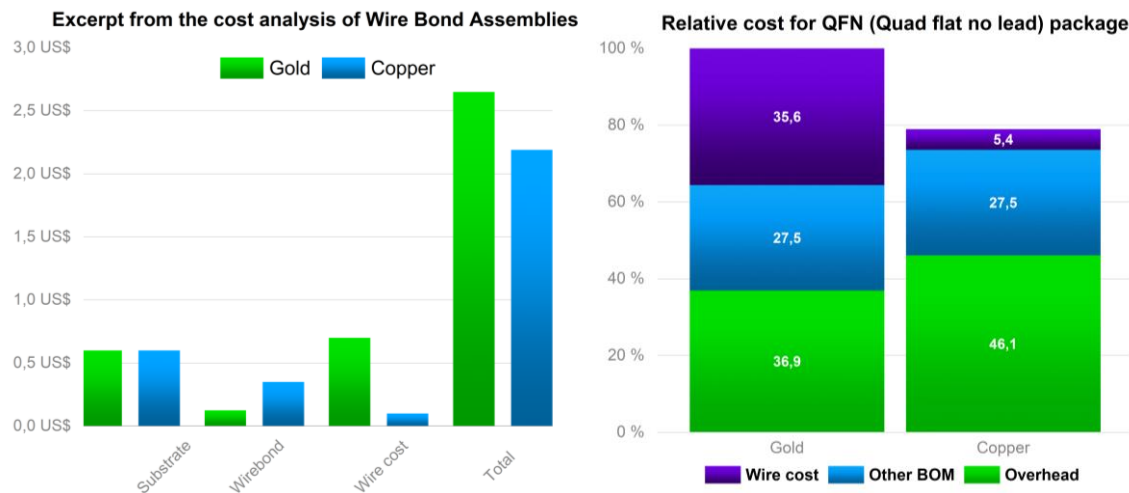


Figure 1.2: Left: Excerpt from a cost comparison of wire bond assemblies with gold and Cu wire. Data taken from *Palesko et al.*⁷ Right: Relative cost of manufacturing a QFN package. Data taken from *Breach et al.*¹¹

It becomes clear that with increasing wire diameter the cost savings relative to Au will increase.^{11, 12} Thus, Cu wire-bonding was used mainly for larger diameters ($>30\ \mu\text{m}$) in power and discrete devices due to its better conductivity and lower material cost. In the following years Cu wire-bonded ICs successfully emerged in consumer grade ICs starting from 2010 because Cu outperformed Au at conductivity properties, cost effectiveness, higher mechanical strength, higher thermal conductivity, and slower intermetallic compound (IMC) growth with aluminum (Al).^{13, 14} In **Table 1.1** the key physical parameters of Au and Cu wire-bonds are compared.^{12, 15} It is striking that Au excels at the key physical parameters which dictate the wire-bonding process, whereas Cu outperforms Au in the actual performance of the device. Thereby, the better thermal conductivity of the wire-bond not only originates from the better material property of Cu but also from the lower IMC growth rate between Cu and Al compared to Au and Al which results in less heat generation.

Table 1.1: Comparison of the key physical parameters of gold wire-bonds versus Cu wire-bonds.¹⁵ The green boxes mark the more suitable wire at the respective parameter. Note that Au excels at physical parameters which dictate the wire-bonding process, whereas Cu outperforms the Au wire-bond in the actual performance of the chip.

Parameter	Gold (Au)	Copper (Cu)
Ductility	8.8 MPA	13.6 MPA
Tensile Strength	>240 N/m ²	160-200 N/m ²
Oxidation	No	Yes
Melting Point	1064 °C	1085 °C
Work Hardening Rate	Low	High
Electrical Resistance	2.3 $\mu\Omega\text{cm}^{-1}$	1.7 $\mu\Omega\text{cm}^{-1}$
Thermal Conductivity	293 W/mK	394 W/mK

Thus, Cu wire-bonded devices exhibit an improved electrical resistance and reliability.^{6, 8, 11, 16-22} These two advantages of Cu wire-bonding were the main driving force to adopt the knowledge from Au wire-bonding to Cu wire-bonding and to optimize the wire-bonding process.^{9, 10, 13}

The advantageous electrical and thermal properties of Cu raise the question why Au had historically been preferred over Cu. The main challenge of Cu bond wires lies in the higher oxidation affinity of Cu compared to Au which leads to enhanced corrosion susceptibility. As a consequence, new difficulties arise with the implementation of Cu wire-bonding into automotive applications where the semiconductor usually is exposed to harsh environments. To understand the failure mechanisms of a chip, the schematic structure of the semiconductor package and its fragile parts are explained in **Figure 1.3**. The basis of the package usually is a Cu leadframe (1) with a solder on top (2) which fixes the silicon chip (3). The upper chip surface is mostly comprised of an Al metallization and a passivating silicon nitride (SiN) layer. The electrical connection from the chip is realized by the bond wires (Cu, Au) which connect the metallization layer (Al) on top of the chip surface (4) to the leadframe (5, Cu).

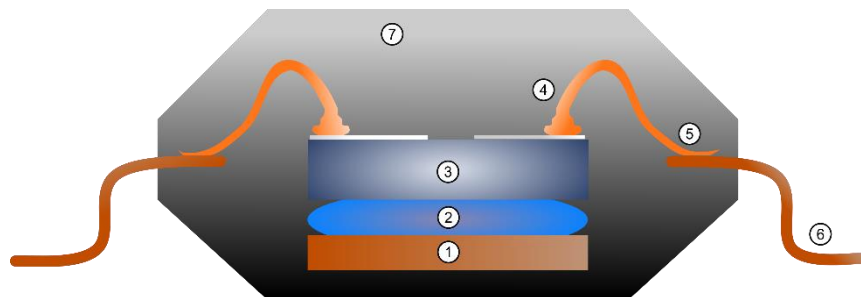


Figure 1.3: Schematic illustration of a semiconductor chip and its individual parts: 1) Die pad, 2) die attach/solder, 3) silicon IC/chip, 4) ball-bond, bond-pad metallization (i.e. Cu/Al), bond wire (i.e. Au, Cu, Al), 5) wedge-bond, bond-leadframe metallization, 6) leadframe/pin, 7) encapsulation material = molding compound (MC).

The bond wire is connected to the chip metallization and the leadframe with a typical ball and stitch wire-bonding process. Here, the actual ball and stitch bond is formed by applying an ultrasonic force on the bond wire which presses the bond wire onto the connective part. The leadframe in turn is connected to the pins which links the chip to the printed circuit board (6, PCB). The metallic parts are encapsulated with a so-called molding compound (7, MC) which is a polymer-based duroplast. The role of the MC is to protect the metallic parts from the surrounding environment.

Hence, there are two critical elements which can lead to chip fatigue. The first is the wire-interconnect fatigue. Generally, the wire-interconnects can be characterized by two different systems:

- i. Homogenous system: Au/Au, Cu/Cu, Al/Al
- ii. Heterogenous system: Cu/Al, Au/Al

For a homogenous system, the ultrasonic force leads to a metal-to-metal contact which is purely formed by interdiffusion. The homogeneous metal-to-metal contact shows good crystalline interface strength and is not prone to interface degradation. On the contrary, the ultrasonic bonding process in heterogeneous systems results in a metallurgical reaction and IMC growth between the bond and the chip metallization.^{23, 24} The formation of various IMC phases leads to several interfaces where some of the interfaces can show weak crystalline interconnection. For example, porous and brittle phases can occur, which could potentially amplify corrosion related failures. Additionally, the combination of two different metals might lead to galvanic couples and, along with an electrolyte, results in crevice/pitting corrosion induced by ion movement and oxidation in humid environment.²⁵ This in turn can lead to the fatigue of the wire-interconnect as the less noble IMC gets oxidized.

The second important contribution to chip failure is the fatigue of the package due to the delamination of the MC.^{26, 27} In a package, several critical polymer-metal interfaces exist. In contrast to the metal-to-metal contacts where a strong crystalline interface is present, the polymer-metal interfaces are formed by weak chemical bonds, mostly chemisorption. These weak interface interactions result in the delamination of the plastic package from the metallic parts of the chip and thereby can induce damage to the metallic parts like the chip surface, cracks in the solder, and lifted or broken wires. Therefore, the adhesion and composition of the MC is an important factor to ensure sturdy wire bond contacts.^{28, 29} Also, the delamination of the MC leads to open pathways for the ambient humidity. In summary, these effects result in the fatigue of the package which is visible as drift or fail of the electrical parameters.

To avoid chip fatigue, harsh environments are simulated with highly accelerated temperature and humidity stress tests such as temperature cycling (TC), highly accelerated stress test (HAST, 130 °C, 85% relative humidity, 2 bar), and high temperature storage life tests (HTSL) to check for thermomechanical, humidity, or temperature related failure mechanisms. Though the reliability of Cu is comparable to Au in HTSL tests, it has been shown that Cu bonds are more prone to oxidation and corrosion than Au in biased and unbiased HAST tests.^{11, 22, 30-34} This led to reliability concerns at demanding applications and consequently to further investigations on the related corrosion

mechanisms.³⁵ It has been found that the primary driving source for corrosion under biased and unbiased HAST conditions is the presence of chloride ions (Cl⁻) and high moisture content in the package.^{32, 33, 36-39} The general failure mechanism in these stress tests is crevice corrosion along the IMC of the Cu/Al interface which causes to electrical failure in sustained stress tests.⁴⁰ It has been found that these corrosive reagents originate from the MC which is the encapsulation material of the semiconductor chip.²⁸ In fact, the MC is supposed to protect the metallic parts from environmental factors but showed to be a crucial factor in challenging applications. For this reason, it became apparent that the composition of the molding compound and its individual components are crucial parameters, see **Table 1.2**.⁴¹

Table 1.2: Overview of the components which are required for the molding compound (MC). Note that the flame retardants and adhesion promoters are present in small amounts (<5 wt%). Data from *Riedl*.⁴¹

Component	Example	Purpose	Content / wt%
Filler	Spherical, crystalline SiO ₂	Mechanical stability, Thermal stability	80-90
Basic resin	Ortho-cresol novolac	Polymer matrix	10-20
Hardener	Hydroxylated multiaromates	Linkage, hardening	
Adhesion promoter	Mercaptosilanes, Triazoles	Adhesion on metal/chip surface	<5
Catalyst	Triphenylphosphines	Speed up curing	
Flame retardant	Phosphates, metal oxides, halogens	Reduce flammability	
Wax	Polyethylene wax	Improve fluidity	
Coupling agent	Epoxide, sulfoxide	Linkage	
Ion catcher	MgAl _{0.45} O _{1.67}	Catch free ions	
Coloring agent	Carbon black	Optical purpose, dissipates electrostatic charge	

The MC is mostly comprised of spherical silicon oxide particles to ensure the thermal and mechanical stability. In addition to these fillers, usually an epoxy resin is added in combination with amines and biphenyls to create a polymer matrix around the filler particles. The filler and polymer matrix make up for 95 wt% of the MC.⁴¹ The remaining components are used to specifically tune the desired properties of the MC.⁴¹ Halogen compounds were used as flame-retardant agents for the MC to make the encapsulation material inflammable. However, due to reliability and safety issues, the halogen compounds have been removed from the MC to prevent halogenide induced corrosion and to develop “green” MCs.^{28, 42} Even though the removal of corrosive halogen compounds, the Cu-Al interface is still prone to corrosion due to moisture ingress through the molding compound.^{39, 43}

Another important aspect for chip reliability is the narrow second bond (first bond = ball-bond, second bond = stitch/wedge-bond) process window of bare Cu bond wire which leads to low and unstable second bond strength. This especially moves into focus for high application requirements because the lower bond strength goes along with increased corrosion susceptibility.⁴⁴ As a consequence, palladium-coated copper (PCC) wire with an approximate Pd layer thickness of 80 nm, and palladium-doped copper bond wires have been developed to improve the bonding process and to prevent halogen induced corrosion.⁴⁵⁻⁴⁹ The new wire types were rigorously tested for their reliability and especially the PCC wire proved to be better than bare Cu in extended reliability tests such as HTSL, biased and unbiased HAST.^{38, 48, 50, 51} Therein, the Pd-coating is supposed to fulfill several functions:^{49, 52, 53}

- i. Pd-coating acts as diffusion barrier for Cl^- ions and moisture and thus prevents chloride induced corrosion.
- ii. Pd-coating slows down the IMC formation between Cu and Al and thereby prevents crevice corrosion along the interface which results in strengthened bond contact.
- iii. Pd-coating and Pd-dopants inside the Cu core could act as Cl^- ion trapper to form PdCl_2 .
- iv. Pd-coating and Pd-dopants enable an improved bonding process of first (ball-bond) and second bond (wedge-bond).

Despite the improved reliability of the PCC wire it is no universal remedy to all Cu wire bond problems. It turned out that the key to reliable bond contacts is the complete Pd coverage of the Cu core. If the Pd-coating is damaged at some point, either during the bond wire production or the bonding process, it instead could accelerate the degradation of the bond wire by galvanic coupling of Cu and Pd with moisture as electrolyte.⁵⁴ For example, Cu-Pd alloys and insufficient melting of Pd are observed if the bonding process is not optimized. This leads to vulnerable grain boundaries at the chamfer region of the ball bond surface where Cl^- ions gather, which in turn may result in large Cu voids.⁴⁹ Also, Cu ball voids and hillock formation were observed in HTSL tests for molded and non-molded PCC wires.^{49, 50, 55} In non-molded PCC wire HTSL tests, the Cu voids were located at damaged Pd layer sites and the resulting hillocks were composed of CuO. In addition to that, Cu voids were observed above the Cu-rich IMC with PCC wire which could lead to weak bond interconnection.⁵³ Note that these Cu voids were not observed for bare Cu wire. These results suggest a corrosion mechanism which is independent of the MC and indicates that the addition of Pd leads to the formation of Cu voids and therefore is the root cause for the degradation of the Cu core. Further, it was found that hillock and Cu void formation only occurs in combination with corrosive species such as O^{2-} and Cl^- which are actively attacking the core. Note that hillock and Cu void formation on the PCC wire surface is not observed in vacuum environment.⁵⁶ Thus, it can be concluded that Cu ion outward diffusion through the Pd-coating is no intrinsic degradation process of the PCC wire. Hence, the content of corrosive reagents such as Cl^- , O^{2-} , and S^{2-} in the MC is an important feature for Cu wire degradation and chip reliability. Still, the PCC wire shows good performance in AEC Q100 grade 0 requirements, but this may be of concern for extended mission profiles.

By reducing the halogenide content in the MC, it was thought that most drivers for Cu bond wire degradation had been eliminated. However, in the course of this adjustment another challenge emerged, which was even observed in HTSL tests: it turned out that MCs with high sulfur content significantly accelerate the bond interconnect corrosion at high temperatures.⁵⁷⁻⁵⁹ Moreover, the severity of Cu wire degradation seems to correlate with the sulfur content in the package, see **Table 1.3**.^{29, 54, 59, 60} Therein, the MCs A-E differ in the overall composition and the extractable sulfate content (sulfur compounds within the MC are oxidized to SO_4^{2-} during the aqueous extraction process), whereas E1-E4 only differ in the sulfate content. Note that corrosion is only observed for MCs with high amounts of extractable sulfate or rather total sulfur content (determined by combustion ion chromatography of the MC).

Table 1.3: Overview of extractable sulfate and total sulfur content in different molding compounds. Note that the MCs E1-4 are only varied in total sulfur content in cooperation with the supplier.⁶⁰ Data extracted from *Lee et al.* and *Mavinkurve et al.*^{54, 60}

MC	Extractable SO_4^{2-} / ppm	Total S / ppm***	Significant Corrosion
A ⁵⁴	8.8*		No
B ⁵⁴	34.5*		Yes
C ⁵⁴	47.5*		Yes
D ⁶⁰	4.3**	26.0	No
E1 ⁶⁰	21.1**	127.9	Yes
E2 ⁶⁰	1.7**	20.5	No
E3 ⁶⁰	1.9**	8.2	No
E4 ⁶⁰	18**	141.2	Yes

* Analytic method not specified (mold compound extract method)

** Determined by Ion Chromatography after extraction with demineralized water in a pressured vessel

*** Determined by Combustion Ion Chromatography

The high sulfur content in these MCs originates from organic sulfur compounds, which are added as adhesion promoters.⁶⁰ The role of these adhesion promoters is to improve the adhesion between the MC and the leadframe to avoid delamination.^{41, 61, 62} Adhesion promoters are bifunctional organic molecules which act as coupling agents to avoid delamination of the MC during thermal stress.⁶¹ **Figure 1.4** illustrates the chemical structure and working principle of typical adhesion promoters. Typical adhesion promoters comprise a thiol or disulfide moiety as they are known to strongly adsorb on noble metal surfaces.⁶³⁻⁶⁸ There, the thiol is adsorbed on the metal surface and forms self-assembled monolayers if combined with long hydrocarbon chains which are densely packed by Van der Waals forces.^{63, 68-70} Along with other functional groups such as hydroxy, amine or trimethoxy silane groups, they form densely packed arrangements which link well to epoxy resins (= MC). Therefore, alkanethiols, disulfides, mercaptosilanes, benzotriazoles and mercaptotriazoles are usually used as adhesion promoters in molding compounds to form a link between the metal surface and the encapsulation.^{41, 60-63, 71}

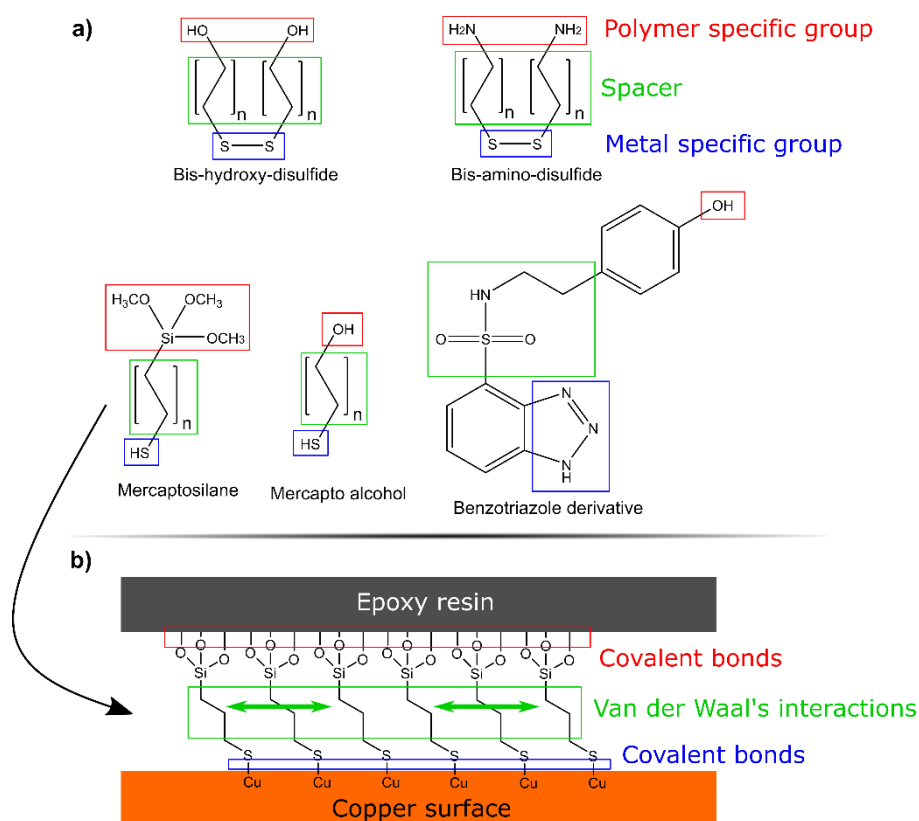
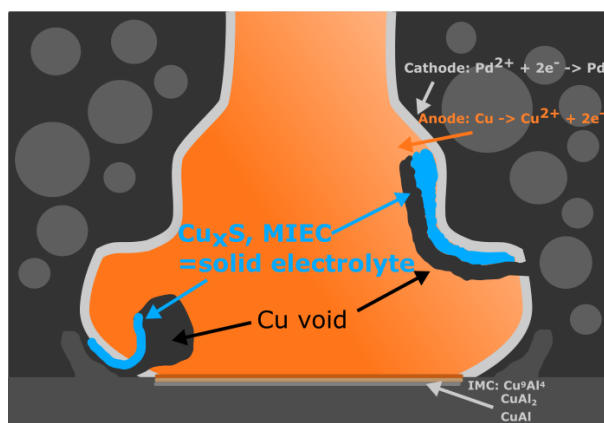


Figure 1.4: a) Typical adhesion promoters which are used to improve the adhesion between the MC and the metal surface.^{61, 63}
 b) Schematic illustration of a chemisorbed and self-assembled monomolecular (SAM) layer of a mercaptosilane between the epoxy resin (= MC) and the Cu surface.

These bifunctional molecules are also known as corrosion inhibitors at room temperature conditions because the molecules are chemisorbed on the surface and thereby form a protective layer on the metallic surface.^{69, 72} Nevertheless, if these molecules are exposed to temperatures above 150 °C they can decompose, and reactive sulfur compounds are released.^{29, 54, 60, 73, 74} It was hypothesized, that corrosive H₂S molecules form as decomposition product from the sulfur compounds at temperatures above 150 °C.^{29, 54, 58, 60} It was initially assumed that H₂S molecules react with nearby metal surfaces to form the corresponding metal sulfides, which can lead to Cu-Al interfacial corrosion in bare Cu wires.⁶⁰ This was already observed in “dry” conditions such as HTSL test but is assumed to accelerate in HAST test due to increased moisture. Therefore, “the paradoxical role of sulfur in molding compounds” was reported by *Mavinkurve* et al. as these bifunctional sulfur compounds are crucial ingredients for the adhesion of the MC to the metal surface but also initiate corrosion in harsher test environments.⁶⁰ This means that sulfur-containing adhesion promoters can be a potential risk for extended mission profiles like AEC grade 0 and beyond. However, due to the high decomposition temperatures (>150 °C) the question arises if this failure mechanism is actually observed in “real life” applications. There, the temperature usually does not exceed 150 °C which may lead to false lifetime predictions from sulfur induced corrosion stress testing at high temperatures. Related investigations revealed that the total extractable sulfur content in MCs is hardly decreased after thermal ageing at temperatures such as 100 °C and 125 °C which implies a reduced liberation of corrosive sulfur species and thus negligible corrosion risk.^{29, 60}

Further investigations revealed that sulfur induced corrosion is especially observed for PCC wires which show big Cu voids at the chamfer squeeze region and at the edge of the Cu-Al interface after stress tests, as illustrated in **Figure 1.5**.^{54, 57, 60} This corrosion mechanism is supposed to start at damaged Pd-coating sites, which is similar to the non-molded hillock formation in PCC wires with oxygen in HTSL tests.^{49, 55 58} At these damaged Pd layer sites, Cu is exposed to the corrosive sulfur species and could form Cu_xS . It was concluded that the Pd-Cu coupling could act as a galvanic cell with Cu_xS as solid electrolyte to accelerate the corrosion.⁵⁴

a) Pd-Cu galvanic coupling
Chamfer squeeze, Ball bond



b) Pd-Cu galvanic coupling
Pitting corrosion, Wedge bond

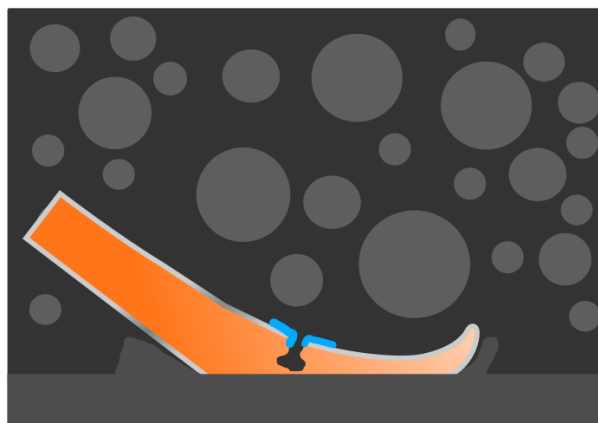


Figure 1.5: Schematic illustration of the failure mechanism in PCC wire at ball- and wedge bond. a) Pd-Cu galvanic coupling in PCC wire with Cu_xS as solid electrolyte. Typical phenomena are voids in the chamfer squeeze region and large Cu voids at the edge of the ball bond-IMC interface. b) Pitting corrosion at the wedge bond of the PCC wire, similar failure mechanism to (a).

There, the Pd-coating may act as cathode and potential catalyst and the Cu core as the anode which results in Cu^+ dissolution and the formation of Cu voids. Thereby, it is assumed that the small holes in the Pd layer can lead to a miniaturized galvanic cell in combination with a capillary effect where Cu^+ dissolution is more pronounced. However, it is not clear whether this is the sole mechanism and if other mechanisms are involved. It was proposed that an additional Cu^+ diffusion through the holes, along the whole Pd surface, may also contribute to the degradation. This seems likely, as earlier investigations found that ion migration on the bond wire surface is in fact possible along with alloy formation and galvanic effects.⁷⁵ Further, it is not clear if Cu ions can diffuse through the Pd layer to form copper sulfide on the surface. There, the formed copper sulfide Cu_xS may act as solid electrolyte as it is a mixed ionic-electronic conductor.⁷⁶⁻⁷⁸ So far, it was not possible to determine the composition of copper sulfide in the corroded areas. Yet, the composition of the copper sulfide may be a crucial factor for the Cu bond wire degradation. This is because the composition of the copper sulfide strongly determines the Cu^+ mobility which in turn drives Cu bond wire degradation.^{79, 80} In addition to that, there are still wide gaps in the literature regarding the decomposition of the sulfur compounds, role of the Pd-coating, and the MC – all of which would be crucial to fully understand the whole corrosion mechanism. As a consequence, empirical corrections based on stress test findings were made to minimize the sulfur induced corrosion in Pd-coated bond wires.

One option to achieve better reliability against sulfur induced corrosion is to specifically tailor the MC and PCC wire combination for high temperature as the sulfidation is strongly influenced by the package combination.²⁹ Another option is to specifically customize the bond wire to resist harsher environments. Hence, new Cu bond wires were developed with Pd-coating (≈ 60 nm) and an additional flash-Au layer (thin Au layer ≈ 10 nm, gold-palladium coated Cu wire = APC wire) to further boost the corrosion resistance of the bond wires, see **Figure 1.6**.⁸¹

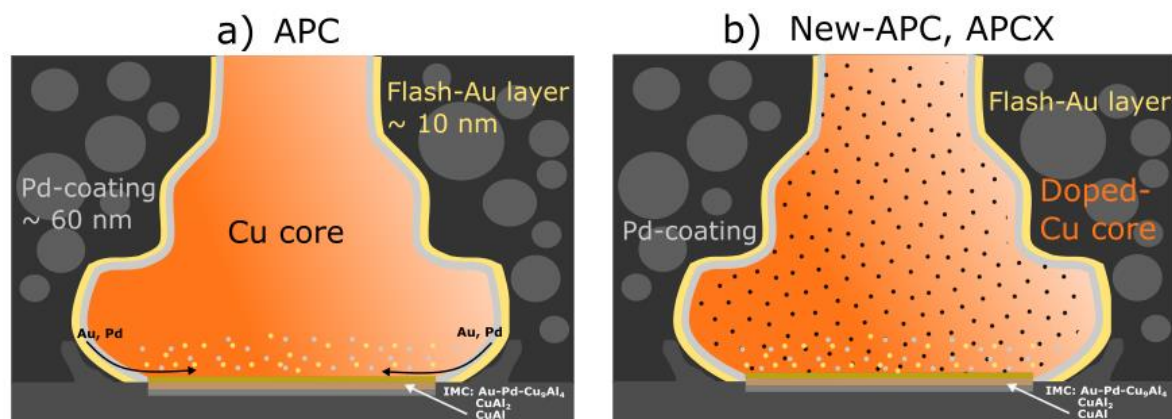


Figure 1.6: a) Palladium-coated Cu wire with flash gold (APC). Au and Pd atoms are distributed over the bonding area during the bonding process and thereby strengthen the bond. b) New-APC (APCX) wire with additive in the Cu core. The additive further enhances the corrosion resistance by passivating damaged spots in the coating.

The flash-Au layer thereby improves the sulfidation resistance, hinders the Pd segregation during bonding, and stabilizes the electrical resistivity of the bonding interface.^{81, 82} Even though the APC wire performed better in accelerated stress tests, it still displayed sulfur corrosion and hillock formation through damaged coating spots.^{56, 82} As it is hardly feasible to produce a perfect Pd-coating, another strategy has to be established. To achieve this, dopant elements were added to the Cu core. These additive elements are supposed to act as passivating agent if the corrosive species attacks at damaged Au-Pd layer spots.^{83, 84} As a result, the new-APC (APCX wire) wire showed similar mechanical properties like the APC wire with improved sulfur and halide induced corrosion resistance.^{56, 83-85} With this optimized corrosion reliability in mind, this wire type is perfectly suited for automotive devices at high temperatures. Nevertheless, further improvement of this bond wire type is still in progress in view of the growing demands of the automotive industry. For instance, recent studies explored the reliability of Pt- and Pd-alloyed APC wires in accelerated stress tests.⁸⁶ The actuality of new bond wire development showcases the relevance of ever-improving bond wire reliability with regard to growing requirements in automotive applications. On these grounds, the present PhD thesis was initiated to clarify the underlying sulfur induced corrosion mechanisms and thereby support further package and bond wire development.

2 Motivation and Goals of this PhD Thesis

The present PhD thesis was initiated to clarify the underlying sulfur induced corrosion mechanisms as this understanding is crucial to support further package and bond wire development. To achieve this, different problems which arise from sulfur-containing adhesion promoters and their sulfur induced corrosion must be considered. One of the main challenges is to identify the corrosion products during sulfur corrosion. This is hardly achievable in the small semiconductor package setup and therefore the detailed corrosion mechanisms are unclear to date. The precise identification of corrosion products, structural information and quantitative conversions are desirable, as they allow a deeper understanding of the corrosion processes. In this thesis, powder X-ray diffraction (PXRD) is established, which enables a detailed corrosion study. Using electrochemical impedance spectroscopy (EIS), the main corrosion products can be identified, and the electrochemical properties can be analyzed. The electrochemical properties are crucial as the electrode reactions play a key role in corrosion processes. This is especially pronounced for the Pd-coated bond wires which may form Cu/Pd galvanic couples and thus can lead to galvanic corrosion. To clarify the role of the Pd-coating during sulfur corrosion, various coated bond wires are investigated with corrosive S-compounds. To gain deeper insights into the underlying corrosion mechanism, high temperature in situ powder X-ray diffraction (HT-in situ-PXRD) and scanning electron microscopy (SEM) is applied. Moreover, HT-in situ-PXRD is utilized to screen a wide range of different S-compounds to classify the specific S-moieties for their corrosive capability. Hence, this PhD thesis comprises several parts which deal with the respective contributions of Cu bond wire degradation. For each, specific elements of sulfur related corrosion are highlighted.

2.1 Part 1: Literature Review and Electrochemical Measurements on Cu_xS

As recent developments in the automotive industry give rise to demanding reliability requirements, extremely long stress tests must be conducted. Thus, new methods are explored to study the time and temperature dependent reliability of different package combinations. One option is to employ computational corrosion simulations to study the long-term behaviour of semiconductor packages. However, reliable data is required to perform these simulations. As copper sulfide was found in packages with PCC wires, it was concluded that Cu_xS works as solid electrolyte between a galvanic cell of Cu and Pd. Hence, it is crucial to determine the properties of the solid electrolyte to assess sulfur induced corrosion degradation. Thereby, the properties of copper sulfide strongly depend on the composition and temperature. Thus, the goal of **Chapter 5** is to provide a conclusive overview of literature data regarding the electrochemical properties of copper sulfide. Then, electrochemical measurements were performed in **Chapter 6** to gain further insights into the composition-temperature dependency of Cu ion diffusion in Cu_xS . For this, EIS and polarization measurements were performed on an all-solid-state galvanic cell with different Cu_xS compositions. Finally, the experimental findings are compared to the literature data.

2.2 Part 2: General Reactivity of Cu Mixtures with Bifunctional Thiols

The second part deals with the general reactivity of Cu and Pd with thiols to gain a basic understanding of the main corrosion processes. As the corrosion mechanism is not yet fully understood, **Chapter 7** aims towards a more complete picture of the sulfur-induced corrosion mechanisms. There, different material combinations are explored to gain further insight into critical material selection criteria. To realize this, Cu-thiol mixtures and Cu-Pd-thiol mixtures are prepared and stored at various temperatures. Afterwards the samples are examined by PXRD. The respective measurements are discussed regarding the copper sulfide composition which may form in the semiconductor package and the influence of the total sulfur content in the surrounding environment. Finally, the reaction products and kinetics of various adhesion promoters are discussed in powdery mixtures as well as the effect of Pd addition.

2.3 Part 3: Corrosion Susceptibility of Cu Bond Wire versus Organic Sulfur Compounds

Sulfur-containing adhesion promoters are required to improve the adhesion between the molding compound and the metallic parts of the semiconductor package and thereby prevent delamination of the MC. Even though these sulfur-containing adhesion promoters are the most suitable reagent to improve adhesion, they also lead to the sulfidation of the bond wire at elevated temperatures. Hence, it is essential to identify the reactivity of various organic sulfur compounds. Accordingly, the aim of the third part (**Chapter 8**) is to explore the reactivity of different organic sulfur moieties versus bare Cu bond wire at elevated temperatures with the aim to identify suitable sulfur compounds which can be used as alternative adhesion promoters and additives for demanding applications. Experimentally, this was tackled by HT-in situ-PXRD which allowed for a quantitative comparison.

2.4 Part 4: A Corrosion Comparison of Coated Cu Bond Wires with Thiols

The introduction of Cu bond wire into automotive applications led to halogen and sulfur induced corrosion of the Cu bond wire. As a potential remedy to this corrosion, different wire types like Pd-coated copper (PCC), gold-palladium coated copper (APC), and doped gold-palladium coated copper (APCX) bond wire were introduced. However, the effects as well as the corrosion reliability of the various coatings and dopants are not fully understood to date. Hence, the goal of part 4 (**Chapter 9**) is to investigate the corrosion reliability and failure mechanisms of various coated Cu bond wires versus selected adhesion promoters at elevated temperatures. Consequently, the reliability of the various coated Cu bond wires is compared and discussed regarding high-temperature applications. Here, isothermal HT-in situ-PXRD is applied to quantify the corrosive degradation. Then, a kinetic analysis and a complementing SEM and energy dispersive X-ray (EDX) analysis is performed to acquire detailed knowledge of the related processes.

2.5 Part 5: Solvent Mediated Corrosion Effects

In semiconductor packages, the adhesion promoter is a component of the MC, which is a solid duroplast after curing. Thus, the mobility of the adhesion promoter is constrained by the surrounding polymer-matrix and the filler particles. Yet, the influence of the polymer-matrix on diffusivity and reactivity is unknown and has scarcely been investigated up to date. Therefore, **Chapter 10** investigates the influence of different solvents on the reactivity of the adhesion promoter. In the experiments, the solvents propylene carbonate (PC) and dimethylsulfoxide (DMSO) serve as “dummy” solvents to study the solvent mediated effects on sulfur induced corrosion as observed by HT-in situ-PXRD. This is complemented by a subsequent kinetic analysis.

2.6 Part 6: Temperature Induced Acceleration of Sulfur-Compound Facilitated Corrosion

Since adhesion promoters decompose at elevated temperatures, the risk for sulfidation reaction with Cu bond wire rises. The decomposition of adhesion promoters is known to strongly increase at temperatures above 150 °C which may not be a realistic temperature profile for real semiconductor applications. Hence, the question arises if different failure mechanisms emerge at the elevated temperatures (>150 °C) required for accelerated stress tests. The goal of **Chapter 11 and 12** is to resolve this question by identifying the respective corrosion mechanisms and to clarify if these mechanisms are related by a temperature dependency. To realize this, isothermal HT-in situ-PXRD is applied at temperatures between 150 °C and 250 °C, respectively, on bare Cu and APC wire in combination with selected adhesion promoters. Finally, a thorough kinetic analysis is performed to gain further knowledge of the related mechanisms and to obtain the corresponding activation energies.

3 General theory

3.1 Mass and Charge Transport in Solids

Principally, the mass and charge transport in solids is based on the flux of electrons and ions in the solid. Thereby, the flux of electrons results in an electronic conductivity (σ_{eon}) and a flux of ions in an ionic conductivity (σ_{ion}), respectively. If both charge carriers (electrons, ions) are mobile in the solid, it is a so-called mixed ionic-electronic conductor (MIEC). The conductivity is then given by the sum of all partial conductivities and is comprised of an ionic and electronic contribution:

$$\sigma = \sigma_{\text{ion}} + \sigma_{\text{eon}} = \sum \sigma_k \quad (3.1)$$

If one partial conductivity is bigger than the other by several orders of magnitude, it encompasses pure electronic and pure ionic conductors and can be expressed by the transference number:

$$t_k = \frac{\sigma_k}{\sigma} \quad (3.2)$$

Hence, the classification of a solid is based on the major transport carrier and is further divided by their specific conductivity σ [$\Omega^{-1}\text{cm}^{-1}$, or S/cm]. Thus, solids can be divided into electronic conductors (metals, semi-conductors) and ionic conductors, see **Table 3.1**. In this thesis, $\text{RbCu}_4\text{Cl}_3\text{I}_2$ and Cu_{2-x}S are used for the electrochemical measurements. The former is a so-called solid electrolyte due to the high ionic conduction $\sigma_{\text{ion}} > 10^{-4}$ S/cm.⁸⁷⁻⁹⁰ The latter is a MIEC with a predominant electronic conduction.^{76-78, 91}

Table 3.1: Typical conductivities of solid electronic- and ionic conductors at room temperature.⁹²

	Material	Specific conductivity $\sigma / \Omega^{-1}\text{cm}^{-1}$
Electronic conductor	Metals	$< 10^5$
	Semiconductors	$10^{-5} - 10^0$
Ionic conductor	Super-ionic conductors	$> 10^{-4}$
	Normal ionic conductors	$10^{-10} - 10^{-5}$
	Poor ionic conductors	$< 10^{-10}$

Thereby, the specific conductivity results from the crystal structure, composition, and bonding characteristics, which is a substance-specific property. Also, external factors such as dopants, temperature, and non-stoichiometry influence the conductivity. In particular, the existence of defects is essential for the ionic conductivity in solids. The most important are zero-dimensional point defects in the crystal lattice, which is Frenkel- and Schottky defect, respectively. The Frenkel defect forms when an atom in the crystal lattice leaves its regular site and becomes an interstitial atom which

simultaneously creates a vacancy in the lattice. The Schottky defect is characterized by two oppositely charged vacancies in the lattice, created by extracting two oppositely charged ions. Both point defect types are illustrated in **Figure 3.1**. Another point defect type is the introduction of foreign atoms (doping) into the crystal lattice to an interstitial site or a regular lattice site. Thus, point defects can be categorized into intrinsic (Frenkel-, Schottky defect) and extrinsic (doping with foreign atoms) defects. Due to the constant concentration of extrinsic defects, and the exponential increase of intrinsic defect concentration with temperature, the conductivity is predominantly governed by extrinsic defects at low temperatures and intrinsic defects at higher temperatures, respectively. In order to differentiate between the different defect types a special notation was introduced by *Kröger* and *Vink*.⁹³ In the case of the copper sulfide Cu_{2-x}S a cationic Frenkel defect type can expressed:



where $\text{Cu}_{\text{Cu}}^{\times}$ represents a regular Cu atom in the crystal lattice, which moves into an interstitial site Cu_{i}^{+} with a positive charge, and thereby creates a negative charged vacancy V_{Cu}' at the former Cu atom site.

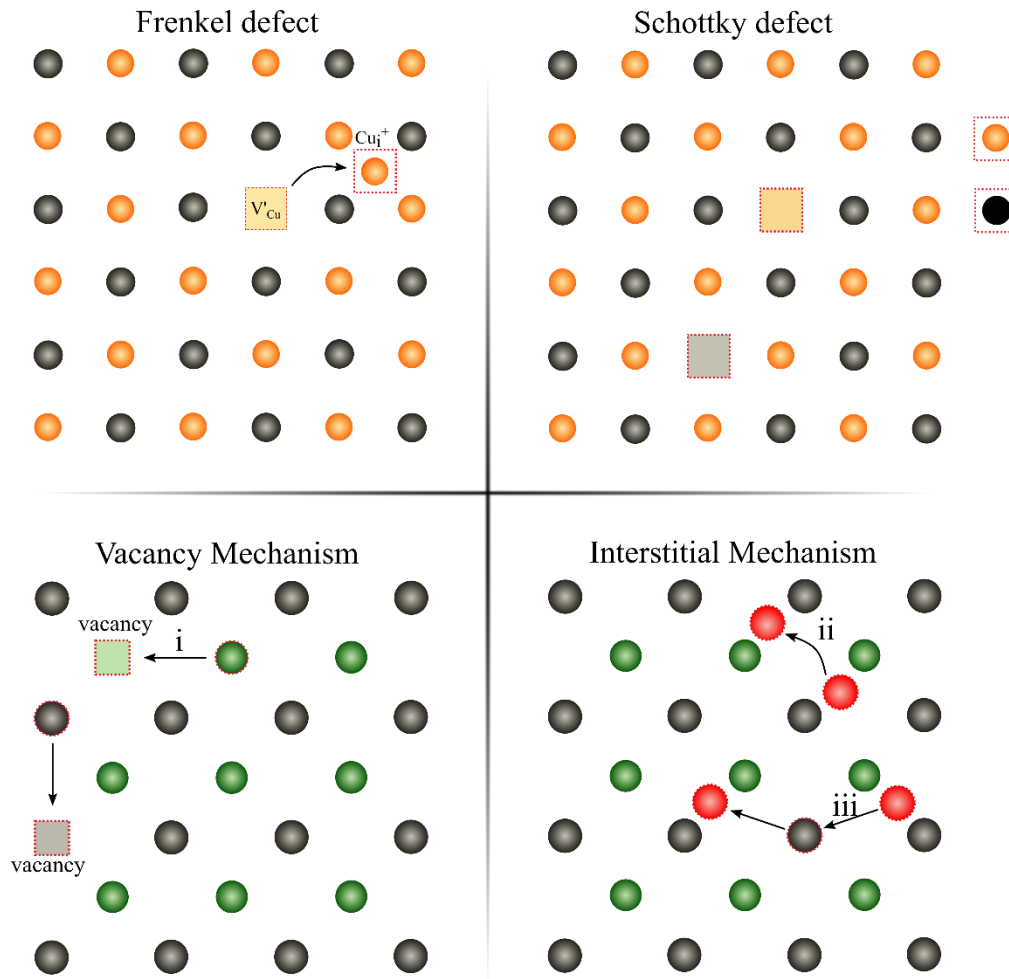


Figure 3.1: Top left: Frenkel defect. Top right: Schottky defect. Bottom: Possible mechanisms for atomic diffusion: i. Vacancy mechanism, ii. interstitial mechanism, and iii. interstitialcy mechanism.

There, the mobility of the ions is of several orders of magnitude lower than the electrons due to their size and binding properties. The transport mechanism of the ions within the crystal lattice is attributed to jumps between neighbouring lattice sites. In general, two different transport mechanisms for ions exist. These are transport through vacancies and transport through interstitial sites. Hence, three different jump mechanisms are obtained (**Figure 3.1**):

- i. An ion at a regular lattice site jumps towards a vacancy site, the former lattice site is the new vacancy site.
- ii. An ion jumps from one interstitial site towards the next interstitial site.
- iii. An ion at an interstitial site jumps towards a regular occupied lattice site and thereby forces the atom at the regular lattice site towards an interstitial site.

Further, the jumps must overcome a potential barrier which includes a thermodynamic and a kinetic term. Also, an ion flux is only observed if an electrical field gradient or chemical potential gradient is applied. Thus, the particle flux density J can be expressed as:^{94, 95}

$$J = -\beta \cdot \left(\frac{d\tilde{\mu}}{dx} \right) \quad (3.4)$$

where β is the kinetic coefficient and $\tilde{\mu}$ is the electrochemical potential. The electrochemical potential is the sum of the chemical potential and the electrical potential:^{94, 95}

$$\tilde{\mu} = \mu + z \cdot F \cdot \varphi = \mu^0 + RT \cdot \ln c + z \cdot F \cdot \varphi = \tilde{\mu}^0 + RT \cdot \ln c \quad (3.5)$$

where μ is the chemical potential, z the charge of the ion, F the Faraday constant, φ the electrostatic potential, c the concentration, R the gas constant, and T the absolute temperature. From eq. (3.4) and (3.5) the two special cases, pure diffusion and pure electrical conduction can be derived. In the case of pure diffusion, the particles and defects carry no charge and thus the term of the electrical potential becomes zero. Therefore, only the chemical potential gradient remains and eventually Fick's first law is obtained with $\beta = \frac{Dc}{RT}$:

$$J = -\beta \cdot \left(\frac{d\tilde{\mu}}{dx} \right) = -D \cdot \left(\frac{dc}{dx} \right) \quad (3.6)$$

Pure conduction is observed for high defect concentrations where the chemical potential gradient becomes zero. Hence, only an electrical potential is present which results in a current density:^{94, 95}

$$J = -\beta \cdot \left(\frac{d\tilde{\mu}}{dx} \right) = -\beta \cdot z \cdot F \cdot \left(\frac{d\varphi}{dx} \right) \rightarrow i = -\beta \cdot z^2 \cdot F^2 \cdot \left(\frac{d\varphi}{dx} \right) \quad (3.7)$$

From the current density, the conductivity is obtained with $\sigma = z^2 \cdot F^2 \cdot \beta$. Finally, the relation between the diffusivity D and the conductivity σ is obtained by the kinetic coefficient β , which is the Nernst-Einstein relation:

$$\beta = \frac{Dc}{RT} = \frac{\sigma}{z^2 F^2} = \frac{uc}{zF} \quad (3.8)$$

Note that the quantity u is the mobility and is like the diffusion coefficient but in electrical units instead of thermal units. Further, the diffusion coefficient in a chemical potential gradient is specified as the chemical diffusion coefficient \tilde{D}_{chem} :

$$\tilde{D}_{chem} = D_{self} \cdot \left(\frac{d \ln a}{d \ln c} \right) = \frac{\sigma}{z^2 F^2} \cdot \left(\frac{d\mu}{dc} \right) = \frac{\sigma}{F} \cdot \left(\frac{dE}{dc} \right) \quad (3.9)$$

where D is the self-diffusion coefficient at equilibrium conditions and $\left(\frac{d \ln a}{d \ln c} \right)$ is the thermodynamic factor. The self-diffusion coefficient is then related to the conductivity through the Nernst-Einstein relation:

$$D_{self} = \frac{R \cdot T \cdot \sigma_k}{z^2 \cdot F^2 \cdot c_k} \quad (3.10)$$

The calculation of the activation energy of diffusion related processes is then given by the Arrhenius equation:

$$D_{self} = D_0 \cdot e^{\left(\frac{-E_a}{k_B T} \right)} \quad (3.11)$$

where D_0 is the frequency factor and E_a the activation energy. Hence, the experimental procedure is first, the determination of the component conductivity σ_k , and from this the calculation of the self-diffusion coefficient D_{self} . If the thermodynamic factor is known in the given composition range, the chemical diffusion coefficient is calculated from the self-diffusion coefficient.

3.2 Cell Arrangements and Electrodes

Depending on the electrochemical problem, different cell arrangements can be constructed. Thereby, various electrodes are used which determines the function of the cell and the mass and charge transport within the cell. Due to the different boundary conditions at the interface, these electrodes can be classified as reversible, ion blocking, and electron blocking electrodes.

Reversible electrodes are characterized by an electron and ion transfer at the electrode interface. Thus, the current is given by the sum of the electronic and ionic current. In this thesis, Cu is used as reversible electrode. Note that the sample system Cu_{2-x}S can also be classified as a reversible electrode.

Ion blocking electrodes only show an electron transfer at the interface which leads to a pure electronic conduction and a non-present ionic conduction. In this thesis, platinum (Pt) is used as an ion blocking electrode.

Electron blocking electrodes are pure ionic conductors with very low electronic conduction. Thereby, the ionic conduction is by several orders of magnitude higher than the electronic conduction. Also, the electronic conduction must be several orders of magnitude lower than in the sample. Additionally, the same conductive ions must be present in the electrode and the sample (e.g. Cu^+). Further, the ionic conduction in the ion blocking electrode must be higher compared to the sample. In order to measure an electrical current, the ion blocking electrode must be contacted with a reversible electrode. Here, $\text{RbCu}_4\text{Cl}_3\text{I}_2$ is applied as an ion blocking electrode.

Hence, different cell arrangements can be constructed from these electrodes. Generally, cells can be distinguished between symmetrical or asymmetrical cells. In this thesis, a symmetrical and an asymmetrical cell arrangement is used, which is also called a galvanic cell arrangement, see **Figure 3.2**. The symmetrical cell $\text{Pt}|\text{Cu}_{2-x}\text{S}|\text{Pt}$ is used to measure the total conductivity of the sample. The asymmetric cell $\text{Pt}|\text{Cu}|\text{RbCu}_4\text{Cl}_3\text{I}_2|\text{Cu}_{2-x}\text{S}|\text{Pt}$ is established to measure the ionic conduction of the sample. There, the sample is contacted between Pt and $\text{RbCu}_4\text{Cl}_3\text{I}_2$, where Pt ensures the electronic conduction to the potentiostat, and the latter enables a pure ion transfer at the interface. As the electric current of the cell is dependent on the charge transfer at the interface $\text{Cu}_{2-x}\text{S}|\text{RbCu}_4\text{Cl}_3\text{I}_2$, the ionic conduction of the sample can be related to the cell resistance. Further, the reversible electrode Cu is used to transfer the ionic current in $\text{RbCu}_4\text{Cl}_3\text{I}_2$ into an electric current. Hence, this cell can be used for ionic resistance measurements and the measurement of the galvanic cell potential. The cell potential can then be used to characterize and modify the sample, see next chapter.

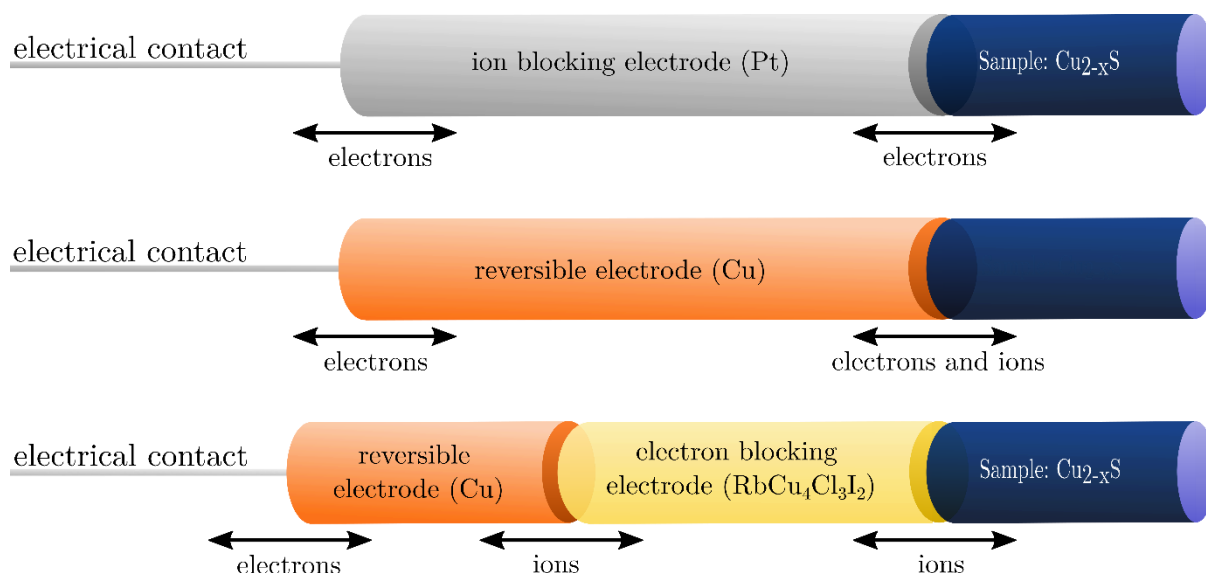


Figure 3.2: Schematic representation of different cell arrangements which use reversible electrodes (Cu), ion blocking electrodes (Pt), and electron blocking electrodes ($\text{RbCu}_4\text{Cl}_3\text{I}_2$). Top: Cell which is used for the total conductivity measurements (symmetrical, only one part is shown). Bottom: Asymmetrical cell arrangement which is used for the electrochemical characterization of the sample.

3.3 Polarization / EMF / Coulometric titration

In order to characterize and adjust the composition of the sample (Cu_{2-x}S), an all solid-state galvanic cell was utilized, see **Figure 3.3**. Therefore, an electron blocking solid electrolyte ($\text{RbCu}_4\text{Cl}_3\text{I}_2$) is used, which solely enables Cu ions to diffuse through the solid electrolyte.

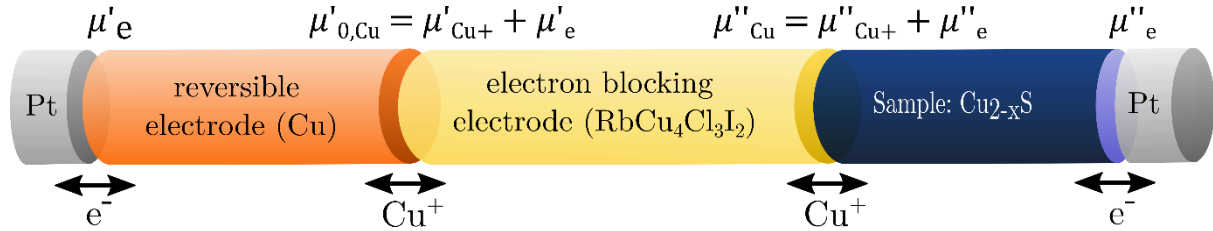


Figure 3.3: Schematic illustration of the all solid-state galvanic cell which was used for the polarization and emf measurements: Pt | Cu | $\text{RbCu}_4\text{Cl}_3\text{I}_2$ | Sample (Cu_{2-x}S) | Pt.

With this asymmetric cell arrangement, several electrochemical measurements can be performed. These are polarization, electromotive force (emf) measurements, and coulometric titration, respectively. This is feasible due to the different electrochemical potentials $\tilde{\mu}_e$ at both platinum (Pt) contacts which results in a cell potential:⁹⁶⁻⁹⁸

$$-UF = \tilde{\mu}_e'' - \tilde{\mu}_e' \quad (3.12)$$

On the left side of the cell, Pt is in contact with Cu, and both are very good electronic conductors. Therefore, the electrochemical potential of the electrons is equal in both metals ($\tilde{\mu}_e'(\text{Pt}) = \tilde{\mu}_e'(\text{Cu})$). On the right side, the Pt electrode is in contact with the sample (Cu_{2-x}S). Due to the predominant electronic conduction in Cu_{2-x}S , the electronic conduction is very high and the same assumption as on the left side can be made: $\tilde{\mu}_e''(\text{Pt}) = \tilde{\mu}_e''(\text{Cu}_{2-x}\text{S})$. Thus, the difference in the chemical potential results from the phase boundary conditions of the solid electrolyte $\text{RbCu}_4\text{Cl}_3\text{I}_2$, where the conditions hold:⁹⁶⁻⁹⁸

$$\mu'_{0,\text{Cu}} = \tilde{\mu}'_{\text{Cu}^+} + \tilde{\mu}_e' \quad \text{and} \quad \mu''_{\text{Cu}} = \tilde{\mu}''_{\text{Cu}^+} + \tilde{\mu}_e'' \quad (3.13)$$

Which then gives the cell potential after rearranging eq. (3.12):

$$-UF = (\mu''_{\text{Cu}} - \mu'_{0,\text{Cu}}) - (\tilde{\mu}''_{\text{Cu}^+} - \tilde{\mu}'_{\text{Cu}^+}) \quad (3.14)$$

As the Cu ion concentration is very high in the solid electrolyte compared to the sample, the chemical potential of the Cu ions at both phase boundaries of the solid electrolyte is equal ($\mu''_{\text{Cu}^+} = \mu'_{\text{Cu}^+}$).⁹⁸ Consequently, the cell potential only depends on the difference between the chemical potential of copper sulfide and Cu:

$$-UF = \mu''_{\text{Cu}}(\text{Cu}_{2-x}\text{S}) - \mu'_{0,\text{Cu}} \quad (3.15)$$

Eq. (3.15) in combination with the chemical potential $\mu_{Cu} = \mu_{0,Cu} + RT \cdot \ln a_{Cu}$ and a Cu activity of one in Cu, gives the cell voltage, which is dependent on the Cu activity in $Cu_{2-x}S$:

$$U_{cell} = \frac{RT}{nF} \cdot \ln a'_{Cu}(Cu_{2-x}S) \quad (3.16)$$

where U_{cell} is the cell voltage, R the gas constant, T the absolute temperature, n the charge number, F the Faraday constant, and a'_{Cu} the activity of Cu in the copper sulfide. Hence, the cell voltage is a function of the Cu activity in the copper sulfide. The cell voltage is also called the electromotive force (emf), or the open cell voltage. Consequently, the cell voltage depends on the composition of the copper sulfide as this changes the Cu activity. If a higher voltage than the cell voltage is applied, the Cu ions wander from the copper sulfide through the solid electrolyte towards the Cu electrode and an electric current is observed in the opposite direction, which can be measured. This process is a so-called polarization, where the applied voltage is the polarization voltage and the process continues until the cell voltage reaches the polarization voltage. If a lower voltage than the cell voltage is applied the opposite direction of ion flux and electric current is observed. In the beginning, the electric current is the highest and decreases exponentially as the cell voltage adapts to the polarization voltage. Thus, the composition of the copper sulfide can be modified accurately with polarization. Therefore, a polarization at the desired polarization voltage (composition) is conducted until the electric current is reaching zero. This indicates that the cell voltage reached the polarization voltage and a steady state is reached where no ion flux is present. Afterwards the open current potential (emf) is measured to ensure the thermodynamic stability of the sample. Note that the emf stays constant in biphasic ranges and changes only with the composition in monophasic ranges.

3.3.1 Emf Measurement – Coulometric Titration

The measurement of the electric current, which is related to the insertion/exclusion of Cu^+ ions into/from the copper sulfide, is called coulometric titration. Where polarization at a constant potential is a potentiostatic titration. When a constant electric current is applied to the cell, it is called galvanostatic titration. With both methods, the composition change (Δx) can be related with Faraday's law:

$$\Delta x = \frac{Q \cdot V_m}{F \cdot V_{sample}} \quad (3.17)$$

where Q is the total charge current, F the Faraday constant, V_m the molar volume of copper sulfide, and V_{sample} the volume of the sample. When the emf of the galvanic cell is plotted versus the composition change Δx , the coulometric titration curve is obtained.

3.3.2 Galvanostatic Titration

Additionally, the chemical diffusion coefficient can be calculated from galvanostatic titration measurements:⁹⁹⁻¹⁰¹

$$\tilde{D}_{chem} = \left[2 \frac{k'}{k} \cdot \frac{L}{\sqrt{\pi}} (t_e^2 + t_{ion}^2) \right]^2 \quad (3.18)$$

where \tilde{D}_{chem} is the chemical diffusion coefficient, L the length of the sample, t_e and t_{ion} the electronic and ionic transference number, respectively. Here, k should be a linear slope of a plot U_{cell} versus $t^{1/2}$ at short polarization times and k' the linear slope of a plot U_{cell} versus t at long polarization times.⁹⁹⁻¹⁰¹ As $Cu_{2-x}S$ is a predominant electronic conductor ($t_e \approx 1$, $t_{ion} \approx 0$) the term $(t_e^2 + t_{ion}^2)$ reduces to one.

3.3.3 Potentiostatic Titration

Also, the chemical diffusion coefficient can be obtained from potentiostatic titration measurements (chronoamperometry) with the Cottrell equation:^{100, 102}

$$\tilde{D}_{chem} = \left[\frac{k'' \cdot \sqrt{\pi}}{z \cdot F \cdot A \cdot V_{Cu}^*} \right]^2 \quad (3.19)$$

where z is the charge number, F the Faraday constant, A the area of the electrode surface, and V_{Cu}^* the Cu vacancy concentration in the copper sulfide. The slope k'' is obtained by a plot of I versus $t^{1/2}$ and should be linear at short polarization times. Note that the Cottrell equation only holds for predominant electronic conduction, which is given for copper sulfide as the electronic conduction is higher by several order of magnitudes compared to the ionic conduction.

3.4 Electrochemical Impedance Spectroscopy (EIS)

Another method to characterize the electrical properties of a material is the electrochemical impedance spectroscopy (EIS). There, a small AC voltage is applied which produces an alternating electric current. From the resulting current, the complex impedance is determined. The complex impedance in turn carries various information such as interface and volume properties of a material. Also, the electronic and ionic properties and the corresponding charge carrier mobilities can be investigated due the frequency dependency of the related processes. In the following, the theoretical foundations for EIS are given.

3.4.1 EIS Theory

The simultaneous investigation of electronic and ionic transport fluxes is feasible due to their different concentration-relaxation times (t_{relax}), which leads to a frequency dependency in EIS measurements. Thus, the different processes can be separated, and the frequency dependence of the conductivity in general is a result of local concentration changes of the charge carriers, which is given by Ohm's law:

$$\hat{j}(\omega t) = \hat{\sigma}(\omega t) \cdot \hat{E}(\omega t) \quad (3.20)$$

where $\hat{j}(\omega t)$ is the electric current density, $\hat{\sigma}(\omega t)$ the conductivity, and $\hat{E}(\omega t)$ the electric field in their respective complex and frequency dependent form. The electric field is proportional to the applied AC voltage:

$$\hat{U}(\omega t) = U_0 \cdot e^{i(\omega t + \theta_U)} \quad (3.21)$$

where $\hat{U}(\omega t)$ is the applied AC voltage, U_0 the amplitude, and ω the angular frequency. Accordingly, the electric current density is proportional to the resulting electric current:

$$\hat{I}(\omega t) = I_0 \cdot e^{i(\omega t + \theta_I)} \quad (3.22)$$

Further, the resulting current can be phase-shifted compared to the applied AC voltage which results in the phase angle $\theta = \theta_I - \theta_U$. Finally, the frequency dependant complex impedance is obtained with Ohm's law:

$$\hat{Z}(\omega) = \frac{\hat{U}(\omega t)}{\hat{I}(\omega t)} \quad (3.23)$$

$$\hat{Z}(\omega) = \frac{U_0}{I_0} \cdot e^{-i(\theta_I - \theta_U)} \quad (3.24)$$

$$\hat{Z}(\omega) = Z_0 \cdot e^{-i\theta} \quad (3.25)$$

$$\hat{Z}(\omega) = Z_0 \cos \theta - i Z_0 \sin \theta \quad (3.26)$$

where $\hat{Z}(\omega)$ is the complex impedance, $Z_0 \cos \theta = Z' = Z^{re}$ the real part, $Z_0 \sin \theta = Z'' = Z^{im}$ the imaginary part, and $Z_0 = |\hat{Z}(\omega)|$ the absolute value of the complex impedance. Hence, physical parameter such as bulk ionic conductivity can be determined from these frequency dependent parameters.

3.4.2 EIS Representation and Analysis

There are two common methods to analyse impedance measurements, which are Bode plot and Nyquist plot, respectively. In Bode plots, the absolute value of the impedance Z_0 (logarithmic) and the phase angle θ (linear) are plotted versus the frequency (logarithmic). Thereby, the saddle points of the absolute value of impedance curve represent the sample resistances and the inflexion point of

the phase angle curve characterizes different time constants in the sample. The Nyquist plot is obtained by plotting the imaginary part Z'' (linear) versus the real part Z' (linear). Note that the Nyquist plot normally starts with high frequencies on the left side and ends with low frequencies at the right-hand side. In order to understand the underlying physical processes which are involved in the measurement, equivalent circuits are used to simulate the obtained impedance spectra. Therefore, different elements are used which can be combined to represent the electrochemical cell. These elements can be assigned to their respective contribution in the electrochemical system and follow Kirchhoff's law for serial and parallel connection, respectively:

$$Z_{total} = Z_1 + Z_2 \quad (3.27)$$

$$\frac{1}{Z_{total}} = \frac{1}{Z_1} + \frac{1}{Z_2} \quad (3.28)$$

For the evaluation of the impedance spectra, a suitable equivalent circuit is built from the individual elements. Then, the values of the respective elements are fitted until the simulated impedance plot shows a good agreement to the experimental impedance measurement. This procedure was performed with the software *Zahner Analysis*.¹⁰³ Finally, material properties such as ionic conductivity and diffusion coefficients can be calculated from the obtained values, see table **Table 3.2**. Note that the Nernst-Diffusion- (ND) and Finite-Diffusion (FD) element are special cases of the ideal Warburg impedance. The ND element describes a symmetrical and closed case, whereas the FD element depicts an asymmetrical and open arrangement.

Table 3.2: Overview of the basic equivalent circuit elements and their physical expressions as well as the corresponding parameter. Note that the Nernst-Diffusion- (ND) and Finite-Diffusion (FD) element are special cases of the ideal Warburg impedance. The ND element describes a symmetrical and closed case, whereas the FD element depicts an asymmetrical and open Warburg impedance.⁹⁸

Element (Symbol)	Complex Impedance: $Z(\omega) =$	Parameter
Resistance (R)	R	R
Capacity (C)	$\frac{1}{i\omega C}$	C
Inductivity (L)	$i\omega L$	L
Constant Phase Element (CPE)	$\frac{1}{Y^{CPE}(i\omega)^\alpha}$	Y_{CPE}, α
Warburg impedance (Z_w)	$\frac{W}{(i\omega)}$	W
Nernst-Diffusion (Z_{ND})	$Z_0 \frac{\tanh(kL)}{kL}$	Z_0, k, L
Finite-Diffusion (Z_{FD})	$Z_0 \frac{\coth(kL)}{kL}$	Z_0, k, L

Hence, the specific conductivity σ_{spec} of an ionic conductor can be derived from the resistance (R) or the value Z_0 of the respective Warburg impedance element:

$$\sigma_{spec} = \frac{L}{A \cdot \rho \cdot R} = \sigma_0 \cdot e^{\left(\frac{-E_a}{k_b T}\right)} \quad (3.29)$$

where L is the length of the sample, A the area of the electrode surface, and ρ the density of the pellet ($\rho = \frac{\rho_{pellet}}{\rho_{compound}}$). Additionally, mass and charge transport include capacitive contribution to the complex impedance. Usually, a solid electrolyte exhibits three different capacitive contributions, which are geometrical, grain boundary, and electrode capacity.

The geometrical capacity C_g is defined by the dimensions of the sample and the contribution of the electrical contacts in contact with the sample. In parallel to the geometrical capacitance is the bulk resistance R_b which is used to calculate the specific conductivity. In addition to the mass and charge transport through the bulk, a transport takes place across boundaries. Hence, another grain boundary resistance R_{gb} is observed with a parallel grain boundary capacity C_{gb} . This is especially observed for low temperatures and small grain sizes. Also, the charge transfer at two adjacent electrodes leads to a charge transfer resistance R_{ct} with a corresponding charge transfer capacity which is called the double layer capacity C_{dl} .

Note that these processes act at different time scales and occur in a series. Thus, one individual process can be expressed by one parallel RC element. If all three processes occur, three RC elements are connected in series. However, these three distinct processes are rarely observed individually in the impedance spectra because a differentiation is only possible if the time constants τ differ at least by one order of magnitude:

$$R \cdot C = \tau \quad (3.30)$$

The time constant τ is material constant and is also called relaxation time and describes the different electrochemical processes. If the time constant τ differs for example by three order of magnitude, three semicircles can be observed in the Nyquist plot. Keep in mind that this is rarely observed in real samples. Typical capacitances which might occur in solid-state cells are given in **Table 3.3**.⁹⁸

Table 3.3: Typical capacitances in solid-state cells. Note that a differentiation is only possible if the time constant τ differs by at least one order of magnitude. This is rarely observed in real solid-state cells and the capacities in this table represent the ideal case.⁹⁸

Capacity / F	Electrochemical Process
10^{-12}	Geometrical capacity C_g
10^{-9}	Grain boundary capacity C_{gb}
10^{-6}	Double layer capacity C_{dl}

3.4.3 Warburg Impedance

The Warburg impedance element is used to describe diffusion-controlled processes in an electrochemical cell. There, it is characterized by a phase angle of 45° at low frequencies. However, this is the ideal case which is rarely seen in solid-state cells. In solid-state cells, two special of Warburg impedance are observed which are Nernst-Diffusion and Finite-Diffusion. The former describes a symmetrical cell with ion or electron blocking electrodes. The latter is observed for asymmetrical cell arrangements with an ion blocking electrode at one side and an electron blocking electrode at the other side of a sample, see **Figure 3.4**.

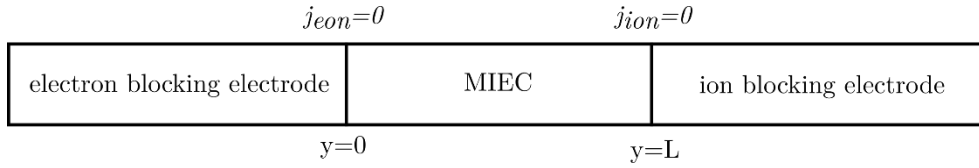


Figure 3.4: Schematic representation of an asymmetric galvanic cell arrangement. The MIEC is contacted between an ion blocking electrode and electron blocking electrode. These blocking electrode lead to a different diffusion expression compared to the ideal Warburg impedance.

The blocking electrode at $y = 0$ and $y = L$ lead to different boundary conditions, which in turn lead to a different analytical expression of the Warburg impedance. At $y = 0$ the electron density flux is non-present and $j_{e on} = 0$. Likewise, the ionic density flux $j_{i on}$ is zero at $y = L$. Also, a linear homogenous diffusion is assumed along the coordinate y which leads to a concentration gradient with an applied AC voltage due to the different chemical potentials at both electrical contacts. This leads to the general expression for the Warburg impedance:⁹⁸

$$Z_W = \frac{\Delta U}{\Delta I} = \frac{\frac{1}{F} \left(\frac{d\mu}{dc} \right)_{c_0} \cdot c_0 \cdot e^{(i\omega t)} \cdot \left(1 - \frac{\cosh \left[-k(\omega) \cdot \frac{L}{2} \right]}{\cosh \left[k(\omega) \cdot \frac{L}{2} \right]} \right)}{-\frac{AF\tilde{D}}{t_e} \cdot \left(\frac{\partial c}{\partial y} \right)_{y=0,L}} \quad (3.31)$$

Now the two different cases for closed and open Warburg impedance can be derived with the respective boundary conditions:⁹⁸

$$Closed = Z_{ND} = Z_0 \cdot \frac{\tanh(kL)}{kL} \quad (3.32)$$

$$Open = Z_{FD} = Z_0 \cdot \frac{\coth(kL)}{kL} \quad (3.33)$$

$$with: k(\omega) = \sqrt{\frac{i\omega}{\tilde{D}}} \quad (3.34)$$

The closed Nernst-Diffusion then describes a symmetrical cell arrangement where an ion can diffuse from one electron blocking electrode into the other electron blocking electrode. Thus, the sample impedance Z_0 is solely defined by the ionic conductivity:

$$Z_0 = \frac{L}{A \cdot \sigma_{ion}} \quad (3.35)$$

Accordingly, the sample impedance Z_0 is derived for two symmetrical ion blocking electrodes with the electronic conductivity. From eq. (3.32) it becomes clear that the Warburg impedance for the Nernst-Diffusion behaves like an ohmic resistor at low frequencies.

The open Finite-Diffusion represents an asymmetric galvanic cell where an ion can diffuse from the electron blocking electrode into the sample but cannot diffuse from the sample into the ion blocking electrode. Here, the sample impedance Z_0 is given by:

$$Z_0 = \frac{L}{A \cdot \sigma_{ion} t_e} \cdot [(1 - t_e)^2 + t_e^2] \quad (3.36)$$

Thus, the sample impedance depends on the contribution of the electronic conduction. If the electronic conduction is by several order of magnitude higher than the ionic conduction, eq. (3.36) simplifies to eq. (3.35) because $t_e \approx 1$. Note that Cu_{2-x}S is a predominant electronic conductor with $t_e \approx 1$. Also, the open Warburg impedance behaves like a capacitor at low frequencies as the ions and electrons are blocked at each blocking electrode. The Nyquist and Bode plots of the three different Warburg impedance elements are shown in **Figure 3.5**.

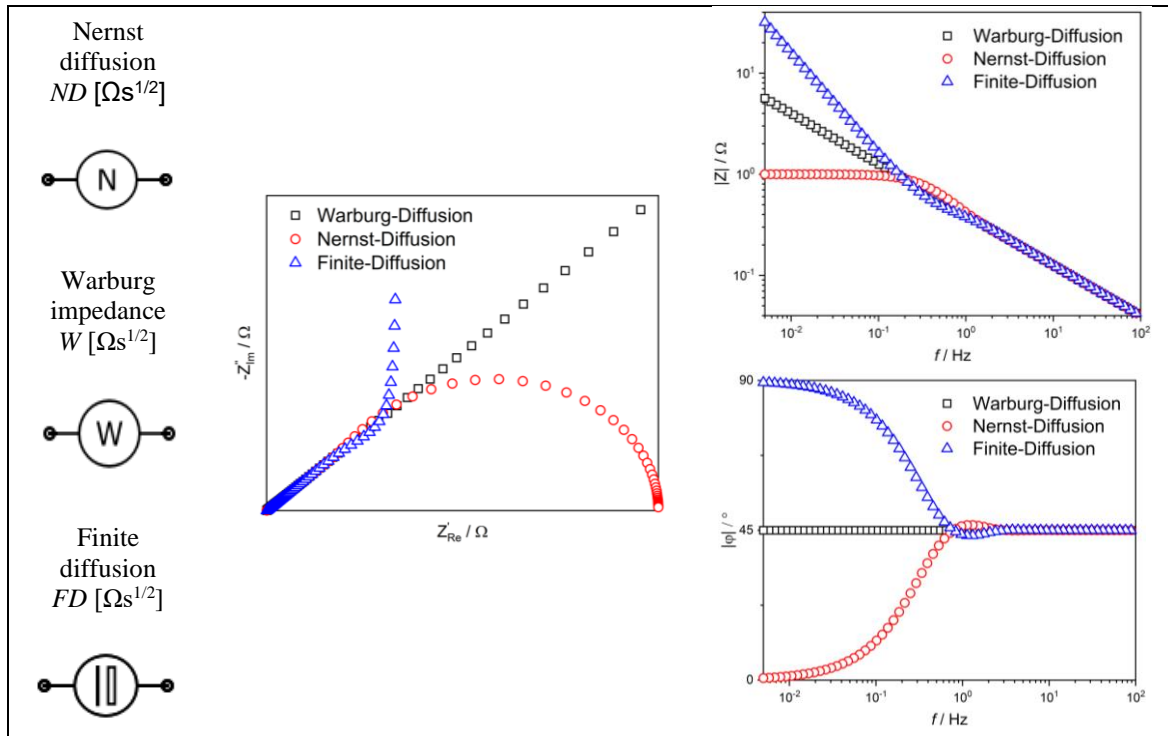


Figure 3.5: Nyquist and Bode plots of the three different diffusion impedances. Here, the Warburg impedance element describes the ideal diffusion case, Nernst-Diffusion element the closed diffusion, and Finite-Diffusion element the open diffusion case.

3.4.4 Chemical Diffusion Coefficients

In addition to the ionic and electronic conductivities, the diffusion coefficients can be deduced from EIS measurements. According to the Nernst-Einstein relation, the self-diffusion coefficient can be calculated with eq. (3.10). However, the chemical diffusion coefficient is often denoted in the literature which makes it difficult to compare with the obtained self-diffusion coefficients. One option to calculate the chemical diffusion coefficient from the self-diffusion coefficient is through the thermodynamic factor (see eq. (3.9)). Though the chemical diffusion coefficient can be obtained with this method, detailed information of the composition and the thermodynamic factor is needed. An option to obtain this is from emf measurements and coulometric titration curves. Good care must be taken to obtain these parameters as a lot of parameters can influence these measurements.

Therefore, another method was applied which uses the derived expression for the closed Finite-Diffusion. Here, eq. (3.33) can be simplified to:⁹⁹

$$Z_{FD} = R_{ion} + \frac{RT}{z^2 F^2 A V_{Cu}^*} \cdot \frac{1}{\sqrt{2\omega \tilde{D}_{chem}}} \cdot (t_e^2 + t_{ion}^2) \cdot (1 - i) \quad (3.37)$$

where R_{ion} is the ionic resistance, R the gas constant, T the absolute temperature, z the charge number, F the Faraday constant, A the area of the electrode surface, V_{Cu}^* the vacancy concentration in $Cu_{2-x}S$, \tilde{D}_{chem} the chemical diffusion coefficient, and t_e and t_{ion} the electronic and ionic transference number, respectively. The chemical diffusion coefficient can then be obtained by plotting Z^e and Z^m versus $\omega^{-1/2}$ which yields the slope S and should give two parallel straight lines. Finally, the chemical diffusion coefficient can be calculated with the obtained slope S and the equation simplifies with $t_e \approx 1$:⁷⁸

$$\tilde{D}_{chem} = \left[\frac{RT}{z^2 F^2 A \sqrt{2} \cdot S \cdot V_{Cu}^*} \right]^2 \quad (3.38)$$

$$\text{with: } V_{Cu}^* = \frac{(\Delta x) \rho_{Cu_2S}}{(2 - \Delta x) M_{Cu} + M_S} \quad (3.39)$$

3.5 Quantitative Phase Analysis (QPA) via PXRD

In order to quantify the PXRD measurements a fundamental condition is needed, in which the diffracted intensity of a phase is proportional to the quantity of this phase in the mixture. In general, the intensity I_{hkl} of a reflection is defined as:

$$I_{hkl} = K_0 \cdot A \cdot \left(\frac{|F_{hkl}|}{V_{EZ}} \right)^2 \cdot H \cdot P \cdot L \quad (3.40)$$

$$\text{with } K_0 = \frac{I_0 \cdot e^4 \cdot \lambda^3 \cdot Q_0}{m_e^2 \cdot c^4} \quad (3.41)$$

where K_0 is a device-specific constant, A the absorption coefficient, F_{hkl} the structure factor, V_{EZ} the volume of the unit cell, H the multiplicity factor, P the polarization factor and L the Lorentz factor. Further, the device specific constant K_0 is defined by I_0 the incident X-ray beam, e the elementary charge, λ the incident X-ray wavelength, Q_0 the width of the incident X-ray beam, m_e the mass of the electron and c the speed of light. Finally, the theoretical foundation for the quantitative phase analysis via PXRD is given by eq. (3.42) developed by *Alexander and Klug*.¹⁰⁴

$$I_1 = \frac{k_1 \cdot w_1}{\mu_1^*} \quad (3.42)$$

where I_1 is the intensity, w_1 the weight fraction, k_1 a constant related to the nature of component I and μ_1^* is the linear mass absorption coefficient of component I in a mixture. Based on this equation, several quantification methods can be used.¹⁰⁵ In this thesis, the powder patterns mainly comprise the Cu and low-/high temperature α -/ β -Cu₂S phase. Hence, four different quantification techniques were used based on equation (3.42) depending on the sample matrix. Hereafter, the theoretical foundations for the respective methods are discussed. Also, an overview of the applied methods is given in **Table 3.4**.

Table 3.4: Overview of the applied methods used for the quantitative phase analysis. For the powdery mixtures, the relative calibration method and the reference intensity ratio method are used. For the HT-in situ-PXRD Cu bond wire experiments the external standard method and the direct comparison method are used.

Method	Samples	Chapter	Radiation
Relative calibration method	Cu/ α -Cu ₂ S mixtures	7.4.1-2	Cu- $K_{\alpha 1}$
Reference intensity ratio method	Cu/Pd/ α -Cu ₂ S mixtures	7.4.3-4	Cu- $K_{\alpha 1}$
External standard method	Fully corroded Cu bond wire/ β -Cu ₂ S	8-12	Mo- $K_{\alpha 1}$
Direct comparison method	Cu bond wire/ β -Cu ₂ S	8-12	Mo- $K_{\alpha 1}$

3.5.1 Relative Calibration Method (RCM)

The RCM was established for the powdery Cu/Cu_xS mixtures in chapter 7.4.1 and 7.4.2. This method is commonly known as single reflection method because it is normally performed with one single reflection of the phase of interest and a reference phase. Here, a series of standards is prepared containing the crystalline phase of interest at known weight fractions. Then, the standards are measured, and a calibration curve is generated for each single reflection of a phase I , which relates the weight fraction w_1 to the intensity I_I of a phase in a mixture

$$w_1 = A \cdot I_1 + B \quad (3.43)$$

In this thesis, the relative intensities of the α -Cu₂S phase in relation to the strongest Cu-reflection ($\sim 43.3^\circ$) are used for the quantification of the α -Cu₂S phase. Hence, only the copper sulfide weight fraction in the sample can be quantified as the intensities of the Cu phase vary with the incident X-ray beam intensity and with the preparation on the flatbed carriers. Herein, the three strongest copper sulfide reflections at $\sim 37.3^\circ$, $\sim 45.8^\circ$ and $\sim 48.5^\circ$ are used for the quantification to ensure a good reproducibility and accuracy. Of course, the linear mass absorption coefficient μ^* of the components in the calibration mixture should be akin to the mass absorption coefficients of the components in the sample matrix. Thus, a suitable matrix is required for the calibration standards. This is considered for the sample mixtures and the experimental details will be discussed in chapter 7.3. In **Table 3.5** some calibration parameters for the RCM are shown. Here, the relative intensities (one measurement) and the mean relative intensities (three measurements) for one reflection are compared. As the mean relative intensities show better values, this method was chosen for the quantitative analysis. Thus, a three-fold determination was performed for all calibration standards and samples.

Table 3.5: Comparison of the calibration parameters. The mean relative intensities were used as they show much better values.

	Rel. Int.	Mean Rel. Int.
R ²	0,9944	0,9972
Std. deviation / wt%	0,60	0,31
Rel. Std. deviation / wt%	5,33	5,03
Confidence interval / wt%	1,46	0,49
LOD / wt%	1,30	0,46
LOQ = 3 · LOD / wt%	4,57	1,61
Linearity test of Mandel	✓	✓
Residual distribution test	✓	✓
Neumann-trendtest	✓	✓

3.5.2 Reference Intensity Ratio (RIR) Method

The RIR method is a general internal standard method, which employs $\alpha\text{-Al}_2\text{O}_3$ (corundum) as the standard for comparing the diffraction intensities of powder materials. This method is used for a semi-quantitative phase analysis of the Cu/Pd mixtures in chapter 7.4.3 and 7.4.4. In general, the *RIR* value is calculated from eq. (3.44).^{106, 107}

$$RIR_{1,2} = \left(\frac{x_2}{x_1}\right) \left(\frac{I_{(hkl)1}}{I_{(hkl)2}}\right) \left(\frac{I_{(hkl)2}^{rel}}{I_{(hkl)1}^{rel}}\right) = \frac{RIR_{1,cor}}{RIR_{2,cor}} \quad (3.44)$$

where x is the weight fraction of the sample, I is the intensity of a specific reflection, I^{rel} is the relative intensity of the reflection, 1 and 2 are the phase of interest. If corundum is chosen as the internal standard, the $RIR_{1,cor}$ value is known as I/I_{cor} or RIR_{cor} (cor = corundum) in 50:50 mixture. Hence, the RIR_{cor} values can be calculated for a phase 1 by eq. (3.45):

$$RIR_{1,cor} = \frac{I_1}{I_{cor}} \quad (3.45)$$

From two different RIR_{cor} values derived from eq. (3.45), the ratio of the weigh fractions can be derived which relates the intensities of two phases 1 and 2 in a mixture:^{106, 107}

$$\left(\frac{x_1}{x_2}\right) = \left(\frac{I_{(hkl)1}}{I_{(hkl)2}}\right) \left(\frac{I_{(hkl)2}^{rel}}{I_{(hkl)1}^{rel}}\right) \left(\frac{RIR_{2,cor}}{RIR_{1,cor}}\right) \quad (3.46)$$

When the RIR_{cor} values for all phases are known, and if eq. (3.47) holds, then the normalized eq. (3.48) allows the analysis of any phase without the addition of a standard.^{106, 108}

$$\sum_{k=1}^n x_k = 1 \quad (3.47)$$

$$x_a = \frac{I_{(hkl)1}}{RIR_1 I_{(hkl)1}^{rel}} \left[\sum_{k=1}^{\# \text{ of phases}} \frac{I_{(hkl),k}}{RIR_k I_{(hkl),k}^{rel}} \right]^{-1} \quad (3.48)$$

Here, the RIR_{cor} values from the *Match!* database are used. Note that the RIR_{cor} values from the database can vary to the actual sample as texture and absorption effects as well as chemical composition can alter the observed intensities from the true intensities of PXRD reflections. Also, the assumption that no amorphous phases are present leads to large deviations in the calculated weight fractions. Thus, the RIR method is considered a semi-quantitative method. Nevertheless, it was applied for the powdery Cu-Pd mixtures, because in these mixtures often more than three phases are observed. In addition to that, a few minor unidentified reflections are observed in some powder pattern which eliminates whole powder pattern fitting methods. Therefore, the analysis of the powdery Cu/Pd mixtures was performed in qualitative fashion.

3.5.3 External Standard Method (ESM)

The ESM is used for the quantification of the Cu bond wire HT-in situ-PXRD measurements. In specific, this method was only applied for few selected isothermal high temperature PXRD measurements where the bond wire fully corroded to β -Cu₂S. Then, the pure Cu wire in the beginning can be used as the external standard for the quantification of the Cu phase and the sole corrosion product β -Cu₂S at the end can then be used as the external standard for the quantification of β -Cu₂S during the measurement. If the Cu bond wire is not fully corroded, no suitable external standard is available. Note that the application of pure β -Cu₂S powder as standard gives unreliable results and shows large deviations in the weight fractions compared to the results obtained from scanning electron microscopy (SEM) cross-sections of the bond wires after the PXRD measurements. Thus, the applied quantification method is indicated in the experimental description. In general, the ESM is applied if the Cu bond wire is fully corroded to β -Cu₂S. The ESM is based on eq. (3.42) and in a binary mixture (Cu/ β -Cu₂S) gives eq. (3.49) described by *Alexander and Klug*.¹⁰⁴

$$\frac{I_1}{I_1^0} = \frac{x_1 \mu_1^*}{x_1(\mu_1^* - \mu_2^*) + \mu_2^*} \quad (3.49)$$

Here, x_1 is the weight fraction of component I in the binary mixture, I_1^0 is the intensity of the reflection in the external standard, I_1 the intensity of the reflection in the sample, and μ_1^* and μ_2^* the linear absorption coefficients of the components I and 2, respectively. For the quantification of the HT-XRD powder pattern the three strongest reflections of the Cu (hkl planes = 111,200,202 = $\sim 19.5^\circ$, $\sim 22.5^\circ$, $\sim 32.1^\circ$) and β -Cu₂S (hkl planes = 012,110,013 = $\sim 16.8^\circ$, $\sim 20.5^\circ$, $\sim 21.6^\circ$) phases are used. This multireflection quantification reduces the influence of preferred orientation effects and thus gives more reliable results. The exact mass absorption coefficients μ^* are obtained from the pure external standards via Rietveld analysis (**Table A 3.1**). The Rietveld refinement was performed with *Jana2006*¹⁰⁹ (**Figure A. 3.1-5**). An exemplary calibration curve for the bare Cu wire is given in **Figure A. 3.6**. What is evident is that the calibration curves do not exhibit a linear slope. This is due to absorption effects. Here, μ_{Cu} is much bigger than $\mu_{\text{Cu}_2\text{S}}$, which ‘dilutes’ the Cu phase in the Cu₂S phase and thus diminishes self-absorption effects. Therefore, the intensity I_{Cu} is more intense in the mixture, whereas $I_{\text{Cu}_2\text{S}}$ is less intense. This leads to a nonlinear behaviour and may have influences on the ‘visibiltiy’ of the phases in the diffraction pattern. As a consequence, this absorption effects might affect the precision and the detection limit of the phases.

3.5.4 Direct Comparison Method (DCM)

As mentioned above, the ESM method is not applicable for the β -Cu₂S quantification if the wire is not fully corroded. Thus, an external standard is missing. Also, the external standard method is not suitable for longer measurements with variation in incident X-ray beam intensity. Hence, for all measurements where high fluctuation in beam intensity is observed and the wire is not fully corroded, the DCM is applied. Therefore, the DCM is chosen as the standard method for the high temperature in situ Cu bond wire experiments unless otherwise declared. In principle, the DCM is a modified RIR method which was first introduced by *Spurr et al.* and then generalized by *Chung* and is based on eq. (3.42).^{108, 110} This method provides a new factor K which relates the intensity relation in a binary mixture:

$$\frac{I_1}{I_2} = \left(\frac{RIR_{1,cor}}{RIR_{2,cor}} \right) \left(\frac{x_1}{x_2} \right) \quad (3.50)$$

$$K = \frac{RIR_{1,cor}}{RIR_{2,cor}} \quad (3.51)$$

Here, I_1 and I_2 are the diffracted X-ray intensities and x_1 and x_2 are the respective weight fractions and $RIR_{1,cor}$ and $RIR_{2,cor}$ are the reference intensity ratios of components 1 and 2. Usually, the RIR_{cor} is used and the factor K can be calculated easily. However, the factor K can also be obtained from the slope of a plot I_1/I_2 against x_1/x_2 . As the reference values from the databases may alter from the experimental setup, the factor K was obtained from this plot, see **Figure A. 3.7-8**. Therefore, the experimental values obtained from the ESM are used where the fully corroded wires give accurate Cu and copper sulfide weight fractions. Also, some selected measurements which were quantified with the ESM were cross-checked with SEM analyses to verify the results. Again, a multireflection analysis with the three strongest reflections of the Cu (hkl planes = 111,200,202 = $\sim 19.5^\circ$, $\sim 22.5^\circ$, $\sim 32.1^\circ$) and β -Cu₂S (hkl planes = 012,110,013 = $\sim 16.8^\circ$, $\sim 20.5^\circ$, $\sim 21.6^\circ$) phases is performed to minimize texture effects and to increase the precision of the quantification. The obtained values from this plot are $K_{Cu_2S} = 0.184$ and $K_{Cu} = 5.453$ and are in good agreement with the values from reference databases ($K_{Cu} = 5.381, 5.753$; $K_{Cu_2S} = 0.186, 0.174$; see **Table A 3.2**). Further, in a binary mixture we can assume: $x_{Cu} + x_{Cu_2S} = 1$ and thus the weight fraction of a component 1 can be calculated by:

$$x_1 = \frac{1}{1 + K_1 \frac{I_2}{I_1}} \quad (3.52)$$

The advantages of this method are that no external or internal standard is required and the fluctuations in incident beam intensity are cancelled out for the quantification of a binary mixture. As it happens, only the Cu and β -Cu₂S are observed in the HT-in situ-PXRD measurements, which makes the DCM a suitable choice to quantify the measurements. This allows to measure over long periods of time and to compare the individual measurements to each other.

3.6 Lotgering Factor – Preferred Orientation

In addition to a quantitative phase analysis, texture effects can be analysed via PXRD. Therefore, the Lotgering factor (LF) was established which is a semi-quantitative approach to analyse the degree of preferred orientation in a textured sample.¹¹¹ In this thesis, a modified Lotgering factor method is used. Herein, P is calculated from the respective intensity of a Bragg reflection I_{hkl} versus the sum of the intensities of the three strongest reflections $\sum I_{hkl}$ of the respective Cu/ β -Cu₂S phases from the PXRD pattern. This yields the fraction of the peak intensities P :

$$P = \frac{I_{(hkl)}}{\sum I_{(hkl)}} \quad (3.53)$$

where P describes a particle-oriented sample and P_0 describes a standard sample with random particle distribution. Hence, the LF can be calculated according to:

$$LF = \frac{P - P_0}{1 - P_0} \quad (3.54)$$

The LF increases from 0 for a randomly oriented sample to 1 for a perfectly oriented sample. However, the LF is no quantitative description of the orientation distribution and therefore is only used for a qualitative analysis.¹¹²

3.7 Solid State Kinetic Analysis

Kinetic studies of chemical reactions were initially developed by empirical studies of homogenous gas phase reactions. The derived concepts were then applied to chemical reactions in the liquid phase and eventually adopted to solid-state reactions. Despite some similarities, the application of these principles to solids differ from solutions and gases and are more complex than those in homogenous phases due to factors like particle size, geometric shape, interface effects, nuclei formation and complex diffusion phenomena.¹¹³ Therefore, more complex theoretical mathematical models were developed in the past century to describe experimentally observed solid-state reactions. The solid-state reactions can be tracked in a normalized form which is the conversion fraction (α). The conversion fraction is ranged from 0 to 1 and the isothermal differential reaction rate law defined in eq. (3.55) and the integrated form in eq. (3.56) can then be expressed as:¹¹⁴

$$reaction\ rate = \frac{d\alpha}{dt} = k(1 - \alpha) \quad (3.55)$$

$$-\ln(1 - \alpha) = kt \quad (3.56)$$

Here, $d\alpha/dt$ is the isothermal reaction rate and the temperature dependency of the reaction rate constant k is defined by the Arrhenius law:¹¹⁵

$$k = Ae^{-\frac{E_a}{RT}} \quad (3.57)$$

where, E_a is the activation energy, A is the preexponential factor, T is the absolute temperature, and R is the gas constant. Initially, the application of the Arrhenius equation to the kinetics of solid-state reaction has been doubted due to the inability to represent the energy distribution by the Maxwell-Boltzmann equation. However, the energy distribution in solids can be expressed by the Fermi-Dirac statistics for electrons and Bose-Einstein statistics for phonons. Both expressions approximate to an exponential energy term which allows the application of the Arrhenius equation to reactions of solids.^{116, 117}

By introducing a mathematical reaction model these expressions can be generalized in the form of eq. (3.58) and eq. (3.59). Here, k is the reaction rate constant, $f(\alpha)$ is the differential reaction model and $g(\alpha)$ is the integral reaction model for isothermal conditions

$$\frac{d\alpha}{dt} = k \cdot f(\alpha) \quad (3.58)$$

$$g(\alpha) = k \cdot t \quad (3.59)$$

In the past, many models have been developed which are based and categorized by their shape of the isothermal α versus time (α - t) plots (deceleratory, acceleratory, linear, sigmoidal) and their underlying mechanistic assumptions, respectively. Based on the mechanistic assumptions, the models can be classified as:

- i. Diffusion
- ii. Geometrical contraction/expansion
- iii. Nucleation & Growth
- iv. Reaction-order

A general mathematical expression has been suggested by *Sestak* and *Berggren* that includes all mechanistic assumptions (models) in a single equation, where m , n , and p are constants:¹¹⁸

$$g(\alpha) = \alpha^m (1 - \alpha)^n (-\ln(1 - \alpha))^p \quad (3.60)$$

In heterogenous kinetics, identifying a solid-state reaction model often helps to understand the reaction mechanism, which involves chemical steps that are difficult to obtain experimentally. A brief overview of the solid-state reaction models is presented in **Table 3.6**. Generally, the choice of the solid-state model is determined by statistical fits to the mathematical models or by model-free methods (isoconversional). In the following an overview and a short derivation of the most prominent solid-state models is given. In addition to that, three different methods, which are used in this thesis for the analysis of the solid-state reactions (α - t plots), are discussed.

Table 3.6: Overview of the solid-state reaction models and their integral expressions of the isothermal reaction rate. The Anti-models describe an expansion of the reacting particle and can be considered a Kirkendall effect model, whereas the original models are based on a shrinking particle and thus are shrinking core models. Also, the experimentally obtained Avrami exponents n are given as well as the calculated Avrami exponents. The Avrami exponent n is used for the analysis of the solid-state reaction models. It is striking, that the experimental Avrami exponents are roughly the same as the calculated Avrami exponents in the range $\alpha = 0-0.5$, whereas the Avrami exponents increase in the range $\alpha = 0.5-0.75$ and $\alpha = 0.8-1$. Therefore, the optimal range for the analysis of solid-state reaction models is in the range from 0 to 0.5 conversion fraction.^{114, 119-128}

Model	Integral Form $g(\alpha)=kt$	n (exp.) 114, 129	n (calc.) $\alpha = 0-0.5$	n (calc.) $\alpha = 0.5-0.75$	n (calc.) $\alpha = 0.8-1$
Diffusion models					
1-D (D1) ^{113, 114}	α^2	0.62	0.54	0.85	2.06
2-D (D2) ^{113, 114}	$(1-\alpha)\ln(1-\alpha)+\alpha$	0.57	0.53	0.71	1.38
3-D Jander (D3) ¹¹⁹	$[1-(1-\alpha)^{1/3}]^2$	0.54	0.51	0.59	0.81
3-D GB ^a (D4-GB) ¹²⁰	$1-2\alpha/3-(1-\alpha)^{2/3}$	0.57	0.52	0.67	1.14
3-D CV ^b (D3-CV) ¹²¹⁻¹²³	$z-(z-1)(1-\alpha)^{2/3}-[1+(z-1)\alpha]^{2/3}$				
Anti-D2 (Jander)	$[(1+\alpha)^{1/2}-1]^2$	-	0.56	0.92	2.27
Anti-D3 (Jander) ¹²⁴	$[(1+\alpha)^{1/3}-1]^2$	-	0.57	0.99	2.50
Anti-D4 (GB) ¹²³	$1+2\alpha/3-(1+\alpha)^{2/3}$	-	0.56	0.94	2.34
Counterdiffusion (CD-D2)	$[(\alpha)^{1/2}]^2$	-	1.09	1.70	4.12
Counterdiffusion (CD-D3)	$[(\alpha)^{1/3}]^2$	-	1.63	2.55	6.18
Geometrical contraction/expansion					
Contracting area (R2) ¹²⁵	$[1-(1-\alpha)^{1/2}]$	1.11	1.04	1.29	2.05
Contracting volume (R3) ¹²⁵	$[1-(1-\alpha)^{1/3}]$	1.07	1.03	1.18	1.61
Anti-R2	$[(1+\alpha)^{1/2}-1]$	-	1.12	1.90	4.75
Anti-R3	$[(1+\alpha)^{1/3}-1]$	-	1.13	1.98	4.99
Reaction-order models					
Zero-order (F0/R1)	α	1.24	1.09	1.70	4.12
First-order (F1)	$[-\ln(1-\alpha)]$	1	1	1	1
Second-order (F2)	$[1/(1-\alpha)]^{-1}$	-	0.91	0.63	0.31
Third-order (F3)	$(1/2)[(1-\alpha)^{-2}-1]$	-	0.83	0.43	0.16
Nucleation & Growth models					
Avrami-Erofe'ev (A2) ¹²⁶⁻¹²⁸	$[-\ln(1-\alpha)]^{1/2}$	2	2	2	2
Avrami-Erofe'ev (A3) ¹²⁶⁻¹²⁸	$[-\ln(1-\alpha)]^{1/3}$	3	3	3	3
Avrami-Erofe'ev (A4) ¹²⁶⁻¹²⁸	$[-\ln(1-\alpha)]^{1/4}$	4	4	4	4
Power law (P2)	$\alpha^{1/2}$	-	2.18	3.40	8.24
Power law (P3)	$\alpha^{2/3}$	-	3.26	5.10	12.34
Power law (P4)	$\alpha^{3/4}$	-	4.35	6.80	16.47

^a GB = Ginstling-Brounshtein, ^b CV = Carter-Valensi

3.7.1 Diffusion Models

The biggest distinction between homogeneous and heterogeneous kinetics is that solid-state reactions often occur between rigid surfaces. Therefore, the reaction takes place between one (solid-liquid) or two (solid-solid) crystal lattices where the motion of reactants is often restricted and may depend on lattice/surface defects. If the chemical reaction of two reactants on the surface of the phase boundary is faster than the motion of the reactants in the crystal lattice, the diffusion of reactants become the rate limiting step in the solid-state reaction. Hence, the growth of the product layer AB at the reactive phase boundary is diffusion-controlled and decreases proportionally with the thickness of the product layer. For metallic oxidation (e.g. Cu to Cu₂S), a moving boundary is observed, where the mobile ions in A move across the phase boundaries b₁ and b₂ towards the reactive interface AB/B in time dt to form product AB, see **Figure 3.6**.

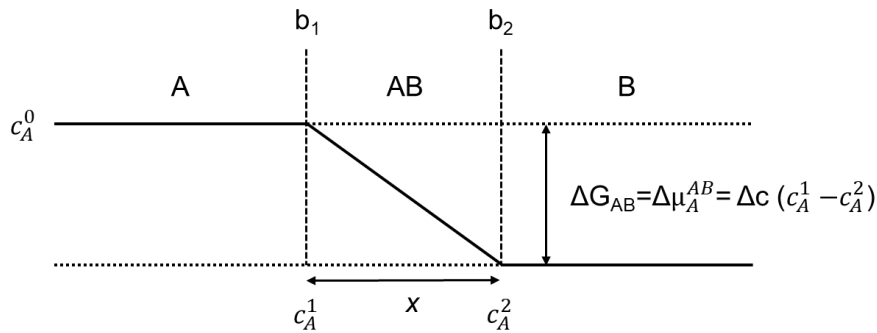


Figure 3.6: Schematic model of the concentration (c_A) profile of A during a heterogeneous solid-state reaction $A+B=AB$. Here, the diffusion of A through the product layer towards the reactive phase boundary AB/B is the rate limiting step of the reaction rate.

From Figure 3.6 the expression in eq. (3.61), which assumes a linear concentration gradient, can be derived:

$$\frac{dx}{dt} = D \left(\frac{M_{AB}}{M_A \rho} \right) \left(\frac{c_A^1 - c_A^2}{x} \right) \quad (3.61)$$

Which gives eq. (3.62) after integration:

$$x^2 = 2Dt \left(\frac{M_{AB}(c_A^1 - c_A^2)}{M_A \rho} \right) \quad (3.62)$$

where, M_{AB} and M_B are the molecular weights of AB and A, D is the diffusion coefficient, ρ is the density of the product AB, x is the thickness of the product layer AB, c_A^1 and c_A^2 are the concentrations of A at the phase boundary b₁ and b₂, respectively. Finally, the parabolic law is obtained if the reaction rate $k = 2D(M_{AB}(c_A^1 - c_A^2))/M_A\rho$:¹³⁰

$$x^2 = kt \quad (3.63)$$

In a one-dimensional case (infinite flat plane) the product layer thickness x is directly proportional to the conversion fraction α :

$$a^2 = k't \quad (3.64)$$

Eq. (3.64) represents the one-dimensional diffusion model (D1). Similarly, the three-dimensional diffusion model (D3) by *Jander* can be derived for spherical particles.¹¹⁹ Note that the three-dimensional Jander model (D3) assumes a shrinking core model, where the product layer moves towards the centre of the reacting particle. Thereby, the basic assumption for a spherical particle is derived:

$$\alpha = \frac{r_0^3 - (r_0 - x)^3}{r_0^3} \quad (3.65)$$

In addition to that, *Jander* used the parabolic law to define x , and with assuming $k' = k/r_0^2$, the Jander (D3) model is obtained:

$$x = r_0(1 - (1 - \alpha)^{1/3}) \rightarrow kt = r_0^2(1 - (1 - \alpha)^{1/3})^2 \rightarrow k't = (1 - (1 - \alpha)^{1/3})^2 \quad (3.66)$$

A more detailed version of the Jander model was expressed by *Carter* and *Valensi* whom include the volume expansion ($z = \frac{V_{product}}{V_{initial}}$) of the product layer AB into their model (D3-CV).¹²¹⁻¹²³ Compared to that, *Ginstling* and *Brounshtein* have demonstrated that the Jander model (D3) is oversimplified due to the parabolic law.¹²⁰ This assumption only holds at low product layer thicknesses x . Hence, *Ginstling* and *Brounshtein* used the steady-state solution of Fick's first law for radial diffusion in a sphere as their basic assumption and derived a three-dimensional model (D4-GB).^{120, 131}

As the shrinking core model is a special case and often the contrary phenomenon is observed experimentally, two additional basic assumptions were made. The first assumption accounts for a moving boundary which moves outward, starting from the surface of the particle. This is also known as Kirkendall effect, where the diffusing ions move towards the surface through the product layer and thus create voids at the former surface of the particle.¹³² According to that the following assumption can be defined:

$$\alpha = \frac{(r_0 + x)^3 - r_0^3}{r_0^3} \quad (3.67)$$

Based on this assumption the Anti-Jander (Anti-D3) model was derived.¹²⁴ The second assumption accounts for counterdiffusion. Here, ion A moves from the centre towards the surface and ion B from the surface towards the centre, respectively. From the assumption in eq. (3.68) a counterdiffusion model can be derived with the simplification $x_A = x_B$ and $k_A = k_B$:

$$\alpha = \frac{(r_0 + x_B)^3 - (r_0 - x_A)^3}{r_0^3} \quad (3.68)$$

In summary, three different models can be generated which are shrinking core (SC), Kirkendall effect (KE), and counterdiffusion (CD) model, respectively. Also, these models can be expressed for a two-dimensional case (D2, Anti-D2, CD2, cylindrical). In order to get further insight into the underlying mechanisms a general equation was used:¹³³

$$\frac{r_2}{r_0} = (1 - \Phi\alpha + z\alpha)^{1/n} \quad (3.69)$$

where, $\Phi \in [0,1]$ is a parameter which describes the proportion of the reacted metal volume to the core contraction (KE: $\Phi = 0$, SC: $\Phi = 1$, CD: $\Phi = 1/2$), z is the volume expansion of the product layer ($z = \frac{V_{product}}{V_{initial}}$), n the dimension (1-D, 2-D, 3-D), and α is the conversion fraction. A schematic representation of the distinct processes is given in **Figure 3.7**. In this way a differentiation between the three different diffusion mechanisms can be made. Thereby, the product layer thickness x is analysed by scanning electron microscopy (SEM) and then the ratio of the radii is plotted versus the conversion fraction α , obtained by the PXRD measurements. Finally, the experimental values are compared to the theoretically calculated models (SC, KE, CD).

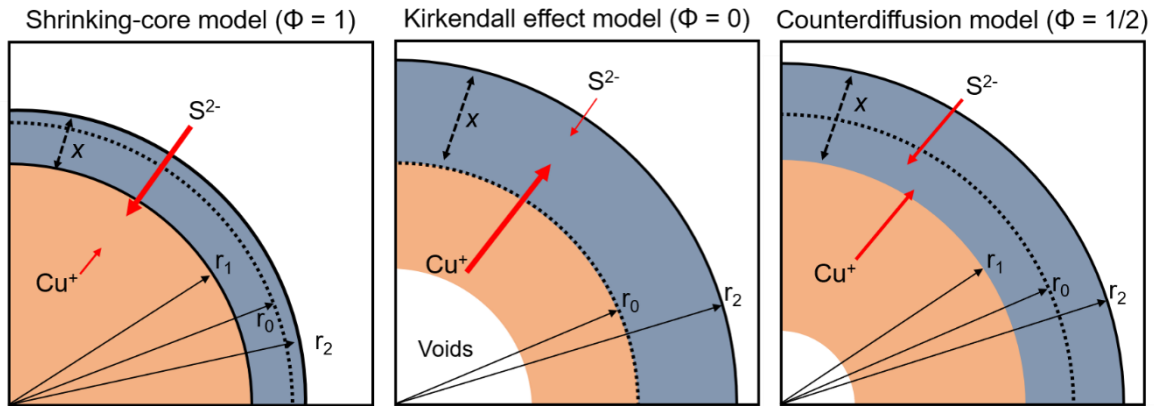


Figure 3.7: Schematic illustration of the three different diffusion mechanism which can occur in solids which are shrinking core (SC, $\Phi = 1$), Kirkendall effect (KE, $\Phi = 0$), and counterdiffusion (CD, $\Phi = 1/2$) model, respectively.

3.7.2 Geometrical Contraction/Expansion Models

The geometrical models are also called phase boundary controlled models because the chemical reaction or rather the nucleation at the surface occurs rapidly and is the rate limiting step. Therefore, the reaction rate is limited by the progress of the reaction interface, which depends on the various particle morphologies (cylindrical, spherical). As the reaction proceeds, the interface moves towards the centre (shrinking core, SC) or outwards of the centre (Kirkendall effect, KE), depending on the mobile species. For any particle eq. (3.70) holds:¹²⁵

$$r = r_0 \pm kt \quad (3.70)$$

where r is the radius at time t , r_0 is the radius at time t_0 , and k is the reaction rate constant. Here, the term kt gets negative for the SC model and positive for the KE model. Based on that, the basic assumptions for a three-dimensional SC and KE model are defined:¹²⁵

$$\text{SC: } \alpha = \frac{r_0^3 - r^3}{r_0^3} \quad (3.71)$$

$$\text{KE: } \alpha = \frac{r^3 - r_0^3}{r_0^3} \quad (3.72)$$

and with $k' = k/r_0$ the contracting sphere model (R3) and the expanding sphere model (Anti-R3) are derived (see table 4.3). Similarly, the two-dimensional models are defined. Keep in mind that the geometrical reaction models can transition towards a diffusion model. Thereby, the reaction rate is controlled by a rapid chemical reaction at the surface of the particle and thus is controlled by the interface velocity. Due to the growing product layer thickness, chemical diffusion becomes more important, which then is the rate limiting process, see **Figure 3.8**.

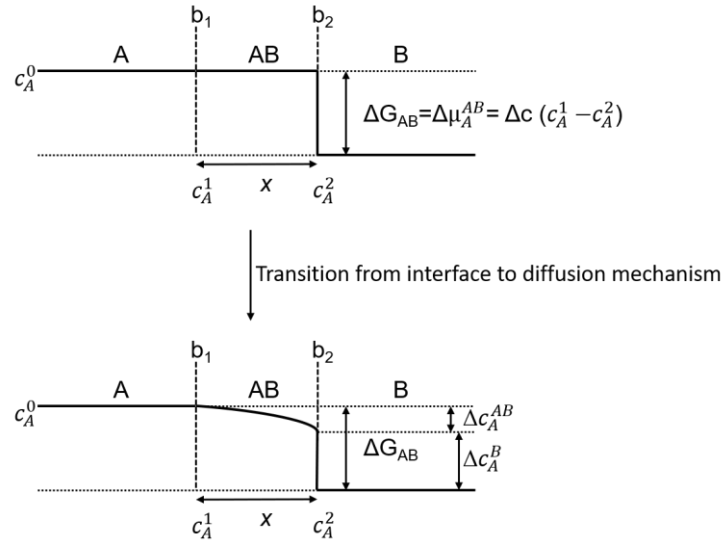


Figure 3.8: Schematic concentration profiles of a phase boundary controlled reaction model (top), which transitions towards a diffusion controlled reaction model (bottom).

Note that the particle size is incorporated in the reaction rate constant k' of the phase boundary and diffusion-controlled models. Therefore, the particle size distribution and the particle shape will have a significant impact on the reaction rate constant. In general, this leads to a shift in the α - t plots.

3.7.3 Nucleation & Growth Models

Nucleation and growth models account for both the nucleation at the surface of a particle and nuclei growth rate. After the formation of a nucleation germ, the nucleation germ grows, and the nucleation rate is thereby different from the growth rate. A prominent version of these models are the Avrami-Erofe'ev models.¹²⁶⁻¹²⁸ These models are widely applied due to their versatility to describe crystallization, crystallographic phase transitions, precipitation, decomposition, adsorption,

hydration, and desolvation. The foundation for nucleation is the fluctuating energy within the crystal or on the surface. Therein, nucleation is the first step which is favoured at impurity and defect sites as well as edges, corners, and grain boundaries. These so-called nucleation sites are characterized by their lowered activation energy. Consequently, small metastable aggregate can form at these sites. When the critical radius is reached and the free Gibb's energy gets negative, a stable nucleation germ is formed. Thereby, the nucleation models can be divided into single- or multistep nucleation rate models. The single-step models assume that the nucleation and the growth of the nuclei occur in a single step. Here, N_0 nucleation sites are available and a number of nuclei N form and subsequently grow.¹¹⁴

$$\frac{dN}{dt} = k_N N_0 e^{-k_N t} \quad (3.73)$$

Here, k_N is the nucleation rate constant. Note that the rate of nucleation is approximately constant if k_N is small and thus results in a linear nucleation rate. Compared to that, when k_N is small, all nucleation sites are instantly occupied which yields an instantaneous nucleation rate. The multistep nucleation models account for both, the nucleation and growth of the nucleus to occur at two different steps. The basis of this concept is, that a small unstable germ nucleus forms and may revert to the reactants or grow further to form a growth nucleus. This leads to eq. (3.78), also called the power law of nucleation.¹¹⁴

$$\frac{dN}{dt} = \left(\frac{N_0 (k_i t)^\beta}{\beta!} \right) \beta t^{\beta-1} \quad (3.74)$$

where N is the number of nuclei formed at time t , N_0 the available nucleation sites, β the successive events required to form a growth nucleus, and k_i the probability to form a growth nucleus. Further, the growth of the nuclei can be defined by the volume through the general expression:¹¹⁴

$$V(t) = \int_0^t \sigma \left(\int_0^t G(x) dx \right)^\lambda \left(\frac{dN}{dt} \right)_{t=t_0} dt \quad (3.75)$$

where, $V(t)$ is the volume of all growth nuclei, σ the nucleus shape ($4\pi/3$ for a sphere), $G(x)$ the nucleus growth rate, λ the growth dimension ($\lambda = 1, 2, 3$), and dN/dt the nucleation rate. The universal eq. (3.75) can be modified with the different nucleation rates dN/dt to account for a single-step or multistep nucleation model.

The Avrami-Erofe'ev models are based on a single-step nucleation and growth mechanism, and additionally include growth restrictions. There exist two distinct growth restrictions, which are ingestion and coalescence, see **Figure 3.9**.¹²⁶⁻¹²⁸

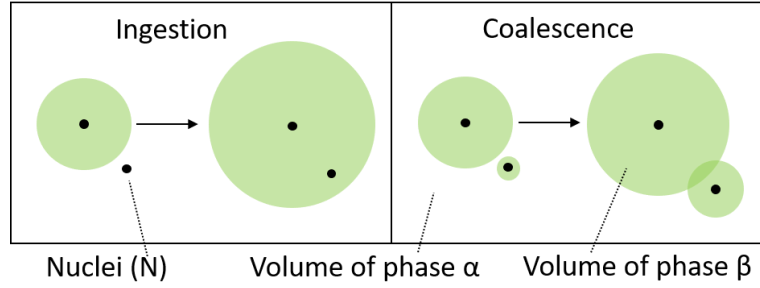


Figure 3.9: Schematic representation of the two distinct growth restrictions which occur in the Avrami-Erofe'ev models. Ingestion is the inclusion of a potential nucleation site. Coalescence is the loss of product interface when two nuclei merge into each other.

Ingestion is the inclusion of a potential nucleation site by the growth of a nucleus. These are called “phantom nuclei”. Coalescence is the loss of product interface when the interface of two or more growing nuclei merge into each other. Due to these growth restrictions an extended conversion fraction α' is required which gives :

$$d\alpha' = \frac{d\alpha}{(1 - \alpha)} \quad (3.76)$$

where, α' is the extended conversion fraction. Based on that, the Avrami-Erofe'ev models have been developed (A2-A4). These Avrami-Erofe'ev models are also called the JMAEK models. This goes back to the scientists who contributed to the development of these models and stands for Johnson, Mehl, Avrami, Erofe'ev, and Kolmogorow.¹³⁴ These models are characterized by their sigmoidal shape in the α - t plot, which comprises a nucleation, growth, and decelerating part, which originates from the growth restrictions.

Similar to that, the power law models (P2-P4) can be derived with the nucleation rate defined in eq. 4.31. In comparison to the Avrami-Erofe'ev models, the power law models do not include growth restrictions and therefore show an exponential behaviour in the α - t plot.

3.7.4 Reaction-Order Models

Order-based models are the most simplistic approach to solid-state kinetics, which originate from homogenous kinetics. In the order-based approach, the reaction rate is proportional to the conversion fraction α raised to a specific power, which is the reaction order. The basic assumption for order-based model is defined as:

$$\frac{d\alpha}{dt} = k(1 - \alpha)^n \quad (3.77)$$

where $d\alpha/dt$ is the reaction rate, k is the reaction rate constant, and n is the reaction order (integral, fractional). When n is 0, the zero-model is obtained (F0/R1). If $n = 1, 2, 3$ the first-order model (F1), second-order model (F2), and third-order model (F3) are obtained after separating the variables and integrating.

3.7.5 Johnson-Mehl-Avrami-Erofe'ev-Kolmogorow (JMAEK) Method

For the mechanistic and kinetic analysis, three different methods are applied. The first method is the Johnson-Mehl-Avrami-Erofe'ev-Kolmogorow^{126-128, 134} (JMAEK) approximation. This equation is commonly used to describe the kinetics of heterogenous isothermal phase transformations in solid state reactions. The JMAEK equation is a phenomenological model based on the following assumptions:¹³⁴

- i. nucleation and growth of a new phase occurs at isothermal conditions
- ii. nuclei of the new phase are distributed randomly
- iii. the growth rate of the new phase depends only on temperature
- iv. impingements of growing particles of the new phase are non-existent

The relation of the conversion fraction α of the new phase on time t at isothermal conditions can be expressed as (JMAEK equation, eq. (3.78)):

$$\alpha(t) = 1 - e^{-(kt)^n} \quad (3.78)$$

where n is the Avrami exponent and k is the kinetic rate constant. The value of the Avrami parameter is given by the relation:¹³⁵⁻¹³⁷

$$n = d \cdot m + a \quad (3.79)$$

where d is the dimension of the phase growth (1-D, 2-D, 3-D), m is dependent on the type of growth (interface control = 1, diffusion control = $\frac{1}{2}$) and a is related to the nucleation rate and can have fractional values (nucleation is absent/pre-existent site saturation = 0, constant nucleation/continuous nucleation = 1). Further, the Avrami exponent n can continuously increase during a transformation for increasing nucleation rates and decrease for decreasing nucleation rates, respectively.¹³⁸ Hence, the resulting values for the Avrami parameter n are a combination of these quantities and can have fractional values. Also, the Avrami exponent should be constant if the reaction mechanism stays constant throughout the whole reaction.¹³⁸ Due to a range of deviations from JMAEK kinetics which are observed in parabolic growth and linear growth transformations, a modified version of the JMAEK approximation was applied, in addition to the original JMAEK equation, to fit the experimental data. The modified equation has been developed by *Starink* and *Zahra*, see eq. (3.80).^{139, 140} The Starink-Zahra equation is more flexible than the original JMAEK model but also encompasses JMAEK kinetics.¹³⁹⁻¹⁴¹ Therefore, better experimental fits are obtained.

$$\alpha(t) = 1 - \left[\frac{(kt)^{n_A}}{n_i} + 1 \right]^{-n_i} \quad (3.80)$$

Here, k is the kinetic rate constant and n_A is the Avrami exponent, which are both akin to the parameters in eq. (3.78). Thereby, n_i ($(n_i = 1/\lambda_i - 1)$, with λ_i a positive constant) is the newly introduced parameter and is called the impingement factor.^{139, 140} This impingement factor accounts for deviations from the ideal preconditions for the JMAEK approximation, and also includes the JMAEK equation if $n_i \rightarrow \infty$. Deviations from the preconditions include:^{139, 140}

- i. capillary effect (Gibbs-Thomson effect, interfacial energy)
- ii. vacancy annihilation due to defects (especially at grain boundaries)
- iii. blocking due to anisotropic growth
- iv. impingement on defects, inclusions and interfaces

Hence, the Starink-Zara equation is used if such deviations are indicated by the experiment or a poor fit of the JMAEK equation. However, caution should be exercised if the Starink-Zara equation is applied, as the incorporation of an additional fitting parameter can lead to a variation of the Avrami parameter n_A . As mentioned above, the Avrami exponent n_A can change during a transformation. Keep in mind that the Avrami parameter n_A obtained from a fit of the JMAEK and Starink-Zahra equation is a mean value over the whole experimental range and can include several mechanisms. Therefore, the JMAEK approximation is also applied in its linearized form for a more detailed analysis to distinguish between different mechanisms within the whole transformation range.¹²⁹

$$-\ln \ln(1 - \alpha) = n \ln(k) + n \ln(t - t_0) \quad (3.81)$$

The Avrami exponent n_A is thereby determined by plotting $-\ln \ln(1 - \alpha)$ against $\ln(t)$, known as Sharp-Hancock plot (SH-plot), see **Figure 3.10**.¹²⁹ The slope of this linear plot gives the exponent n and the intercept of the y-axis yields the kinetic rate constant k . The advantage of this method is that more than one linear part in the SH-plot indicates more than one uniform mechanism and implies a change of mechanism during the conversion which means the Avrami exponent n changes throughout the whole process. Further, the induction time t_0 is subtracted for the analysis, as the exponent n is highly dependent on the chosen incubation time t_0 . Finally, the Avrami exponent n is related to commonly used solid-state reaction models, see table 4.3.^{114, 129} For each group of mechanistic assumptions, typical values of the Avrami exponent n were determined experimentally: ≈ 0.5 for diffusion control, ≈ 1 for interface control, $\approx 2/3/4$ for nucleation & growth control.¹²⁹ However, diffusion controlled reactions can also have values of 1.5/2/2.5 for higher dimensions and continuous nucleation.¹³⁵ Note that the Avrami exponent n deviates from a linear slope above 50 wt% conversion except for the Avrami-Erofe'ev models (A2-A4). Therefore, the ideal range for the analysis is from 0 to 50 wt% conversion. Above this range a differentiation between the respective mechanistic groups is difficult and requires precise experimental data.

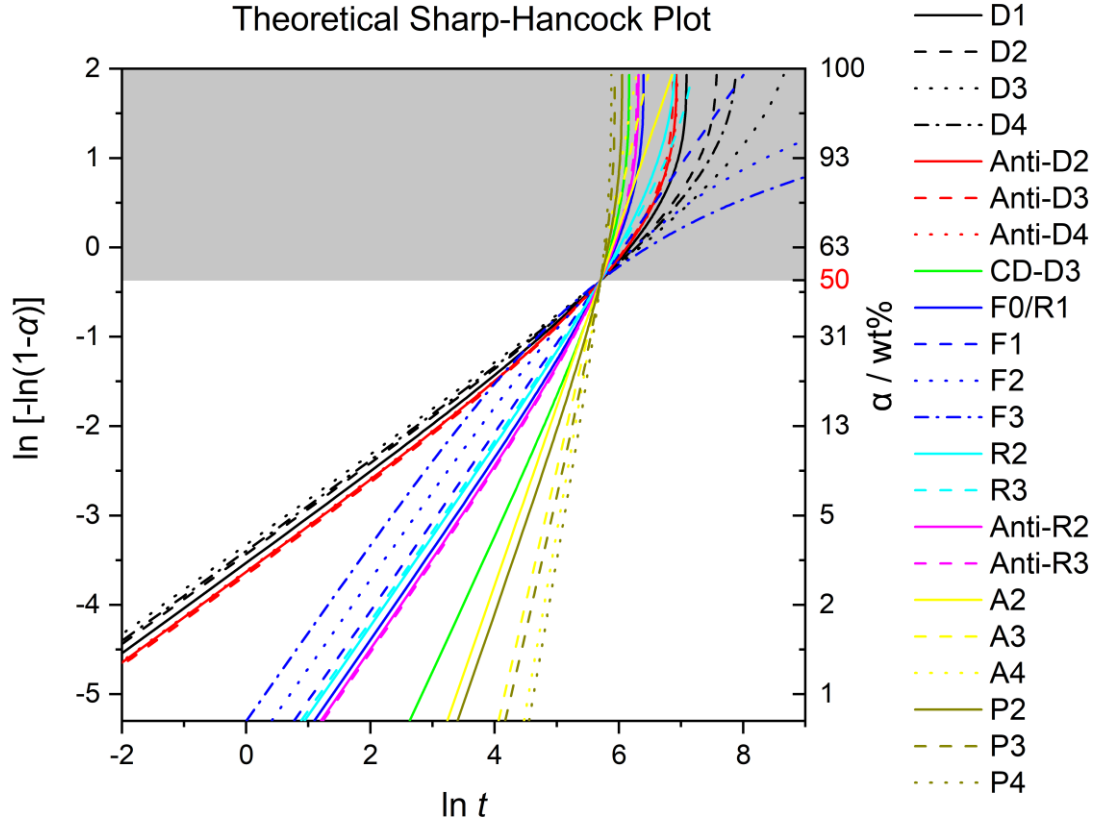


Figure 3.10: Theoretical SH-plot with the calculated slopes for the different reaction models. The slopes can be divided into four groups: diffusion, reaction-order, geometrical, nucleation. Note that the theoretical curves deviate from a linear slope above 50 wt% conversion except for the Avrami-Erofe'ev models (A2-A4).¹²⁹

3.7.6 Isoconversional Methods

The second method is a model-free method. These are also called isoconversional methods and the basic principle is that the reaction rate at constant conversion fraction is a function of temperature. The advantage of that method is that no modelistic assumption is required for the kinetic analysis and the activation energy E_a can be calculated at any conversion fraction α . The theoretical foundation for the isoconversional methods is given by the differential and integral rate laws:

$$\frac{d\alpha}{dt} = Ae^{-\frac{E_a}{RT}} \cdot f(\alpha) \quad (3.82)$$

$$g(\alpha) = Ae^{-\frac{E_a}{RT}} \cdot t \quad (3.83)$$

From both expressions, an isoconversional method can be derived. From the differential rate law, Friedman's method is obtained by a plot of $\ln(d\alpha/dt)$ versus $1/T$ at a specific α :¹⁴²

$$\ln\left(\frac{d\alpha}{dt}\right) = \ln(A \cdot f(\alpha)) - \frac{E_a}{RT} \quad (3.84)$$

If the integral rate law is used as basis, the standard integral isoconversional method is obtained by a plot of $-\ln t$ versus $1/T$ at a specific α :¹⁴³

$$-\ln t = \ln \left(\frac{A}{g(\alpha)} \right) - \frac{E_a}{RT} \quad (3.85)$$

Thereby, the frequency factor A and the activation energy E_a are generally assumed to be constant throughout the whole reaction process. However, it was shown that E_a and A can vary during the process due to more complex reactions in solid-state kinetics.^{144, 145} The advantage of the isoconversional methods is that it can reveal such variations of E_a in the Arrhenius plot regardless of the underlying mechanisms. Here, a deviation from a linear behaviour in the Arrhenius plot is attributed to more than one mechanism (chemical or physical) and indicates a more complex reaction. Thus, solid-state kinetics can be identified as single-step kinetics (no variation in E_a , one kinetic triplet) or a more complex system such as multistep kinetics (variation in E_a , more than one kinetic triplet).¹⁴⁶ However, such variations of the activation energy E_a can be artifactual depending on the used isoconversional method, especially at low conversion fraction α .¹⁴⁶ Therefore, a combination of model-fitting methods and model-free methods is required to obtain the kinetic triplet $g(\alpha)$, E_a , and A in order to fully describe the kinetics in solid-state reactions.

3.7.7 Master Plots

The third method is a graphical analysis which employs master plots (also called reduced time plots) for a mechanistical comparison between different experimental curves.¹⁴⁷⁻¹⁴⁹ By this method, the concept of a general time θ is introduced. In this thesis, a reference point at $\alpha = 0.5$ is used and therefore θ is the time at 50% conversion. Herein, two different master plots are used. First, is a master plot based on the differential form $f(\alpha)$:¹⁴⁸

$$\frac{d\alpha/d\theta}{(d\alpha/d\theta)_{\alpha=0.5}} = \frac{f(\alpha)}{f(0.5)} \quad (3.86)$$

Thus, the theoretical master plot can be derived from $f(\alpha)/f(0.5)$ versus α . Similar to this is the second master plot, which is based on the integral form $g(\alpha)$ and is defined as:¹⁴⁸

$$\frac{\theta}{\theta_{\alpha=0.5}} = \frac{g(\alpha)}{g(0.5)} \quad (3.87)$$

Eventually, the master plot can be derived from $g(\alpha)/g(0.5)$ versus α . Note, that these expressions are only valid for isothermal conditions. Further, the functions in both master plots coincide at $\alpha = 0.5$. However, there are distinct ranges where the functions of the different reaction models can be clearly distinguished. In the range $\alpha < 0.5$ the differential master plot shows the best allocation and in the range $\alpha > 0.5$ the integral master plot dominates. Thus, to determine the best agreement with the kinetic models, both master plots are used to investigate the whole reaction process. The theoretical master plots in differential form $f(\alpha)$ and the integral form $g(\alpha)$ are shown in **Figure 3.11**. Note that

the theoretical curves in the integral form $g(\alpha)$ show the same behaviour compared to α - t curves, but in a reduced time scale. Keep in mind that, despite each respective kinetic analysis method offers some advantage, only a combined kinetic study permits a meaningful description of the underlying mechanism. Also, the kinetic studies must be combined with additional experimental techniques like SEM or EBSD to gain detailed information about the involved mechanisms.

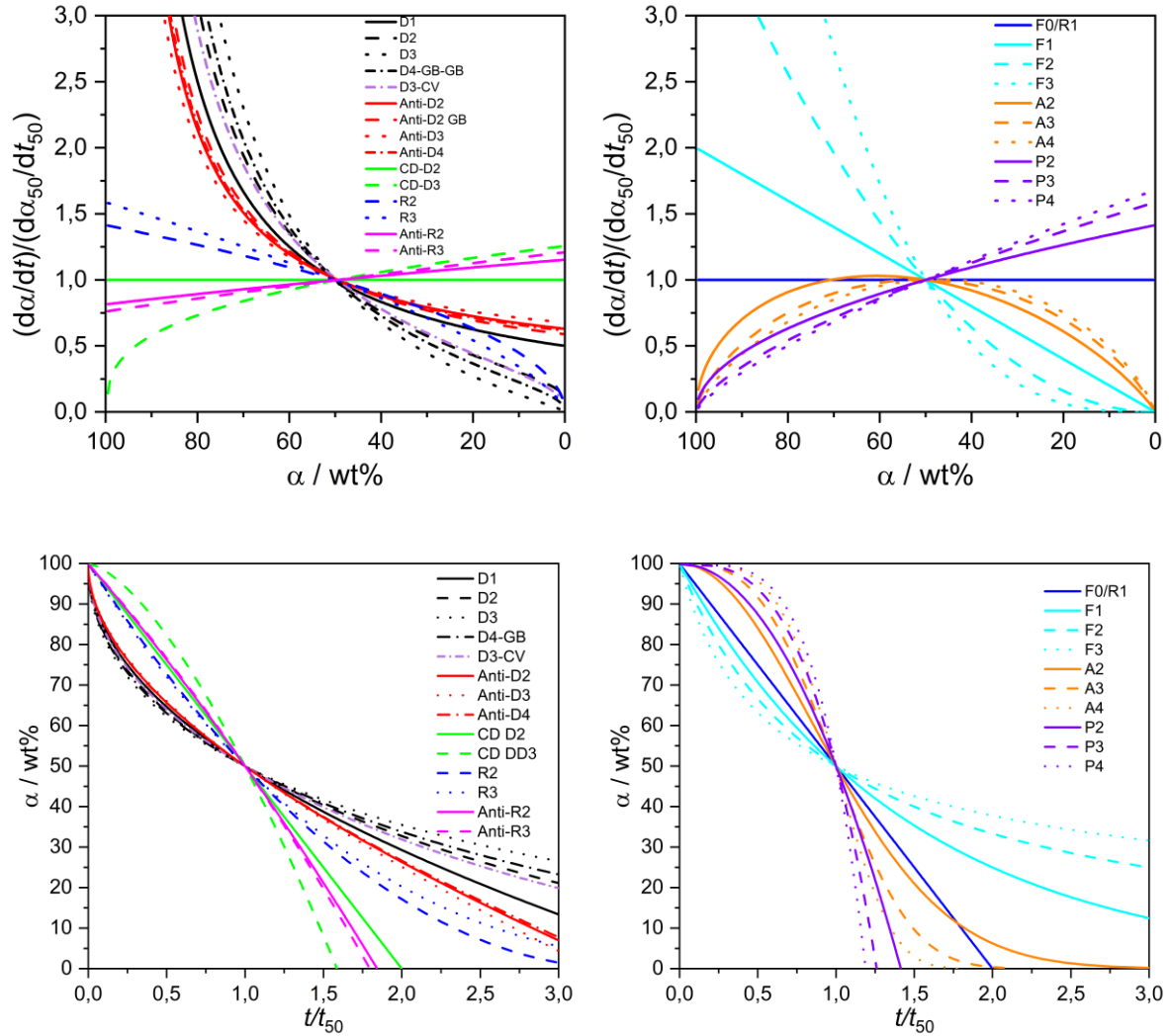


Figure 3.11: Theoretical master plots $f(\alpha)$ (top) and $g(\alpha)$ (bottom) for the different reaction models. A differentiation between the models in the range $\alpha < 0.5$ is better with the differential master plot. Compared to that, the integral master plot is more suitable in the range $\alpha > 0.5$. Also, a differentiation between the different mechanistic assumptions can be made but an allocation within a mechanistic group (i.e. diffusion, D1-D4) requires precise experimental data.

4 General Experimental

4.1 Methods

4.1.1 Electrochemical Impedance Spectroscopy (EIS) and Polarization

The electrochemical impedance spectroscopy (EIS) spectra and the polarization experiments were recorded on a Zahner IM6 which was upgraded to a Zahner Zennium potentiostat. The equipment is located outside the argon glove box. Within the glove box a tubular furnace was used to heat the cell. The temperature of the oven and thus within the cell was controlled with an Eurotherm2404 control unit. The cell itself is connected to the potentiostat with 4 different measuring cables at the CE (counter electrode), RE (reference electrode), TE (test electrode) and TES (test electrode sense) port. Note that these 4 cables are twisted to prevent inductive contributions of the cables during the measurements. Also, the thermo cable and the measuring cables are connected from within the argon glove box to the control units outside of the glove box. The measurement cell is constructed within a hollow glass cylinder and consists of banana plugs (Cu) which are connected to platinum wires, see **Figure 4.1**. At the end of the platinum wire a platinum sheet is attached which connects to the sample. Outside of the platinum sheets corundum pellets are attached to insulate the cell. Also, metal springs are used to compress the cell and ensure good electrical contact within the sample cell arrangement. The idle capacity of the cell is ca. 12 pF and the ohmic resistance of the short-circuited cell is about 0.5 – 0.8 Ω . The *ThalesFlink* software was used to control the measurements and to adjust the open current potential of the cell and the temperature program.¹⁵⁰ Finally, the *Zahner Analysis* software (Version 2.9.2) was used to evaluate the data.¹⁰³

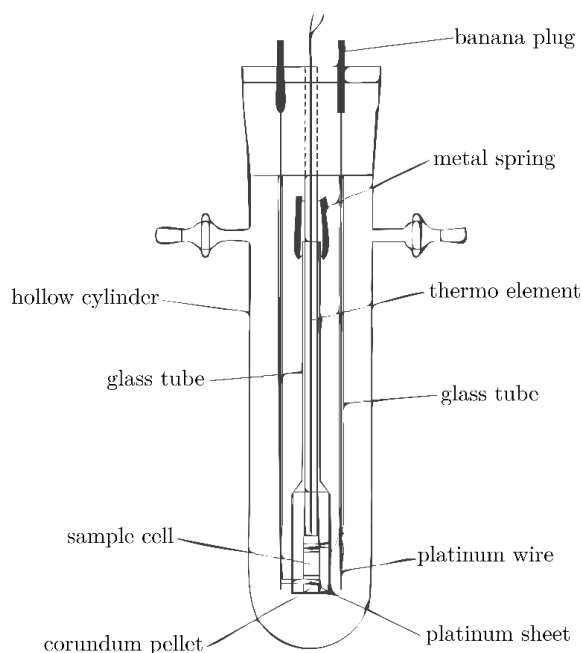


Figure 4.1: Assembly of the cell for the electrochemical measurements.

4.1.2 Powder X-ray diffraction (PXRD)

Powder X-ray diffraction was used as standard method to characterize the samples. In this work, all measurements were performed on a Stoe STADI P powder diffractometer. The two monochromated (Ge single crystal) X-ray sources Cu- $K_{\alpha 1}$ ($\lambda = 1.540598 \text{ \AA}$) and Mo- $K_{\alpha 1}$ ($\lambda = 0.70930 \text{ \AA}$) were used to measure the samples. A Dectris Mythen 1K CCD-detector ($\Delta\theta = 0.015^\circ$, $2^\circ \leq 2\theta \leq 126^\circ$) was used for the collection of the intensities and all samples are measured in transmission geometry. The air-stable samples are ground in an agate mortar and then fixed between two polyethylene foils with a small amount of silicon grease on a flatbed carrier. The air-sensitive samples were measured in sealed glass capillaries (quartz- or borosilicate glass with a diameter of 0.3 – 0.5 mm). The detailed experimental procedure will be explained in the respective chapter.

The powder X-ray diffraction measurements at high temperatures were measured in a heatable STOE capillary graphite oven 0.65 (max. heat rate $50^\circ\text{C}/\text{min}$, Eurotherm 24.16 controller, $\Delta T = \pm 1^\circ\text{C}$) up to a temperature of 250°C . Note, that all measurements were performed at isothermal conditions. Before the measurements, the oven was calibrated with a NH_4NO_3 and an $\alpha\text{-Si}$ standard. The measurement window is 5 mm wide and 65 mm from the top end of the capillary which means that there are $\approx 5\text{-}15$ mm to the bottom end of the capillary. Due to the architecture of the oven, only small glass capillaries can be inserted into the vertical graphite oven and are therefore measured in Debye-Scherrer geometry, see **Figure 4.2**. All glass capillaries were flame-sealed before the measurement. For the high temperature measurements solely Mo- $K_{\alpha 1}$ -radiation was used. The *WinX^{POW}* software package was used to control the oven and to adjust the temperature progression.¹⁵¹

For the analysis of the powder patterns the program packages *WinX^{POW}* from STOE & Cie and *Match!* from Crystal Impact were used.^{151, 152} Further, the COD and ICDD-PDF-2 databases were used for phase identification and analysis of the powder patterns. The indexation of the reflections in the powder pattern was realized with the indexation algorithms TREOR,¹⁵³ ITO,¹⁵⁴ DICVOL¹⁵⁵. Also, the powder patterns were analysed with *Jana2006*.¹⁰⁹ In particular, LeBail fits and Rietveld refinements were performed with *Jana2006*. Therefore, the cell-, background-, and profile parameters as well as the peak asymmetry was refined using the least squares method until a good fit of the calculated powder pattern compared to the measured powder pattern was accomplished. Also, the mass absorption coefficients μ^* are determined from the pure external standards through Rietveld analysis.

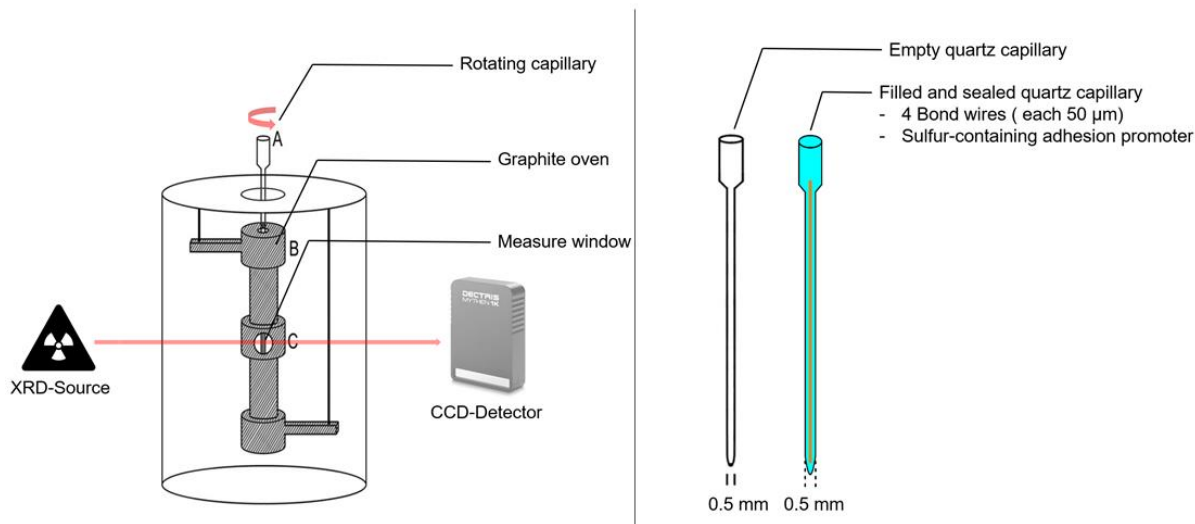


Figure 4.2: Experimental setup for the high-temperature measurements (left side). Here, a graphite oven is used wherein a small quartz capillary is inserted. Also, the sample rotates during the measurement to ensure a good statistical distribution. On the right side, a typical bond wire experiment is shown with 4 bond wires (each with a diameter of 50 μm) in the quartz capillary, filled up with sulfur-containing adhesion promoter.

4.1.3 Scanning Electron Microscopy (SEM) and Energy Dispersive X-ray Spectroscopy (EDX)

In order to analyse the morphology of the samples three different scanning electron microscopes (SEM) and energy dispersive X-ray (EDX) spectroscopes were used. This is due to the different facilities where the measurements were conducted.

The scanning electron microscope (SEM) which was used at the University of Regensburg is a Zeiss EVO® MA 15 for ultra-high vacuo and variable pressure in combination with a LaB₆ cathode. The software Zeiss SmartSEM (Version 6.02) was used to control the microscope and to conduct the analyses. For the energy dispersive X-ray spectra, a Bruker Quantax 200 – Z30 (30 mm², Xflash 630) was used in combination with the Bruker Quantax ESPRIT (Version 2.1) software.

The scanning electron microscope used at the Fraunhofer IMWS in Halle is a Zeiss Supra 55VP. For the EDX-analyses an AMETEK-EDAX Octane Elite + SDD was operated with a Team software.

At Infineon Technologies AG Regensburg, two different SEM's were used. The first one is a ZEISS GeminiSEM 500 with a thermal field emission gun and the second one is a Hitachi SU8010 with a cold cathode field emission source.

Keep in mind that the EDX analysis allows the determination of the elemental composition of the material of interest. However, the information depth amounts to several micrometers depending on the used voltage. Also, the information is obtained from a pyriform area underneath the surface. Therefore, the composition can deviate from the true value depending on the sample composition.

4.1.4 Electron Backscatter Diffraction (EBSD)

To gain further information on the grain size distribution and grain orientation electron backscatter diffraction (EBSD) was performed. Here, an EDAX Pegasus EDX/EBSD-system attached to a Zeiss Ultra 55-FE-SEM microscope was used in combination with a Hikari XP EBSD Camera. The EBSD analyses were performed at Infineon Technologies AG in Regensburg.

4.1.5 Nuclear Magnetic Resonance (NMR) Spectroscopy

All NMR spectra were measured at ambient temperature using a Bruker Avance 300 (300 MHz) NMR spectrometer. All chemical shifts are reported in δ scale as parts per million (ppm) relative to the solvent peak as internal standard.

4.1.6 Thermogravimetric Analysis with FT-IR (TGA/FT-IR)

Thermogravimetric analysis coupled with fourier transform infrared detection (TGA/FT-IR) was used to study the thermal stability and decomposition products of organic compounds. The TGA/FT-IR measurements were performed at Infineon Technologies AG on a Netzsch TG Libra 209F1 (TGA) coupled with a Bruker Vertex 70 (FT-IR). The samples were measured in a corundum crucible which was purged with nitrogen during the analysis. Thereby, the sample was heated from 25 °C to 600 °C with a heating rate of 20 °C/min. After the measurement, the respective spectra were analysed with the help of the NIST/EPA Vapor-Phase IR Library.

4.2 Materials

4.2.1 Cu Bond Wires

In this thesis bare Cu wire and various coated Cu bond wires are used. Here, an overview about the initial state of the used bond wires is given, see **Table 4.1**. In chapter 8 only bare Cu wire is used in combination with different adhesion promoter. In chapter 9 all wire types are compared versus selected adhesion promoters. Then the bare Cu and APC wire are examined in detail in chapter 11 at various temperatures.

Table 4.1: Overview of the different used Cu bond wires.

Wire type	Core	Coating 1 / nm	Coating 2 / nm	d / μm
Bare Cu	Cu	-	-	50
PCC	Cu	Pd / ≈ 80 nm	-	50
APC	Cu	Pd / ≈ 60 nm	Flash-Au / ≈ 10 nm	50
APCX	Cu + dopant X	Pd / ≈ 60 nm	Flash-Au / ≈ 10 nm	50

Here, bare Cu wire is used with 99.99 wt% Cu. This is also valid for the Cu core in PCC and APC wire. Note that the PCC (≈ 80 nm) wire is solely coated with a Pd-coating whereas the APC and APCX wire is coated with a Pd-coating (≈ 60 nm) and an additional Flash-Au (≈ 10 nm) layer on top of the Pd-coating. In addition to that, the APCX wire comes with additive elements in the Cu core of about ≈ 1.5 wt%. In **Figure 4.3** the SEM and EBSD pictures are shown for the cross-sections and wire surfaces for all initial wire types. It is striking that the surface of the bare Cu wire shows a larger number of defects compared to the coated Cu wires. Nonetheless, some defective spots are also observed for all coated Cu wire variants. Also, the grain sizes on the surface of the Cu wire are larger than on the surface of the coated wires and show random orientation distribution. For the coated Cu wires, the surface exhibits smaller grain sizes with an anisotropic, longitudinal alignment of the grains along the wire surface. Thereby, the surface of the PCC, APC, and APCX wire is mostly comprised of Pd(101) surface. Further, the grain orientation within the bare Cu wire is randomly distributed. Contrary to that, the grains in the Cu core of the PCC wire show a preferred orientation of the [100] direction in EBSD measurements, which is in line with PXRD measurements, see **Figure 4.4**. Whereas the Cu core of the APC and APCX is mostly comprised of grains with [101] direction and grains with [111] direction have nearly vanished, see **Figure 4.5**. This is also verified by PXRD and through the semi-quantitative analysis via the Lotgering factor. Texture effects are important features as the interactions between the metal surface and the sulfur molecule depends among others on the exposed surface of the metal. For instance, the sulfur molecule may adsorb more strongly on Cu(111) than on a Cu(101) surface. Consequently, the reaction may be accelerated by the enhanced adsorption on the surface.

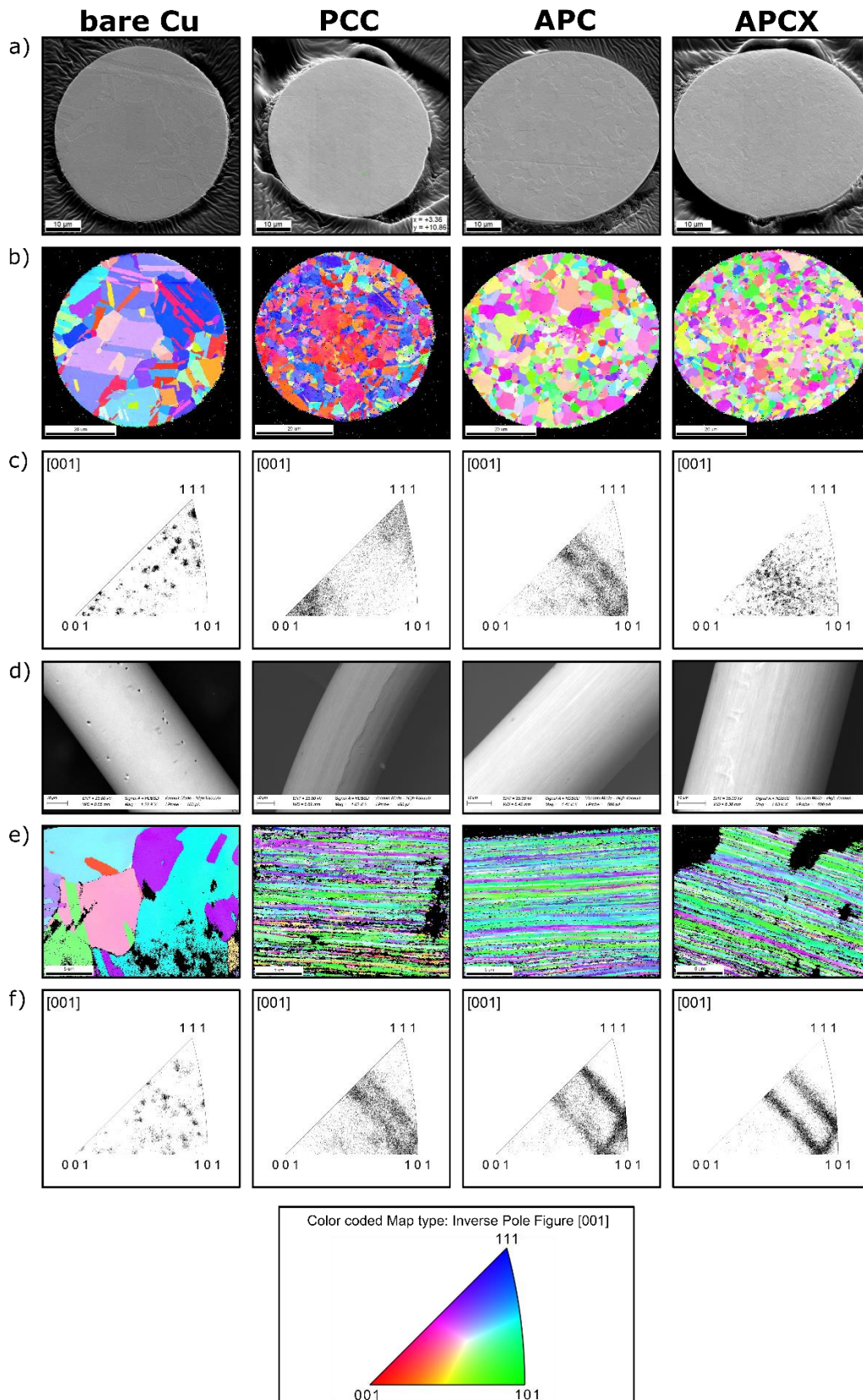


Figure 4.3: Overview of the different wire types; bare Cu, PCC, APC, APCX: a) SEM pictures of the cross-sections, b) EBSD of cross-sections, c) Grain orientation distribution at the cross-sections, d) SEM pictures of the wire surface (Recorded at the University of Regensburg), e) EBSD of the wire surface, f) Grain orientation distribution on the wire surface. All measurements were made at Infineon Technologies AG, except of the SEM pictures of the surface (d).

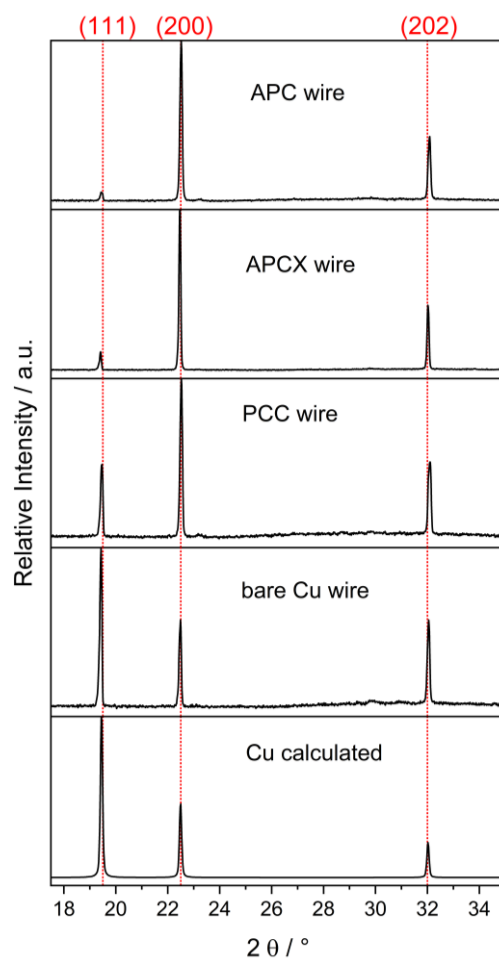


Figure 4.4: Powder patterns of the four different Cu bond wires (top) and the calculated powder pattern for randomly distributed Cu powder (bottom). Note that the bare Cu bond wire shows no preferred orientation whereas the coated Cu bond wires show a preferred orientation of the [200] and [202] directions. Also, the texture effects are even more pronounced for the Flash-Au coated wires. There, the (111) reflection has nearly vanished.

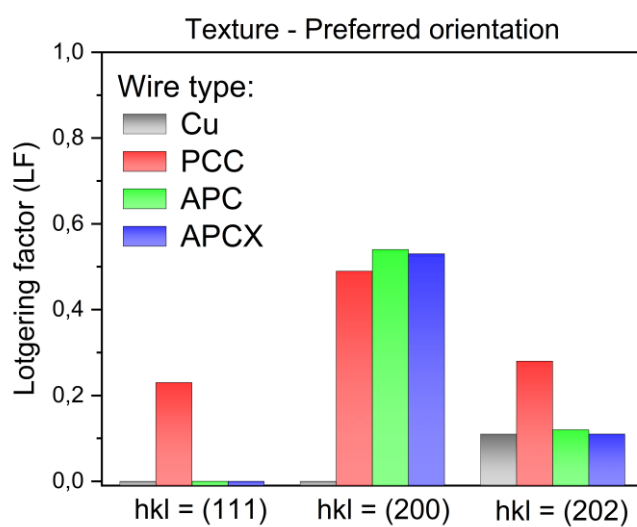


Figure 4.5: Semi-quantitative analysis of the PXRD patterns of the initial wires via the Lotgering factor (LF). Note that the PCC wire exhibits more of the (111) reflection, whereas the APC and APCX wire show a preferred orientation of the (200) reflection.

Another crucial feature is the grain size distribution of the Cu bond wire. As mentioned above, the Pd-coating exhibits small, elongated grains compared to randomly distributed bare Cu wire grains. The random distribution of the grains is also true for the Cu core of the bare Cu wire. Also, the grain sizes of the bare Cu wire are much bigger compared to the grains within the Cu core of the coated bond wires, see **Figure 4.6**. Here, the grain size distribution of the Cu bond wires decreases in the order: Cu > APC > PCC > APCX. Besides texture effects, grain size distribution is a crucial element with regard to the reactivity of the bond wires. If the bond wire is comprised of smaller grains, the grain boundary volume is higher relative to the whole wire volume. As grain boundary diffusion is faster than bulk diffusion, this may lead to an increased ion flux through the material or on the surface. Hence, the reactivity may be strongly influenced by the grain size distribution.

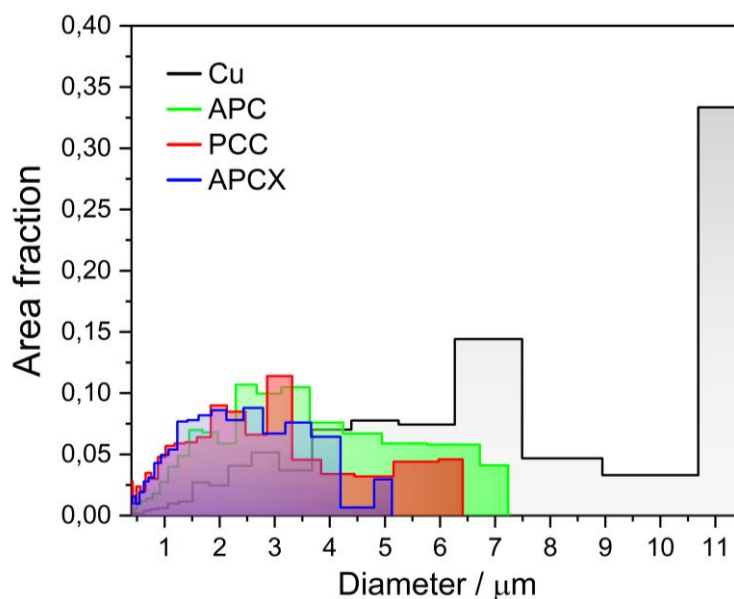


Figure 4.6: Grain size distribution for the different Cu bond wires obtained from EBSD measurements. The bare Cu wire is comprised of much bigger grains than the coated Cu wires. Then, the grain size of the Cu bond wires decreases in the order: Cu > APC > PCC > APCX.

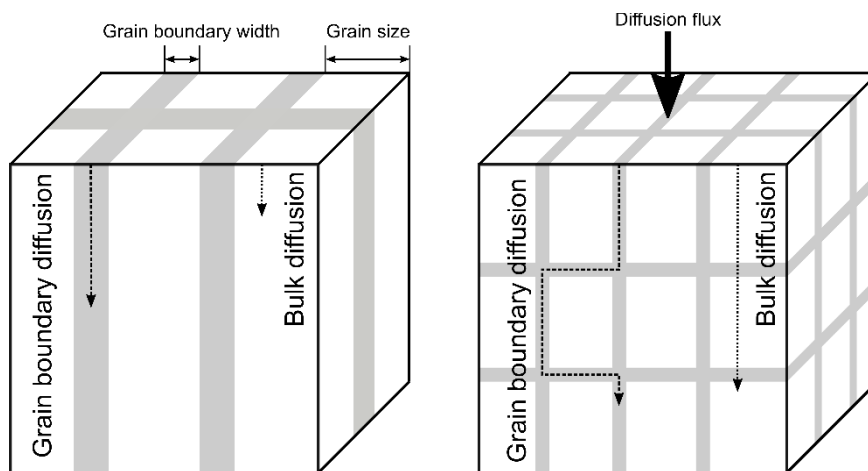
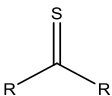
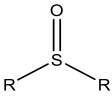
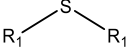
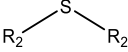
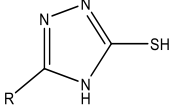
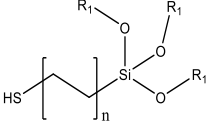
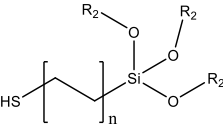





Figure 4.7: Schematic illustration of grain boundary diffusion and bulk diffusion. In general, grain boundary diffusion is faster and smaller grain sizes may lead to a significant increase of ion diffusion through the material.

4.2.2 Organic Sulfur Compounds

In this thesis, several organic sulfur compounds are used to study the corrosion behaviour of these compounds at elevated temperatures. In **Table 4.2** all the different sulfur compounds are summarized. Note, that the di-, tri-, tetrasulfide is a mixture consisting of 84 % disulfide, 12 % trisulfide and 4 % tetrasulfide (**Figure A. 8.1**). Also, a measurement with a bare Cu bond wire in an unsealed capillary under ambient air conditions (O_2) was performed to compare the reactivity of the organic sulfur compounds with well-researched oxygen corrosion.

Table 4.2: Overview of all organic sulfur compounds (and O_2) which are used in this thesis for the corrosion experiments. Note that mercaptosilane 1, triazole-thiol, and the disulfide are the most frequently used S-compounds.

Organic sulfur compound	Abbreviation S-compound	Aggregation state	Melting Point / °C	Boiling Point / °C	S-moiety
Thioketone	TK	solid	204		
Sulfoxide	SO	liquid		189	
Thioether 1	TE1	liquid		190	
Thioether 2	TE2	liquid		296	
Triazole-thiol	TT	solid	>300		
Mercaptosilane 1	MS1	liquid		214	
Mercaptosilane 2	MS2	liquid		210	
Oxygen	O2	gaseous		-183	
Disulfide	DS	liquid		230	
Di-,Tri-, Tetrasulfide	DTTS	liquid		360	

5 Literature Review of the Cu-S System

5.1 Abstract

In this chapter, the binary phase diagram Cu-S and its relevant stoichiometric composition ranges are discussed. First, the low chalcocite α -Cu_{2-x}S and high chalcocite β -Cu_{2-x}S are highlighted, which exhibit an extremely narrow composition range with Cu_{2-1.993}S and Cu_{2-1.988}S, respectively. Further, it is hypothesized that the high chalcocite β -Cu₂S behaves like a “solid-liquid hybrid phase” with high Cu ion diffusion. Eventually, emf measurements are reviewed and their potential application to determine the composition in Cu_{2-x}S as a function of cell potential is discussed. Finally, different experimental methodologies to study the diffusion behaviour of Cu_{2-x}S are briefly compared before discussing the electrochemical properties of Cu_{2-x}S with regard to the available literature data. Here, special attention is given to electrical and ionic conductivity as well as self-diffusion and chemical diffusion coefficients as a function of both composition and temperature.

5.2 Introduction

In the past, as well as many recent investigations dealt with the Cu-S system due to its importance in mineralogy, geology, and various industry applications such as photovoltaics, anodes for lithium-ion batteries, or biomedical applications.^{156, 157} For most potential applications, Cu_{2-x}S ($0 < x < 1$) and its copper-rich compositions and phases are the most relevant. These are promising materials because they are nontoxic and display excellent optoelectronic and thermoelectric properties.^{158, 159} Cu_{2-x}S in general is a *p*-type semiconducting material and a mixed ionic-electronic conductor (MIEC) with predominant electronic conduction. A wide range of stoichiometric compositions exist which yields distinct electrical and photoelectronic properties. For instance, the transition from copper-rich Cu₂S to sulfur-rich CuS leads to an increased electrical conductivity and a wider band gap (1.2-2.0 eV).^{77, 159} In addition, the modification of the copper sulfide composition changes the ionic conductivity and with this the mobility of Cu ions.

As mentioned above, copper sulfide Cu_{2-x}S is found after HTS above 150 °C. Hence, it is hypothesized that Cu_{2-x}S acts as solid electrolyte to enable a galvanic cell between Pd and Cu. This is possible as Cu_{2-x}S is a MIEC with significant Cu ion conductivity. Thus, the electrochemical properties of the solid electrolyte Cu_{2-x}S are important parameters for sulfur induced bond wire corrosion. The electronic and ionic conductivity change depending on temperature and composition. Because of this, it is vitally important to determine the specific copper sulfide phase in the package, which in turn provides information on the electrochemical properties. Hence, the composition of the respective copper sulfides will be resolved in chapter 7-9. The result ($= \alpha/\beta$ -Cu₂S) is anticipated here as the following review and discussion mostly focuses on the copper-rich compositions. Thus, the aim of this chapter is to give an overview of the Cu-S system as well as the temperature and composition dependent properties of Cu_{2-x}S from the available literature data to date.

5.3 Results & Discussion

5.3.1 The Cu-S System – Phase Diagram and Crystal Structures

The Cu-S system is a well investigated, but complex system which can form many different phases, see **Figure 5.1**. At room temperature the most important phases are low chalcocite (α -Cu₂S, monoclinic), djurleite (Cu_{1.95}S, monoclinic), anilite (Cu_{1.75}S, orthorhombic) and covellite (CuS, hexagonal) from copper- to sulfur-rich, respectively. At higher temperatures above 103 °C, phase transition takes place from low chalcocite to high chalcocite (β -Cu₂S, hexagonal). With increasing sulfur content, the phase transition temperature decreases to ≈ 90 °C for the biphasic mixture of high chalcocite and high-digenite (γ -Cu_{1.8}S, cubic). Then, the transition temperature decreases again to ≈ 72 °C for the monophasic γ -Cu_{1.8}S.

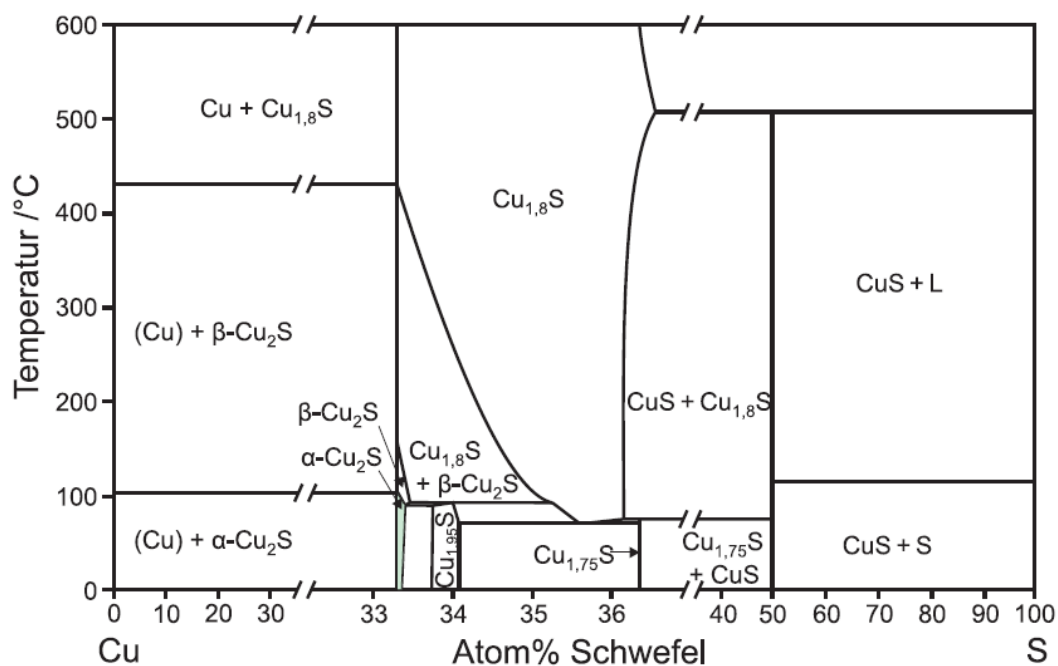


Figure 5.1: Cu-S phase diagram. The most prominent phases are low (α -Cu₂S) and high chalcocite (β -Cu₂S), djurleite (Cu_{1.95}S), high-digenite (γ -Cu_{1.8}S), anilite (Cu_{1.75}S), and covellite (CuS).^{160, 161} Reproduced with kind permission from *Siol*.¹⁶²

Moreover, the individual phases in the most cases do not possess a defined stoichiometric composition but rather a composition range. The low chalcocite α -Cu_{2-x}S and high chalcocite β -Cu_{2-x}S phase exhibit an extremely narrow composition range with Cu_{2-1.993}S and Cu_{2-1.988}S, respectively, see table **Table 5.1** for an overview.^{160, 161} Therefore, synthesis of pure low/high chalcocite is a challenge as a slight deviation from the Cu content leads to djurleite (Cu_{1.95}S). Further, demixing of the chalcocite phase to Cu and djurleite is energetically favoured as the djurleite phase is more stable which could additionally lead to a spontaneous development of Cu vacancies.¹⁵⁸ Hence, the djurleite phase is often observed beneath the chalcocite phase which can be hardly distinguished from each other due to their similarities. In addition, the metastable tetragonal (Cu_{1.96}S) and low-digenite phase (Cu_{1.8}S) occur in the phase diagram upon cooling.

Table 5.1: Overview of some stable and metastable copper sulfides in the Cu-S system as well as their temperature range and space groups. Data taken from Chakrabarti and Blachnik et al.^{160, 161}

Name	Formula used in this work	Composition range x in Cu_xS	Temperature range	Space group
High temperature phases				
High-digenite	$\gamma\text{-Cu}_{1.8}\text{S}$	2.002-1.732	$> 72\text{-}90\text{ }^\circ\text{C}$	$Fm\bar{3}m$
High-chalcocite	$\beta\text{-Cu}_2\text{S}$	2.000-1.988	$> 103\text{ }^\circ\text{C}$	$P6_3/mmc$
Low temperature phases				
Low-chalcocite	$\alpha\text{-Cu}_2\text{S}$	2.000-1.993	$< 103\text{ }^\circ\text{C}$	$P2_1/c$
Djurleite	$\text{Cu}_{1.95}\text{S}$	1.965-1.934	$< 90\text{ }^\circ\text{C}$	$P2_1/n$
Anilite	$\text{Cu}_{1.75}\text{S}$	1.750	$< 72\text{ }^\circ\text{C}$	$Pnma$
Covellite	CuS	1.000	$< 507\text{ }^\circ\text{C}$	$P6_3/mmc$
Metastable phases				
Tetragonal phase	$\text{Cu}_{1.96}\text{S}$	1.99-1.92 ¹⁶³	$90\text{-}140\text{ }^\circ\text{C}$	$P4_32_13$
Low-digenite	$\text{Cu}_{1.8}\text{S}$	1.89-1.71 ¹⁶³	$< 72\text{ }^\circ\text{C}$	$R\bar{3}m$

The most relevant phases within the scope of this work are low chalcocite $\alpha\text{-Cu}_2\text{S}$ and high chalcocite $\beta\text{-Cu}_2\text{S}$. Both phases possess a hexagonal symmetry with an elongated hexagonal close packed (*hcp*) arrangement of S atoms along the c axis, whereas the *hcp* is slightly distorted in the case of low chalcocite, see **Figure 5.2**.¹⁶⁴ Therein, the Cu atoms of low chalcocite ($\alpha\text{-Cu}_2\text{S}$) occupy the a, d, and e sites, each with trigonal coordination. Hence, the coordination number stays constant with threefold coordinates. Whereas the Cu atoms in high chalcocite ($\beta\text{-Cu}_2\text{S}$) are randomly distributed over the a, b, and c sites with trigonal, tetrahedral, and linear coordination, respectively. See **Figure A 5.1-3** for the respective unit cells of low and high chalcocite as well as coordination modes.

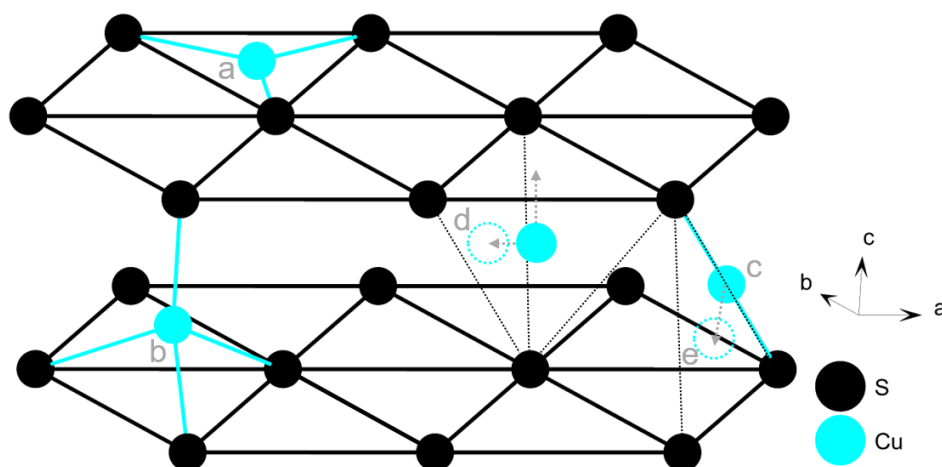


Figure 5.2: Schematic view of the $\alpha/\beta\text{-Cu}_2\text{S}$ hexagonal close packed lattice and the respective Cu positions as solid-liquid hybrid phase according to Wang.¹⁶⁴ In low chalcocite, Cu atoms occupy a, d, and e sites with trigonal coordination. In high chalcocite, Cu atoms are distributed over the a, b, and c sites with trigonal, tetrahedral, and linear coordination, respectively. The dashed arrows indicate possible relaxation and diffusion pathways. Adapted with permission from L. Wang, *Phys. Rev. Lett.*, 108, 085703-2, 2012. Copyright (2012) by the American Physical Society.

Related DFT studies on the occupation and relaxation of the different Cu atom sites reveal a spontaneous relaxation of b and c sites into the nearby d and e sites without a significant potential barrier between the respective sites.¹⁶⁴ Hence, the d and e sites are thermodynamically more stable at lower temperatures which results in a phase transition at ~ 103 °C. Detailed analysis of the diffusion pathways reveals a predominant diffusion of the Cu atoms along the b axis and the a axis.¹⁶⁴ Hence, diffusion of the Cu atoms is favored in between the layers of hexagonal packed S atoms. Moreover, molecular dynamic simulations of high chalcocite suggest that the Cu atoms are located near the a , d , and e sites with minimal potential barriers along the diffusion pathways.¹⁶⁴ Hence, the Cu atom diffusion behaviour is more like a liquid phase and thus can be described by a Cu sublattice melting within the solid S sublattice. Therefore, the high chalcocite phase can be characterized as a “solid-liquid hybrid phase” similar to superionics rather than a solid solution.¹⁶⁴⁻¹⁶⁶ Hence, in theory, higher Cu diffusion in β -Cu₂S compared to α -Cu₂S is anticipated as well as lower activation energies E_a for Cu diffusion in the high temperature phase. This is due to the lower potential barriers for the Cu atoms to hop from one site to a neighbouring site in high chalcocite.

5.3.2 Emf Measurements on Cu_{2-x}S

Because of the large variations in the composition of Cu_{2-x}S within a phase, the exact measurement of the stoichiometric composition is a challenge. Similar problems arised on Ag_{2-x}S samples, where emf measurements on a galvanic cell Ag|AgI|Ag_{2-x}S by *Wagner* proved to be suitable to determine the composition as a function of the cell potential.¹⁶⁷ Thus, the same method was adapted to Cu_{2-x}S samples. Therein, the basic principle is the distinct Cu activity within the Cu reference electrode and the Cu_{2-x}S sample and thus the difference between the chemical potentials (for further details see chapter 3.3):

$$-nFU = \mu''_{Cu}(Cu_{2-x}S) - \mu'_{0,Cu} \quad (5.1)$$

Consequently, the cell potential can be measured as a function of the composition as it solely depends on the Cu activity a_{Cu} in the Cu_{2-x}S sample. Then, the composition of the Cu_{2-x}S sample can be adjusted by coulometric titration where Cu ions are removed from the sample. Simultaneously, the cell potential is measured, and the composition can be derived from Faraday’s law. However, in contrast to the Ag system, no suitable solid electrolyte (must be a pure Cu⁺ ionic conductor) was available for the Cu system in the range ~ 100 - 300 °C. Therefore, aqueous CuSO₄ solutions were applied as liquid electrolytes by *Mathieu* et al. and *Potter*.^{97, 168} Naturally, this led to a limited temperature range up to 100 °C. Whereas *Ishikawa* et al. introduced a new solid electrolyte which enabled an emf measurement up to ~ 200 °C.¹⁶⁹ Moreover, different sample preparations and geometries were used by the respective authors. Therein, *Mathieu* et al. used thin Cu_{2-x}S samples (~ 1 - 3 μ m) prepared by vapor deposition on glass carriers.⁹⁷ Contrary to that, *Potter* and *Ishikawa* et al. utilized polycrystalline Cu_{2-x}S pellets (~ 0.5 mm).^{168, 169} Thereby, sample thickness is an important parameter as the measured cell potential strongly depends on the steady state condition of the sample. Thus, thicker samples may result in inhomogeneous composition distribution within the sample.

However, all three authors performed a coulometric titration on the respective galvanic cell to alter the composition and measure the emf. In general, the coulometric titration commenced from the copper-rich composition with the removal of Cu ions from the sample. Thereby, *Mathieu* et al. performed a coulometric titration over the whole range starting from low chalcocite Cu_2S towards covellite CuS .⁹⁷ Similar to that, *Ishikawa* et al. conducted the coulometric titration towards a specific composition (from Cu_2S up to $\text{Cu}_{1.8}\text{S}$) but also varied the temperature from 25 °C to 175 °C at a given composition, and measured the emf accordingly.¹⁶⁹ Contrary to that, *Potter* synthesized a specific Cu_{2-x}S phase and composition and subsequently made small variations of the composition by coulometric titration.¹⁶⁸ This procedure was chosen as long homogenization times are necessary for the polycrystalline pellets to achieve the respective cell potential. Also, the removal of Cu ions from the Cu_{2-x}S electrode leads to volume changes which may yield porous and fragile electrodes. See **Table 5.2** for a detailed overview of the respective methodology, applied by the different authors.

Table 5.2: Emf measurements and their characteristics which are conducted by three different authors.

	Galvanic cell	Sample	Electrolyte	Procedure
<i>Ishikawa</i> et al. ¹⁶⁹ 1976	$\text{Cu} \text{Cu}_5^{2+} \text{Cu}_{2-x}\text{S}$	Polycrystalline Cu_{2-x}S pellets (~ 0.5 mm thick)	Organic, solid electrolyte: $\text{CuBr}\cdot\text{C}_6\text{H}_{12}\text{N}_4\text{CH}_3\text{Br}$	Coulom. titr. up to $\text{Cu}_{1.8}\text{S}$ and variation of temp. (25-175 °C)
<i>Mathieu</i> et al. ⁹⁷ 1971	$\text{Cu} \text{Cu}_{aq}^{2+} \text{Cu}_{2-x}\text{S}$	Vapor deposition of Cu_{2-x}S (~1-3 μm thick) on SiO_2 carrier	Deaerated aqueous CuSO_4 solution with H_2SO_4 to pH = 2	Coulom. titr. of Cu_2S up to CuS
<i>Potter</i> ¹⁶⁸ 1977	$\text{Cu} \text{Cu}_{aq}^{2+} \text{Cu}_{2-x}\text{S}$	Polycryst. Cu_{2-x}S pellets and Cu_{2-x}S wires	Deaerated aqueous $\text{CuSO}_4/\text{CuCl}$ solution	Small variation of different phases by coulom. titr.

Accordingly, emf measurements were conducted and the corresponding E-composition curves in **Figure 5.3** were obtained. Therein, monophasic ranges are characterised by a change in the cell potential with variation of the composition as the chemical potential alters with the Cu/S ratio. For instance, low chalcocite shows an immediate response of the cell potential with miniscule variation of the composition from Cu_2S to $\text{Cu}_{1.994}\text{S}$. Whereas biphasic ranges exhibit a steady cell potential in a wide composition range. This is due to the equilibrium between the two phases which in sum does not alter the chemical potentials. Consequently, monophasic and biphasic ranges can be distinguished from another and characterized by emf measurements. There, *Mathieu* and *Potter* measured a similar cell potential of ~130-140 mV, starting from Cu_2S (0 mV), for the low end of the chalcocite phase, which corresponds to $\text{Cu}_{1.994}\text{S}$. Then, the emf remains constant due to the biphasic mixture of chalcocite and djurleite up to $\text{Cu}_{1.96}\text{S}$ for *Potter* data and $\text{Cu}_{1.93}\text{S}$ for *Mathieu* data where the transition to monophasic djurleite takes place.^{97, 168} Subsequently, the emf stays constant again with the transition towards a djurleite/anilite (~150 mV) mixture. Further comparison of the E-composition curves at 60 °C and 90 °C obtained by *Mathieu* reveals a qualitative similar curve at higher temperature, which is slightly shifted towards higher cell potentials. Moreover, a comparison to the E-composition curve from *Potter* data shows shifted composition boundaries but with the same phase sequence.

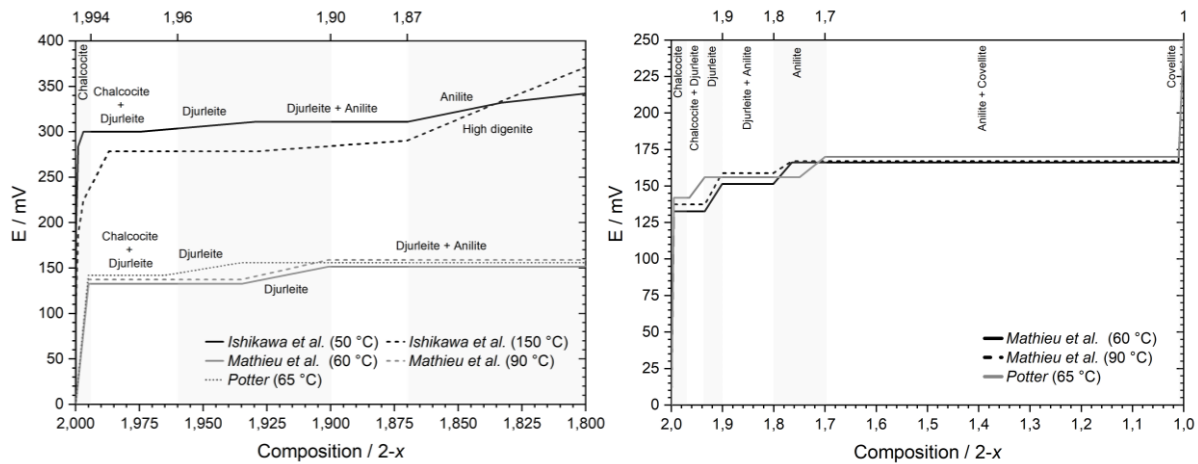


Figure 5.3: Emf measurements on Cu_{2-x}S samples. For experimental details see table 5.2. Therein, the measured cell potential E / mV is plotted versus the obtained composition $/ 2-x$ in Cu_{2-x}S . Monophasic ranges are characterized by a change in the emf, whereas biphasic ranges exhibit a steady cell potential. Left: E-composition diagram from Cu_2S to $\text{Cu}_{1.8}\text{S}$. Therein, the present phases are labelled in the vicinity of the respective emf curve and the approximate phase ranges are indicated by shaded areas. Right: E-composition diagram from Cu_2S to CuS . Therein, the present phases are labelled, and the approximate phase ranges are indicated by shaded areas. Data taken from Mathieu et al., Potter, and Ishikawa et al.^{97, 168, 169}

Contrary to Mathieu and Potter E-composition curves, Ishikawa et al. measured much higher cell potentials with $\sim 300 \text{ mV}$ for the low end of chalcocite ($\text{Cu}_{1.997}\text{S}$) at 50°C .¹⁶⁹ However, the phase sequence is in accordance with Mathieu and Potter measurements but with shifted composition boundaries. The peculiarity from Ishikawa et al. is the measurement of the E-composition curve at 150°C . Thus, a phase transition from $\alpha\text{-Cu}_{2-x}\text{S}$ to $\beta\text{-Cu}_{2-x}\text{S}$ takes place as well as the transition from djurleite and anilite to high digenite $\gamma\text{-Cu}_{2-x}\text{S}$, respectively. Hence, the phase sequence proceeds from high chalcocite ($\text{Cu}_{2-1.99}\text{S} = 0\text{--}278 \text{ mV}$) to the chalcocite/digenite mixture to monophasic digenite ($\text{Cu}_{1.87\text{--}1.80}\text{S} = 290\text{--}371 \text{ mV}$).

The large deviation of the emf, measured by Ishikawa et al., from the emf obtained by Mathieu and Potter can be explained by the different experimental setup. Mathieu et al. and Potter used a liquid electrolyte with bivalent Cu^{2+} ions, whereas Ishikawa et al. introduced a solid electrolyte with a monovalent Cu^+ ion conduction. Strikingly, the emf obtained with the monovalent Cu^+ electrolyte, is approximately doubled compared to the bivalent Cu^{2+} electrolyte measurements. From eq. 5.1 it is evident that a bivalent cation introduces the factor $n = 2$ for the calculation of the cell potential which coincides with the deviation of the solid electrolyte from the liquid electrolyte.

Moreover, the phase boundaries within the E-composition curves of the polycrystalline samples (Potter and Ishikawa et al.) at 50°C and 65°C are in good agreement. Contrary to that, the composition boundaries are shifted for the thin Cu_{2-x}S sample prepared by vapor deposition.

In summary, all methods qualitatively match with each other. However, slight deviations can occur depending on the Cu_{2-x}S sample preparation. Moreover, the bivalent Cu^{2+} conduction in the liquid electrolyte must be taken into account versus monovalent Cu^+ conduction in the solid electrolyte.

5.3.3 Experimental Methodologies for the Measurement of Chemical Diffusion

Besides the determination of the exact stoichiometric composition, the measurement of the chemical diffusion coefficient \tilde{D}_{chem} in Cu_{2-x}S is not straightforward as Cu_{2-x}S is a MIEC semiconductor with predominant electronic conduction. Thus, the electronic conduction σ_{eon} superimposes the ionic conduction σ_{ion} and therefore corresponds to the total conductivity $\sigma_{\text{eon}} = \sigma_{\text{total}}$. Hence, the pure ionic conductivity, which is linked to the self-diffusion coefficient and the chemical diffusion coefficient by eq. 5.2 (for detail see chapter 3):

$$\tilde{D}_{\text{chem}} = D_{\text{self}} \cdot \left(\frac{d \ln a}{d \ln c} \right) = \frac{R \cdot T \cdot \sigma_k}{z^2 \cdot F^2 \cdot c_k} \cdot \left(\frac{d \ln a}{d \ln c} \right) \quad (5.2)$$

is difficult to obtain by simple electrochemical measurements. Because of this, highly sophisticated techniques, and in this context complex mathematical derivations, had to be developed to determine the underlying ionic conductivity and chemical diffusion coefficient. Hence, several methodologies were developed, whereby the usage of platinum (Pt) point electrodes (P.E.) posed the most common technique.

The mathematical fundamentals and methodology for the application of P.E. were initially established by *Miyatani* and then adopted by the group of *Rickert*, *Tinter* and *Wiemhöfer* and later by *Pauporte* and *Vedel*.^{91, 170-172} The electrochemical cell of a P.E. measurement, in general, can be expressed as: $\text{Pt}|\text{MIEC}|\text{Pt}'(\text{P.E.})$. Thereby, the technique is based on a composition change of Cu_{2-x}S in the vicinity of the P.E., induced by a constant dc current or voltage. This is due to a potential gradient which will build up at the P.E. according to $UF = \mu_e' - \mu_e = \frac{1}{z} \mu_{\text{Cu}}' - \mu_{\text{Cu}}$. Further, a modification of the composition takes place by Cu ion movement and thus chemical diffusion. Moreover, the altered stoichiometric composition yields a distinct conductivity of the sample and therefore a resistance drift is observed. Hence, the resistance drift is measured as a function of time in order to calculate the chemical diffusion coefficient. However, two prerequisites of the MIEC sample must be fulfilled for the P.E. technique:

- i. MIEC is a predominant electronic conductor with sufficient electronic conduction (e.g. $\sigma_{\text{eon}} = 0.1 \text{ S} \cdot \text{cm}^{-1}$) and therefore the chemical diffusion coefficient can be calculated by:

$$\tilde{D}_{\text{chem}} = \frac{\sigma_{\text{eon}} \cdot \sigma_{\text{ion}}}{(\sigma_{\text{eon}} + \sigma_{\text{ion}}) \cdot z^2 \cdot F^2} \cdot \left(\frac{d \ln \mu}{d \ln c} \right), \text{ with } \sigma_{\text{eon}} \gg \sigma_{\text{ion}}, = \frac{\sigma_{\text{ion}}}{z^2 \cdot F^2} \cdot \left(\frac{d \ln \mu}{d \ln c} \right) \quad (5.3)$$

- ii. Conductivity of the MIEC changes with composition: $\sigma_{\text{eon}} \sim \frac{1}{R} \sim 2 - x$, $\Delta R \sim \Delta x \sim \sqrt{\tilde{D}_{\text{chem}} t}$

Herein, the respective authors commonly conducted the measurements on $\alpha\text{-Cu}_2\text{S}$ which fulfills the requirements as it is a good predominant electronic conductor. Also, the conductivity increases with decreasing Cu content. This will be discussed in more depth in the next chapter. However, *Pauporte* et al. performed additional measurements on $\beta\text{-Cu}_2\text{S}$ up to 190 °C with a subsequent comparison to *Rickert* and *Wiemhöfer* data as well as to EIS measurements.¹⁷²

Another technique is EIS, which commonly utilized galvanic cells with a liquid or solid electrolyte between a Cu reference electrode and the Cu_{2-x}S sample. Therein, the electrolyte is supposed to be a pure Cu ion ionic conductor to eliminate electronic contributions from the measurement. Note the similarities to the emf measurements by *Mathieu et al.* and *Ishikawa et al.* which also introduced such galvanic cells.^{97, 169} Hence, the advantage of this method is the simultaneous determination of the composition and the chemical diffusion, which is more cumbersome for P.E. measurements. The most prominent works, which applied EIS on a galvanic cell $\text{Cu}|\text{Cu}^+$ or $\text{Cu}^{2+}|\text{Cu}_{2-x}\text{S}$, were performed by *Cassaignon and Sanchez et al.* and *Pauporte et al.*^{78-80, 172-174} The former used an aqueous CuSO_4 solution as liquid electrolyte and the latter a solid electrolyte RbCu_4Cl_5 . However, the EIS measurement with liquid electrolyte limits the temperature range up to 100 °C. Therefore, *Pauporte et al.* investigated the high chalcocite $\beta\text{-Cu}_{2-x}\text{S}$ in combination with the solid electrolyte up to ~160 °C. Yet, the disadvantage of the solid electrolyte is the occurrence of electrode surface effects which must be taken into account.¹⁷⁴ Note that the general methodology of EIS with solid electrolyte was adopted in this work. For theoretical fundamentals and experimental details see chapter 3.4 and chapter 4.1.1.

Other notable studies were carried out by *Castel* who performed potentiostatic measurements on a galvanic cell $\text{Cu}|\text{Cu}^{2+}|\text{Cu}_{2-x}\text{S}$ alike to the cell introduced by *Mathieu et al.*^{97, 175} Here, *Castel* investigated the relaxation of the current with time and calculated the chemical diffusion coefficient as a function of composition.¹⁷⁵ In this study, the composition was modified by coulometric titration.

Furthermore, chronopotentiometric measurements were conducted by *Allen et al.*, wherein a Cu_{2-x}S layer was grown onto a CdS carrier and then contacted by two gold probes.¹⁷⁶ Here, the composition was measured as a function of the conductivity. Also, *Okamoto et al.* applied chronopotentiometric measurements on pressed pellets of polycrystalline Cu_2S and $\text{Cu}_{1.8}\text{S}$.¹⁷⁷

In the following chapter, the obtained chemical diffusion coefficient as well as ionic and electronic conduction in Cu_{2-x}S as a function of composition and temperature will be reviewed. Thereby, most of the available data originates from the authors discussed in this chapter.

5.3.4 Conductivity and Diffusion in Cu_{2-x}S

As mentioned above, low chalcocite $\alpha\text{-Cu}_{2-x}\text{S}$ is a MIEC with predominant electronic conduction. Also, low chalcocite is a semiconducting material with p-type behaviour and a band gap of ~ 1.2 eV. Thereby, the electronic conductivity increases with the deviation from ideal low chalcocite Cu_2S (~ 0.5 S/cm) composition towards anilite/digenite $\text{Cu}_{1.8}\text{S}$ (~ 2400 S/cm), see **Figure 5.4**. However, the transition from Cu_2S to $\text{Cu}_{1.8}\text{S}$ is not accompanied by a significant change in the band gap energy E_g which is in the range ~ 1.2 - 1.5 eV.¹⁵⁸ Yet, the removal of Cu ions leads to a reduction of the Fermi level below the valence band maximum.¹⁷⁸ Consequently, the electronic conduction increases with deviation from stoichiometric Cu_2S composition. This is also confirmed at 140 - 160 °C where the same conductive behaviour is observed, relative to room temperature values. Therefore, measurements with P.E. technique at high temperatures (as will be seen below) is feasible because the electronic conductivity changes with stoichiometric composition above 100 °C. However, the lower electronic conduction of the high chalcocite phase $\beta\text{-Cu}_{2-x}\text{S}$ could be a potential problem for the P.E. technique.

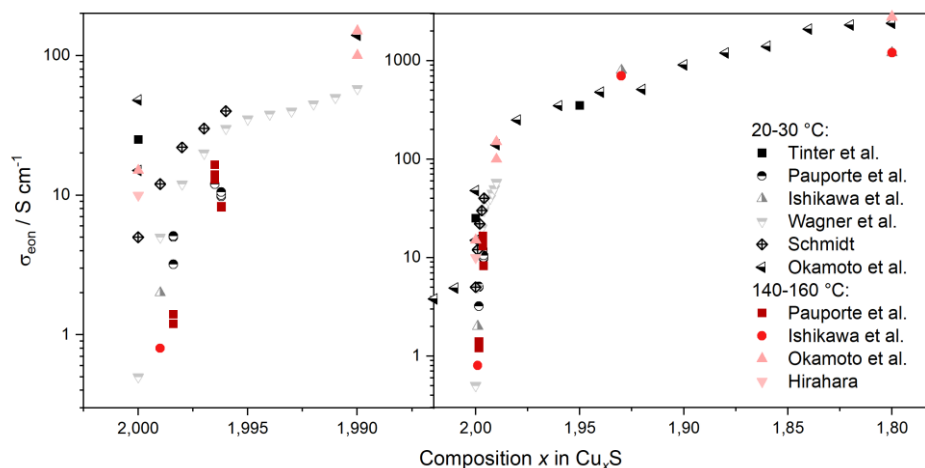


Figure 5.4: Electronic conductivity in Cu_{2-x}S at 20 - 30 °C (black, grey) and 140 - 160 °C (red) as a function of composition. Electronic conductivity increases with deviation from chalcocite composition. Data extracted from literature.^{77, 78, 91, 169, 172, 177, 179}

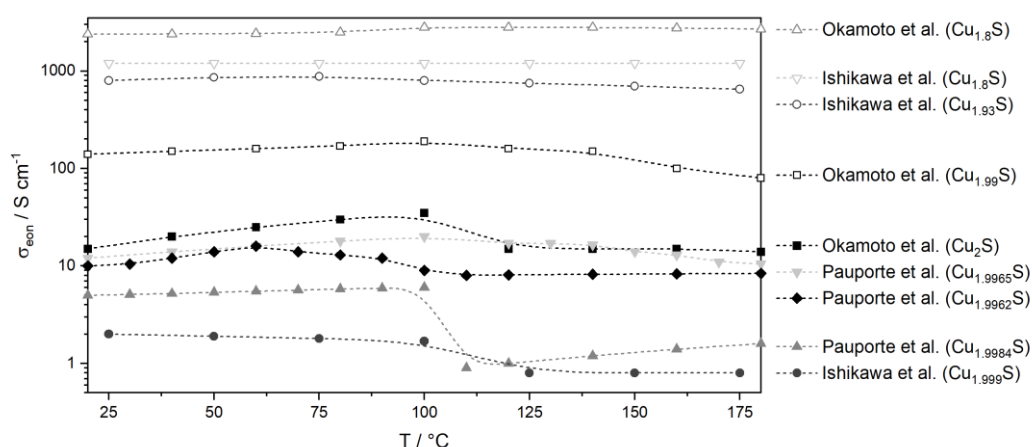


Figure 5.5: Electronic conductivity of different Cu_{2-x}S compositions as a function of temperature. The electronic conductivity in general decreases from $\alpha\text{-Cu}_{2-x}\text{S}$ to $\beta\text{-Cu}_{2-x}\text{S}$ whereas the conductivity remains constant for anilite/digenite. Data extracted from literature.^{78, 169, 172, 177}

Further analysis of the electronic conductivity in **Figure 5.5** as a function of temperature, in general, reveals a slight decrease from α -Cu_{2-x}S to β -Cu_{2-x}S at 100 °C, which is also observed for a composition Cu_{1.99}S. Whereas djurleite (Cu_{1.93}S) and anilite/digenite ($2-x = 1.8$) stay approximately constant over the whole range from 25 °C to 175 °C.

According to a typical semiconducting behaviour, the ionic conductivity α -Cu_{2-x}S increases linearly with temperature in the range from 20-80 °C, see **Figure 5.6 (left)**. Hence, from $\sim 3 \cdot 10^{-5}$ S/cm to $\sim 5 \cdot 10^{-4}$ S/cm. Also, variation of the composition from Cu₂S to Cu_{1.93}S an ionic conductivity in the same order of magnitude. Therein, the values obtained by *Miyatani* deviate from the measurements of other groups and exhibit an exponential increase at the phase transition temperature (100 °C).¹⁷⁰ However, high temperature data of the β -Cu₂S is scarce and shows a big deviation. Herein, extrapolation of the values obtained by *Rickert et al.* would approximately match the experimental data from *Hirahara* which are in the range $\sim 2 \cdot 10^{-3}$ S/cm at 150 °C.⁷⁶ Contrary to that, the values obtained by *Okamoto et al.* are higher by two orders of magnitude with ~ 0.2 S/cm at 150 °C and an exponential leap, indicated from the *Miyatani* data, could be feasible.^{170, 177} Still, the values measured by *Okamoto et al.* for Cu₂S are extremely high and approximate to the measured values for electronic conduction (~ 1 -10 S/cm). This is rather unlikely if β -Cu_{2-x}S behaves like an MIEC with predominant electronic conduction. Nevertheless, a “solid-liquid hybrid phase” is discussed before wherein a high ionic conduction could be feasible in accordance with liquid electrolytes.

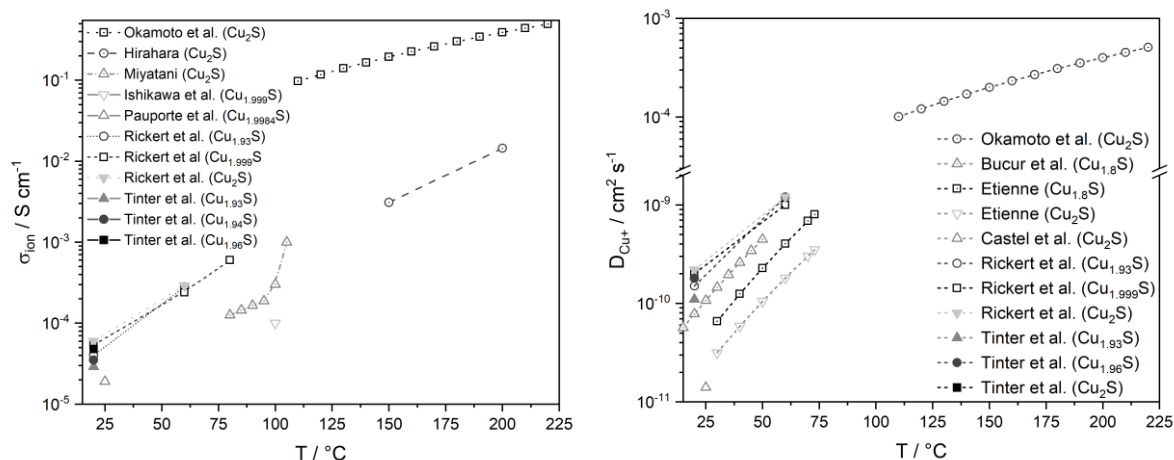


Figure 5.6: Left: Ionic conductivity, right: Self-diffusion coefficient in Cu_{2-x}S for various compositions (labelled in brackets) as a function of temperature. Data taken from literature.^{76, 78, 91, 169, 170, 172, 175, 177, 179-182}

Like the ionic conductivity, the Cu⁺ self-diffusion coefficient D_{Cu^+} increases linearly with temperature from 20 °C to 75 °C, see **Figure 5.6 (right)**. Contrary to the ionic conductivity, the deviation from ideal composition leads to lower diffusion coefficients. Therein, lower values for Cu₂S are obtained by *Etienne* with $\sim 3 \cdot 10^{-10}$ cm² s⁻¹ at 27 °C compared to $\sim 3 \cdot 10^{-9}$ cm² s⁻¹ obtained by *Rickert et al.*^{76, 182} Nevertheless, similar trends are observed, and the self-diffusion coefficients for Cu_{1.8}S measured by *Bucur et al.* are in the same range compared to the Cu_{1.8}S data from *Etienne*.^{181, 182} Interestingly, the self-diffusion coefficients attained by *Okamoto et al.* would match a hypothetical extrapolation of the low temperature values but with a lower slope at high temperatures and $\sim 2 \cdot 10^{-2}$ cm² s⁻¹ at 150 °C.¹⁷⁷

In accordance with the self-diffusion coefficient, the chemical diffusion coefficient depends on the stoichiometric composition in Cu_{2-x}S , see **Figure 5.7**. Herein, most authors found a chemical diffusion coefficient in low chalcocite within a range of $1 \cdot 10^{-8}$ - $1 \cdot 10^{-7} \text{ cm}^2 \text{ s}^{-1}$ at room temperature. The most extensive research on the chemical diffusion coefficient \tilde{D}_{Chem} as a function of composition was conducted by *Cassaignon et al.*^{79, 80} Therein, it is found that the chemical diffusion coefficient decreases from chalcocite to djurleite, anilite, and covellite. Further analysis of \tilde{D}_{Chem} as a function of cell potential ($\text{Cu}|\text{Cu}^{2+}|\text{Cu}_{2-x}\text{S}$) reveals only slight variations within a respective phase and big leaps due to phase transition. Also, it is found that \tilde{D}_{Chem} strongly depends on the method which is used to calculate the concentration of the diffusing species. It is concluded that the Cu concentration should be assumed to be proportional to the deviation from pure chalcocite $\alpha\text{-Cu}_2\text{S}$, which promotes the existence of a vacancy mechanism.⁸⁰ Hence, \tilde{D}_{Chem} should increase with higher vacancy concentration. However, the decrease of \tilde{D}_{Chem} with phase transition seems to be mostly governed by the changes in activation energy for the respective phases. This also matches with the experimental data from *Pauporte et al.*¹⁷²

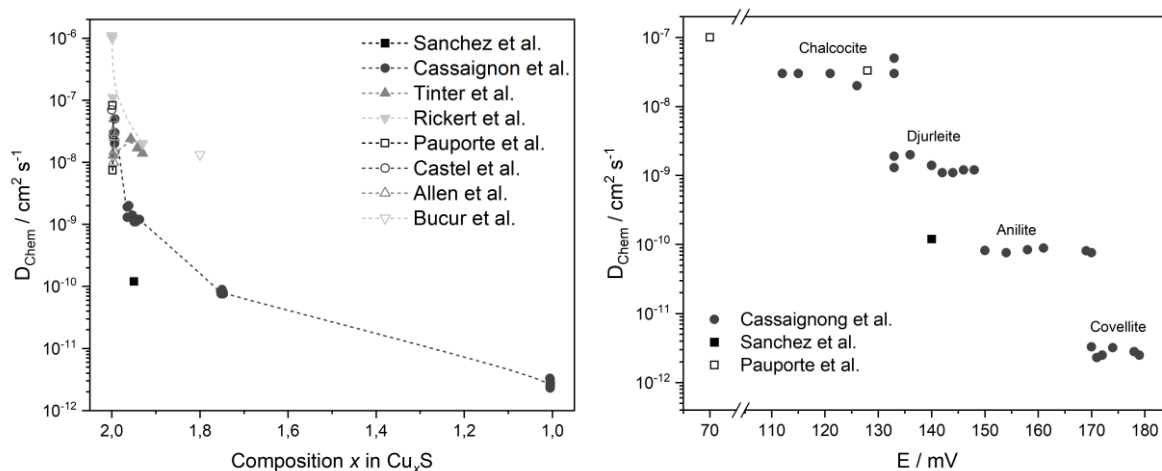


Figure 5.7: Chemical diffusion coefficient on Cu_{2-x}S from chalcocite to covellite as a function of composition (left) and cell potential (right, $\text{Cu}|\text{Cu}^{2+}|\text{Cu}_{2-x}\text{S}$). Data taken from literature.^{76, 78, 80, 91, 172, 173, 175, 176, 181}

Finally, the chemical diffusion coefficients are analysed as a function of temperature, see **Figure 5.8**. Therein, the experimental values attained by *Pauporte et al.*, *Castel et al.*, and *Bucur et al.* are in a similar order of magnitude between $1 \cdot 10^{-8}$ - $1 \cdot 10^{-7} \text{ cm}^2 \text{ s}^{-1}$ at 20°C and $1 \cdot 10^{-7}$ - $1 \cdot 10^{-6} \text{ cm}^2 \text{ s}^{-1}$ at 80°C , respectively.^{78, 172} Herein, *Pauporte et al.* measured the chemical diffusion coefficient in an all-solid-state galvanic cell with the composition $\text{Cu}_{1.9965}\text{S}$ and an activation energy of 1.7 eV at 120-160 $^\circ \text{C}$.⁷⁸ This value is extremely high compared to 0.28 eV attained by the P.E. method.^{78, 172} Also, the values obtained by the all-solid-state cell are much higher than the other literature data at high temperatures. This could be due to the softening of the solid electrolyte RbCu_4Cl_5 at elevated temperatures or electrode effects.⁷⁸ Nevertheless, further optimization and investigation with the solid electrolyte of a $\text{Cu}_{1.88}\text{S}$ sample gave similar values compared to the P.E. technique.¹⁷⁴ The values measured by *Pauporte et al.* are in the range $\sim 1 \cdot 10^{-7} \text{ cm}^2 \text{ s}^{-1}$ and are comparable to the values from

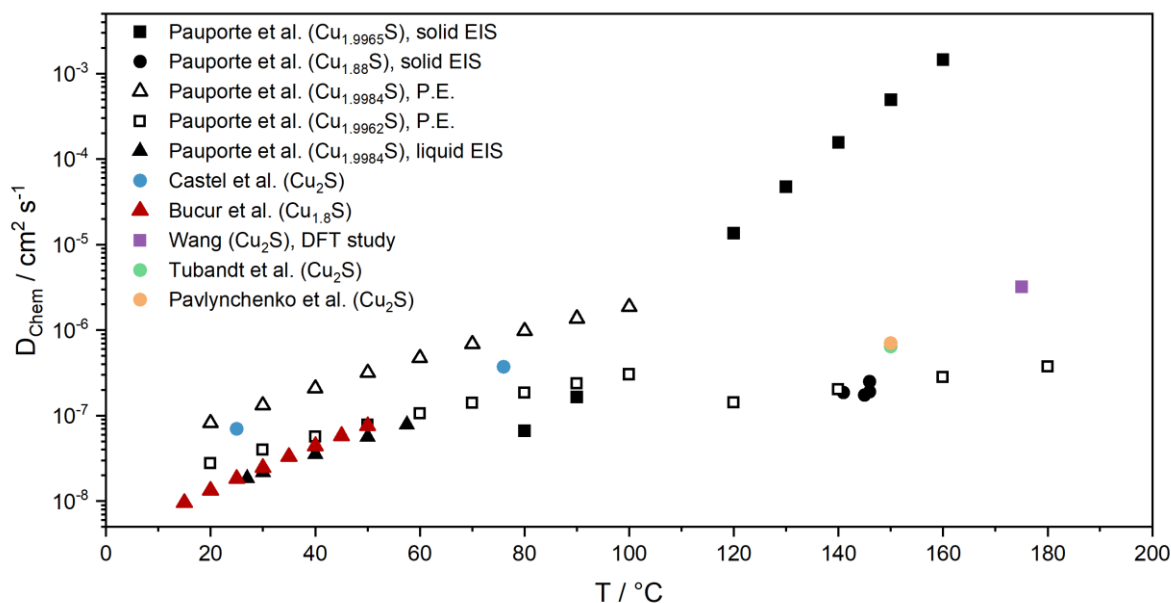


Figure 5.8: Chemical diffusion coefficient in Cu_{2-x}S at various compositions (labelled in brackets) as a function of temperature, obtained by different methods. P.E. = point electrode, EIS = electrochemical impedance spectroscopy. Data taken from literature.^{78, 164, 172, 174, 175, 181, 183, 184}

Tubandt et al. and *Pavlyuchenko et al.* with values of $\sim 4 \cdot 10^{-7} \text{ cm}^2\text{s}^{-1}$ at 150 °C.^{174, 183, 184} Also, the theoretical chemical diffusion coefficient calculated by *Wang* in a DFT study is in a similar range with $\sim 2 \cdot 10^{-6} \text{ cm}^2\text{s}^{-1}$ at 175 °C.¹⁶⁴ Consequently, the diffusion coefficients obtained in a first study by *Pauporte et al.* seem rather high and lower values in the range $1 \cdot 10^{-7} - 1 \cdot 10^{-6} \text{ cm}^2\text{s}^{-1}$ are anticipated at 150 °C. Yet, there is also evidence by *Okamoto et al.* and *Miyatani*, which indicate a big leap with the transition from low to high chalcocite.^{170, 177} It is also feasible that the ionic conductivity and diffusion coefficients strongly depend on the sample preparation, condition, and experimental technique. Therefore, further investigations are necessary to clarify the diffusion behaviour of Cu_{2-x}S .

5.4 Conclusion

The most relevant phases within the scope of this work are low chalcocite $\alpha\text{-Cu}_2\text{S}$ and high chalcocite $\beta\text{-Cu}_2\text{S}$, which undergo a phase transition at $\sim 103 \text{ °C}$. Therein, it is hypothesized that the high chalcocite $\beta\text{-Cu}_2\text{S}$ behaves like a “solid-liquid hybrid phase” with high Cu ion diffusion.

Review of the literature data reveals a high electronic conductivity of Cu_{2-x}S which increases with deviation from ideal stoichiometric Cu_2S composition. Also, a slight decrease of the electronic conduction σ_{con} is confirmed with the transition to the high chalcocite phase. Yet, the phase transition to $\beta\text{-Cu}_2\text{S}$ is accompanied by an increase of the ionic conductivity σ_{ion} and self-diffusion coefficient $D_{\text{Cu}+}$. Further, the chemical diffusion coefficient decreases from chalcocite to covellite and exhibits only slight variations within each phase. Finally, an increase of the chemical diffusion coefficient \tilde{D}_{Chem} up to $\sim 2 \cdot 10^{-6} \text{ cm}^2\text{s}^{-1}$ as a function of temperature is confirmed by review of the literature data. However, it remains unclear if this increase in \tilde{D}_{Chem} is continuous or if it is interrupted by a leap in the chemical diffusion coefficient at the phase transition.

6 Polarization and EIS on Cu_{2-x}S

6.1 Abstract

In this chapter, the thermostability, ionic conductivity, and electronic conductivity of the solid electrolyte Rb₄Cu₁₆Cl_{12.8}I_{7.2} is evaluated for the usage in the galvanic cell Cu|Rb₄Cu₁₆Cl_{12.8}I_{7.2}|Cu_{2-x}S. Then, the sole Cu_{2-x}S sample is measured for its electronic conductivity. Subsequently, the galvanic cell is measured via EIS at 0 mV up to 120 mV in 20 mV increments. Then, an equivalent circuit is built to fit the obtained EIS spectra. Accordingly, the ionic conductivity σ_{ion} , self-diffusion coefficient D_{Cu^+} , and chemical diffusion coefficient \tilde{D}_{Chem} are calculated from the obtained parameters. Herein, activation energies of 0.33 eV and 0.27 eV are determined and chemical diffusion coefficients of $5.9 \cdot 10^{-10} \text{ cm}^2 \text{ s}^{-1}$ and $9.6 \cdot 10^{-6} \text{ cm}^2 \text{ s}^{-1}$ are obtained for the low and high chalcocite phase, respectively. Therefore, the slope S of the Randles plot was used to calculate the chemical diffusion coefficient. Comparison to the available literature data reveals a good agreement with the experimental data.

6.2 Introduction

As discussed in the previous chapter, intensive research was performed on the electrochemical properties of Cu_{2-x}S. However, literature data on the diffusion of Cu in high chalcocite is still scarce. The literature suggests that the high chalcocite displays lower electronic conductivity compared to the low chalcocite phase. Moreover, an extremely high activation energy of 1.7 eV was measured for the high chalcocite phase by *Pauporte et al.*⁷⁸ This value seems extremely high as a “solid-liquid hybrid” phase behaviour is expected for the high chalcocite phase. Therefore, lower activation energies are anticipated for the high temperature phase. Moreover, not much data is available for the phase transition regime. Different trends are observed in the phase transition region between 80 °C and 120 °C, e.g., leaps towards lower chemical diffusion coefficients (*Pauporte et al.*, P.E.) or a fast acceleration (*Pauporte et al.*, EIS solid) in the temperature range above 100 °C.^{78, 172} Also, literature on the ionic conductivities σ_{ion} measured by *Miyatani* and *Okamoto et al.* suggest an exponential increase for the high chalcocite phase β -Cu_{2-x}S. Therefore, additional electrochemical measurements were performed on Cu_{2-x}S to study the phase transition behaviour and the electrochemical properties of the low and high chalcocite phase. Thus, the galvanic cell Cu|Rb₄Cu₁₆Cl_{12.8}I_{7.2}|Cu_{2-x}S was established to investigate the diffusion behaviour in copper sulfide from 40 °C to 200 °C. Herein, the investigation mostly focuses on the copper-rich compositions.

6.3 Experimental

6.3.1 Chemicals and Sample Preparation

Several chemicals are used for the preparation of the solid electrolyte $\text{Rb}_4\text{Cu}_{16}\text{Cl}_{12.8}\text{I}_{7.2}$ and the Cu_{2-x}S sample, which are listed in **Table 6.1**. Pure Cu and S are used for the preparation of Cu_{2-x}S and RbCl, CuCl, and CuI for the solid electrolyte $\text{Rb}_4\text{Cu}_{16}\text{Cl}_{12.8}\text{I}_{7.2}$.

Table 6.1: List of commercially available chemicals, their purity, form, and manufacturer.

Name	Sum formula	Form	Purity	Manufacturer
Copper	Cu	powder	99.7	Merck
Sulfur	S ₈	powder	99.5	Sigma-Aldrich
Rubidium chloride	RbCl	powder	99.8	Sigma-Aldrich
Copper(I) chloride	CuCl	powder	pure	Merck
Copper(I) iodide	CuI	powder	98+%	Lancaster

6.3.1.1 Purification of Cu

Copper oxides like CuO and Cu₂O are common passivation layers in commercially available Cu powder. Because of that, the passivated Cu powder was reduced in a H₂:Ar mixture (ratio 1:5) at 600 °C for 6 h prior to use. Then the Cu powder was sieved to ensure a homogeneous grain size distribution (40-80 μm).

6.3.1.2 Purification of Copper Halides

Copper(I) halides were washed with the corresponding hydrohalic acid as a means of purification. The insoluble impurities were removed by filtering the soluble complex which is built by the halides and the acid. Dilution with water caused dissociation of the complex and precipitation of copper(I) halide as a white powder. After filtrating the powder and washing it with distilled water and ether, Cu(I)X (X = Cl, I) is finally dried in vacuo and preserved under Ar atmosphere.

6.3.1.3 Synthesis of $\text{Rb}_4\text{Cu}_{16}\text{Cl}_{12.8}\text{I}_{7.2}$

$\text{Rb}_4\text{Cu}_{16}\text{Cl}_{12.8}\text{I}_{7.2}$ was synthesized from RbCl (0.1774 g, 1.46 mmol, 1 eq.), CuCl (0.3196 g, 3.23 mmol, 2.2 eq.) and CuI (0.5030 g, 2.64 mmol, 1.8 eq.). The respective powders are mixed together and pestled in a mortar and put into a quartz ampoule under nitrogen atmosphere. Then, the ampoule was evacuated under standard vacuo and sealed. The ampoule was subsequently heated for two days at 300 °C before being quenched in cold water. The resulting clump was ground, isostatically pressed to a pellet at a pressure of 8 t/cm². Then, the pellet was put into an ampoule and sealed under vacuo. Eventually, the ampoule was annealed for five days at 200 °C and then cooled down at room temperature. Finally, the pellet was ground, and the purity was verified by PXRD.

6.3.1.4 Synthesis of Cu_{2-x}S

Cu₂S was synthesized from Cu (7.985 g, 126 mmol, 2 eq.) and S (2.015 g, 63 mmol, 1 eq.). The powders were put into a quartz ampoule which was then evacuated under standard vacuum and sealed. The mixture was heated for two days at 500 °C before being quenched at air. The resulting Cu_{2-x}S phase was checked by PXRD.

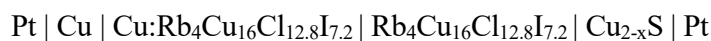
6.3.1.5 PXRD

High temperature PXRD with Mo-K_{α1} ($\lambda = 0.70930$ Å) radiation in Debye-Scherrer geometry was used to check the temperature stability of the solid electrolyte Rb₄Cu₁₆Cl_{12.8}I_{7.2}, see chapter 4.1.2 for details. Herein, a non-isothermal measurement was performed at 30 °C to check the initial state of the sample. Subsequently, the measurement was performed from 120 °C to 220 °C in 10 °C steps.

PXRD measurements with Cu-K_{α1} ($\lambda = 1.540598$ Å) radiation on a flatbed carrier in transmission geometry before and after EIS was used to check for possible electrode reactions.

6.3.2 Cell Setup and General Measurement Procedure

Before every measurement the solid electrolyte Rb₄Cu₁₆Cl_{12.8}I_{7.2} was pressed to pellets at a pressure of 8 t/cm². Accordingly, Cu, Cu_{2-x}S, and the Cu:Rb₄Cu₁₆Cl_{12.8}I_{7.2} mixture were pressed to pellets at 12 t/cm² prior to use and only pellets with a density > 90% were used for the measurements. Then, the pellets were assembled according to an asymmetrical arrangement. The electrochemical cell was set up in a glovebox under constant argon atmosphere, see chapter 4.1.1. The cell was arranged asymmetrically in the order (see chapter 3.2 and 3.3 for details):



Cu was used as reference electrode, Rb₄Cu₁₆Cl_{12.8}I_{7.2} as solid electrolyte and Cu_{2-x}S as working electrode. Between Rb₄Cu₁₆Cl_{12.8}I_{7.2} and Cu a 1:1 mixture of the reference electrode and the solid electrolyte was placed to ensure a smooth charge transfer from e⁻ to Cu⁺ between the electrodes. Cu|Cu:Rb₄Cu₁₆Cl_{12.8}I_{7.2}|Rb₄Cu₁₆Cl_{12.8}I_{7.2}|Cu_{2-x}S was combined at a ratio of 1:1:6. Small Pt plates connected to Pt wires were used to transfer the ac and dc current to the sample.

Before every measurement, the galvanic cell was polarized for at least 12 h at 150 °C and then at least 12 h at 40 °C to ensure a good homogenization of the sample composition. Afterwards, the open current potential (OCP = cell potential) of the galvanic cell was measured for 30 min to guarantee a steady state condition of the sample electrode Cu_{2-x}S. For all EIS measurements, an ac voltage of 10 mV was applied. Finally, the impedance spectra were recorded at intervals of 10 °C in a frequency range of 5·10⁻³ and 3·10⁵ Hz. Finally, an equivalent circuit was used to attain the resistance R from the fitted EIS spectra. The attained resistance is then used to calculate the conductivity.

6.4 Results & Discussion

6.4.1 Solid electrolyte Rb₄Cu₁₆Cl_{12.8}I_{7.2}

6.4.1.1 Thermostability of Rb₄Cu₁₆Cl_{12.8}I_{7.2}

PXRD was used to check the thermostability of the solid electrolyte Rb₄Cu₁₆Cl_{12.8}I_{7.2}. Therein, the solid electrolyte was heated up from 120 °C to 220 °C in 10 °C intervals, see **Figure 6.1**. The reflections are congruent to each other with only slight shifts in 2θ values, which can be assigned to a temperature dependent volume increase. Further, the cubic cell parameters for all measurements could be indexed and refined until convergence with Rb₄Cu₁₆Cl_{12.8}I_{7.2} [JCPDS, 37-1206]. This shows that the solid electrolyte remains unchanged and indicates a good thermostability of Rb₄Cu₁₆Cl_{12.8}I_{7.2} within the applied temperature range from 40-200 °C. The refined cell parameters ($a = 10.0159$ Å) can be assigned to the beforementioned composition. Also, no additional RbCl, CuCl, or CuI phases are formed in this stoichiometric range which is in agreement with literature.⁸⁸

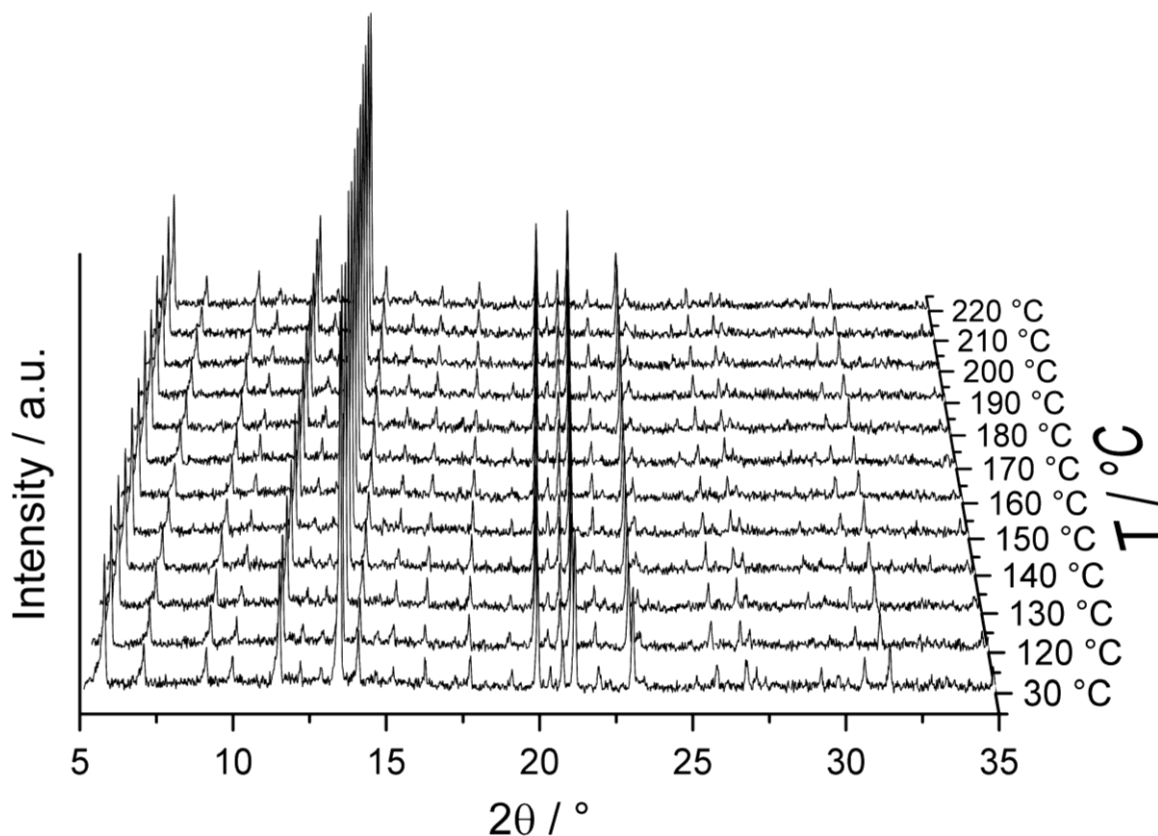


Figure 6.1: PXRD measurement of Rb₄Cu₁₆Cl_{12.8}I_{7.2} from 30-220 °C. The solid electrolyte remains unchanged up to 220 °C.

6.4.1.2 Conductivity of Rb₄Cu₁₆Cl_{12.8}I_{7.2}

The conductivity of pure Rb₄Cu₁₆Cl_{12.8}I_{7.2} was determined by EIS, arranged between two Au sheets, at temperatures between 30-220 °C. The respective Nyquist plot for the second cooling cycle is shown in **Figure 6.2 (left)**. The solid electrolyte displays the typical behaviour of a pure ionic conductor, which is depicted by the linear diffusion curve. Hence, the Nyquist plots can be fitted with an equivalent circuit consisting of a resistor and a CPE in series or alternatively to a Debye circuit which adds a parallel ideal capacitor for the geometrical Pt capacity. Further, the electronic conductivity of the solid electrolyte must be extremely low as no semicircle for electronic leakage is observed. Hence, the ionic conductivity is calculated from the serial resistance which is fitted to the Nyquist plots. The obtained ionic conductivities σ_{ion} from 30-220 °C are shown in **Figure 6.2 (right)**.

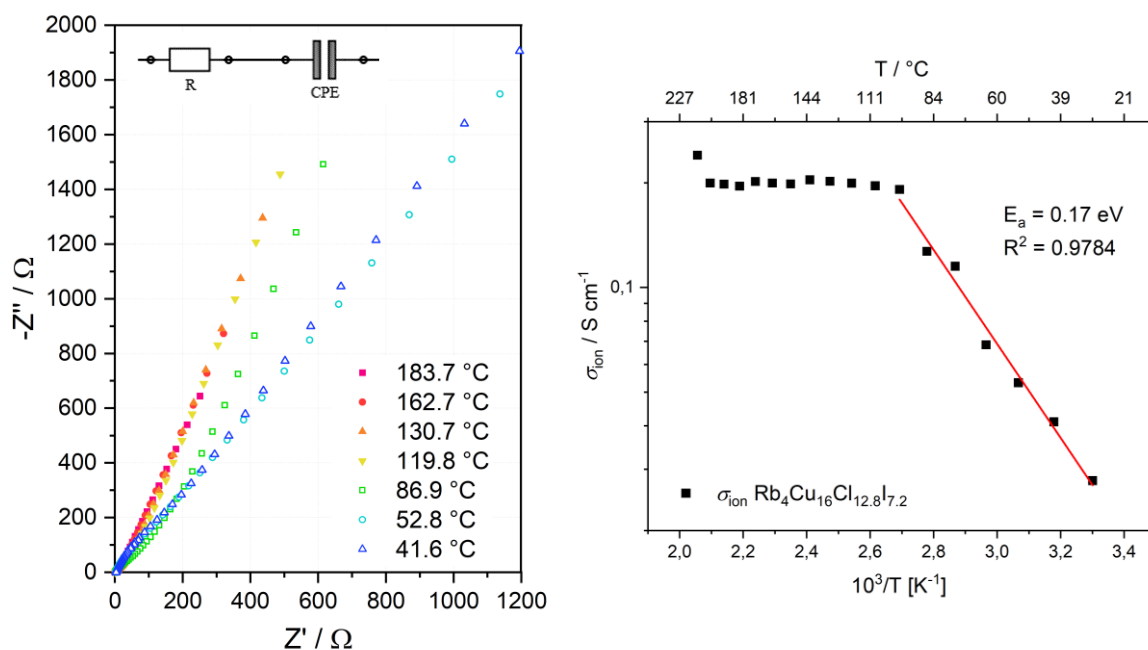


Figure 6.2: Left: Nyquist plot for the second cooling cycle of the EIS measurement of Rb₄Cu₁₆Cl_{12.8}I_{7.2} from 220-30 °C. The solid electrolyte displays a typical diffusion curve for a pure ionic conductor. Right: Arrhenius plot for the ionic conductivity σ_{ion} of Rb₄Cu₁₆Cl_{12.8}I_{7.2}.

From 30 °C to 110 °C the ionic conductivity increases linearly with temperature from 0.02 S/cm to 0.2 S/cm as expected from an ionic conductor. Unexpectedly, the conductivity stagnates at ~0.2 S/cm above 110 °C and the detailed mechanism has not been clarified so far. Compared to the experimental conductivity, the ionic conductivity of Rb₄Cu₁₆Cl_{12.8}I_{7.2} was reported to range between 0.28-0.37 S/cm by *Takahashi et al.*^{88, 89} Thus, the values determined in this thesis are slightly lower, but still in the same magnitude. Further, the activation energy was calculated to 0.17 eV from the Arrhenius equation in the temperature range from 30 °C to 110 °C. The electronic conductivity is low, since the electrolyte is a pure ionic conductor, with values of $1 \cdot 10^{-12}$ S/cm for electronic conductance at 60 °C according to *Takahashi et al.*^{88, 89} Therefore, Rb₄Cu₁₆Cl_{12.8}I_{7.2} is a suitable solid electrolyte for the galvanic cell arrangement as it is a pure Cu ion conductor with negligible electronic conduction. Hence, Rb₄Cu₁₆Cl_{12.8}I_{7.2} can be used as an electron blocking electrode (EBE).

6.4.2 EIS on a Pure Cu_{2-x}S Cell

The total electronic conductivity σ_{eon} of pure Cu_{2-x}S without the solid electrolyte was measured in a symmetrical arrangement between two Au plates contacted by two Pt sheets. Beforehand, the cell potential of the galvanic cell Cu|Cu⁺|Cu_{2-x}S was measured at room temperature to determine the composition of the sample. Hence, an open current potential of 13 mV was measured prior to the EIS measurement which corresponds to a nearly stoichiometric composition of $2-x \approx 2$ for α -Cu₂S. Then, EIS was performed at temperatures between 40-200 °C at an ac voltage of 10 mV. The respective Nyquist plots for one heating cycle are shown in **Figure 6.3**. From 40-80 °C monoclinic low chalcocite exhibits the behaviour of a pure resistor. Then, a phase transition occurs above 100 °C to the hexagonal high chalcocite, which displays semicircles in the Nyquist plot. This is a typical behaviour for semiconducting materials. Accordingly, the semicircles are fitted with an equivalent circuit which consists of a resistor in series with a RC element. Note that the semicircles are depressed compared to ideal semicircles. This can be attributed to the porous surface of the solid electrodes which yields non-ideal capacitive behaviour and therefore must be fitted with a CPE element.

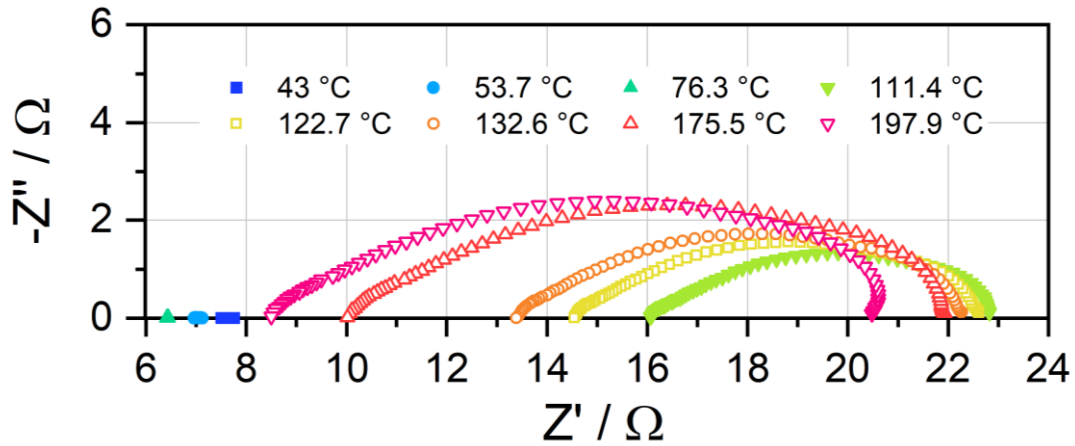


Figure 6.3: Nyquist plots for the EIS measurements on pure Cu_{2-x}S (OCP = 13 mV) from 30-200 °C.

Eventually, the EIS spectra are fitted with the equivalent circuits and the attained resistances are used to calculate the electronic conductivity of the Cu_{2-x}S sample, see **Figure 6.4**. Therein, the electronic conductivity increases with temperature up to 0.06 S/cm at 84 °C. Then the phase transition to high chalcocite begins in this region and the conductivity decreases with temperature. This trend matches with the literature data in chapter 5.3.4 where a decline of the electronic conductivity is observed for the β -Cu_{2-x}S phase. Also, the experimental values (0.03-0.06 S/cm) are in a similar range compared to the literature data, see table **Table 6.2**.

Table 6.2: Experimental values of the electronic conductivity σ_{eon} for specific compositions compared to the literature data.

	Composition	E / mV	$\sigma_{\text{eon}} / \text{Scm}^{-1}$ at 25 °C	$\sigma_{\text{eon}} / \text{Scm}^{-1}$ at 150 °C
Experimental	$\approx \text{Cu}_{1.9999}\text{S}$	13	0.05	0.035
Ishikawa et al ¹⁶⁹	$\approx \text{Cu}_{1.9999}\text{S}$	80-20 (25-150 °C)	0.1	0.04
Pauporte et al ¹⁷² .	$\text{Cu}_{1.9984}\text{S}$	70	4	1

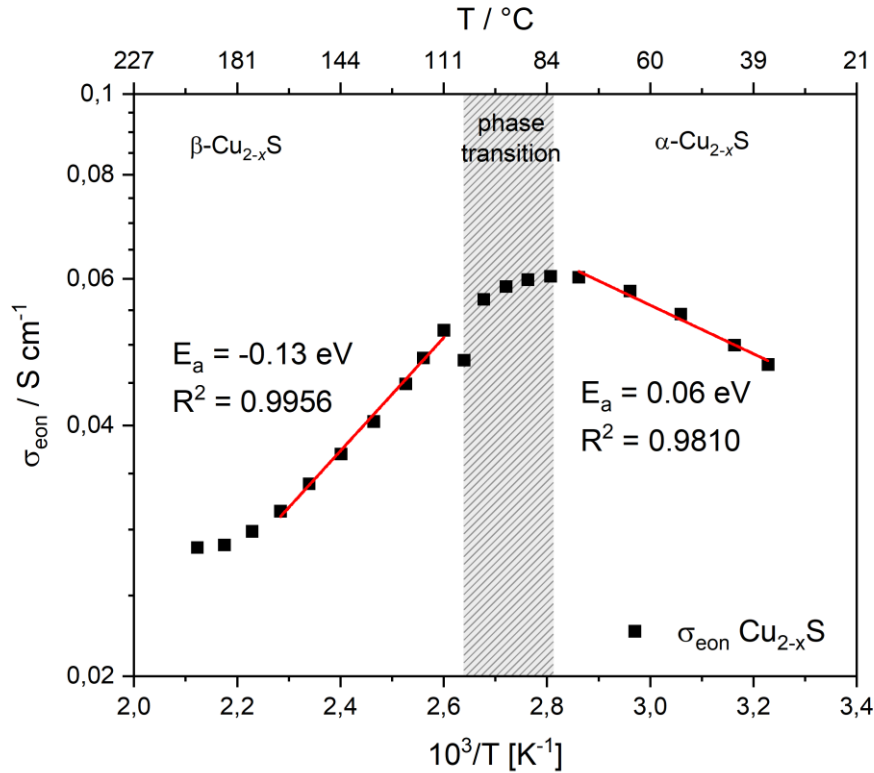


Figure 6.4: Arrhenius plot for the electronic conductivity σ_{eon} for pure Cu_{2-x}S (OCP = 13 mV) from 30–200 °C.

Thereby, the lower experimental values for σ_{eon} are expected due to the lower cell potential (OCP = 13 mV) and thus a higher stoichiometric composition of $\alpha\text{-Cu}_{1.9999}\text{S}$. Hence, the vacancy concentration, which act as electron acceptors, is lower and thus yields lower conductivity. Further, the initial increase of the conductivity is to be expected due to the semiconducting behaviour of the material. The following drop of total conductivity might be contributed to the phase change either to the tetragonal phase Cu_{1.96}S, djurleite phase Cu_{1.95}S, or high chalcocite phase $\beta\text{-Cu}_2\text{S}$ (see table 5.1). A PXRD measurement of the Cu_{2-x}S phase before the measurement reveals the existence of a small amount of the tetragonal Cu_{1.96}S beneath the $\alpha\text{-Cu}_{2-x}\text{S}$ phase (see **Figure A. 6.4**). Thereby, the transition to high chalcocite is the most obvious as it is anticipated from the phase diagram. However, as discussed before, demixing of the chalcocite phase could spontaneously lead to the more thermodynamically stable djurleite or tetragonal phase which could explain the drop in conductivity. Also, more of the tetragonal phase could be produced which in turn might lead to the drop in conductivity. Moreover, it is also feasible that the ionic conduction in the higher symmetric hexagonal $\beta\text{-Cu}_2\text{S}$ proceeds predominantly by Cu ion movement due to the solid-liquid hybrid phase behaviour. This in turn diminishes the importance of the vacancy concentration and in turn could alter the electronic conduction. Also, it was shown by DFT studies that the ionic movement primarily occurs between the *hcp* layers of S atoms which in turn might affect the electronic conductivity.¹⁶⁴

6.4.3 Electrochemical Measurements on the Galvanic Cell Cu|Cu⁺|Cu_{2-x}S

6.4.3.1 Ionic Conductivity σ_{ion} and Self-Diffusion Coefficient D_{Cu^+}

The EIS measurements with the galvanic cell Cu|Rb₄Cu₁₆Cl_{12.8}I_{7.2}|Cu_{2-x}S were carried out in a temperature range between 40-200 °C. Note that the same sample as in the previous section is used for the galvanic cell. Prior to the EIS measurements, the cell voltage was held constant at 0 mV to adjust the composition of the sample, and the steady state of the cell was monitored before the measurements was performed (see **Figure A. 6.2**). Then, the EIS measurements were conducted from 300 kHz to 5 mHz. The respective Nyquist plots for the β -Cu_{2-x}S phase above 100 °C are shown in **Figure 6.5**. At 100 °C the α -Cu_{2-x}S phase undergoes a phase transition towards the β -Cu_{2-x}S which is depicted in the Nyquist plot by the semicircles at high frequencies and the diffusion curve at low frequencies. Note that the semicircles are shifted towards lower resistances as the temperature increases. Thereby, the small bump at the high frequency region of the semicircle represents the charge transfer resistance between the Cu|EBE electrode interface, the semicircle the ionic contribution and the straight diffusion curve at low frequencies depicts the diffusion of Cu ions in Cu_{2-x}S. As seen before, the semicircles are depressed due to the roughness factor of the solid electrodes. The same phenomenon is observed for the diffusion curves at low frequencies which are slightly shifted towards angles below 45 °.

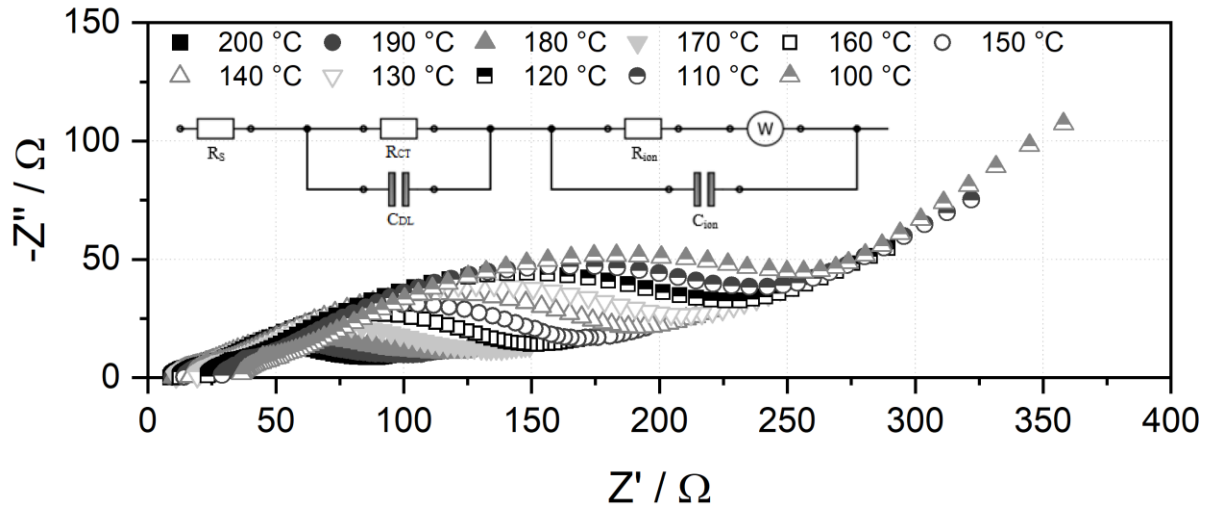


Figure 6.5: Nyquist plots for the EIS measurement from 300 kHz to 5 mHz on the galvanic cell Cu|Rb₄Cu₁₆Cl_{12.8}I_{7.2}|Cu_{2-x}S (OCP = 0 mV, \approx Cu_{1.9999}S) and the corresponding equivalent circuit. Here shown for the high chalcocite phase β -Cu_{2-x}S from 100 °C to 200 °C. Therein, the Nyquist plots of the β -Cu_{2-x}S phase typically display a semicircle at high frequencies and a linear diffusion curve at low frequencies.

Accordingly, the EIS spectra of α -Cu_{2-x}S and β -Cu_{2-x}S were fitted with the respective equivalent circuits shown in **Figure 6.6** (see **Figure A. 6.1** for the respective Bode plots). Therein, the Nyquist plot of α -Cu_{2-x}S solely exhibits a straight diffusion tail which can be fitted by a resistance in series with a capacitor. Hence, the ionic conductivity can simply be calculated by the fitted resistance. Whereas the EIS spectra of β -Cu_{2-x}S must be fitted with

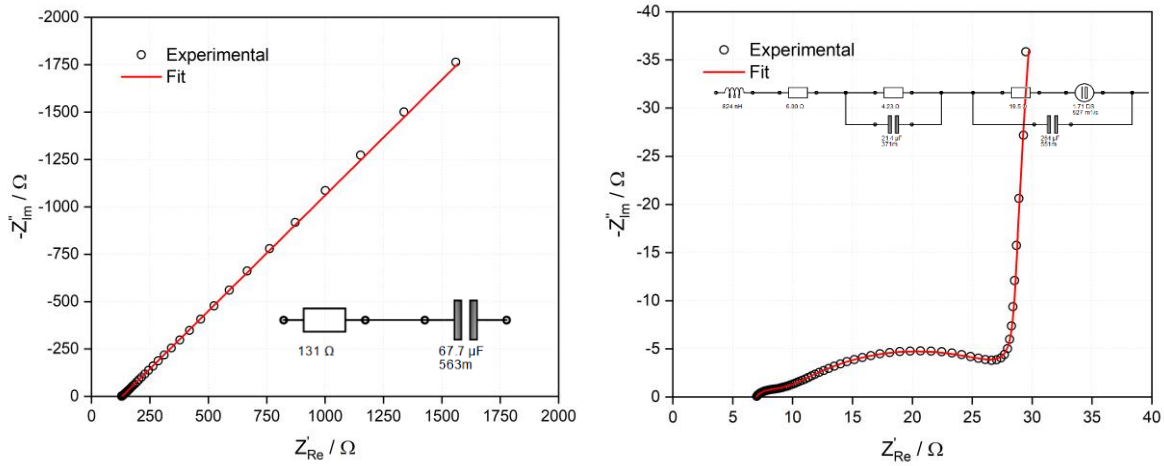


Figure 6.6: Left: Fitted Nyquist plot and equivalent circuit for the galvanic cell Cu|Cu⁺|Cu_{2-x}S at 40 °C. Right: Fitted Nyquist plot and equivalent circuit for the corresponding galvanic cell at 190 °C.

a RC element for the charge transfer resistance, a RC element for the ionic conductivity, and a FD element for the diffusion of Cu ions. Additionally, an inductor and a series resistor are added due to an inductive contribution of the current at high frequencies and the small resistance of the EBE. Consequently, the ionic conductivity can be calculated from the fitted resistance R_{ion} . Note that either a FD element or an ideal Warburg impedance element was used to fit the diffusion tail in the EIS spectra. Theoretically, the galvanic cell should display the closed expression Z_{FD} because of the asymmetric arrangement of the cell, which should lead to a capacitive behaviour of the diffusion tail. However, depending on the temperature and the cell potential also a Warburg type diffusion behaviour was observed. Consequently, a Warburg element was used in the equivalent circuit. Note that the different diffusion impedance elements did not significantly influence the ionic resistance.

Hence, eq. 3.29 is used to calculate the ionic conductivity from the fitted ionic resistance, see **Figure 6.7 (left)**. Therein, the temperature dependent ionic conductivities are shown for the galvanic cell measured at an OCP of 0 mV. The conductivity increases steadily with increasing temperature as is expected for semiconductors. It ranges between values of $9.5 \cdot 10^{-4}$ - $1.3 \cdot 10^{-2}$ S/cm from 40 °C to 200 °C. The brief drop at ca. 120 °C results from the phase transition from low to high chalcocite which theoretically should occur at 103 °C. However, the phase transition happened roughly at the expected temperature during the cooling cycle. Thus, the unexpectedly high transition temperature in the heating cycle could be a consequence of insufficient annealing time before the respective EIS measurement. In addition to that, a phase transition from low chalcocite to tetragonal Cu_{1.96}S besides high chalcocite is also feasible as mentioned in the previous section.

Consequently, the activation energies are calculated from the slopes in the Arrhenius plots for the respective phase regions which is assumed to be low and high chalcocite. Here, the composition is assumed to be \approx Cu_{1.9999}S due to the cell potential of 0 mV with activation energies of 0.27 eV and 0.21 eV are obtained for low and high chalcocite, respectively. The obtained values match well with

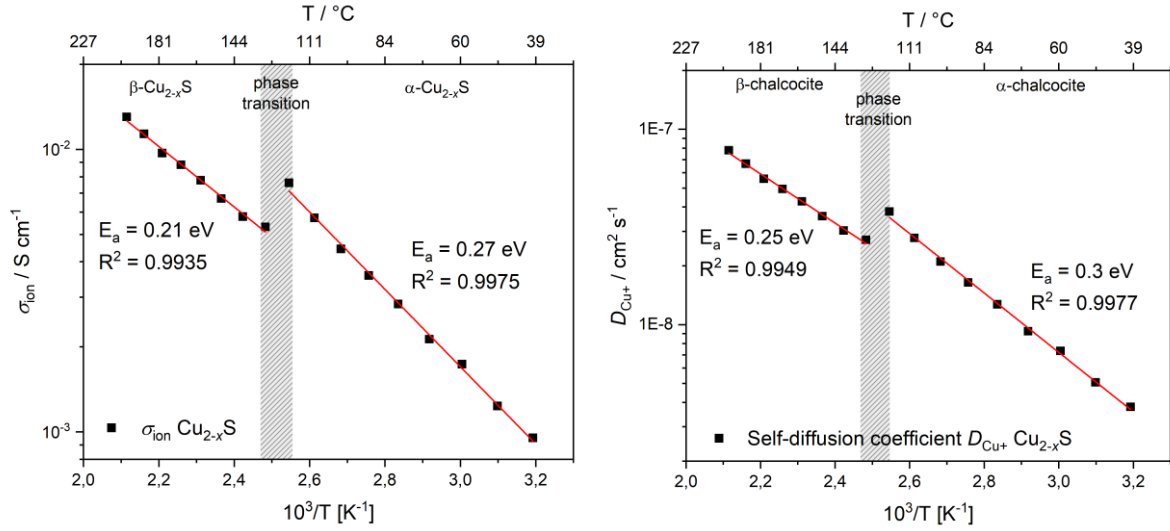


Figure 6.7: Left: Arrhenius plot for the ionic conductivity σ_{ion} of Cu_{2-x}S (OCP = 0 mV, $\approx \text{Cu}_{1.9999}\text{S}$) from 40 °C to 200 °C measured by the galvanic cell arrangement $\text{Cu}|\text{Cu}^+|\text{Cu}_{2-x}\text{S}$. Right: Respective Arrhenius plot for the self-diffusion coefficient D_{Cu^+} of Cu_{2-x}S (OCP = 0 mV, $\approx \text{Cu}_{1.9999}\text{S}$) from 40 to 200 °C.

the data from *Miyatani* for low chalcocite $E_a = 0.3 \text{ eV}$ ($\approx \text{Cu}_2\text{S}$) and *Okamoto et al.* for high chalcocite $E_a = 0.24 \text{ eV}$ ($\approx \text{Cu}_2\text{S}$).^{170, 177} Accordingly, the self-diffusion coefficient is calculated from the ionic conductivity with eq. 3.10, see **Figure 6.7 (right)**. There, the same trends are observed for the self-diffusion coefficient D_{Cu^+} with values ranging from $3.8 \cdot 10^{-9} - 7.8 \cdot 10^{-8} \text{ cm}^2 \text{ s}^{-1}$ from 40-200 °C. Also, the activation energies E_a are calculated from the Arrhenius plot and are 0.3 eV and 0.25 eV for low and high chalcocite, respectively. Again, the value for high chalcocite matches well with 0.24 eV obtained by *Okamoto et al.* in the high chalcocite region from 110-220 °C.¹⁷⁷ Contrary to that, *Bucur et al.* found a much higher value of 0.48 eV but for a composition of $\approx \text{Cu}_{1.8}\text{S}$.¹⁸¹ Thus, the activation energy seems to increase from chalcocite to anilite/digenite.

Further comparison of the obtained experimental ionic conductivities to the literature data reveals higher values by one order of magnitude compared to the works of *Rickert* and *Tinter et al.*, see **Figure 6.8 (left)**.^{76, 91} However, *Rickert* and *Tinter* mostly used compositions of $\text{Cu}_{1.96}\text{S}$, $\text{Cu}_{1.94}\text{S}$, and $\text{Cu}_{1.93}\text{S}$ which could explain the lower ionic conductivity. Also, the experimental values of the high chalcocite phase are lower by about one order of magnitude compared to the data of *Okamoto et al.*¹⁷⁷ However, *Okamoto et al.* did not determine the exact stoichiometric composition and only give an assumed composition of Cu_2S . Therefore, the deviation from the experimental data could be a consequence of the altered composition. Yet, a similar temperature dependency of the ionic conductivity is observed for the high chalcocite phase. Strikingly, the experimental data of the high chalcocite phase coincides with the ionic conductivities from *Hirahara* at 150 °C and 200 °C.

The comparison of the self-diffusion coefficient D_{Cu^+} (or often called component diffusion coefficient) to the literature data in principle reveals a similar picture, see **Figure 6.8 (right)**. Therein, the experimental values are higher by about one order of magnitude compared to the literature data of *Rickert*, *Tinter*, *Castel*, and *Etienne*.^{76, 91, 175, 182}

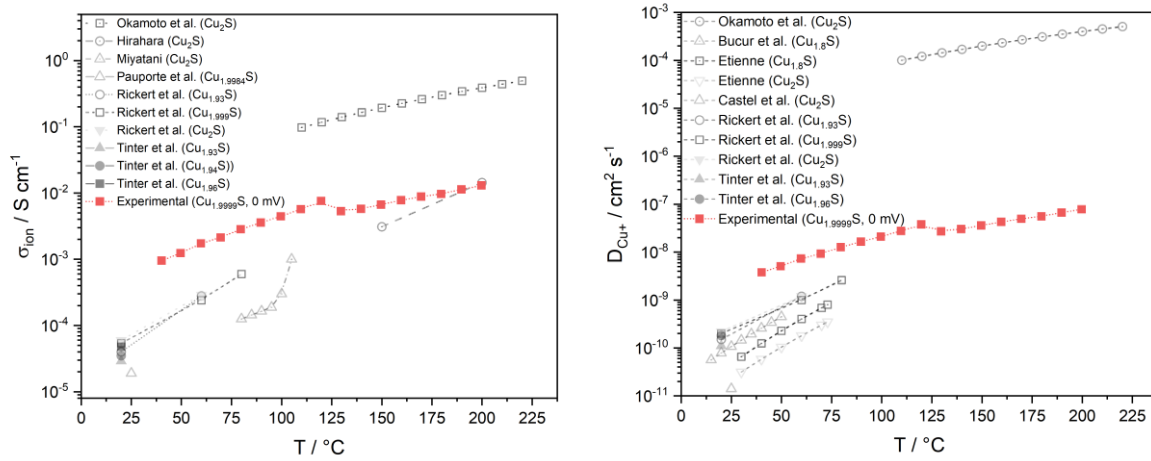


Figure 6.8: Left: Comparison of the experimental values for the ionic conductivity σ_{ion} to the literature data. Right: Experimental values D_{Cu^+} determined by EIS compared to the literature data.^{76, 78, 91, 169, 170, 172, 175, 177, 179-182}

Note that *Castel* and *Etienne* only give an approximate composition of $\approx \text{Cu}_2\text{S}$. Further, *Rickert et al.* measured compositions of $\approx \text{Cu}_2\text{S}$ and $\text{Cu}_{1.999}\text{S}$ but also obtained lower values of about $1.0 \cdot 10^{-9} \text{ cm}^2 \text{s}^{-1}$ at 60°C .⁷⁶ Thus, it is feasible that the deviation of the experimental data originates from the methodology but also keep in mind that an extremely high stoichiometric composition of $0 \text{ mV} \approx \text{Cu}_{2-1.9999}\text{S}$ is used for the EIS measurements. Thus, the higher values for the experimental diffusion coefficients could also stem from the stoichiometric composition of the copper sulfide phase. As seen before, the values from *Okamoto et al.* for the high chalcocite phase are much higher than the experimental values by four orders of magnitude.¹⁷⁷ These values seem extremely high and it is anticipated that the experimental data are closer to the real diffusion coefficient. Also, an imaginary extrapolation of the literature data for the low chalcocite phase would coincide with the obtained experimental diffusion coefficients. Thus, it is concluded that EIS measurements on the galvanic cell $\text{Cu}|\text{Cu}^+|\text{Cu}_{2-x}\text{S}$ can be used to determine the electrochemical properties of copper sulfide phases and the obtained values are in an appropriate range.

6.4.3.2 Emf Dependent EIS Measurements on the Galvanic Cell $\text{Cu}|\text{Cu}^+|\text{Cu}_{2-x}\text{S}$

Like the measurement of the Cu_{2-x}S sample in the galvanic cell in the previous sections, EIS measurements were conducted with the same cell at different cell potentials. Therefore, the cell potential was adjusted with a constant voltage from 0 mV to 120 mV in increments of 20 mV. Further, the OCP potential was monitored before each EIS measurement to ensure the steady state of the cell potential (see **Figure A. 6.2**). Thereby, the cell potentials were modified to change the composition of the Cu_{2-x}S sample. Herein, the same cell potential – composition relationship obtained by *Ishikawa et al.* (see chapter 5.3.2) is expected for the galvanic cell in this thesis.¹⁶⁹ Accordingly, the cell potential at 0 mV and 120 mV correspond to Cu_2S and $\text{Cu}_{1.9995}\text{S}$ respectively. Also, the Nyquist plots exhibit the same behaviour as described in the previous chapter. Thus, the ionic resistance is obtained from the fit of the equivalent circuit and D_{Cu^+} is calculated from the ionic conductivity. Then, the self-diffusion coefficient is plotted as a function of temperature for the respective cell potentials in **Figure 6.9**. Therein, it is evident that the diffusion coefficient increases with higher cell

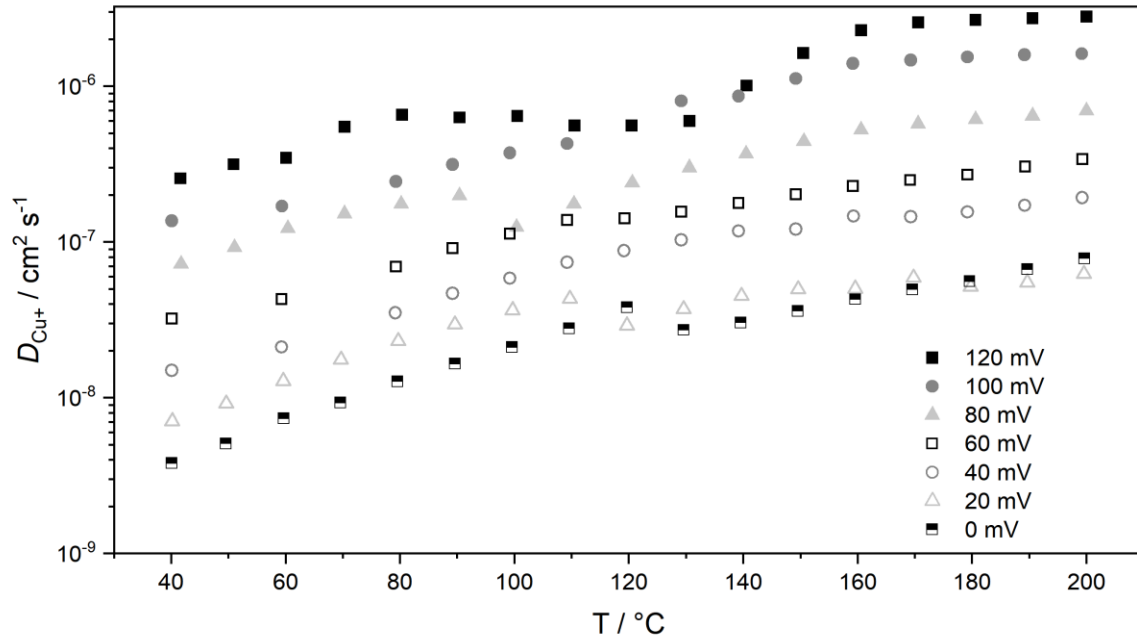


Figure 6.9: Self-diffusion coefficient D_{Cu^+} plotted versus temperature for different cell potentials from 0 mV (Cu_2S) to 120 mV ($\text{Cu}_{1.995}\text{S}$). The cell potential was adjusted by a constant voltage and the steady state was confirmed by monitoring of the OCP prior to the EIS measurements.

potential from $4.4 \cdot 10^{-9} - 2.8 \cdot 10^{-6} \text{ cm}^2 \text{ s}^{-1}$ at 40 °C and thus with deviation from ideal chalcocite composition. Note that, the diffusion mechanism can either proceed via Cu ion movement or a vacancy mechanism. Hence, a lower diffusion coefficient is anticipated if the diffusion takes place by a Cu^+ diffusion mechanism. This is due to the lower Cu concentration which should yield a lower diffusion coefficient. However, the contrary is confirmed which supposes the presence of a vacancy mechanism. This is in line with the observations from *Cassaignon et al.* and *Pauporte et al.* which assume a vacancy mechanism in low chalcocite.^{78-80, 172, 174} Hence, the diffusion coefficients increase with deviation from ideal low chalcocite composition and thus increasing vacancy concentration. Note that *Cassaignon et al.* also measured an initial increase of the diffusion coefficient for small deviations from ideal composition with a subsequent decrease with higher deviation from ideal composition.⁸⁰ However, opposing trends are found in literature where *Rickert et al.* measured decreasing and *Castel* increasing diffusion coefficients with lower Cu concentration.^{76, 175} Also, the literature review in chapter 5.3.4 points to a decreasing diffusion coefficient with lower Cu concentration from chalcocite to covellite.

Herein, it is concluded that the diffusion coefficient initially increases with small deviations from ideal composition because of the increased vacancy concentration. As the vacancy concentration increases, the Cu atoms could be more strongly bound within the copper sulfide structure. Consequently, a decrease of the diffusion coefficient is anticipated with higher deviation from ideal chalcocite composition.

After the measurements on pure Cu_{2-x}S, the galvanic cell at 0 mV, and the emf dependent EIS measurements. The cell was checked via PXRD for any side reactions on the electrode surface and phase transitions. Hence, no change is confirmed for Rb₄Cu₁₆Cl_{12.8}I_{7.2} (see **Figure A. 6.3**). Yet, a high amount of tetragonal Cu_{1.96}S is confirmed beneath low chalcocite in the Cu_{2-x}S sample despite the polarization at 0-120 mV which should give a composition between Cu_{2-1.9995}S (see **Figure A. 6.4**). As mentioned before, the low and high chalcocite phases are prone to spontaneous demixing towards djurleite or digenite. In this case, the tetragonal phase presumably formed during the polarization and heating cycles. Therefore, the tetragonal phase must be considered with regard to the obtained ionic conductivities and diffusion coefficients. However, the general trend for the temperature dependency of the diffusion coefficients remains constant and also matches with the values found in literature. Also, the low values of the electronic conductivity indicate the presence of chalcocite and a composition near ideal Cu₂S. Therefore, it is assumed that the tetragonal phase does not prevail in the EIS measurements.

Further, a small precipitate was found in between the EBE|Cu_{2-x}S interface and was confirmed to be pure Cu (see **Figure A. 6.5**). Yet, no significant difference was observed in the EIS spectra for higher cell potentials and increasing galvanic cell age during the series measurements. Also, the adjustment of a distinct cell potential is only possible if the Cu and Cu_{2-x}S electrode are separated by an electrolyte. There, the OCP was checked prior to every EIS measurement which proves the existent separation of the electrodes. Hence, it is assumed that the small Cu precipitate does not significantly alter the EIS measurements. However, it could be feasible that the small Cu precipitate might lead to a slight elevation of the measured diffusion coefficients which has to be taken into account.

6.4.3.3 Chemical Diffusion Coefficient

Finally, the chemical diffusion coefficients are calculated from the measurement of the galvanic cell at 0 mV. Thereby, the chemical diffusion coefficient can be calculated by different equations as the thermodynamic factor ($d\ln a/d\ln c = dE/dc$) is not easily available ($\tilde{D}_{\text{Chem}} = D_{\text{self}} \cdot d\ln a/d\ln c$). Also, different methods and equations were utilized in literature to calculate the chemical diffusion coefficient. Therefore, four different methods are used in this thesis to calculate \tilde{D}_{Chem} and to get further insight into differences and better comparability between these methods, see **Table 6.3** for an overview (see chapter 3.3 and 3.4 for more details). The first method (EIS, P) uses the obtained ionic conductivity and accounts for the thermodynamic factor dE/dc (37.8 V) which is extracted from *Pauporte* for a composition range of Cu_{2-1.997}S.¹⁷² Note that this method is commonly used by *Rickert* and *Tinter* et al. to calculate \tilde{D}_{Chem} .^{76, 91} Additionally, coulometric titration (CT) was performed at 120 °C on a newly prepared galvanic cell with the same arrangement and identical Cu_{2-x}S powder as in the previous chapters. Prior to the titration, the cell voltage was adjusted to 0 mV. Then, CT was performed with a constant current of 1 μ A up to 200 mV (see **Figure A. 6.7**). Then, the cell voltage U_{cell} was plotted versus t and $t^{1/2}$ at short polarization times to obtain the slopes k' and k . Subsequently, the chemical diffusion was calculated from the obtained parameters. Then, potentiostatic titration (PT) was performed on the same cell at 120 °C and 160 °C starting from 200 mV.

Table 6.3: Overview of the different methodologies and equations which are used for the calculation of the chemical diffusion coefficient \tilde{D}_{chem} . Note that dE/dc was extracted from the literature for a composition range of Cu_{2-1.997}S.¹⁷²

Methodology	Equation	Obtained parameter
1. EIS(P), 0 mV \approx Cu _{1.9999} S	$\tilde{D}_{chem} = \frac{\sigma_{ion}}{F} \cdot \left(\frac{dE}{dc} \right)$	σ_{ion} (exp.), dE/dc (lit.) ¹⁷²
2. EIS(Slope), 0 mV \approx Cu _{1.9999} S	$\tilde{D}_{chem} = \left[\frac{RT}{z^2 F^2 A \sqrt{2} \cdot S \cdot V_{Cu}^*} \right]^2$	Slope S (from Nyquist plot) and V_{Cu}^*
3. Coulometric titration (CT), 0 mV \approx Cu _{1.9999} S	$\tilde{D}_{chem} = \left[2 \frac{k'}{k} \cdot \frac{L}{\sqrt{\pi}} \right]^2$	k' and k
4. Potentiostatic titration (PT), 200 mV \approx Cu _{1.999} S	$\tilde{D}_{chem} = \left[\frac{k'' \cdot \sqrt{\pi}}{z \cdot F \cdot A \cdot V_{Cu}^*} \right]^2$	k'' , and V_{Cu}^*

Therefore, a constant voltage of 0 mV was applied on the galvanic cell. Then, the measured cell current I is plotted versus $t^{1/2}$ for short polarization times to determine the slope k'' . Finally, \tilde{D}_{Chem} is calculated from the obtained parameters. Here, a composition of Cu_{1.999}S is assumed for the initial cell potential of 200 mV.

Further, the slope S is determined from the EIS measurement on the galvanic cell at 0 mV. This method (EIS, Slope) was used by *Cassaignon* et al. and *Pauporte* et al. to determine the chemical diffusion coefficient.^{80, 172-174} Note that the vacancy concentration is used here instead of the Cu concentration. To determine the slope S , the impedance Z_{Re} and Z_{Im} of the low frequency tail, which represents the diffusive contribution in the Nyquist plots, is plotted versus $\omega^{-1/2}$, see **Figure 6.10**. This plot is also called Randles plot and the obtained slopes S from this plot can then be used to calculate \tilde{D}_{Chem} . Note that in this thesis the slope S of the impedance Z_{Re} vs $\omega^{-1/2}$ is used to determine \tilde{D}_{Chem} .

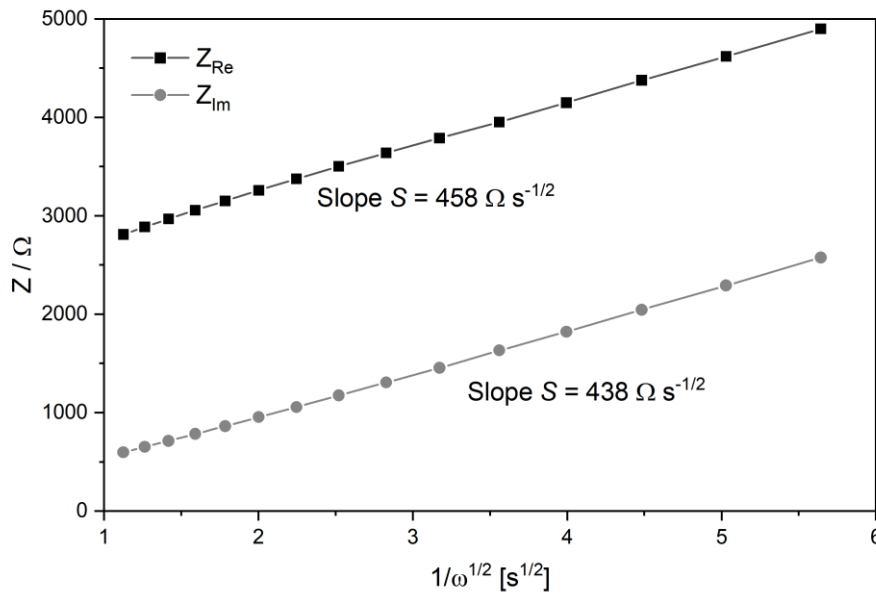


Figure 6.10: Diffusion curve (low frequency range) of the Nyquist plot at 40 °C represented as Randles plot with Z_{Re} and Z_{Im} plotted versus $1/\omega^{1/2}$. The curves exhibit a straight line with similar slopes S and can thus be used for the calculation of the chemical diffusion coefficient \tilde{D}_{chem} .

Consequently, \tilde{D}_{Chem} is calculated with method 1 and 2 from the same EIS measurement on the galvanic cell at 0 mV in the temperature range from 40 °C to 200 °C. The obtained experimental values are shown in the Arrhenius plot of \tilde{D}_{Chem} , see **Figure 6.11**. Therein, it is evident that the chemical diffusion coefficient strongly depends on the respective method which is used for the calculation. Here, the values obtained by EIS(P), which used the ionic conductivity and the thermodynamic factor dE/dc , exhibits the same behaviour as the ionic conductivity. The respective values range between $3.7 \cdot 10^{-7}$ - $5.1 \cdot 10^{-6}$ cm² s⁻¹ and the obtained activation energies for low and high chalcocite are 0.12 eV and 0.09 eV. Compared to that, the values obtained by EIS(Slope, Cu_{1.9999}S) are lower at 40 °C with a much higher acceleration up to 200 °C. Thereby, the diffusion coefficients range between $5.9 \cdot 10^{-8}$ – $9.6 \cdot 10^{-4}$ cm² s⁻¹ from 40 °C to 200 °C. Hence, higher activation energies are determined with 0.33 eV and 0.27 eV for low and high chalcocite, respectively. Note that a composition of Cu_{1.9999}S is assumed for the calculation of the vacancy concentration.

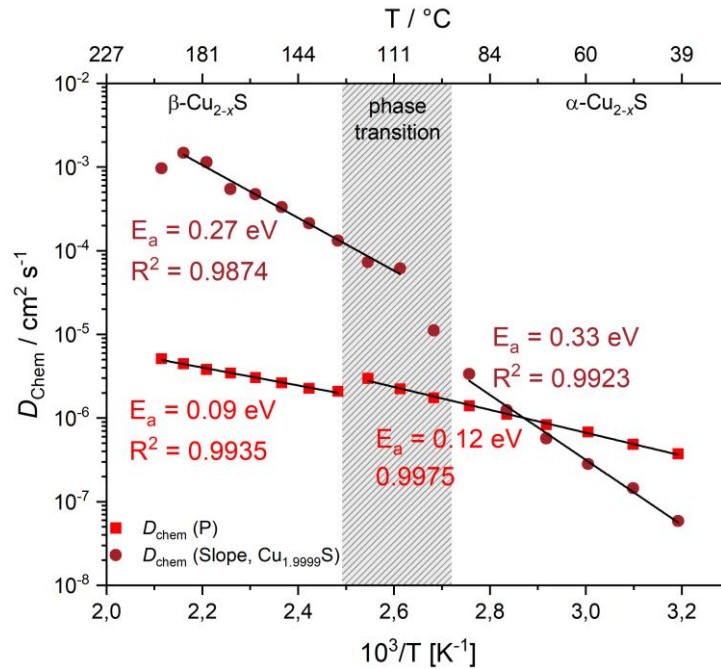


Figure 6.11: Arrhenius plot for the obtained chemical diffusion coefficients from 40 °C to 200 °C. Two different methods are applied: $\tilde{D}_{\text{Chem}}(\text{P})$ is calculated from σ_{ion} with $dE/dc = 37.8$ V. $\tilde{D}_{\text{Chem}}(\text{Slope, Cu}_{1.9999}\text{S})$ is calculated from the slopes of the Randles plot with a vacancy concentration corresponding to Cu_{1.9999}S.

Apparently a big deviation exists between the two methods. Thus, an overview of the activation energies found in literature is given in **Table 6.4** for better comparability. Therein, a mean activation energy E_a of 0.41 eV is found for the low chalcocite phase. Also, the lowest value, determined by *Pauporte et al.* by P.E. technique, is 0.26 eV for a composition of Cu_{1.9962}S. Therefore, an activation energy of 0.12 eV, determined by EIS(P), is rather unlikely. Contrary to that, the values determined by EIS(Slope) are comparable to the activation energies found in literature. Note that the thermodynamic factor is theoretically independent of the temperature and thus always gives the same activation energy for a given ionic conductivity. Thus, it is concluded that the method which employs the thermodynamic factor is assessed as unsuitable. Also, the determination of the thermodynamic

factor remains critical as it is strongly dependent on the composition and the measured emf curves. However, a similar problem occurs for the EIS-Slope method. Therein, a critical parameter is the chosen vacancy concentration V_{Cu}^* for the calculation of \tilde{D}_{Chem} . Yet, the experimental values of 0.33 eV and 0.27 eV are in good agreement with the activation energies of 0.28 eV and 0.26 eV determined by Pauporte et al for low and high chalcocite, respectively.

Table 6.4: Overview of the activation energies E_a for \tilde{D}_{Chem} found in literature at the respective temperature ranges and compositions. Moreover, the mean activation energy is calculated for the low chalcocite values (Cu_{2-1.993}S) and the experimental values determined for the low chalcocite phase are given for better comparison.

	Temperature range / °C	Composition x in Cu _x S	E_a / eV
<i>Etienne</i> , 1970 ¹⁸²	30-73	≈ 2	0.51
	30-73	≈ 1.8	0.52
<i>Rickert</i> et al., P.E., 1983 ⁷⁶	20-80	2.0-1.996	0.45
<i>Tinter</i> et al., P.E., 1983 ⁹¹	20-80	1.96-1.93	0.32
<i>Allen</i> et al., 1984 ¹⁷⁶	25-70	1.996	0.40
<i>Bucur</i> et al., 1995 ¹⁸¹	15-50	≈ 1.8	0.48
<i>Pauporte</i> , EIS solid, 1996 ⁷⁸	120-160	1.9965	1.70
<i>Pauporte</i> , EIS liquid, 1996 ⁷⁸ 1999 ¹⁷²	30-60	1.998	0.47
	27-57	1.9984	0.40
<i>Pauporte</i> , P.E., 1999 ¹⁷²	20-100	1.9985	0.37
	20-100	1.9962	0.28
	120-190	1.9962	0.26
Mean activation energy E_a for composition Cu _{2-1.993} S (low chalcocite)			0.41 \pm 0.07
Exp. EIS (P)	40-120	1.9999	0.12
Exp. EIS (Slope)	40-90	1.9999	0.33

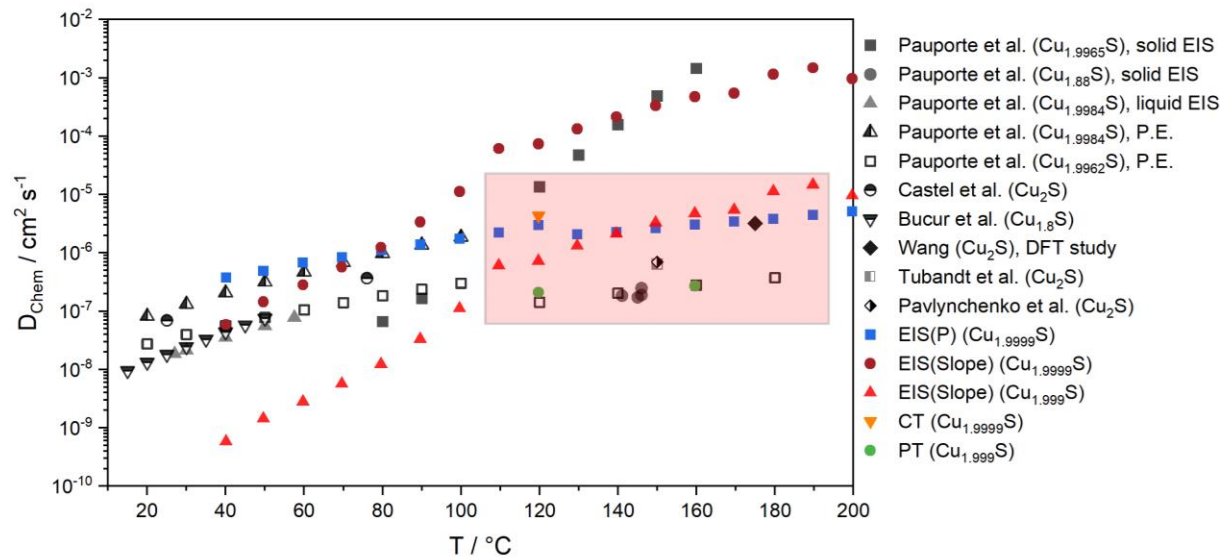


Figure 6.12: Experimental values obtained by EIS, coulometric titration (CT), and potentiostatic titration (PT) compared to the literature data.^{78, 164, 172, 174, 175, 181, 183, 184} Note that the values determined by the slope of the Randles plot are strongly dependent on the assumed vacancy concentration (EIS-Slope, Cu_{1.999}S vs. EIS-Slope, Cu_{1.9999}S).

A comparison of the calculated values \tilde{D}_{Chem} for a chosen composition Cu_{1.9999}S and Cu_{1.999}S is given in **Figure 6.12**. Therein, it becomes evident that the values differ by about one order of magnitude between the respective compositions. Moreover, the experimental values are compared to the literature data. Strikingly, the values obtained by EIS(Slope) are either extremely low for Cu_{1.999}S in the low temperature range or extremely high for Cu_{1.9999}S in the high temperature region. Therefore, the diffusion coefficients were evaluated by CT and PT for further comparison, see **Table 6.5**.

Table 6.5: Experimental values of \tilde{D}_{Chem} for the different methods at 120 °C.

Methodology	$\tilde{D}_{\text{Chem}} / \text{cm}^2 \text{s}^{-1}$
EIS(P, Cu _{1.9999} S), 0 mV	$2.98 \cdot 10^{-6}$
EIS(Slope, Cu _{1.9999} S), 0 mV	$7.3 \cdot 10^{-5}$
EIS(Slope, Cu _{1.999} S), 0 mV	$7.3 \cdot 10^{-7}$
CT (Cu _{1.9999} S), 0 mV	$4.4 \cdot 10^{-6}$
PT (Cu _{1.999} S), 200 mV	$2.1 \cdot 10^{-7}$

Thereby, the values determined by PT match with the diffusion coefficients measured by *Pauporte et al.* (P.E) and *Tubandt et al.*^{172, 183} Compared to that, the value determined by CT is higher by about one order of magnitude. Interestingly, the methods (PT, EIS(Slope, Cu_{1.999}S)) with a composition of Cu_{1.999}S match well with the literature data for high chalcocite. Thus, the chemical diffusion coefficient is most likely in the range between $1 \cdot 10^{-7} \text{ cm}^2 \text{s}^{-1}$ and $1 \cdot 10^{-6} \text{ cm}^2 \text{s}^{-1}$ for a composition of Cu_{1.999}S. Contrary to that, higher diffusion coefficients are obtained for the methods CT and EIS(Slope, Cu_{1.9999}S) with a composition of Cu_{1.9999}S.

In summary, an assumed composition of Cu_{1.999}S gives comparable values to the chemical diffusion coefficients in literature. Also, the EIS method which employs the slope S from the Randles plot to calculate \tilde{D}_{Chem} gives reasonable activation energies of 0.33 eV and 0.27 eV for the low and high chalcocite, respectively. Thus, the EIS(Slope) method is assessed more suitable for the determination of the chemical diffusion coefficients.

6.5 Conclusion

First, the temperature stability of the solid electrolyte Rb₄Cu₁₆Cl_{12.8}I_{7.2} was confirmed at up to 200 °C and the ionic conductivity was determined to be 0.02 - 0.2 S/cm from 30 °C to 200 °C. Also, no significant electronic contribution was observed in the EIS spectra of the electrolyte. Hence, the solid electrolyte proved to be a suitable selection for the solid electrolyte in the all-solid-state galvanic cell Cu|Rb₄Cu₁₆Cl_{12.8}I_{7.2}|Cu_{2-x}S. Then, the electronic conductivity of a sole Cu_{2-x}S sample, sandwiched between two ion blocking Pt electrodes, was measured via EIS. PXRD measurements of the Cu_{2-x}S sample before the EIS measurement reveals a small amount of the tetragonal Cu_{1.96}S phase. However, a low electronic conductivity in the range of 0.03 - 0.06 S/cm was measured which is typical for chalcocite compositions with low Cu deficiency.

Subsequently, the galvanic cell was measured via EIS in the temperature range from 40 °C to 200 °C. Then, an equivalent circuit was built to fit the experimental EIS spectra. Accordingly, the ionic resistance was determined from this fit which was then used to calculate the ionic conductivity. The resulting ionic conductivity σ_{ion} ranges from $9.5 \cdot 10^{-4}$ - $1.3 \cdot 10^{-2}$ S/cm at 40 °C to 200 °C with an activation energy of 0.27 eV and 0.21 eV for the low and high chalcocite phase. Also, a leap towards lower ionic conductivity is observed in the phase transition region. Comparison to literature data reveals higher experimental values for the low chalcocite phase but good agreement with data from *Hirahara* for the high chalcocite phase.¹⁸⁰ Accordingly, the self-diffusion coefficient was calculated from the ionic conductivity via the Nernst-Einstein relation. Therefore, similar activation energies and trends are displayed for the obtained values of D_{Cu^+} . Further measurements at higher cell potentials show an increasing self-diffusion coefficient with deviation from ideal chalcocite composition. However, emf dependent EIS measurements by *Cassaignon* et al. show a lower \tilde{D}_{Chem} for copper-deficient copper sulfide structures.⁸⁰ Thus, it is concluded that a Cu deficiency leads to an initial increase with a maximum and then drops with lower Cu concentration due to the more strongly bound Cu ions.

Finally, the chemical diffusion coefficients are investigated. For this, four different methodologies are applied: EIS (thermodynamic factor), EIS (Slope from Randles plot), coulometric titration, and potentiostatic titration. The method which uses the slope S from the Randles plot to determine \tilde{D}_{Chem} shows the best agreement with literature data. For instance, an E_a of 0.33 eV and 0.27 eV is obtained and chemical diffusion coefficients of $5.9 \cdot 10^{-10}$ – $9.6 \cdot 10^{-6}$ cm² s⁻¹ for the low and high chalcocite phase, respectively. However, the chosen vacancy concentration is a critical parameter for the calculation of \tilde{D}_{Chem} . Here, the best agreement with literature data is obtained with a composition of Cu_{1.999}S.

Nonetheless, the exact composition remains a critical parameter for all the methodologies which are utilized above, either as a function of concentration, vacancy concentration, or as thermodynamic factor. Therefore, a precise measurement of the stoichiometric composition and the respective copper sulfide phases must accompany the electrochemical measurements of the diffusion coefficients.

7 General Reactivity of Cu and Pd Mixtures with Bifunctional Thiols

7.1 Abstract

High temperature storage (HTS) of Cu and Cu-Pd powdery mixtures with bifunctional thiols results in various copper sulfide, palladium sulfide and intermetallic Cu-Pd mixtures. The formed phases are strongly dependent on temperature and stoichiometric ratios of the starting mixture and thiol compounds. The sulfidation rate of Cu increases with temperature and the presence of palladium. In a next step, the reaction kinetics of the mixtures are analyzed with quantitative phase analysis (QPA) via powder X-ray diffraction (PXRD). Further, the corrosion behaviour is analyzed with Johnson-Mehl-Avrami-Erofe'ev-Kolmogorow (JMAEK) kinetics. It is found that, in general the formation of copper sulfide follows an interface-controlled mechanism and at certain product layer thicknesses changes towards a diffusion-controlled mechanism. A comparison to a semi-quantitative analysis of the mixtures with palladium shows that palladium speeds up the formation of copper sulfide significantly. Also, palladium hydride (PdH_x) palladium sulfide (PdS) and the intermetallic copper-palladium phase Cu_3Pd are discussed regarding their catalytic capabilities. The results are discussed considering corrosion risk and reliability in semiconductor packages, where Cu and Pd-coated copper (PCC) wires are used in combination with bifunctional thiols as adhesion promoters.

7.2 Introduction

One of the main causes for failure in high temperature storage tests (HTS) is the sulfidation of the Cu and especially the PCC wire.^{29, 82} The sulfidation is supposed to originate from additives in the encapsulation material. The molding compound (MC) includes sulfuric adhesion promoters in low (10-150 ppm) ppm-range.⁶⁰ At high temperatures the wire corrodes via oxidation with these sulfur-containing adhesion promoters. This leads to the formation of Cu voids, pitting corrosion, hillocks, and Cu_xS .⁵⁴ The underlying mechanism is likely galvanic corrosion induced by the Pd layer and copper sulfide as solid electrolyte. However, the corrosion related failures are not fully understood up to now. As the corrosion kinetics depend among other things on the properties of the solid electrolyte Cu_xS , it is vitally important to determine the formed phases during corrosion. Thus, the aim of this chapter is, to understand the failure mechanisms, to verify the formed phases during corrosion and to learn about the acceleration of the corrosion kinetics from low to high temperatures. In our study, powdery mixtures of Pd, Cu and thiol were stored at high temperature, analyzed and quantified with powder X-ray diffraction.

7.3 Experimental

7.3.1 Powdery Mixtures with Two Different Thiols

The Cu powder (Cu, 99.7%, < 80 μm , Merck) used was reduced in a gas stream of $\text{H}_2\text{:Ar}$ mixture with a ratio of 1:5 at 500 $^\circ\text{C}$ in order to reduce the passivating Cu_2O , CuO layer on the surface. The reduced spherical Cu particles were sieved to a diameter of 40-80 μm prior to use. Then 5 different mixtures with solid triazole-thiol (**TT**) and with/without palladium powder (Pd, 99.95%, < 80 μm , Alfa Aesar) were prepared by grinding them together thoroughly in a mortar:

- 1-4) Cu powder (250 mg, 3.93 mmol) and **TT** powder to get the stoichiometric ratios $\text{Cu:TT} = 1:0.1, 1:0.33, 1:0.55$ and $1:1$.
- 5) Cu powder (150 mg, 2.33 mmol), Pd powder (25 mg, 0.23 mmol) and **TT** powder (27 mg, 0.23 mmol) resulting in a stoichiometric ratio of $\text{Cu:Pd:BT} = 1:0.1:0.1$.

The mixtures with liquid mercaptosilane 1 (**MS1**) were prepared slightly different. The Cu powder was presented in a silica ampoule and then liquid **MS1** was dripped over the powder. In a second mixture the Cu and Pd powder were thoroughly ground together and then **MS1** was dripped over the mixture:

- 6) Cu powder (0.65 g, 10.22 mmol) and liquid **MS** (0.2 mL, 1.02 mmol) resulting in a Cu:MS1 ratio of $1:0.1$.
- 7) Cu powder (0.076 g, 1.20 mmol), Pd powder (0.013 g, 0.12 mmol) and liquid **MS** (0.21 mL, 0.12 mmol) resulting in a Cu:Pd:MS1 ratio of $1:0.1:0.1$.

All mixtures were weighed into silica ampoules under N_2 -atmosphere. The filled ampoules were evacuated under liquid nitrogen cooling and sealed with a hydrogen-oxygen flame. The sealed ampoules were put in a drying oven at isothermal conditions. The applied temperatures ranged from 125 $^\circ\text{C}$ to 250 $^\circ\text{C}$ and the time span from 2 h to 2500 h.

7.3.2 PXRD – Calibration and Quantification

Powder-X-ray diffraction (PXRD) was used as standard method to characterize the reaction products. For device specific details, see chapter 4.12. Further, $\text{CuK}\alpha_1$ ($\lambda = 1.5406 \text{ \AA}$) radiation was used for all samples and all samples were measured in transmission geometry on a flatbed carrier. The samples were thoroughly ground in a mortar before the measurement to ensure good homogeneity for the quantification.

In order to quantify the $\alpha\text{-Cu}_2\text{S}$ content in the samples without palladium, three linear calibration curves were generated according to the relative calibration method (RCM). This method is suitable as the sole reaction product is copper sulfide. Hence, the first calibration curve is a mixture of Cu powder, **TT** powder and $\alpha\text{-Cu}_2\text{S}$ powder up to ca. 25 wt% $\alpha\text{-Cu}_2\text{S}$ to simulate the same matrix as in

the original mixtures with **TT** (**Figure A. 7.1**). For the second calibration curve Cu powder and α -Cu₂S powder are ground together up to ca. 15 wt% α -Cu₂S (**Figure A. 7.2**). Note that in the mixture with **MS1** only the Cu and α -Cu₂S phase is observed in the powder pattern as **MS1** is a liquid compound. Thus, the calibration mixture only consists of Cu and copper sulfide. Then, all homogenized mixtures are measured at the same parameters. Also, attention was paid to good reproducibility at all steps. For the actual calibration curve the three strongest reflections at $\sim 37.3^\circ$, $\sim 45.8^\circ$ and $\sim 48.5^\circ$ of the low chalcocite phase α -Cu₂S are used. To attain high reproducibility the relative intensities versus the strongest Cu reflections are used to eliminate the declining initial beam intensity and the fluctuating sample preparations which cannot be completely avoided. Further, three-fold determination was performed to guarantee good reproducibility. Then, the α -Cu₂S content in the actual samples were determined. Therefore, again a three-fold determination was conducted for reproducibility. For all determinations the relative intensities were used with constant measuring parameters.

This method could not be applied to the palladium mixtures as the thiol and palladium react at varying degrees with Cu. Thus, the relative intensities vs. Cu could not be used. Hence, the semi-quantitative *RIR* method was applied with the program package Match!. Here, the reference-intensity-ratio (*RIR*) vs. corundum is calculated for the COD-files in the Match! database. This *RIR* is used to quantify Cu, Pd and further reaction products. Of course, the accuracy of this method is lower compared to the linear calibration curve.

7.3.3 Kinetic Analysis

The JMAEK approximation is used to study the reaction kinetics of the powdery mixtures at elevated temperatures. In particular, the linearized form of the JMAEK equation is used to generate the SH-plot. Then, the Avrami exponent n is derived from the slope of this plot. Further, the reaction rate constant k is obtained from the y-axis of the SH-plot. Finally, the reaction mechanisms are discussed in view of the obtained parameters.

7.4 Results and Discussion

7.4.1 HTS of Cu Powder with Triazole-Thiol

HTS of Cu powder and **TT** powder at 250 °C for 24 h shows significant formation of α -Cu₂S (low chalcocite), see **Figure 7.1**. Also, the reflection intensities of the thiol phase decrease, which means either the thiol moiety reacts with Cu or **TT** decomposes and the corresponding sulfur-decomposition products react with Cu. Note that, the copper-rich low chalcocite forms at a molar ratio Cu:**TT** = 1:0.1. Thus, a Cu excess is present which leads to a copper-rich copper sulfide.

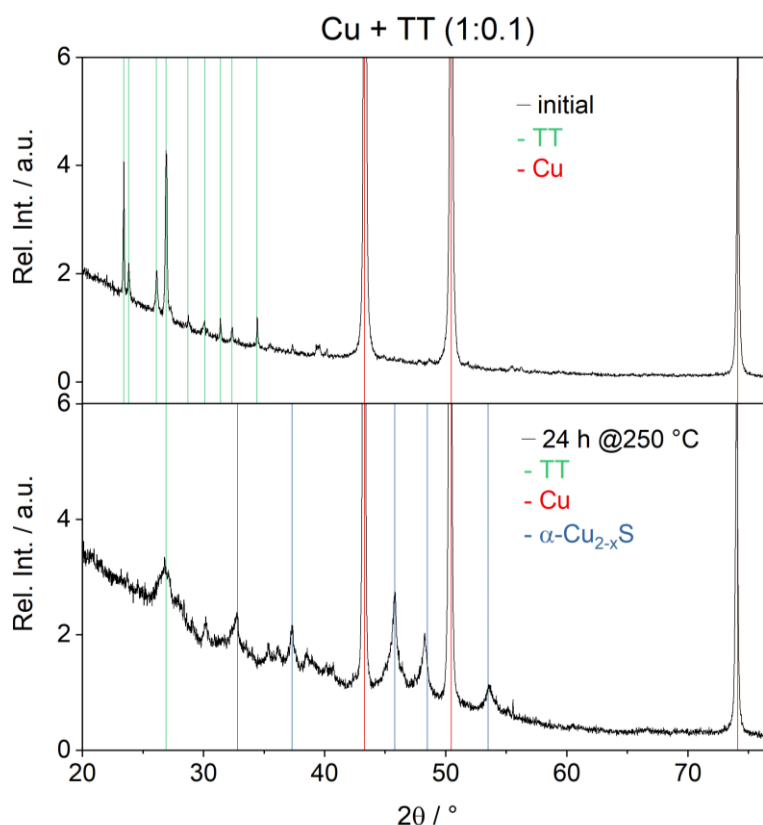


Figure 7.1: Comparison of an initial Cu-**TT** mixture with a stoichiometric ratio of 1:0.1 (top) and the same mixture after 24 h at 250 °C (bottom).

As it is hardly possible to determine the formed copper sulfide phases in the semiconductor package, further investigations regarding the copper sulfide composition were performed to gain knowledge, which phases are likely to form in the electronic device. Thus 4 different molar ratios of the Cu:**TT** mixture were prepared to study the influence of the sulfur content in the sample, see **Figure 7.2**. The samples were stored at 250 °C for 7 d and investigated with PXRD. As the sulfur content increases the copper sulfide changes from α -Cu_{2-1.99}S (low-Ch, 1:0.1, 1:0.3) to Cu_{1.95}S (djurleite, 1:0.3) to γ -Cu_{1.8}S (high-digenite, 1:0.5), to CuS (covellite, 1:1). Hence, the copper sulfide composition changes from copper-rich to copper-poor, which results in mixtures of different sulfides. As the sulfur content increases, the low chalcocite incorporates the sulfur from **TT** and transitions to copper-poor sulfides along the phase diagram.

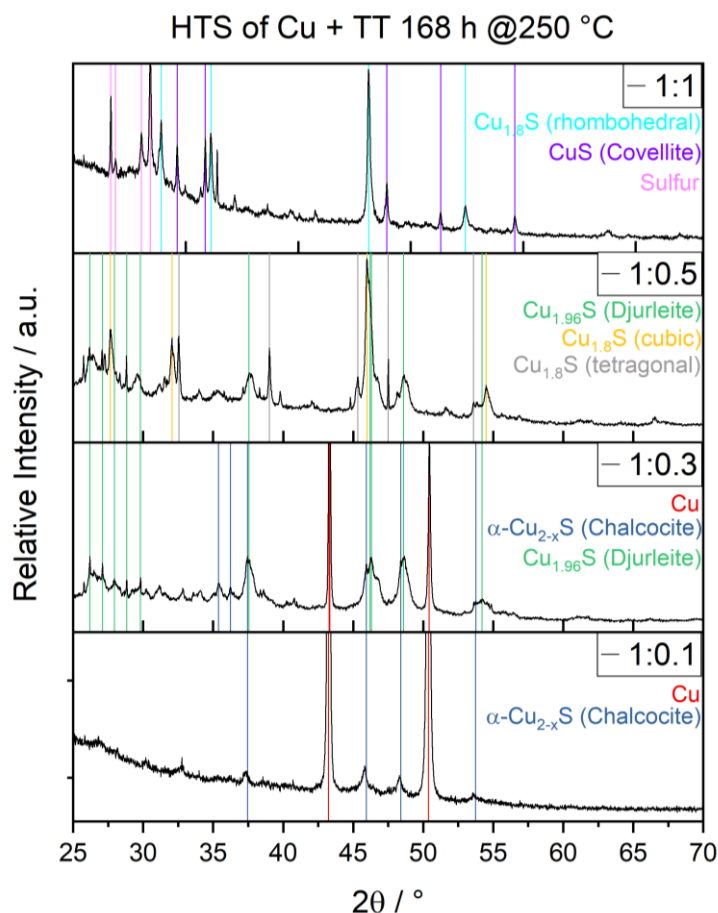


Figure 7.2: Comparison of Cu-TT mixtures with different stoichiometric ratios ranging from Cu:TT = 1:1 to 1:0.1.

Surprisingly, the low-temperature phase anilite ($\text{Cu}_{1.75}\text{S}$) is not observed. Instead, only low-chalcocite, djurleite, high-digenite and covellite are observed, which form mixtures of $\alpha\text{-Cu}_2\text{S}/\text{Cu}_{1.95}\text{S}$, $\text{Cu}_{1.95}\text{S}/\gamma\text{-Cu}_{1.8}\text{S}$ and $\gamma\text{-Cu}_{1.8}\text{S}/\text{CuS}$. Thus, it can be concluded that these are the main copper sulfides formed, which are present as pure phase or as mixtures mentioned above. In comparison, the sulfur content in MC is up to 120 ppm sulfur in sulfur rich MCs.^{54, 60} Compared to the powder mixtures, the sulfur content in semiconductor packages is very low. Hence, it is highly likely that the formed copper sulfide phase in packages is the low chalcocite phase $\alpha\text{-Cu}_{2-x}\text{S}$. This copper sulfide is a non-stoichiometric compound and a mixed electronic and ionic conductor (MIEC) with properties strongly dependent on composition.^{76-79, 169} The MIEC properties with high electronic and ionic conduction are the main reason why it is troublesome in semiconductor packages. Due to mixed conduction, it can serve as solid electrolyte between a Pd coating and a Cu source. This may lead to galvanic corrosion in Pd-coated Cu-wire (PCC) packages.⁵⁴ Additionally, the high Cu-ion diffusion in $\alpha\text{-Cu}_{2-x}\text{S}$ enables a self-propagating copper sulfide phase in the package. At temperatures above 100 °C $\alpha\text{-Cu}_2\text{S}$ undergoes a phase transition to the high temperature phase $\beta\text{-Cu}_{2-x}\text{S}$ (high chalcocite). The high temperature phase could even have higher Cu-ion mobility than the low-temperature phase, leading to an increased copper sulfide propagation, see chapter 5.^{78, 79, 172}

As a consequence, a higher corrosion rate is expected at high temperatures. Also, several additional phenomena could dictate the corrosion rate at high temperatures:

- Cu-ion mobility in α -Cu₂S.
- Reaction of thiol with Cu.
- Decomposition of thiol.
- Diffusion of thiol within the MC.

In order to investigate the rate determining corrosion step a kinetic analysis was performed. In addition to that, the goal of the kinetic analysis was to gain knowledge about the temperature dependence of the related mechanisms. An elemental question is if the underlying corrosion mechanism remains the same at higher temperatures. This is essential for reliability tests at high temperatures as it is assumed that the corrosion mechanism remains the same. Thus, this assumption must be examined critically. Hence, to perform the kinetic and mechanistic analysis a Cu:TT (molar ratio = 1:0.1) mixture was stored for various times at temperatures ranging from 150 °C to 250 °C. Then the samples were quantified with PXRD and finally analyzed with JMAEK kinetics. The copper sulfide formation after HTS at various storage times is summarized in **Figure 7.3**.

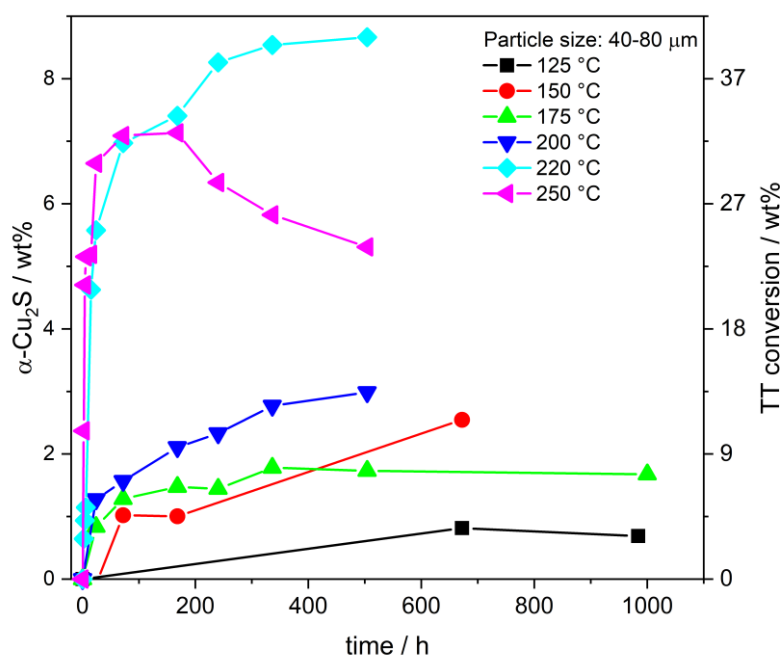


Figure 7.3: α -Cu₂S formation after various HTS conditions.

At low temperatures a small amount of copper sulfide forms, which does not increase over time. As the temperature increases the corrosion rate speeds up in the beginning 48 h and then stagnates or slows down after 1 wt% copper sulfide forms. This is uniformly observed in the temperature range from 150-200 °C. A further increase to 220 °C and 250 °C speeds up the corrosion significantly. In the first 24 h the corrosion rate is extremely high but then slows down at about 7 wt%. After \approx 180 h the corrosion behaviour at 220 °C and 250 °C diverges from each other. Unexpectedly, the copper

sulfide content increases at 220 °C and decreases at 250 °C. A reasonable explanation for this observation is the lower reactivity of **TT** at the Cu_2S surface at 220 °C. Hence, the Cu-ion outward-diffusion is faster than the reaction of **TT** with copper sulfide. This leads to an increase of the copper sulfide content in the sample. At 250 °C the Cu-ion outward-diffusion is slower than the reaction of **TT** with $\alpha\text{-Cu}_2\text{S}$, which leads to the incorporation of the S-atoms of **TT** into the copper sulfide. As a result, the $\alpha\text{-Cu}_2\text{S}$ content decreases and new copper-poor phases form if a certain product layer thickness is reached, which implies longer diffusion times to the surface (**Figure A. 7.6**).

In order to gain kinetic insight, the Sharp-Hancock plot is studied in the temperature range from 150 °C to 250 °C, see **Figure 7.4**. From 150-200 °C the slope n of the SH-plot is about 0.25 which indicates a diffusion-controlled mechanism. In comparison, experimental values for the Avrami exponent n for diffusion-controlled reactions range from 0.5-0.65.^{114, 129} However, the Avrami exponent can have divergent values, depending on dimension and nucleation rate. At the start of the reaction at 220 °C and 250 °C the slope n changes to 1. This is characteristic for a fast interface-controlled mechanism. Then, the slope n decreases uniformly to a diffusion-controlled mechanism at 220 and 250 °C after 4.7 wt% copper sulfide formed. This remains unchanged at 220 °C until the end. Compared to that, the slope changes again at 250 °C and gets negative, which means the loss of $\alpha\text{-Cu}_2\text{S}$ as mentioned above.

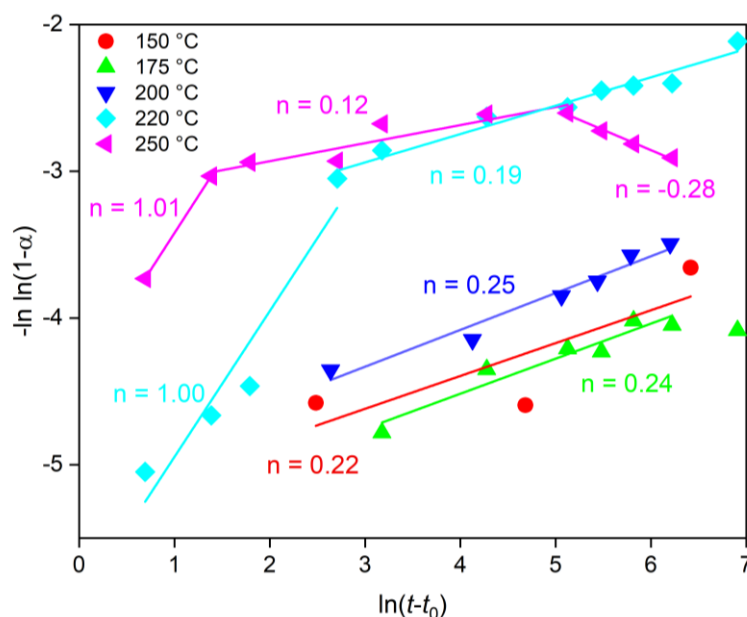


Figure 7.4: Sharp-Hancock plot for the mixture Cu:**TT** (molar ratio 1:0.1) from 150-250 °C.

This means that in the temperature range from 150-200 °C a diffusion mechanism controls the formation of $\alpha\text{-Cu}_2\text{S}$ with the Cu-ion mobility as the rate limiting factor. When the temperature increases to 220 °C and higher, the corrosion mechanism changes. At high temperatures an interface-controlled mechanism governs the reaction. This implies, that the phase boundary reaction of the thiol at the Cu surface is the rate determining step. As the reaction proceeds and the copper sulfide layer grows thicker, the diffusion of the Cu-ion through the $\alpha\text{-Cu}_2\text{S}$ layer becomes the rate limiting step. Finally, the kinetic parameters for the Cu:**TT** mixtures are summarized in **Table 7.1**.

Table 7.1: Overview of the Avrami exponents n obtained from the SH-plot and the reaction rate constants obtained from the Avrami equation for the Cu:TT mixture.

T / °C	t / h	Avrami exponent n	Mechanism	Rate constant k / h ⁻¹
150	72-672	0.2(2)	D(3)	$5.5(8) \cdot 10^{-11}$
175	24-504	0.24(3)	D(3)	$1.1(1) \cdot 10^{-10}$
200	24-504	0.25(2)	D(3)	$1.6(1) \cdot 10^{-9}$
220	15-1000	0.19(2)	D(3)	$1.3(1) \cdot 10^{-8}$
220	2-15	1.0(2)	R(1)	$2.5(1) \cdot 10^{-3}$
250	2-4	1.0(3)	R(1)	$1.2(4) \cdot 10^{-2}$

Note that, there are two important points in the SH-plot, namely 4.7 wt% and 7.3 wt% which marks a junction at 220 °C and 250 °C. This means that at a distinct copper sulfide layer thickness the mechanism changes and thus underlines the importance of the Cu⁺ diffusion through the copper sulfide layer. Here, spherical Cu particles are assumed with a mean radius of $r_0^2 = 30 \mu\text{m}$ due to prior sieving. The relation of formed copper sulfide weight fraction (α), diffusion (D) and product layer thickness (l) is shown in Eq. 7.1-9 for three-dimensional diffusion, which assumes spherical particles. Hence, the following equations apply:¹¹⁴

$$l^2 = 2D \cdot \frac{M_{\text{Cu}_2\text{S}} \cdot \Delta c_{\text{Cu}}}{M_{\text{Cu}} \cdot \rho_{\text{Cu}_2\text{S}}} \cdot t \quad (7.1)$$

$$k = 2D \cdot \frac{M_{\text{Cu}_2\text{S}} \cdot \Delta c_{\text{Cu}}}{M_{\text{Cu}} \cdot \rho_{\text{Cu}_2\text{S}}} \quad (7.2)$$

$$l^2 = kt \quad (7.3)$$

Here, we assume a three-dimensional diffusion according to the Jander (D3) model:¹¹⁹

$$(1 - (1 - \alpha)^{1/3})^2 = k't \quad (7.4)$$

$$\text{with } k' = \frac{k}{r_0^2} \quad (7.5)$$

Which can be modified in order to take the molar volumes $z = V_{\text{Cu}_2\text{S}}/V_{\text{Cu}}$ into account. An equation which considers the volumes has been derived by *Carter and Valensi* (CV):¹²¹

$$[(1 + (z - 1) \cdot \alpha)^{2/3} + (z - 1)(1 - \alpha)^{2/3} - z] \cdot r_0^2 = 2 \cdot (1 - z) \cdot kt \quad (7.6)$$

Finally, the product layer thickness can be calculated:

$$l = \sqrt{\frac{[1 + (z - 1) \cdot \alpha]^{2/3} + (z - 1)(1 - \alpha)^{2/3} - z \cdot r_0^2}{2 \cdot (1 - z)}} \quad (7.7)$$

In comparison to that, the equation for a three-dimensional interface-controlled mechanism (R3) changes to:¹¹⁴

$$r = r_0 - [(1 - (1 - \alpha)^{1/3}) \cdot r_0] \quad (7.8)$$

$$l = r_0 - r \quad (7.9)$$

with r the radius of the Cu particle after a certain amount copper sulfide formed. In **Table 7.2** the calculated copper sulfide layer thickness is shown for the diffusion mechanism (D3 – CV, eq. 7.7) and the interface-controlled mechanism (R3, eq. 7.9). The values are very close to each other as both models assume a spherical model. This means for the calculation of the product layer thickness that the related mechanism plays a minor role. However, the velocity, until the layer thickness is big enough to cause a change in mechanism, is different for both processes.

Table 7.2: Comparison of the calculated copper sulfide layer thicknesses between diffusion (D3) and interface control (R3).

α / wt%	D3 – CV	R3
4.7	0.470 μm	0.478 μm
7.3	0.731 μm	0.749 μm

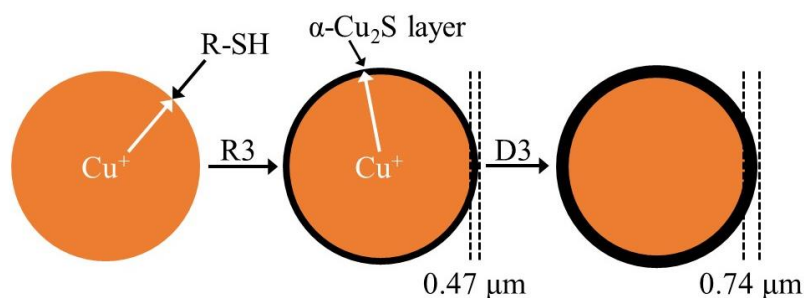


Figure 7.5: Schematic presentation of the corroding Cu particles. At 4.7 wt% a copper sulfide layer of 0.47 μm thickness is formed and 0.73 at 7.3 wt%.

According to Eq. 7.7 and 7.9 $\approx 0.47 \mu\text{m}$ thick copper sulfide layer formed at 4.7 wt% on the surface of the spherical Cu particles and $\approx 0.73 \mu\text{m}$ at 7.3 wt%, see **Figure 7.5**. As you may have noticed, in this special case the layer thickness in μm coincidentally corresponds to the formed weight percentages by a factor of 10. Hence, the product layer thickness can easily be tracked with reaction progress and vice versa making it an easy way to analyze reaction progress with optical techniques. Also, the product layer thickness and reaction progress can be simulated with the corresponding reaction model. In the corresponding diffusion- and interface-controlled reaction models, the geometrical circumstances can be adjusted to fulfill experimental conditions. The reaction rate constant which is needed to simulate these parameters from the model can be derived from the Arrhenius plot, if the corrosion follows an Arrhenius behaviour.

To verify the assumption of an Arrhenius behaviour, an Arrhenius plot was generated, as thermal activated processes show an Arrhenius-like behaviour with increasing temperature. Therefore, $\ln(k)$ was extracted from the SH-plot and plotted against T^{-1} , see **Figure 7.6**. For the Arrhenius plot the logarithmic rate constants for the same mechanism types are compared (e.g. 150-220 °C, $n \approx 0.25$). As the temperature increases from 150-220 °C the rate constants for the diffusion-related mechanism ($n \approx 0.25$) grow and yield an activation energy of 1.42 ± 0.28 eV. When the temperature increases, the sulfidation is controlled by an interface-controlled mechanism ($n \approx 1$) and gives an activation energy of 1.17 ± 0.26 eV. Also, the reaction rate constants are much higher for the interface process. Hence, the interface mechanism will be dominant above 220 °C and the diffusion mechanism below 220 °C. In qualification test practice, this means that the failure mechanism changes from 200 °C to 220 °C. This emphasizes that HTSL tests cannot be easily upscaled to higher temperatures and that further investigations are necessary to clarify the temperature induced acceleration of the sulfur induced corrosion of specific devices .

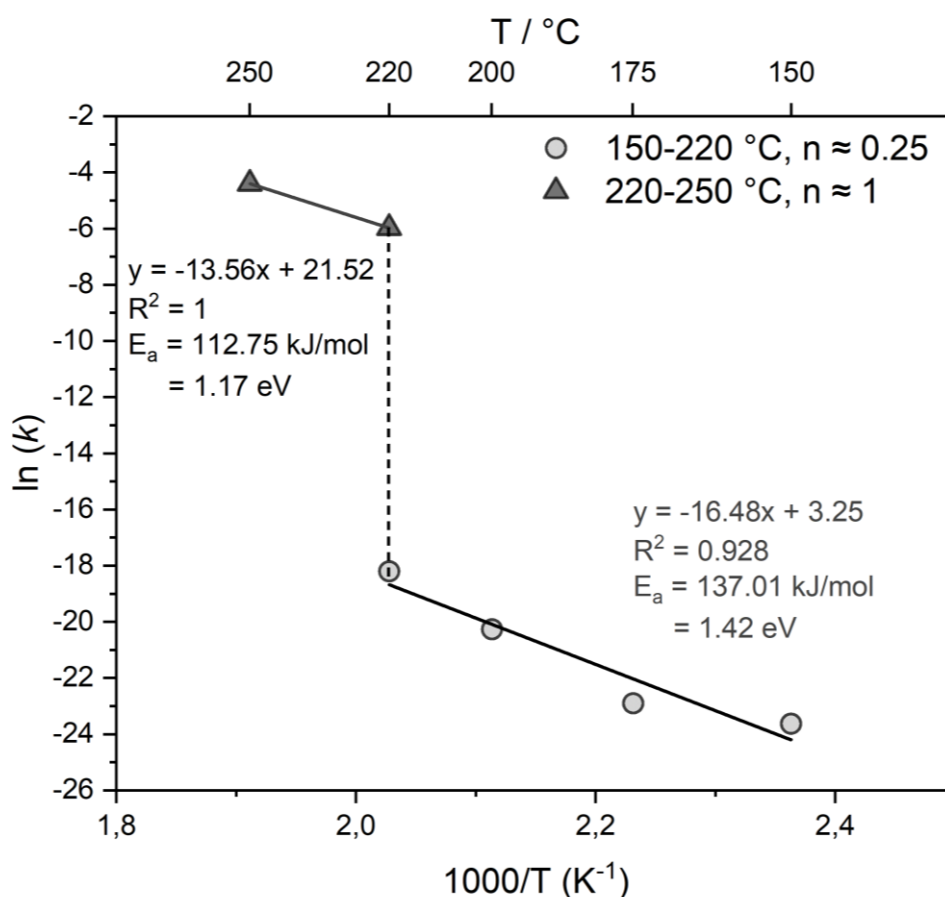


Figure 7.6: Arrhenius plot for the reaction of the Cu:TT mixture from 150-250 °C.

7.4.2 HTS of Cu Powder with Mercaptosilane

Like the mixture before, a Cu:MS1 (molar ratio = 1:0.1) mixture was prepared and stored at isothermal conditions ranging from 125-200 °C and storage times of 24 h up to 2500 h. After HTS, the samples were filtered from the liquid MS1 and then analysed separately. The liquid product was analysed via NMR- and infrared-spectroscopy revealing MS1 as the sole component. Thus, only the filtered powder was used for further investigation. In **Figure 7.7** the powder pattern is shown for the Cu:MS1 mixture after 24 h at 200 °C. Similar to the Cu:TT mixture the sole reaction product is the copper-rich low chalcocite phase α -Cu₂S beneath the remaining Cu particles. Therefore, the remaining reaction products must evaporate into the gas phase, which was not investigated into detail. However, this raises the probability even more for the copper-rich α -Cu₂S to be formed in the electronic device as the adhesion promoter concentration is low.

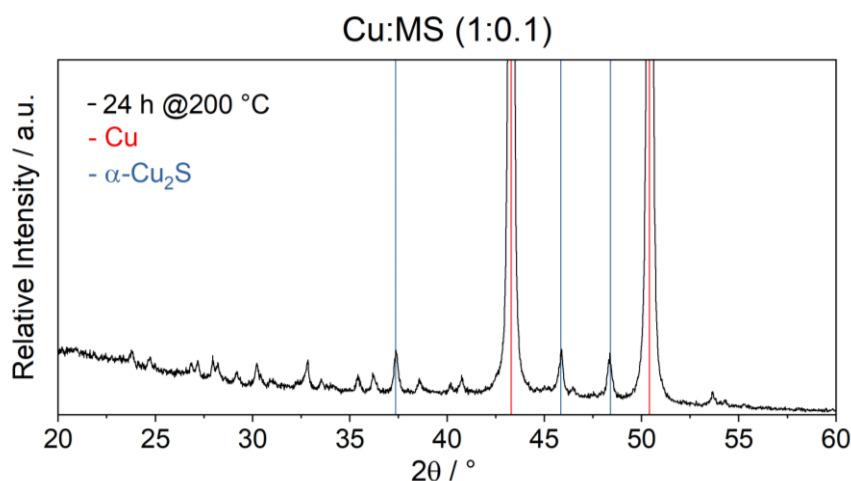


Figure 7.7: PXRD pattern of the Cu:MS1 mixture after 24 h at 200 °C. Here, only the most intense reflections are marked, which are used for quantification.

After the sample evaluation, the Cu:MS1 mixtures were quantified with PXRD after various HTS conditions, see **Figure 7.8**. At 125 °C no reaction products and copper sulfides are observed. At slightly elevated temperature (150 °C) a minor copper sulfide formation is observed which accelerates significantly after 1000 h. This might be due to the formation of enough nucleation centers, which leads to an increased growth of the copper sulfide layer. Even higher temperatures, such as 175 °C lead to a considerable increase of the reaction speed. It is not evident if it follows a linear or a parabolic behaviour. Due to the strong increase compared to 150 °C it seems feasible that the mechanism changes, which cannot be explained by faster diffusion. Further increase to 200 °C enhances the reaction speed even more. At first glance it seems to follow a parabolic behaviour. However, the steep α -Cu₂S formation in the first 72 h indicates another mechanism which changes to a diffusion-like behaviour.

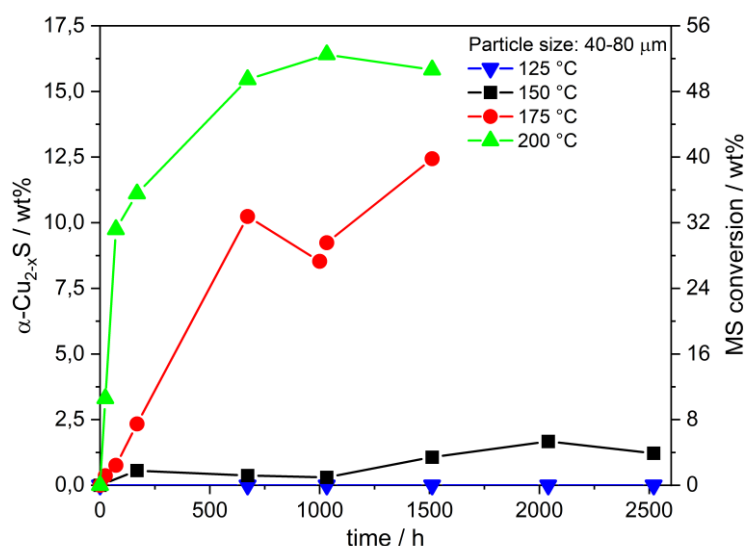


Figure 7.8: Low chalcocite formation after various HTS conditions.

To investigate the kinetics of copper sulfide formation, the SH-plot was generated, see **Figure 7.9**. Herein, the beginning stages of copper sulfide formation show similar slopes n ($n \approx 1$ -1.3). This Avrami exponent is comparable to that one obtained for the Cu:TT mixture at 220-250 °C in the beginning stages. Hence, a similar mechanism may occur at the beginning stages. With the slope $n \approx 1$, indicating an interface-controlled mechanism. In contrast to the Cu:TT mixture, this mechanism arises at much lower temperature (150-200 °C). Then, again at a certain point the slope in the SH-plot changes which reveals a mechanism change (175 °C, 200 °C). This point is at about 10 wt% copper sulfide formation which corresponds to a copper sulfide layer thickness of 1.00 μm and 1.04 μm according to the diffusion (D3-CV, eq. 7.7) and interface model (R3, eq. 7.9).

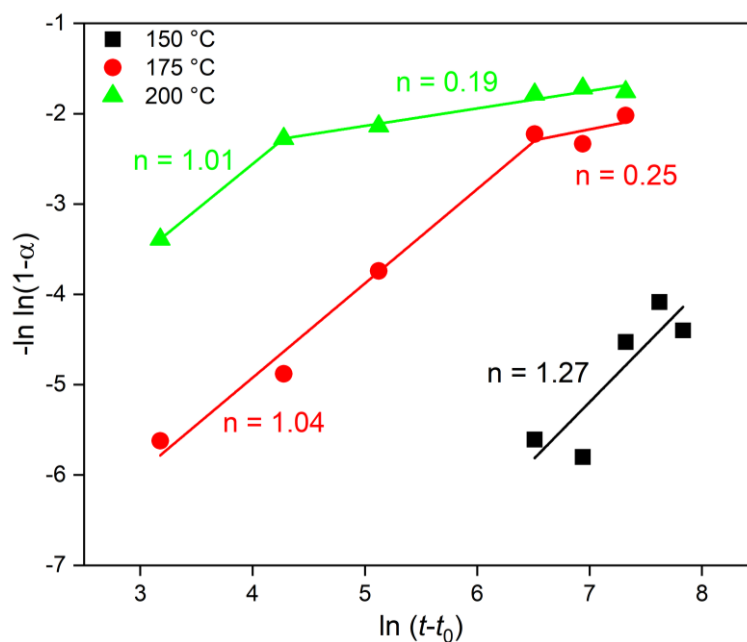


Figure 7.9: SH-plot of the quantified Cu:MS1 mixture after HTS.

There, the slope changes to $n \approx 0.2$. This is also observed for the Cu:TT mixture and points to a diffusion-controlled mechanism. This seems logical as the outward-diffusion of the mobile Cu-ions become the rate limiting step at a certain α -Cu₂S layer thickness. Thus, it is no coincidence that we observe this phenomenon for both mixtures. Of course, the layer thickness may differ with different adhesion promoters as the reactivity is changing. Finally, the kinetic parameters for the Cu:MS1 mixtures are summarized in **Table 7.3**.

Table 7.3: Overview of the Avrami exponents n obtained from the SH-plot and the reaction rate constants from the Avrami equation for the Cu:MS1 mixture.

T / °C	t / h	Avrami exponent n	Mechanism	Rate constant k / h ⁻¹
150	672-2500	1.3(4)	R(3)	$1.5(5) \cdot 10^{-5}$
175	24-672	1.04(9)	R(2)	$1.6(1) \cdot 10^{-4}$
200	24-72	1.0(1)	R(1)	$1.5(2) \cdot 10^{-3}$

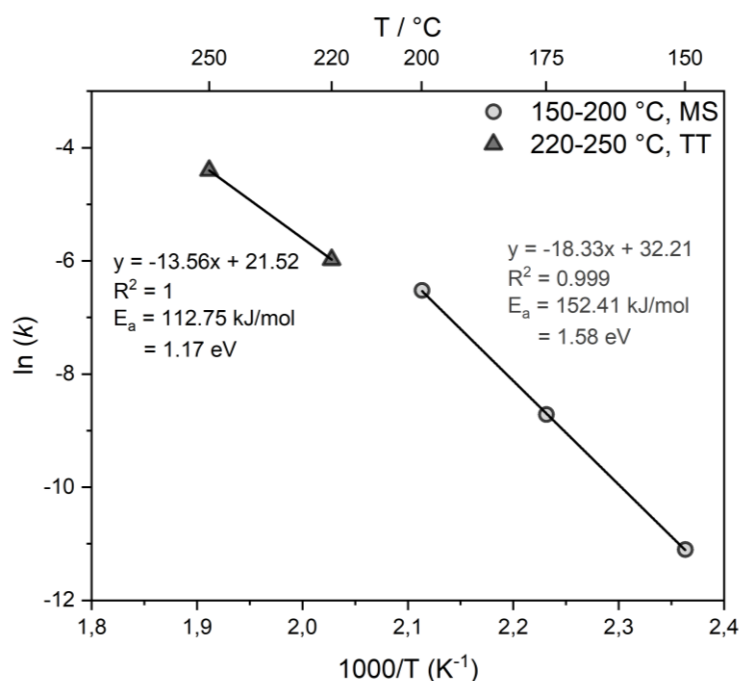


Figure 7.10: Arrhenius plot for the Cu:MS1 and Cu:TT mixtures with slopes $n \approx 1$ in the SH-plot.

In **Figure 7.10** the Arrhenius plot is shown to compare the beginning stages of the Cu:MS1 and the Cu:TT mixtures with a slope of $n \approx 1$ in the SH-plot. As we can see in the Arrhenius plot, the reaction rate constants for the interface-controlled mechanism of the corrosion reaction with the two different thiols are very similar. The magnitude of the reaction rate constant is in the same order and the activation energy is relatively similar with 1.17 ± 0.26 eV for TT and 1.58 ± 0.22 eV for MS1. Hence, the reactivity is very similar for both thiols as it is expected for the same compound class. Further, the difference between a solid (TT) and a liquid (MS1) thiol is less than expected. Thus, we can exclude that the interface-control does not originate from the fluid film resistance but by the reaction of the thiol at the Cu particle surface. However, in contrast to MS1 the TT molecule shows no

interface-control below 150 °C. This behaviour may originate from the limited diffusion of the solid **TT** molecules within the mixture and on the surface of the Cu particles. Thus, there is an additional barrier the sulfidation reaction must overcome in order to change to an interface-controlled mechanism. Unlike **TT**, the liquid **MS1** is not hindered by diffusion towards the reactive Cu particle surface which may explain the different reactivity at lower temperatures. If we look at these findings regarding the conditions in semiconductor packages a major question arises, which is the diffusion and distribution of sulfur compounds within the MC. Also, the distribution and accumulation of the adhesion promoter on the Cu surface during and after the molding process is poorly understood. If we assume a solid-like behaviour, the diffusion of the thiol molecule will be the rate limiting step which implies diffusion-control of the sulfidation reaction and vice versa for a liquid-like behaviour. When the temperature increases, the diffusion in the MC gets higher. Also, the interface reaction of the thiol at the Cu surface could speed up. Hence, the diffusion may no longer be the limiting step and the probability of a change in mechanism towards an interface-controlled reaction is much higher at elevated temperatures such as 250 °C. This makes the diffusion of the sulfur compound in the MC a critical parameter for qualification tests and lifetime simulations. Currently a mean activation energy of 0.7 eV is assumed for the lifetime prediction of Cu bond wires according to the Arrhenius model. However, the Arrhenius plots show much higher acceleration modes with $D3 = 1.42$ eV and $R3 = 1.17$ eV, 1.58 eV. Thus, we can narrow the activation energy of the different failure mechanism to 1.1-1.6 eV instead of a mean value of 0.7 eV which is commonly used for the Arrhenius model.

7.4.3 HTS of Cu and Pd Powder with Triazole-Thiol

As PCC wires show an increased sulfidation rate in HTSL tests, a mixture of Cu:Pd:**TT** (molar ratio = 1:0.1:0.1) was investigated to simulate a PCC wire under the influence of a sulfurous environment. The mixtures were stored at different temperatures and analyzed via PXRD. After 672 h, a wide range of Cu and Pd compounds formed, see **Figure 7.11**.

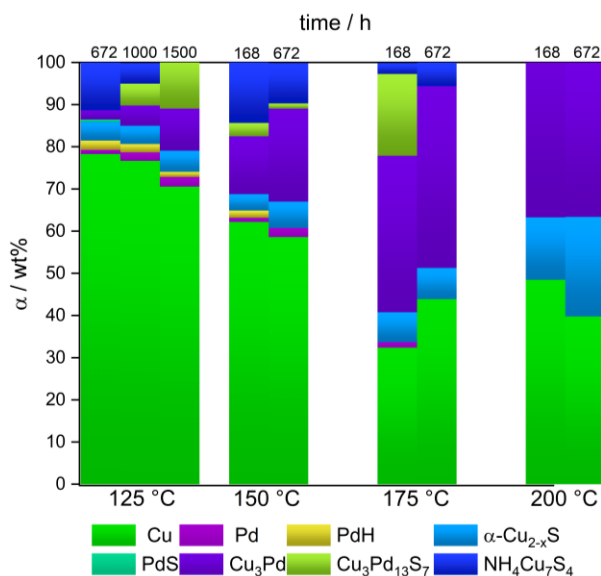


Figure 7.11: Semi-quantitative results for the Cu:Pd:**TT** (molar ratio = 1:0.1:0.1) mixture after HTS.

At 125 °C the most phases are observed and consist of the intermetallic compound Cu₃Pd, the palladium hydride PdH_x ($x \approx 0.6$), palladium sulfide PdS, ammonium heptacopper sulfide NH₄Cu₇S₄, and the low chalcocite α -Cu₂S. Therefore, it is assumed that various reactions occur in these mixtures, such as:

- i. Intermetallic compound formation through diffusion of Cu ions along grain boundaries into Pd particles:¹⁸⁵⁻¹⁸⁹
 - $3 \text{ Cu} + \text{Pd} \rightarrow \text{Cu}_3\text{Pd}$
- ii. Oxidative addition and reductive elimination of the thiol at the surface of the Pd particle and simultaneous formation of PdH_x and PdS:¹⁹⁰⁻¹⁹²
 - $\text{R-SH} + \text{Pd}^0 \rightarrow [\text{R-S-Pd}^{2+}\text{-H}] \rightarrow \text{PdH}_x + \text{PdS} + \text{R}$
- iii. Low chalcocite formation from sulfidation reaction and subsequent NH₄⁺ intercalation into Cu_xS to form NH₄Cu₇S₄:^{193, 194}
 - $\text{Cu} + \text{TT} \rightarrow \text{Cu}_{2-x}\text{S} + \text{NH}_3 + \frac{1}{2} \text{H}_2 \xrightleftharpoons{\Delta T} \text{NH}_4\text{Cu}_7\text{S}_4$

Note that, the H₂ evolution originates from the reversible palladium hydrogenation and the NH₃ formation stems from the decomposition of the triazole-thiol (**Figure A. 7.9**). At higher temperature (150 °C) the PdH_x is not observed anymore as the hydrogen incorporation is not thermodynamically stable and thus reversible at high temperatures. Also, PdS is not formed, instead the mixed phase Cu₃Pd₁₃S₇ is found. This phase may form through the incorporation of Cu ions into the PdS-lattice as the Cu ion readily substitutes palladium ion lattice sites.^{195, 196} However, the mixed sulfide Cu₃Pd₁₃S₇ seems to be thermodynamically unstable and segregates to Cu₃Pd and α -Cu₂S. So, by increasing the temperature to 175 °C the most dominant phases are shifted towards Cu₃Pd and α -Cu₂S. This is even more pronounced at 200 °C. Thus, the copper sulfide and the intermetallic phase Cu₃Pd seem to be the thermodynamically most stable corrosion products. Also, the ammonium heptacopper sulfide is vanishing due to the reversibility of this compound at high temperatures.¹⁹⁴ It is important to note that there are some unidentified reflections in the powder pattern from 125-175 °C. These reflections cannot be assigned with the JCPDS and the COD database. Further, the reflections disappear at 200 °C making it more than likely that it is an organic phase which decomposes into gaseous components at high temperatures. As the adhesion promoter comprises a triazole it is likely that it decomposes at high temperature and some polymer-like network (e.g. covalent organic frameworks = COF's) will form. As a lot of different phases are observed it is difficult to properly quantify the powder pattern with a calibration curve. Therefore, a semi-quantitative approach was used with the software package Match!. Herein, the phases are indexed and quantified with the *RIR* vs corundum. As some reflections are observed which cannot be assigned, the accuracy of this method suffers. Thus, this system is investigated in a qualitative fashion. The crucial point is whether Pd speeds up the α -Cu₂S formation and thus enhances the Cu degradation. From the postulated reaction pathways above, one can imagine that Pd might act as a catalyst and therefore reduces the activation energy of intermediary states and consequently increases the reaction rate. In addition to that, the formation of palladium hydride is

observed which is known to enhance the hydrogen evolution reaction (HER).¹⁹⁷⁻¹⁹⁹ This also increases the catalytic capability of PdH_x by lowering the adsorption energy towards the thiol moiety of **TT** and thus promotes copper sulfide formation. In fact, a small amount of Pd is sufficient to speed up the $\alpha\text{-Cu}_2\text{S}$ formation, see **Figure 7.12**.

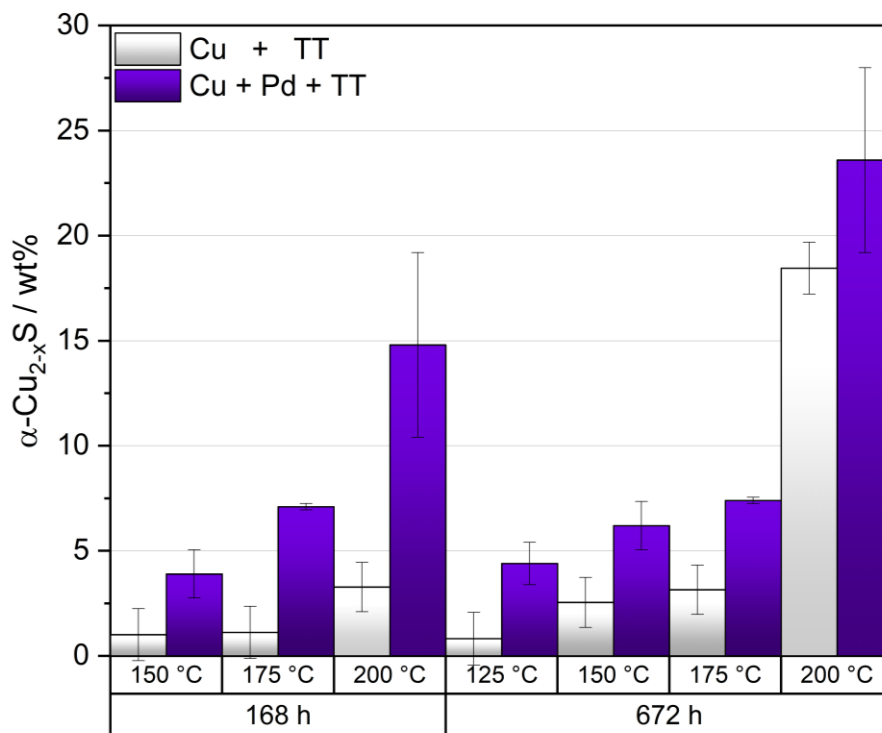


Figure 7.12: Semi-quantitative results for $\alpha\text{-Cu}_2\text{S}$ formation obtained for the Cu:**TT** (molar ratio = 1:0.1) and the Cu:Pd:**TT** (molar ratio = 1:0.1:0.1) mixtures. The maximal theoretical $\alpha\text{-Cu}_2\text{S}$ amount is 24 wt%.

Like the PCC wire, the mixtures with small amount of Pd speed up the corrosion significantly. After 168 h HTS at 150 °C the copper sulfide formation more than doubled compared to the mixture without Pd. As the temperature increases to 200 °C an exponential behaviour for the $\alpha\text{-Cu}_2\text{S}$ formation is observed. The same behaviour is found after 672 h. These findings convincingly explain why PCC wires are much more prone to corrosion. An initial palladium hydride formation might increase the catalytic power of the palladium coating which enables the formation of the copper sulfide. Additionally, the reversible formation of PdH_x might lead to strain or embrittlement of the Pd-coating and thus might lead to an increased catalytic activity and thus increased corrosion rate.¹⁹⁹ However, the catalytic centers are not limited to PdH_x and Pd but it also can happen at the surface of the intermetallic Cu_3Pd particles which are also known for their catalytic capabilities.²⁰⁰⁻²⁰⁴ This mixture of potential catalytically active compounds makes it hard to predict where the reaction happens and what reaction products will result. Thus, a wide variety of phases are observed as a result of more than one catalytically active surface.

7.4.4 HTS of Cu and Pd Powder with Mercaptosilane

In the same manner, the Cu:Pd:MS1 (molar ratio = 1:0.1:0.1) mixture was investigated. After HTS the samples were filtered, and the liquid and solid phase were analyzed separately. Like the Cu:MS1 mixture, the liquid phase showed no signs of any corrosion products by means of NMR and IR spectroscopy. Thus, the solid phase was exclusively examined by PXRD. Then, the samples were quantified like the Cu:Pd:TT mixture, see **Figure 7.13** (**Figure A. 7.8**).

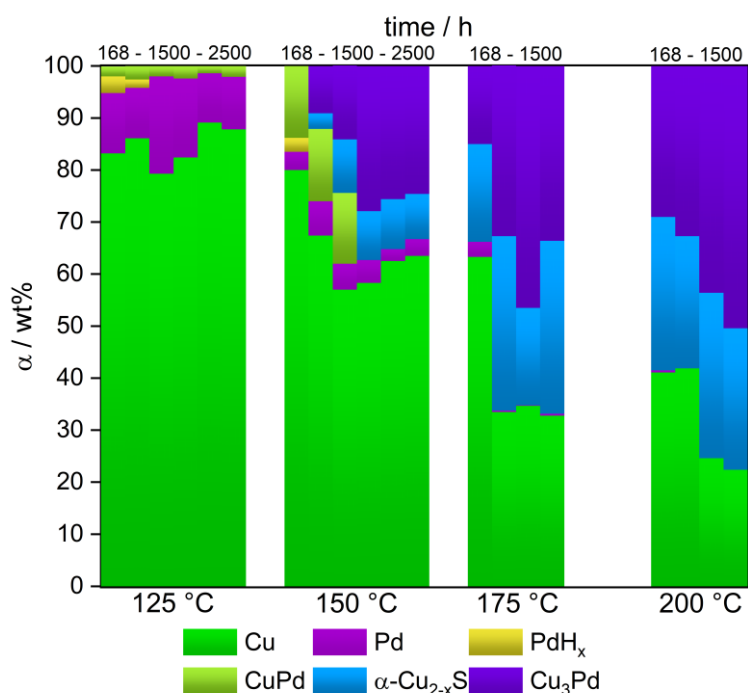


Figure 7.13: Semi-quantitative results for the Cu:Pd:MS1 (molar ratio = 1:0.1:0.1) mixture after HTS for various conditions.

In general, fewer phases are formed in the Cu:Pd:MS1 system compared to the Cu:Pd:TT system. The main difference is the absence of palladium sulfides in the MS1 system. However, similar phase formation is found. At 125 °C, PdH_x and the new intermetallic phase CuPd forms. With increasing HTS time the PdH_x formation is reversible, but no other corrosion products are formed out of it. Also, no α-Cu₂S formation is observed at 125 °C. This changes at 150 °C, where PdH_x, CuPd and α-Cu₂S is formed in the beginning stages of corrosion. Then, CuPd transitions to the copper-rich Cu₃Pd phase, while the copper sulfide content stays relative constant. The same is found at 175-200 °C where Cu₃Pd and low chalcocite forms exclusively. Note that, Cu₃Pd and α-Cu₂S are the same final corrosion products in the Cu:Pd:TT system. Therefore, it is concluded that Cu₃Pd and α-Cu₂S are the most thermodynamically stable products. Also, the first copper sulfide formation is found together with the first Cu₃Pd formation. This increases the probability that Cu₃Pd is the catalytically active compound in the system. Further, the copper sulfide content increases at the same time as the Cu₃Pd content, which indicates a cooperative effect between the thiol and these two phases. In addition to that, the formation of the intermetallic Cu₃Pd phase shows that Cu ion diffusion into and through a

Pd-coating is feasible.¹⁸⁶⁻¹⁸⁹ At the boundary of the Pd-Cu interface of a PCC wire the Cu₃Pd phase may form and devour the Pd-coating which results in a more reactive surface. At this surface the catalytic cleavage of the sulfur-hydrogen bond is energetically favored, and the adjacent Cu ions can absorb the sulfur atom to form the copper sulfide. It is important to note that at 200 °C the amount of α -Cu₂S does not change. This is due to the complete conversion of the thiol moieties with Cu (theoretical α -Cu₂S amount = 33 wt%). To consolidate the hypotheses that the presence of palladium and its corrosion products accelerate the Cu corrosion, the α -Cu₂S amounts in the Cu:MS1 and Cu:Pd:MS1 mixtures are compared, see **Figure 7.14**.

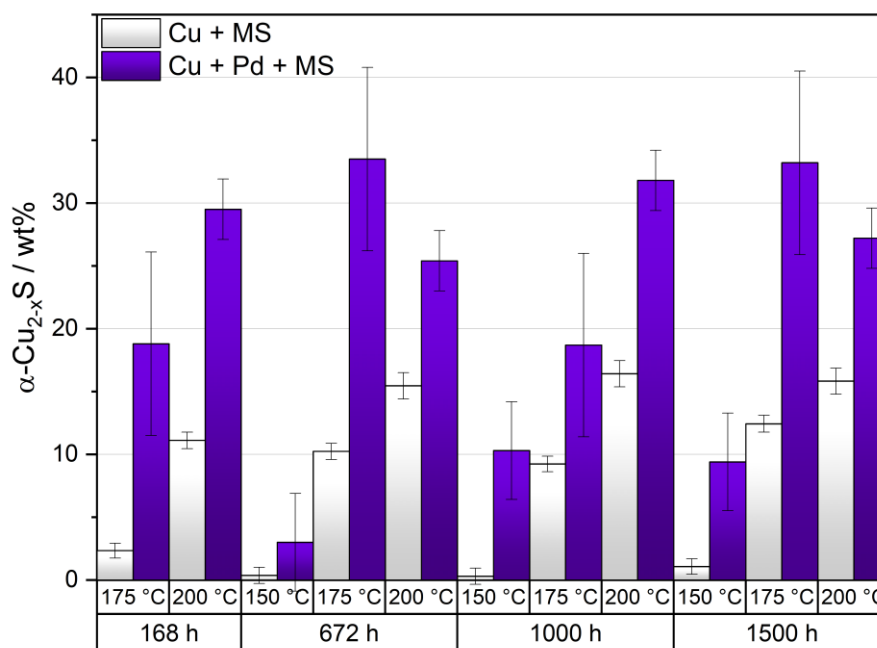


Figure 7.14: Semi-quantitative results for α -Cu₂S formation obtained for the Cu:MS1 (molar ratio = 1:0.1) and the Cu:Pd:MS1 (molar ratio = 1:0.1:0.1) mixtures. The maximal theoretical α -Cu₂S amount is 33 wt%.

A small amount of Pd already makes a difference at 150 °C for 672 h. As the temperature and storage time increases, the effect of Pd induced corrosion acceleration becomes more severe. After 672 h at 175 °C the theoretically accessible α -Cu₂S amount is reached, which means complete conversion of the thiol. This underlines the drastic effect of palladium on the Cu degradation. This is in line with the higher sulfidation of the PCC wires in the package. In **Figure 7.15**, a proposed sulfidation and alloying process is shown for a PCC wire, which is concluded from the HTS experiments of the different Cu:Pd:thiol mixtures. First, oxidative addition and reductive elimination takes place at the Pd surface. This leads to PdH_x formation with RS⁻ adsorbed at the surface. As a consequence, PdH_x enhances the catalytic C-S bond cleavage of the thiol. Simultaneously, Cu inserts into the palladium-coating on the Cu facing side of the Pd layer to form the intermetallic phase CuPd. During constant heating, the palladium hydride formation is thermodynamically not stable and turns back to Pd under HER. The resulting Pd layer shows higher strain and is more brittle and thus shows more defect sites than the original Pd layer due to the reversed lattice expansion.

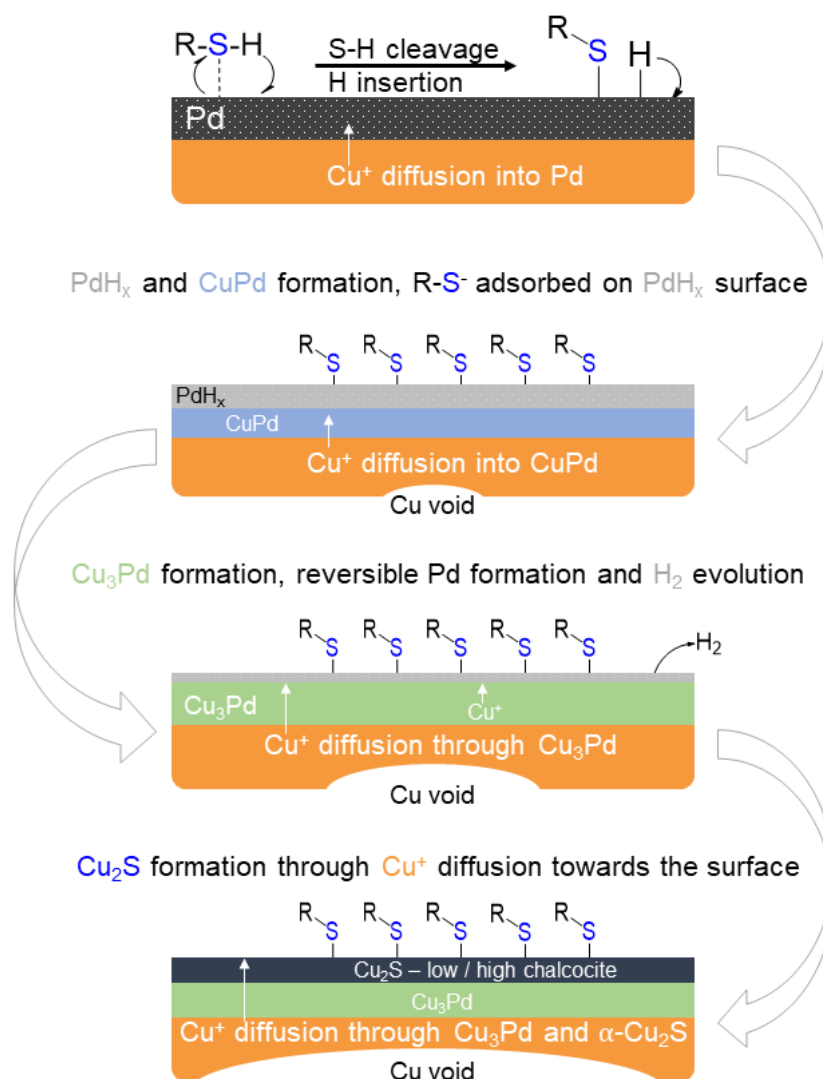


Figure 7.15: Schematic illustration of a proposed general sulfidation and alloying process of a PCC wire.

Thus, Cu^+ readily diffuses into the neighboring Pd layer and eventually forms the copper-rich Cu_3Pd .^{186, 205} The Cu_3Pd phase combines the catalytic capability to form copper sulfide at the surface and the continuous supply of Cu ions. Finally, copper sulfide forms at the surface of the formed Cu_3Pd layer as the intermetallic phase can segregate at the surface into Cu and Pd islands.^{200, 206, 207} Hence, the segregated Cu particles can react near the adjacent catalytically active Pd sites towards $\alpha\text{-Cu}_2\text{S}$. The high conversion of the thiol to copper sulfide suggests that copper sulfide also reacts with the thiol moiety. As a constant supply of Cu ions through Cu_3Pd and Cu_2S is feasible, the copper sulfide layer grows thicker until the thiol provision is exhausted. In addition to that, surface defects and cracks from corrosion induced volume expansion could lead to a combined Cu_3Pd - Cu_2S galvanic corrosion if both phases are exposed to the thiol. In summary, this leads to a thick Cu_3Pd and Cu_2S layer which are generated from the supply of Cu ions from the Cu wire core, leading to large Cu voids. In the worst case the Cu voids grow too large and cause failure. As it was shown, Pd heavily accelerates the sulfidation process of Cu. Thus, Pd carries a high risk as a protective coating in a sulfurous environment.

7.5 Conclusion

In this chapter, the general reactivity of Cu with thiol and Pd under HTS was investigated. It was found that the Cu content in the formed copper sulfide strongly depends on the thiol content in the mixture. Here, HTS of Cu powder with low thiol quantities leads to the formation of the copper-rich low chalcocite α -Cu₂S. Therefore, low and high chalcocite are expected for semiconductor packages due to the comparably low sulfur content in the MC. Analysis of the quantified data revealed that the sulfidation tends to be interface-controlled with an activation energy between 1.17 eV and 1.58 eV. After a certain copper sulfide layer thickness is reached, the reaction mechanism changes towards a diffusion-controlled mechanism and the sulfidation slows down. Also, the aggregation state of the thiol directs the corrosion mechanism. This is indirectly connected to the diffusion rate of the adhesion promoter in the MC. Due to the limited diffusion of the thiol in the MC a diffusion-controlled process is expected in integrated circuits. When Pd is added to the mixture, a wide variety of phases such as PdH_x, Pd_xS, CuPd and Cu₃Pd form which can considerably increase the catalytic capability of Pd. This means that in semiconductor packages various potent catalysts can form on the surface of the PCC wire. Additionally, the reversible formation of PdH_x leads to a brittle Pd-coating, which may increase the sulfidation risk and speed. However, a precise quantification was not possible due to the several phases which are formed during HTS. Therefore, the analysis was performed in a semi-quantitative fashion with the RIR method. This analysis revealed a significant acceleration of the sulfidation, when Pd is added to the mixture. Thus, more Cu voids may form, thus increasing the risk of failure in semiconductor devices. Because of the semi-quantitative analysis, an accurate kinetic analysis is not feasible. Therefore, it cannot be concluded if the sulfidation reaction is simply accelerated over the whole temperature range or if other failure mechanisms play a role at higher temperatures.

In these studies, it was shown how Pd enhances the corrosion rate and that a Pd-coating poses a high risk for high temperature applications in a sulfurous environment. This especially concerns qualification standards for future automotive applications where high temperature testing moves into focus. This not only poses a problem to this specific material combination but to other systems as well. As the failure mechanism changes at higher temperatures as shown above, high temperature testing may lead to false conclusions. To avoid this, lower temperatures must be used for stress tests which would imply impossibly long qualification times. To compensate for that, corrosion modeling might prove to be a potential tool for lifetime simulations of the electronic device at lower temperatures.

8 Corrosion Susceptibility of Bare Cu bond Wire versus Various Organic Sulfur Compounds

8.1 Abstract

Isothermal high-temperature in-situ powder X-ray diffraction (HT in-situ PXRD) measurements were performed on Cu bond wires with various organic S-compounds. The isothermal storage of the bond wires at 250 °C leads to bond wire corrosion with high chalcocite (β -Cu₂S) as the main corrosion product. The HT-in situ-PXRD measurements allow to simultaneously quantify the Cu bond wire degradation and β -Cu₂S formation. Hence, different organic sulfur compounds are compared for their sulfur induced corrosion. The measurements indicate that the corrosion susceptibility of bare Cu bond wire towards organic sulfur compounds, at least for the tested S-compounds, decreases from: thioketone \approx sulfoxide \approx thioether $>$ unconjugated thiol \approx oxygen $>$ conjugated thiol $>$ di-, tri- and tetrasulfide. Hence, suitable S-compounds can be identified as potential ingredients for the formulation of the MC. Also, HT-in situ-PXRD could be evaluated as a suitable methodology for substance screening. Finally, the corrosion kinetics are analyzed via the JMAEK equation and the Master plots $f(\alpha)$ and $g(\alpha)$.

8.2 Introduction

As mentioned before, organic sulfur compounds play an important role in molding compounds to ensure good adhesion to the metallic parts and thereby prevent delamination of the MC. Also, sulfur compounds are key reagents for the formation of a stable polymer-backbone in the MC. Even though these sulfur-containing adhesion promoters are the most suitable reagent to improve adhesion, they also lead to the sulfidation of the bond wire at temperatures above 150 °C.^{29, 60} As high temperature stress testing becomes a standard requirement for automotive applications, it is essential to identify critical combinations of sulfur compounds with Cu bond wire at high temperatures. Accordingly, the aim of this chapter is to explore the reactivity of different organic sulfur moieties versus bare Cu bond wire at elevated temperatures and to evaluate HT-in situ-PXRD as a suitable method for substance screening. This should allow us to identify suitable sulfur compounds which may be used as alternative additives for MC formulation. However, up to now it was hardly feasible to study the reactivity of different adhesion promoters because the corrosion occurs only in ultrathin layers within semiconductor packages. Hence, the formation of Cu_xS was only hypothesized and not experimentally verified.⁵⁴ As the corrosion kinetics depend, among other factors, on the properties of the solid electrolyte Cu_xS, it is vitally important to determine the formed phases during corrosion. From chapter 7 it was concluded that the low/high chalcocite phase (<100 °C = α -Cu₂S, >100 °C = β -Cu₂S) forms in semiconductor packages. To verify this assumption and to arrive at a more detailed picture of the corrosion behaviour, isothermal HT-in situ-PXRD measurements are performed. Finally, the reaction kinetics are analyzed, and the underlying failure mechanism are studied.

8.3 Experimental

8.3.1 Bare Cu Bond Wire Experiments with Organic Sulfur Compounds

All experiments were performed with bare Cu bond wire with a diameter of 50 μm . Prior to the experiments, the bare Cu wire was treated with hydrochloric acid for 15 min to reduce the passivating Cu_2O , CuO layer on the surface of the wire. Then, the wire was washed three times with distilled water and acetone (p.a.). For every measurement, four Cu bond wires are used per capillary. This approach ensured good intensities for the PXRD measurements as well as a uniform and reliable reaction monitoring. The wires were filled into a silica capillary, which is 0.5 mm in diameter and ≈ 80 mm in length. Then, the capillary was filled with the reagent. All steps were performed under an inert nitrogen atmosphere. After the capillary was filled with the wires and the reagent, the capillary was flame-sealed to prevent evaporation of the reagents and to protect the wires from oxygen oxidation. In case of the solid triazole-thiol (TT), the capillary was filled with the solid reagent, evacuated prior to use and flame sealed under vacuo. In **Table 8.1** a complete list of all experiments is given. Also, a measurement with a bare Cu bond wire in an unsealed capillary under ambient air conditions was performed to compare the reactivity of the organic sulfur compounds with well-researched oxygen corrosion. Note, that **DTTS** is a mixture consisting of 84 % disulfide, 12 % trisulfide and 4 % tetrasulfide (**Figure A. 8.1**).

Table 8.1: List of all conducted isothermal HT-in situ-PXRD measurements.

Bond wire type	Organic sulfur compound	Abbreviation (S-compound)	T / °C	Molar ratio (wire:reagent)	Cu:S ratio
Cu	Thioketone*	TK	250	1:0.1	1:0.1
Cu	Sulfoxide	SO	250	1:2.2	1:2.2
Cu	Thioether 1	TE1	250	1:0.9	1:0.9
Cu	Thioether 2	TE2	250	1:0.9	1:0.9
Cu	Mercaptosilane 1	MS1	250	1:0.8	1:0.8
Cu	Mercaptosilane 2	MS2	250	1:0.6	1:0.6
Cu	Triazole-thiol**	TT	250	1:2.3	1:2.3
Cu	Oxygen	O₂	250	1:∞	1:∞
Cu ^a	Disulfide	DS	250	1:0.8	1:1.6
Cu ^a	Di-,Tri-,Tetrasulfide	DTTS	250	1:0.3	1:0.68

*TK is a solid reagent and was dissolved in propylene carbonate prior to use.

** TT is a solid reagent and was used as solid due to poor solubility.

^a External standard method (ESM) is used for the quantification.

8.3.2 Isothermal HT-in situ-PXRD Measurements and Quantification

HT-in situ-PXRD was used as standard method to characterize the reaction products and to follow the corrosion process. For device specific details, see chapter 4.1.2. Further, Mo- $K_{\alpha 1}$ ($\lambda = 0.70930 \text{ \AA}$) radiation was used for all samples and measured in Debye-Scherrer geometry in a silica capillary. Also, the measurements were conducted at $250 \text{ }^{\circ}\text{C}$ under isothermal conditions.

In all experiments with organic sulfur compounds, the powder patterns solely comprise a Cu and Cu_2S phase. Hence, the ESM and DCM method can be used to quantify the binary mixture. For further details, see chapter 3.5.3 and 3.5.4. Herein, the experiments **1-8** are quantified with the DCM method because of an incomplete conversion of the Cu bond wire. The experiments with **DS** and **DTTS** are quantified with the ESM method as the wire fully corroded to $\beta\text{-Cu}_{2-x}\text{S}$ which could be used as external standard. Note that with **DTTS** a phase transition from the hexagonal chalcocite $\beta\text{-Cu}_{2-x}\text{S}$ to the cubic copper sulfide phase $\gamma\text{-Cu}_{2-x}\text{S}$ is observed. This additional phase was also quantified with the ESM.

The three strongest reflections Cu_2O (111), (020), and (200) in the measurement of bare Cu bond wire at ambient are used for the quantification of cuprite (Cu_2O). Further, the DCM is used in accordance with the quantification of copper sulfide. The factor $K_{\text{Cu}_2\text{O}}$ is determined from the RIR-values of the COD database, see **table A 4.2**.

8.3.3 SEM and EDX Analysis

The PXRD measurements are complemented with SEM and EDX analysis, which was conducted at the University of Regensburg. Herein, the wires were analyzed after the HT-in situ-PXRD measurements. Therefore, the wires were removed from the capillaries and stored in a nitrogen glovebox under continuous nitrogen flow to dry the surface of the wires. Then, the SEM and EDX analysis was performed with a variable pressure aperture at 25 kV.

8.3.4 Kinetic Analysis

Herein, two methods are used to study the reaction kinetics of the organic sulfur compounds versus bare Cu bond wire. The first method is the analysis via the JMAEK equation in its exponential and linearized form, see chapter 3.7.5. Therefore, the exponential form is used to fit the experimental data over the whole reaction range. As one process could dominate the JMAEK-fit, the linearized form of the JMAEK equation is used to generate the SH-plot. The SH-plot is used to study the corrosion process in more detail as the corrosion mechanism could change over the whole reaction range. Then, the Avrami exponent n and the reaction rate k is derived from the JMAEK-fit and the SH-plot. The second method is the application of the master plots $f(\alpha)$ and $g(\alpha)$, see chapter 3.7.7. Hence, the normalized theoretical models are compared to the normalized experimental data. Here, the master plot $f(\alpha)$ is especially suited to study the beginning stages (0-50 wt%) of the Cu bond wire degradation and the master plot $g(\alpha)$ to investigate the later stages (50-100 wt%). Finally, the reaction mechanisms are discussed in view of the obtained parameters.

8.4 Results and Discussion

8.4.1 Comparison of Cu bond Wire Degradation with Organic Sulfur Compounds

In general, the high temperature measurements at 250 °C of bare Cu bond wire versus organic sulfur compounds exhibit similar HT-in situ-PXRD progressions. At the beginning stages of the measurement, only the Cu reflections (111), (200), and (202) are observed, see **Figure 8.1**. These reflections originate from the Cu bond wire and show a similar intensity distribution compared to a calculated Cu phase (see **Figure 4.4**), which indicates a random distribution of the grains within the wire. Then, the intensities of the Cu reflections start to decrease over time and new reflections arise. The emerging reflections can be assigned to the high chalcocite phase β -Cu_{2-1.988}S (JCPDS 84-207). This is in accordance with chapter 7, where the low chalcocite phase was observed. Hence, the assumption is thereby confirmed that low/high chalcocite forms in semiconductor packages. This is underlined by the high Cu:S ratios in some experiments (e.g. Cu+DS, Cu:S = 1:1.6), where only the copper-rich high chalcocite phase is observed despite the high sulfur content. Therefore, it is very unlikely that other copper-poor phases are formed in semiconductor packages due to the comparably low sulfur content in the MC. Also, the composition of the high chalcocite phase can be narrowed down to Cu:S = 2-1.988:1. In the most cases only the three strongest reflections (012), (110), and (013) of the β -Cu₂S phase are observed in the powder pattern. These three reflections are used for

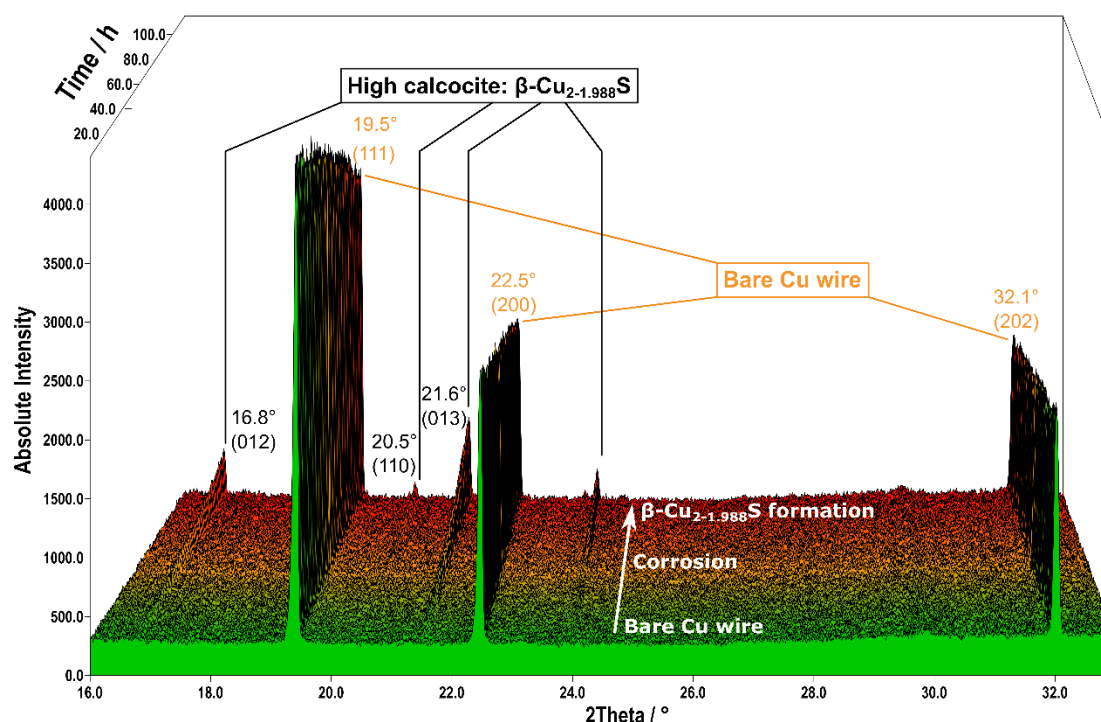


Figure 8.1: Representative HT-in situ-PXRD measurement. Here, bare Cu bond wire is measured with MS2 at 250 °C for 116 h. The green part in front represents the start of the measurement, where the uncorroded bare Cu wire (JCPDS 85-1326) is present. The orange part represents the start of the corrosion where copper sulfide (JCPDS 84-207) starts to form. Accordingly, the red part represents severe Cu wire degradation and formation of high chalcocite β -Cu_{2-1.988}S. The Cu (111), (200), and (202) reflections as well as the β -Cu_{2-1.988}S (012), (110), and (013) reflections are usually observed in the HT-in situ-PXRD measurements and are used for the quantification of the measurements.

the quantification of the copper sulfide phase. As the measurement proceeds, the Cu reflections further decrease, and the copper sulfide reflections increase. Accordingly, all organic sulfur compounds were measured at 250 °C versus bare Cu bond wire. Then the integral intensities of the respective reflections were determined, and a quantitative phase analysis was performed. Note that the respective measurements are shown in the appendix in **Figure A. 8.2-10**. In general, the measurements feature the respective Cu and β -Cu₂S reflections and only differ in the degradation kinetic. Therefore, the HT-in situ-PXRD measurements are only shown once for each reagent. Thus, the respective measurements are only shown for exceptional cases which differ from the general case.

The HT-in situ-PXRD measurements of the compounds **TK**, **SO**, **TE1**, and **TE2** revealed no change in the powder pattern after 100 h. Hence, these compounds showed no signs of corrosion in the PXRD measurements. Therefore, thioketones and thioethers are assumed to be stable versus bare Cu bond wire at 250 °C. Compared to that, the measurement with **O₂**, **MS1**, and **MS2** revealed a Cu bond wire degradation of ≈ 40 wt% after 100 h. Therein, the measurement of bare Cu bond wire at ambient air (denoted as **O₂**) also resulted in Cu bond wire corrosion, but cuprite (Cu₂O) as corrosion product, see **Figure A. 8.6**. Note that the mercaptosilanes **MS1** and **MS2** show a similar Cu bond wire degradation speed as oxygen corrosion. In contrast to that, the sulfur compounds **TT**, **DS**, and **DTTS** exhibit a severe Cu bond wire corrosion of ≈ 100 wt% after 100 h at 250 °C, see **Figure 8.2**.

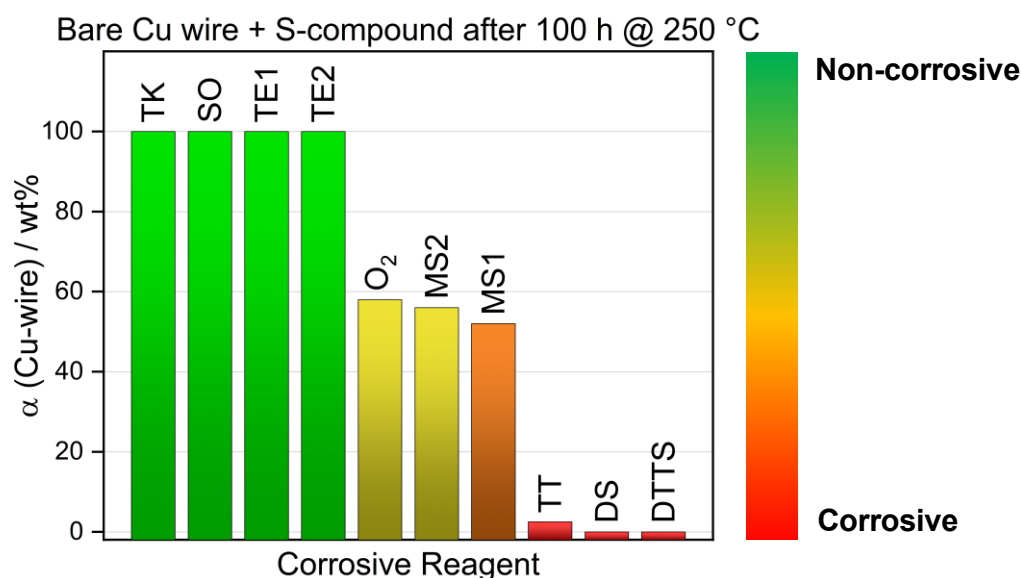


Figure 8.2: Comparison of the Cu bond wire degradation with different organic S-compounds and O₂ with bare Cu wire after 100 h at 250 °C. The reactivity changes in the order **TK** < **SO** < **TE1** < **TE2** < **O₂** < **MS2** < **MS1** < **TT** < **DS** < **DTTS**.

Accordingly, it is concluded that the corrosion susceptibility of bare Cu bond wire towards specific sulfur moieties increase in the order: Thioketone \approx sulfoxide \approx conjugated/unconjugated thioether > oxygen > unconjugated thiol > conjugated thiol > disulfide > trisulfide > tetrasulfide. Note that the di-, tri-, and tetrasulfide are especially prone to Cu corrosion with sulfur in an oxidation state of -1 and 0. To verify the findings of the HT-in situ-PXRD measurements, SEM and EDX measurements were performed. Herein, the SEM analysis of the bare Cu bond wire with **TK** after 120 h at 250 °C

revealed a layered film around the Cu wire, see **Figure 8.3**. However, the Cu core is still intact which is verified by the PXRD measurements. Also, no additional phases besides Cu are observed in the powder pattern. Hence, it is concluded that an amorphous phase forms around the Cu wire which cannot be detected by means of PXRD measurements. Further, sulfur element is observed on the surface of the Cu wire by EDX analysis. This means that **TK** is in fact decomposing on the surface but in minor amounts which cannot be measured by means of PXRD (Detection limit: $\text{Cu}_2\text{S} > \approx 5 \text{ wt}\%$). Despite **TK** does not lead to a significant Cu bond wire degradation, the formation of an amorphous phase on top of the wire could lead to the delamination of the MC. This especially must be considered for extended lifetimes at high temperatures.

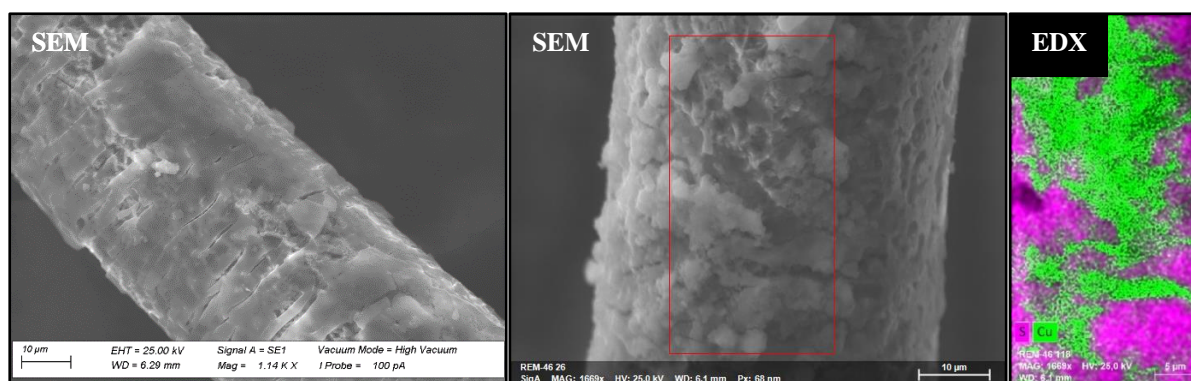


Figure 8.3: SEM and EDX analysis of the Cu wire surface after the HT-in situ-PXRD measurement with **TK** after 120 h at 250 °C. Left: A layered film is observed on the surface of the Cu wire. Right: EDX mapping of an excerpt of the wire surface which illustrates that the Cu wire is occupied by S on the surface.

Compared to that, the SEM analysis of the bare Cu bond wire with the thioethers **TE1** and **TE2** do not exhibit a pronounced layer on the wire surface. Also, the wire is nearly undamaged with some minor cavities on the surface. On closer inspection, small spheres on the surface are observed, see **Figure 8.4**. An EDX analysis of the spheres revealed the existence of Cu and S in a ratio of 2:1 on the surface of the wires (**Figure A. 8.11-6, Table A 8.1-2**).

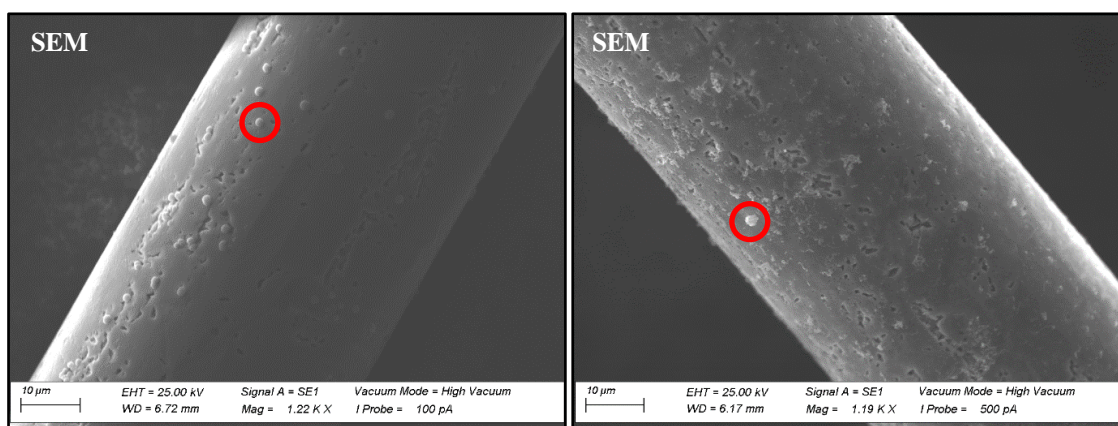


Figure 8.4: SEM analysis of the Cu wire surface after the HT-in situ-PXRD measurement. Left: Cu wire with **TE1** after 115h at 250 °C. Right: Cu wire with **TE2** after 140 h at 250 °C. Both wires show minor signs of corrosion, which are small spheres on the Cu surface. These spheres consist of Cu and S in a molar ratio $\approx 2:1$, according to the EDX measurements.

Hence, the formation of Cu_2S spheres on the surface of the wire. Again, the formation of Cu_2S is not observed in the PXRD measurements as the copper sulfide content is below the detection limit. Nevertheless, these two thioethers (**TE1**, **TE2**) are regarded as non-corrosive in this context as minor amounts of copper sulfide form on the surface of the wire compared to the thiol reagents. Also, no further decomposition products are observed either by SEM or PXRD.

In contrast to that, the Cu wire shows clear signs of corrosion with the conjugated thiol **TT** already after 17 h at 250 °C, see **Figure 8.5**. There, the Cu wire is covered with a layer of Cu, S, and N. The EDX spectra of this layer reveals a Cu to S ratio of $\approx 2:1$ with about 50 atom-% N incorporated into

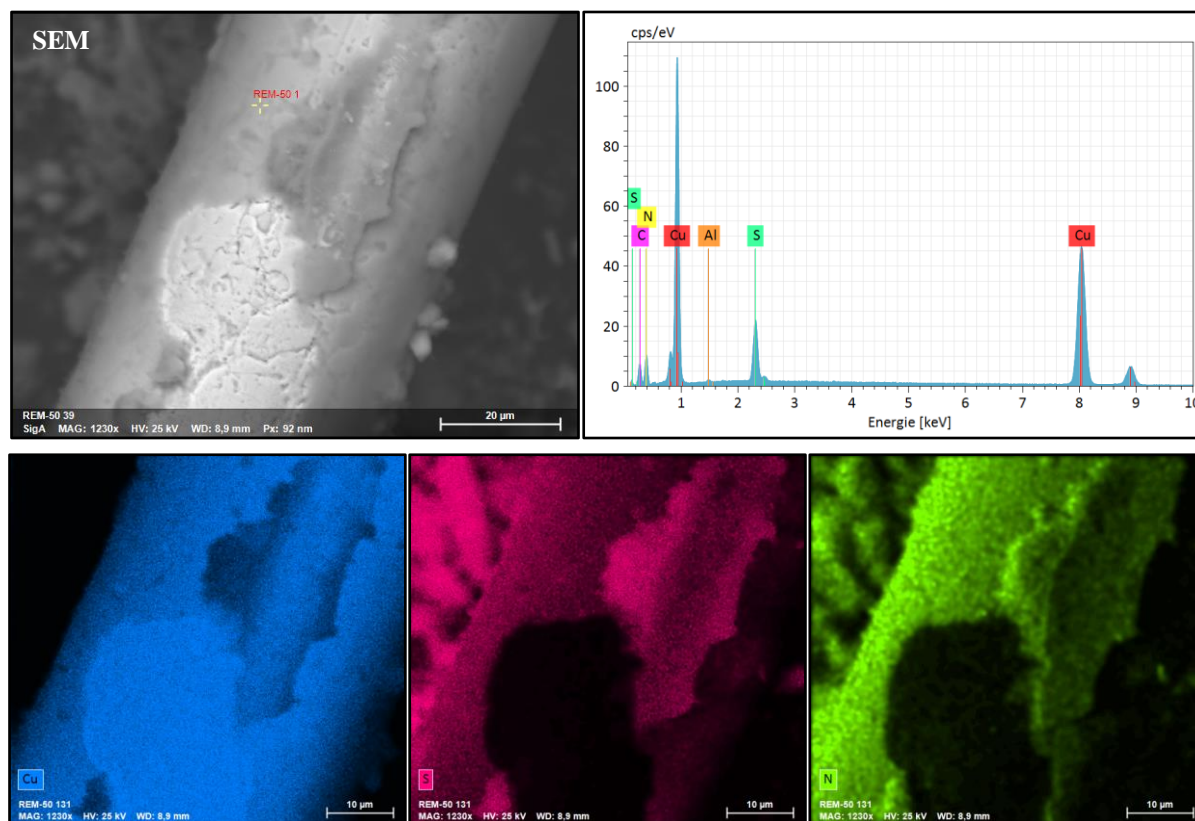


Figure 8.5: SEM and EDX analysis of the Cu wire surface after 17 h HTS with **TT** at 250 °C. Top left: SEM analysis of the Cu wire surface after HTS with a layer on top of the Cu wire surface. Top right: EDX analysis of the marked spot on the left side. The EDX analysis reveals that the layer is comprised of Cu, S, and N. Bottom: EDX mappings of the SEM picture on the top left which underline the findings of the EDX analysis.

Table 8.2: EDX analysis of the marked spot in Figure 8.5. The EDX analysis reveals that the layer on top of the Cu wire surface is comprised of Cu and S in a ratio of $\approx 2:1$ as well as N.

Element	Mass norm. / %	Atom-%	Abs. error / %	Rel. error / %
N	22.29	51.39	1.61	46.35
S	18.30	18.43	0.39	13.81
Cu	59.41	30.19	0.78	8.42

the corrosion layer, see **Table 8.2**. This indicates the formation of Cu_2S as corrosion product along with the formation of an amorphous N phase. This is concluded because no other corrosion product besides Cu_2S is observed in the PXRD measurements. The homogenous distribution of Cu, S, and N within this layer points to a simultaneous decomposition of **TT** and formation of Cu_2S . Therefore, it is assumed that the thiol reacts with the Cu surface to form copper sulfide. Then, an immediate polymerisation of the organic reaction product occurs to form a N-polymeric organic layer. This could lead to the delamination of the MC as the volume expansion by the additional formation of an organic layer on the surface of the metallic Cu surface could generate high strain. Also, the Cu degradation and volume expansion between the IMC increases the risk of lifted bond wires. As a result, this could cause resistance drifts due to the organic layer or the failure of the device by lifted bond wires. Hence, the application of this compound as adhesion promoter is critical, especially at high temperatures where the decomposition of the molecule is more likely to occur and thereby accelerates the corrosion kinetic.

Below the degradation process of the bare Cu bond wires with the corrosive reagents (O_2 , MS1, MS2, **TT**, **DS**, **DTTS**) will be discussed in further detail.

8.4.2 Oxygen Corrosion of Bare Cu Wire – A Comparison to Literature

As shown above, the reagents oxygen, di-, tri-, tetrasulfide, conjugated-, and unconjugated thiols lead to a degradation of the Cu wire. There the oxygen corrosion exhibits a similar degradation of the Cu wire compared to the unconjugated thiols (Group 1). Also, the reagents **TT**, **DS**, and **DTTS** (Group 2) display comparable Cu wire degradation to each other. Yet, the respective corrosion mechanism can greatly differ within the respective group. Therefore, the measurements are quantified and analysed via the JMAEK equation. Also, a graphical analysis of the experimental data with the Master plots $f(\alpha)$ and $g(\alpha)$ is performed.

As oxygen corrosion is well-researched, a reference measurement of Cu wire in ambient air environment at atmospheric pressure was performed. Hence, the validity of the HT-in situ-PXRD measurements can be confirmed and compared to the literature. There, most authors report a parabolic diffusion model as the most suitable solid-state reaction model to describe the Cu oxidation in the temperature range from 150 °C to 350 °C.²⁰⁸⁻²¹¹ However, recent studies also suggest a linear growth behaviour of cuprite in the beginning oxidation stages.²¹² Nevertheless, it is highly likely to change from a linear growth towards a parabolic growth behaviour at an increased cuprite layer thickness. Note that these investigations were conducted on thin Cu films (nm range) which resulted in nanoscale cuprite layers. Further, the formation of cuprite (Cu_2O) below 300 °C is consistent throughout the literature.²⁰⁸⁻²¹³ As mentioned above, the formation of cuprite is also observed in the PXRD measurements of Cu wire at ambient air (**Figure A. 8.6**). Therein, the Cu oxidation process displays a parabolic behaviour, see **Figure 8.7a**. Compared to the thin Cu films, the Cu wire has a diameter of 50 μm . Hence, a larger cuprite layer is formed at a conversion of ≈ 40 wt%. Because of this, a parabolic diffusion behaviour is more likely to occur. This is due to the lengthened diffusion path through the cuprite layer.

In order to further investigate the oxidation kinetic to the literature, the experimental oxidation rates are calculated for a one-dimensional (D1) and three-dimensional model. This is demonstrated in eq. (8.1) for a one-dimensional (D1) diffusion process:

$$\alpha^2 = x^2 = \frac{k}{r_0} \cdot t \rightarrow k = \frac{x^2 \cdot r_0}{t} \quad (8.1)$$

Here, α is the conversion fraction, x is the cuprite layer thickness, r_0 the initial wire diameter and k the oxidation rate. The obtained values are compared to the oxidation rates from the literature, see **Figure 8.6**.²¹⁰⁻²¹³ Herein, the experimental oxidation rates are in line with the oxidation rate from the literature and range from 0.02 nm/s to 0.45 nm/s. Thereby, the initial oxidation rate of the D1 model (0.41 nm/s) approximates to the linear growth kinetics obtained by *Unutulmazsoy et al* (0.44 nm/s).²¹² Also, the oxidation rate decreases in the later oxidation stages as the Cu^+ diffusion through the cuprite layer becomes rate limiting. However, the kinetic analysis with the JMAEK-fit, SH-plot and Master plots revealed that the Cu bond wire oxidation is rather governed by a D3 model, see **Figure 8.7**. Accordingly, the oxidation rates of the D3 model (initial: 0.14 nm/s; end: 0.02 nm/s) are in good accordance with the oxidation rates from the literature which also assume a parabolic law.^{210, 211} Interestingly, the initial oxidation rate obtained by *Maack et al.* increases with smaller grain size distribution (10 nm: 0.25 nm/s; 100 nm: 0.15 nm/s).²¹⁰ Keep this in mind as the Cu bond wire features a larger grain size distribution compared to the palladium-coated wires.

In summary, the Cu oxidation follows a parabolic behaviour which is in accordance with reports from literature. Also, similar oxidation rates are obtained. Thereby, the validity of the HT-in situ-PXRD measurements is confirmed. Consequently, the oxygen corrosion is a well-suited reference point to analyse the kinetics of the S-reagent measurements.

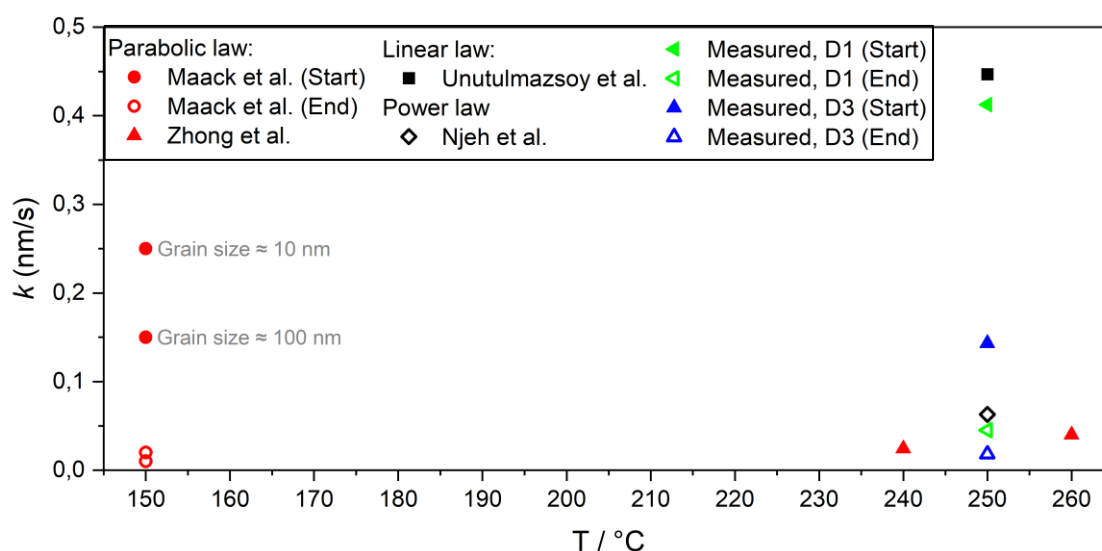


Figure 8.6: Oxidation rates of Cu to Cu_2O taken from Literature.²¹⁰⁻²¹³ Here, the literature data is compared to the experimental findings. Thereby, a one-dimensional (D1) and three-dimensional (D3) diffusion model was used to calculate the oxidation rates.

8.4.3 Degradation Mechanism and Kinetics of the Corrosive Reagents O₂, MS1, and MS2

Compared to the parabolic oxygen corrosion, the corrosion process of the Cu wire with **MS1** and **MS2** follows an approximately linear behaviour, see **Figure 8.7a**. Also, the Cu corrosion induced by oxygen is faster than the mercaptosilanes in the beginning but is then slowed down by the diffusion through the cuprite layer after about 40 h. Whereas the sulfidation of the Cu wire proceeds continuously. Thus, the diffusion of either Cu⁺ or mercaptosilane through the copper sulfide layer is not limiting the degradation kinetic. Because of this a more severe Cu wire corrosion is observed after 120 h. This is expressed by the Avrami exponent n which is obtained by the JMAEK-fit. There, the exponent changes from $n = 0.38$ for oxygen corrosion to 1.68 and 1.40 for **MS1** and **MS2**, respectively. Here, the oxygen corrosion with an exponent of $n = 0.38$ is best described by the D3 model with a theoretical value of $n = 0.51$. Hence, a three-dimensional diffusion-controlled model. In contrast to that, the Avrami exponents of **MS1** and **MS2** are closest to a three-dimensional counterdiffusion model (CD-D3) with a theoretical value of $n = 1.63$. Also, a three-dimensional nucleation and growth model with a pre-existent site saturation is also feasible: $n = d \cdot m + a = 3 \cdot \frac{1}{2} + 0 = 1.5$, where d is the dimension, m a diffusion mechanism and a the nucleation rate.

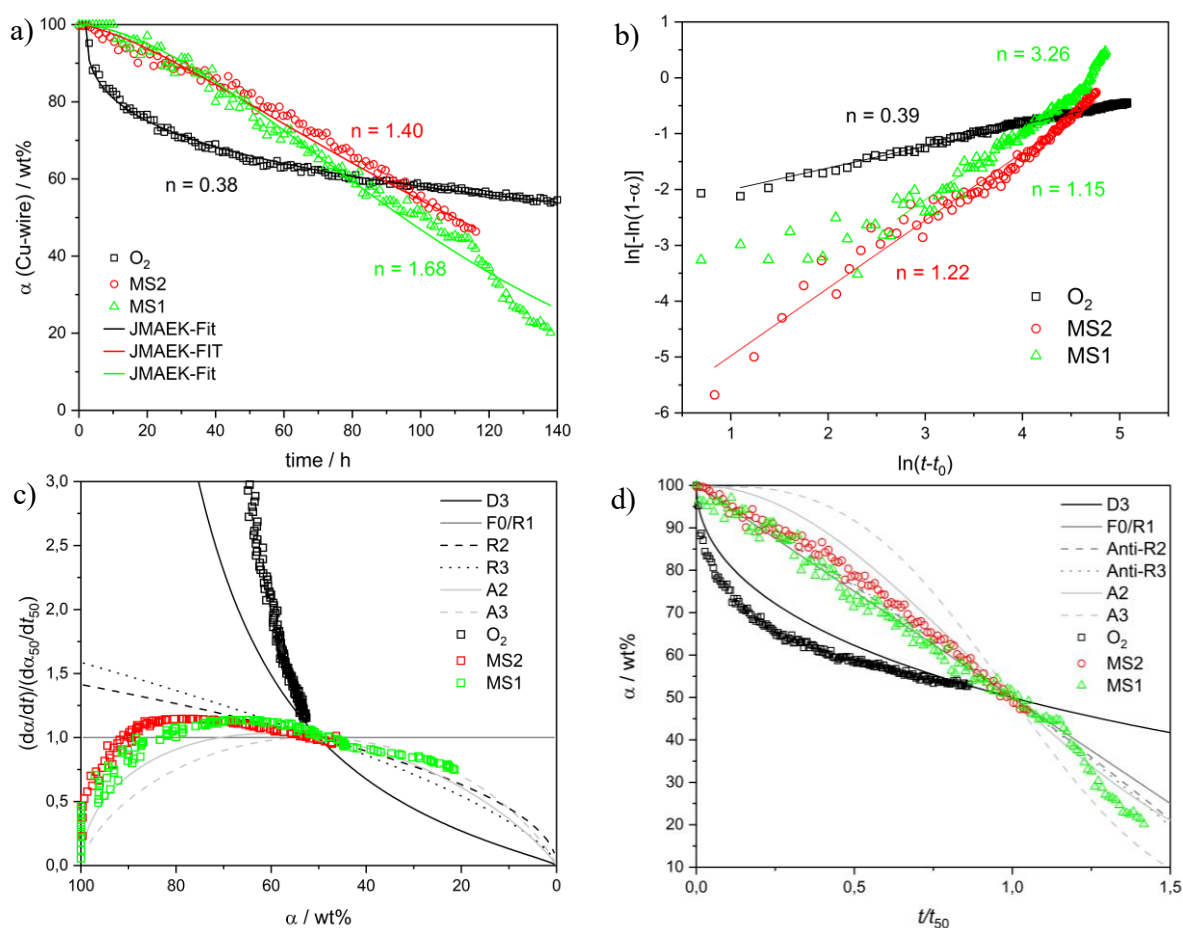


Figure 8.7: a) Quantified experimental data from the HT-in situ-PXRD measurements of bare **Cu** bond wire with **O₂**, **MS1**, and **MS2** and the obtained Avrami exponents n from the JMAEK-fit. b) SH-plot and respective Avrami exponents n of the obtained experimental data. c) Master plot $f(\alpha)$ of the normalized experimental data compared to theoretical solid-state reaction models. d) Master plot $g(\alpha)$ of the normalized experimental data compared to theoretical solid-state models.

Keep in mind that the JMAEK-fit cannot describe a change in the corrosion mechanism within the corrosion process but rather fits the Avrami exponent to the predominant mechanism. This is observed for **MS1**, where the degradation accelerates after ≈ 60 wt% and thereby deviates from the JMAEK-fit.

Whereas the SH-plot allows to differentiate between different mechanisms. Hence, further investigation via the SH-plot (**Figure 8.7b**) reveals the same exponent for oxygen corrosion but a more complex mechanism for **MS1**. For **MS1**, two different exponents of $n = 1.15$ and $n = 3.26$ are observed in the SH-plot. The former indicates a three-dimensional interface-controlled mechanism (R3, Anti-R3, theoretical n Anti-R3 = 1.13), whereas the latter describes a two-dimensional nucleation and growth-controlled model for **MS1** after a Cu degradation of ≈ 60 wt%. This can be explained by an interface-controlled mechanism in the beginning which is governed by the chemical surface reaction. Thereby, β -Cu₂S spheres form on the surface of the Cu wire and eventually form a continuous layer as the spheres coalesce. Then, the volume expansion of the chalcocite phase could lead to cracks and pores in the corrosion layer after a certain β -Cu₂S layer thickness is reached. Hence, an increased percolation of either Cu ions or mercaptosilane through these pores becomes feasible. This again leads to an increased nucleation of copper sulfide and thereby accelerates the degradation. Note that **MS2** exhibits a similar exponent with $n = 1.22$ which again points to an interface-controlled mechanism (R3, Anti-R3). However, the measurement of bare Cu wire **MS2** was stopped after a Cu conversion of ≈ 60 wt%. Therefore, it cannot be confirmed if the corrosion mechanism also accelerates at this point for **MS2** as observed for **MS1**.

The graphical analysis via the Master plots also points to a D3 model for oxygen corrosion, see **Figure 8.7c,d**. However, some disparities between the theoretical model and the experimental data are observed. Here, a faster degradation takes place in the beginning of the oxidation. As mentioned above, the Cu oxidation can also start with a linear growth which can explain the discrepancies. Then, the oxidation slows down and approximates to the D3 model with an increased cuprite layer thickness. Compared to that, the beginning sulfidation stages with the mercaptosilanes are best described by a one-dimensional nucleation and growth model (A2) in the Master plot $f(\alpha)$. This can be considered as a homogenous surface nucleation on the Cu wire. Note that this is similar to the interface-controlled mechanism, where the growth of copper sulfide is also limited by the surface. Whereas the former is limited by the nucleation and growth rate (A2) and the latter by the chemical reaction (R3, Anti-R3). Then, the experimental data of **MS1** and **MS2** approximates to an interface-controlled mechanism (R3) which then merges into a nucleation and growth model (A3) model. Further analysis of the Master plot $g(\alpha)$ shows that the sulfidation with **MS1** follows a one-dimensional interface model (R1) and then merges into an A3 model. In contrast to that, the **MS2** model seems to follow an Anti-R3 model which is characterized by the outward movement of the reactive surface.

The combined kinetic analysis clearly shows that the oxygen corrosion follows a D3 model, where the beginning stages differ from the model. This can be explained by a linear growth or a fast grain boundary diffusion as the oxidation starts. This changes for the mercaptosilanes. Here, it is concluded that the sulfidation with **MS1** starts with a homogenous surface nucleation mechanism (A2) which merges into an interface-controlled mechanism (R1). Hence, it is first controlled by the formation of nuclei where the growth of these nuclei is governed by the chemical surface reaction. After the volume expansion created cracks in the copper sulfide layer, a percolation of Cu ions or mercaptosilane directs the degradation kinetic. This is expressed by a counterdiffusion model (CD-D3) which eventually leads to an increased nucleation (A3) of copper sulfide. A similar conclusion is derived for the mercaptosilane **MS2**. Here, the sulfidation also starts with a homogenous surface nucleation but then changes to an interface-controlled model where the reactive surface moves outward of the wire. This points to a Kirkendall effect where an outward diffusion towards the reactive surface leads to Cu voids. This could also be the case for **MS1** where the counterdiffusion of Cu ions and **MS1** takes place. Hence, a Kirkendall effect can be observed if the outward diffusion of Cu ions is faster than the inward diffusion of the mercaptosilane. Also, the reaction rate constant increases slightly from $2.02 \cdot 10^{-3} \text{ h}^{-1}$ for O_2 corrosion to $8.18 \cdot 10^{-3} \text{ h}^{-1}$ and $6.99 \cdot 10^{-3} \text{ h}^{-1}$ for **MS1** and **MS2**, respectively. The derived models from the respective kinetic analysis method are summarized in **Table 8.3**. For further details regarding the reaction rate constants and Avrami exponents n see **Table A 8.3** in the appendix.

Table 8.3: Overview of the derived models from the respective kinetic analysis method. Here, shown for O_2 , **MS1**, and **MS2**.

Wire	O_2	MS1	MS2
T / °C	250	250	250
Sharp-Hancock Plot			
Mechanism	D3	R3, Anti-R3 A3	R3, Anti-R3
JMAEK-Fit			
Mechanism	D3	CD-D3, A2	Anti-R3, CD-D3
Master Plots			
Mechanism f(α)	D3	A2, R3, A3	A2, R2
Mechanism g(α)	D3	R1, A3	Anti-R3
Summary			
Assumed Mechanism	D3	A2, R1 → CD-D3, A3	Anti-R3

8.4.4 Degradation Mechanism and Kinetics of the Corrosive Reagents TT, DS, and DTTS

As mentioned in chapter 8.4.1, the conjugated thiol **TT**, disulfide **DS**, and di-,tri-, and tetrasulfide mixture **DTTS** lead to a severe corrosion of the Cu wire after 100 h. By closer inspection it is observed that **TT** exhibits much faster corrosion kinetics in the beginning than **DS** and **DTTS**, see **Figure 8.8a**. Also, the corrosion of the Cu wire with **TT** shows a parabolic behaviour where ≈ 90 wt% of the Cu wire is converted to β -Cu₂S after 5 h. Further, an Avrami exponent $n = 0.56$ and $n = 0.59$ is obtained by the JMAEK-fit and SH-plot respectively, see **Figure 8.8a,b**. This is perfectly in line with a D3 model and indicates a diffusion-controlled corrosion mechanism. Compared to the oxygen corrosion, the exponent is slightly higher (0.38 vs 0.56) for the **TT** corrosion. This difference could originate from a faster grain boundary oxidation for the oxygen corrosion where the O₂ molecule can readily diffuse through the grain boundaries of the Cu wire.²¹⁰ In contrast to that, the solid **TT** molecule is more likely to adsorb on the surface and is then limited by surface diffusion. Then, the corrosion is limited either by the surface diffusion of **TT** or by the diffusion of Cu⁺ through the copper sulfide.

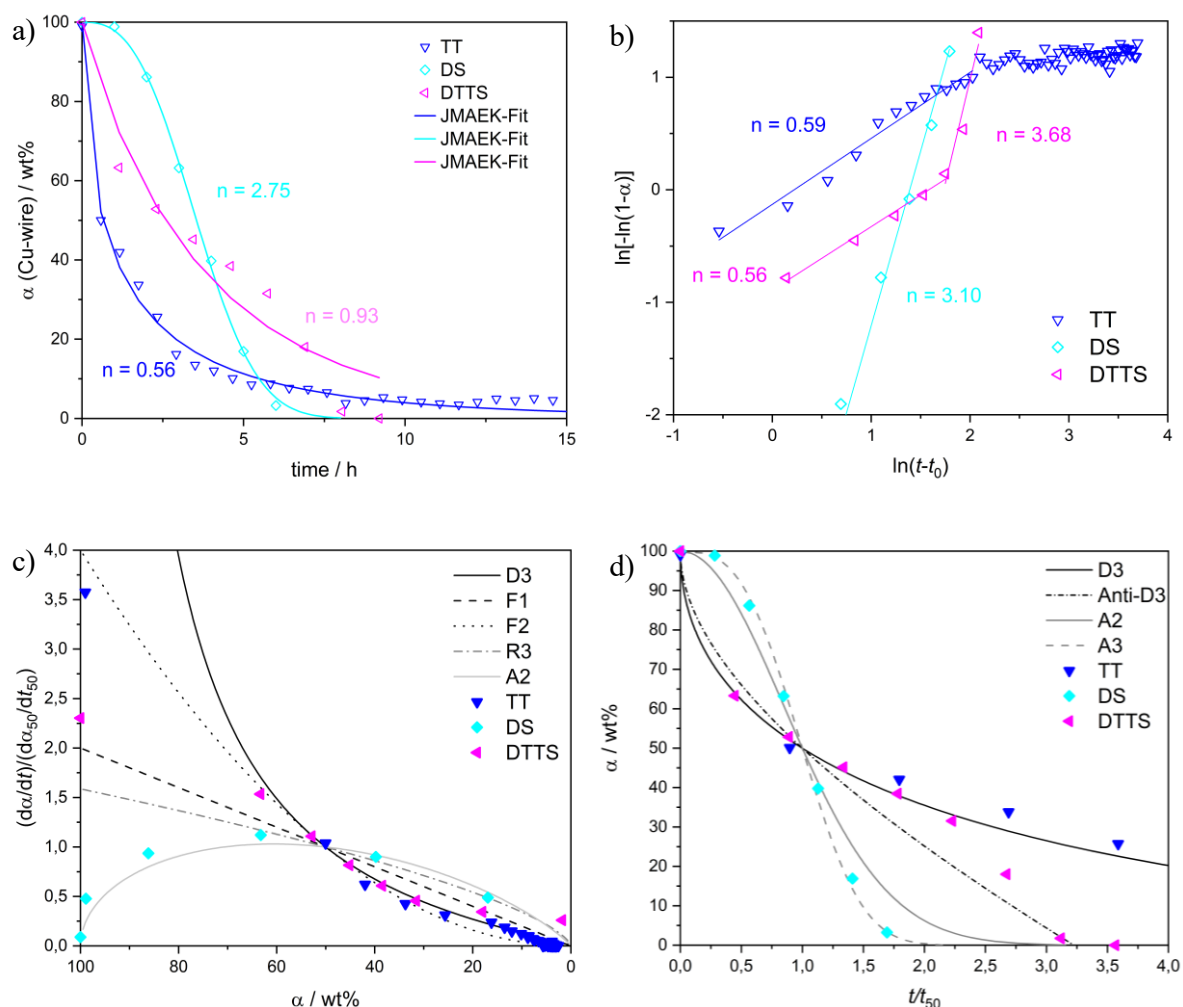


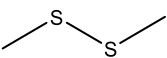
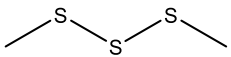
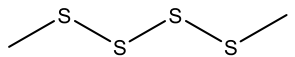
Figure 8.8: a) Experimental data from the HT-in situ-PXRD measurements of bare Cu bond wire with **TT**, **DS**, and **DTTS** and the obtained Avrami exponents n from the JMAEK-fit. b) SH-plot and respective Avrami exponents n of the obtained experimental data. c) Master plot $f(\alpha)$ of the normalized experimental data compared to solid-state reaction models. d) Master plot $g(\alpha)$ of the normalized experimental data compared to solid-state reaction models.

However, the corrosion with **TT** reaches a plateau after 10 h. This can be caused by two different reasons. First is the preparation of the capillary. Here, the solid **TT** was filled into the small capillary. This unavoidably can cause an incomplete filling of the capillary around the Cu wires. Hence, the solid **TT** is consumed around the wire and the corrosion stops. Second is the formation of an amorphous N-polymeric layer which is observed in **Figure 8.5**. This could lead to an impenetrable β -Cu₂S/N-polymeric layer which impedes further Cu⁺ or **TT** diffusion. Consequently, the corrosion reaction comes to an end. Also, the master plots clearly follow a D3 model which is in line the obtained Avrami exponents, see **Figure 8.8c,d**.

In contrast to that, the degradation kinetics of Cu wire with **DS** shows a sigmoidal shape where the complete Cu wire is corroded after ≈ 7 h. This points to a nucleation and growth-controlled corrosion mechanism. This is also expressed by an Avrami exponent of $n = 2.75$ and $n = 3.10$ for the JMAEK-fit and the SH-plot, respectively. Thus, an A3 model which is a two-dimensional nucleation and growth-controlled mechanism. Therefore, the diffusion is not limiting the corrosion kinetic but rather the chemical reaction at the surface of the Cu wire: $n = d \cdot m + a = 2 \cdot 1 + 1 = 3$, where d is two-dimensional, m an interface mechanism and a the constant nucleation rate. Note that an exponent $n = 3$ can also be derived for a three-dimensional mechanism with pre-existent site-saturation ($a = 0$). Further, the comparison of the experimental data to the theoretical model in the master plots $f(\alpha)$ and $g(\alpha)$ also follow a nucleation and growth-controlled model, see **Figure 8.8c,d**. Hence, it is concluded that the chemical reaction (R-S, S-S bond cleavage) and the subsequent nucleation and growth of copper sulfide directs the corrosion kinetic.

For the sulfide mixture **DTTS**, the Cu wire is expected to corrode faster due to the unstable S-S(S), and (S)S-S(S) bond in the tri- and tetrasulfide, see **Table 8.4**. Here, the sulfur atom in an oxidation state of 0 shows much weaker bond dissociation enthalpies of 222 kJ/mol and 155 kJ/mol for the tri- and tetrasulfide, respectively.²¹⁴ Whereas the sulfur atoms with an oxidation state of -1 in the disulfide exhibit a bond dissociation energy of 271 kJ/mol. Accordingly, it is expected that the tetrasulfide is the most reactive molecule which initiates the Cu corrosion. When the tetrasulfide is consumed, the trisulfide is the next reactive compound. Hence, the trisulfide will be consumed and a similar corrosion kinetic is assumed because of the same oxidation state of 0 for the reactive sulfur atom. Then, only disulfides remain and the degradation kinetic is assumed to slow down due to the altered oxidation states and an increased bond dissociation energy.

Table 8.4: Calculated bond dissociation enthalpies (kJ mol⁻¹) at 298 K for di-, tri-, and tetrasulfide.²¹⁴

Bond:	S-S	S-S(S)	(S)S-S(S)
	271		
		215	
		222	155

Actually, this is observed in the α - t -plot and SH-plot of Cu wire with **DTTS**, see **Figure 8.8a,b**. There, the Cu wire degrades very fast in a parabolic behaviour to ≈ 50 wt% after 2.5 h. After 2.5 h the corrosion slows down, and the Cu wire is completely corroded after 7 h. Also, it follows a sigmoidal shape until complete conversion. This is also confirmed by the SH-plot with an Avrami exponent of $n = 0.56$ and $n = 3.68$. Again, the exponent of $n = 0.56$ matches well with a D3 model and $n = 3.68$ with an A4 model. Additionally, the master plot $f(\alpha)$ indicates that the corrosion starts with a first-order reaction model (F1) and then merges into a D3 model, see **Figure 8.8c,d**. Further, the master plot $g(\alpha)$ confirms the D3 model which then drifts from this model towards a sigmoidal shape. In summary, the corrosion is governed by the decomposition of the tri-, and tetrasulfide in the beginning. This is due to the weak bond dissociation energy of the (S)S-S and (S)S-S(S) bond. Then the copper sulfide layer thickness increases which consequently leads to an increased diffusion pathway. Hence, the diffusion of Cu^+ or sulfides control the reaction kinetic. When all tri-, and tetrasulfide is consumed, the corrosion slows down. There, the degradation is governed by nucleation and growth which is induced by the disulfide. This is in accordance with the corrosion kinetic of pure **DS**, which also follows a nucleation and growth model.

To sum up, the most reactive compound is **TT** which follows a D3 model with a reaction rate constant of $8.03 \cdot 10^{-1} \text{ h}^{-1}$. The mixture **DTTS** also follows a D3 model due to the high reactivity of tri-, and tetrasulfide. Hence, very reactive reagents lead to a diffusion-controlled model as the decomposition of the S-reagent is fast enough that diffusion becomes the rate limiting step. Then, mostly disulfide remains and a nucleation and growth model is observed (A). This is in line with the pure disulfide **DS** which is also characterized as a nucleation and growth-controlled corrosion mechanism. Accordingly, similar reaction rate constants of $2.47 \cdot 10^{-1} \text{ h}^{-1}$ and $2.62 \cdot 10^{-1} \text{ h}^{-1}$ are obtained for **DS** and **DTTS**. The derived models from the respective kinetic analysis method are summarized in **Table 8.5**. For further details regarding the reaction rate constants and Avrami exponents n see **Table A 8.4** in the appendix.

Table 8.5: Overview of the derived models from the respective kinetic analysis method. Here, shown for **TT**, **DS**, and **DTTS**.

Wire	TT	DS	DTTS
T / °C	250	250	250
Sharp-Hancock Plot			
Mechanism	D1, Anti-D3	A3	D3 A4
JMAEK-Fit			
Mechanism	D3, Anti-D3	A3	D - R
Master Plots			
Mechanism $f(\alpha)$	D3	A2	D3
Mechanism $g(\alpha)$	D3	A3	D3, A2-A4
Summary			
Assumed Mechanism	D3	A3	D3 \rightarrow A4

A peculiarity is observed for the HT-in situ-PXRD measurement of Cu wire with **DTTS**, see **Figure A. 8.10**. Here, the Cu wire corrodes simultaneously to the β -Cu₂S formation. After 7 h, the hexagonal high chalcocite β -Cu_{2-1.988}S phase undergoes a phase transition towards the cubic high digenite γ -Cu_{2-1.732}S phase, see **Figure 8.9**. At this point, the complete Cu wire is corroded but the reactive sulfide reagent is still present. Note that the high digenite phase is characterized by a much wider composition range of Cu = 2-1.732. Therefore, it is concluded that the decomposition of the sulfide is still ongoing. This leads to a subsequent incorporation of sulfur atoms into the β -Cu₂S lattice. Consequently, the high chalcocite is transformed to the high digenite due to the altered composition. However, this is not observed for pure **DS**. Note that the theoretical Cu:S ratio in the capillary of bare Cu wire with pure **DS** is 1:1.6. Thus, there would be sufficient **DS** present to initiate the phase transformation to the high digenite. Nevertheless, this is not observed for the pure **DS** even after 60 h (**Figure A. 8.9**). This indicates that some traces of tri-, and tetrasulfide still remain in the mixture which leads to the high digenite transition. Also, this is not observed for the other reagents **MS1**, **MS2**, **TT**. Hence, it is assumed that a phase transition only occurs after complete Cu wire conversion with a very reactive compound.

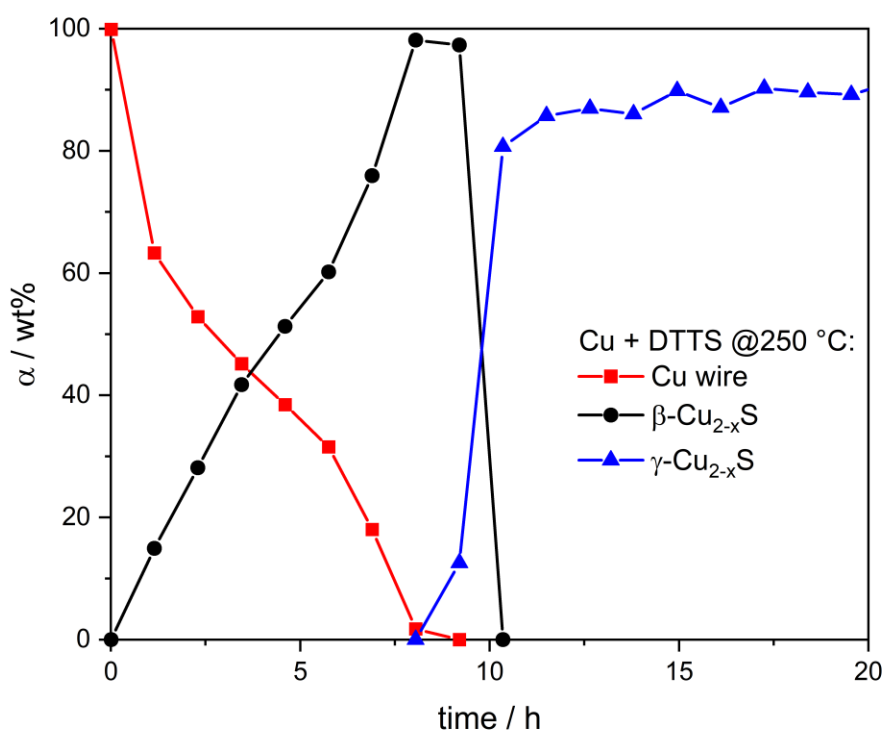


Figure 8.9: Corrosion process of **Cu** bond wire with **DTTS** at 250 °C. The Cu wire degradation proceeds simultaneously to the β -Cu_{2-1.988}S formation. After \approx 8 h the hexagonal high chalcocite undergoes a phase transition towards the cubic high digenite γ -Cu_{2-1.732}S. As the reaction proceeds, more sulfur is incorporated into the copper sulfide which leads to the phase transition.

8.5 Conclusion

In this chapter, the corrosion susceptibility of bare Cu bond wire towards various S-reagents at 250 °C for 100 h, at least for the tested compounds, was found to increase in the order: Thioketone \approx sulfoxide \approx conjugated/unconjugated thioether > oxygen > unconjugated thiol > conjugated thiol > disulfide > trisulfide > tetrasulfide. Furthermore, the Cu wire corrosion uniformly started with the formation of β -Cu₂S, and no Cu wire degradation was observed for **TK**, **SO**, **TE1**, and **TE2**.

Further comparison of the obtained HT-in situ-PXRD measurement of **O₂** corrosion to the literature confirmed the validity of the measurements. Here, a parabolic corrosion behaviour is observed for **O₂** corrosion which is characteristic for a diffusion-controlled process. Compared to that, the mercaptosilanes **MS1** and **MS2** exhibit a linear behaviour which was found to be nucleation and growth controlled in the beginning which then merges into an interface-controlled mechanism. The corrosion of the Cu wire with **MS1** then accelerates after 120 h. It was concluded that this is caused by the volume expansion of the copper sulfide which enables the percolation of either Cu ions or mercaptosilane.

The S-reagents **TT**, **DS**, and **DTTS** result in a severe Cu wire corrosion. Here, the Cu wire is completely corroded after 7 h for all three reagents. In contrast to the mercaptosilanes, the mercaptotriazole **TT** exhibits a parabolic corrosion behaviour. This is caused by a faster surface reaction. Hence, diffusion becomes rate limiting. There, the difference lies in the conjugation of the **TT** molecule which could react to a more stable radical species. Also, a simultaneous formation of a β -Cu₂S/N-polymeric phase is feasible. Similar corrosion speeds are observed for **DS** and **DTTS**, where **DS** follows a nucleation and growth behaviour and **DTTS** a more complex reaction sequence. Because of the fragile polysulfide (S)₂-S(S) bond, the tetrasulfide reacts readily with the Cu wire. This is similar for the trisulfide but changes for the disulfide. Hence, the reaction slows down when the polysulfides are consumed. Eventually, mostly disulfide is present and reacts in accordance with the pure **DS** to a nucleation and growth-controlled mechanism. However, β -Cu_{2-1.988}S undergoes a phase transition to γ -Cu_{2-1.732}S due to the subsequent incorporation of sulfur atoms. This is not observed for the other reagents and could indicate remnants of reactive tetrasulfide.

These studies showed that di-, tri-, and tetrasulfides are inadequate compounds for the formulation of the MC. Also, conjugated thiols such as **TT** pose a high corrosion potential at elevated temperatures. Hence, these compounds are especially prone to corrosion at high temperature applications and carry a high risk of bond failure. This is better for the mercaptosilanes **MS1** and **MS2**, however, significant corrosion of the Cu wire is still observed for this compound class. This can lead to bond wire failure at extended lifetimes.

In summary, the sharp distinction between reactivity, determination of corrosion products and subsequent kinetic analysis makes HT-in situ-PXRD a suitable tool for substance screening which facilitates the identification of corrosive ingredients and selection of suitable compounds for the formulation of the MC.

9 Corrosion of Coated Cu Bond Wires – A Comparison

9.1 Abstract

In this chapter bare Cu, PCC, APC, and APCX wire are measured with **TT**, **DS**, and **MS1** at 250/175 °C via HT-in situ-PXRD. Eventually, the measurements are analysed for their corrosion kinetics. Then, differences and mechanisms between the individual bond wires are presented in detail. Herein, it is found that **TT** and **DS** lead to a much faster degradation of all bond wires compared to **MS1**. Therefore, it is concluded that the S-reagent is the most dominant package material selection criterion. Nevertheless, differences between the various bond wires still exist. It was found that the APCX wire degrades much faster compared to the other wire types studied. Also, the bare Cu wire performs in general worse than the coated wires PCC and APC. Hence, the reliability of the wires versus sulfur induced corrosion at 250 °C is ranked in the order: APC \approx PCC > Cu > APCX. In the following, the corrosion kinetics for the individual bond wires are discussed in detail. Also, general corrosion models are developed by complementing the HT-in situ-PXRD measurements with SEM and EDX micrographs. Our studies show that the corrosion of the coated wires with **MS1** begins especially at the defect sites of the coating which results in more or less pronounced hillocks and subsequent creeping corrosion of β -Cu₂S. Here, the Pd-coating leads to a faster surface reaction compared to the other wire types which leads to a dendritic growth of β -Cu₂S for both **TT** and **MS1**. Contrary to that, the addition of a flash-Au layer slows down the initial surface reaction. However, the addition of Ni and Ga into the core of the APCX wire leads to a detrimental corrosion behaviour and a variety of corrosion products such as Ni₃S₂/NiS and Ga₂S₃/GaS as well as Ga-Pd alloys.

9.2 Introduction

As seen in chapter 8, the selection of a suitable adhesion promoter is a crucial feature for the bond wire reliability. Another aspect is the high temperature reliability of variant coated Cu bond wires (Cu, PCC, APC, and APCX) versus sulfur induced corrosion. As mentioned above, the introduction of Cu bond wire into automotive applications led to several corrosion related problems.^{29, 58, 60} For instance, sulfur induced corrosion of Cu bond wire at high temperatures (> 150 °C). Therefore, different bond wire types like bare Cu, Pd-coated Cu (PCC), Au-Pd-coated Cu (APC), and Au-Pd-coated Cu with a doped Cu core (APCX) were introduced to fulfill these demanding requirements. However, the effects as well as the corrosion reliability of the various coatings and dopants are not fully understood. Hence, the goal of this chapter is to investigate the corrosion reliability and failure mechanisms of various coated Cu bond wires versus selected adhesion promoters at elevated temperatures. With this in mind, the three S-reagents **MS1**, **TT**, and **DS** are used to compare the respective bond wires to each other. Finally, the reliability of the various coated Cu bond wires is compared and discussed regarding high-temperature applications. First, isothermal HT-in situ-PXRD is applied to quantify the corrosive degradation. Then, a kinetic analysis is performed to acquire knowledge of the related processes. After the PXRD measurements, SEM and EDX analysis of the bond wire cross-sections is performed to complement the X-ray measurements.

9.3 Experimental

9.3.1 Coated Cu Bond Wire Experiments with S-Reagent

All experiments were performed with coated Cu bond wire with a diameter of 50 μm . These are bare Cu (Cu), Pd-coated Cu (PCC), Pd-coated Cu with a flash-Au layer (APC), and Pd-coated Cu bond wire with flash-Au and two dopants 1 and 2 in the Cu core (APCX), for details see chapter 4.2.1. For the preparation of the bare Cu wire see chapter 8.3.1. The coated Cu bond wires PCC, APC, and APCX were used as received from the manufacturer. For every measurement, four bond wires were used per capillary. This approach ensured good intensities for the PXRD measurements as well as a uniform and reliable reaction monitoring. The wires were filled into a silica capillary, which is 0.5 mm in diameter and ≈ 80 mm in length. Then, the capillary was filled with the reagent. All steps were performed under an inert nitrogen atmosphere. After the capillary was filled with the wires and the reagent, the capillary was flame-sealed to prevent evaporation of the reagents and to protect the wires from oxygen oxidation. In case of the solid triazole-thiol (TT), the capillary was filled with the solid reagent, evacuated prior to use and flame sealed under vacuo. In **Table 9.1** a complete list of all experiments is given.

Table 9.1: List of all conducted isothermal HT-in situ-PXRD measurements.

Bond wire type	Organic sulfur compound	Abbreviation (S-compound)	T / °C	Molar ratio (wire:reagent)	Cu:S ratio
Cu	Mercaptosilane 1	MS1	250	1:0.8	1:0.8
PCC	Mercaptosilane 1	MS1	250	1:0.8	1:0.8
APC	Mercaptosilane 1	MS1	250	1:0.8	1:0.8
APCX ^a	Mercaptosilane 1	MS1	250	1:0.8	1:0.8
Cu	Triazole-thiol*	TT	250	1:2.3	1:2.3
PCC	Triazole-thiol*	TT	250	1:2.3	1:2.3
APC ^a	Triazole-thiol*	TT	250	1:2.3	1:2.3
APCX ^a	Triazole-thiol*	TT	250	1:2.3	1:2.3
Cu	Disulfide	DS	250 / 175	1:0.8	1:1.6
PCC	Disulfide	DS	250 / 175	1:0.8	1:1.6
APC	Disulfide	DS	250 / 175	1:0.8	1:1.6
APCX	Disulfide	DS	250 / 175	1:0.8	1:1.6

* TT is a solid reagent and was used as solid due to poor solubility.

^a External standard method (ESM) is used for the quantification

9.3.2 Isothermal HT-in situ-PXRD Measurements

HT-in situ-PXRD was used as standard method to characterize the reaction products and to follow the corrosion process. For device specific details, see chapter 4.1.2. Further, Mo- $K_{\alpha 1}$ ($\lambda = 0.70930 \text{ \AA}$) radiation was used for all samples and measured in Debye-Scherrer geometry in a silica capillary. Also, the measurements were conducted at 250 °C and 175 °C under isothermal conditions.

In all experiments with **MS1**, **TT**, and **DS**, the powder patterns solely comprise a Cu and Cu₂S phase. Hence, the ESM and DCM method can be used to quantify the binary mixture. For further details, see chapter 3.5.3 and 3.5.4. Herein, the experiments are mostly quantified with the DCM method. Exceptions, which are measured with the ESM, are marked in **Table 9.1**. Note that in the measurement of **APCX** with **MS1** a phase transition from the hexagonal chalcocite $\beta\text{-Cu}_{2-x}\text{S}$ to the cubic copper sulfide phase $\gamma\text{-Cu}_{2-x}\text{S}$ is observed. This additional phase was also quantified with the ESM

9.3.3 SEM and EDX Analysis

The PXRD measurements are complemented with SEM analysis, which was conducted at the University of Regensburg. Herein, the wires were analyzed after the HT-in situ-PXRD measurements. Therefore, the wires were removed from the capillaries and stored in a nitrogen glovebox under continuous nitrogen flow to dry the surface of the wires. Then, the SEM and EDX analysis was performed with a variable pressure aperture at 25 kV.

Also, additional SEM and EDX measurements were conducted at the Fraunhofer IMWS in Halle on a Zeiss Supra 55VP. For the EDX-analyses an AMETEK-EDAX Octane Elite + SDD was operated with a Team software. Also, additional preparation of the wires was required. Herein, the capillaries were opened and dried overnight under an inert nitrogen atmosphere.

For the analysis of the surface morphology, the dried and untreated wires were used. Then, focused ion beam (FIB, Ga) technique was used to excavate areas of the wire surface. Finally, SEM (3 kV, SE-imaging) and EDX (10 kV, BSE-imaging) analysis was performed on the FIB-treated samples.

To analyse the cross-sections, the corroded wires were embedded with an epoxy resin. Then, the cross-sections were prepared by Ar-ion milling. Eventually, SEM (10 kV, BS-imaging) and EDX (7 / 15 kV) measurements were conducted.

9.3.4 Kinetic Analysis

Herein, the JMAEK equation in its exponential (JMAEK-fit) and linearized (SH-plot) form is used to analyse the corrosion kinetics and mechanisms. Also, the master plots $f(\alpha)$ and $g(\alpha)$ are used for a graphical analysis in comparison to theoretical solid-state models. For further details see chapter 3.7 and chapter 8.3.4.

9.4 Results and Discussion

9.4.1 Overview of the Cu Core Corrosion Process of Various Coated Cu Bond Wires

In high temperature stress tests, PCC bond wire showed to be especially prone to sulfur induced corrosion.^{54, 60, 82} However, the underlying mechanism is not fully understood. Also, a detailed investigation regarding the reliability and influence of the variant coatings is missing. Hence, the bond wires Cu, PCC, APC, and APCX are studied with **MS1**, **TT**, and **DS** at 250 °C and 175 °C via HT-in situ-PXRD. Therein, all measurements result in the degradation of the Cu core and the simultaneous formation of the high chalcocite β -Cu₂S phase (Figure A9.1-4). The respective quantified measurements are shown in **Figure 9.1**. Herein, the degradation of bare Cu, PCC, and APC bond wire versus **MS1** at 250 °C exhibit similar progressions, see **Figure 9.1a**. After 120 h approximately 45 wt% of the Cu wire remains. In contrast to that, the APCX wire shows a much faster degradation with **MS1** at 250 °C. There, the wire is completely corroded at 80 h and shows an abrupt degradation after 60 h. Thus, the reliability of the wires versus **MS1** is ranked in the order: PCC > Cu > APC > APCX.

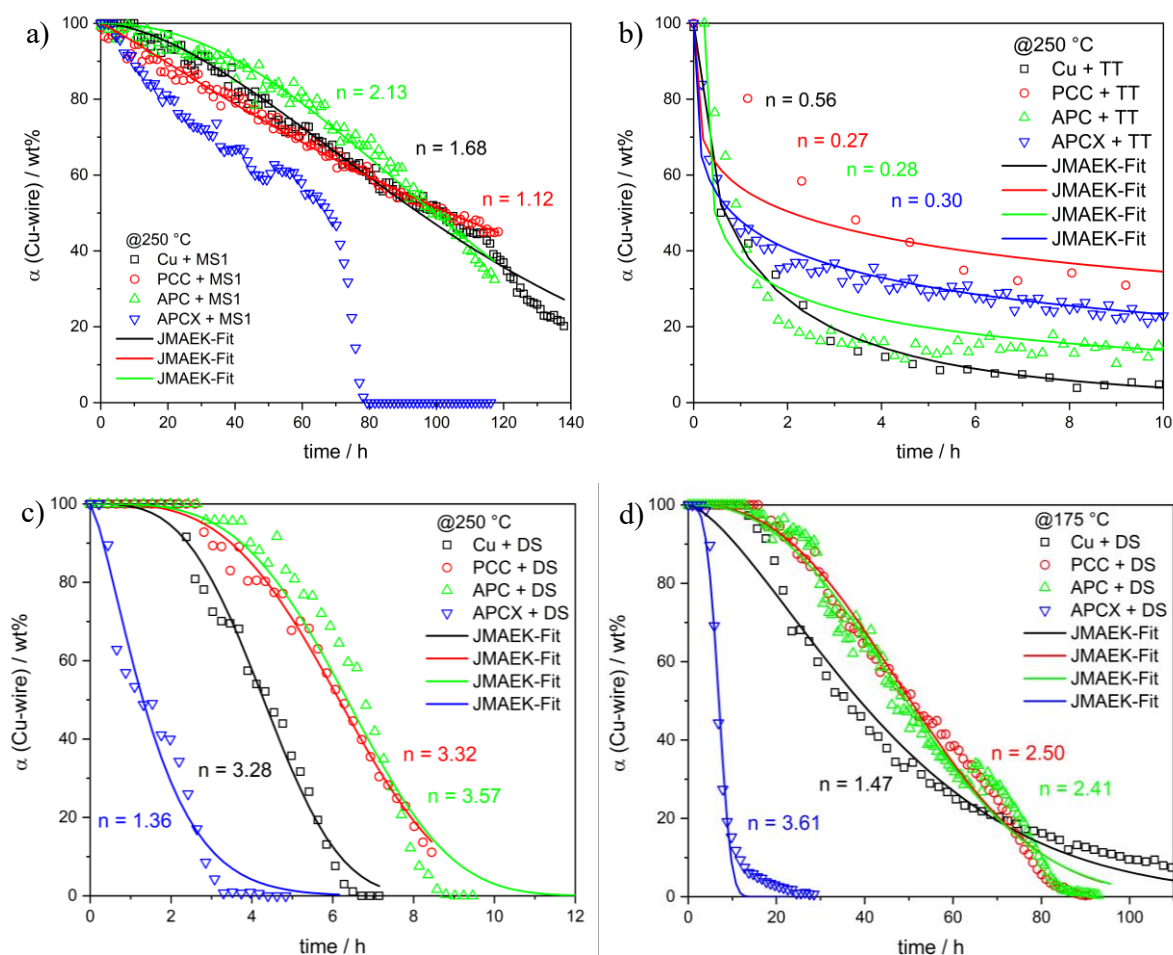


Figure 9.1: α - t -plots from the quantified HT-in situ-PXRD measurements of **Cu**, **PCC**, **APC**, and **APCX** bond wire with **MS1**, **TT**, and **DS** and the obtained Avrami exponents n from the JMAEK-fit. a) Bond wires with **MS1** at 250 °C. b) Bond wires with **TT** at 250 °C. c) Bond wires with **DS** at 250 °C. d) Bond wires with **DS** at 175 °C.

Compared to that, the corrosion experiments of the bond wires with **TT** uniformly exhibit a parabolic behaviour, see **Figure 9.1b**. Thereby, a major part of the corrosion with **TT** occurs in the first 4 h at 250 °C. Note that **TT** is a solid reagent and was filled as solid into the capillary. Therefore, an incomplete filling of the capillary cannot be ruled out. With this in mind, a comparison of these measurements must be treated with caution. However, the PCC wire seems to be the most reliable bond wire at these conditions. This is in accordance with the **MS1** experiments. Whereas the APCX wire shows a better corrosion reliability versus **TT** compared to the Cu and APC wire. Here, Cu wire is the most susceptible wire which is in stark contrast to the **MS1** experiments. This difference originates from the altered reactivity of the S-reagent. Herein, **TT** is much more reactive than **MS1** which leads to a parabolic behaviour (see chapter 8). This is characteristic for a diffusion-controlled mechanism. Hence, the diffusion of either Cu ions or **TT** becomes the rate limiting step. For the bare Cu wire, the Cu ions can readily diffuse towards the reactive surface which results in a fast and complete corrosion. Conversely, the Cu ion diffusion is hindered by the Pd-coating of the coated bond wires PCC, APC, and APCX. This results in a slower and uncomplete corrosion of the bond wire. Thus, the bond wire reliability versus **TT** is ranked in the order: PCC > APCX > APC > Cu.

In general, the α - t curves of the bond wires with **DS** in **Figure 9.1c,d** display a sigmoidal corrosion process. At 250 °C all bond wire degradations with **DS** show a sigmoidal behaviour which indicates a nucleation and growth-controlled process. Also, all bond wires are completely corroded after 10 h at 250 °C. There, the PCC and APC bond wire behave similar to each other. Whereas the Cu bond wire corrodes faster, and a complete degradation is reached after 6 h. The fastest degradation is observed for the APCX bond wire which is completely corroded after 3 h. This is in accordance with the **MS1** experiments, where the APCX wire exhibits a much faster corrosion process compared to the other bond wires. Hence, the reliability of the various wire types is ranked in the order: PCC \approx APC > Cu > APCX.

At 175 °C the PCC and APC wire demonstrate a better reliability versus **DS** compared to the Cu wire at first sight, see **Figure 9.1d**. At closer inspection, this is true for the first 60 h but then the degradation of the Cu wire slows down. Accordingly, a complete conversion of the bare Cu wire is delayed and is slower compared to the PCC and APC wire after 80 h. As before, the APCX wire corrodes much faster and is completely corroded after 30 h. This is a third of the time needed for a complete Cu core corrosion of the PCC and APC wire. Also, all bond wire measurements with **DS** at 175 °C show a sigmoidal behaviour. This is in line with the measurements at 250 °C and again points to a nucleation and growth-controlled mechanism. However, the ceasing corrosion stages of the bare Cu and APCX bond wire deviate from the classical JMAEK-model. There, a slower degradation is observed compared to the JMAEK-fit. This can be explained by various deviations from the ideal preconditions (e.g. capillary effect, blocking due to anisotropic growth, impingement on inclusions and interfaces) which leads to an impingement and accordingly to a slower Cu core degradation in the ceasing stages (see chapter 3.7.5).¹⁴⁰ Finally, the reliability of the bond wire versus **DS** at 175 °C is ranked in the order: Cu > PCC \approx APC > APCX.

In summary, the overall corrosion kinetic is governed by the corrosive S-reagent instead of the bond wire surface or coating. Hence, the selection of a suitable adhesion promoter remains as a crucial part in the MC formulation. Herein, **MS1** leads to a linear corrosion behaviour which is an interface-controlled mechanism. There, the complete Cu core corrosion ranges from 80 to 120 h at 250 °C. Note that the APCX wire is an exception and exhibits an abrupt degradation after 60 h. The solid reagent **TT** leads to a parabolic degradation process and is much faster with the largest part of the corrosion reaction occurring in the first 4 h at 250 °C. Also, the bond wires with **DS** show a sigmoidal corrosion behaviour at both 250 and 175 °C with a mean full conversion time of 8 h and 60 h, respectively. Again, this leads to the conclusion that the corrosion mechanism is rather directed by the S-reagent than the nature of the bond wire. Hence, the biggest impact on corrosion prevention is to select suitable adhesion promoters.

Of course, differences between the respective wires are still existent. Remember that the solid reagent **TT** could lead to an incomplete filling of the capillary and is therefore excluded from the holistic view. Thus, the bond wire corrosion in **Figure 9.1a,c,d** with **MS1** and **DS** leads to the conclusion that the doped APCX bond wire corrodes much faster compared to the bare Cu, PCC, and APC wire. Further, the PCC and APC bond wire in general behave similar. This is plausible as these are in principle the same wire types with an additional flash-Au layer on top of the PCC wire. Although, recent studies report that the APC wire is more reliable in sulfidation tests at 140 °C compared to PCC bond wires.⁸² The Cu wire in contrast corrodes faster in the commencing corrosion stages but especially slows down in the ceasing stages at low temperatures. Recall, that the sulfidation of the bond wires in stress tests is especially observed for the PCC wires.^{54, 60} Conversely, this is not confirmed by these measurements and rather indicates the protective function of the Pd-coating as a barrier. Hence, the commencing corrosion stages are delayed for the PCC and APC wire. However, this is in stark contrast to the APCX wire which has the same coating as the APC wire. The fast degradation of the APCX wire points to a significant role of the dopants in the Cu core. Further, the fast degradation of the APCX wire contrasts with recent investigations which report an enhanced sulfur induced corrosion reliability of this wire type in stress tests at 175 °C.⁸³⁻⁸⁶ There, the dopants are supposed to passivate the outer layer of the Cu core if the Pd-coating is damaged. But if this passivation fails, these dopants can act as nucleation germs which in turn leads to a much faster corrosion. Thus, the APCX wire poses a high risk at high temperature applications, at least in the temperature range from 250-175 °C.

Therefore, the reliability of the bond wires in the temperature range from 250 °C to 175 °C in the framework of these measurements is assessed in the order:



In the following, the bond wire corrosion kinetics with **MS1** and **TT** are discussed in detail. The degradation kinetics of all bond wires with **DS** from 250-175 °C is discussed in chapter 12.

9.4.2 Corrosion Kinetics of Cu Bond Wires with MS1

The Cu core corrosion of the bare Cu, PCC, and APC bond wire display a similar behaviour, see **Figure 9.2a**. Therein, the PCC wire exhibits a linear progression with an Avrami exponent $n = 1.12$ of the JMAEK-fit which is indicative for an interface-controlled (R3, Anti-R3) mechanism. For the bare Cu wire the exponent changes to 1.68 which either can be a CD-DD3 or a diffusion-controlled nucleation and growth-controlled model ($n = 3 \cdot \frac{1}{2} + 0$). The nucleation characteristic is even more pronounced for the APC wire with an exponent of $n = 2.13$. However, the corrosion kinetic of the Cu, PCC, and APC wire is similar with about 50 wt% Cu conversion after 100 h. This leads to the conclusion that the reaction of the mercaptosilane **MS1** with Cu is the rate limiting step instead of diffusion related processes. Hence, the Pd-coating does not act as diffusion or reaction barrier because the corrosion kinetic of the bare Cu wire is like the coated wires PCC and APC. The corrosion behaviour of the APCX wire in contrast displays a parabolic behaviour in the first 60 h and then degrades abruptly. This points to a diffusion-controlled mechanism. Therein, it is assumed that the dopants play a significant role as the APC and APCX wire only differ in the composition of the Cu core. After 60 h, the corrosion mechanism changes instantly and leads to a complete breakdown of the wire. This reveals a change in the corrosion mechanism which cannot be described by the classical JMAEK-model.

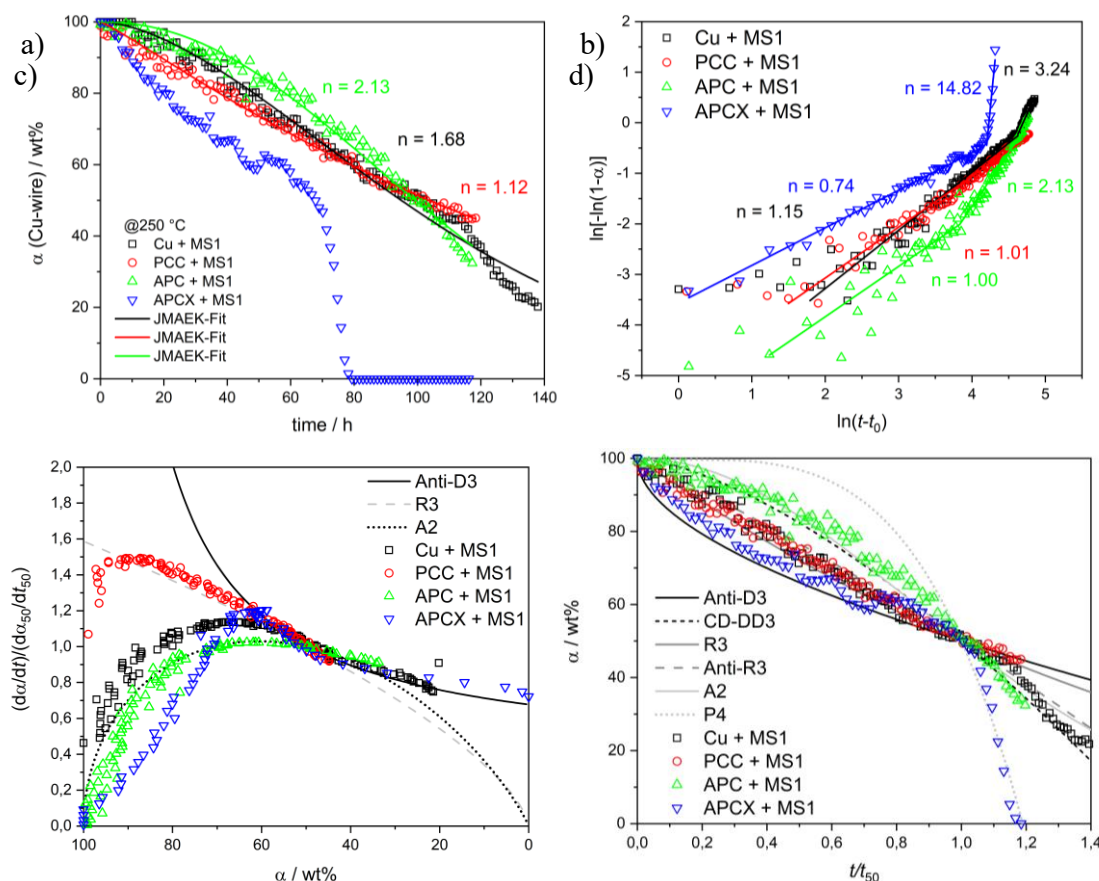


Figure 9.2: a) α -t-plots from the quantified HT-in situ-PXRD measurements of bare Cu, PCC, APC, and APCX bond wire with MS1 at 250 °C and the Avrami exponents n from the JMAEK-fit. b) SH-plot c) Master plot $f(\alpha)$ d) Master plot $g(\alpha)$

The findings from the JMAEK-fit are mostly confirmed in the SH-plot in **Figure 9.2b**. Therein, the Cu, PCC, and APC wire display an Avrami exponent of $n = 1.15, 1.01, 1.00$, in the initial corrosion stages, respectively. Note that the slope in the SH-plot of the whole corrosion process of the PCC wire does not change. Hence, an interface-controlled mechanism (R1-R3) which does not change throughout the corrosion. The APC wire by contrast changes from a slope of 1.00 to 2.13 (A2, CD-D3) at ca. 15 wt%. Thus, the corrosion starts with an interface-controlled mechanism which then transforms to a nucleation and growth-controlled process. The same transformation is observed for the bare Cu wire where the slope transforms from 1.15 to 3.24 (A3, P2, CD-D3) but at a later stage of about 50 wt%. Divergent slopes are observed for the APCX wire. Here the initial stages exhibit a slope of 0.74 (D-R) which then increases to 14.82 (P4) at ca. 50 wt%. This confirms the assumption that the corrosion of the APCX wire undergoes a mechanistic change. Therein, the diffusion-controlled regime contrasts with the APC wire which has the same coating. Thus, it is feasible that the dopants suppress the diffusion of Cu ions to the surface. As the dopants should be located at the Cu grain boundaries, they are supposed to suppress the fast grain boundary diffusion of Cu ions. Consequently, the degradation is slowed down and is directed by the decreased diffusion velocity. However, the dopants can also act as impurities which lower the activation energy for the formation of a growth nucleus. Here, a power law is derived which is a multistep nucleation and growth model. Hence, a fast nucleation occurs in a first step and then the nuclei grow in a second step. The formation of a large number of nuclei and subsequent growth of these nuclei leads to an exponential degradation of the wire.

In the master plot $f(\alpha)$, the interface mechanism (R3) is again confirmed for the PCC wire, see **Figure 9.2c**. Therein, the Cu and APC wire corrosion is initiated by a nucleation and growth-controlled mechanism (A2). The A2 model is characterized as a one-dimensional nucleation and growth model with an interface-controlled mechanism ($n = 1 \cdot 1 + 1$). This can be interpreted as a homogenous surface nucleation of the wire in the initial corrosion stages. As corrosion phenomena usually start with a nucleation on the surface, this model is often observed throughout this thesis. Further, the Cu wire corrosion process merges into an Anti-D3 model which is characterized by a diffusion controlled Kirkendall effect model. Note that the slope in the α - t plot of the APCX wire sharply increases. Therefore, it is not suitable for the master plot $f(\alpha)$ and excluded from this approach.

In the master plot $g(\alpha)$, the Cu wire corrosion starts with an Anti-R3 model and then merges into a CD-D3 model, see **Figure 9.2d**. The PCC wire corrosion is also initiated by an Anti-R3 model which then transforms to an Anti-D3 model. Whereas the APC wire corrosion begins with an R3 model which readily changes towards an A2 model. Then followed by a slight change at 50 wt% to an CD-D3 or P2 model. Note that the corrosion models for the Cu, PCC, and APC wire generally transform from an interface-controlled model towards diffusion-controlled models. Further, the findings from the SH-plot are confirmed for the APCX bond wire. Here, the degradation of the Cu core starts with an Anti-D3 model and then merges into a P4 model at 50 wt%. Note that the derived mechanistic assumptions from the kinetic analysis are summarized in **Table 9.2**.

Table 9.2: Overview of the derived models from the respective analysis method. Here, shown for all bond wires with **MS1**.

Wire	Cu	PCC	APC	APCX
T / °C	250	250	250	250
Sharp-Hancock Plot				
Mechanism	Anti-R3	R3	R3	D - R
	A3		A2, P2	A4
JMAEK-Fit				
Mechanism	CD-D3	R3, Anti-R3	A2, P2	-
Master Plots				
Mechanism f(α)	A2, Anti-D3	R3	A2	A2-A4, Anti-D3
Mechanism g(α)	Anti-R3, CD-D3	Anti-R3, Anti-D3	CD-D3, P2	Anti-D3, P4
Summary				
Assumed Mechanism	Anti-R3	R3, Anti-R3	R3	Anti-D3
	↓		↓	↓
	CD-D3		CD-D3, P2	P4

Interestingly, all wires – except the PCC wire – accelerate at the ceasing corrosion stages. However, this could also occur for the PCC wire at the later stages and indicates some additional phenomena at an increased product layer thickness. Possible phenomena are:

- Additional diffusion or percolation pathways through cracks and pores, generated by the volume expansion.
- Capillary effect through the formed pores and subsequent flushing of the Cu core by liquid S-reagent.
- If percolation pathways are established, additional convection of the liquid S-reagent through the Cu core.
- When a certain number of cavities is reached in the Cu core, the surface of the Cu core increases significantly. Consequently, surface diffusion of Cu ions dominates which is faster than grain boundary or bulk diffusion.

Therefore, the risk of a complete wire breakdown increases significantly when a high degree of corrosion is reached. Of course, phenomena ii. and iii. are unlikely to occur in the solid MC. However, phenomena i. and iv. can also arise in the semiconductor package.

In the following section, the derived models are checked by SEM and EDX images of the cross-sections after the HT-in situ-PXRD measurements. Note that for the Cu and APC wire a second PXRD measurement was performed, and the subsequent cross-sections are shown here. However, these two measurements were only performed up to a conversion of ≈ 20 -30 wt%. Thus, they are not suitable for the kinetic analysis and a comparison to the other wires.

9.4.3 Cross-Sections of Cu Bond Wires with MS1 after HT-in situ-PXRD

After the HT-PXRD measurements of the various bond wires with **MS1**, cross-sections of the wires were prepared. Then, SEM and EDX analysis was performed on these cross-sections. The obtained SEM images are displayed in **Figure 9.3**. Therein, the bare Cu wire is surrounded by a homogeneous β -Cu₂S layer. Also, Cu voids underneath the β -Cu₂S layer are visible. The formation of Cu voids also points to an outward diffusion of Cu ions towards the reactive surface. Note that the Cu voids are evenly distributed underneath the β -Cu₂S layer which implies a corrosion on the whole Cu wire surface.

This changes for the PCC wire. There, most of the β -Cu₂S and Cu void formation is observed at distinctive spots. These spots are supposed to be damaged areas of the Pd-coating. There, the mercaptosilane **MS1** can attack the Cu core and β -Cu₂S forms. Accordingly. The volume expansion of the copper sulfide leads to a hillock formation. Then, a galvanic coupling is feasible which amplifies the corrosion kinetics. However, an evenly distributed β -Cu₂S layer is also observed around the whole Pd-coating. Hence, it seems possible that Cu ions either can diffuse through the Pd-coating or on the Pd surface to form β -Cu₂S.

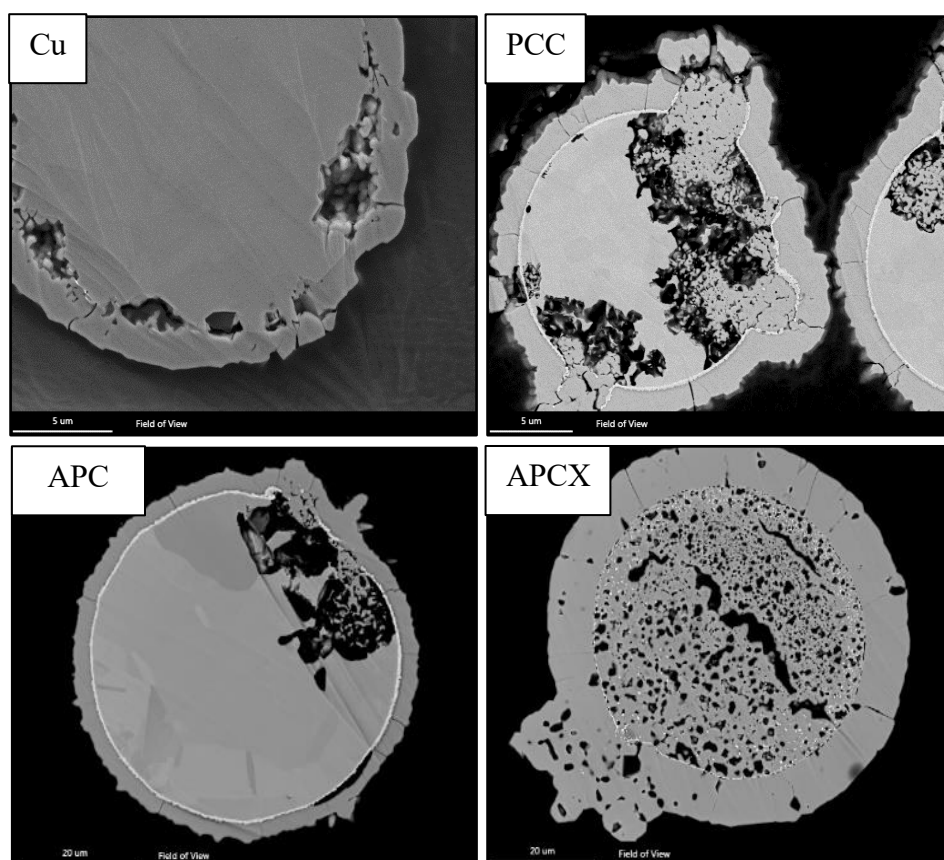


Figure 9.3: SEM analysis of the cross-sections of the respective bond wires after the HT-in situ-PXRD measurements. Note that the cross-section of the bare Cu and APC bond wire was prepared after a second measurement with **MS1**. The preparation and SEM analysis were performed at the Fraunhofer IMWS in Halle.

The APC wire in contrast to the PCC wire shows an even distribution of β -Cu₂S on the whole Pd/Au surface. Also, the Cu voids are formed at damaged spots of the Pd-coating. This again underlines the hypotheses of an initial reaction at these damaged spots. However, no β -Cu₂S and hillock formation within the Cu core is observed.

Complete Cu core corrosion is observed for the APCX wire, which completely converted to β -Cu₂S. There, a homogenous layer is formed around the former Pd/Au-coating. Also, a complete segregation of the Pd/Au-coating occurs together with a porous β -Cu₂S within the former Cu core. Thereby, the initial corrosion stage is assumed to be like the APC wire corrosion. However, at a certain product layer thickness pores in the β -Cu₂S layer form which enables the percolation of liquid mercaptosilane. Hence, an amplified nucleation in the core is observed which is even accelerated by the dopants.

As it is not evident from the HT-in situ-PXRD if a SC or KE mechanism is present, the SEM images are quantified in combination with the PXRD measurements. The combinatorial analysis allows to get further insight into the prevalent mechanisms. There, the ratio of the radii r_2/r_0 of the corroded wire and the initial wire is plotted versus the measured conversion fraction α , see **Figure 9.4** (chapter 3.7.1). Hence, the ratio describes the proportion of the reacted metal volume to the core contraction.

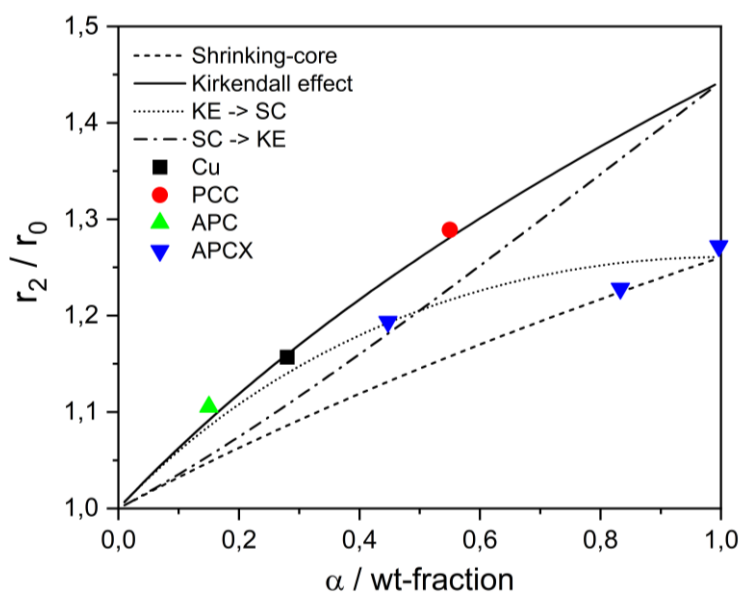


Figure 9.4: Proportion of the r_2/r_0 ratio to the Cu to β -Cu₂S conversion fraction. Here, the Cu, PCC, and APC wire follow a Kirkendall effect model. Conversely, the APCX wire transforms from a Kirkendall effect model towards a shrinking-core model. The experimental points are derived from the cross-sections in Figure 9.3 and the HT-in situ-PXRD measurements.

Therein, the bare Cu, PCC, and APC wire are found to clearly follow a KE mechanism. Hence, the outward diffusion of Cu⁺. This is also observed in the SEM images by Cu voids in **Figure 9.3** but is not as obvious for the PCC wire where some β -Cu₂S is also found within the core. Also, the analysis reveals that the APCX wire follows a KE mechanism in the beginning which then merges into SC mechanism. Thus, the formation of the homogenous β -Cu₂S layer around the coating and then the nucleation in the Cu core.

In the following sections, the SEM and EDX analysis are discussed in detail and a compatible corrosion mechanism is proposed after combining the findings from HT-PXRD and SEM/EDX.

9.4.3.1 SEM and EDX of Bare Cu Wire with MS1 and Proposed Mechanistic Model

In **Figure 9.5a**, the bare Cu wire with MS1 after 100 h at 250 °C is shown. An EDX mapping of Cu and S element reveals a homogenous β -Cu₂S layer (composition determined from HT-in situ PXRD) around the Cu core. Also, large Cu voids are located at the interface between the Cu core and the corrosion layer. This points to an outward diffusion of Cu ions and thereby a KE mechanism. However, Si element was also found within these voids. This can occur either by the percolation of mercaptosilane or the epoxy resin which was used for the preparation. Up to date this is not clarified. Hence, a percolation of the mercaptosilane through the generated cracks cannot be excluded. Further inspection of the bare Cu wire surface after 30 min reveals a homogenous corrosion layer in the initial stages, see **Figure 9.5b**. It is striking that some areas display a more pronounced corrosion layer than others. The distribution of corroded and non-corroded areas resembles the morphology of the grain distribution of the initial Cu wire surface. This could indicate a preferred growth at specific Cu grain orientations. (e.g. Cu(111)). Recent studies suggest a pronounced thiolate adsorption on Cu(111) and Cu(100) surfaces.⁶⁷ Therein, heating above 130 °C leads to a network of an adsorbed RS-Cu_{ad} species and subsequent C-S bond cleavage to form Cu₂S.^{67,215,216} Hence, a thermal activation of the C-S bond cleavage and copper sulfide formation. At 250 °C this process is even faster and results in a fast sulfidation of the Cu core.

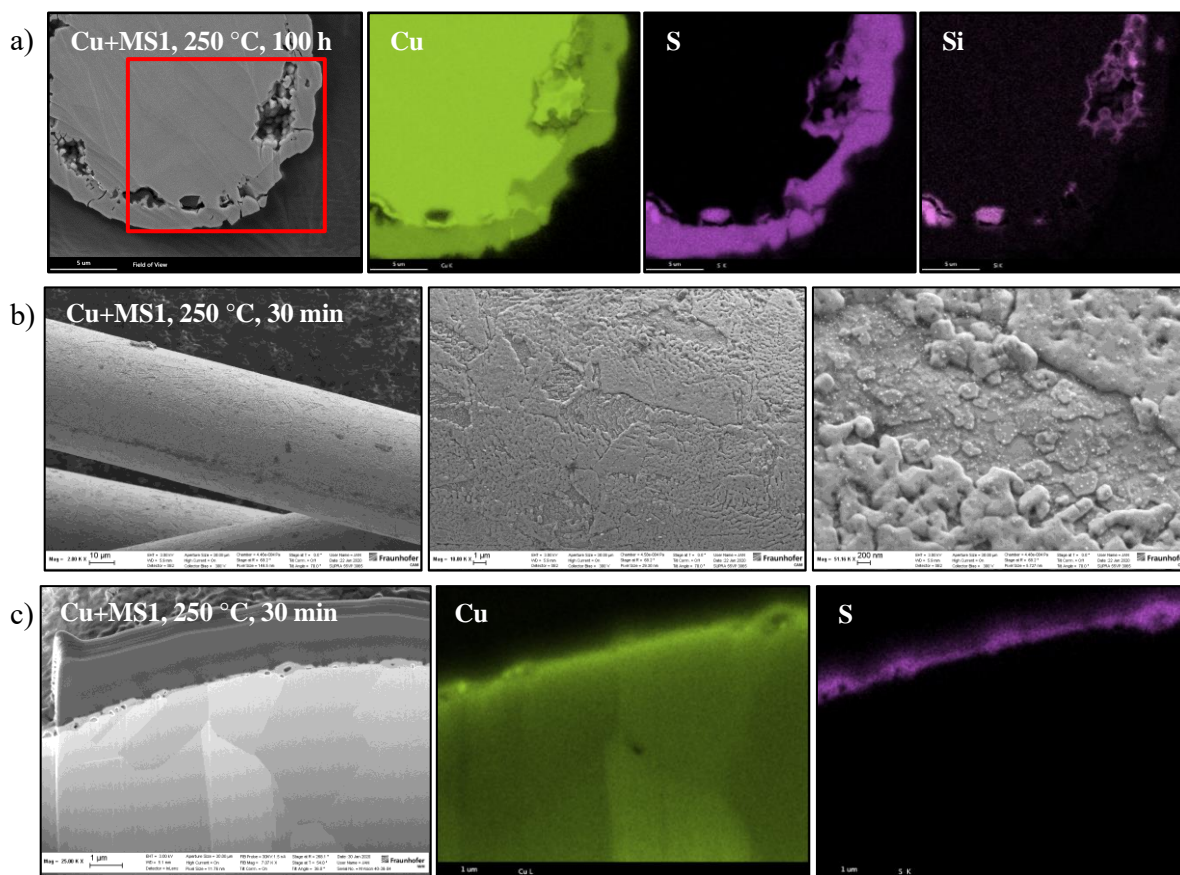


Figure 9.5: SEM and EDX analysis of the bare Cu wire with MS1 at 250 °C. a) Images of the cross-section after 100 h. Therein, a thick copper sulfide layer and large Cu voids are visible. Also, Si is detected in the Cu voids. b) Surface of the bare Cu wire after 30 min. Here, copper sulfide growth is preferred for certain areas. c) Small copper sulfide layer is visible and miniscule voids in the EDX mapping of Cu. Preparation, FIB, SEM, and EDX measurements were performed at the Fraunhofer IMWS.

Further analysis of the Cu wire after 30 minutes at 250 °C with FIB technique and subsequent SEM analysis reveals a small copper sulfide layer as corrosion layer, see **Figure 9.5c**. At closer inspection, small voids are visible between the corrosion layer and the Cu core. Also, a miniscule void is visible in the EDX mapping of Cu element. This void is located at the grain boundary within Cu core. Therefore, it is likely that the Cu^+ diffusion takes place along the grain boundaries. This is due to a faster grain boundary diffusion compared to the slower bulk diffusion. This phenomenon is also known from oxygen induced Cu corrosion.²¹⁰ Therein, it was also reported that a larger grain size distribution goes along with a slower corrosion rate.²¹⁰ Hence, grain boundary engineering (GBE) and controlled preparation of bigger grain size distributions could significantly improve the reliability of the bond wire. However, further investigations are needed regarding the grain boundary diffusion mechanism. Also, the suggested preferred adsorption and copper sulfide formation at distinct Cu surfaces needs further research. This could prove as important information to prevent the initial Cu corrosion stages at high temperatures.

Accordingly, a corrosion model is proposed in **Figure 9.6** from the HT-in situ-PXRD measurements, SEM, and EDX images of the cross-sections. First, thiolate (RS^-) chemisorbs on the surface to form $\text{Cu}_{\text{ad}}\text{-SR}$ species. These form coherent networks on the surface and at extended exposure to high temperatures ($>130\text{ }^\circ\text{C}$) leads to a subsequent C-S bond cleavage. Hence, the corrosion rate is initially controlled by the chemical surface reaction (R3) to form $\beta\text{-Cu}_2\text{S}$. This decomposition reaction accelerates with temperature and leads to a fast formation of a $\beta\text{-Cu}_2\text{S}$ corrosion layer. When the Cu surface is completely covered with a copper sulfide layer, Cu ion diffusion becomes rate limiting. Here, it is concluded that the majority of the Cu^+ diffusion takes place at the grain boundaries within the Cu core. Then, Cu ions diffuse through the $\beta\text{-Cu}_2\text{S}$ layer towards the reactive surface. Hence, Cu voids are formed by a Kirkendall effect (Anti-D3). Naturally, this leads to a weakening of the Cu bond wire interconnects due to the formation of Cu voids. Therefore, poses a high risk of lifted bond wires at extended lifetimes in sulfuric environment at temperatures above 130 °C.

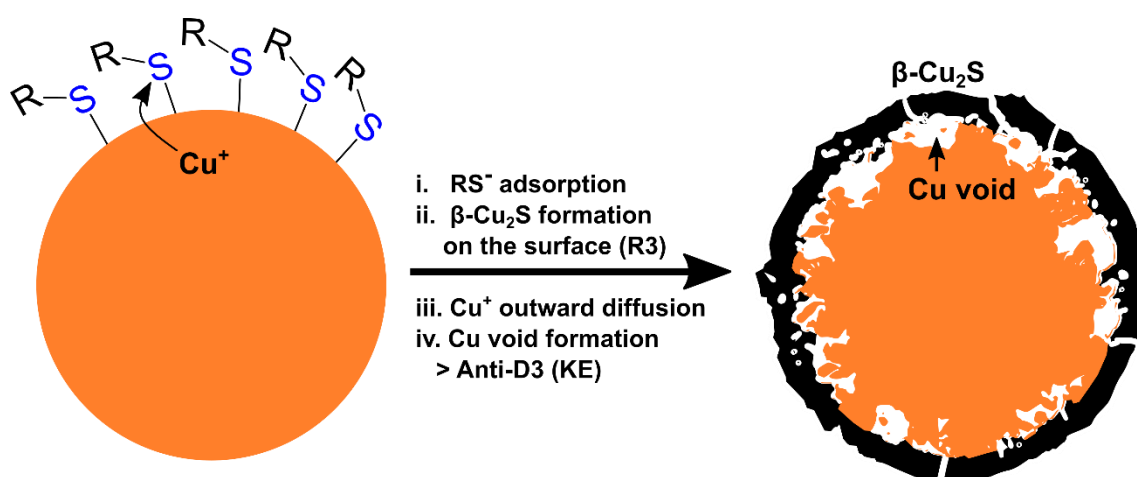


Figure 9.6: Proposed schematic corrosion model for bare Cu wire with MS1. First the mercaptosilane chemisorbs on the surface. Then, $\beta\text{-Cu}_2\text{S}$ forms and the corrosion rate is controlled by the surface reaction (R3, Anti-R3). At a certain product layer thickness, the Cu ion outward diffusion (Anti-D3) becomes rate limiting. Hence, Cu voids are formed according to the Kirkendall effect.

9.4.3.2 SEM and EDX of PCC Wire with MS1 and Proposed Mechanistic Model

The SEM and EDX analysis on the cross-section of the PCC wire after 120 h at 250 °C points to a more complex corrosion sequence, see **Figure 9.7a**. Therein, an EDX mapping of Cu and S element reveals a β -Cu₂S layer (determined from HT-in situ-PXRD) on top of the Pd surface and a significant amount of β -Cu₂S within the Cu core. Note that the β -Cu₂S within the core shows a porous morphology compared to the homogenous β -Cu₂S layer on the Pd surface. Also, circular hillock formation is observed at distinct spots. In addition to that, Cu void formation is exclusively observed in the vicinity of these hillocks. Further, the hillock formation leads to a spherical distortion of the Pd-coating. This leads to the conclusion, that Pd in fact acts as diffusion barrier for Cu ions. However, β -Cu₂S formation still happens at the damaged areas of the Pd-coating. This is in line with previous results of an oxidized PCC wire, where hillock formation and Cu voids are exclusively observed at damage Pd layer spots.⁵⁵ Here, the β -Cu₂S formation is even more pronounced due to a galvanic coupling and catalytic activity of Pd. However, the formation of hillocks is striking as the β -Cu₂S formation should rather propagate outwards as the Cu ion diffusion is fast in β -Cu₂S. Consequently, no hillocks should occur. Therefore, it is assumed that a more complex corrosion sequence takes place. Further, Cu₃Pd formation is observed in the powder pattern after 120 h, see **Figure A. 9.6**. Note that the formation of CuPd and Cu₃Pd also occurs in the powdery mixtures of Cu/Pd with **TT** and **MS1** (see chapter 7.4.3).

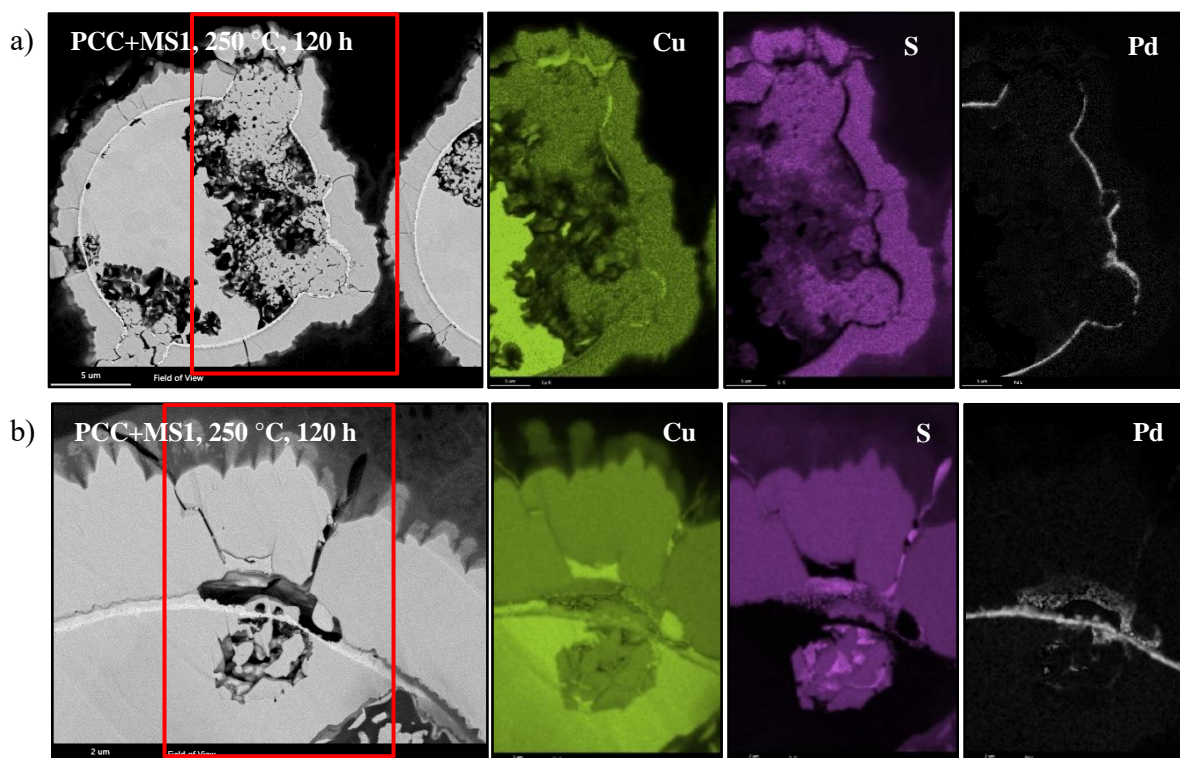


Figure 9.7: SEM and EDX analysis of the **PCC** wire with **MS1** at 250 °C after 120 h. a) SEM and EDX images of the cross-section. Therein, a thick copper sulfide layer and large Cu voids are visible. Also, hillock formation is observed at distinct spots with a distorted Pd layer. Also, a large amount of S element is found within the Cu core. b) Magnification of a cross-section area which shows the formation of a dendritic morphology at the copper sulfide surface. Also, the decomposition of the Pd-coating.

Hence, an alloying of Cu₃Pd is also likely to occur for the PCC wire. Here, two mechanisms are possible:

- i. Alloying by Cu⁺ interdiffusion from within the core through the Pd-coating^{185, 186, 188, 189, 205}
- ii. Alloying of the outer Pd-coating by surface diffusion of Cu⁺⁷⁵

Here, a continuous Cu⁺ interdiffusion from within the core should produce Cu voids in the vicinity of the Pd-coating. This is not observed and therefore mechanism i. is not dominating the corrosion mechanism but still could occur at high temperatures.^{185, 186, 205} By closer inspection of **Figure 9.7b** a thin layer on top of the Pd-coating is observed. Also, an EDX mapping of Cu element reveals a significant amount of Cu on top of the Pd surface. Hence, the formation of Cu₃Pd alloy by Cu ion surface diffusion is feasible according to mechanism ii.⁷⁵ There are several types of driving forces for the Cu⁺ diffusion through the damaged spots towards the surface:

- i. Concentration gradient from Cu core to Pd surface. Hence, Cu⁺ diffusion through the damaged area which is amplified by the capillary effect and tensile stress.
- ii. Reduction of the free energy of the formed Cu₃Pd alloy based on the thermodynamic rule.
- iii. Formation of β -Cu₂S and thereby reduction of free energy
- iv. Emf reduction of the galvanic couple Cu/Pd by Cu₃Pd formation
- v. High current density i_{Cu} because of the high surface area ratio $S_{Pd}/S_{Cu} \gg 1$

Also, Pd is known to be prone to sulfur poisoning.²¹⁷ Further investigations regarding the Pd-thiol interaction revealed that thiols strongly adsorb on the Pd(111) surface.⁶⁷ It was concluded, that a diluted PdS_x layer is formed on top of the Pd surface which is able to adsorb thiolates.⁶⁷ This is possible as the *d*-band of Pd is populated near the Fermi level which enables an easier C-S bond cleavage of adsorbed thiolates compared to Cu surfaces.⁶⁷ Though PdS_x can form during the sulfidation process, it also can act as a passivation layer.²¹⁸

Recall that in the powdery mixtures of Cu and Pd with bifunctional thiols in chapter 7.4, PdH_x and PdS formation is confirmed in the initial corrosion stages at 150-175 °C. Eventually, a reversible reaction to Cu₃Pd and β -Cu₂S was experimentally verified as PdH_x and PdS are thermodynamically unstable. Whereas for the PCC wire small spheres and miniscule segregation of the Pd layer is observed in the EDX mapping of Pd element. However, due to the thin Pd layer these phases could not be confirmed in the powder patterns but are possible to occur in the initial corrosion stages.^{190, 199}

The adsorption of thiolates can also take place for a Cu₃Pd alloy with a subsequent formation of β -Cu₂S.^{201, 204} There, the Cu₃Pd alloy combines the catalytic activity of Pd and the supply of Cu ions to form β -Cu₂S. Thus, the β -Cu₂S preferentially propagates along the wire surface due to the better C-S bond cleavage on the Pd/Cu₃Pd interface. Thereby, the supply of Cu ions is ensured by the fast Cu⁺ diffusion in β -Cu₂S with the Cu core as the source. Note that this is strikingly similar to the proposed sulfidation and alloying process in **Figure 7.15**. Another striking feature is the dendritic morphology of the outer β -Cu₂S surface. This points to a very fast precipitation of β -Cu₂S and thus to a dendritic growth which is not observed for the bare Cu bond wire.

Thus, a corrosion model is proposed in **Figure 9.8** which is derived from the combined analysis of SEM, EDX, and HT-in situ-PXRD measurements. In the initial stages, thiolate strongly adsorbs on the Pd surface and at damaged areas of the Pd-coating (i.). Simultaneously, Cu ions diffuse through the damaged Pd layer along the surface of the wire (ii.). Then, β -Cu₂S forms at the damaged area and a galvanic cell is formed which accelerates the corrosion even further (iii.). At the same time, Cu_{4-x}Pd alloy is formed on the Pd surface and thereby enhances the β -Cu₂S formation on the surface (v.). Accordingly, this process is only governed by the chemical surface reaction (R3). Hence, a homogeneous β -Cu₂S layer forms due to the concurrent propagation of β -Cu₂S along the wire surface (iv.) and the β -Cu₂S formation on Cu_{4-x}Pd. However, due to the outward diffusion of Cu ions a diffusion pathway is present and Cu voids form in the vicinity of the damaged Pd layer. This enables the diffusion of RSH into the Cu core (vi.). There, a galvanic coupling of Cu and Pd is existent which enables a fast β -Cu₂S formation. Therefore, β -Cu₂S accumulates underneath the Pd layer which leads to a hillock formation and the distortion of the Pd-coating. At a certain layer thickness the mechanism changes to an outward movement of the reactive surface (Anti-R3). This is due to the diffusion of Cu⁺ through the β -Cu₂S product layer towards the reactive surface. Subsequently, Cu voids form in the vicinity of the damaged Pd layer according to the KE. When a thick product layer thickness is reached, cracks form and β -Cu₂S scales chip off. This is due to the high Pilling-Bedworth ratio $R_{PB} = 2$ which creates high interfacial stress.²¹⁹ This enables further percolation of RSH into the Cu core and also the catalytic C-S bond cleavage on the Cu_{4-x}Pd surface. The decomposition products subsequently lead to a dendritic β -Cu₂S growth due to the fast surface reaction with diffusing Cu ions.

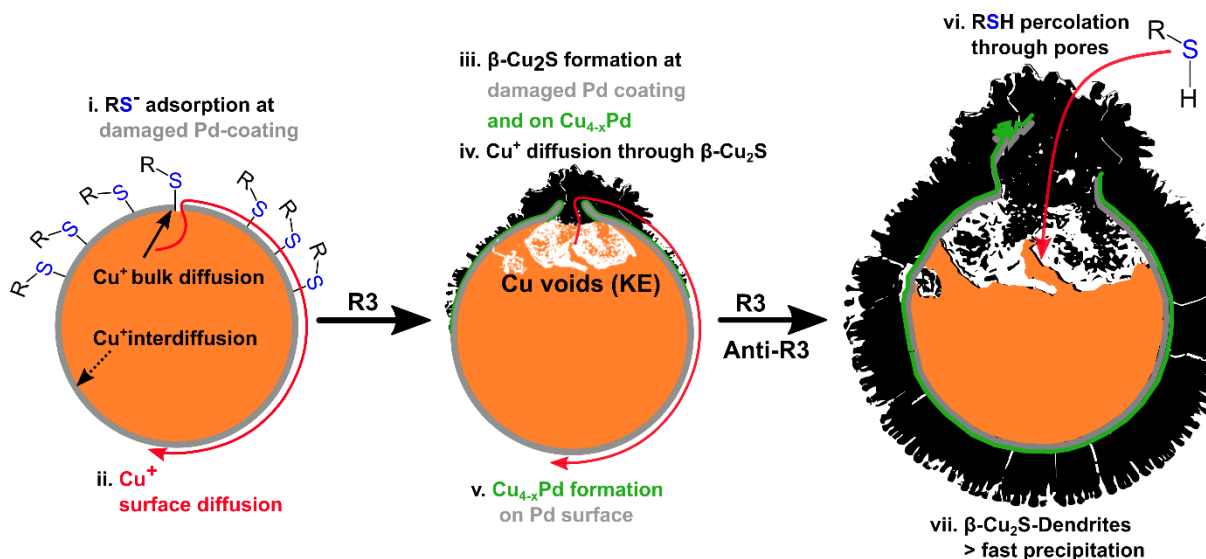


Figure 9.8: Proposed schematic corrosion model for **PCC** wire with **MS1**. First the mercaptosilane chemisorbs on the surface with simultaneous Cu⁺ surface diffusion and Cu_{4-x}Pd alloying process. Then, β -Cu₂S forms at the damaged Pd-coating and the corrosion rate is controlled by the surface reaction (R3). At a certain product layer thickness, the outward movement of the interface (Anti-R3) becomes rate limiting. Hence, Cu voids are formed according to the Kirkendall effect. At some point cracks form due to the volume expansion of the product layer and RSH percolation into the Cu core becomes feasible.

9.4.3.3 SEM and EDX of APC wire with MS1 and proposed mechanistic model

The SEM and EDX analysis on the cross-section of the APC wire after 86 h at 250 °C show a similar behaviour like the PCC wire, see **Figure 9.9**. Therein, the Cu voids are in the vicinity of damaged Pd layer spots. Also, a homogeneous β -Cu₂S (determined from PXRD) layer is present around the Cu core on the Pd surface. An EDX mapping of Pd element clearly shows that the Pd layer is damaged near the Cu voids. This underlines the hypotheses that β -Cu₂S is initially forming at these specific spots. Also, S element is found within the Cu voids which indicates mercaptosilane diffusion into the Cu core. This is in accordance with the PCC wire. However, severe hillock formation is observed for the PCC wire which is not as pronounced for the APC wire.

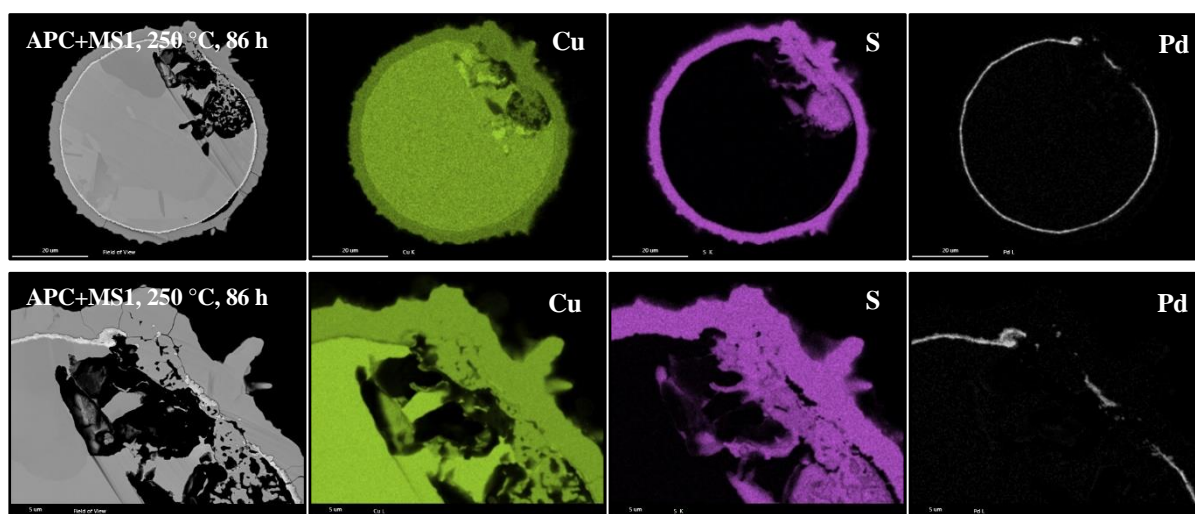


Figure 9.9: SEM and EDX analysis of the APC wire with MS1 at 250 °C after 86 h. a) SEM and EDX images of the cross-section. Therein, a thick copper sulfide layer and large Cu voids are visible. The Cu voids are observed at damaged Pd layer spots. Also, a large amount of S element is found within the Cu core. b) Magnification of a)

Recall that the corrosion kinetic from PCC to APC wire changes from an interface mechanism (R3) towards a nucleation and growth controlled (A2/P2) mechanism. The disparity lies within a slower nucleation of β -Cu₂S for the APC wire with a subsequent fast growth. As the PCC and APC wire only differ in the additional flash-Au coating and the grain orientation distribution, these disparities must originate from these properties. This subsequently leads to a more homogeneous β -Cu₂S layer with fewer cracks and smaller hillocks. From the PCC wire it is concluded that the hillock formation underneath the Pd layer originates from a fast β -Cu₂S formation and the counterdiffusion of Cu⁺ and MS1. Hence, several assumptions can be made, based on the variation of an additional flash-Au layer and altered grain orientation distribution:

- i. Altered reactivity of RSH on Au surface compared to Pd.⁶⁷
- ii. Altered diffusivity of Cu⁺ on Au surface and through Au/Pd-coating^{75, 185, 186, 205}
- iii. Faster grain boundary diffusion due to altered grain orientation distribution compared to PCC wire. Therefore, faster Cu⁺ diffusion and faster propagation of β -Cu₂S

Compared to the Cu and Pd surface, the Au surface exhibits a lowered C-S bond cleavage of adsorbed thiolates $\text{Au}_{\text{ad}}\text{-SR}$.⁶⁷ This is because of the *d*-band which is much lower than the Fermi level and therefore displays poor catalytic capability for C-S bond cleavage. Hence, the thiolates desorb above 130 °C on the Au surface and form disulfides.⁶⁷ Note that the formation of disulfides is not reported for Cu and Pd surfaces. Also, bimetallic Pd-Au catalysts showed to be less prone to sulfur poisoning.²²⁰ This explains the slower reactivity on the Au surface in the initial corrosion stage compared to the PCC wire. Hence, **MS1** should only react to $\beta\text{-Cu}_2\text{S}$ at damaged spots in the Au/Pd layer. This changes when Cu and Pd is exposed to the now present mercaptosilane/disulfide mixture.

However, a SEM micrograph of the APC wire surface after 30 min with **MS1** at 250 °C reveals a homogeneous distribution of $\beta\text{-Cu}_2\text{S}$ around the wire and occasional hillocks, see **Figure 9.10a**. Also, the $\beta\text{-Cu}_2\text{S}$ scales are arranged longitudinal along the Au/Pd layer. This is strikingly similar to the grain boundary distribution of the initial Au/Pd surface (see chapter 4.2.1). If the Au/Pd layer acts as diffusion barrier, only hillocks should be observed on the wire surface. Hence, Cu^+ interdiffusion through the Au/Pd-coating or surface diffusion must be present to achieve a homogeneous layer. Both, Cu^+ interdiffusion through Au/Pd thin layers and Cu^+ diffusion on Au surfaces are reported in literature.^{75, 221-224} Therein, a loose polycrystalline microstructure of Pd with nanochannels is reported which enables the Cu^+ diffusion through the coating and, in the literature case, CuO and Cu void formation.^{223, 224} However, such Cu voids are not observed underneath the Pd layer but should occur if thick $\beta\text{-Cu}_2\text{S}$ scales are formed in the μm scale. This observation rules out the interdiffusion as the dominating mechanism but still can be present to some degree. Hence, Cu^+ surface diffusion and $\beta\text{-Cu}_2\text{S}$ propagation along the surface must be the predominant mechanism which is underlined by large Cu voids in the vicinity of the small hillocks. Note that this is like the PCC wire, where a counterdiffusion of Cu^+ and mercaptosilane leads to the formation of hillocks. This is confirmed by **Figure 9.10b**, where S element is observed within the Cu core. Also, pores are existent in the $\beta\text{-Cu}_2\text{S}$ layer. Nevertheless, much smaller hillocks form at damaged Pd spots which could be a consequence of a faster Cu^+ diffusion on the Au surface.

Also, the altered grain orientation distribution could lead to a faster Cu^+ diffusion within the grain boundaries and thus a faster supply of Cu ions. Hence, the propagation of $\beta\text{-Cu}_2\text{S}$ is proceeding much smoother, and the hillock formation is reduced. Additionally, the formation of Cu_{4-x}Pd and CuAu_3 alloys can take place underneath the Pd layer (Cu_{4-x}Pd) and on the Au surface (Cu_{3-x}Au), see **Figure 9.10b,c**.^{75, 221, 225} There, thin layers are observed alongside the Pd layer. Note that the formation of a cubic alloy is confirmed in chapter 12.3. However, a distinction between the Cu_{4-x}Pd and CuAu_3 alloy via PXRD is not possible in this case.

In summary, this leads to an interface-controlled mechanism (R3) in the beginning with a slower nucleation because of the reduced reactivity on the Au surface. Then, the mechanism changes towards a nucleation and growth model. This is also observed in chapter 8.4.4 for the bare Cu wire with pure disulfide **DS**. Therefore, it is likely that the disulfide formation at Au surface leads to a change in the corrosion mechanism. Herein, from an interface-controlled towards a nucleation and growth model.

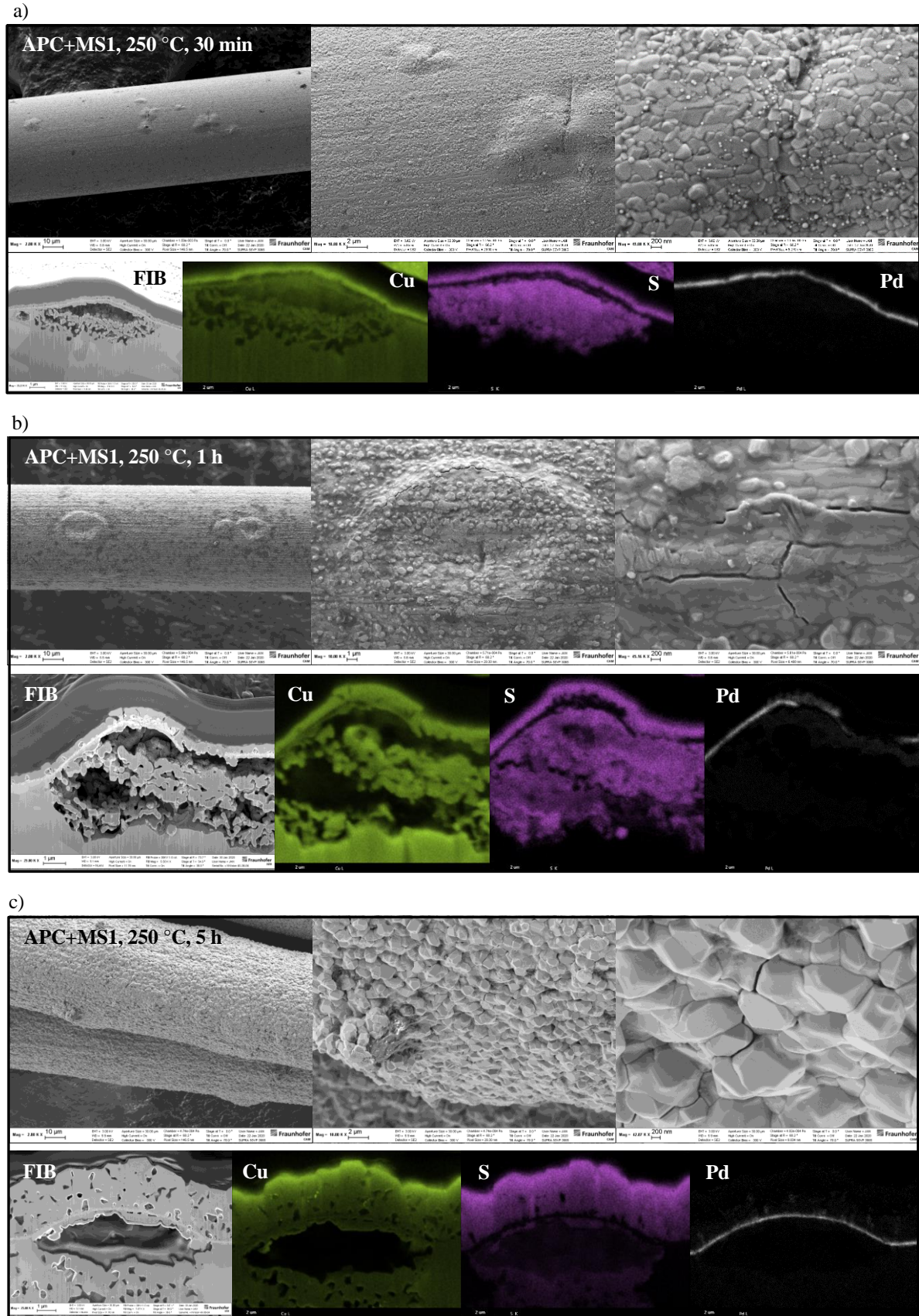


Figure 9.10: SEM and EDX micrographs of the wire surface and cross-sections performed on a corroded APC wire with MS1 at 250 °C, after a) 30 min, b) 1 h, and c) 5 h

Accordingly, a corrosion model is proposed in **Figure 9.11** from the findings of the HT-PXRD measurements and the SEM and EDX micrographs. In the initial corrosion stage, thiol chemisorbs on the Au surface but with minor C-S bond cleavage at the surface (i.). This results in a slower initial degradation of the Cu wire. Further, thiolate desorbs from the Au surface to form disulfide (ii.). Simultaneously, Cu^+ diffuses through the damaged Pd layer spots on the Au surface along the longitudinal grain boundaries (iii.). Due to the Cu^+ diffusion, the concurrent alloying process of the Pd/Au-coating takes place (vi.). Here, presumably the formation of Cu_{4-x}Pd and CuAu_3 .

Similar to the PCC wire, the $\beta\text{-Cu}_2\text{S}$ formation starts at the damaged Pd-coating areas (iv.). Thereby, the propagation of $\beta\text{-Cu}_2\text{S}$ along the wire surface is controlled by the chemical reaction at the wire surface (v., R3). Then the corrosion mechanism undergoes a change from R3 to A2 due to the formation of disulfides on the Au surface. As the $\beta\text{-Cu}_2\text{S}$ layer grows thicker, cracks and pores develop. These enable a counterdiffusion (CD-D3) of Cu^+ and **MS1** which produces Cu voids and $\beta\text{-Cu}_2\text{S}$ within the Cu core with predominant Cu^+ outward diffusion according to the KE (vii.). In summary, the slower surface reaction on Au leads to a more homogeneous $\beta\text{-Cu}_2\text{S}$ layer (viii.). However, at a certain product layer thickness the $\beta\text{-Cu}_2\text{S}$ scales can develop cracks or chip off which enables RSH percolation and thereby further breakdown of the Cu core.

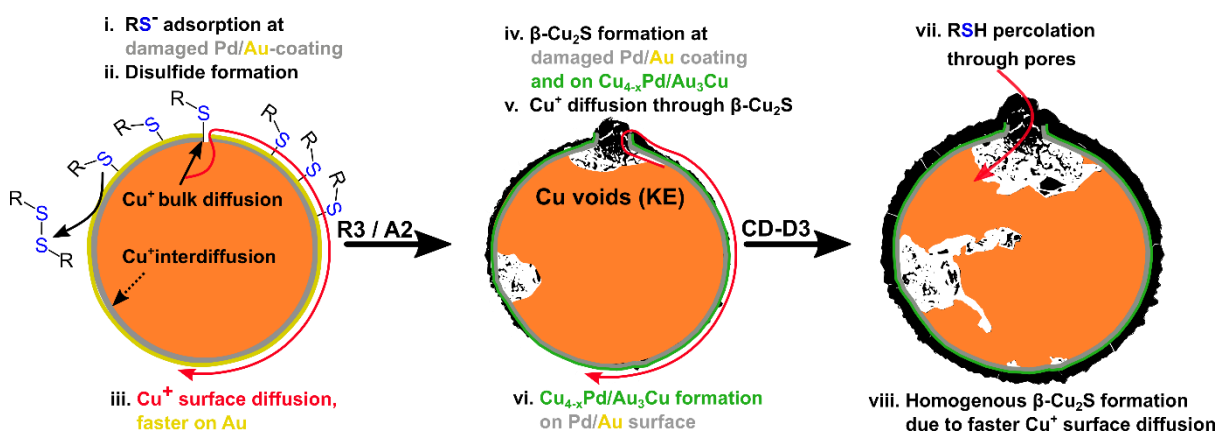


Figure 9.11: Proposed schematic corrosion model for APC wire with **MS1**. First, the mercaptosilane chemisorbs on the surface with simultaneous disulfide formation and Cu^+ surface diffusion with subsequent $\text{Cu}_{4-x}\text{Pd}/\text{Cu}_{3-x}\text{Au}$ alloying process. Then, $\beta\text{-Cu}_2\text{S}$ forms at the damaged Pd-coating and the corrosion rate is controlled by the surface reaction (R3). Then, the reaction is controlled by nucleation and growth (A2). Also, Cu voids are formed which indicate Cu^+ outward diffusion according to the Kirkendall effect. At some point cracks form due to the volume expansion of the product layer and RSH percolation into the Cu core becomes feasible which is expressed by the counterdiffusion model CD-D3.

Despite these findings, it is not evident if Cu^+ diffuses through the coating or along the surface. Also, the alloy formation could not be confirmed. Hence, the role of Cu^+ diffusion and alloy formation still remain nebulous. However, if Cu ions diffuse through the coating or through damaged spots of the coating, severe Cu corrosion takes place. Therefore, the role of Cu^+ diffusion and its prevention should be the focus of further investigations.

9.4.3.4 SEM and EDX of APCX Wire with MS1 and Proposed Mechanistic Model

Compared to the APC wire, the APCX wire shows a much more severe Cu core corrosion. Herein, the difference between these two wires solely lies within the dopants of the Cu core for the APCX wire. Hence, the APCX wire was analysed via ICP-OES to gain further understanding of the involved processes and its individual elements. Therein, Ga (0.59 wt%) and Ni (0.30 wt%) are present within the Cu core in similar amounts like the Pd-coating (0.96 wt%), and Au-coating (0.32 wt%). Further analysis with EDX mapping of an APCX wire with **MS1** at 250 °C after 60-99 h confirmed the existence of Ga and Ni element as dopants within the Cu core, see **Figure 9.12**.

From the r_2/r_0 ratio in Figure 9.4 it is concluded that the corrosion mechanism changes from a KE to a SC mechanism. Also, an Anti-D3 model is revealed in the kinetic analysis which merges into a P4 model. However, this is not as obvious in the SEM and EDX micrographs. Therein, a homogeneous β -Cu₂S layer forms around the Au/Pd-coating but also a large amount of β -Cu₂S within the Cu core after 60 h. This is confirmed by an EDX mapping of S element, see **Figure 9.12a**. Therefore, it is concluded that the initial corrosion stage is like the APC wire where the β -Cu₂S formation starts at the damaged Au/Pd layer areas. Then, the propagation of β -Cu₂S takes place along the Au surface. Again, Cu⁺ surface and interdiffusion could lead to alloy formation, see **Figure A. 9.9**. Hence, a β -Cu₂S layer forms around the wire surface with predominant Cu⁺ outward diffusion. When the β -Cu₂S layer grows thicker, huge cracks form. These cracks enable the percolation of mercaptosilane into the Cu core and thereby the formation of β -Cu₂S. At these cracks, voids are accumulated in a semi-circular fashion to end up at another crack in the β -Cu₂S layer. These voids subsequently function as percolation pathways for **MS1** and further enhance the complete breakdown of the Cu core by convection of **MS1**. Further, the corrosion of the Cu core clearly proceeds along the grain boundaries of the Cu core, see **Figure 9.12**. For a magnification see **Figure A. 9.7**.

Hence, the question arises why this is not observed for the APC wire. Therein, the sole disparity between the APC and APCX wire is the added Ni and Ga element within the Cu core. Hence, these dopants must play a significant role in the corrosion mechanism of the APCX wire. In general, these dopants are supposed to act as passivation barrier at the damaged coating areas.^{83, 84, 86} However, at high temperatures and high sulfur content detrimental effects on the bond wire reliability is displayed. In fact, Ni and Ga aggregates are visible in the EDX micorgraphs, see **Figure 9.12b**. Therein, the EDX mapping of Ni element superimposes with the dark areas of S element. Hence, an EDX spectrum was performed on these areas which revealed the existence of nickel sulfide in a composition of Ni_{1.25}S, see **Figure A. 9.8**. Note that the exact composition determined from EDX spectroscopy can differ from the actual composition. Hence, the two sulfides Ni₃S₂ and NiS can form during the corrosion. Also, a segregation of the Pd-coating happens after 99 h, see **Figure 9.12c**. Thereby, it is striking that the EDX mapping of Ga overlaps with Pd and S (see Figure A. 9.7). Thus, it is likely to form Ga-Pd alloys and gallium sulfides. For reasons of clarity, first Ni and its Cu-Ni alloys will be discussed. Then Ga and its alloys are the subject of further inspection.

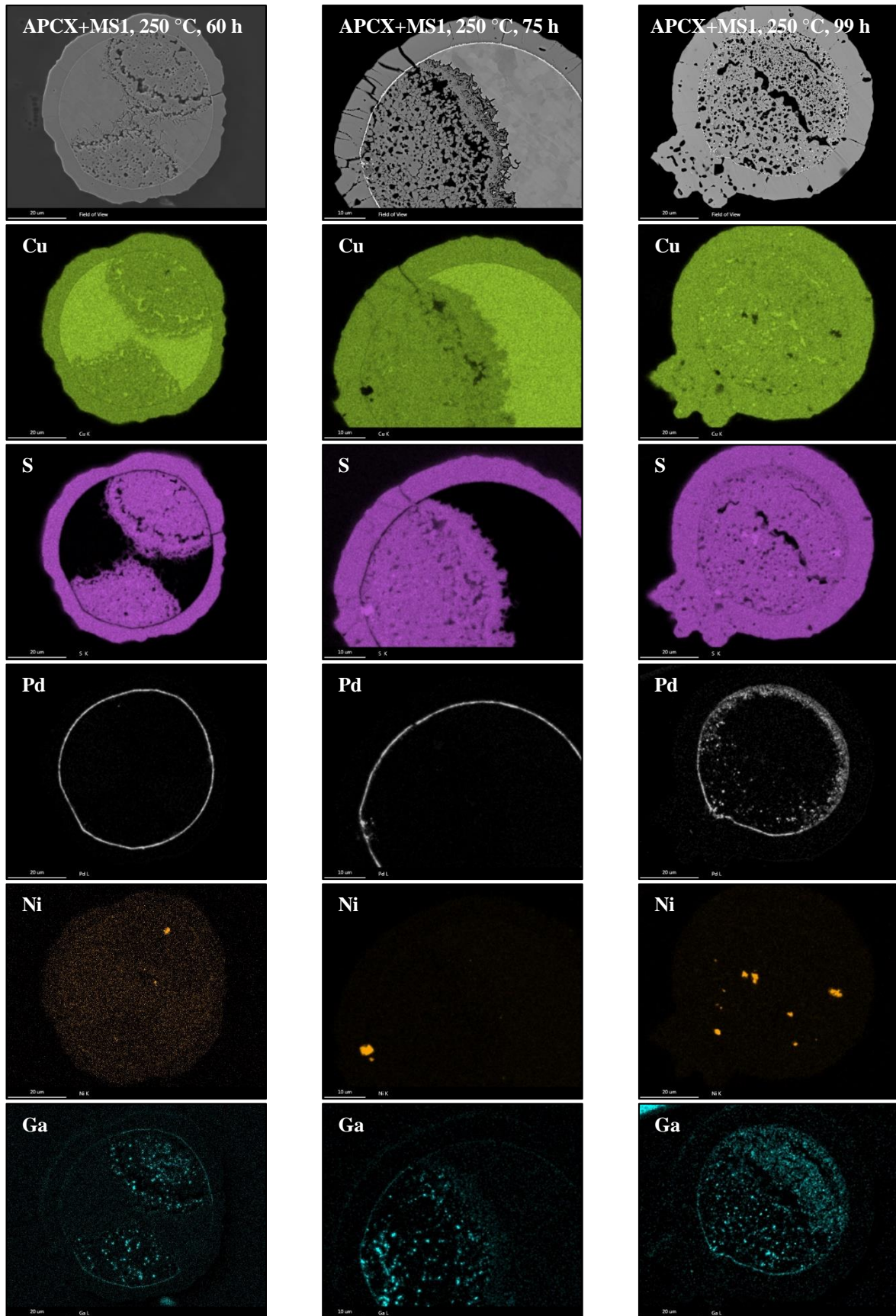


Figure 9.12: SEM and EDX micrographs of the cross-sections performed on a corroded APCX wire with MS1 at 250 °C, after a) 60 h, b) 75 h, and c) 99 h. Therein, Ni and Ga are found as dopants within the Cu core.

Generally, thiol adsorption on Ni and Pd surfaces is similar. Like Pd, Ni forms diluted NiS_x layer on the surface.⁶⁷ There, thiolates are adsorbed on the diluted NiS_x layer. Thereby, the d -band of Ni is populated near the Fermi level which leads to a C-S bond cleavage already at room temperature.⁶⁷ Again, the formed NiS_x layer on the surface can act as a passivation layer which is in line with PdS_x passivation. However, it is also reported that the adsorption of thiolate solely takes place on Ni(0) surfaces and not on NiO surface.⁶⁷ Note that the capillary is prepared under nitrogen atmosphere with **MS1**. Thus, NiO can be excluded from the discussion. Further, the Gibb's free energy of formation of Ni_3S_2 is higher than for Cu_2S which explains the strong driving force of Ni to form its sulfide.²²⁶

Therein, the Cu-Ni system forms a complete range of solid solutions. Due to this no segregation of Ni towards the grain boundaries (GB) is expected. Also, Ni is commonly established to reduce the GB diffusivity of Cu in Cu-Ni alloys.²²⁷ Yet, Ni was found to segregate in Cu-Ni alloys and to diffuse along the GBs towards the surface.^{228, 229} In the presence of oxygen, this leads to the formation of Cu_2O and NiO on the surface.²³⁰ Thereby, Ni accumulates at the surface and the corresponding NiO acts as passivation layer. Whereas Ni and Cu predominantly end up to their respective sulfides Cu_2S , Ni_3S_2 , and NiS in the mutual presence of sulfur and oxygen.²³¹⁻²³⁴ Contrary to the oxides, the sulfides are more porous and show enhanced Cu^+ diffusivity which leads to an increased corrosion rate.²³³ Additionally, sulfide formation gives rise to further segregation due to the poor miscibility of Cu_2S and Ni_3S_2 . Hence, big cracks are more likely to appear which goes along with additional diffusion pathways. These enable the diffusion of **MS1** into the Cu core and further degradation of the wire. In addition to that, Ni is completely soluble in Pd which adds the possibility of Ni diffusion through the Pd layer towards the surface. Consequently, nickel sulfide forms on the surface. Enhanced sulfur corrosion has also been observed on Ni/Pd/Au-coated Cu solder pins and Cu connectors.^{235, 236} Therein, the corrosion is induced by H_2S with a subsequent formation of porous Cu_2S on the surface. Like the APCX wire, Ni clumps together to form dome-shaped nickel sulfide with Cu_2S on the top. Like the coated bond wires, the corrosion is initiated at the coating defect sites and results in the creeping corrosion of Cu_2S . This is in accordance with the hypotheses that the sulfur induced corrosion of the APCX wire starts at the Au/Pd defect sites with subsequent Ni accumulation at these areas. Then nickel sulfide and Cu_2S forms at these spots which leads to a creeping corrosion along the wire surface.

The addition of Ga into the Cu core increases the complexity of the APCX wire even further. It was shown that minor addition of Ga into Cu increases the oxidation resistance.²³⁷ Unlike the Cu-Ni system, the Cu-Ga system exhibits lower miscibility. Hence, greater segregation of Ga towards the GBs is expected. Actually, Ga accumulates to evenly distributed small aggregates within the Cu core whereas Ni rather gathers near the surface to form greater grains. This points to a high degree of segregation but lower GB diffusivity of Ga within the Cu core. Thus, Ga could possibly slow down intergranular corrosion (IGC) by oxide or sulfide formation. Investigations on Pd-Cu-Ga alloy oxidation showed a preferential formation of the oxides: PdO, Cu_2O , CuO, Ga_2O_3 , CuGa_2O_4 .^{238, 239} Hence, it is likely that the corresponding sulfides form, see **Table 9.3** for an overview.

Table 9.3: Overview of the proposed Cu, Pd, Ni, and Ga corrosion products with sulfur and their Pd alloys. For better comparability, the corresponding oxides are given which are found in literature from Cu-Ni²³¹⁻²³⁴ and Pd-Cu-Ga^{238, 239} alloys.

Element	Comparison with oxide ^{231-234, 238, 239}	Proposed corrosion products	
		O ²⁻	S ²⁻
Cu	CuO, Cu ₂ O, CuGa ₂ O ₄	Cu ₂ S, CuGaS ₂	CuPd, Cu ₃ Pd
Pd	PdO	Pd ₄ S	-
Ni	NiO	NiS, Ni ₃ S ₂	Completely miscible
Ga	Ga ₂ O ₃	GaS, Ga ₂ S ₃	Ga ₅ Pd, GaPd

From the EDX micrographs it has been shown that Ga element overlaps either with Pd or S element. Hence, Ga in fact forms GaS or Ga₂S₃ in between the GBs. However, this leads to further segregation of Cu and Ga in the core which then results in increased mercaptosilane diffusion within the GBs. Additionally, Ga could form alloys with Pd. The formation of Pd₂Ga has been experimentally observed in Pd-Cu-Ga alloys at 400 °C.²⁴⁰ Of course, this is more unlikely to occur at 250 °C but alloy formation can still take place. At 250 °C the alloys Ga₅Pd and GaPd are the most likely to form. Again, Pd and Ga element superposition is confirmed in the EDX micrographs. Also, the dissolution of the Pd-coating after 99 h indicates additional processes as this is not observed for the APC wire. Here, it is assumed that the formation of Ga-Pd alloys leads to the segregation of the Pd-coating. Also, Ni can possibly enhance a further segregation of the Pd-coating as it may dissolve in the Pd layer. Thus, the Pd-coating slowly degrades and therefore enables the diffusion of mercaptosilane into the Cu core. This finally results in a faster breakdown of the wire.

Further, the segregation of Ni and Ga to the GBs leads to an increased IGC along the grain boundaries as seen from the SEM and EDX micrographs. Recent investigations on the addition of Pt and Pd to the APC wire also result in a faster sulfidation along the grain boundaries.⁸⁶ This underlines the hypotheses that the addition of dopants into the Cu core leads to the segregation of these dopants into the GBs. This consequently leads to a faster IGC along the grain boundaries. In summary, the enhanced diffusion of mercaptosilane within the GBs leads to an increased nucleation in the Cu core which is amplified by the Ga and Ni dopants. Therein, Ni and Ga could act as impurities to reduce the energy barrier for the nucleus formation. Thus, the diffusion mechanism (Anti-D3) merges into a nucleation and growth-controlled mechanism (P4).

Accordingly, a corrosion model is proposed in **Figure 9.13** from the findings of the HT-PXRD measurements and the SEM and EDX micrographs. First, the thiol chemisorbs on the Au/Pd surface where additional disulfide formation can occur (i.). Also, Cu ions may diffuse either through the Au/Pd-coating or along the wire surface to form Cu₂S (ii.). At the defect sites of the Au/Pd-coating, initial β -Cu₂S corrosion starts which results in creeping corrosion along the wire surface (iii.). This is accompanied by Cu⁺ outward diffusion and thus the formation of voids according to the KE (iv., Anti-D3). The creeping corrosion of β -Cu₂S goes along with alloying processes of the Au/Pd-coating

to form Cu_3Pd , CuPd or $\text{Cu}_3\text{Au}/\text{CuAu}$ (v.). Besides the $\beta\text{-Cu}_2\text{S}$ formation, Ni accumulates at the exposed areas of the Cu core which leads to the oxidation of Ni to $\text{Ni}_3\text{S}_2/\text{NiS}$ (vii.). Also, the volume expansion and segregation $\beta\text{-Cu}_2\text{S}$ scales leads to cracks in the $\beta\text{-Cu}_2\text{S}$ layer (vi.). This enables the percolation and convection of **MS1** into to the Cu core and subsequent corrosion of the Cu core especially along the grain boundaries (x.). Hence, sulfur induced IGC results in the agglomeration of Ga to form $\text{Ga}_2\text{S}_3/\text{GaS}$ (viii.). Therein, a fast nucleation of $\beta\text{-Cu}_2\text{S}$ takes place due to the addition of Ni and Ga which act as impurities to reduce the activation energy to form nuclei (xii., P4). At a certain point, the Cu_3Pd , Cu-Au, and Ga-Pd alloying processes result in the dissolution of the Pd-coating (xiii.). This impairs the corrosion resistance even further which leads to a complete breakdown of the APCX wire and also to a fast formation of a porous $\beta\text{-Cu}_2\text{S}$ core (xiv.).

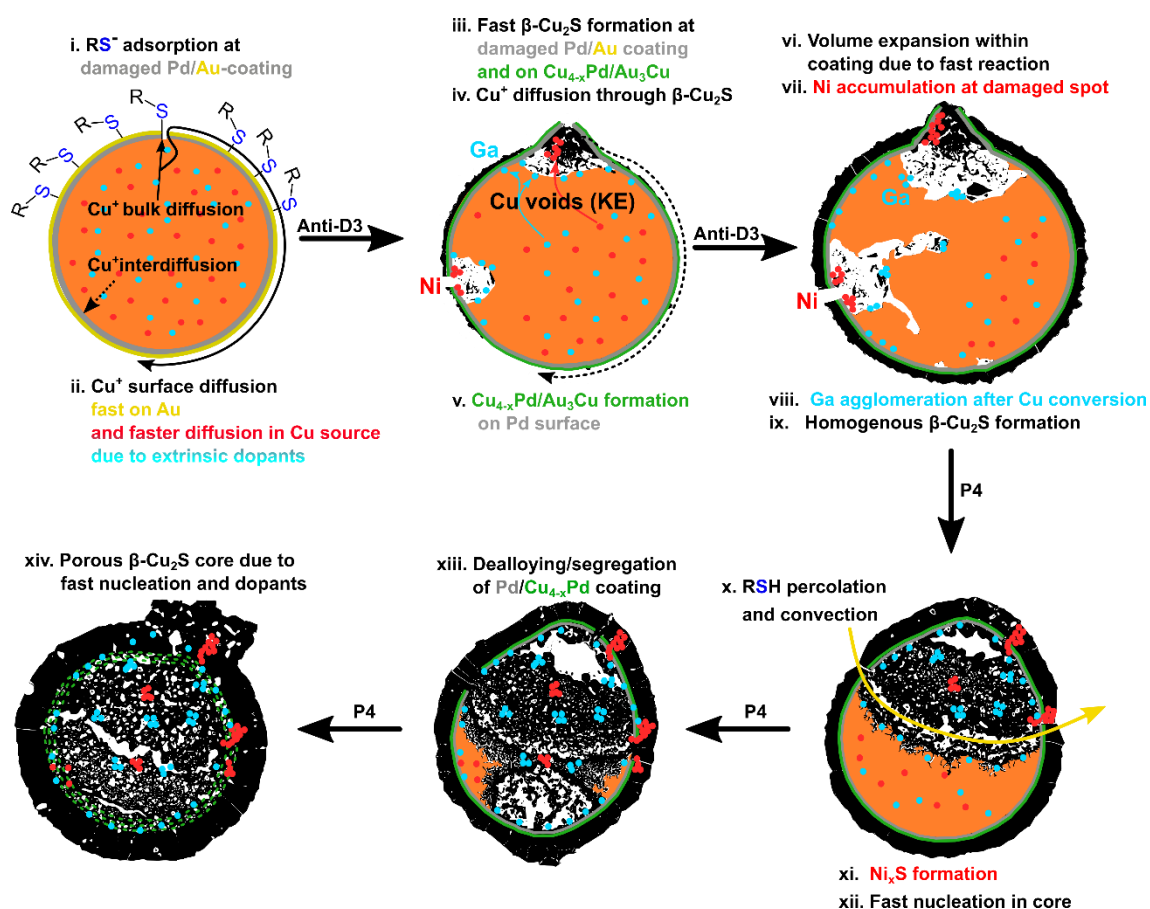


Figure 9.13: Proposed schematic corrosion model for APCX wire with **MS1**. First, $\beta\text{-Cu}_2\text{S}$ forms at the damaged Pd-coating and the corrosion rate is controlled by the outward diffusion of Cu ions according to a KE mechanism (Anti-D3). Further, Ni and accumulates at the surface to form Ni_xS which leads to a further segregation and bigger pores and cracks in the Cu_2S layer. At some point cracks form due to the volume expansion of the product layer and RSH percolation and convection into the Cu core becomes feasible. Also, Ga forms Ga_xS and Ga_xPd alloy which leads to the dissolution of the Pd-coating and IGC (P4).

However, the question remains if this is actually observed in the presence of moisture and oxygen. These could lead to a more passivating and homogeneous oxide layer and thereby preventing further degradation of the Cu core. Still, the APCX wire poses a high risk versus sulfur induced corrosion in the sole presence of sulfur species which leads to detrimental, porous sulfide layers.

9.4.4 Corrosion Kinetics of Cu Bond Wires with TT

As mentioned in chapter 8, the corrosion rate and mechanism are mostly dominated by the sulfur reagent. Note that **TT** is a solid reagent and was filled as solid into the capillary. Therefore, an incomplete filling of the capillary cannot be ruled out. Hence, a comparison of these measurements must be treated with caution. Here, triazole-thiol **TT** generally induces a parabolic behaviour with Avrami-exponents ranging from $n = 0.27$ - 0.56 , see **Figure 9.14a**. Thereby, the major part of the corrosion with **TT** occurs in the first 4 h at 250 °C. Further investigations via the SH-plot reveals an interface-controlled ($n = 0.91$ - 0.95) corrosion in the initiating stages which then merges into a diffusion-controlled ($n = 0.18$ - 0.59) mechanism, see **Figure 9.14b**. Note that for the bare Cu wire solely the diffusion part is present in the SH-plot. This is explained by the very fast reaction which impedes the detailed tracking of the corrosion process. Thereby, sufficient time is needed to accumulate the needed intensities for QPA. Thus, the initial process is “invisible” to the measurement. Therefore, it is assumed that the initial corrosion behaviour of the bare Cu wire is presumably beginning with an interface-controlled mechanism in accordance with the coated wires.

Consequently, all wires behave similar with distinct preferences for the APC and APCX wire. Thereby, the APC wire displays a higher degree of the interface-controlled regime whereas the APCX wire contains more diffusional contributions. In **Table 9.4** the derived models are summarized.

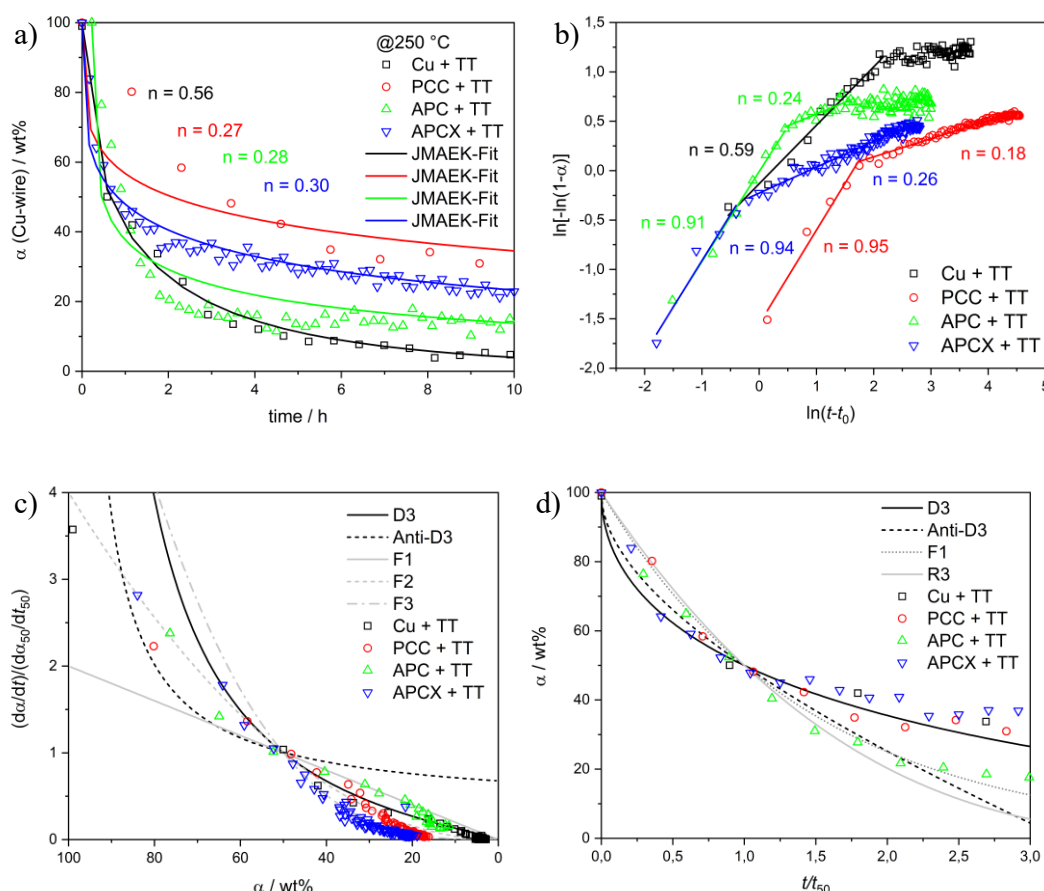


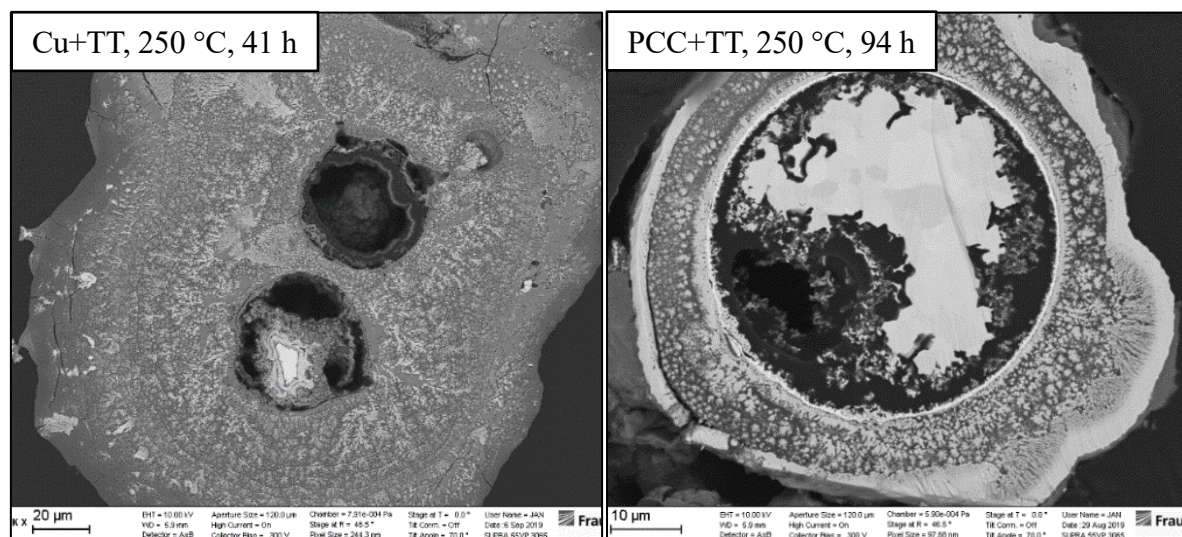
Figure 9.14: a) α - t -plots from the quantified HT-in situ-PXRD measurements of bare **Cu**, **PCC**, **APC**, and **APCX** bond wire with **TT** at 250 °C and the Avrami exponents n from the JMAEK-fit. b) SH-plot c) Master plot $f(\alpha)$ d) Master plot $g(\alpha)$

Table 9.4: Overview of the derived models from the respective analysis method. Here, shown for all bond wires with **TT**. For further details see **Table A 9.3**.

Wire	Cu	PCC	APC	APCX
T / °C	250	250	250	250
Sharp-Hancock Plot				
Mechanism	D3, Anti-D3	R3 D3, Anti-D3	R3 D3, Anti-D3	R3 D3, Anti-D3
JMAEK-Fit				
Mechanism	D3, Anti-D3	D3, Anti-D3	D3, Anti-D3	D3, Anti-D3
Master Plots				
Mechanism f(α)	F2	F2	F1, F2	F2, F3
Mechanism g(α)	D3	R3, D3	F1	D3
Summary				
Assumed Mechanism	R3 ↓ Anti-D3	R3 ↓ Anti-D3	R3 ↓ Anti-D3	R3 ↓ Anti-D3

9.4.5 Cross-Sections of Cu and PCC Bond Wire with TT after HT-PXRD

After the HT-in situ-PXRD measurements, SEM micrographs were conducted on the cross-sections of the bare Cu and PCC bond wire, see **Figure 9.15**. Therein, the bare Cu wire exhibits severe Cu core degradation with large Cu voids. This clearly indicates an outward diffusion of Cu ions towards the reactive surface according to the KE. Around the Cu void is a large mixed phase of $r \approx 70 \mu\text{m}$. Note that a maximal product layer thickness of $r = 43 \mu\text{m}$ can be reached by pure $\beta\text{-Cu}_2\text{S}$. Hence, this large product layer must be a mixture of two different phases. This is also displayed by a dendritic structure of the first phase within the second phase.

**Figure 9.15:** SEM micrographs on the cross-sections of the **Cu** and **PCC** bond wire after HT-in situ-PXRD measurements with **TT** at 250 °C. The preparation and SEM analysis were performed at the Fraunhofer IMWS in Halle.

The PCC wire also exhibits large and evenly distributed Cu voids but with differences in the product layer. First, a homogenous layer forms on the Pd surface which is followed by a mixed product layer. The mixed phase has similar features like the corroded bare Cu wire, which is the dendritic structure of one phase in another phase. Then, the mixed phase is followed by a homogeneous layer on top. In the next sections, the corroded Cu and PCC bond wire with **TT** are discussed in detail.

9.4.5.1 SEM and EDX of Bare Cu Wire with **TT** and Proposed Mechanistic Model

The EDX mapping on the cross section of the bare Cu wire after 41 h at 250 °C with **TT** confirms the beforementioned hypothesis of a mixed product phase, see **Figure 9.16**. Therein, Cu voids are visible, and some Cu remains in the core to form connective diffusion pathways to the outer layer. Thereby, the EDX mapping reveals an outer layer which mostly consists of N element. Within this organic layer of N, β -Cu₂S is incorporated in a dendritic morphology. Thereby, the dendritic morphology indicates a fast co-precipitation of β -Cu₂S along the N layer. This is expected as the N content in **TT** is high and the solid state of aggregation of **TT** impedes the diffusion away from the reactive zone. This results in a co-precipitation of β -Cu₂S and the by-product of the decomposition reaction of Cu with **TT**. From chapter 7.4.3 it is known that **TT** decomposes to NH₃ to form NH₄Cu₇S₄ and with further heating, Cu₂S. Though NH₄Cu₇S₄ is not observed in the powder pattern of Cu wire with **TT**, similar reaction pathways can take place. For instance, the decomposition of **TT** to NH₃ and **TT** radicals to form a N-polymeric organic layer. Another striking feature is the continuous degradation of the Cu core and the relatively homogenous distribution of β -Cu₂S within the organic layer. Thereby, the organic layer generally should slow down the Cu ion diffusion towards the reactive surface. This is not observed and a continuous supply of Cu⁺ is assured during the whole corrosion process.

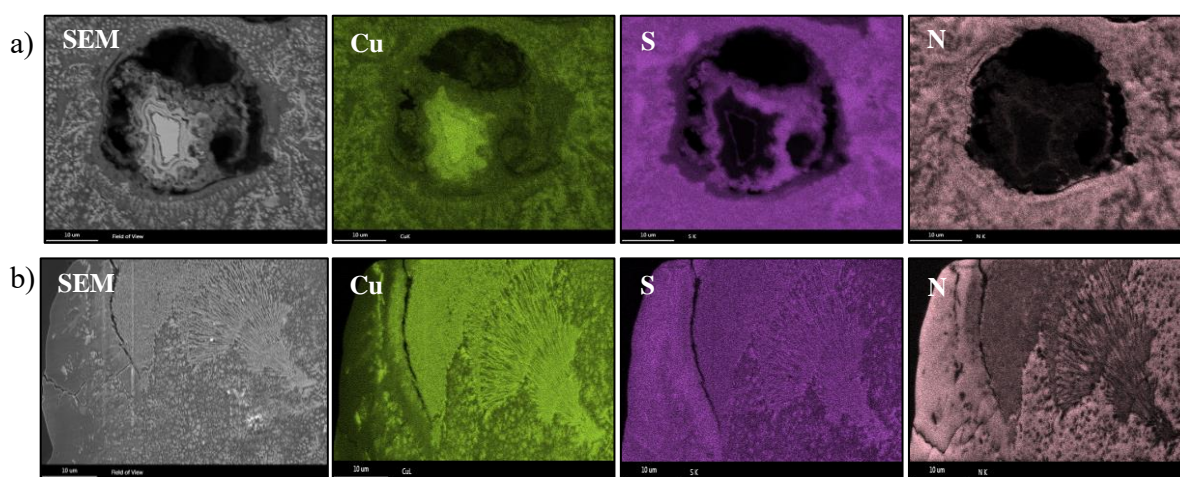


Figure 9.16: SEM magnifications and EDX micrographs on the cross-sections of Fig 9.15. Here, the bare **Cu** bond wire with **TT** after 41 h at 250 °C. a) Magnification and EDX micrographs of the Cu core, b) Magnification and EDX mappings of the mixed phase with its dendritic structure. The EDX analysis reveals an N-polymeric organic layer with dendritic β -Cu₂S within the layer.

From PXRD, SEM, and EDX measurements a corrosion model is proposed in **Figure 9.17**. First, thiolate chemisorbs on the Cu surface (i.). Then, the fast chemical reaction on the surface is limited by the diffusion of Cu^+ towards the surface (D3). The fast surface reaction and the solid state of aggregation of TT leads to the co-precipitation of $\beta\text{-Cu}_2\text{S}$ and a N-polymeric organic layer (ii.). Thereby, the organic layer does not impede the Cu ion outward diffusion which leads to the continuous formation of $\beta\text{-Cu}_2\text{S}$ within the organic layer (iii.). Consequently, Cu voids are formed according to a KE model (iv., Anti-D3).

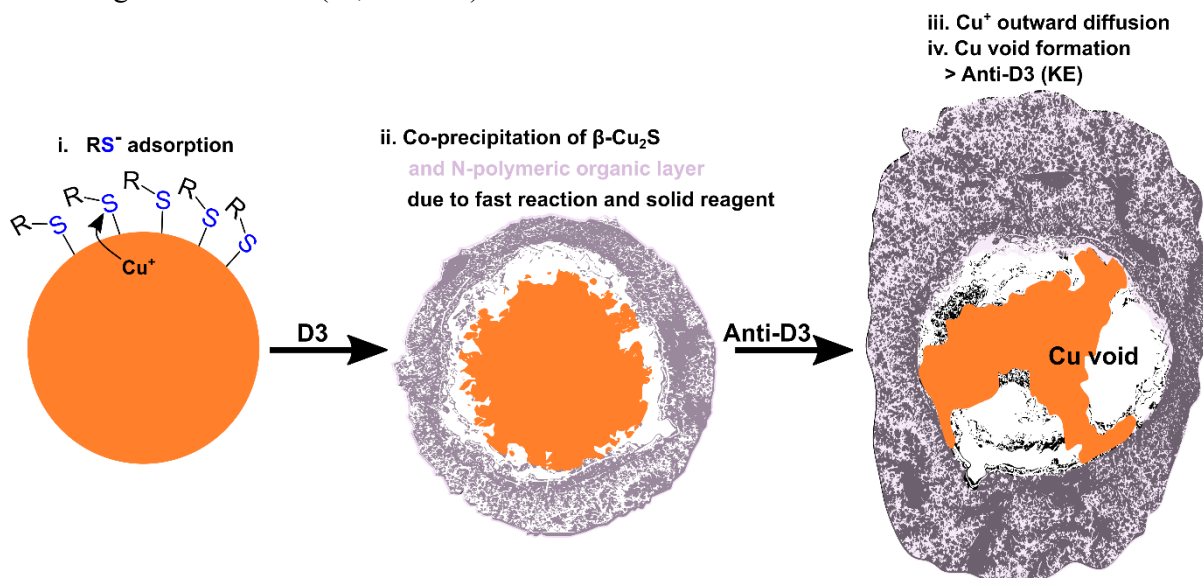


Figure 9.17: Proposed schematic corrosion model for bare **Cu** wire with **TT**. First the triazole-thiol chemisorbs on the surface. Then, $\beta\text{-Cu}_2\text{S}$ forms and the corrosion rate is controlled by the Cu ion diffusion (D3). At a certain product layer thickness, the Cu ion outward diffusion (Anti-D3) becomes rate limiting. Hence, Cu voids are formed according to the Kirkendall effect along with the co-precipitation of $\beta\text{-Cu}_2\text{S}$ and the N-polymeric organic layer.

9.4.5.2 SEM and EDX of PCC Wire with TT and Proposed Mechanistic Model

Compared to the corroded Cu wire, the PCC wire exhibits three distinct product layers after the corrosion with **TT** at 250 °C, see **Figure 9.18**. Another striking feature is the even distribution of Cu voids underneath the Pd-coating. Also, no significant hillock formation is observed compared to the PCC wire with **MS1**. Additionally, a homogenous $\beta\text{-Cu}_2\text{S}$ layer is present on the Pd surface.

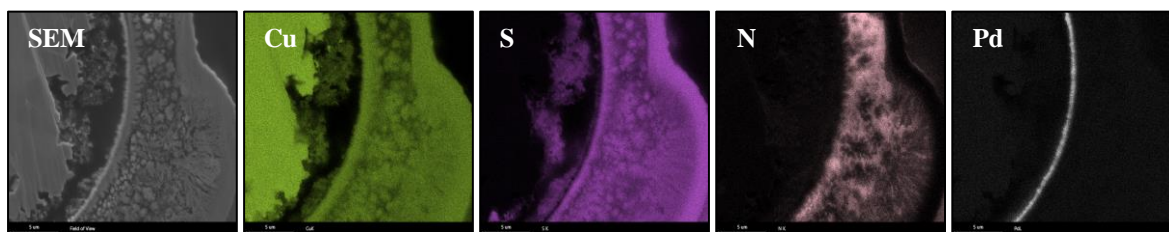


Figure 9.18: SEM magnifications and EDX micrographs on the cross-sections of Fig 9.15. Here, the **PCC** bond wire with **TT** after 94 h at 250 °C. Magnification and EDX micrographs of the mixed phase with its dendritic structure. The EDX analysis reveals an N-polymeric organic layer with dendritic $\beta\text{-Cu}_2\text{S}$ within the layer and a homogeneous layer at the outermost layer.

This can be explained, by a higher degree of decomposition of **TT** on the Pd surface compared to the bare Cu surface. This is confirmed in chapter 7.4.3 where Pd leads to a faster and stronger decomposition of **TT**. Thus, gaseous decomposition products can form which can diffuse away from the reactive zone. Consequently, a homogeneous β -Cu₂S layer is formed. Additionally, the even distribution of Cu voids leads to the conclusion that Cu ions diffuse through the Pd-coating. This is also indicated by the thin outgrowths underneath and on top of the Pd-coating. Hence, Cu voids grow underneath the Pd-coating. The driving force for the Cu⁺ interdiffusion is most likely the fast chemical reaction on the Pd surface to reduce the free energy of the system.

Like the bare Cu wire, a mixed phase of N element and β -Cu₂S forms on top of the homogeneous β -Cu₂S layer. Also, the dendritic morphology is displayed in accordance with the bare Cu wire. This is also observed in the powder pattern in **Figure 9.19**. Therein, β -Cu₂S forms along Cu₃Pd and an amorphous phase, which is indicated by the broad background. From the combined analysis of PXRD and EDX it is concluded that the amorphous phase is presumably a N-polymeric organic phase.

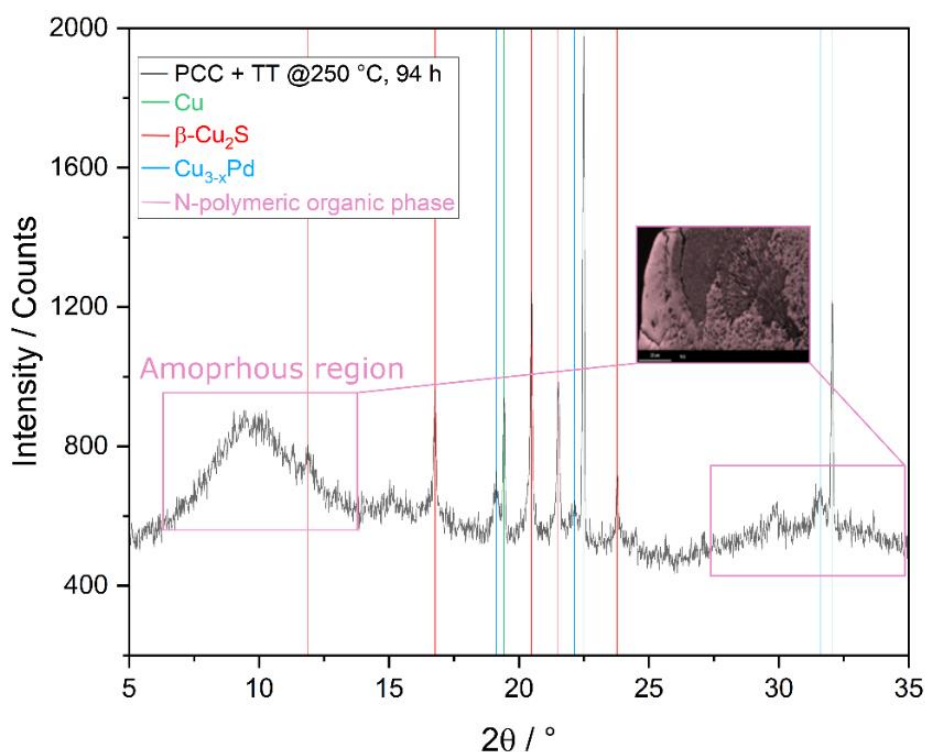


Figure 9.19: Powder pattern of the PCC wire with TT after 94 h at 250 °C. The powder pattern displays the Cu, β -Cu₂S, and Cu₃Pd phase along with the amorphous N-polymeric organic phase.

As the Pd surface is completely covered with β -Cu₂S, the decomposition of **TT** slows down and consequently the mixed phase forms. In section 9.4.5 it is mentioned that the incomplete filling of the capillary with solid **TT** could lead to an incomplete conversion. This is presumably the case for the corrosion reaction of the PCC wire with **TT**. Thereby, the solid reagent **TT** is completely consumed at the surface of the wire. However, the reagent **TT** can further decompose to its gaseous decomposition products. Consequently, the gaseous products such as NH₄S, H₂S or HS⁻ can further react on the surface of the mixed phase to grow a homogeneous β -Cu₂S layer. This is accompanied by Cu ion outward diffusion through the Pd-coating to form voids according to the KE model.

From PXRD, SEM, and EDX measurements a corrosion model is proposed in **Figure 9.20** for the corrosion of PCC bond wire with **TT**. First, thiolate chemisorbs on the Pd surface (i.). Thereby, the Pd surface enables C-S bond cleavage and decomposition of the triazole-thiol. Simultaneously, Cu^+ interdiffusion leads to the Cu_3Pd alloy formation and the growth of voids in the vicinity of the Pd layer (ii.). Consequently, a homogeneous $\beta\text{-Cu}_2\text{S}$ layer forms as the gaseous decomposition products can diffuse away from the Pd surface (iii.). As the whole Pd surface is covered, the slower reaction results in a co-precipitation $\beta\text{-Cu}_2\text{S}$ and the by-product of the **TT** decomposition. Hence, a mixed phase grows, which consists of dendritic $\beta\text{-Cu}_2\text{S}$ and a N-polymeric organic phase (iv.). The growth of the product layer is thereby not hindered by the organic layer and is accompanied by continuous Cu ion outward diffusion (v., Anti-D3). Eventually, the solid reagent **TT** is completely consumed on the wire surface. Further heating leads to the decomposition of **TT** to its gaseous products like NH_4S , H_2S and HS^- which leads to the growth of a homogenous $\beta\text{-Cu}_2\text{S}$ product layer on top of the mixed phase. Hence, a three-layer product layer grows in the order: homogeneous $\beta\text{-Cu}_2\text{S}$ / $\beta\text{-Cu}_2\text{S}$:N-polymeric organic phase / homogeneous $\beta\text{-Cu}_2\text{S}$.

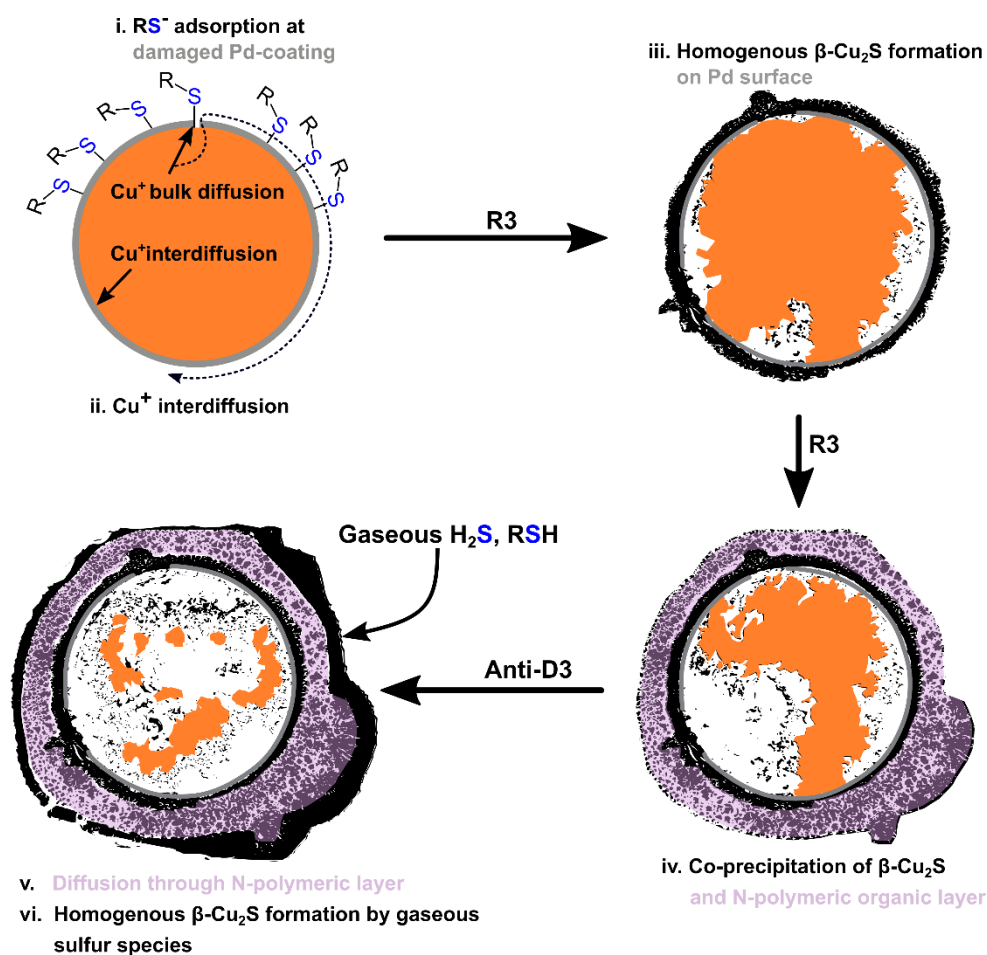


Figure 9.20: Proposed schematic corrosion model for **PCC** wire with **TT**. First the triazole-thiol chemisorbs on the surface. Then, $\beta\text{-Cu}_2\text{S}$ forms and the corrosion rate is controlled by the chemical surface reaction (R3). At a certain product layer thickness, the Cu ion outward diffusion (D3, Anti-D3) becomes rate limiting. Hence, Cu voids are formed according to the Kirkendall effect. The decomposition on the Pd surface results in a three-layered product layer which consists of: $\beta\text{-Cu}_2\text{S}$ / $\beta\text{-Cu}_2\text{S}$:N-polymeric organic phase / $\beta\text{-Cu}_2\text{S}$.

9.5 Conclusion

In summary, **TT** leads to a faster degradation of all bond wires compared to **MS1**. This is in line with chapter 8 where the S-reagent dictates the overall corrosion mechanism. Hence, the S-reagent is the most important package material selection criterion. Nevertheless, differences between the various bond wires still exist but are negligible compared to the selection of the S-reagent.

Herein, the APCX wire degrades much faster compared to the other wire types, at least at 250 °C. Also, the bare Cu wire performs in general worse than the coated wires PCC and APC. Hence, the reliability of the wires against sulfur induced corrosion is increasing in the order: APCX, Cu, PCC, APC. Note that this solely applies to pure sulfur induced corrosion at 250 °C. This may change as moisture and oxygen are added to the mixture which may lead to a passivating oxide layer on the surface, thus, preventing further breakdown of the Cu core.

In general, the kinetic analysis of the bond wires with **TT** reveals an interface-controlled mechanism in the initial corrosion stages. Then, the mechanism merges into a KE model which is characterized by the outward diffusion of the Cu ions (Anti-D3). In contrast, the kinetic analysis of the bond wires with **MS1** exhibits an interface mechanism in the beginning which transforms into nucleation and growth-controlled mechanisms. An exception is the APCX, where outward diffusion is followed by the nucleation in the core. The commonality of nucleation and acceleration of the corrosion rate is due to the percolation of **MS1** into the Cu core as the β -Cu₂S scales create cracks and chip off. Also, the corrosion of the coated wires with **MS1** begins at the defect sites of the coating. This results in more or less pronounced hillocks. The hillock formation is thereby governed by the RSH percolation, Cu⁺ surface diffusion, Cu⁺ interdiffusion and β -Cu₂S propagation along the wire surface. Additional factors are bulk and grain boundary diffusion of the Cu core which acts as Cu ion source. Whereas Cu ion surface diffusion is predominant with **MS1**, interdiffusion is the dominant mechanism in combination with the S-reagent **TT**. Furthermore, the Pd-coating in general leads to a faster surface reaction which drives the dendritic growth of β -Cu₂S for both **TT** and **MS1**. This is not observed for the bare Cu wire which simply reacts to β -Cu₂S. Also, the decomposition of **TT** leads to a mixed β -Cu₂S/N-polymeric organic phase.

Moreover, a solid reagent such as **TT** does not percolate into the core like the liquid compound **MS1**. This is an important finding as adhesion promoters are incorporated into the solid MC. Thus, diffusion of the S-reagent is limited within the MC and the formation of SAMs during the molding process must be considered as a rate limiting factor. Therefore, a corrosion mechanism like with the solid reagent **TT** is assumed for semiconductor packages. Thereby, it is found that the initial corrosion for both **TT** and **MS1** is governed by the reactivity of the S-reagent ($R, n \approx 1$). Also, the differences between the corrosion rates of **TT** and **MS1** are much bigger compared to the differences between the individual bond wires. This means that the initial reactivity of the reagent governs the degradation of the bond wire. Thus, the selection of a suitable adhesion promoter is the key selection criterion to regulate the initial corrosion and to improve the reliability.

Additionally, it is assumed that a higher initial coverage of the Cu surface with SAMs of adhesion promoters after curing results in a higher overall degradation of the Cu wire. This is due to the faster corrosion in the beginning by the interface-mechanism, which slows down when the SAM supply of adhesion promoters on the surface is exhausted. Hence, the mechanism merges into a diffusion-controlled mechanism which should be rate limited by the mobility of the adhesion promoter within the MC towards the Cu surface.

Another important aspect which must be considered is the uniform corrosion of the bare Cu wire versus the localized pitting corrosion of the coated wires PCC, APC, and APCX. A uniform corrosion of the bare Cu wire carries a much lower risk for resistance drift and bond wire break-off because the Cu degradation is distributed over the whole surface. In contrast, the corrosion of the coated wires is localised at the damaged spots. Consequently, pitting corrosion at these spots yields big holes which then might cause resistance drift or bond wire break-off. This is especially true for thin stitch bonds. Hence, coated bond wires such as PCC, APC, and APCX bond wire pose a high risk for localised corrosion and subsequent bond failure.

As shown above, the initial corrosion of the coated bond wires PCC, APC, and APCX begins at the Pd, Au/Pd layer defect sites. This is an important feature which must be considered for galvanic corrosion (Pd-Cu couple). There, the surface ratio of cathodic (S_{Pd}) to anodic (S_{Cu}) area at cracks or pinholes is a key parameter if the corrosion is under cathodic control, see **Figure 9.21**.

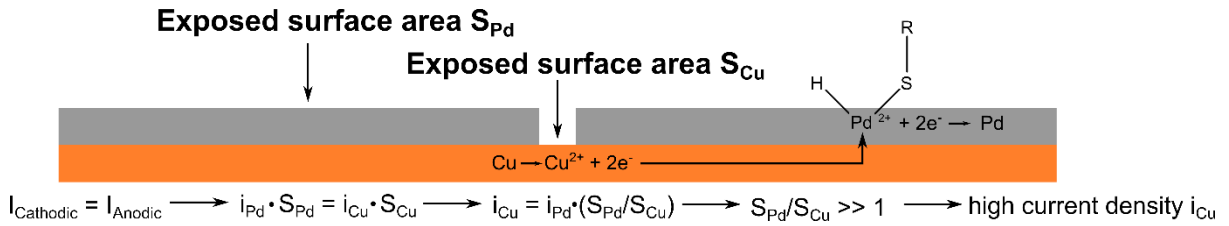


Figure 9.21: Schematic illustration of the galvanic couple Pd-Cu and the respective cathodic and anodic processes. The high surface area ratio of S_{Pd} versus S_{Cu} results in a high current density i_{Cu} at the damaged coating spot.

In the case of cathodic control, a variation of the cathode area has a significant effect, because the galvanic current is in general proportional to the cathode surface. Here, the basic assumption is the equality of the cathodic (Pd) and anodic (Cu) currents I . However, this does not mean that the current densities i (A/cm^2) are equal. The cathodic and anodic currents can be expressed by the current densities i multiplied by the surface area S . With this, it becomes evident that a high ratio $S_{Pd}/S_{Cu} \gg 1$ of the Pd surface to the exposed Cu surface results in a high current density i_{Cu} for the Cu core. Consequently, the Cu core exhibits much higher corrosion current densities at these spots, which results in severe pitting corrosion. Thus, the surface area of the Pd-coating becomes an important parameter for Cu bond wire corrosion, because of the surface area ratio S_{Pd}/S_{Cu} . Therefore, the length and thickness ($S_{Pd} = 2 \cdot r \cdot \pi \cdot h$) of the bond wire within the semiconductor package must be considered for long-term reliability as long and thick coated bond wires possess a much higher Pd, Au/Pd surface area.

Furthermore, the addition of a flash-Au layer slows down the initial surface reaction. However, disulfide formation at the Au surface leads to an enhanced nucleation of β -Cu₂S and thereby to an increased nucleation rate as the corrosion proceeds. As the elements Ni and Ga are added as dopants into the Cu core of the APCX wire, the complexity of the corrosion mechanism increases. This also leads to a detrimental corrosion behaviour of the APCX wire. It is found that Ni and Ga form a variety of corrosion products such as nickel and gallium sulfides as well as Pd-Ga alloys. Eventually, the wire completely corrodes with a porous β -Cu₂S within the core which is a consequence of the Cu-Ni-Ga alloy segregation.

However, common phenomena are the initial Cu corrosion at the defect sites as well as Cu⁺ inter- or surface diffusion. Therefore, potential successful strategies to prevent corrosion and ion migration is the improvement of the coating. Up to now it is not feasible to produce a perfect Pd- or Au-coating. This leads to a porous or defective Au or Pd layer. Recent studies aimed at the improvement of the protective layer. These studies found that an amorphous Pd(P) layer prevents the diffusion of Cu ions through a Au/Pd(P) layer.²²⁴ Hence, interdiffusion is prevented which then leads to a successful corrosion prevention. Also, the pre-treatment of the Cu surface with a flash-Au and consecutive Pd/Au-plating results in more densely packed Pd grains.²²³ Consequently, Cu⁺ diffusion is hindered by the denser Pd-layer. Another investigation successfully applied graphene layers as protective coating to prevent Cu oxidation.²⁴¹

Apart from the different protective measures, the commonality within these investigations is the impregnable protective coating. Hence, Cu ion inter- and surface diffusion are significant factors to prevent Cu core oxidation. Also, grain boundary and bulk diffusivity within the Cu core are important factors to reduce the corrosion rate. The IGC along the grain boundaries is especially pronounced for the doped APCX wire which is in line with literature.⁸⁶ Hence, the use of additive elements carries a high risk for IGC in the presence of sulfur. Therefore, a potential strategy to prevent corrosion of the Cu core is to specifically tune grain size and grain boundaries by GBE. Another potential tool is to select suitable dopants which do not segregate to the GBs and are more resistant to oxidation. Yet, dopants can also be specifically selected to segregate to GBs and thereby prevent grain boundary diffusion. Such additives can also be used to form better passivating layers versus sulfur induced corrosion than Ga and Ni to further enhance corrosion resistance. Therefore, further investigations regarding the grain boundary diffusivity, segregation and passivation of specific dopants are needed to understand the involved processes which then can be used to improve the dopant selection criteria.

Nevertheless, further investigations are needed to improve bond wire reliability, especially with regard to the Cu⁺ diffusivity within the Cu core and the Au/Pd-coating. Thereby, the diffusion pathways of Cu ions are an important factor to limit the corrosion rate. Also, alloy formation can hardly be analysed by means of PXRD due to their thin layers. Hence, other methods must be developed to identify the different alloys and their catalytic properties.

10 Solvent Mediated Corrosion Effects

10.1 Abstract

In this chapter, Cu and APC wire is measured at 250/225/200 °C with pure solid **TT**, **TT/PC**, and **TT/DMSO** mixtures. The obtained measurements are analysed for their corrosion kinetics via the JMAEK-fit, SH-plot, and ICM. These experiments show that the corrosion mechanism transforms from mixed interface- and diffusion-control at 250 °C towards pure diffusion control at 200 °C. The subsequent evaluation of the obtained rate constants reveals an increasing activation energy in the order: APC (**TT/DMSO**) < APC (**TT/PC**) < Cu (solid **TT**) < APC (solid **TT**). As a consequence of the high activation energy, solid **TT** corrosion is heavily accelerated at higher temperatures which leads to detrimental Cu core corrosion. The reverse trend is observed for the **TT/PC** and **TT/DMSO** solutions. For the solutions, a high corrosion rate is observed at 200 °C but the lower activation energy results in a slower acceleration of the corrosion rate at high temperatures.

Further, it is shown that dissolution of **TT** in PC or DMSO, which serves as “dummy matrix” to simulate the MC, can influence corrosion rates and activation energy for Cu bond wire corrosion. This occurs because the solvents PC and DMSO can induce changes in solvation (stabilization, hindrance of decomposition products), diffusion (liquid vs. solid), wetting (formation of SAMs) and catalytic capabilities (pH-value). Finally, important aspects of MC composition and their potential impact are discussed with regard to sulfur induced corrosion.

10.2 Introduction

In semiconductor packages, the adhesion promoter is a component of the MC. Due to this, the mobility of the adhesion promoter is constrained by the surrounding polymer-matrix and the filler particles of the MC. Yet, the influence of the polymer-matrix on diffusivity and reactivity of the adhesion promoter is unknown and has not been studied extensively in the literature. This chapter aims at narrowing this gap by investigating the influence of different solvents on the reactivity of the adhesion promoter to simulate different MC environments for the bond wires. In this study, the solvents propylene carbonate (PC) and dimethyl sulfoxide (DMSO) serve as “dummy matrices” to obtain first insights into solvent mediated effects on sulfur induced corrosion. Hence, Cu and APC bond wire is used in combination with solid adhesion promoter **TT** as pure solid and liquid mixtures. HT-in situ-PXRD is used, followed by a subsequent kinetic analysis. Furthermore, activation energies are determined from 250 °C to 200 °C to further clarify different aspects of solvent mediated corrosion control. For instance, decomposition kinetics of the adhesion promoter in the gas phase versus liquid phase are investigated.

10.3 Experimental

10.3.1 Cu and APC Bond Wire with Various TT Solutions

All experiments were performed with bond wires with 50 μm diameter. Here, bare Cu (Cu) and Pd-coated Cu with a flash-Au layer (APC) are used. For details see chapter 4.2.1. For experimental details see chapter 9.3.1. In case of the solid triazole-thiol (**TT**), the capillary was filled with the solid reagent, evacuated prior to use and flame sealed under vacuo. Note that the use of the solid reagent can lead to an incomplete filling of the capillary. Also, 3.2 M solutions of **TT** are prepared to yield the mixtures **TT/PC** and **TT/DMSO**. Therein, the **TT/PC** mixture is used as suspension due to the poor solubility of **TT** in PC (anhydrous, 99.7 %). Keep in mind that this procedure may result in an inhomogeneous distribution of **TT** within the capillary. Whereas the **TT/DMSO** mixture was heated up to 80 $^{\circ}\text{C}$ prior to use to completely dissolve **TT** in DMSO (anhydrous, 99.9 %). Then, the heated **TT/DMSO** solution was filled into the capillary. Note that sulfoxides are shown to be stable versus bare Cu wire at 250 $^{\circ}\text{C}$, see chapter 8.4.4. In **Table 10.1** a complete list of all experiments is given as well as the theoretical molar ratios.

Table 10.1: List of all conducted isothermal HT-in situ-PXRD measurements.

Bond wire type	Organic sulfur compound	Mixture	T / $^{\circ}\text{C}$	Molar ratio (wire:reagent)	Cu:S ratio
Cu ^a	Triazole-thiol	TT (solid)	250/225/200	1:2.3	1:2.3
APC ^a	Triazole-thiol	TT (solid)	250/225/200	1:2.3	1:2.3
APC	Triazole-thiol	TT/PC (liq.)	250/225/200	1:0.5	1:0.5
APC	Triazole-thiol	TT/DMSO (liq.)	250/200	1:0.5	1:0.5

^a External standard method (ESM) is used for the quantification

10.3.2 Isothermal HT-in situ-PXRD Measurements

HT-in situ-PXRD was used as standard method to characterize the reaction products and to follow the corrosion process. For device specific details, see chapter 4.1.2. Further, Mo- $K_{\alpha 1}$ ($\lambda = 0.70930 \text{ \AA}$) radiation was used for all samples and measured in Debye-Scherrer geometry in a silica capillary. Also, the measurements were conducted at 250-200 $^{\circ}\text{C}$ under isothermal conditions. In all experiments with **TT** and **TT** mixtures, the powder patterns solely comprise a Cu and Cu₂S phase. Hence, the ESM and DCM method can be used to quantify the binary mixture. For further details, see chapter 3.5.3 and 3.5.4.

10.3.3 Kinetic Analysis and Activation energy

Herein, the JMAEK equation in its exponential (JMAEK-fit) and linearized (SH-plot) form is used to analyse the corrosion kinetics and mechanisms. Also, the isoconversional method (ICM) is used to gain further insight into the acceleration mode of the sulfur induced corrosion, see chapter 3.7.6. In this chapter, the time at 10 wt% Cu-wire conversion was chosen for the ICM. This ensured a reliable analysis of the experimental data as the incomplete filling and inhomogeneous distribution of **TT** in the capillary can lead to unreliable conclusions in the later conversion stages. Finally, the obtained kinetic parameters from JMAEK-fit, SH-plot and ICM are used to generate the Arrhenius plot. Hence, the activation energy E_a is obtained from the Arrhenius plot.

10.4 Results and Discussion

10.4.1 Solvent Mediated Corrosion Effects

Herein, PC and DMSO are used to study solvent mediated effects on sulfur induced Cu corrosion. These solvents are chosen due to their ability to dissolve **TT** in relatively high amounts and their high boiling point. The key parameters for both solvents and a comparison to acetonitrile (AN) and sulfolane is shown in **Table 10.2**.

Table 10.2: Key parameters for the solvents PC, DMSO, sulfolane and AN.

Solvent	Boiling point / °C	Dielectric constant / Fm^{-1}	Dipole moment / D	Classification
PC	240	65	4.9	polar aprotic
DMSO	189	47	3.96	polar aprotic
Sulfolane	285	43	4.35	polar aprotic
AN	82	38	3.92	polar aprotic

Hence, the APC wire was measured at 250-200 °C with pure solid **TT**, liquid **TT**/PC suspension, and liquid **TT**/DMSO solution. Note that the bare Cu wire was solely measured with pure solid **TT** for a comparison to the APC wire.

At 250 °C, the pure solid **TT** results in a severe corrosion of both Cu and APC wire where approximately 10 wt% Cu remains after 5 h, see **Figure 10.1a**. Whereas PC slows down the APC wire corrosion significantly with ≈ 60 wt% after 5 h. The corrosion of the APC wire decreases even more when DMSO is used as solvent with ≈ 70 wt% after 5 h. However, the corrosion of the APC wire with **TT**/DMSO halts at approximately 70 wt%. This is observed at both 250 and 200 °C. Theoretically, the sulfur content in this solution should result in a complete APC wire corrosion to Cu_2S . Hence, two assumptions are feasible. First, the incomplete dissolution of **TT** in DMSO which yields a much lower concentration of **TT** and subsequently to a maximal conversion up to 70 wt%. Second is the formation of a passivation layer in combination with DMSO which prevents further corrosion of the bond wire. However, the abrupt end of the corrosion reaction rather points to a low concentration of **TT** in DMSO because some degree of corrosion is still expected for a passivation layer. Also, the formed β - Cu_2S layer in general exhibits no passivating properties.

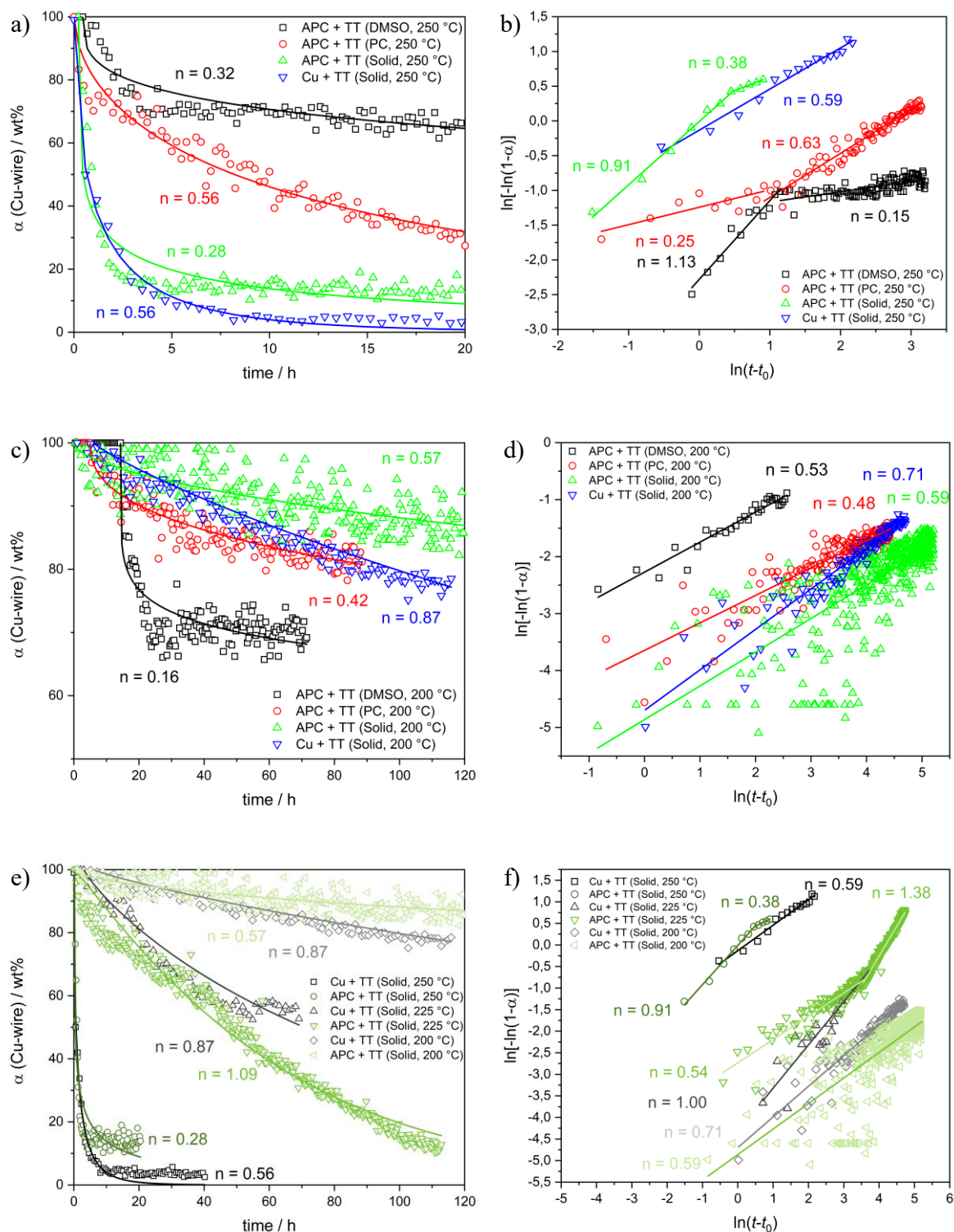


Figure 10.1: a) α -t plots and JMAEK-fit of APC+TT (DMSO, PC, solid) and Cu+TT (solid) at 250 °C b) corresponding SH-plot, c) α -t plots and JMAEK-fit of APC+TT (DMSO, PC, solid) and Cu+TT (solid) at 200 °C d) corresponding SH-plot e) α -t plots and JMAEK-fit of APT+TT (solid) and Cu+TT (solid) from 250-200 °C. f) corresponding SH-plot

Hence, the JMAEK-fit over the whole reaction range must be treated with caution. Yet, the JMAEK-fits are performed to get first insights into the corrosion kinetics with different solvents. Therein, the α - t plots of Cu and APC wire at 250 °C display a parabolic behaviour with Avrami exponents in the range $n = 0.28$ - 0.56 . This indicates a diffusion-controlled (D) corrosion behaviour for solid **TT**, PC, and DMSO mixtures. A detailed look at the corrosion mechanism at 250 °C via the SH-plot reveals similar progression for Cu (solid), APC (solid), and APC (DMSO), see **Figure 10.1b**. Therein, Cu (solid) presumably starts with an interface-controlled mechanism (see chapter 9.4.4). Hence, all three exhibit an interface-controlled (R) mechanism ($n = 0.91$ - 1.13) which then merge into diffusion-controlled mechanisms. Contrary to that, the PC mixture displays a much lower Avrami exponent of $n = 0.25$ and subsequent increase to $n = 0.63$. This could be attributed to the good wettability of PC on Cu surfaces which could inhibit the β -Cu₂S nucleation.²⁴² After adequate β -Cu₂S nuclei formed, the wetting of PC on the surface reduces and the corrosion rate increases.

However, a change in the corrosion mechanism (mostly diffusion, D) does not take place but a significant increase of the corrosion rate for the pure solid **TT**. Therefore, it is concluded that the solvent does not change the corrosion mechanism itself but rather impedes the interaction of the thiol with the Cu surface. Thereby, the PC and DMSO can solvate **TT** which slows down the corrosion. Further, PC and DMSO may stabilize decomposition products and radicals which otherwise could immediately react on the Cu surface. Also, anodic dissolution of Cu⁺ is different in various solvents. Related investigations determined an increasing Cu dissolution in the solvents: sulfolane > PC > AN.^{243,244} Herein, it is assumed that sulfolane and DMSO behave relatively similar. Hence, the lower Cu⁺ dissolution in sulfolane/DMSO could explain the enhanced corrosion rate of **TT**/PC compared to **TT**/DMSO.

Strikingly, the reverse trend is observed at 200 °C, see **Figure 10.1c**. Therein, the corrosion susceptibility increases in the order: APC (solid) < Cu (solid) < APC (PC) < APC (DMSO). Further analysis with the SH-plot yields the same results with Avrami exponents in the range $n = 0.48$ - 0.71 , see **Figure 10.1d**. Hence, the transition from an interface/diffusion at 250/225 °C to a pure diffusion mechanism at 200 °C, see **Figure 10.1e,f**. This is in line with the powdery mixtures of Cu with **TT** which also utilized the pure solid **TT**, see chapter 7.4.1. Hence, the general reactivity of the triazole at the respective temperature dictates the overall corrosion mechanism with slight differences between the Cu and APC wire. Yet, the solvent can influence the corrosion rate.

Therein, the temperature reduction from 250 to 200 °C leads to lower **TT** decomposition.^{29, 54, 60, 73, 74} This consequently results in a much lower corrosion rate of the pure solid **TT** with Cu and APC bond wire. Therefore, it is concluded that the primary driving force for copper sulfide formation is the decomposition of the triazole-thiole. Here, **TT** presumably undergoes a unimolecular decomposition to form SH• radicals, H₂S, and HN=C=S (see **Figure A 7.9**).²⁴⁵ As a consequence, the gaseous decomposition products form slower at 200 °C and may diffuse away from the reactive zone. This especially can occur if a temperature gradient is present in the capillary. This phenomenon is not as pronounced at higher temperature due to the higher overall amount of decomposition products.

This is due to the vapor pressure of solid **TT** and its decomposition product which is much lower at 200 °C compared to 250 °C. Therefore, diffusion is impaired towards the reactive surface which in turn results in a much lower corrosion rate.

Though the solvents PC and DMSO could impede the corrosion reaction by solvation, they could also stabilize the decomposition products to yield a higher amount of reactive species. Additionally, a high amount of **TT** is dissolved in PC or DMSO at 200 °C. This enables a readily diffusion of **TT** towards the surface within the solvent. Thereby, the wire surface can exert catalytic capabilities to produce copper sulfide and **TT** decomposition products. Hence, it is concluded that at high temperature decomposition of solid **TT** prevails, and at lower temperature dissolution effects become predominant. Thus, an increased corrosion rate is observed for the solutions at lower temperatures. Strikingly, the incubation time increases up to 20 h with the **TT**/DMSO mixture at 200 °C. A prolonged incubation time is even observed at 250 °C for the **TT**/DMSO mixture. After the incubation, the Cu wire undergoes a fast degradation. From literature it is known that DMSO can act as oxidant for disulfide formation.²⁴⁶ This is even more pronounced at higher temperatures. Hence, at high temperatures such as 250 and 200 °C DMSO could oxidize **TT** to yield the corresponding disulfide. This can explain the instantaneous corrosion after the incubation time. At this point presumably most of **TT** is converted to the disulfide. Hence, the disulfide may lead to a fast corrosion.

In **Table 10.3** an overview of the derived models for Cu an APC wire with **TT** in combination with different solvents and various temperatures is given. For further details see **Table A 10.1-4**.

Table 10.3: Summary of the assumed mechanism for APC and Cu wire with **TT** in combination with different solvents which is derived from the combinatorial kinetic analysis.

Wire	APC (DMSO)	APC (PC)	APC (Solid)	Cu (Solid)
T / °C	250	250	250	250
Summary				
Assumed Mechanism	R1 → D3	D3, Anti-D3	R1 → D3	D3, Anti-D3
Wire	APC (DMSO)	APC (PC)	APC (Solid)	Cu (Solid)
T / °C	200	200	200	200
Summary				
Assumed Mechanism	D3	D3	D1, Anti-D3	D – R, F2
Wire	APC (Solid)	APC (Solid)	APC (Solid)	APC (Solid)
T / °C	250	225	225	200
Summary				
Assumed Mechanism	R1 → D3	D3 → Anti-R3	D3 → Anti-R3	D3
Wire	Cu (Solid)	Cu (Solid)	Cu (Solid)	Cu (Solid)
T / °C	250	225	225	200
Summary				
Assumed Mechanism	D3, Anti-D3	D – R, F2	D – R, F2	D – R, F2

10.4.3 Temperature Effects on Corrosion Acceleration of Solid, PC, and DMSO Mixture

To further investigate the solvent mediated effects on Cu corrosion, the rate constants are determined from the SH-plot, JMAEK-fit, and ICM. Eventually, the obtained values $\ln k$ are plotted versus $1/T$ at 250/225/200 °C to obtain the Arrhenius plots, see **Figure A. 10.1**. Then the activation energies E_a are calculated from the obtained slopes of the Arrhenius plots. Note that only two measurements at 250 and 200 °C were performed for the **TT**/DMSO mixture. However, the **TT**/DMSO mixture is still included into the analysis to gain first insights into the temperature induced acceleration of solvent mediated corrosion.

Finally, the obtained activation energies E_a are given in **Figure 10.2**. Therein, the mean activation energies for the APC wire increase in the order DMSO (1.4 ± 0.4 eV) < PC (2.0 ± 0.2 eV) < solid (3.2 ± 0.5 eV). Whereas the bare Cu wire displays a lower mean activation energy with solid **TT** (2.8 ± 0.4 eV) compared to the APC wire. Moreover, the SH-plot and the JMAEK-fit are consistent but with the t_{10} values of the ICM as an exception. Therein, the bare Cu exhibits a higher activation energy than the APC wire. This is due to the comparably small increment of Cu conversion whereas the JMAEK and SH method evaluate the whole conversion range. As mentioned before, the incomplete filling and inhomogeneous distribution of **TT** in the capillary can lead to affected rate constants from the later conversion stages. This consequently may lead to altered activation energies for the JMAEK and SH method. Nevertheless, similar trends are observed for all evaluation methods which is the increase of the activation energy from solvent mediated to pure solid **TT** corrosion.

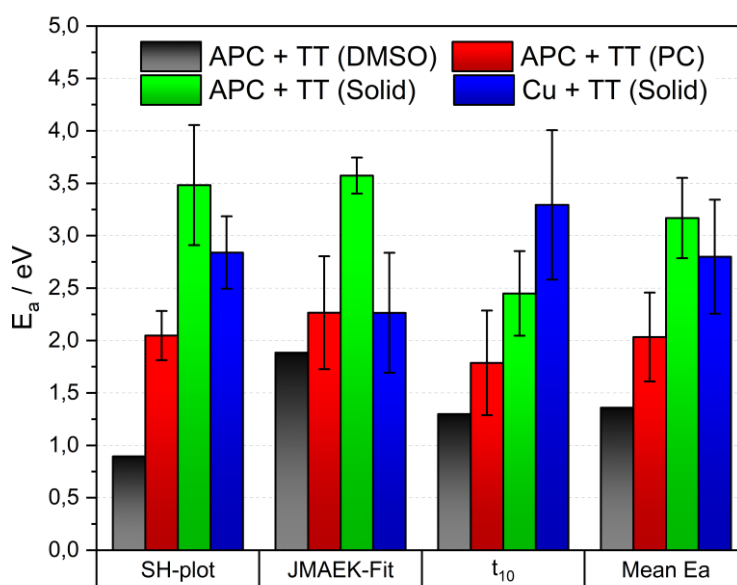


Figure 10.2: Obtained activation energies E_a from SH-plot JMAEK-fit and ICM (time at conversion = 10 wt%) and mean value. Here for the pure solid **TT** with Cu and APC wire as well as APC with **TT**/PC and **TT**/DMSO mixture.

Further, the activation energies for solid **TT** commute between 2.25-3.6 eV. Note that for diffusion-controlled mechanisms typical activation energies less than 1 eV are expected, while for interface-controlled mechanisms activation energies above 1 eV are anticipated. Hence, these high activation

energies underline the predominant role of the chemical reaction which leads to the decomposition of **TT** and formation of β -Cu₂S. Thereby, activation energies ranging from 2.3-2.9 eV have been determined for the thermal decomposition of ethyl mercaptans, benzyl mercaptans, and benzyl sulfides.^{247, 248} Hence, the activation energies of the thermal decomposition for mercaptans coincides with the determined activation energies for Cu and APC wire corrosion with solid **TT**. Therein, the higher activation energy for the APC wire can be explained by the poorer ability of the Au surface to cleave the C-S bond compared to the Cu surface.⁶⁷ Consequently, the activation energy rises because more energy is needed to cleave the C-S bond.

Whereas for the Au surface it was hypothesized that it favours disulfide formation which may be more pronounced in solution. Due to the enhanced diffusivity of **TT** in solution compared to diffusion of solid **TT** in the gas phase, **TT** molecules can more easily approximate each other on the Au surface to yield disulfide. This can especially occur in **TT**/DMSO solution as DMSO can oxidize thiol to form disulfide.²⁴⁶ Compared to thiol decomposition, lower activation energies in the order of ≈ 1 -1.2 eV have been determined for the decomposition of dimethyl disulfide.²¹⁴ This is approximately in the same order of magnitude as the activation energy for the APC wire corrosion with **TT**/DMSO (1.4 ± 0.4 eV). Whereas disulfide formation presumably is not as pronounced in the **TT**/PC mixture. Thus, the activation energy for the **TT**/PC mixture lies in between the solid **TT** and the **TT**/DMSO mixture.

10.5 Conclusion

In this chapter, Cu and APC wire was measured at 200 °C and 250 °C with pure solid **TT**. It was found that the corrosion mechanism transforms from mixed interface- and diffusion-control at 250 °C towards pure diffusion control at 200 °C. This is in line with the powdery mixtures from chapter 7.4.1. The same trend is observed for the APC wire with **TT**/DMSO and **TT**/PC mixtures from 250 °C to 200 °C. The subsequent evaluation of the obtained rate constants reveals an increasing activation energy in the order: APC (**TT**/DMSO) < APC (**TT**/PC) < Cu (solid **TT**) < APC (solid **TT**). It was hypothesized that disulfide formation on the Au surface is especially pronounced in solution and DMSO. Thus, the activation energy decreases due to the easier S-S bond cleavage. Note that the sulfoxide DMSO was shown to be stable versus bare Cu wire at 250 °C, see chapter 8.4.4. Additional influence can be exerted by the solvation of **TT** and its transitional decomposition products which also can lower the activation energy. As a consequence of the high activation energies, solid **TT** corrosion is heavily accelerated at higher temperatures which leads to detrimental Cu core corrosion. The reverse trend is observed for the **TT**/PC and **TT**/DMSO solutions. For the solutions, a high corrosion rate is observed at 200 °C but the lower activation energy results in a slower acceleration of the corrosion rate at high temperatures.

Hence, it is shown that dissolution of **TT** in PC or DMSO, which served as “dummy matrices”, can influence corrosion rates and activation energy for Cu bond wire corrosion. Thereby, the solvents PC and DMSO can induce changes in solvation (stabilization, hindrance of decomposition products),

diffusion (liquid vs. solid), wetting (formation of SAMs) and catalytic capabilities (pH-value). However, these experiments served as a first approach to gain first insights into solvent mediated effects, but the detailed solvent and polymer mediated effects are beyond the scope of this work. Nevertheless, it is demonstrated that different environments and mobility of the adhesion promoter can influence the corrosion behaviour. Therefore, it is substantial to gain further understanding of MC mediated effects.

Contrary to the wire-**TT** mixtures, the bond wires are surrounded by solid MC after the package assembly. Therefore, “classical” solvent mediated effects are unlikely to occur in the package. However, similar effects like stabilization of transition products and decomposition products by the surrounding polymer-matrix of the MC can heavily influence the corrosive behaviour of the package. A possible mean to investigate this is to combine specific adhesion promoters with well-defined polymer matrices and systematically compare reactivity and corrosion rates. However, framework conditions like viscosity (liquid, viscous, solid), pH-value and adhesion promoter should be kept constant as these can affect the corrosion behaviour as shown above. Therein, pH-value is another important feature which could heavily influence the catalytic capability of the MC to decompose the adhesion promoter. Thus, it is relevant to methodically investigate pH effects with consistent polymer matrix-adhesion promoter mixtures. Also, various adhesion promoters must be studied in combination with an invariable polymer matrix to further understand the influence of the MC. Hence, it is important to strictly separate the individual parameters to avoid superimposition of different effects and to define clear correlations of individual ingredients of the MC on the corrosion behaviour.

Further, the actual wetting of the bond wire surface with adhesion promoter can be affected during the molding process and the polymer matrix. This can lead to similar effects as observed with the **TT/PC** and **TT/DMSO** mixtures, where the formation of continuous SAMs is presumably impaired by the solvent. Thus, the concentration and mobility of the adhesion promoter within the MC especially during the molding process is an important aspect. For instance, higher concentration and mobility of the adhesion promoter during the molding process yields homogeneous SAMs and vice versa. Yet, a well-formed SAM can induce enhanced sulfur corrosion but also improves adhesion of the MC towards the metallic parts. The mobility of the adhesion promoter could be modified by the viscosity of the MC during the molding process to yield the desired outcome.

Another crucial aspect is the mobility of the adhesion promoter within the cured and solid MC. From the **TT** experiments as solid, PC, and DMSO solution it is shown that the diffusion not only of the adhesion promoter but also its decomposition product in the gas and liquid phase can play a significant role during the bond wire corrosion. Therefore, it is crucial to define clear temperature regimes for the decomposition of the individual adhesion promoters as the diffusivity of the adhesion promoter can vary considerably from its decomposition products. Also, the mobility of the individual adhesion promoters must be systematically investigated for different MCs. Another strategy to investigate adhesion promoter diffusion in detail is to use well-defined polymer matrices to specifically tune the matrix towards the desired properties.

11 Grain Growth and Reorientation in APC Bond Wire

11.1 Abstract

In this chapter, APC bond wire is measured by HT-in situ-PXRD at 225 °C, 250 °C, and 300 °C while incorporated into MC. Then, EBSD micrographs are performed on the cross-sections of the bond wires after the PXRD measurement to analyse the microstructure of the bond wire. Thereby, it is shown that the microstructure changes upon annealing above 225 °C. Closer inspection of the determined integral intensities obtained from the PXRD measurement revealed a sigmoidal and parabolic decline of the Cu(200) reflection at 250 °C and 300 °C, respectively. Hence, two different grain growth and reorientation kinetics are observed, depending on the respective temperature. Further analysis by EBSD and *LF* shows that different grain orientation distributions are obtained at 250 °C and 300 °C. Thus, in addition to different grain growth kinetics, varying orientation distributions are obtained with different temperatures. Finally, potential risks and prevention strategies are discussed.

11.2 Introduction

As mentioned above, adhesion promoters decompose at elevated temperatures and the risk for sulfidation reaction with Cu bond wire rises. However, the decomposition of adhesion promoters is known to strongly increase at temperatures above 150 °C which may not be a realistic temperature profile for real semiconductor applications. Hence, the question arises if additional mechanisms play a role if temperatures above 150 °C are applied to accelerate stress tests. In addition to enhanced decomposition of S-compounds above 150 °C, grain growth and grain reorientation may occur at elevated temperatures. As the grains grow, the Cu bond wire exhibits altered bulk and surface properties. Thus, grain growth leads to changes in the grain boundary density, orientation, and residual stress. As the grain boundaries have higher energies than the bulk, they are more prone to chemical reactions. Therefore, an altered grain boundary density leads to a change in the corrosion resistance of the surface which is usually accompanied by increased electron activity and diffusion. Previous investigations on Cu bond wire and Cu films showed that grain growth already occurs at annealing temperatures in the range $\approx 300\text{--}400$ °C.^{249, 250} Further investigations regarding the corrosion susceptibility of Cu with different grain sizes revealed better corrosion resistance for ultrafine-grained Cu compared to coarse-grained Cu.²⁵¹ Also, it is known from various Fe-, Zn-, Cu-, Ni-, and Cu-Ni-alloys in the literature that a change in grain size affects the corrosion resistance and corrosion mechanisms.²⁵² As high stress test temperatures such as 225 and 250 °C are used, grain growth is more likely to occur. As mentioned, this can drastically alter the corrosion behaviour of Cu bond wires. Thus, the aim of this chapter is to investigate grain growth and reorientation at annealing temperatures in the range 225–300 °C.

11.3 Experimental

11.3.1 APC Bond Wire HT-in situ-PXRD Measurements with Cured MC

All experiments were performed with bond wires with 50 μm diameter. Here, Pd-coated Cu with a flash-Au layer (APC) is used as received from the manufacturer, for details see chapter 4.2.1. Also, the uncured MC was ground in a planetary ball mill for 8 cycles, each for 5 min at 700 rpm. To exclude unwanted side reactions during this procedure, the obtained fine powder was checked via PXRD after milling. Then, the capillary was filled with 4 bond wires and the ground and uncured MC. All steps were performed under an inert nitrogen atmosphere. After the capillary was filled with the wires and the reagent, the capillary was evacuated prior to use and flame-sealed under vacuo. Finally, the capillary was preheated to 150 $^{\circ}\text{C}$ and annealed for 30 min to cure the MC. Subsequently, the capillary was heated to the experimental conditions (225/250/300 $^{\circ}\text{C}$) and held there isothermally.

11.3.2 Isothermal HT-in situ-PXRD Measurements

HT-in situ-PXRD was used as standard method to characterize the reaction products and to follow the corrosion process. For device specific details, see chapter 4.1.2. Further, Mo- $K_{\alpha 1}$ ($\lambda = 0.70930 \text{ \AA}$) radiation was used for all samples and measured in Debye-Scherrer geometry in a silica capillary. Also, the measurements were conducted at 225-300 $^{\circ}\text{C}$ under isothermal conditions. In all experiments of APC bond wire with cured MC, the powder patterns solely comprise the Cu and amorphous SiO_2 phase. Hence, the quantification of the Cu phase is redundant as only Cu reflections are present in the powder pattern. Also, it is important to note that no corrosion products are visible in the powder pattern.

11.3.3 EBSD Measurements and Lotgering Factor LF

To gain further information on the grain size distribution and grain orientation, electron backscatter diffraction (EBSD) was performed before and after the HT-in situ-PXRD measurements. Here, an EDAX Pegasus EDX/EBSD-system attached to a Zeiss Ultra 55-FE-SEM microscope was used in combination with a Hikari XP EBSD Camera. The EBSD analyses were performed at Infineon Technologies AG in Regensburg.

Also, the LF for the individual Cu reflections was determined from HT-in situ-PXRD measurements to complement the EBSD measurements and to further analyse the grain growth kinetics. For details see chapter 3.6.

11.4 Results and Discussion

Preceding HT-in situ-PXRD experiments revealed a strong variation of the Cu(111), (200), and (202) intensities in the powder pattern of the APC wire even with non-reactive reagents. Such strong variation in the Cu intensities is not observed for the bare Cu, PCC, and APCX wire. Hence, APC wire was selected as subject for further investigation. To investigate this phenomenon and to simulate package conditions, HT-in situ-PXRD measurements on APC bond wire in MC environment were conducted at 225 °C, 250 °C and 300 °C. Therein, the PXRD measurement at 225 °C for 71 h exhibits constant intensities over the whole measurement, see **Figure 11.1a**. Hence, no grain growth or reorientation is observed at 225 °C. This is also confirmed by EBSD analysis on the cross-sections of the APC bond wire which displays no change after the measurement.

Contrary to that, the PXRD measurement at 250 °C exhibits a continuous intensity decrease of all three Cu reflections over 96 h, see **Figure 11.1b**. Thereby, the strongest decline is measured for the Cu(200) reflection and a small decrease for the Cu(111) and Cu(202) reflections. A comparison of the EBSD micrographs of initial bare Cu and annealed APC wire reveals even larger grain size for the annealed APC bond wire and preferred grain orientation distribution. Herein, the grains preferably adopt the Cu(313) orientation for the annealed APC wire. This is a significant modification of the APC bond wire at 250 °C. Thus, the APC bond wire could display significant differences in corrosion resistance compared to a wire below 250 °C which consists of the initial grain size distribution and orientation. This is among other factors due to the altered grain boundary density which decreases with bigger grain sizes. Hence, grain boundary diffusion could be oppressed, and bulk diffusivity becomes more important. Also, the grain boundary angles change with grain reorientation which leads to a change in the grain boundary energy. Therefore, different angles result in an altered reactivity towards corrosive reagents.²⁵³ However, no clear evidence is found in literature if a bigger grain size leads to better corrosion resistance.²⁵²

Further temperature increase of the APC bond wire with MC up to 300 °C exponentially accelerates grain growth and reorientation, see **Figure 11.1c**. Compared to 250 °C, the grain growth and reorientation is mostly completed after ≈ 3 h. Also, the Cu(111) reflection stays constant in the PXRD measurement while Cu(202) exhibits a small decrease and Cu(200) a very strong decline. Further inspection via EBSD after the PXRD measurements reveals large grain sizes and reorientation of the annealed APC bond wire. Strikingly, a different grain orientation distribution is detected after the PXRD measurement at 300 °C compared to 250 °C. Thereby, annealing at 300 °C predominantly yields Cu(111) and Cu(001) orientations. This is similar to the initial PCC bond wire, see chapter 4.2.1. The varying grain orientation distribution at 300 °C and 250 °C in turn results in a greater complexity of the system. This presumably leads to an altered corrosion resistance of the APC bond wire at different temperatures as the grain size and orientation varies with temperature. Hence, different grain boundary angles will result from varying grain orientation distribution and thus to an altered reactivity and diffusivity of the grain boundaries as well as an altered reactivity of the wire surface.

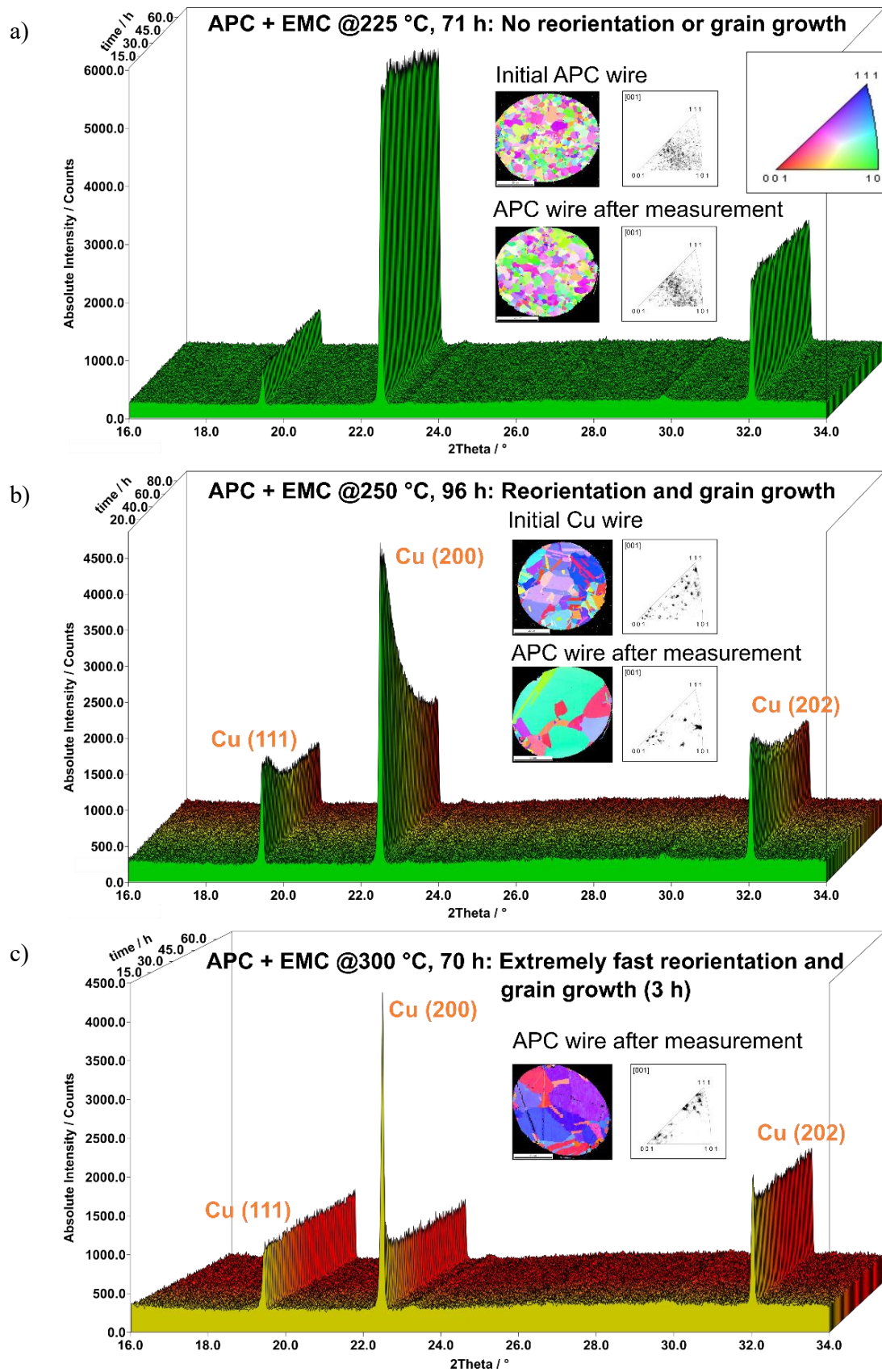


Figure 11.1: HT-in situ-PXRD and EBSD measurements of APC bond wire with cured MC at a) 225 °C, b) 250 °C, and c) 300 °C. At 225 °C no grain growth and reorientation is displayed. Whereas the measurement at 250 °C reveals significant grain growth and reorientation. This is even more pronounced at 300 °C.

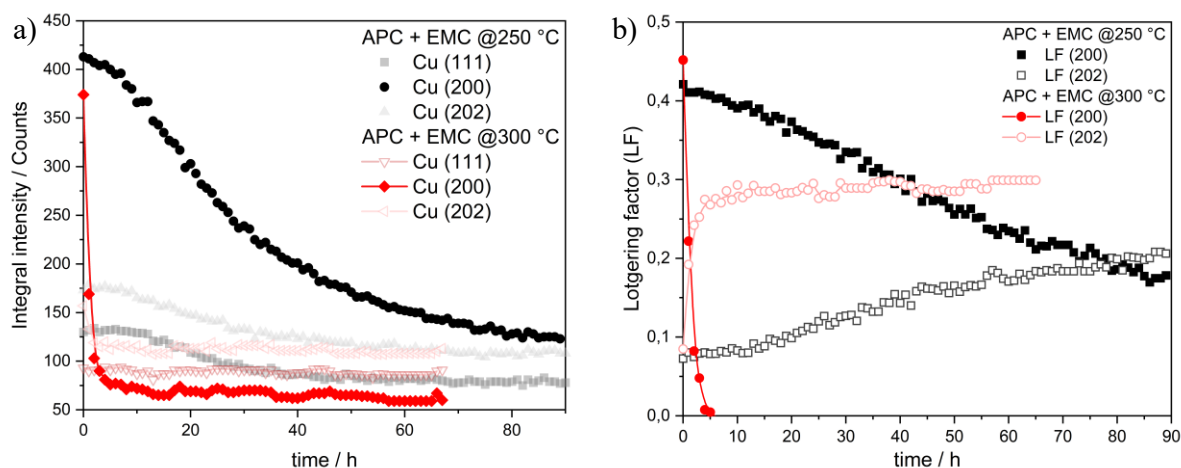


Figure 11.2: a) Intensity progress of the respective Cu reflections of the APC bond wire at 250 and 300 °C. Here, the Cu(200) reflections are highlighted as the strongest intensity decrease is observed for this reflection. Therein, a sigmoidal curve is measured at 250 °C and a parabolic behaviour at 300 °C. b) *LF* progress of the individual Cu reflections of the APC bond wire relative to a random distributed Cu powder. As the Cu(200) reflection decreases, the Cu(202) becomes the dominant reflection relative to the other individual reflections.

After the PXRD measurement, the integral intensities were determined to further investigate the grain growth and reorientation process, see **Figure 11.2a**. Therein, the Cu(111) and Cu(202) reflections undergo small changes compared to the Cu(200) reflections at 300 °C and 250 °C respectively. Hence, only the Cu(202) reflections are considered for further discussion. At 250 °C the Cu(202) displays a sigmoidal decrease of the integral intensities. This is indicative for a nucleation and growth-controlled process. Note that a theoretical JMAEK-fit of the normalised integral intensities from 0 to 100 yields an Avrami exponent of $n \approx 1.40$. This exponent can be achieved by a three-dimensional, diffusion-controlled nucleation and growth with pre-existent site saturation which complies to spherical particles growing from small dimensions.¹³⁵ Hence, a grain growth and reorientation process known from sintering and Ostwald ripening.

Whereas the grain growth and reorientation process at 300 °C follows a parabolic behaviour. Here, a theoretical JMAEK-fit of the normalised integral intensities from 0 to 100 yields an Avrami exponent of $n \approx 0.60$. This fits well with a one-dimensional, purely diffusion-controlled process which corresponds to fast grain boundary diffusion as well as predominant growth of grain boundary particles.¹³⁵ Compared to 250 °C the nucleation process does not dictate the growth kinetics but rather the diffusion of Cu ions. Thus, both processes at 250 °C and 300 °C are linked by diffusional processes but the rate limiting step varies.

This is also confirmed by a plot of the *LF* versus time, see **Figure 11.2b**. Therein, the Cu(200) reflection also displays sigmoidal and parabolic decline at 250 °C and 300 °C respectively. Further, the continuous plot of the *LF* also reveals a mirrored increase of the Cu(202) reflection relative to the Cu(200) reflection. This is expected as shrinking and growing grains are linked by the reorientation process. However, the Cu(202) intensity at 300 °C is higher than the Cu(202) intensity at 250 °C which points to the varying grain orientation distribution which is in line with the EBSD micrographs.

11.5 Conclusion

In this chapter, grain growth and reorientation were confirmed to take place above 225 °C by HT-in situ-PXRD and EBSD analysis. Closer inspection of the determined integral intensities obtained from the PXRD measurement revealed a sigmoidal and parabolic decline of the Cu(200) reflection at 250 °C and 300 °C, respectively. Hence, two different grain growth and reorientation kinetics are observed, depending on the respective temperature. Further analysis by EBSD and *LF* shows that different grain orientation distributions are obtained at 250 °C and 300 °C. Thus, in addition to different grain growth kinetics, varying orientation distributions are obtained at different temperatures.

As stress tests at elevated temperatures such as 250 °C are employed, grain growth and reorientation effects become crucial factors because they can completely alter corrosion behaviour. Note that grain growth is predominantly observed for the APC bond wire. Hence, high temperature stress testing at 250 °C for the APC bond wire is critical as the grain size and grain orientation distribution alters from realistic mission profiles ($T < 150$ °C). There, the corrosion resistance depends on grain size, grain orientation, grain boundary angles, and grain boundary density.²⁵⁰⁻²⁵³ These parameters affect the bulk and surface properties as well as the grain boundary energies. As a consequence, these changes modify the electrochemical behaviour of the bond wire and therefore affect corrosion susceptibility. Consequently, thorough investigation is necessary prior to the high temperature stress tests to exclude grain growth and reorientation effects.

In the literature no clear evidence is found whether small or large grains show better corrosion resistance.²⁵² In general, the corrosion behaviour of Cu samples was found to transition from uniform to localized IGC for fine-grained and coarse-grained Cu, respectively.^{251, 254} Hence, bond wires with small grain size distribution are expected to show more uniform corrosion compared to bond wires with large grain sizes. This also means that bond wires with large grain sizes exhibit a higher risk for IGC which consequently leads to a more localized corrosion. Another factor which increases the probability of IGC is the segregation of impurities. As observed for grain growth and reorientation, heat treatment may result in an additional segregation of impurities or dopants towards the grain boundaries. Hence, corrosion phenomena such as pitting corrosion are more likely to occur which especially poses a high risk for sulfur induced degradation of thin stitch bonds.

However, grain growth and grain reorientation strategies also present an opportunity to improve the corrosion resistance without the introduction of additional coatings or dopants into the system. The advantage of a grain microstructure improvement strategy is to move from a complex metallurgical system (e.g. APCX = Au-Pd-Cu-Ni-Ga) with unpredictable alloying and corrosion products towards a “simplistic” Cu bond wire. Another upside is that GBE could improve the general corrosion resistance of the Cu bond wire in various corrosive environments: recent studies showed that GBE can be specifically used to modify grain boundaries and also to predict IGC resistance.^{253, 255} Furthermore, it has been found that GBE technology can drastically improve the corrosion resistance

of Cu against sulfur induced corrosion by dibenzyl disulfide.²⁵⁶ It is hypothesized that the introduction of a larger number of twin grain boundaries can terminate diffusion and percolation channels. Consequently, the impaired diffusivity within the grain boundaries leads to a better corrosion resistance. This again demonstrates the importance of grain boundary diffusivity which seems to be the essential aspect of Cu wire corrosion.

With this knowledge in mind, a thorough investigation of the grain boundary connectivity and diffusion pathways for the respective wire types could provide vital information to understand the corrosion susceptibility of the different wire types. Hence, information on grain boundary connectivity and diffusion pathways can then be used to specifically modify the bond wires by GBE technology. Additionally, further research on grain size and annealing effects could provide crucial knowledge to improve the corrosion resistance of the bond wires.

12 Temperature Induced Acceleration of Sulfur Facilitated Corrosion

12.1 Abstract

In this chapter, the Cu, PCC, APC, and APCX bond wire is measured isothermally via HT-in situ-PXRD in combination with **DS** at 250 °C, 225 °C, 200 °C, and 175 °C. Afterwards, the corrosion rates are determined from the kinetic analysis and the generated Arrhenius plots. The obtained activation energies E_a are then discussed for the respective bond wire. To further investigate the long-term corrosion behaviour, HTS at 150 °C was performed for the 4 bond wires with **DS**. The same procedure was conducted with Cu and APC bond wire **MS1**. For this, HT-in situ-PXRD measurements are performed at 250 °C, 225 °C, 200 °C, and 175 °C with subsequent kinetic analysis. Then the Arrhenius plots are analysed, and the slopes are discussed with regard to the obtained activation energies E_a . Accordingly, long-term storage at 150 °C and 175 °C was performed for Cu and APC bond wire with **MS1** and **TT** and compared to the measurements at higher temperatures. Finally, the experiments of the various bond wires with **DS**, **MS1**, and **TT** are compared to each other and discussed with regard to their temperature dependant corrosion behaviour.

12.2 Introduction

As mentioned before, the harsh environments for automotive applications are simulated with highly accelerated temperature and humidity stress tests to check for device fatigue by thermomechanical, humidity, or temperature related failure mechanisms. For instance, temperatures above 150 °C are applied to accelerate corrosion related processes. Within the scope of these tests, sulfuric adhesion promoters proved to be detrimental for Cu bond wire reliability. Therefore, “the paradoxical role of sulphur in molding compounds” was reported by *Mavinkurve* et al. as they are crucial elements for the adhesion of the MC to the metal surface but also initiate corrosion at harsher test environments.⁶⁰ This means that they can be a potential risk for extended mission profiles like AEC grade 0 and beyond. Since adhesion promoters decompose at elevated temperatures, the risk for sulfidation reaction with Cu bond wire rises. However, due to the high decomposition temperatures (>150 °C) the question arises if these failure mechanisms arise in actual application conditions. There, the temperature usually does not exceed 150 °C which may lead to false acceleration models for sulfur induced corrosion stress testing. Related investigations revealed that the total extractable sulfur content in MCs is hardly decreased after thermal ageing at temperatures such as 100 °C and 125 °C which implies a reduced liberation of corrosive sulfur species and thus negligible corrosion risk.^{29, 60} Hence, the goal of this chapter aims to resolve this question by identifying the respective corrosion mechanisms and to clarify if these mechanisms are related by a temperature dependency. To realize this, isothermal HT-in situ-PXRD and HTS is utilized at 150-250 °C on bare Cu, PCC, APC, and APCX bond wire in combination with selected adhesion promoters. Finally, a thorough kinetic analysis is performed to gain further knowledge of the related mechanisms and their temperature dependant behaviour.

12.3 Experimental

12.3.1 Cu Bond Wires with MS1 and DS at 250-175 °C

All experiments were performed with Cu bond wire with a diameter of 50 μm . These are bare Cu, PCC, APC, and APCX bond wire, for details see chapter 4.2.1. For the preparation of the bare Cu wire and experimental details see chapter 9.3.1. Further, the 4 different bond wires are measured either with **MS1** or **DS** at 250/225/200/175 °C, see **Table 12.1** for further details.

Table 12.1: List of all conducted isothermal HT-in situ-PXRD measurements.

Bond wire type	Organic sulfur compound	Abbreviation (S-compound)	T / °C	Molar ratio (wire:reagent)	Cu:S ratio
Cu	Mercaptosilane 1	MS1	250-175	1:0.8	1:0.8
APC	Mercaptosilane 1	MS1	250-200	1:0.8	1:0.8
Cu	Disulfide	DS	250-150	1:0.8	1:1.6
PCC	Disulfide	DS	250-175	1:0.8	1:1.6
APC	Disulfide	DS	250-150	1:0.8	1:1.6
APCX	Disulfide	DS	250-150	1:0.8	1:1.6

12.3.2 Isothermal HT-in situ-PXRD Measurements

HT-in situ-PXRD was used as standard method to characterize the reaction products and to follow the corrosion process. For device specific details, see chapter 4.1.2. Further, Mo- $K_{\alpha 1}$ ($\lambda = 0.70930 \text{ \AA}$) radiation was used for all samples and measured in Debye-Scherrer geometry in a silica capillary. Also, the measurements were conducted at 250 °C-175 °C under isothermal conditions.

In all experiments with **MS1** and **DS** at 250-175 °C, the powder patterns solely comprise a Cu and Cu₂S phase and minor amounts of Cu₃Pd. Hence, the DCM method is used to quantify the binary mixture. For further details, see chapter 3.5.3 and 3.5.4.

12.3.3 SEM and EDX Analysis

The PXRD measurements are complemented with SEM measurements, which were conducted at the University of Regensburg. Herein, the wires were analyzed after the HT-in situ-PXRD measurements. Therefore, the wires were removed from the capillaries and stored in a nitrogen glovebox under continuous nitrogen flow to dry the surface of the wires. Then, the SEM analysis was performed with a variable pressure aperture at 25 kV.

12.3.4 Kinetic Analysis and Activation Energy

Herein, the JMAEK equation in its exponential (JMAEK-fit) and linearized (SH-plot) form is used to analyse the corrosion kinetics and mechanisms. Also, the isoconversional method (ICM) is used to gain further insight into the acceleration mode of the sulfur induced corrosion, see chapter 3.7.6. Finally, the obtained kinetic parameters from JMAEK-fit, SH-plot and ICM are used to generate the Arrhenius plot. Hence, the activation energy E_a is obtained from the Arrhenius plot.

12.4 Results and Discussion

12.4.1 Corrosion Kinetics of Bare Cu Wire with DS at 250-175 °C

In the following sections, the quantified HT-in situ-PXRD measurements for **DS** with Cu, PCC, APC, and APCX bond wire at 250-175 °C are analysed for their corrosion kinetics. Therein, a fast degradation of bare Cu wire with **DS** at 250 °C is confirmed in chapter 8. Hence, it is selected as suitable reagent to explore the temperature dependent corrosion of the different wire types due to the faster acquisition time compared to other reagents. Note that all measurements led to the degradation of the bond wire and β -Cu₂S formation.

In **Figure 12.1a** the quantified PXRD measurement are displayed for bare Cu bond wire with **DS** at 250-175 °C. Thereby, the bare Cu wire exhibits a complete degradation after ≈ 8 h at 250 °C. Then, the degradation time increases to ≈ 20 h at 225 °C and further increase to ≈ 30 h at 200 °C. Further decrease of the temperature in turn yields an exponential rise of the degradation time to ≈ 140 h at 175 °C. Strikingly, all slopes follow a sigmoidal behaviour but with decreasing Avrami exponents from $n = 3.28$ at 250 °C to $n = 1.47$ at 175 °C, respectively. Thus, the overall corrosion kinetic is still governed by nucleation and growth (A2-A4, sigmoidal) but the individual parameters such as dimensionality ($d = 1,2,3$), interface vs. diffusion ($m = 1, \frac{1}{2}$), and nucleation rate ($a = 1, 0$) can vary depending on temperature. However, solely from HT-in situ-PXRD the individual parameters cannot

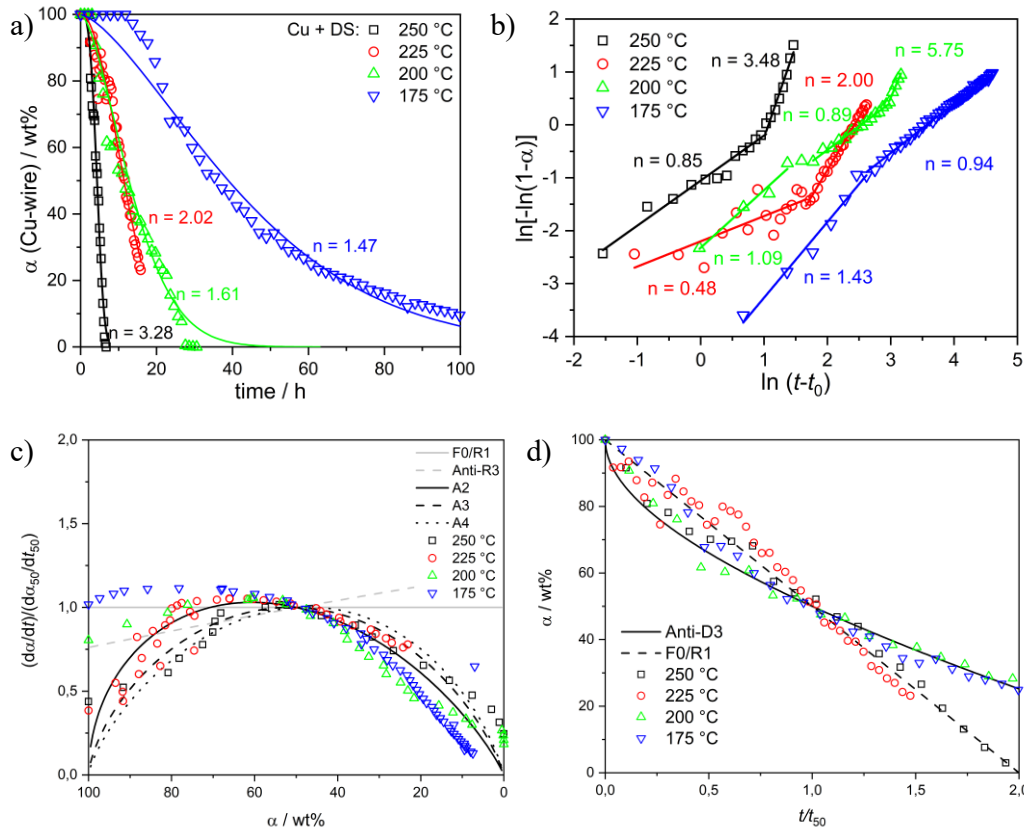


Figure 12.1: a) α -t-plots from the quantified HT-in situ-PXRD measurements of bare **Cu** bond wire with **DS** at 250-175 °C and the Avrami exponents n from the JMAEK-fit. b) SH-plot c) Master plot $f(\alpha)$ d) Master plot $g(\alpha)$.

be clearly distinguished as any combination of these can yield similar Avrami exponents ($n = d \cdot m + a$). Therefore, complementing methods are necessary to determine these parameters in detail. Closer inspection via the SH-plot reveals a more complex corrosion sequence, see **Figure 12.1b**. Therein, the corrosion mechanism at 250 °C and 225 °C is directed by mixed diffusion and interface control ($n = 0.85$) and pure diffusion ($n = 0.48$) control in the beginning, respectively. This changes at 200 °C and 175 °C where the Cu degradation is predominantly governed by interface control ($n = 1.09, 1.43$). Then, the slopes in the SH-plot increase at 250, 225, and 200 °C to exponents of $n = 3.48, 2.00$, and 5.75 respectively. These exponents point to a nucleation and growth-controlled mechanism. Hence, the degradation is first governed either by diffusion or interface control and then merge into a nucleation directed mechanism. Such a phenomena is also observed for the different bond wire with **MS1** at 250 °C. There, it is concluded that the acceleration and nucleation in the later stages of the degradation stem from an increased percolation of **MS1** into the core, see chapter 9.4.2. This is also likely to occur for **DS** where the fast sulfidation reaction could lead to a porous β -Cu₂S layer to enable percolation pathways. Interestingly, this is not observed at 175 °C, where the slope decreases from $n = 1.43$ to 0.94 after the initial Cu wire degradation. Hence, no nucleation and percolation of **DS** is supposed to happen in the Cu core. This can be explained by the slower sulfidation reaction at 175 °C which yields more homogeneous β -Cu₂S layers. Additionally, the lower vapor pressure at 175 °C reduces the percolation of **DS** (b.p. 189 °C) into the core compared to 250-200 °C. This is an important finding as percolation is also not supposed to occur in semiconductor packages. There, the mobility of the adhesion promoter is hindered by the polymer matrix and the filler particles. Hence, nucleation-based mechanisms of the Cu core are unlikely to occur in packages but rather Cu⁺ outward diffusion due to the produced β -Cu₂S layer. However, fast decomposition of the adhesion promoter at high temperatures and high vapor pressure of its decomposition products within the MC could also enable percolation of the gaseous reactants into the core. Thus, nucleation within the Cu core is more unlikely to occur in semiconductor packages but still should be regarded a potential degradation mechanism. Further analysis via the master plot $f(\alpha)$ confirms the nucleation and growth-controlled mechanisms, see **Figure 12.1c**. Also, the master plot $g(\alpha)$ shows that the ceasing corrosion stages are governed by interface mechanisms (R1) at 250 °C and 225 °C which transform to KE diffusion-controlled (Anti-D3) degradations at 200 °C and 175 °C, see **Figure 12.1d**. This again underlines that Cu⁺ outward diffusion at lower temperature becomes rate limiting instead of **DS** percolation and nucleation in the Cu core. Therefore, it is concluded that vapor pressure and mobility of the adhesion promoter and its decomposition products are important parameters to define possible reaction pathways and mechanisms. Thereby, elevated temperatures such as 250 °C pose a higher risk for percolation of gaseous reaction products through β -Cu₂S layers into the Cu core.

For an overview of all obtained rate constants and derived models see **Table A 12.1**. Note that the Arrhenius plots which are generated from the obtained rate constants are summarized in section 12.4.5.

12.4.2 Corrosion Kinetics of PCC Bond Wire with DS at 250-175 °C

Like the bare Cu bond wire, the PCC bond wire degradation displays a sigmoidal behaviour in the temperature range from 250 to 175 °C, see **Figure 12.2a**. Strikingly, the degradation behaviour at 250 °C and 225 °C is alike with no further acceleration at 250 °C and a complete conversion of the Cu core after ≈ 10 h. A further temperature decrease to 200 °C leads to an increased conversion time of ≈ 30 h. The conversion time then increases exponentially to ≈ 90 h at 175 °C. Thereby, no clear tendency is observed for the Avrami exponent which commutes between $n = 1.88$ -3.44. However, the sigmoidal behaviour of the degradation kinetics and the relatively high Avrami exponent indicate that nucleation and growth-controlled corrosion kinetics are the dominant processes. This is in line with the bare Cu wire where also nucleation and growth-controlled kinetics are confirmed. From chapter 8 it is known that the S-reagent dictates the overall mechanism, thus similar corrosion kinetics are expected for all bond wires. Hence, similar conversion times and kinetics from 250-200 °C are observed for the PCC and bare Cu bond wire. Whereas at 175 °C the conversion time and corrosion kinetic changes significantly for the PCC wire. There, the conversion time for the PCC wire is reduced from 140 h to 90 h compared to the bare Cu wire. This is a consequence of the altered corrosion kinetic, which instead of a deceleration in the case of the bare Cu wire, shows an acceleration of the corrosion kinetics in the later corrosion stages, see **Figure 12.2b**. Thus, the corrosion of the PCC wire

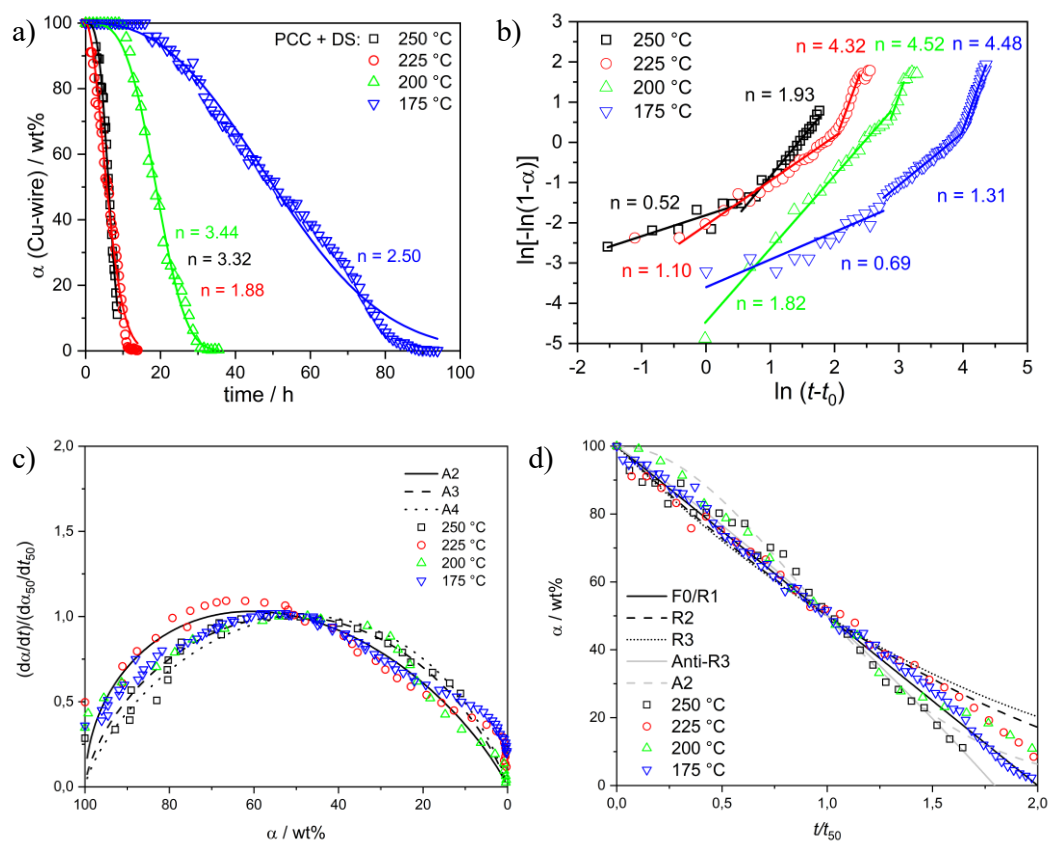


Figure 12.2: a) α - t -plots from the quantified HT-in situ-PXRD measurements of PCC bond wire with DS at 250-175 °C and the Avrami exponents n from the JMAEK-fit. b) SH-plot c) Master plot $f(\alpha)$ d) Master plot $g(\alpha)$.

accelerates in the later stages for the whole temperature range from 250 to 175 °C. Hence, the Pd-coating affects the corrosion mechanism at 175 °C compared to the bare Cu bond wire. First, the Pd-coating hinders the corrosion reaction at the surface due to the diffusion barrier for Cu ions. This presumably results in a slow and diffusion-controlled ($n = 0.69$ at 175 °C) creeping corrosion of β -Cu₂S along the wire surface, like the experiments with **MS1**. Thereby, the galvanic coupling of Cu/Pd can lead to a faster corrosion reaction at the damaged coating spots. This could lead to a more porous corrosion layer which then enables **DS** percolation at some point. Second, alloy formation of Cu_xPd could lead to the segregation of the Pd-coating which then allows the percolation of **DS** into the core. Additionally, Pd and Cu-Pd alloys could act as catalysts to enable easier S-S bond cleavage at 175 °C which subsequently leads to faster nucleation of β -Cu₂S. Contrary to that, the corrosion of the bare Cu wire presumably exhibits a more homogeneous layer at 175 °C which then acts as a diffusion barrier. Further, the Avrami exponents of the ceasing stages in the SH-plot of the PCC wire change from $n = 1.93$ (A2) at 250 °C to $n \approx 4.5$ (A4, P4) at 225-175 °C. This could indicate a mechanistical change from a 1-dimensional corrosion mechanism (A2) at 250 °C, towards a 3-dimensional mechanism (A4, P4) at 225-175 °C, where the nucleation and growth of small particles direct the corrosion kinetic.

Further analysis via the master plot $f(\alpha)$ underlines the nucleation and growth-controlled mechanisms in the whole temperature range, see **Figure 12.2c**. Therein, all measurements approximately follow an Avrami-model (A2-A4). However, a clear distinction between the model dimensions is not feasible from the experimental data. Also, the master plot $g(\alpha)$ shows that the normalized experimental data exhibit similar progressions, see **Figure 12.2d**. Therein, the slope of the ceasing corrosion stages decreases from 250 °C to 225-175 °C. This again indicates that the higher vapor pressure at 250 °C leads to an increased percolation and nucleation within the Cu core. Thus, the temperature decrease leads to a lower vapor pressure and with this a decreased percolation and nucleation. However, this is not as pronounced for the PCC wire as compared to the bare Cu wire. Hence, it is concluded that the PCC wire makes up for the lower vapor pressure by an increased catalytic activity of the Pd-coating. For an overview of all derived mechanistic models and the obtained rate constants see **Table A 12.2**. Also, the Arrhenius plots, which are generated from the obtained rate constants, are discussed in section 12.4.5.

12.4.3 Corrosion Kinetics of APC Bond Wire with DS at 250-175 °C

Unexpectedly, the APC wire exhibits the same corrosion kinetics as the PCC wire, see **Figure 12.3a**. Thereby, the APC wire degradation displays a sigmoidal behaviour at 250-175 °C. Also, the Cu conversion time does not increase from 250 °C to 225 °C and is ≈ 10 h for 100 wt% Cu conversion. Then, the conversion time of the APC wire increases, like the PCC wire, to 30 h and 90 h for 200 °C and 175 °C, respectively. Also, similar Avrami exponents are observed in the range $n = 2.41$ -3.57 which again confirm a nucleation and growth-controlled mechanism. Further analysis via the SH-plot underlines the similarities of the APC to the PCC wire corrosion kinetics, see **Figure 12.3b**. Therein, the slope for APC wire corrosion increases from $n = 0.60$ -1.72 to $n = 3.56$ -4.79 as seen before for the PCC wire. This again, is attributed to an increased percolation into the Cu core as the corrosion proceeds. Also, the master plot $f(\alpha)$ shows the same nucleation and growth-control characteristics, see **Figure 12.3c**. Additionally, a decrease of the slope in the later stages of the Cu degradation within the master plot $g(\alpha)$ is observed from 250 °C to 175 °C, see **Figure 12.3d**. Thus, it is concluded that the additional flash-Au layer on the surface of the APC wire does not exhibit a significant contribution to the corrosion kinetics but rather is directed by the Pd-coating. For an overview of all derived mechanistic models see **Table A 12.3**. Also, the Arrhenius plots, which are generated from the obtained rate constants, are discussed in section 12.4.5.

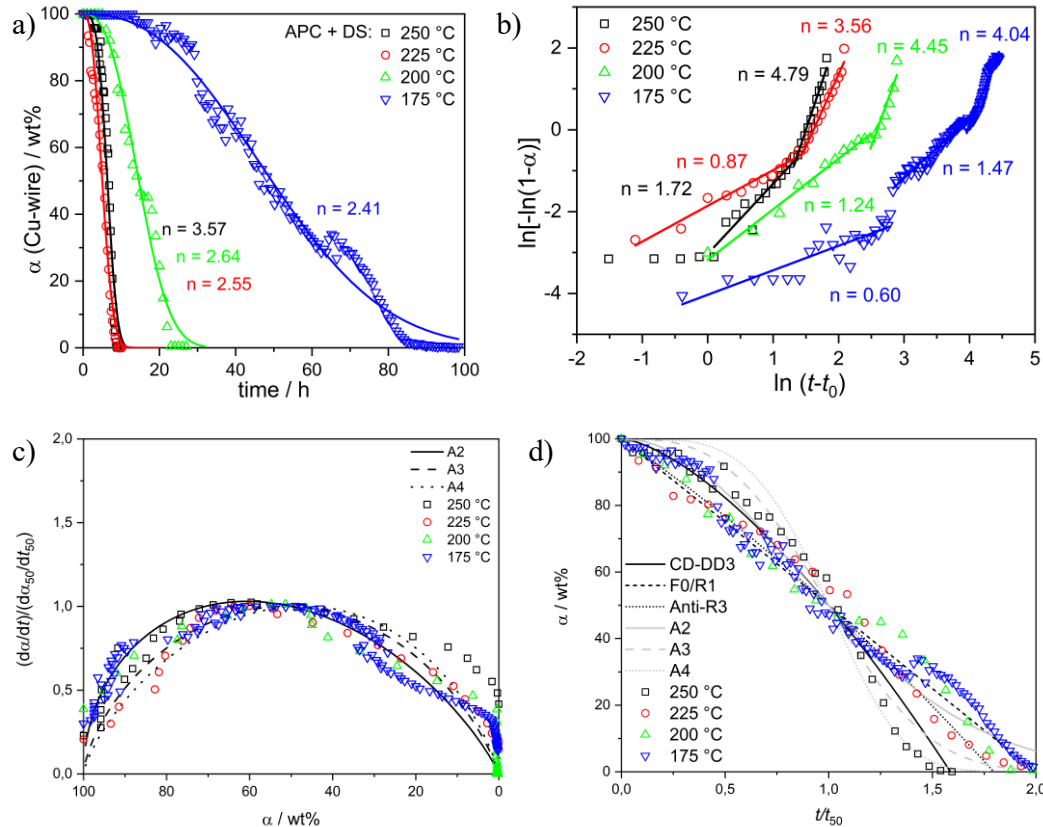


Figure 12.3: a) α - t -plots from the quantified HT-in situ-PXRD measurements of APC bond wire with DS at 250-175 °C and the Avrami exponents n from the JMAEK-fit. b) SH-plot c) Master plot $f(\alpha)$ d) Master plot $g(\alpha)$.

Subsequent SEM analysis after the HT-in situ-PXRD measurements reveals a completely corroded Cu core of the APC wire at 225 °C and 175 °C, see **Figure 12.4a,b**. Hence, the percolation of **DS** into the Cu core is thereby confirmed, which eventually leads to the nucleation and growth of β -Cu₂S within the Cu core. The subsequent analysis of the APC wire surface after the corrosion shows that

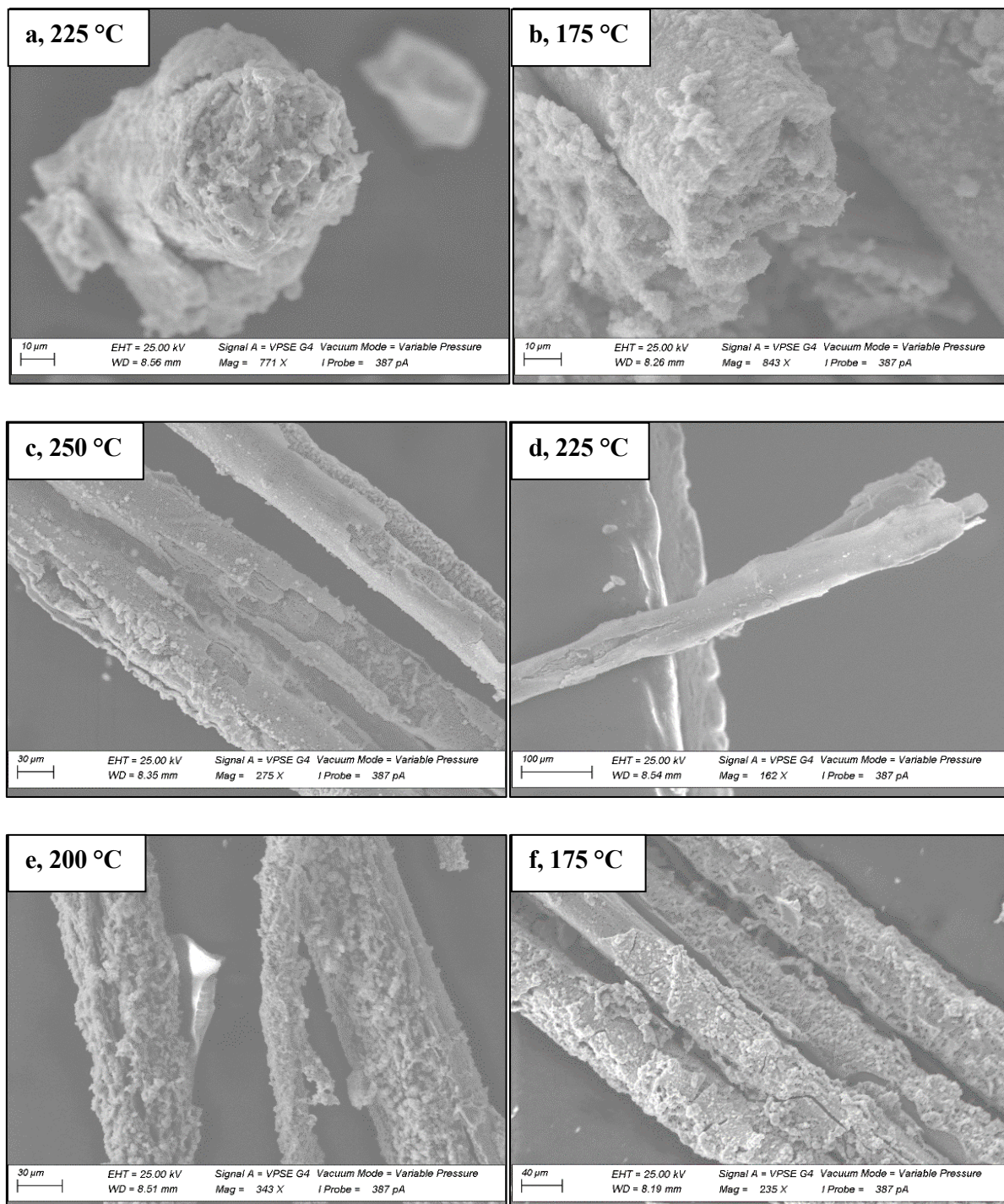


Figure 12.4: SEM micrographs of the corroded APC wires after the HT-in situ-PXRD measurements at isothermal conditions from 250-175 °C. a,b) Broken wires with completely corroded Cu core at 225 °C and 175 °C. c-f) Corroded wire surface at 250, 225, 200, 175 °C. Thereby, the β -Cu₂S layer tends to be more homogeneous at 250 °C and 225 °C whereas more spherical particles are present at 200 °C and 175 °C.

the β -Cu₂S layer tends to be more homogeneous at 250 °C and 225 °C whereas more spherical particles are present at 200 °C and 175 °C. This can be explained by a higher saturation of thiolates on the wire surface at higher temperatures. This consequently yields smaller but a larger number of nuclei. These nuclei grow and eventually coalesce to form a homogeneous layer. Whereas lower temperatures result in a decreased saturation of thiolates on the surface and thus bigger nuclei. As the big nuclei grow, they form spherical particles and more porous corrosion layers.

To further differentiate between a SC and KE model, the r_2/r_0 ratio from the SEM micrographs is plotted versus the obtained wt-fraction from the PXR measurements, see **Figure 12.5**. Therein, a SC model is confirmed for the whole temperature range from 250-175 °C which can be clearly distinguished from a KE model, at least for the ceasing corrosion stages. Thus, the percolation of **DS** into the Cu core takes place. However, it is not evident if a SC mechanism occurs from the beginning of the APC wire corrosion. Thereby, it is possible that the corrosion mechanism undergoes a transition from a KE model towards a SC model like the APCX wire with **MS1** (chapter 9.4.3). Also, a SC mechanism is assumed for the PCC wire corrosion as well due to the apparent commonalities of the APC and PCC wire corrosion.

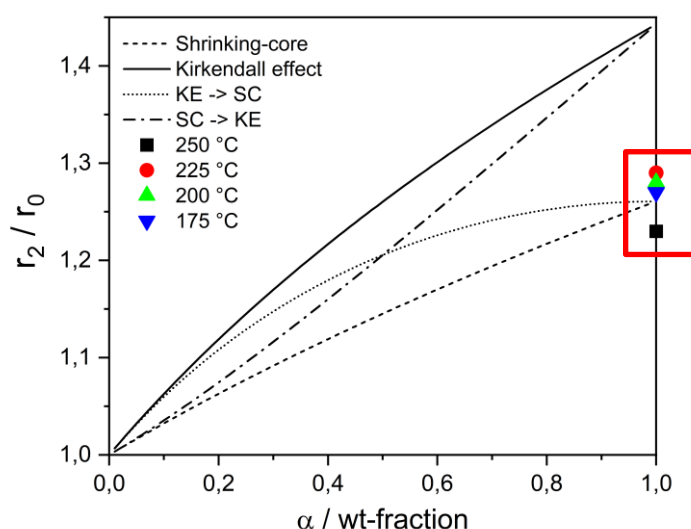


Figure 12.5: Proportion of the r_2/r_0 ratio to the Cu to β -Cu₂S conversion fraction. Here, a SC mechanism is confirmed for the ceasing corrosion stages of the APC wire at 250-175 °C

As mentioned before, percolation of the S-reactant into the Cu core is unlikely to take place in semiconductor packages. This is due to the decreased mobility of the S-reagent within the MC compared to the pure liquid reagent. However, further investigation regarding the diffusivity of gaseous composition products within the MC and through the corrosion product layer are necessary to completely rule out this hypothesis. Nevertheless, for Cu bond wire corrosion surrounded by MC, it is more likely to follow a diffusion-controlled mechanism according to a KE model as seen for solid **TT** corrosion (see chapter 9.4.4-5). Despite these experimental differences between liquid S-reagent and solid MC, it becomes evident that Pd- and Au/Pd-coatings do not act as diffusion barriers to prevent corrosion of the Cu core, at least for corrosive sulfur species from 250-175 °C.

12.4.4 Corrosion Kinetics of APCX Bond Wire with DS at 250-175 °C

Compared to the Cu, PCC, and APC wires, which show relatively similar corrosion kinetics, the APCX wire displays a significant acceleration for the Cu core degradation with **DS** in the whole temperature range from 250 to 175 °C, see **Figure 12.6a**. Also, a sigmoidal behaviour is observed which is in line with the other bond wires. Interestingly, the full conversion of the APCX wire at 250 °C (≈ 3 h) takes longer compared to 225 °C (≈ 2 h.) Below 225 °C the full conversion time increases to ≈ 3 h at 200 °C and ≈ 25 h at 175 °C. A similar trend is observed for the PCC and APC wire but with much lower corrosion rates compared to the APCX wire. This is also in line with the measurements of the bond wires with **MS1**, wherein the APCX wire showed the worst reliability and the highest corrosion rates (chapter 9.4.2). Further investigation via the SH-plot already reveals high Avrami exponents at the beginning of the bond wire corrosion with $n = 2.07$ -2.95, see **Figure 12.6b**. However, at 175 °C the Avrami exponent transitions from $n = 2.88$ to 0.74 which indicates a diffusion-controlled mechanism with increasing conversion fraction. This is like the bare Cu wire at 175 °C which also exhibits a transition to a diffusional model. This could be attributed to two distinct phenomena for the APCX wire. First, an increasing product layer thickness which leads to a lengthened diffusion pathway and with this to a diffusion control by Cu^+ outward movement. This is the same mechanism which is expected for the bare Cu wire. Second, the formation of a passivating corrosion layer by the Ni and Ga additives in the Cu core which slows down the percolation of **DS**.

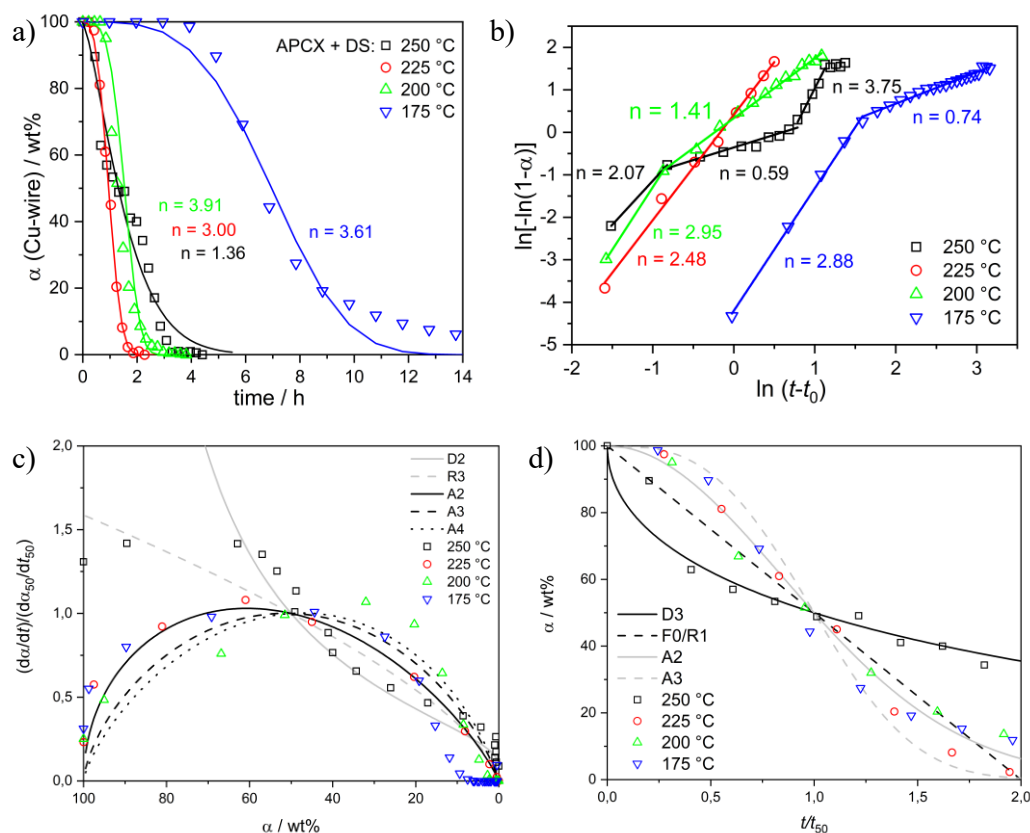


Figure 12.6: a) α - t -plots from the quantified HT-in situ-PXRD measurements of APCX bond wire with **DS** at 250-175 °C and the Avrami exponents n from the JMAEK-fit. b) SH-plot c) Master plot $f(\alpha)$ d) Master plot $g(\alpha)$.

Moreover, the master plots $f(\alpha)$ and $g(\alpha)$ confirm the nucleation and growth kinetics at 225-175 °C wherein the ceasing stages at 175 °C deviate from the Avrami models, see **Figure 12.6c,d**. However, a closer look at the experimental data at 250 °C, compared to the theoretical slopes in the master plots, reveals a corrosion sequence which starts by interface control and then merges into a diffusion-control. Thus, different limiting corrosion steps are confirmed at 250 °C compared to 225 °C which could explain the higher conversion time at 250 °C. As seen for the APC wire, higher temperatures led to more homogeneous layers. This could also be the case for the APCX wire which then slows down the reaction by diffusion-control of the Cu ions through the product layer. Consequently, lower temperatures and thus lower thiolate saturation at the wire surface shifts the predominant corrosion mechanism towards nucleation and growth control. For an overview of the derived models and the obtained kinetic rate constants see **Table A 12.4**.

As the APC and APCX wire only differ in the composition of the Cu core, it is concluded that the additives Ni and Ga significantly reduce the corrosion resistance versus sulfur induced corrosion (chapter 9.4.3.4). This is confirmed for lower temperatures as well, which implies a high corrosion risk for pure sulfur corrosion. However, APC wires with additives in the core proved to be more corrosion resistant in package stress tests than conventional APC wire.⁸³⁻⁸⁵ This can be explained by the mutual presence of sulfur, moisture and oxygen which could lead to a corrosion resistant passivation layer. Because of this, further investigations are strongly recommended to identify the involved processes as this can drastically alter the corrosion resistance. Herein, it leads to the transition from a corrosion resistant bond wire in package stress tests to an extremely corrosive bond wire in pure S-reagent environment. Thereby, the additives within the Cu core are supposed to passivate the exposed Cu surface at the damaged coating areas. Of course, there is a big deviation of the S-reagent mobility within the MC compared to the pure DS. Nevertheless, the additives should act as a passivating agent and thereby prevent diffusion and percolation into the core regardless of the S-reagent state of aggregation and mobility. However, the degradation of the APCX wire does not slow down. Hence, the additives do not fulfill their intended purpose. Therefore, it is concluded that at least in the scope of this thesis the APCX wire exhibits a poor reliability. Hence, the APCX bond wire carries a high risk for bond degradation and subsequent failure of the device in combination with sulfur-containing species.

12.4.5 Acceleration Modes of Cu Bond Wires versus Disulfide Facilitated Corrosion

To gain further insight into the temperature induced acceleration of Cu bond wire corrosion, Arrhenius plots are generated from the obtained rate constants in chapter 12.4.1-4. Thereby, the rate constants are derived via the JMAEK-fit, SH-plot, and ICM. In **Figure 12.7** a representative Arrhenius plot is shown, which is derived from the respective JMAEK-fits of Cu, PCC, APC, and APCX wire with **DS**. Therein, it is evident that APCX wire corrosion displays much higher corrosion rates compared to the other bond wires. Also, a linear relationship of the temperature facilitated acceleration mode of PCC, APC, and APCX bond is confirmed in the temperature range from 175 °C to 225 °C. Strikingly, no further acceleration is observed above 225 °C for PCC, APC, and APCX bond wire. In contrast to that, the acceleration of bare Cu bond wire corrosion approximates to a linear relationship in the whole temperature range from 175 °C to 250 °C. Moreover, the slopes of PCC, APC, and APCX wire are higher compared to the slope of bare Cu wire. These findings are also confirmed by the Arrhenius plots obtained from the SH-plot and ICM, see **Figure A. 12.1-4** for further details.

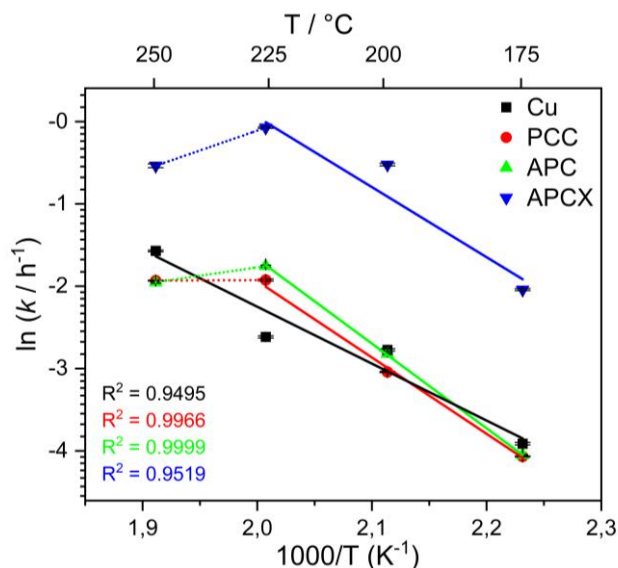


Figure 12.7: Arrhenius plot of the obtained rate constants from the JMAEK-fits of bare Cu, PCC, APC, and APCX bond wire with **DS** from 175-250 °C. Note that the coefficient of determination applies to the solid lines.

However, a linear relationship is expected for the whole temperature range if diffusion related processes dominate the corrosion rate. Due to the deviation from linearity for the PCC, APC, and APCX wire at 250 °C, it is concluded that other aspects besides diffusion processes must play a significant role. Thereby, mostly nucleation and growth-controlled mechanisms are confirmed for the bond wire degradation with **DS**. Moreover, the growth of the nuclei can either be controlled by diffusion and interface mechanisms. As growth by diffusion is excluded due to non-linear behaviour in the Arrhenius plot, growth of the nuclei must proceed through interface-controlled mechanisms. Thus, the chemical reaction at the surface dictates the overall corrosion rate and further temperature increase does not lead to a faster chemical reaction. Contrary to that, a linear behaviour is measured for bare Cu bond wire from 175-250 °C. Thus, diffusion of reactants dominates the growth of nuclei.

Eventually, the activation energies are calculated from the slope of the obtained Arrhenius plots. Therein, an increasing mean activation energy is confirmed from bare Cu (0.63 ± 0.07 eV) to PCC (0.8 ± 0.1 eV), APC (0.88 ± 0.07 eV), and APCX (0.9 ± 0.2 eV) bond wire, see **Figure 12.8**. For further details see **Table A 12.5**. As discussed above, PCC, APC, and APCX bond wire corrosion are governed by interface-control and Cu bond wire corrosion by diffusion-control, respectively. This is in line with, in general, higher activation energies for interface reactions versus diffusion-controlled reactions. Hence, the influence of the wire surface becomes more dominant from Cu to APCX wire.

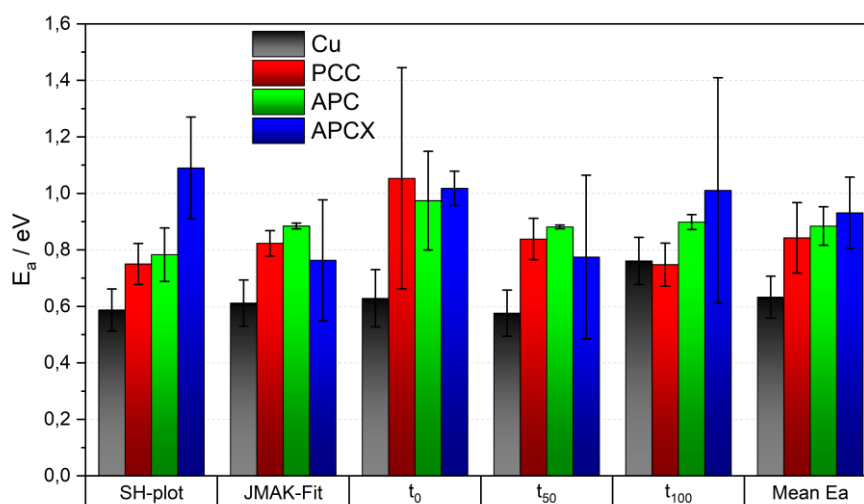


Figure 12.8: Activation energies determined from JMAEK-fit, SH-plot, and ICM (times at t_0 = induction period, t_{50} = 50 wt%, t_{100} = 100 wt% conversion). Therein, the mean activation energy increase from bare Cu to PCC, APC, and APCX bond wire.

This is in line with literature where a decreasing reactivity with thiolates is reported from Cu to Ag and Au, see **Figure 12.9**.⁶⁷ Also, the reactivity increases from group 11 to group 10 elements.^{67, 257} Thus, it is concluded that the reactivity decreases in the order Cu, Pd, Au which results in an increased activation energy for **DS** corrosion from Cu to PCC and APC bond wire.

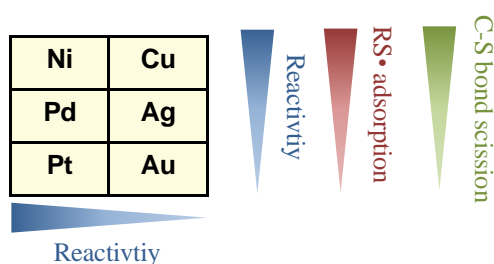


Figure 12.9: Trends for reactivity, RS• adsorption, and C-S bond scission within of group 10 and 11 of the periodic table.⁶⁷

However, a lower activation energy would be expected for the APCX wire due to the addition of Ni into the core which should readily react with **DS**. Yet, a higher activation energy is verified for the APCX wire which can also be attributed to the addition of Ga into the core or an initial passivation of the surface. Also, the additives Ni and Ga could act as impurities to decrease the activation energy for the formation of nuclei. Though, the overall activation energy for the APCX bond wire corrosion does not decrease, the additives lead to much higher corrosion rates compared to the other bond wires.

This is demonstrated by theoretical considerations of heterogeneous (APCX) versus homogeneous (Cu) crystallization, see **Figure 12.10**. Therein, the maximum of the crystallization rate shifts towards higher temperatures from homogeneous to heterogeneous crystallization. Hence, higher crystallization rates are observed for heterogeneous crystallization. This is expressed by a shift from long time scales for homogeneous to shorter time scales for heterogeneous crystallization in a plot of temperature versus time, a so-called time-temperature-transformation (T-T-T) plot.

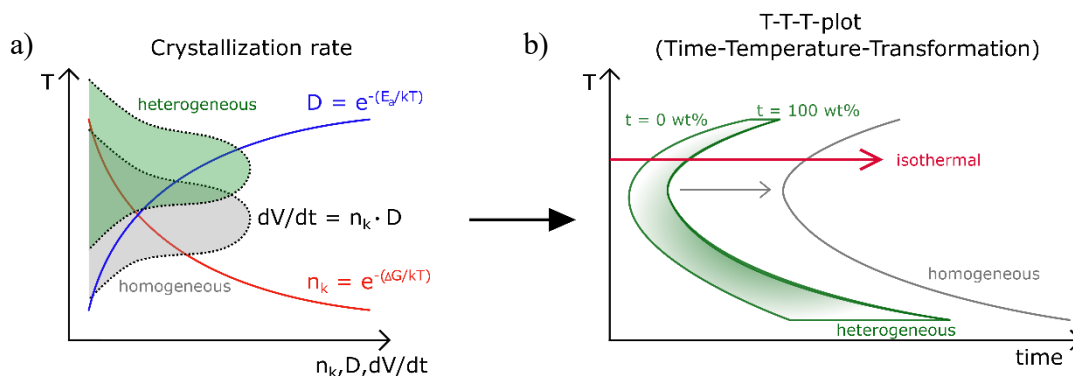


Figure 12.10: a) Schematic illustration of the nucleation rate n_k , diffusion coefficient D , and overall crystallization rate dV/dt versus temperature. Theoretically, the overall crystallization rate is shifted from high to low temperatures for heterogeneous and homogeneous crystallization. b) The shift of the crystallization rate corresponds to a shift from short time scales to longer time scales in the T-T-T plot for heterogeneous and homogeneous crystallization.

Therefore, the addition of Ni and Ga into the core should shift the T-T-T curve to shorter time scales as discussed from theoretical considerations. In fact, this is observed for the T-T-T curve of the APCX wire but is not as pronounced for the undoped PCC and APC wire, see **Figure 12.11**. This leads to the conclusion that the addition of dopants into the core not only elevates the complexity of the system but also yields much higher corrosion rates due to heterogeneous crystallization/corrosion kinetics.

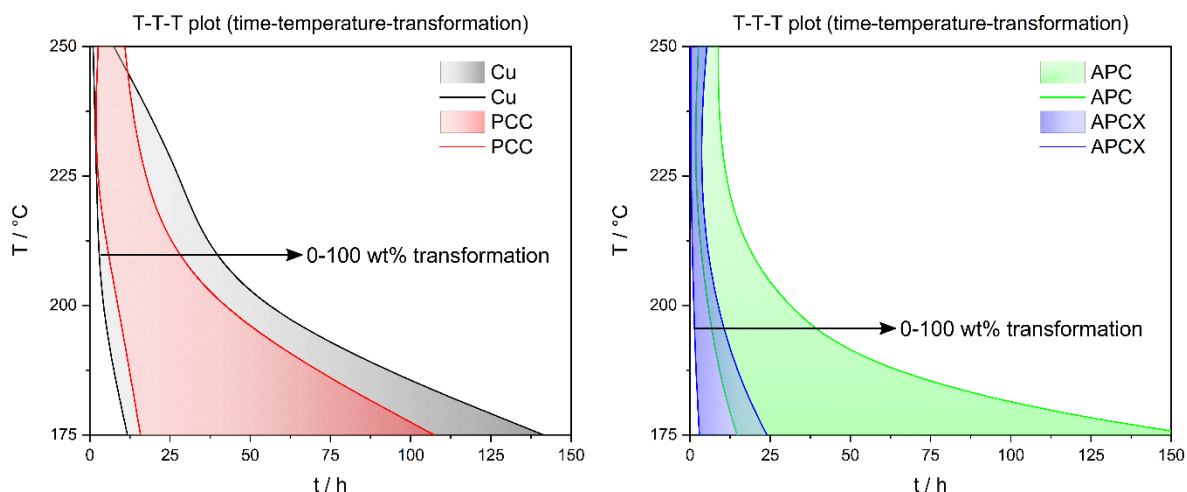


Figure 12.11: T-T-T plot of bare Cu, PCC, APC, APCX bond wire corrosion with DS from 250-175 °C. The left line represent the start of the corrosion (t_0 = induction period) and the right line the full degradation of the bond wire (t_{100} = 100 wt% conversion).

12.4.6 HTS of Bond Wires with Disulfide at 150 °C

Interestingly, the corrosion behaviour changes drastically at 150 °C. While HTS of the bond wires with DS at 175 °C results in sole Cu degradation and β -Cu₂S formation, HTS at 150 °C does not lead to the degradation of the bond wires, see **Figure 12.12 (left)**. Therein, the strongest reflection in the powder pattern of the bare Cu wire (Cu(111)) shows no decrease during HT-in situ-PXRD at 150 °C. Note that a theoretical calculation of the Cu conversion fraction according to the obtained Arrhenius plots would correspond to at least 40-60 wt% Cu conversion after 155 h. Additionally, the powder patterns of the bare Cu, APC, and APCX bond wire after HTS at 150 °C for 155 h reveal a new phase, see **Figure 12.12 (right)**. There, the APC and APCX wire display the same emerging phase (green dashed line) which could not be identified with the ICDD-PDF-2 and COD databases. Moreover, a comparison with the powder pattern of bare Cu wire reveals a different emerging phase (black dashed line) for the bare Cu wire. Again, the new emerging phase in the powder pattern of bare Cu wire could not be identified by the database entries.

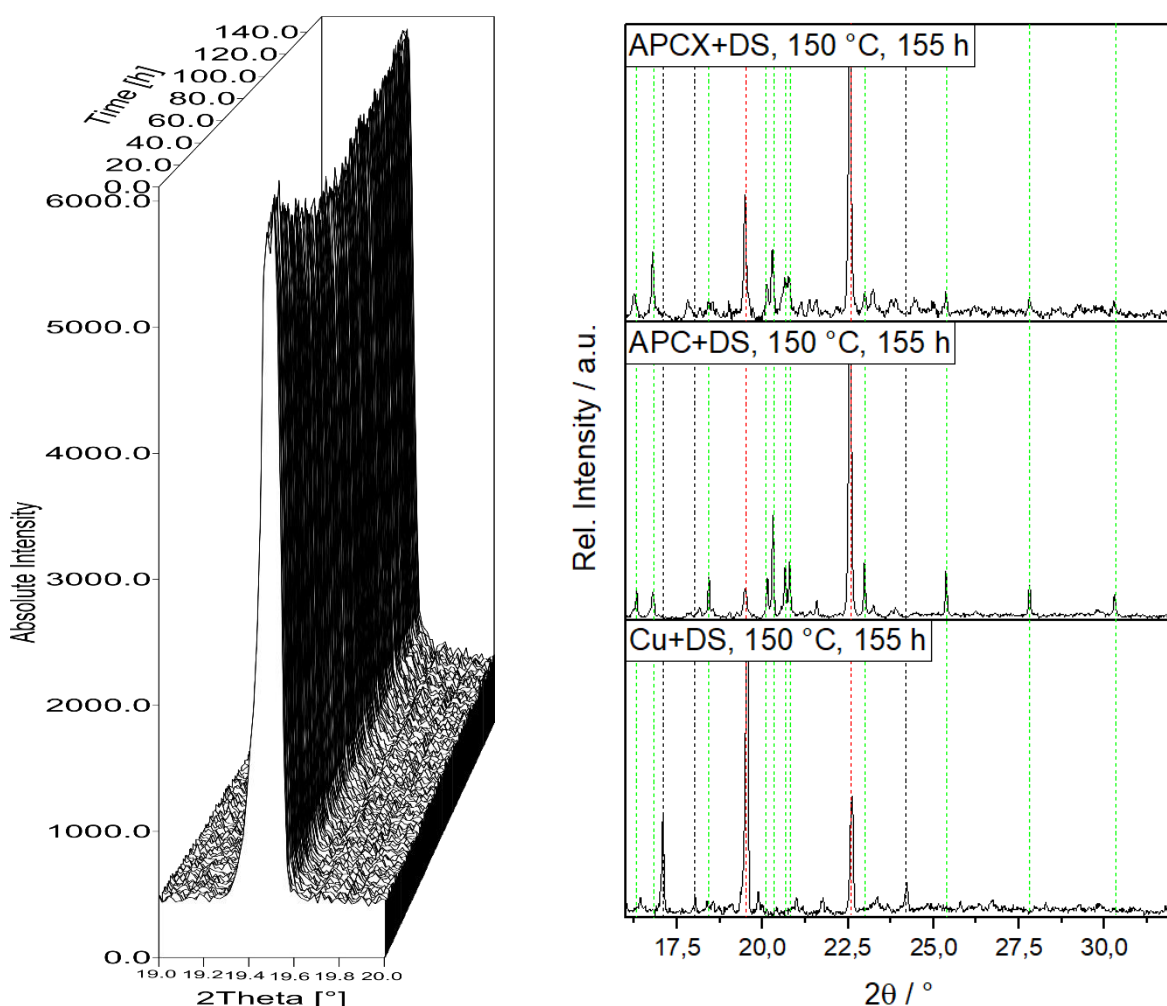


Figure 12.12: Left: Cu(111) intensity progression during HT-in situ-PXRD measurement of bare Cu wire with DS at 150 °C. Right: Powder patterns of the bare Cu, APC, and APCX bond wire with DS after HTS at 150 °C for 155 h. Therein, the powder pattern of the bare Cu, APC, and APCX bond wire do not exhibit β -Cu₂S formation. Also, a new unidentified phase (green dashed line) is emerging after HTS of the APCX and APC bond wire at 150 °C (top, middle). Whereas the bare Cu bond wire yields another unidentified phase (black dashed line) compared to the APC and APCX bond wire (bottom).

Because of the constant Cu reflection intensity during HT-in situ-PXRD, a quantitative conversion of the bond wires can be excluded. Hence, HTS of **DS** with Cu bond wires does not yield product phases which comprise Cu atoms. Therefore, the newly formed phases must be a product of **DS** decomposition products. Optical micrographs of the APC wire with **DS** after HTS at 150 °C for 155 h displays colorless thread-like crystals surrounding the wire, see **Figure 12.13**. Also, the formation of crystals is solely observed in the vicinity of the wire surface.

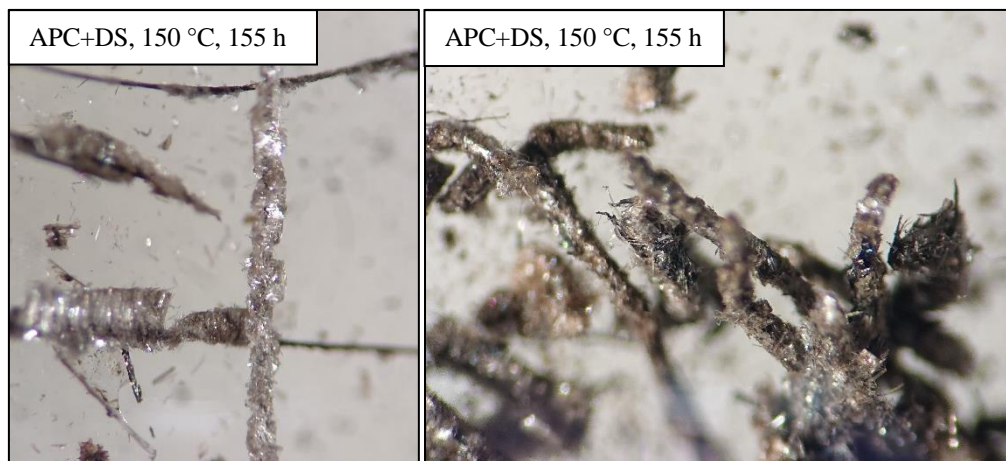


Figure 12.13: Optical micrographs of the **APC** bond wire with **DS** after HTS at 150 °C for 155 h. Left: The **APC** bond wire is mostly uncorroded but with large colorless crystals surrounding the wire. Right: **APC** bond wire is intact with large amounts of thread-like crystals which surround the wire.

This points to a reaction of **DS** on the surface of the wire where the Cu, Au, or Pd surface acts as a catalyst. It is known from literature that disulfides decompose at the Cu surface even at room temperature to form adsorbed thiolate $RS_{ads}-Cu$.²⁵⁸⁻²⁶⁰ Also, it has been found that adsorbed thiolate species of dimethyl disulfide and diethyl disulfide decompose to the corresponding alkane and alkene above ~ 120 °C.^{259,260} Thus, **DS** presumably adsorbs as thiolate on the wire surface and subsequently decomposes at 150 °C. Eventually, the decomposition products react towards a new organic product in the vicinity of the wire surface to form colorless crystals. As mentioned above, two different organic phases are observed for the Au/Pd-coated wires and the bare Cu wire. This can be explained by the different catalytic capability of the bare Cu surface compared to the Au/Pd surface to yield another organic decomposition product.

The presence of an organic product phase is underlined by a subsequent heating of the APCX wire with **DS** after the isothermal HTS at 150 °C. Therefore, non-isothermal HT-in situ-PXRD measurement was performed from 30 °C to 250 °C, see **Figure 12.14**. Therein, the new organic phase is present after isothermal HTS and the powder pattern remains unchanged from 30 °C to 150 °C. This changes above 150 °C where the organic phase from isothermal HTS decomposes and only the Cu reflections remain. Further heating up to 230 °C leads to the degradation of the APCX bond wire and β -Cu₂S formation. Hence, an organic phase is likely to form at 150 °C which consequently decomposes above 150 °C. This is in line with the measurements in chapter 12.4.1-4 where Cu degradation and β -Cu₂S formation is confirmed at 175-250 °C.

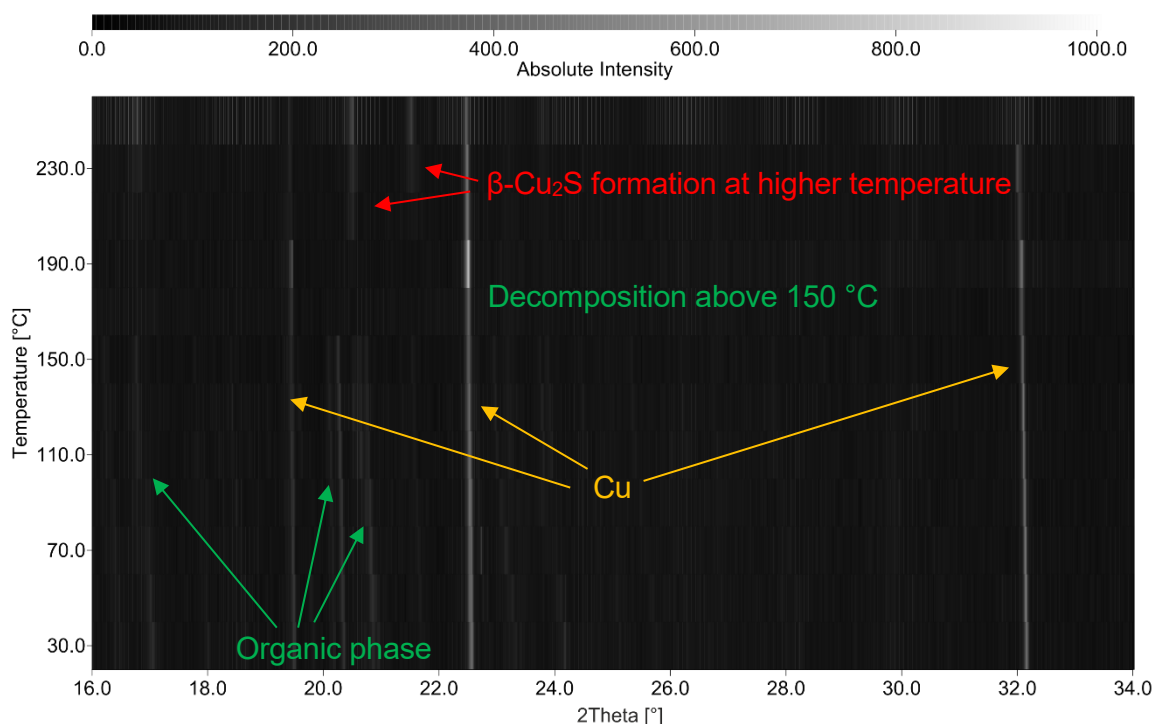


Figure 12.14: HT-in situ-PXRD after the initial isothermal HTS at 150 °C for 155 h. There, the APCX wire with DS is heated at non-isothermal conditions from 30 °C to 250 °C. Therein, the organic phase which emerged from the isothermal HTS decomposes above 150 °C. Further heating up to 230 °C leads to the degradation of the APCX bond wire and β -Cu₂S formation.

This observation has major consequences for package stress testing, at least for disulfide-based compounds. Therein, high temperature stress testing at 175-250 °C would result in the corrosion of the respective bond wire with disulfides. However, stress testing at 150 °C most likely would not show any signs of bond wire degradation. But this can also be falsely ascribed to an insufficient evaluation period to measure traceable amounts of bond wire degradation. Consequently, lifetime predictions for the electronic device are erroneously calculated from high temperature stress testing at 175-250 °C. Yet, operating temperatures range from -40 °C to 150 °C where no Cu degradation and β -Cu₂S formation takes place as confirmed by HT-in situ-PXRD at 150 °C. Nevertheless, the formation of crystallites between the bond wire and the MC could lead to a weakening of the adhesion strength and with this to the delamination of the MC. However, operation temperatures below 120 °C lower the risk for the decomposition of the adsorbed thiolate species. Thus, no bond wire degradation and decomposition of adsorbed thiolates are expected below 120 °C. Consequently, the package exhibits a completely different corrosion behaviour and lifetimes below 120 °C. Naturally, further measurements below 150 °C and 120 °C are necessary to confirm this hypothesis.

Therefore, it is concluded that accelerated package stress testing above 150 °C is critical to predict package lifetimes. This is due to the completely altered mechanism, going from 150 °C to 175 °C (see chapter 12.4.5). Consequently, the different failure mechanisms are accompanied by altered activation energies. Therefore, the package stress test results strongly depend on the respective temperature and failure mechanism.

12.4.7 Corrosion Kinetics of Cu and APC Bond Wire with MS1 at 250-175 °C

In this section, Cu and APC bond wire are isothermally measured with **MS1** at 250 °C, 225 °C, 200 °C, and 175 °C (only APC) to further study the temperature dependent corrosion behaviour of different S-reagents, see **Figure 12.15a**. Therein, the corrosion behaviour of the APC bond wire with **MS1** follows a sigmoidal behaviour at 250 °C, 225 °C, and 200 °C. Also, the Avrami exponents match well with a nucleation and growth-controlled degradation with $n = 2.12$ - 3.88 at 250-200 °C. Similar to that, the bare Cu wire corrosion at 250 °C with **MS1** exhibits also a sigmoidal progression but with a lower exponent of $n = 1.68$ of the JMAEK-fit. A further temperature decrease yields a lower exponent of $n = 1.25$ at 225 °C and approximates to a linear behaviour. Even lower temperatures such as 200 °C and 175 °C result in lower Avrami exponents with $n = 0.93$ and 0.96 , respectively. Hence, the exponents are in between interface and diffusion-controlled models which is expressed by the slight parabolic behaviour which approximates to a linear behaviour of the slopes.

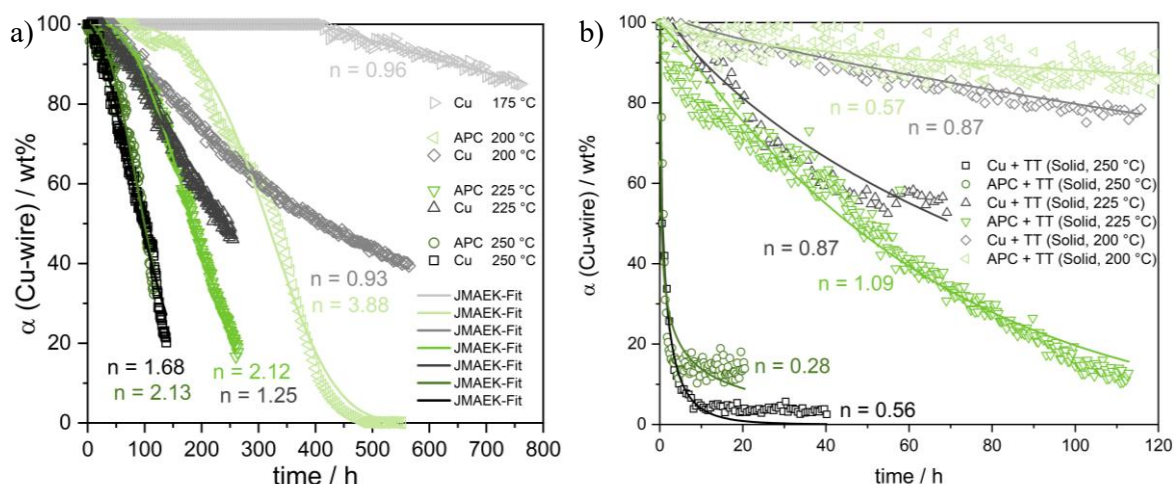


Figure 12.15: a) α - t plots of bare **Cu** and **APC** bond wire with **MS1** at isothermal conditions at 250 °C, 225 °C, 200 °C, and 175 °C and their respective JMAEK-fits. b) α - t -plots of bare **Cu** and **APC** bond wire with solid **TT** at 250 °C, 225 °C and 200 °C and their respective JMAEK-fits.

A comparison between the bare Cu and APC bond wire corrosion with **MS1** reveals slight differences at 250 °C. Thereby, the corrosion kinetics are relatively similar but with a prolonged nucleation phase for the APC bond wire in the beginning. The nucleation phase of the APC bond wire is even more pronounced at 225 °C and 200 °C. However, at about ≈ 60 wt% the APC bond wire degradation at 225 °C and 200 °C progresses much faster compared to the bare Cu bond wire corrosion. Hence, with prolonged high temperature storage time, the APC bond wire corrosion proceeds much faster compared to the bare Cu wire. Herein, the corrosion of the bare Cu wire does not accelerate and eventually degrades slower than the APC wire. For further comparison, the α - t plots of the Cu and APC bond wire measurements with solid **TT** are displayed in **Figure 12.15b** (see chapter 10.4 for further details). Thereby, the corrosion kinetics of bare Cu and APC bond wire at 250 °C are similar which is in line with the **MS1** experiments. However, a pronounced nucleation phase is not observed in combination with solid **TT** which yields similar corrosion kinetics as bare Cu bond wire.

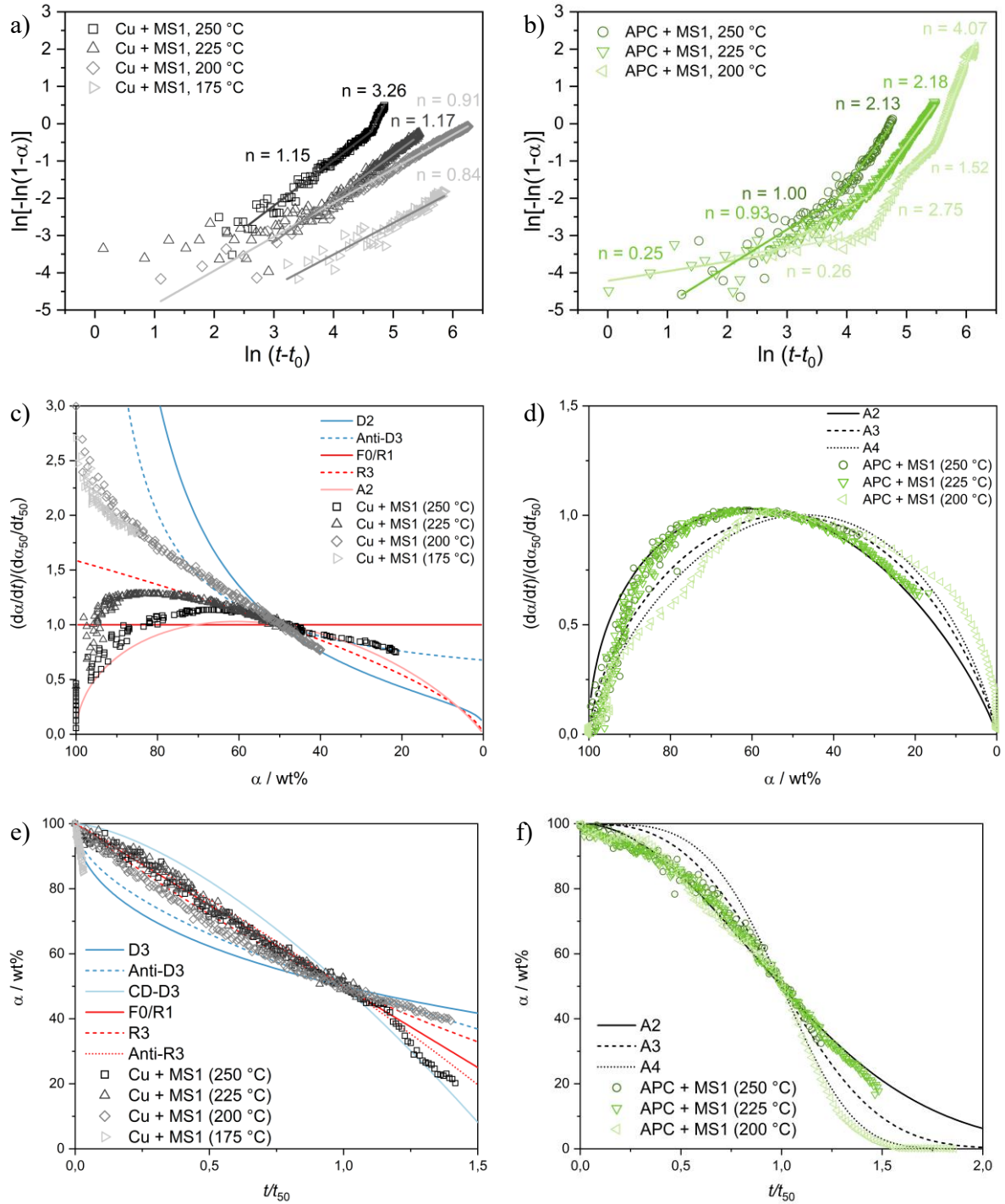


Figure 12.16: a) SH-plot, c) master plot $f(\alpha)$, and e) master plot $g(\alpha)$ of bare **Cu** with **MS1** at 250 °C, 225 °C, 200 °C, and 175 °C. b) SH-plot, d) master plot $f(\alpha)$, and f) master plot $g(\alpha)$ of **APC** bond wire with **MS1** at 250 °C, 225 °C, and 200 °C.

Further investigation via the SH-plot reveals an unchanged corrosion mechanism for bare Cu bond wire through the whole corrosion process with **MS1** at 225-175 °C, see **Figure 12.16a**. Therein, the Avrami exponents are in the range $n = 1.17$ - 0.84 from 225-175 °C. Hence, the degradation of the Cu wire is mostly directed by interface control but with more diffusional contribution for the lower values of the Avrami exponents. However, at 250 °C the exponent changes from $n = 1.15$ to 3.26 which can be attributed to a change from an interface mechanism to a nucleation-base mechanism. This can be

explained by the increased percolation of **MS1** into the core and with this increased nucleation in the core. This is confirmed by the master plots $f(\alpha)$ and $g(\alpha)$ where the experimental values of the bare Cu wire with **MS1** at 175 °C and 200 °C are in between interface- and diffusion-controlled models, see **Figure 12.16c, e**. Hence, the corrosion kinetics are governed by fractional values of interface or diffusion control. Whereas the induction period of bare Cu wire corrosion at 250 °C and 225 °C is rather governed by nucleation which then merge into interface-controlled models.

The detailed analysis of the APC bond wire corrosion with **MS1** at 250 °C and 225 °C via the SH-plot yields exponents of $n = 1.00$ and 0.93 for the initiating corrosion stages, respectively (see **Figure 12.16b**). Hence, mostly interface-controlled mechanisms which is similar to the bare Cu wire. However, at about 15 wt% Cu conversion the exponents rise to $n = 2.13$ and 2.18 (A2) which indicates a nucleation and growth-controlled mechanism. Thereby, 15 wt% Cu conversion approximates to a β -Cu₂S layer thickness of $\approx 2\mu\text{m}$. Thus, it is concluded that the initial reaction on the Au/Pd-surface is directed by the interface reaction. Eventually the whole wire surface is covered with a β -Cu₂S layer and the subsequent degradation is governed by nucleation. Hence, it can be assumed that the initial Au/Pd-surface impedes the β -Cu₂S formation by a slow interface reaction. Similar observations are made at 200 °C but with a diffusion-controlled mechanism ($n = 0.26$) in the beginning which merges into a nucleation and growth-controlled mechanism (A4, $n = 4.07$). Note that the mechanism changes from a 1D-model towards a 3D-model from 250 °C to 200 °C. Similar transitions are observed for the APC bond wire with DS. Thereby, it is concluded that the 1D-model originates from the formation of a homogeneous β -Cu₂S layer due to the large number of small nuclei. Contrary to that, the lower temperature enable the formation of fewer and bigger nuclei and thus the formation of spherical particles which corresponds to the 3D-model. Further, the nucleation-models and the transition from 1D to 3D-models are confirmed by the master plots $f(\alpha)$ and $g(\alpha)$, see **Figure 12.16d, f**. For an overview of all derived models and the obtained rate constants see **Table A 12.6, 7**.

Interestingly, a prolonged nucleation phase occurs for the whole temperature range from 250-200 °C. As such an acceleration phenomenon is not observed for the bare Cu bond wire, this effect can be assigned to the Au/Pd-coating. A closer inspection of the powder patterns reveals the formation of Cu₃Pd which coincides with the accelerated degradation of the APC bond wire. This is shown in **Figure 12.17** for the APC bond wire with **MS1** at 200 °C. Therein, the APC bond wire degradation accelerates after ≈ 150 -200 h which overlays with the formation of Cu₃Pd after ≈ 200 h. Note that the intermetallic formation could even start after 150 h but may not be measured due to the detection limit. Moreover, the Cu₃Pd amount slightly increases up to 3.5 wt% after 450 h which approximates to a full conversion of the Pd-coating (theoretically: 120 nm Pd thickness = 3.5 wt%). As the Cu wire is completely corroded, the Cu₃Pd content decreases as well. Strikingly, the Cu₃Pd amount does not decrease during the corrosion but instead at the end of the Cu core conversion. This implies either that the Cu₃Pd phase is non-reactive or rather a constant supply of Cu ions by the Cu core through the intermetallic phase. However, the diminishing Cu₃Pd phase at the end rather indicates a constant supply of Cu⁺ through the alloy to the reactive surface. Eventually, the Cu supply is exhausted and **MS1** reacts with Cu₃Pd to form β -Cu₂S.

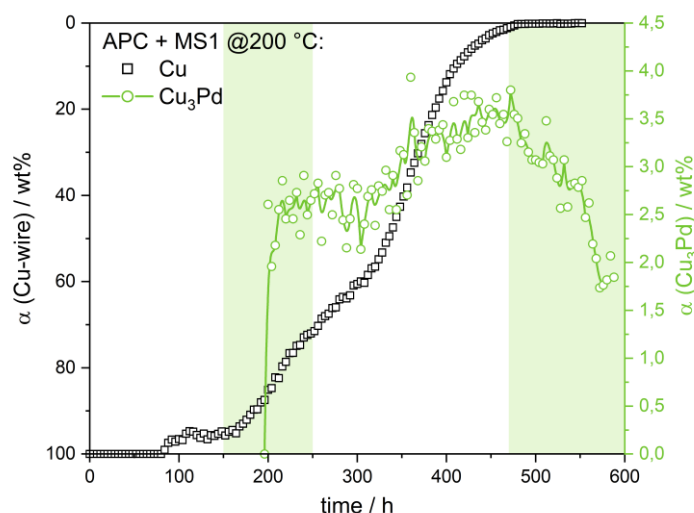


Figure 12.17: α - t -plot of APC bond wire with **MS1** at 200 °C (black dots) overlaid with the formation of Cu_3Pd alloy (green dots). The acceleration of the APC bond wire degradation coincides with the formation of Cu_3Pd . This can be explained due to the diffusion of Cu ions through Cu_3Pd or catalytic activity of the alloy. Note that Cu_3Pd is quantified by DCM. The green areas correspond to the onset and decline of Cu_3Pd formation.

This hypothesis is supported by recent studies which report a decreasing corrosion current density for Cu-Pd alloys.²⁵⁷ Thus, the lower corrosion current density for Cu-Pd alloys suggest a lower reactivity of Cu_3Pd compared to Cu. Hence, Cu reacts more readily than Cu_3Pd which leads to a constant Cu_3Pd content and stability of the alloy during the corrosion. Moreover, it is concluded that the alloy formation enables an additional Cu^+ diffusion through the coating and thereby accelerates the corrosion rate. It is also feasible that the alloy formation increases the catalytic capability to cleave the C-S bond and thus enables an easier $\beta\text{-Cu}_2\text{S}$ formation.

To sum up, bare Cu and APC bond wire show similar reliability versus **MS1** induced corrosion at 250 °C. At lower temperature, the nucleation phase of the APC bond wire extends, which yields better reliability at 225-200 °C in the short-term. However, the long-term corrosion resistance is better for the bare Cu wire as the corrosion rate increases significantly for the APC bond wire with proceeding corrosion. Thereby, it is shown that the acceleration of the APC wire corrosion may take place due to Cu_3Pd alloy formation.

The huge difference between short-term and long-term corrosion behaviour could also have a huge impact on package stress testing. If insufficient evaluation periods are chosen for reliability testing, the APC bond wire may be falsely assumed to be the more reliable bond wire. However, long-term measurements would yield a reversed assessment for the APC bond. At least in the scope of these experiments. Also, higher temperatures for stress testing results in relatively similar corrosion rates which alters completely for lower temperatures. Therefore, it is concluded that lower temperatures which are closer to the actual operating temperatures are more suitable to test the reliability. Thus, a case-by-case assessment and testing procedure for the individual package must be ensured to reproduce actual mission profiles.

12.4.8 Acceleration Modes of Cu and APC Bond Wire versus MS1 Facilitated Corrosion

To gain further insight into the temperature induced acceleration of Cu and APC bond wire corrosion with MS1, Arrhenius plots are generated from the obtained rate constants in chapter 12.4.7, see **Figure A. 12.6**. Thereby, the rate constants are derived via the JMAEK-fit, SH-plot, and ICM. Also, a linear relationship for bare Cu and APC bond wire is confirmed from 250-175 °C. Finally, the activation energies are calculated from the slope of the obtained Arrhenius plots, see **Figure 12.18**.

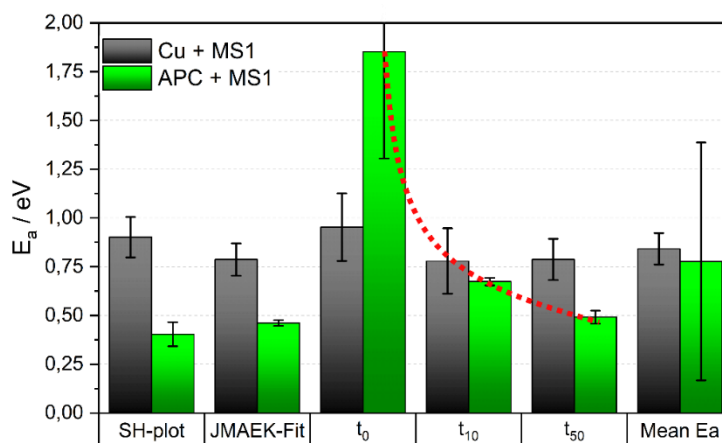


Figure 12.18: Activation energies determined from JMAEK-fit, SH-plot, and ICM (times at t_0 = induction period, t_{10} = 10 wt%, t_{50} = 50 wt% conversion). Therein, activation energy for APC bond wire corrosion decreases from t_0 to t_{10} and t_{50} (dotted red line).

Therein, the obtained activation energies E_a from the JMAEK-fit and SH-plot is determined from the overall corrosion rate. This yields an activation energy of ≈ 0.76 - 0.87 eV and ≈ 0.38 - 0.45 eV for the bare Cu and the APC bond wire, respectively. Similar values are determined from the ICM for the bare Cu wire where the activation energy slightly decreases from t_0 ($E_a = 0.95$ eV) to t_{50} ($E_a = 0.79$ eV). Whereas the APC bond wire exhibits a significant decrease of E_a from the incubation time t_0 ($E_a = 1.85$ eV) to t_{50} ($E_a = 0.49$ eV). This is in line with the kinetic analysis from chapter 12.4.7 where the APC bond wire displays a pronounced incubation and nucleation period. Hence, the prolonged nucleation period is a consequence of the high activation energy to form nuclei on the wire surface. As the corrosion proceeds, Cu_3Pd and $\beta\text{-Cu}_2\text{S}$ formation reduce the activation energy to increase the corrosion rate. Thus, the activation energy decreases with proceeding corrosion progress. As this phenomenon is not as pronounced for the bare Cu wire, the initial high E_a can be attributed to the Au/Pd-surface which impedes the initial nucleation on the wire surface. However, a slight decrease of E_a is also observed for the bare Cu wire. Therefore, it can be hypothesized that the initial formation of $\beta\text{-Cu}_2\text{S}$ could in general enhance the corrosion reaction.

Because of the high E_a of the incubation time t_0 for the APC bond wire, nucleation of $\beta\text{-Cu}_2\text{S}$ is more unlikely to occur at lower temperatures. Thus, it can be hypothesized that APC bond wire corrosion is hindered by the initial $\beta\text{-Cu}_2\text{S}$ formation. However, if nuclei are formed, for instance by inappropriate handling of the package, the APC bond wire corrosion proceeds much faster than bare Cu wire corrosion. Consequently, this could lead to a much greater degradation of the bond wire and thus to failure of the device.

12.4.9 HTS of Cu and APC Bond Wire with MS1 and TT at 150 °C

In addition to the in-situ measurements, long-term HTS at 150 °C and 175 °C was performed to investigate the corrosion behaviour at lower temperatures. Thereby, it is found that the bare Cu wire surface becomes darker and displays first signs of corrosion at 150 °C with solid **TT** after 4700 h, see **Figure 12.19b**. Also, it becomes evident that solid **TT** (white solid) does not exhibit significant decomposition. As a result, the Cu wire corrosion slows down, and the bare Cu wire stays mostly uncorroded. This changes drastically at 175 °C where the whole Cu surface is surrounded by a black corrosion product, presumably Cu_2S , see **Figure 12.19c**. Also, few and very small colourless crystallites become visible after 4700 h at 175 °C. Hence, the reagent **TT** most likely decomposes to a much higher amount and therefore results in a pronounced corrosion layer around the Cu wire. This is in line with chapter 10.4 where it is hypothesized that a decreased decomposition rate of **TT** (or S-reagent) in turn yields a much lower corrosion risk.

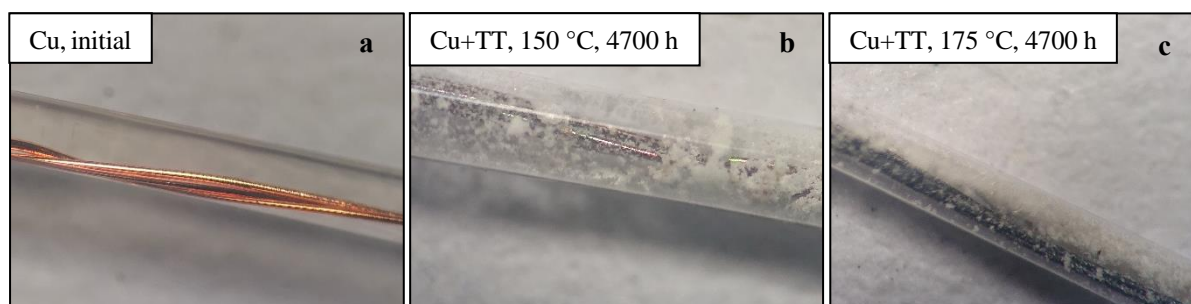


Figure 12.19: a) initial bare Cu wire, b), c) bare **Cu** with solid **TT** after 4700 h HTS at 150 °C and 175 °C.

Like the bare Cu wire, the APC bond wire clearly shows a dark staining of the surface after 4700 h at 150 °C, see **Figure 12.20b**. However, **TT** exhibits no clear signs of discoloration or decomposition after HTS at 150 °C. Thus, the APC bond wire is mostly uncorroded but with first signs of corrosion which could lead to an acceleration of the wire degradation with proceeding HTS. This is due to the formation of initial nuclei which then could enable a fast growth of a corrosion layer like the APC bond wire with **MS1**. After 4700 h HTS of the APC bond wire at 175 °C with solid **TT**, severe corrosion of the wire is observed, see **Figure 12.20c**. There, a black corrosion layer surrounds the APC wire, which presumably is Cu_2S . Moreover, a large number of colorless and needle-shaped crystallites are formed. This is not observed for the bare Cu wire for the same experimental conditions

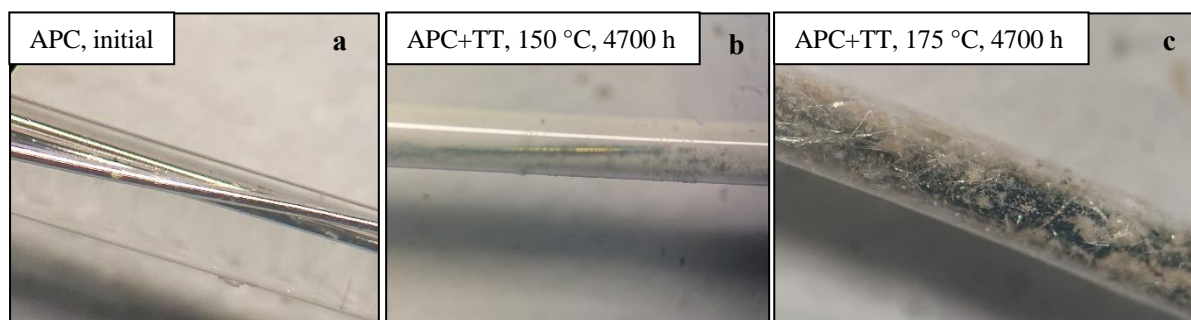


Figure 12.20: a) initial APC wire, b), c) **APC** wire with solid **TT** after 4700 h HTS at 150 °C and 175 °C.

and implies a much higher amount of solid **TT** decomposition on the Au/Pd-surface of the APC wire. Eventually, the higher amount of decomposition products results in a more severe corrosion of the APC bond wire and many crystallites.

Contrary to **TT** corrosion, HTS of bare Cu wire with **MS1** at 150 °C for 4700 h already displays a black corrosion layer around the Cu surface, see **Figure 12.21a**. Also, big black chunks are present on the surface which indicates the initial formation of few nuclei with subsequent growth. Like the bare Cu wire, a black corrosion layer forms on the surface of the APC wire at 150 °C, see **Figure 12.21b**. However, the APC wire is only partially covered with a more homogeneous corrosion layer compared to the bare Cu wire. A similar morphology is observed for the APC bond wire after 4700 h HTS at 175 °C, see **Figure 12.21c**. Therein, most of the APC wire surface is covered but some parts are completely uncorroded. From chapter 9.4.3.3 it is concluded that the APC wire corrosion with **MS1** starts at the damaged areas of the Au/Pd-coating. Hence, this phenomenon can explain the partial coverage of the APC wire surface by creeping corrosion of β -Cu₂S along the surface.

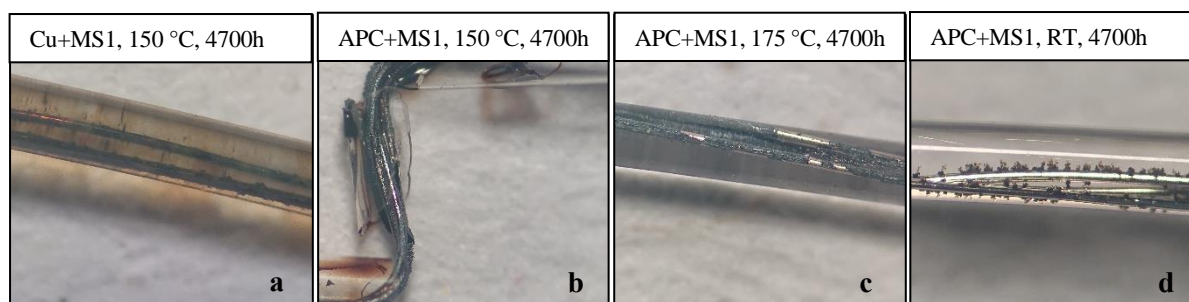


Figure 12.21: a) bare **Cu** wire with **MS1** after 4700 h HTS at 150 °C. b, c, e) **APC** wire with **MS1** after 4700 h HTS at RT, 150 °C, and 175 °C.

Strikingly, corrosion products are also visible after 4700 h storage of the APC bond wire with **MS1** at room temperature, see **Figure 12.21d**. Therein, black chunks are locally distributed over the whole APC wire surface. As these chunks solely emerge from distinct spots on the wire surface, it strongly suggests an initial corrosion at damaged coating areas. Also, these chunks rather propagate to the outward direction instead of creeping corrosion on the wire surface. Naturally, these chunks could coalesce at some point to form a homogeneous layer, but it demonstrates the nucleation-based character of initial APC wire corrosion with **MS1**. This also underlines the former hypothesis of enhanced corrosion due to the formation of a miniaturized galvanic cell which is formed at the damaged areas. Interestingly, a higher degree of creeping corrosion is confirmed at 150-175 °C compared to room temperature. This can be attributed to an elevated mobility of Cu ions on the Au/Pd-surface, through the Au/Pd-coating, or within the β -Cu₂S layer at higher temperatures. However, the supply of Cu ions still takes place through the damaged spots. Thus, the morphology of the corrosion layer may change but the morphology of Cu core degradation should be independent of temperature. Note that no corrosion of the bare Cu wire is observed at room temperature conditions which again underlines the role of the Au/Pd-surface.

12.5 Conclusion

First, it was shown that Cu, PCC, APC, and APCX bond wire corrosion with **DS** in general follows an Avrami type model, which is nucleation and growth controlled. Further analysis of the APC bond wire with SEM after the PXRD measurements revealed the formation of β -Cu₂S within the core. Hence, it is concluded that the liquid reagent percolates into the core at elevated temperatures and thereby enables nucleation of β -Cu₂S within the core. As all 4 bond wire types exhibit similar corrosion behaviour, percolation is also assumed for the other wire types. Moreover, these findings underline the role of the S-reagents, which governs the overall corrosion mechanism. Hence, it is hypothesized that liquid disulfides in general lead to an Avrami type model (A2-A4). However, this could drastically change with the aggregation state of the S-compound. For instance, the mobility of the S-molecule may drastically change within the MC to yield diffusion controlled mechanisms.

Eventually, Arrhenius plots are generated from the obtained rate constants. Bare Cu wire follows an Arrhenius behaviour from 175-250 °C as it displays a linear relationship in the Arrhenius plot. Contrary to that, the PCC, APC, and APCX bond wire only show a linear behaviour from 175-225 °C. At 250 °C no further acceleration of the corrosion is confirmed and indicates that the decomposition reaction of **DS** is the rate limiting factor. Moreover, the corrosion rate of Cu, PCC, and APC bond wire are in the same order of magnitude whereas the APCX bond wire corrosion with **DS** displays much higher corrosion rates. Further analysis of the slopes of the Arrhenius plots reveals an increasing activation energy E_a from Cu ($E_a = 0.63$ eV) to PCC ($E_a = 0.80$ eV), APC ($E_a = 0.88$ eV), and APCX ($E_a = 0.90$ eV) bond wire. This implies that the surface reactivity is lower with the transition from Cu to Pd and Au surface. As a result, the contribution of the surface reaction to the overall corrosion rate increases and the activation energy rises. However, a much higher corrosion rate of the APCX wire hints towards the fact that additional mechanisms may play an important role. It is concluded that the additives Ni and Ga act as impurities to enable a heterogeneous nucleation. Consequently, the corrosion rate drastically increases as rapid nuclei formation is feasible due to the additives. This leads to the conclusion that the addition of dopants into the core not only elevates the complexity of the system but also yields much higher corrosion rates due to heterogeneous crystallization/corrosion kinetics

This changes drastically at HTS of the bond wires with **DS** at 150 °C. There, no bond wire degradation and β -Cu₂S is confirmed, and significant formation of colourless crystals is observed. Further, a new phase emerges from the powder patterns which is assumed to be an organic phase originating from these colourless crystals. Thus, HTS at 150 °C yields a completely altered corrosion behaviour for **DS**. It is concluded that high temperature stress testing is critical to simulate long-term corrosion. For instance, temperatures below 120 °C may lead to even lower decomposition of **DS**, which in turn is inert at these conditions. Hence, the decomposition of the S-reagent is a key parameter to determine the corrosion behaviour. There, it is not only important to investigate the pure S-compound but also the individual combinations with the metallic surface.

Moreover, the corrosion kinetics of Cu and APC wire with **MS1** are analysed from 250 °C to 175 °C. It is found that the bare Cu bond wire corrosion with **MS1** tends to be interface-controlled (R1-R3). Whereas the APC bond wire degradation is governed by nucleation and growth-control (A2-A4). Also, the APC bond wire displays a prolonged incubation and nucleation period compared to the Cu wire. However, after a while the growth of nuclei accelerates, and the long-term corrosion resistance of the APC wire becomes worse than for the Cu wire.

Further, the obtained rate constants from JMAEK-fit, SH-plot, and ICM are used to generate Arrhenius plots for the Cu and APC wire corrosion with **MS1** from 250 °C to 175 °C. Therein, a linear relationship is confirmed for the whole temperature range. The subsequent analysis of the activation energies E_a reveals a slightly higher mean $E_a = 0.83$ eV for the Cu wire versus $E_a = 0.80$ eV for the APC wire. Note that this is in the same range as bond wire corrosion with **DS**. Recall that the S-S bond in **DS** is assumed to be cleaved at the surface to chemisorb the thiolate on the wire surface. **MS1** is also assumed to adsorb as thiolate on the surface. Hence, a similar mechanism takes place on the wire surface which subsequently yields similar activation energies. However, the kinetics of the involved processes differs greatly from **DS** to **MS1** which is then expressed by different rate limiting corrosion steps. Also, a closer look at the ICM revealed a much higher activation energy for the incubation time t_0 of the APC wire. Hence, the high E_a for the incubation time results in a pronounced nucleation period of the APC wire. Then, E_a decreases after the formation of nuclei which results in an acceleration of the corrosion process. Moreover, the acceleration phase overlaps with the formation of Cu₃Pd which strongly suggests a significant influence of the intermetallic phase. Thereby, the alloy can either enable the diffusion of Cu ions to the surface or act as catalyst to cleave the C-S bond.

It is hypothesized that the high initial E_a hinders the formation of nuclei. This may be even more pronounced at lower temperatures where the decomposition of the S-reagent and the formation β -Cu₂S nuclei could be completely hindered by the high activation energy. However, if the wire is handled inadequate, nuclei can be formed on the wire surface. For instance, nuclei may be formed due to high temperatures during the manufacturing process or occasional temperature peaks during the application. This in turn may lead to a significant long-term corrosion of the bond wire as the growth of the nuclei accelerates afterwards. This may be even more pronounced for the APCX wire where the additives can act as impurities and increase nuclei formation. Conversely, the bare Cu wire displays a steady degradation through the whole corrosion process with a linear relationship of the temperature induced acceleration of the wire degradation over the entire temperature range.

Therefore, the chosen evaluation periods are critical to determine the reliability of coated bond wires as insufficient evaluation time may lead to incorrect reliability assumptions. Here, the long incubation time for the nucleation of copper sulfide may prevent the occurrence of corrosion in the semiconductor chip at insufficient test temperature and time. However, nuclei may form during the inadequate handling of the package or temperature peaks during applications. The subsequent growth of these nuclei is much faster than their formation which may lead to high localised corrosion of the coated wires. Hence, coated bond wires remain critical for extended lifetimes and application in harsh

environments. By comparison, high temperature stress testing of the bare Cu wire is less critical as it exhibits steady acceleration modes versus various reagents and over a wide temperature range. This again underlines the complexity of the coated bond wires, which not only turn out to be unpredictable in stress testing but also may produce a wide variety of corrosion products. Therefore, future development of the bare Cu bond wire presents a greater potential than additional coating or additive systems. Hence, complex corrosion reactions can be avoided by the application of bare Cu wire. In addition, high temperature stress testing is less critical and produces more reliable results.

Long-term HTS of the bare Cu and APC bond wire with **TT** and **MS1** at 150 °C and 175 °C underline these hypotheses. Therein, discoloration of the Cu and APC wire surface is visible after 4700 h with **TT** at 150 °C but the wires stayed mostly uncorroded. Compared to that, the Cu and APC wire display a black corrosion layer around the wire after HTS with **MS1** at 150 °C. This huge difference can be attributed to the much higher activation energy of **TT** corrosion (APC = 3.2 eV, Cu = 2.8 eV) versus **MS1** (APC = 0.83 eV, Cu = 0.80 eV). Hence, decomposition and C-S bond cleavage of **TT** is much more unlikely to occur at 150 °C. However, at 175 °C both reagents **TT** and **MS1** lead to a severe black corrosion layer around the Cu and APC wire. This is to be expected as the corrosion accelerates much faster for **TT** as compared to **MS1**. Strikingly, corrosion of the APC bond wire is even confirmed after room temperature storage for 4700 h with **MS1**. For these wires, black chunks are observed at distinct spots on the wire surface. This confirms the hypothesis that corrosion starts at damaged coating areas and underlines the effect of galvanic corrosion at these areas. Thus, the sole presence of the Au/Pd-coating does not catalyse the decomposition of the S-reagent as this should produce a homogeneous layer around the wire surface. Hence, it rather supports the assumption that Cu₂S formation is enabled by the galvanic coupling at the exposed areas of the Cu core. Conversely, corrosion is not observed for the bare Cu wire which remains unchanged after storage at the same conditions. This also underlines the acceleration of APC bond wire degradation after initial nuclei formed.

While HTS at 150 °C with **MS1** and **TT** results in the corrosion of the Cu and APC bond wire, no degradation of the bond wires is confirmed with **DS**. Despite **DS** exhibits much higher corrosion rates at 175 °C to 250 °C compared to **MS1** and **TT**, it does not lead to the degradation of the bond wires at lower temperatures. Also, similar activation energies E_a are found for **MS1** and **DS** which might lead to the conclusion that both behave similar at the respective temperature. Yet, **MS1** still corrodes the wire at lower temperature whereas **DS** does not. Thus, the temperature dependant corrosion behaviour differs greatly for various S-compounds. Consequently, the specific S-reagents, which are suitable as adhesion promoters or additives for the MC, must be investigated individually. Thereby, critical parameters are the temperature dependant

- i. decomposition of the pure S-compound
- ii. decomposition of the S-compound in combination with the desired bond wire
- iii. decomposition of the S-compound within the specific MC
- iv. mobility of the S-compound within the MC

13 Conclusive Discussion on Adhesion Promoter Experiments

Here, the results from chapter 7-12 are summarized and discussed. First, it is found in chapter 7 that Cu powder mixed with **MS1** and **TT** gives the copper-rich, low-temperature α -Cu₂S (< 100 °C). The α -Cu₂S phase is also confirmed when Pd is added to the mixture. According to that, the high-temperature version β -Cu₂S (> 100 °C) is found consistently throughout all HT-in situ-PXRD measurements of the bond wires. Hence, the formation of copper-rich Cu₂S is also assumed for corrosion in semiconductor packages. A further quantification of the powdery mixtures reveals a fast corrosion of the Cu particles in the temperature range from 250 °C to 175 °C which slows down significantly at 150 °C and 125 °C for both **MS1** and **TT**. Here, minor amounts of α -Cu₂S are detected with **TT** after 2500 h at 125 °C but no copper sulfide was found with **MS1** at the same conditions. Similar observations are made on the Cu and APC wire with **TT** and **MS1** after HTS at 175 °C and 150 °C (chapter 12.4.9). The studies revealed the corrosion accelerates noticeable at 175 °C compared to 150 °C.

When Pd is added to the powdery mixtures, the α -Cu₂S formation rate increases for both **TT** and **MS1**. For the Cu-Pd-**TT** mixture, this effect is already observed at 125 °C after 672 h. However, the Cu_xS phase is not detected for the Cu-Pd-**MS1** mixture at 125 °C but instead at 150 °C after 672 h. This is consistent with the Cu-**MS1** mixture and displays the lower reactivity of the **MS1** reagent compared to **TT**. Moreover, the formation of Cu₃Pd is confirmed for both Cu-Pd-**MS1/TT** mixture after long-term HTS or elevated temperatures. Thus, it is hypothesized that HTS ultimately results in the thermodynamically favoured products α/β -Cu₂S and Cu₃Pd. Strikingly, the same phases are indexed in the powder patterns of the HT-in situ-PXRD measurements of the coated Cu bond wires which underlines this hypothesis. Hence, the proposed general sulfidation and alloying process in Figure 7.15 (chapter 7.4.4) is still valid for the Pd-coated Cu bond wires.

However, quantitative phase analysis of the in-situ bond wire experiments at 250 °C shows no significant acceleration of the bond wire corrosion by the Pd-coating. This can be attributed to several factors. First, the Pd-coating in fact acts as diffusion barrier for the S-reagent and thereby impairs Cu core corrosion. However, the exposed Cu pinholes at the damaged coating areas result in a severe pitting corrosion. Thus, the overall Cu core conversion is relatively moderate but highly localised. Second, the Cu-Pd-**MS1/TT** mixture is finely ground and blended. Thus, a large number of galvanic couples is present in the mixture with adjacent S-reagent. This leads to a higher overall corrosion rate and thus to a higher conversion of Cu in the mixtures with added Pd.

Long-term HTS of the APC bond wire with **MS1** at 200 °C reveals an acceleration of the Cu core degradation after a slow nucleation period. Thus, the Au/Pd-coated wires in fact display a worse long-term reliability at 200 °C compared to the bare Cu wire. This is consistent with room temperature storage of the bond wires with **MS1**. There, the bare Cu wire is unchanged after 4700 h while black chunks formed on the surface of the APC bond wire which raises considerable reliability concerns.

Furthermore, lower corrosion rates are obtained for the powdery Cu-**TT** mixtures compared to the Cu wire with **TT** at 200 °C, see **Figure 13.1**. Thus, other factors are assumed to play an important role. As this is not observed for the powdery Cu-**MS1** mixture compared to Cu wire with **MS1**, this phenomenon is ascribed to the **TT** reagent. A substantial difference between the powdery mixture and the wire experiments is the experimental setting. Thereby, HTS of the powdery mixtures was conducted in comparably large and loosely packed ampoules (~cm) versus small capillaries (~mm). Thus, the gaseous decomposition products are distributed over a much bigger volume in the ampoules. This leads to a lower average concentration and vapor pressure of the decomposition products within the reaction vessel. Consequently, the lower vapor pressure results in a decreased corrosion rate. Compared to that, the vapor pressure increases significantly in the densely packed capillaries and thus increases the corrosion rate. This further indicates a key role of S-reagent decomposition and subsequent diffusion of its products. Contrary to that, the corrosion rates with liquid **MS1** are similar for both bare Cu and Cu powder. This points to a corrosion which solely proceeds within the liquid phase instead of gaseous decomposition products. Accordingly, this hypothesis was validated with **TT/PC** and **TT/DMSO** solutions. It is found that the activation energies E_a of Cu corrosion with **TT** solutions approximate to the liquid **MS1** corrosion.

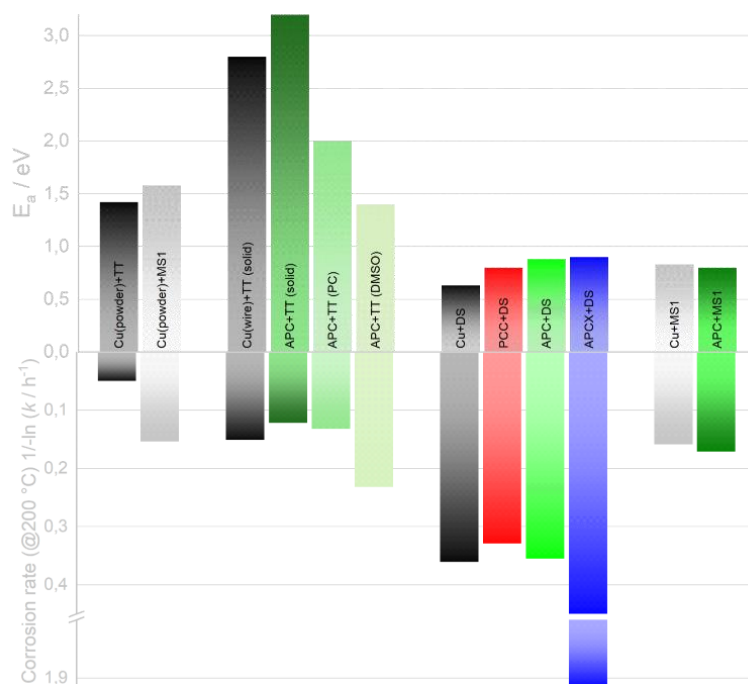


Figure 13.1: Top columns: Activation energies E_a for Cu powder and Cu, PCC, APC, and APCX bond wire experiments with the S-compounds **TT**, **MS1**, and **DS**. Bottom columns: Corresponding corrosion rates at 200 °C.

Interestingly, the activation energy E_a is relatively similar for the corrosion of the powdery Cu-**TT** and Cu-**MS1** mixtures whereas a significant difference arises for the bare Cu wire with **TT** and **MS1**. This can be explained by the thorough reduction by H_2 of the Cu powder surface prior to the experiments, thus the Cu particles show enhanced reactivity. Contrary to that, homogeneous reduction of the bare Cu wire is harder to achieve which may result in a higher initial activation barrier for the

Cu corrosion. However, a high E_a is also obtained for the APC bond wire which is supposed to have an oxidation resistant Au finishing. Thus, it can either be attributed to the Au surface or to the better homogenization of the powdery mixtures compared to the wire experiments. There, sample preparation and surface coverage of the wire within the capillary is more challenging which in turn could lead to a higher activation barrier.

The contrary observation is made for the powdery Cu-**MS1** mixture versus the bare Cu wire with **MS1** experiments. Therein, E_a decreases for the wire experiments which could be explained by good wettability and SAM formation by the liquid on the wire surface. Also, the wire surface exhibits an altered grain size distribution and grain orientation which can have a strong impact on reactivity.

Further investigation of the bond wire corrosion with the liquid reagent **DS** reveals a similar activation barrier E_a compared to **MS1**. Therein, the experiments were performed on Cu, PCC, APC, and APCX bond wire and reveals similar activation energies for all bond wires. Thus, the state of aggregation seems to have the strongest influence on the activation energy. However, a slight increase from Cu to PCC, APC, and APCX wire is still measurable. Hence, the flash-Au layer and the dopants increase the activation barrier. There, the Au surface may exhibit weaker thiolate adsorption which in turn impedes the initial β -Cu₂S formation.

Further comparison of Cu, PCC, APC, and APCX bond wire corrosion with **MS1**, **TT**, and **DS** demonstrates that the corrosion rates are generally in the same order of magnitude for the respective reagent, see **Figure 13.2**. Here, the triazole-thiol **TT** and the disulfide **DS** show similar corrosion rates whereas corrosion rates of the mercaptosilane **MS1** are lower by one order of magnitude. Thus, the selected S-reagent has the most impact on the corrosion rate and therefore is the most important criterion. Still, differences between the respective bond wires are found. Generally, the APCX bond wire displays higher corrosion rates while the PCC bond wire showed to be the most reliable wire type throughout all experiments. This is against the common observations made in literature where the PCC bond wire is more prone to corrosion. These findings suggest that other factors like IMC formation and corrosive species such as H₂O, O²⁻, and Cl⁻ play an important role. This is also true for the APCX bond wire which may develop a passivating layer in combination with other corrosive reagents. Thus, further investigations are necessary to understand combinatorial effects.

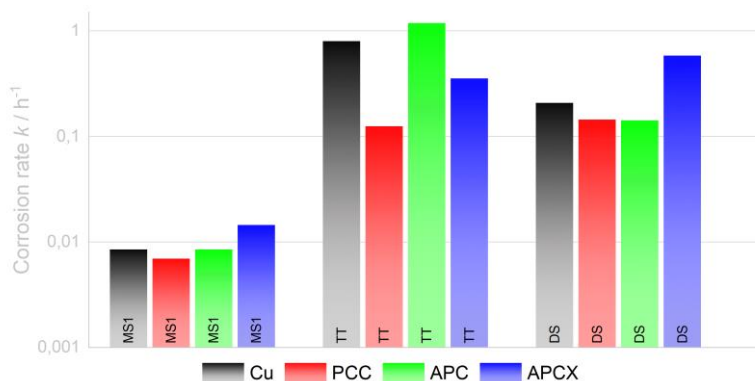


Figure 13.2: Corrosion rates at 250 °C for Cu, PCC, APC, and APCX bond wire with **MS1**, **TT**, and **DS**.

14 Summary and Outlook

This thesis investigates the distinct phenomena which accompany sulfur induced Cu bond wire corrosion in semiconductor packages. Understanding these key aspects of sulfur induced Cu bond wire degradation is crucial to support further package and bond wire development.

Foremost, the general reactivity of Cu and Pd mixtures with thiols is investigated to gain a basic understanding of the system. Preliminary tests show that the Cu content in the formed Cu_{2-x}S strongly depends on the thiol content in the mixture. Importantly, the copper-rich phases $\alpha/\beta\text{-Cu}_{2-x}\text{S}$ are found consistently in subsequent experiments as the main corrosion products. Thus, $\alpha\text{-Cu}_{2-1.993}\text{S}$ ($< 100\text{ }^\circ\text{C}$) and $\beta\text{-Cu}_{2-1.988}\text{S}$ ($> 100\text{ }^\circ\text{C}$) are anticipated in semiconductor packages due to the comparably low sulfur content in the MC. Further studies with additional Pd in the powdery mixtures yield a wide variety of phases such as PdH_x , Pd_xS , CuPd , and Cu_3Pd , which significantly increase the catalytic capability of Pd-coated Cu wires in the semiconductor package. Subsequent quantitative studies reveal a significant acceleration of the sulfidation rate when Pd is added to the mixture. These findings show that Pd-coated Cu wires have a considerably increased corrosion risk and thus serve as a basic understanding for further Cu bond wire corrosion investigations.

Based on these results, the electrochemical measurements are focused on the low chalcocite $\alpha\text{-Cu}_{2-1.993}\text{S}$ and high chalcocite $\beta\text{-Cu}_{2-1.988}\text{S}$. EIS measurements reveal a high electronic conductivity σ_{eon} of $\alpha\text{-Cu}_2\text{S}$ which decreases only negligibly with the transition to $\beta\text{-Cu}_2\text{S}$ (0.03 S/cm). In contrast, the phase transition from $\alpha\text{-Cu}_2\text{S}$ to $\beta\text{-Cu}_2\text{S}$ is accompanied by a significant increase of the ionic conductivity σ_{ion} , self-diffusion coefficient D_{Cu^+} , and chemical diffusion coefficient \tilde{D}_{Chem} ($\sim 1 \cdot 10^{-5} \text{ cm}^2 \text{ s}^{-1}$, $200\text{ }^\circ\text{C}$). EIS measurements and subsequent calculation of \tilde{D}_{Chem} shows good agreement with literature data. As a result, $\alpha/\beta\text{-Cu}_2\text{S}$ is confirmed as a MIEC with high electronic conduction and moderate ionic conduction. It should be stressed that the Cu^+ diffusion in $\beta\text{-Cu}_2\text{S}$ is a crucial property for Cu bond wire corrosion. Hence, the obtained values are vitally important for further theoretical studies such as computational corrosion simulation. Such theoretical corrosion simulations are a potentially powerful tool in combination with experimental verification strategies to predict the lifetime at lower temperatures which are experimentally inaccessible.

For the subsequent evaluation of the Cu bond wire reliability, HT-in situ-PXRD is applied to quantitatively monitor Cu bond wire degradation and $\beta\text{-Cu}_2\text{S}$ formation isothermally at $150\text{ }^\circ\text{C}$ to $250\text{ }^\circ\text{C}$. Accordingly, the reactivity of different organic sulfur moieties versus bare Cu bond wire is explored at elevated temperatures. HT-in situ-PXRD measurements show that the corrosion reliability of bare Cu bond wire versus organic sulfur compounds decreases in the order thioketone, sulfoxide, thioether, unconjugated thiol, oxygen, conjugated thiol, di-, tri- and tetrasulfide. Hence, suitable S-compounds are identified as potential ingredients for the formulation of the MC.

As the addition of Pd leads to increased sulfidation, corrosion reliability and failure mechanisms of Cu, PCC, APC, and APCX bond wire versus triazole-thiol, disulfide, and mercaptosilane are investigated at 250 °C. It is found that **TT** and **DS** lead to a much faster degradation of all bond wires compared to **MSI**. Therefore, it is concluded that the S-reagent is the most dominant package material selection criterion. Yet, discrepancies between the various bond wires are still present. Herein, the reliability of the wires versus sulfur induced corrosion at 250 °C is ranked in the order APC, PCC, Cu, APCX. This finding contrasts with the results obtained on powdery Cu/Pd mixtures where Pd accelerates the Cu corrosion. To further investigate this discrepancy, general corrosion models are developed by complementing the HT-in situ-PXRD measurements with SEM and EDX micrographs. These studies show that the corrosion of the coated Cu wires especially begins at the defect sites of the coating. Accordingly, a high degree of localised corrosion is observed at the defect sites. As a result, the mean corrosion rate is lower compared to the bare Cu wire. Nonetheless, pitting corrosion poses a high risk for bond failure due to the large Cu voids which are formed during the process. Contrary to that, the addition of a flash-Au layer is shown to slow down the initial surface reaction. This can be attributed to the lower reactivity of the Au surface towards S-compounds and thus proves to be a successful strategy to prevent the initial sulfur induced corrosion. Moreover, it is found that the addition of Ni and Ga into the core of the APCX wire leads to a detrimental corrosion behaviour and a variety of corrosion products such as $\text{Ni}_3\text{S}_2/\text{NiS}$ and $\text{Ga}_2\text{S}_3/\text{GaS}$ as well as Ga-Pd alloys for this wire type. As a consequence, the Pd-coating of the APCX wire breaks down and the activation energy is lowered for Cu_{2-x}S nucleation.

Additionally, grain growth and reorientation effects are observed to take place above 225 °C. This is confirmed by HT-in situ-PXRD measurements of APC bond wire at 225/250/300 °C while incorporated into MC and subsequent EBSD analysis. Closer inspection revealed a sigmoidal and parabolic decline of the Cu(200) reflection intensity at 250 °C and 300 °C, respectively. Different grain growth and reorientation kinetics are observed as a function of temperature. Further analysis by EBSD and *LF* shows that different grain orientation distributions are obtained at 250 °C and 300 °C. Thus, in addition to different grain growth kinetics, varying orientation distributions are measured for the APC bond wire at distinct temperatures. This is an important finding as the grain size and orientation plays a vital role in corrosion processes. This also means that altered grain properties must be considered during high temperature stress testing as this may lead to false acceleration models.

As the predominant degradation mechanisms can change with temperature, the temperature induced corrosion acceleration of the different wire types is investigated from 150 °C to 250 °C as this is a key aspect for high temperature stress testing and lifetime predictions. Note that lifetime predictions in general are extrapolations from elevated temperatures such as 150 °C to 250 °C. Therefore, it is vitally important to understand the corrosion behaviour and underlying mechanisms at different temperatures. In our experiments, bare Cu, PCC, APC, and APCX bond wire with **DS** in general follow an Arrhenius behaviour from 175-225 °C with an increasing activation energy E_a from Cu ($E_a = 0.63$ eV) to PCC ($E_a = 0.80$ eV), APC ($E_a = 0.88$ eV), and APCX ($E_a = 0.90$ eV) bond wire.

At 250 °C no further acceleration of the corrosion is confirmed which indicates that the decomposition reaction of **DS** is the rate limiting factor instead of diffusion-controlled processes. Strikingly, the corrosion behaviour of the bond wires changes drastically with **DS** at 150 °C. There, no bond wire degradation and β -Cu₂S is observed. In addition, a significant amount of colourless crystals form. Thus, the temperature reduction from 175 °C to 150 °C yields a completely altered corrosion behaviour for **DS**.

Accordingly, measurements of Cu and APC bond wire with **MS1** are performed from 175 °C to 250 °C with subsequent kinetic analysis. Here, the APC bond wire with **MS1** displays a prolonged incubation and nucleation period compared to the bare Cu wire. However, after a while the growth of nuclei accelerates, and the long-term corrosion resistance of the APC wire becomes worse than the Cu wire. The respective Arrhenius plots show a linear relationship for the whole temperature range with similar activation energies for the Cu wire ($E_a = 0.83$ eV) and APC wire ($E_a = 0.80$ eV). However, a closer look reveals a much higher activation energy for the incubation time t_0 of the APC wire. Hence, the high E_a for the incubation time results in a pronounced nucleation period of the APC wire. Then, E_a decreases after the formation of nuclei which accelerate the corrosion process. Moreover, the acceleration phase overlaps with the formation of Cu₃Pd which strongly suggests a significant influence of the intermetallic phase.

Finally, long-term storage at 150 °C and 175 °C was performed for Cu and APC bond wire with **MS1** and **TT**. There, only slight discoloration of the Cu and APC wire surface is visible after 4700 h with **TT** at 150 °C. Compared to that, it is found that Cu and APC wire displays a black corrosion layer around the wire after HTS with **MS1** at 150 °C. This huge difference is attributed to the much higher activation energy of **TT** corrosion (APC = 3.2 eV, Cu = 2.8 eV) which yields less decomposition products at 150 °C. However, at 175 °C a severe black corrosion layer around the Cu and APC wire is confirmed for both reagents. This is to be expected as the corrosion accelerates much faster for **TT** as compared to **MS1**. Strikingly, corrosion of the APC bond wire is even confirmed after room temperature storage for 4700 h with **MS1** where black chunks are observed at distinct spots on the wire surface. This confirms the hypothesis that corrosion starts at defect sites and underlines the effect of galvanic corrosion at these areas. Conversely, corrosion is not observed for the bare Cu wire which remains unchanged after storage at the same conditions.

In summary, the corrosion behaviour changes drastically from 150 °C to 175 °C for the S-reagents **DS** and **TT**. For both S-reagents the decomposition reactions play a vital role in the corrosion process which is hindered at 150 °C. This is demonstrated by the high E_a for **TT** corrosion but is not as obvious for **DS** corrosion which has a similar E_a to **MS1** corrosion. Therefore, the obtained E_a in general does not permit a clear statement on the decomposition and corrosion behaviour of the respective adhesion promoter. Consequently, the respective adhesion promoters or rather MC must be checked individually for their high temperature corrosion behaviour. Moreover, special attention must be paid to the lower temperature region from 125 °C to 175 °C as this seems to be a critical temperature range. In this range the corrosion behaviour in general changes drastically (e.g. **DS**, **TT**),

which can be especially attributed to the temperature stability and decomposition reactions of the respective adhesion promoter. Here, investigations on the general temperature stability of the S-compound allow first insights into the high temperature corrosion behaviour. However, the combination of different bond wires and the MC matrix makes the high temperature behaviour hard to predict. Therefore, it is concluded that long-term reliability tests at 125-175 °C remain essential to predict the reliability of the specific semiconductor package.

In summary, the HT-in situ-PXRD methodology in capillaries proves to be a successful strategy to screen various S-compounds with respect to their corrosive capability. Moreover, the reagents can either be in liquid or solid form which enables a wide range of different bond wire type and reagent combinations. Also, the bond wires can be measured with other potentially corrosive reagents such as H₂O, O₂ and Cl⁻. Further, the simultaneous determination of structural information, grain properties, and quantitative conversions makes it a powerful tool to gain deep understanding of the underlying mechanisms with a single methodology.

Mechanistic and kinetic investigations allow a profound analysis of the related corrosion processes. Our mechanistic studies clearly show that Cu ion inter- and surface diffusion in PCC bond wires are significant factors for preventing Cu core oxidation. In addition, grain boundary and bulk diffusivity within the Cu core are important features that enable the reduction of the corrosion rate. The IGC along the grain boundaries is especially pronounced for the doped APCX wire. Hence, the use of additive elements carries a high risk for IGC in the presence of sulfur. Therefore, a potential strategy to prevent corrosion of the Cu core is to specifically tune grain size and grain boundaries by GBE. The advantage of a grain microstructure improvement strategy is to move from a complex metallurgical system (e.g. APCX = Au-Pd-Cu-Ni-Ga) with unpredictable alloying and corrosion products towards a “simplistic” Cu bond wire. By comparison to APC bond wire, high temperature stress testing of the bare Cu wire is less critical as it exhibits steady acceleration modes versus various reagents and over a wide temperature range, which makes it more predictable. Consequently, complex corrosion reactions can be avoided by the application of bare Cu wire. Additionally, GBE could improve the general corrosion resistance of the Cu bond wire versus various corrosive environments instead of custom-built applications. For instance, a bare Cu bond wire with small grains and low grain boundary diffusivity, optimized by GBE, would give a universally corrosion resistant Cu wire. Consequently, thin corrosion layers are favoured over highly localised pitting corrosion which exhibits much bigger reliability concerns. Therefore, future development of the bare Cu bond wire by GBE seems a more promising approach than additional coating or additive systems.

15 Bibliography

1. *PwC Research* **2019**, URL: <https://www.pwc.com/gx/en/industries/tmt/publications/assets/pwc-semiconductor-report-2019.pdf> (Access date: 25.11.2020).
2. Andrews, W., Aisch, G., *The New York Times* **2014**, URL: <https://www.nytimes.com/interactive/2014/12/30/business/a-record-year-for-auto-recalls.html> (Access date: 20.10.2020).
3. Lall, P.; Deshpande, S.; Nguyen, L.; Murtuza, M., *IEEE, 64th Electronic Components and Technology Conference (ECTC)* **2014**, 569-585.
4. Govindaiah, N.; Dressler, M.; Bittlingmaier, M.; Zundel, U.; Yadur, A., *IEEE, 17th International Conference on Thermal, Mechanical and Mult-Physics Simulation and Experiments in Microelectronics and Microsystems (EuroSimE)* **2016**, 1-9.
5. Unger, W., Becker, R., Goroll, M., *German Electrical and Electronic Manufacturers Association (ZVEI)* **2006**, URL: https://www.zvei.org/fileadmin/user_upload/Presse_und_Medien/Publikationen/2006/Dezember/Robustness_Validation/Implementation/2006-10_Automotive_Application_Questionnaire_engl_Edition.pdf (Access date: 20.10.2020).
6. Gan, C. L.; Hashim, U., *J. Mater. Sci. Mater. Electron.* **2015**, 26, 4412-4424.
7. Palesko, C. A.; Vardaman, E. J., *IEEE, 60th Electronic Components and Technology Conference (ECTC)* **2010**, 10-13.
8. Breach, C. D.; Wulff, F. W., *Microelectron. Rel.* **2010**, 50, 1-20.
9. Appelt, B. K.; Tseng, A.; Chen, C. H.; Lai, Y. S., *Microelectron. Rel.* **2011**, 51, 13-20.
10. Liu, P. S.; Tong, L. Y.; Wang, J. L.; Shi, L.; Tang, H., *Microelectron. Rel.* **2012**, 52, 1092-1098.
11. Breach, C. D., *Gold Bull.* **2010**, 43, 150-168.
12. Electronics, H., URL: https://www.heraeus.com/media/media/het/doc_het/products_and_solutions_het_documents/bonding_wires_documents/Brochure_Bonding_Wire.pdf (Access date: 21.10.2020).
13. Chauhan, P.; Zhong, Z. W.; Pecht, M., *J. Electron. Mater.* **2013**, 42, 2415-2434.
14. Khoury, S. L.; Burkhard, D. J.; Galloway, D. P.; Scharr, T. A., *IEEE, Transactions on Components Hybrids and Manufacturing Technology* **1990**, 13, 673-681.
15. McLeish, J., **2015**, URL: <https://www.dfrsolutions.com/hubfs/Resources/services/Suitability-of-Cu-Wire-Bond-ICs-in-Auto-Other-Harsh-Environments.pdf> (Access date: 21.10.2020).
16. Ishiko, M.; Usui, M.; Ohuchi, T.; Shirai, M., *Microelectron. J.* **2006**, 37, 262-268.
17. Breach, C., *Microelectron. Rel.* **2019**, 37, 36-45.
18. Breach, C. D., *Gold Bull.* **2016**, 49, 63-73.
19. Breach, C. D.; Wulff, F., *Microelectron. Rel.* **2004**, 44, 973-981.
20. Breach, C. D.; Wulff, F. W., *Gold Bull.* **2009**, 42, 92-105.
21. Lim, A. B. Y.; Neo, W. J.; Yauw, O.; Chylak, B.; Gan, C. L.; Chen, Z., *Microelectron. Rel.* **2016**, 56, 155-161.
22. Wulff, F.; Breach, C. D., *Gold Bull.* **2006**, 39, 175-184.
23. Liu, C. P.; Chang, S. J.; Liu, Y. F.; Chen, W. S., *J. Mater. Process. Technol.* **2019**, 267, 90-102.
24. Tan, Y. Y.; Koerner, H.; Walter, J.; Ananiev, S.; Bauer, R., *IEEE, 65th Electronic Components and Technology Conference (ECTC)* **2015**, 1403-1411.

25. Liu, C. P.; Chang, S. J.; Liu, Y. F.; Su, J., *J. Alloy Compd.* **2020**, 825.
26. Kanert, W.; Dettmer, H.; Plikat, B.; Seliger, N., *Microelectron. Rel.* **2003**, 43, 1839-1846.
27. Kwatra, A.; Samet, D.; Rambhatla, V. N. N. T.; Sitaraman, S. K., *Microelectron. Rel.* **2020**, 111.
28. Rongen, R. T. H.; O'Halloran, G. M.; Mavinkurve, A.; Goumans, L.; Farrugia, M. L., *IEEE, 64th Electronic Components and Technology Conference (ECTC)* **2014**.
29. Rongen, R. T. H.; Mavinkurve, A.; O'Halloran, G. M.; Owens, N.; Weber, Y.; Oberndorff, P.; Farrugia, M. L.; van Olst, E.; van Soestbergen, M., *IEEE 69th Electronic Components and Technology Conference (ECTC)* **2019**, 479-485.
30. Breach, C. D.; Lee, T. K., *J. Electron. Mater.* **2012**, 41, 2018-2028.
31. Manoharan, S.; Li, N. M. J.; Patel, C.; Hunter, S.; McCluskey, P., *IEEE, 20th Electronics Packaging Technology Conference (EPTC)* **2018**, 874-881.
32. Tan, C. W.; Daud, A. R.; Yarmo, M. A., *Appl. Surf. Sci.* **2002**, 191, 67-73.
33. Gan, C. L.; Classe, F. C.; Chan, B. L.; Hashim, U., *Gold Bull.* **2014**, 47, 141-151.
34. Chan, M.; Tan, C. M.; Lee, K. C.; Tan, C. S., *Microelectron. Rel.* **2016**, 61, 56-63.
35. Fateh, A.; Aliofkhazraei, M.; Rezvanian, A. R., *Arab. J. Chem.* **2017**.
36. Gan, C. L.; Ng, E. K.; Chan, B. L.; Hashim, U.; Classe, F. C., *J. Nanomater.* **2012**, 2012.
37. Gan, C. L.; Francis, C.; Chan, B. L.; Hashim, U., *Gold Bull.* **2013**, 46, 103-115.
38. Uno, T., *Microelectron. Rel.* **2011**, 51, 148-156.
39. Han, B.; Kim, D. S., *J. Electron. Packag.* **2017**, 139.
40. Hang, C. J.; Wang, C. Q.; Mayer, M.; Tian, Y. H.; Zhou, Y.; Wang, H. H., *Microelectron. Rel.* **2008**, 48, 416-424.
41. Riedl, E., **2014**, University of Regensburg.
42. Ryu, J. H.; Choi, K. S.; Kim, W. G., *J. Appl. Polym. Sci.* **2005**, 96, 2287-2299.
43. Boettcher, T.; Rother, M.; Liedtke, S.; Ullrich, M.; Bollmann, M.; Pinkernelle, A.; Gruber, D.; Funke, H.-J.; Kaiser, M.; Lee, K.; Li, M.; Leung, K.; Li, T.; Farrugia, M. L.; O'Halloran, O., *IEEE, 12th Electronics Packaging Technology Conference (EPTC)* **2010**, 585-590.
44. An, B.; Ding, L.; Wang, T.; Lu, T.; Sun, L.; Wu, Y., *IEEE, 12th Electronics Packaging Technology Conference (EPTC)* **2011**, 391-394.
45. Tang, L.-J.; Ho, H.-M.; Zhang, Y.-J.; Lee, Y.-M.; Lee, C.-W., *IEEE, 12th Electronics Packaging Technology Conference (EPTC)* **2010**, 777-782.
46. Carson, F.; Yee, J. H.; Park, S. S.; Fontanilla, E., *IEEE, 62nd Electronic Components and Technology Conference (ECTC)* **2012**.
47. Lim, A. B. Y.; Chang, A. C. K.; Yauw, O.; Chylak, B.; Gan, C. L.; Chen, Z., *Microelectron. Rel.* **2014**, 54, 2555-2563.
48. Leong, G. C.; Uda, H., *Plos One* **2013**, 8.
49. Cheng, P. Y.; Lai, P. Y.; Ye, J. M.; Chen, T. C.; Hsieh, C. L., *Microelectron. Rel.* **2018**, 80, 1-6.
50. Lee, C.-C.; Tran, T.; Boyne, D.; Higgins, L.; Mawer, A., *IEEE, 64th Electronic Components and Technology Conference (ECTC)* **2014**, 1539-1548.
51. Stephan, D.; Wulff, F. W.; Milke, E., *IEEE, 12th Electronics Packaging Technology Conference (EPTC)* **2010**, 343-348.
52. Abe, H.; Kang, D. C.; Yamamoto, T.; Yagihashi, T.; Endo, Y.; Saito, H.; Horie, T.; Tamate, H.; Ejiri, Y.; Watanabe, N., *IEEE, 62nd Electronic Components and Technology Conference (ECTC)* **2012**, 1117-1123.
53. Xu, H.; Qin, H.; Clauberg, H.; Chylak, B.; Acoff, V. L., *Acta Mater.* **2013**, 61, 79-88.
54. Lee, C. C.; Tran, T. A.; Mathew, V.; Ibrahim, R.; Eu, P. L., *IEEE 66th Electronic Components and Technology Conference (ECTC)* **2016**, 606-613.

55. Krinke, J. C.; Dragicevic, D.; Leinert, S.; Friess, E.; Glueck, J., *Microelectron. Rel.* **2014**, *54*, 1995-1999.
56. Eto, M.; Haibara, T.; Oishi, R.; Yamada, T.; Uno, T.; Oyamada, T., *IEEE 67th Electronic Components and Technology Conference (ECTC)* **2017**, 1297-1302.
57. Han, M.; Wang, M.; Zhang, L.; Beiyue, Y.; Li, J.; Song, M.; Mathew, V., *IEEE 18th Electronic Packaging Technology Conference (EPTC)* **2016**, 797-800.
58. Lau, K.-T.; Cha, C. L., *Int. J. Mech. Prod. Eng. Res. Dev. (IJMPERD)* **2020**, *10*, 4479-4492.
59. Saruwatari, T.; Takahashi, T.; Ono, A.; Asano, Y.; Iwasaki, T.; Ooida, M.; Hiruta, Y., *Pan Pacific Microelectronics Symposium (Pan Pacific)* **2017**, 1-7.
60. Mavinkurve, A.; Goumans, L.; Farrugia, M. L.; van Olst, E.; van Soestbergen, M.; Rongen, R. T. H.; Bumrungkittikul, B., *IEEE 67th Electronic Components and Technology Conference (ECTC)* **2017**, 1171-1178.
61. Müller, R.; Heckmann, K.; Habermann, M.; Paul, T.; Stratmann, M., *J. Adhes.* **2000**, *72*, 65-83.
62. Denayer, J.; Delhalle, J.; Mekhalif, Z., *Appl. Surf. Sci.* **2011**, *257*, 10686-10691.
63. Wong, C. K. Y.; Fan, H. B.; Yuen, M. M. F., *Ieee T Compon Pack T* **2008**, *31*, 297-308.
64. Dai, Q. P.; Xue, C. C.; Xue, G.; Jiang, L. X., *J. Adhes. Sci. Technol.* **1995**, *9*, 1465-1474.
65. WU, X.; Wiame, F.; Maurice, V.; Marcus, P., *Appl. Surf. Sci.* **2020**, *508*, 145132.
66. Wu, X. C.; Wiame, F.; Maurice, V.; Marcus, P., *Appl. Surf. Sci.* **2020**, 527.
67. Vericat, C.; Vela, M. E.; Corthey, G.; Pensa, E.; Cortes, E.; Fonticelli, M. H.; Ibanez, F.; Benitez, G. E.; Carro, P.; Salvarezza, R. C., *RSC Adv.* **2014**, *4*, 27730-27754.
68. Kwok, S. C. T.; Ciucci, F.; Yuen, M. M. F., *Electrochim. Acta* **2014**, *121*, 57-63.
69. Metikos-Hukovic, M.; Babic, R.; Petrovic, Z.; Posavec, D., *J. Electrochem. Soc.* **2007**, *154*, C138-C143.
70. Vernack, E.; Costa, D.; Tingaut, P.; Marcus, P., *Corros. Sci.* **2020**, 174.
71. Whelan, C. M.; Kinsella, M.; Ho, H. M.; Maex, K., *J. Electrochem. Soc.* **2004**, *151*, B33-B38.
72. Antonijevic, M. M.; Petrovic, M. B., *Int. J. Electrochem. Sci.* **2008**, *3*, 1-28.
73. Wu, X. Y.; Wang, Y. Z.; Di, Y. T.; Lan, T. Y.; Zu, L. W., *J. Nanomater.* **2019**, 2019.
74. Thompson, C. J.; Meyer, R. A.; Ball, J. S., *J. Am. Chem. Soc.* **1952**, *74*, 3287-3289.
75. Hsieh, K. C.; Martens, T., *J. Electron. Mater.* **2000**, *29*, 1229-1232.
76. Rickert, H.; Wiemhofer, H. D., *Solid State Ionics* **1983**, *11*, 257-268.
77. Wagner, R.; Wiemhofer, H. D., *J. Phys. Chem. Solids* **1983**, *44*, 801-805.
78. Pauporte, T.; Vedel, J., *Ionics* **1996**, *2*, 241-247.
79. Cassaignon, S.; Pauporte, T.; Guillemoles, J. F.; Vedel, J., *Ionics* **1998**, *4*, 364-371.
80. Cassaignon, S.; Sanchez, S.; Guillemoles, J. F.; Vedel, J.; Meier, H. G., *J. Electrochem. Soc.* **1999**, *146*, 4666-4671.
81. Chang, C. Y.; Hung, F. Y.; Lui, T. S., *J. Electron. Mater.* **2017**, *46*, 4384-4391.
82. Chen, K. J.; Hung, F. Y.; Chang, C. Y., *Electronics-Switz* **2019**, 8.
83. Klengel, S.; Klengel, R.; Schischka, J.; Stephan, T.; Petzold, M.; Eto, M.; Araki, N.; Yamada, T., *IEEE, 22nd European Microelectronics and Packaging Conference & Exhibition (EMPC)* **2019**, 1-8.
84. Klengel, S.; Klengel, R.; Schischka, J.; Stephan, T.; Petzold, M.; Eto, M.; Araki, N.; Yamada, T., *IEEE, 69th Electronic Components and Technology Conference (ECTC)* **2019**, 175-182.
85. Lorenz, G.; Naumann, F.; Klengel, S.; Petzold, M.; Eto, M.; Araki, N.; Yamada, T., *IEEE, 22nd European Microelectronics and Packaging Conference & Exhibition (EMPC)* **2019**.

-
86. Klengel, R.; Klengel, S.; Schischka, J.; Stephan, T.; Petzold, M.; Eto, M.; Araki, N.; Yamada, T., *IEEE, 70th ECTCElectronic Components and Technology Conference (ECTC)* **2020**.
87. Kanno, R.; Takeda, Y.; Masuyama, Y.; Yamamoto, O.; Takahashi, T., *Solid State Ionics* **1983**, *11*, 221-226.
88. Takahashi, T.; Kanno, R.; Takeda, Y.; Yamamoto, O., *Solid State Ionics* **1981**, *3-4*, 283-287.
89. Takahashi, T.; Yamamoto, O.; Yamada, S.; Hayashi, S., *J. Electrochem. Soc.* **1979**, *126*, 1654-1658.
90. Geller, S.; Akridge, J. R.; Wilber, S. A., *Phys. Rev. B* **1979**, *19*, 5396-5402.
91. Tinter, U.; Wiemhofer, H. D., *Solid State Ionics* **1983**, *9-10*, 1213-1220.
92. Agrawal, R. C.; Gupta, R. K., *J. Mater. Sci.* **1999**, *34*, 1131-1162.
93. Kröger, F. A.; Vink, H. J., *J. Phys. Chem. Solids* **1958**, *5*, 208-223.
94. Maier, J., *Angew. Chem. Int. Ed.* **1993**, *32*, 528-542.
95. Maier, J., *Angew. Chem. Int. Ed.* **1993**, *32*, 313-335.
96. Maier, J., *Z. Phys. Chem.* **1984**, *140*, 191-215.
97. Mathieu, H. J.; Rickert, H., *Z. Phys. Chem.* **1972**, *79*, 315-&.
98. Deckwart, J. M., *Dissertation* **2007**, University of Münster.
99. Preis, W.; Sitte, W., *Solid State Ionics* **1997**, *101*, 503-507.
100. Preis, W.; Sitte, W., *J. Electrochem. Soc.* **1998**, *145*, 2179-2185.
101. Preis, W.; Sitte, W., *J. Chem. Soc. Faraday Trans.* **1996**, *92*, 1197-1203.
102. Cottrell, F. G., *Z. Phys. Chem.* **1903**, *42U*, 386.
103. *Zahner Analysis*, V. R., Zahner-elektrik GmbH & Co. KG, Kronach, Germany, **2018**.
104. Alexander, L.; Klug, H. P., *Anal. Chem.* **1948**, *20*, 886-889.
105. Zhou, X.; Liu, D.; Bu, H.; Deng, L.; Liu, H.; Peng, Y.; Du, P.; Song, H., *Solid Earth Sci.* **2018**, *3*, 16-29.
106. Hubbard, C. R.; Snyder, R. L., *Pow. Diff.* **1988**, *3*, 74,78.
107. Hillier, S., *Clay Miner.* **2000**, *35*, 291-302.
108. Chung, F. H., *J. Appl. Cryst.* **1974**, *7*, 519-525.
109. Petricek, V.; Dusek, M.; Palatinus, L., *Z. Kristallogr.* **2014**, *229*, 345-352.
110. Spurr, R. A.; Myers, H., *Anal. Chem.* **1957**, *29*, 760-762.
111. Lotgering, F. K., *J. Inorg. Nucl. Chem.* **1959**, *9*, 113-123.
112. Furushima, R.; Tanaka, S.; Kato, Z.; Uematsu, K., *J. Ceram. Soc. Jpn.* **2010**, *118*, 921-926.
113. Khawam, A.; Flanagan, D. R., *J. Pharm. Sci.* **2006**, *95*, 472-498.
114. Khawam, A.; Flanagan, D. R., *J. Phys. Chem. B* **2006**, *110*, 17315-17328.
115. Laidler, K. J., *J. Chem. Ed.* **1984**, *61*, 494-498.
116. Galwey, A. K.; Brown, M. E., *Proc. R. Soc. Lond. A* **1995**, *450*, 501-512.
117. Galwey, A. K.; Brown, M. E., *Thermochim. Acta* **2002**, *386*, 91-98.
118. Sestak, J.; Berggren, G., *Thermochim. Acta* **1971**, *3*, 1-12.
119. Jander, W., *Z. Anorg. Allgem. Chem.* **1927**, *163*, 1-30.
120. Ginstling, A. M.; Brounshtein, B. I., *J. Appl. Chem. USSR* **1950**, *23*, 1327.
121. Carter, E. R., *J. Chem. Phys.* **1961**, *34*, 2010-2015.
122. Carter, E. R., *J. Chem. Phys.* **1961**, *35*, 1137-1138.
123. Segal, E., *Rev. Roum. Chim.* **2012**, *57*, 491-493.
124. Komatsu, W.; Uemura, T., *Z. Phys. Chem.* **1970**, *72*, 59-&.
125. Carstensen, J. T., *J. Pharm. Sci.* **1974**, *63*, 1-14.
126. Avrami, H., *J. Chem. Phys.* **1939**, *7*, 1103.

127. Avrami, H., *J. Chem. Phys.* **1940**, 8, 212.
128. Avrami, H., *J. Chem. Phys.* **1941**, 9, 177.
129. Hancock, J. D.; Sharp, J. H., *J. Am. Ceram. Soc.* **1972**, 55, 74-&.
130. Booth, F., *Trans. Faraday Soc.* **1948**, 44, 796-801.
131. Crank, J., *The mathematics of diffusion*, 2nd ed., Clarendon Press: Oxford, England,, **1975**, Chapter 6, p. 89.
132. Kirkendall, E. O., *Trans. Am. Inst. Min. Metall. Eng.* **1942**, 147, 104-109.
133. Susman, M. D.; Vaskevich, A.; Rubinstein, I., *J. Phys. Chem. C* **2016**, 120, 16140-16152.
134. Barmak, K., *Metall. Mater. Trans. B* **2018**, 49, 3616-3680.
135. Starink, M. J., *J. Mater. Sci.* **1997**, 32, 4061-4070.
136. Gutierrez-Urrutia, I., *J. Mater. Sci.* **2011**, 46, 3144-3150.
137. Balagurov, A. M.; Samoylova, N. Y.; Bobrikov, I. A.; Sumnikov, S. V.; Golovin, I. S., *Acta Cryst.* **2019**, B75, 1024-1033.
138. Pradell, T.; Crespo, D.; Clavaguera, N.; Clavaguera-Mora, M. T., *J. Phys. Condens. Matter* **1998**, 10, 3833-3844.
139. Starink, M. J.; Zahra, A. M., *Thermochim. Acta* **1997**, 292, 159-168.
140. Starink, M. J., *J. Mater. Sci.* **2001**, 36, 4433-4441.
141. Starink, M. J., *Int. Mater. Rev.* **2004**, 49, 191-226.
142. Friedman, H. L., *J. Polym. Sci., Part C: Polym. Lett.* **1964**, 6, 183-195.
143. Vyazovkin, S., *Thermochim. Acta* **2000**, 355, 155-163.
144. Vyazovkin, S., *Int. Rev. Phys.ical Chem.* **2000**, 19, 45-60.
145. Vyazovkin, S., *New J. Chem.* **2000**, 24, 913-917.
146. Khawam, A.; Flanagan, D. R., *Thermochim. Acta* **2005**, 429, 93-102.
147. Sharp, J. H.; Brindley, G. W.; Achar, B. N. N., *J. Am. Ceram. Soc.* **1966**, 49, 379-&.
148. Gotor, F. J.; Criado, J. M.; Malek, J.; Koga, N., *J. Phys. Chem. A* **2000**, 104, 10777-10782.
149. Criado, J. M.; Perez-Maqueda, L. A.; Gotor, F. J.; Malek, J.; Koga, N., *J. Therm. Anal. Calorim.* **2003**, 72, 901-906.
150. ThalesFlink, V. Z., Zahner-elektrik GmbH & Co. KG, Kronach, Germany, **2014**.
151. V. Stoe WinX^{POW}, S. C. G., Darmstadt, **2014**.
152. Match!, V., Crystal Impact, Bonn, **2018**.
153. Werner, P. E.; Eriksson, L.; Westdahl, M., *J. Appl. Cryst.* **1985**, 18, 367-370.
154. Visser, J. W., *J. Appl. Cryst.* **1969**, 2, 89-&.
155. Boultif, A.; Louer, D., *J. Appl. Cryst.* **1991**, 24, 987-993.
156. Zhao, J. B.; Zhang, Y. Y.; Wang, Y. H.; Li, H.; Peng, Y. Y., *J. En. Chem.* **2018**, 27, 1536-1554.
157. Chen, X. Q.; Yang, J. P.; Wu, T.; Li, L.; Luo, W.; Jiang, W.; Wang, L. J., *Nanoscale* **2018**, 10, 15130-15163.
158. Xu, Q.; Huang, B.; Zhao, Y. F.; Yan, Y. F.; Noufi, R.; Wei, S. H., *Appl Phys Lett* **2012**, 100.
159. Sun, S. D.; Li, P. J.; Liang, S. H.; Yang, Z. M., *Nanoscale* **2017**, 9, 11357-11404.
160. Chakrabarti, D. J.; Laughlin, D. E., *Bull. Alloy Phase Diagrams* **1983**, 4.
161. Blachnik, R.; Muller, A., *Thermochim. Acta* **2000**, 361, 31-52.
162. Siol, S., *Dissertation* **2014**, Technical University of Darmstadt.
163. Ohtani, T.; Motoki, M.; Koh, K.; Ohshima, K., *Mat. Res. Bull.* **1995**, 30, 1495-1504.
164. Wang, L. W., *Phys. Rev. Lett.* **2012**, 108.
165. Hainovsky, N.; Maier, J., *Phys. Rev. B* **1995**, 51, 15789-15797.
166. Zhou, K.; Wang, J.; Gao, J.; Landmann, U.; Chou, M. Y., *Phys. Rev. B* **2020**, 102.

167. Wagner, C., *J. Chem. Phys.* **1953**, *21*.
168. Potter, R. W., *Econ. Geol.* **1977**, *72*, 1524-1542.
169. Ishikawa, T.; Miyatani, S., *J. Phys. Soc. Jpn.* **1977**, *42*, 159-167.
170. Miyatani, S., *J. Phys. Soc. Jpn.* **1956**, *11*, 1059-1063.
171. Rickert, H.; Wiemhofer, H. D., *Ber Bunsenges. Phys. Chem.* **1983**, *87*, 236-239.
172. Pauporte, T.; Vedel, J., *Solid State Ionics* **1999**, *116*, 311-320.
173. Sanchez, S.; Cassaignon, S.; Vedel, J.; Meier, H. G., *Electrochim. Acta* **1996**, *41*, 1331-1339.
174. Pauporte, T.; Vedel, J., *Solid State Ionics* **1998**, *109*, 125-134.
175. Castel, E., *Dissertation* **1977**, University Pierre et Marie Curie (Paris VI).
176. Allen, L. H.; Buhks, E., *J. Appl. Phys.* **1984**, *56*, 327-335.
177. Okamoto, K.; Kawai, S., *Japanese J. Appl. Phys.* **1973**, *12*, 1130-1138.
178. Lukashev, P.; Lambrecht, W. R. L.; Kotani, T.; van Schilfgaarde, M., *Phys. Rev. B* **2007**, *76*.
179. Wiemhofer, H. D., *Dissertation* **1982**, University of Dortmund.
180. Hirahara, E., *J. Phys. Soc. Jpn.* **1951**, *6*, 428-437.
181. Bucur, R. V.; Berger, R., *Solid State Ionics* **1995**, *76*, 291-296.
182. Etienne, A., *J. Electrochem. Soc.* **1970**, *117*, 870-&.
183. Tubandt, C.; Reinhold, H.; Jost, W., *Z. Anorg. Allgem. Chem.* **1928**, *177*, 253-285.
184. Pavlyuchenko, M. M.; Pokrovsky, I. I.; Thikhonov, A. S., *Dokl. Acad. Nauk Belorussk. SSR* **1965**, *9*, 235.
185. Molnar, G. Y.; Katona, G. L.; Langer, G. A.; Csik, A.; Chen, Y. C.; Beke, D. L., *Mater. Res. Express* **2015**, *2*.
186. Beke, D. L.; Langer, G. A.; Molnar, G.; Erdelyi, G.; Katona, G. L.; Lakatos, A.; Vad, K., *Philos. Mag.* **2013**, *93*, 1960-1970.
187. Bussmann, E.; Sun, J.; Pohl, K.; Kellogg, G. L., *J. Phys. Condens. Matter* **2009**, *21*.
188. Chakraborty, J.; Welzel, U.; Mittemeijer, E. J., *J. Appl. Phys.* **2008**, *103*.
189. Chakraborty, J.; Welzel, U.; Mittemeijer, E. J., *Thin Solid Films* **2010**, *518*, 2010-2020.
190. Zhang, Q. F.; Xu, W.; Li, X. N.; Jiang, D. H.; Xiang, Y. Z.; Wang, J. G.; Cen, J.; Romano, S.; Ni, J., *Appl. Catal. A: Gen.* **2015**, *497*, 17-21.
191. Zhao, X. J.; Zhou, L. Y.; Zhang, W. Y.; Hu, C. Y.; Dai, L.; Ren, L. T.; Wu, B. H.; Fu, G.; Zheng, N. F., *Chem-Us* **2018**, *4*, 1080-1091.
192. Sheng, W.; Myint, M.; Chen, J. G.; Yan, Y., *Energy Environ. Sci.* **2013**, *6*, 1509.
193. Gattow, G., *Acta Cryst.* **1957**, *10*, 549.
194. Boller, H.; Sing, M., *Solid State Ionics* **1997**, *101*, 1287-1291.
195. Matkovic, P.; Elboragy, M.; Schubert, K., *J. Less Common Metals* **1976**, *50*, 165-176.
196. Huhn, W. P.; Widom, M.; Gao, M. C., *Comput. Mater. Sci.* **2014**, *92*, 377-386.
197. Zhang, J. W.; Chen, M. S.; Li, H. Q.; Li, Y. J.; Ye, J. Y.; Cao, Z. M.; Fang, M. L.; Kuang, Q.; Zheng, J.; Xie, Z. X., *Nano Energy* **2018**, *44*, 127-134.
198. Wang, G. X.; Liu, J. Y.; Sui, Y. M.; Wang, M.; Qiao, L.; Du, F.; Zou, B., *J. Mater. Chem. A* **2019**, *7*, 14876-14881.
199. Podjaski, F.; Weber, D.; Zhang, S. Y.; Diehl, L.; Eger, R.; Duppel, V.; Alarcon-Llado, E.; Richter, G.; Haase, F.; Morral, A. F. I.; Scheu, C.; Lotsch, B. V., *Nat. Catal.* **2020**, *3*, 55-63.
200. Ankah, G. N.; Meimandi, S.; Renner, F. U., *J. Electrochem. Soc.* **2013**, *160*, C390-C395.
201. Wu, R. T.; Wang, L. C., *Chem. Phys. Lett.* **2017**, *678*, 196-202.
202. Shit, S. C.; Singuru, R.; Pollastri, S.; Joseph, B.; Rao, B. S.; Lingaiah, N.; Mondal, J., *Cat. Sci. Technol.* **2018**, *8*, 2195-2210.
203. Yuan, D. W.; Zhang, Y., *Appl. Surf. Sci.* **2018**, *462*, 649-658.

-
204. Zhu, W. J.; Zhang, L.; Yang, P. P.; Chang, X. X.; Dong, H.; Li, A.; Hu, C. L.; Huang, Z. Q.; Zhao, Z. J.; Gong, J. L., *Small* **2018**, *14*.
205. Molnar, G.; Erdelyi, G.; Langer, G. A.; Beke, D. L.; Csik, A.; Katona, G. L.; Daroczi, L.; Kis-Varga, M.; Dudas, A., *Vacuum* **2013**, *98*, 70-74.
206. Miller, J. B.; Morreale, B. D.; Gellman, A. J., *Surf. Sci.* **2008**, *602*, 1819-1825.
207. Mogck, S.; Kooi, B. J.; De Hosson, J. T. M., *Acta Mater.* **2004**, *52*, 4651-4658.
208. Choudhary, S.; Sarma, J. V. N.; Pande, S.; Ababou-Girard, S.; Turban, P.; Lepine, B.; Gangopadhyay, S., *Aip Adv.* **2018**, *8*.
209. Rice, K. P.; Han, J. S.; Campbell, I. P.; Stoykovich, M. P., *Oxid. Met.* **2015**, *83*, 89-99.
210. Maack, B.; Nilius, N., *Phys. Status Solidi B* **2020**, *257*.
211. Zhong, C.; Jiang, Y. M.; Luo, Y. F.; Deng, B.; Zhang, L.; Li, J., *Appl. Phys. A* **2008**, *90*, 263-266.
212. Unutulmazsoy, Y.; Cancellieri, C.; Chiodi, M.; Siol, S.; Lin, L.; Jeurgens, L. P. H., *J. Appl. Phys.* **2020**, *127*.
213. Njeh, A.; Wieder, T.; Fuess, H., *Surf. Interface Analy.* **2002**, *33*, 626-628.
214. Vandeputte, A. G.; Reyniers, M. F.; Marin, G. B., *J. Phys. Chem. A* **2010**, *114*, 10531-10549.
215. Ganguly, A.; Chakraborty, I.; Udayabhaskararao, T.; Pradeep, T., *J. Nanopart. Res.* **2013**, *15*.
216. Sung, M. M.; Yun, W. J.; Lee, S. S.; Kim, Y., *Bull. Korean Chem. Soc.* **2003**, *24*, 610-612.
217. Chauhan, B. P. S.; Rathore, J. S.; Bando, T., *J. Am. Chem. Soc.* **2004**, *126*, 8493-8500.
218. Liu, Y.; Sun, C. J.; Bolin, T.; Wu, T. P.; Liu, Y. Z.; Sternberg, M.; Sun, S. H.; Lin, X. M., *Nano Lett.* **2013**, *13*, 4893-4901.
219. Guo, M.; Chen, J.; Martino, T.; Biesinger, M.; Noel, J. J.; Shoesmith, D. W., *J. Electrochem. Soc.* **2019**, *166*, C550-C558.
220. Gao, F.; Goodman, D. W., *Chem. Soc. Rev.* **2012**, *41*, 8009-8020.
221. Zharkov, S. M.; Moiseenko, E. T.; Altunin, R. R., *J. Solid State Chem.* **2019**, *269*, 36-42.
222. Benazzouz, C.; Benouattas, N.; Hammoudi, H.; Tobbeche, S.; Bouabellou, A., *Vacuum* **2006**, *81*, 489-493.
223. Huang, Y. H.; Yang, S. P.; Lee, P. T.; Kuo, T. T.; Ho, C. E., *Corr. Sci.* **2019**, *146*, 112-120.
224. Ho, C. E.; Hsieh, W. Z.; Lee, P. T.; Huang, Y. H.; Kuo, T. T., *App. Surf. Sci.* **2018**, *434*, 1353-1360.
225. Morimura, T.; Hasaka, M.; Nagata, A., *J. All. Comp.* **2002**, *347*, 141-148.
226. Morreale, B., *Dissertation* **2006**, Univeristy of Pittsburgh.
227. Huang, C. S.; Jang, G. Y.; Duh, J. G., *J. Electron. Mat.* **2004**, *33*, 283-289.
228. Divinski, S.; Ribbe, J.; Schmitz, G.; Herzig, C., *Acta Mater.* **2007**, *55*, 3337-3346.
229. Sakurai, T.; Hashizume, T.; Jimbo, A.; Sakai, A.; Hyodo, S., *Phys. Rev. Lett.* **1985**, *55*, 514-517.
230. Zhu, Q.; Zou, L. F.; Zhou, G. W.; Saidi, W. A.; Yang, J. C., *Surf. Sci.* **2016**, *652*, 98-113.
231. Chauhan, P. K.; Gadiyar, H. S., *Corr. Sci.* **1985**, *25*, 1194-1195.
232. Chauhan, P. K.; Gadiyar, H. S., *Corr. Sci.* **1985**, *25*, 55-68.
233. Yuan, S. J.; Pehkonen, S. O., *Corr. Sci.* **2007**, *49*, 1276-1304.
234. BinSabt, M. H.; Al-Kharafi, F. M.; Nazeer, A. A.; Galal, A., *Int. J. Electrochem. Sci.* **2017**, *12*, 1331-1347.
235. Vogel, G., *Microelectron. Rel.* **2016**, *64*, 650-655.
236. Reid, M.; Punch, J.; Grace, G.; Garfias, L. F.; Belochapkine, S., *J. Electrochem. Soc.* **2006**, *153*, B513-B517.
237. Liu, Z. W.; Bando, Y., *Chem. Phys. Lett.* **2003**, *378*, 85-88.

-
238. Kerber, S. J.; Barr, T. L.; Mann, G. P.; Brantley, W. A.; Papazoglou, E.; Mitchell, J. C., *J. Mat. Eng. Perf.* **1998**, *7*, 329-333.
239. Brantley, W. A.; Cai, Z.; Papazoglou, E.; Mitchell, J. C.; Kerber, S. J.; Mann, G. P.; Barr, T. L., *Dent. Mat.* **1996**, *12*, 333-341.
240. Hisatsune, K.; Baba, K.; Hasaka, M.; Morimura, T.; Tanaka, Y.; Udoh, K.; Yasuda, K., *J. All. Comp.* **1995**, *230*, 94-99.
241. Lee, B.; Li, W., *Mater. Lett.* **2020**, 273.
242. Zhuang, D. M.; Huang, X. L.; Chen, Z. H.; Gong, H.; Sheng, L.; Song, L.; Wang, T.; He, J. P., *J. Power Sources* **2020**, 458.
243. Sathyamoorthi, S.; Saravanan, K. R.; Velayutham, D.; Suryanarayanan, V., *J. Appl. Electrochem.* **2012**, *42*, 595-606.
244. Suryanarayanan, V.; Noel, M., *J. Solid State Electrochem.* **2009**, *13*, 1913-1923.
245. Vasiliou, A. K.; Anderson, D. E.; Cowell, T. W.; Kong, J.; Melhado, W. F.; Phillips, M. D.; Whitman, J. C., *J. Phys. Chem. A* **2017**, *121*, 4953-4960.
246. Pulka-Ziach, K., *J Pept Sci* **2018**, 24.
247. Braye, E. H.; Sehon, A. H.; Darwent, B., *J. Am. Chem. Soc.* **1955**, *77*, 5282-5285.
248. Sehon, A. H.; Darwent, B., *J. Am. Chem. Soc.* **1954**, *76*, 4806-4810.
249. Zhang, W.; Li, S. Y.; Yang, Z. X.; Mao, Y.; Xu, S. Y., *Mater. Res. Innov.* **2015**, *19*, S225-S229.
250. Tseng, C. H.; Tseng, I. H.; Huang, Y. P.; Hsu, Y. T.; Leu, J.; Tu, K. N.; Chen, C., *Mater. Charact.* **2020**, 168.
251. Yang, D. S.; Dong, Y. C.; Chang, H.; Alexandrov, I.; Li, F.; Wang, J. T.; Dan, Z. H., *Mater. Corr.* **2018**, *69*, 1455-1461.
252. Ralston, K. D.; Birbilis, N., *Corrosion-Us* **2010**, 66.
253. Yuan, Y.; Jiang, Y. D.; Zhou, J.; Liu, G. Y.; Ren, X., *Mater. Lett.* **2019**, *253*, 424-426.
254. Lapeire, L.; Lombardia, E. M.; De Graeve, I.; Terry, H.; Verbeken, K., *J. Mater. Sci.* **2017**, *52*, 1501-1510.
255. Zhang, Y. H.; Feng, X. Y.; Song, C. M.; Wang, H.; Yang, B.; Wang, Z. G., *MRS Comm.* **2019**, *9*, 251-257.
256. Zhou, J.; Liu, G. Y.; Yuan, Y.; Jiang, Y. D.; Gao, X., *Ieee T Dielect El In* **2020**, *27*, 1022-1028.
257. Wu, Y. L.; Subramanian, K. N.; Barton, S. C.; Lee, A., *Microelectron. Rel.* **2017**, *78*, 355-361.
258. Adams, H.; Miller, B. P.; Kotvis, P. V.; Furlong, O. J.; Martini, A.; Tysoe, W. T., *Tribol. Lett.* **2016**, 62.
259. Furlong, O.; Miller, B.; Li, Z. J.; Tysoe, W. T., *Surf. Sci.* **2011**, *605*, 606-611.
260. Furlong, O. J.; Miller, B. P.; Li, Z. J.; Walker, J.; Burkholder, L.; Tysoe, W. T., *Langmuir* **2010**, *26*, 16375-16380.

A Appendix

A.3 Appendix Chapter 3

Table A 3.1: Mass absorption coefficients μ^* for the initial uncorroded wires. The values are obtained via Rietveld refinement of the initial powder pattern with the software package *Jana2006*. The value for β -Cu₂S is obtained from a fully corroded Cu wire.

Wire type	Absorption coefficient / cm ⁻¹
Bare Cu	43.62
PCC	43.66
APC	43.55
APCX	43.55
Pure β -Cu ₂ S from fully corroded wire	23.49

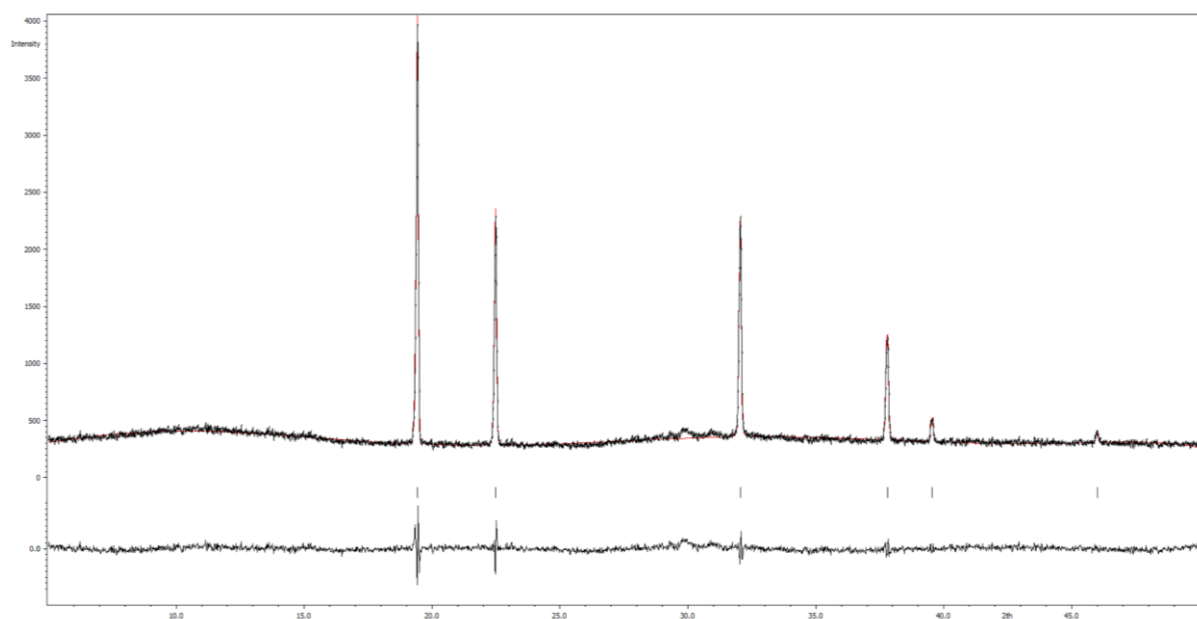


Figure A. 3.1: Rietveld refinement of the bare uncorroded Cu wire at the beginning of the measurement.

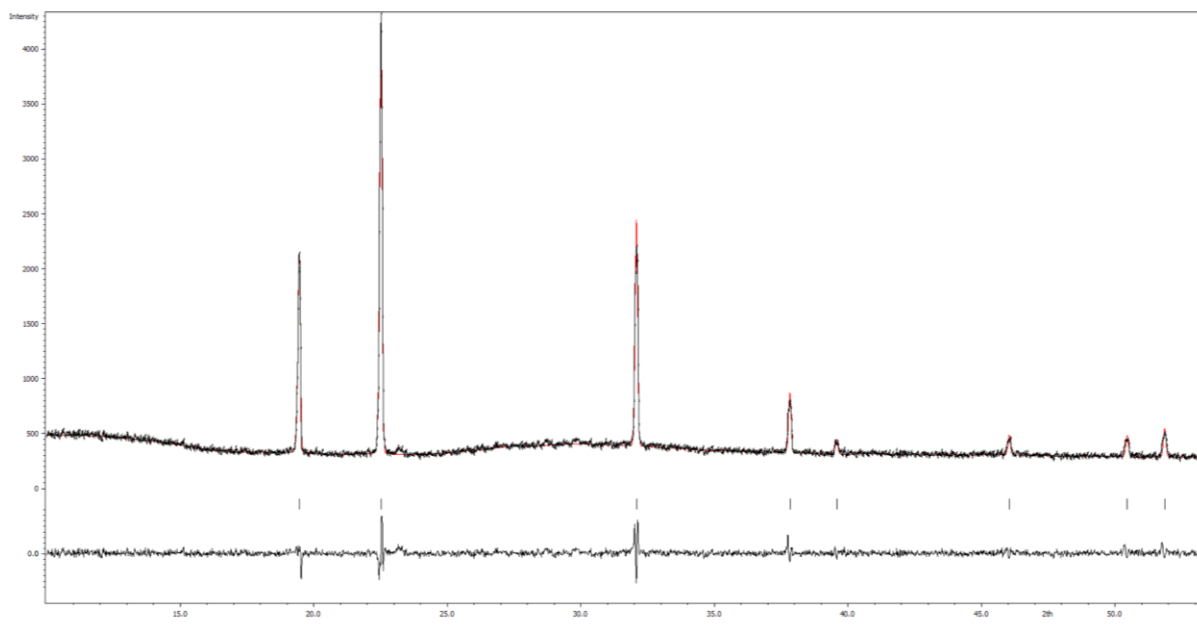


Figure A. 3.2: Rietveld refinement of the palladium-coated copper (PCC) wire at the beginning of the measurement.

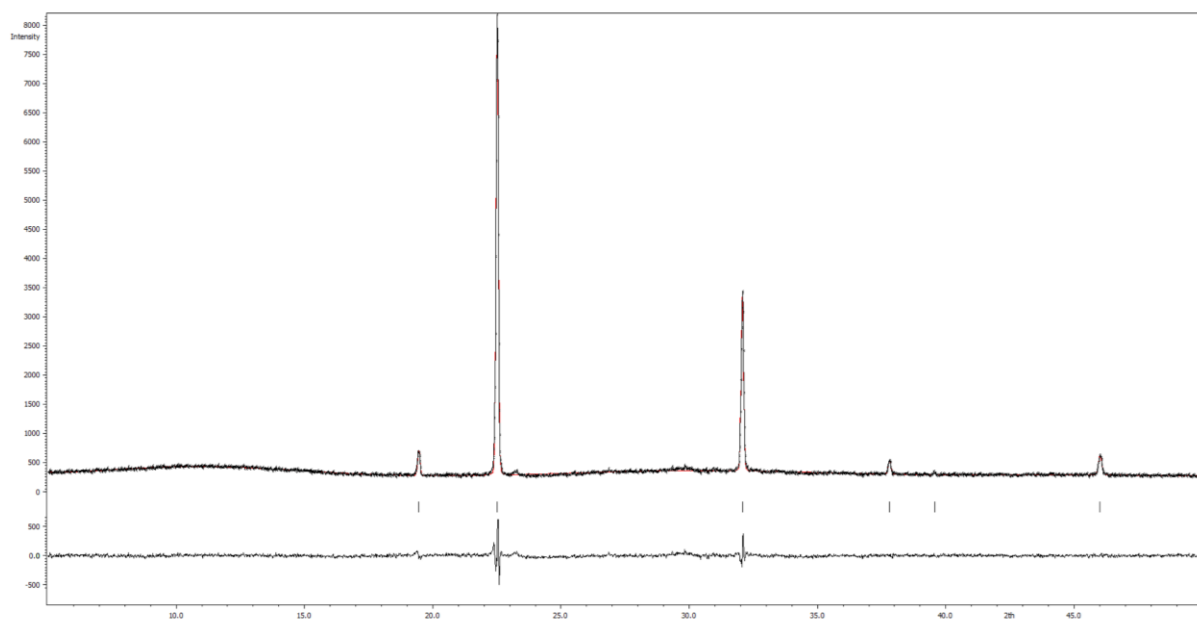


Figure A. 3.3: Rietveld refinement of the pure gold-palladium-coated copper (APC) wire at the beginning.

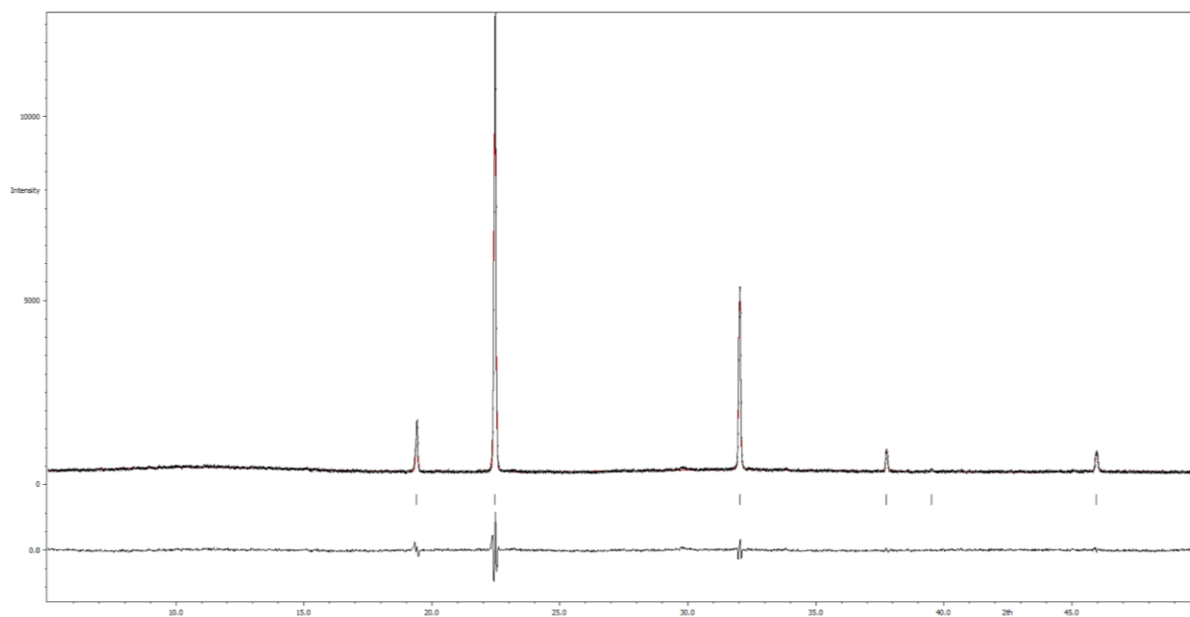


Figure A. 3.4: Rietveld refinement of the initial gold-palladium-coated copper with a doped Cu core (APCX).

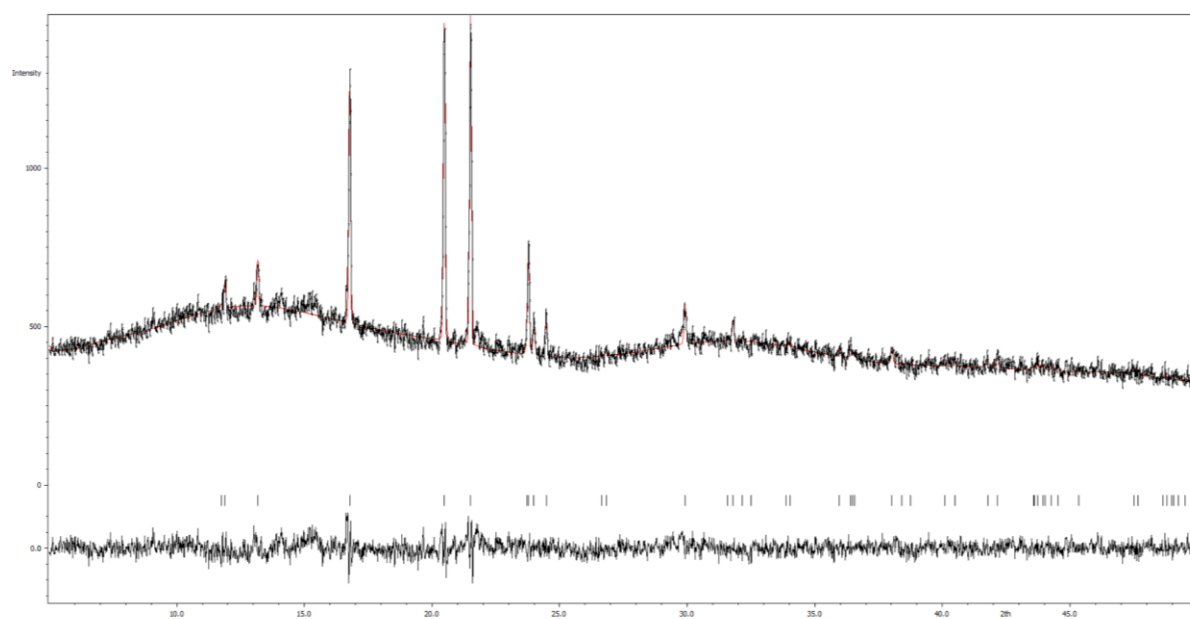


Figure A. 3.5: Rietveld refinement of pure β -Cu₂S which evolved from a fully corroded copper wire.

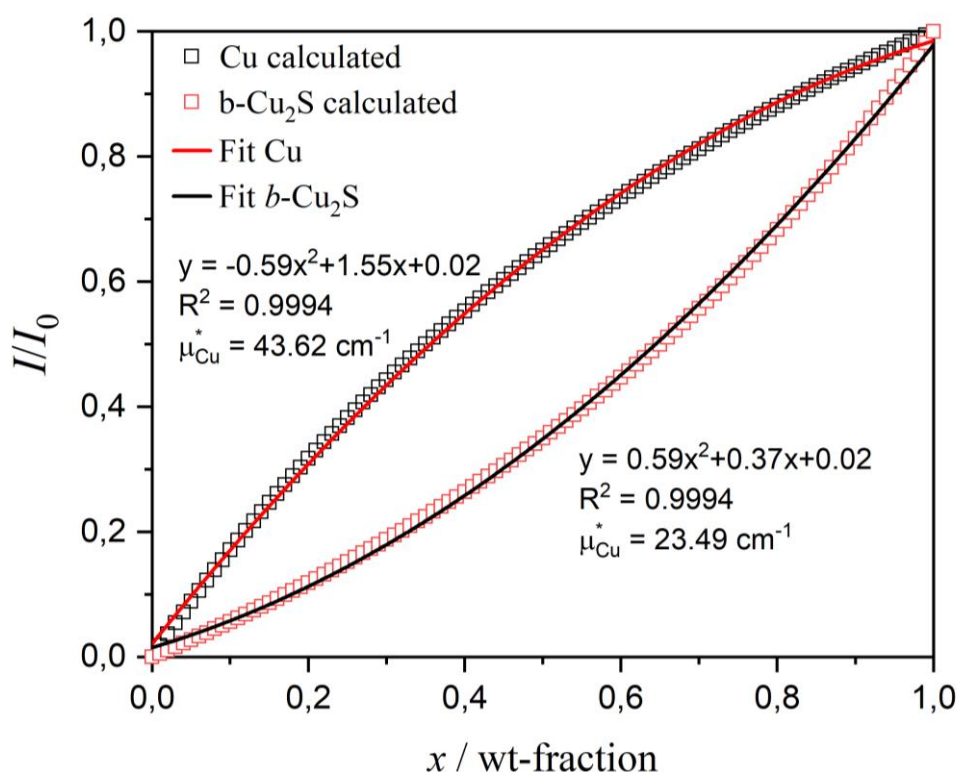


Figure A. 3.6: Exemplary calibration curve for the external standard method. Here, the absorption coefficient for the bare Cu wire and the corresponding corrosion product β -Cu₂S are used.

Table A 3.2: Comparison of database values and obtained values from the experiments. The values from the experiments are obtained from the three strongest reflections of the external standard method of the full corroded wires. The use of multiple reflections was chosen as it reduces the influence of preferred orientations. The values are in good accordance with the reference values from the databases. For the quantification of the Cu wt-fractions where fluctuating beam intensity occurs, the multireflection $K(\text{Cu})$ value on grey coloured background is used. The multireflection $K(\beta\text{-Cu}_2\text{S})$ value is used for the quantification of the β -Cu₂S wt-fractions of partially corroded wires. Also, the RIR from the COD-Database is used for the quantification of Cu₃Pd.

	<i>RIR</i> (Cu)	<i>RIR</i> (β -Cu ₂ S)	<i>K</i> (Cu)	<i>K</i> (β -Cu ₂ S)	Entry # (Cu)	Entry # (β -Cu ₂ S)
Experimental (Cu)	-	-	5.453	0.184	-	-
Experimental (β-Cu₂S)	-	-	5.453	0.184	-	-
COD	12	2.23	5.381	0.186	96-901-3022	96-152-9747
JCPDS	8.86	1.54	5.753	0.174	00-085-1326	00-084-207
	<i>RIR</i> (Cu)	<i>RIR</i> (Cu ₃ Pd)	<i>K</i> (Cu)	<i>K</i> (Cu ₃ Pd)	Entry # (Cu)	Entry # (Cu ₃ Pd)
COD	12	13.53	0.887	1.128	96-901-3022	96-152-5026
	<i>RIR</i> (Cu)	<i>RIR</i> (Cu ₂ O)	<i>K</i> (Cu)	<i>K</i> (Cu ₂ O)	Entry # (Cu)	Entry # (Cu ₂ O)
COD	12	11	1.086	0.921	96-901-3022	99-500-0010

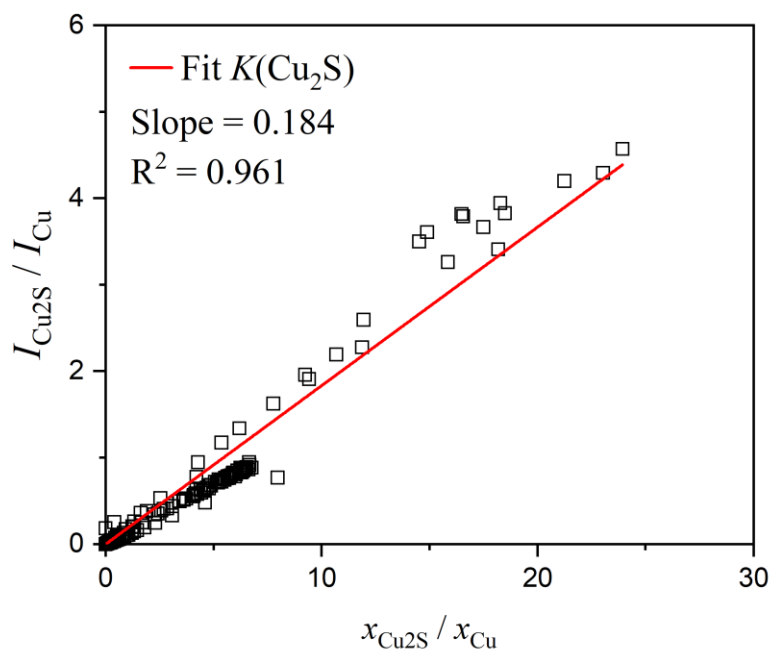


Figure A. 3.7: Plot of the intensity ratios against the wt-fraction ratios. The plot yields the slope $K(\text{Cu}_2\text{S})$ which is defined by $RIR_{\text{Cu}_2\text{S}}/RIR_{\text{Cu}}$. The obtained slope $K(\text{Cu}_2\text{S})$ is in good agreement with reference values.

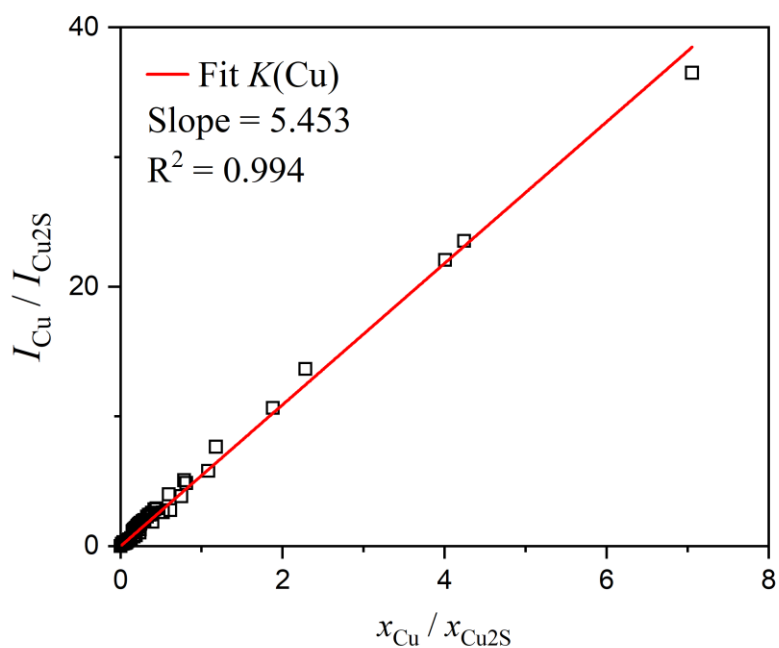


Figure A. 3.8: Plot of the intensity ratios against the wt-fraction ratios. The plot yields the slope $K(\text{Cu})$ which is defined by $RIR_{\text{Cu}}/RIR_{\text{Cu}_2\text{S}}$. The obtained slope $K(\text{Cu})$ is in good agreement with reference values.

A.5 Appendix chapter 5

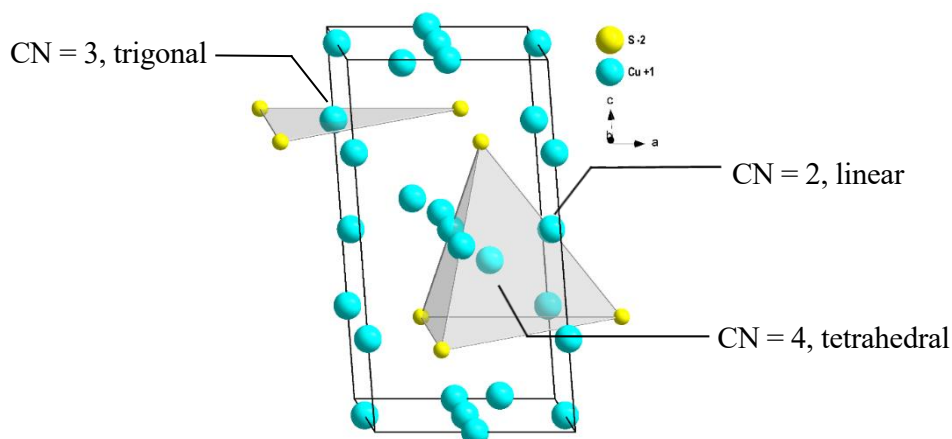


Figure A. 5.1: Unit cell of hexagonal high chalcocite β -Cu₂S ($P6_3/mmc$) with tetrahedral, trigonal, and linear coordination of the Cu atoms with $a = 3.95 \text{ \AA}$, $b = 3.95 \text{ \AA}$, $c = 6.75 \text{ \AA}$, $\gamma = 120^\circ$, and $Z = 2$ which corresponds to $(\text{Cu}_2\text{S})_2$ units.

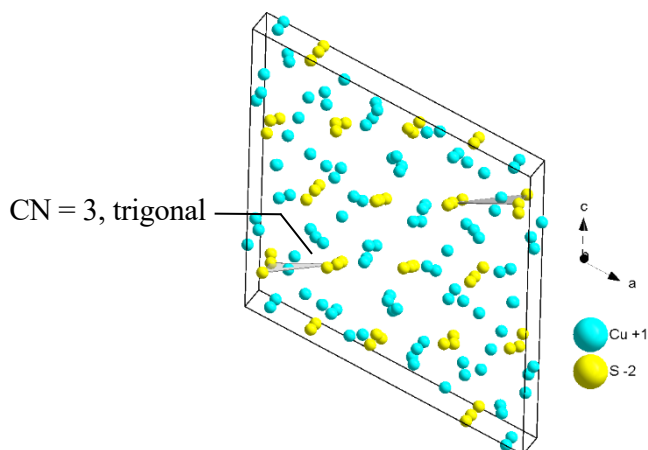


Figure A. 5.2: Unit cell of monoclinic low chalcocite α -Cu₂S ($P2_1/c$) with exclusive trigonal coordination of the Cu atoms with $a = 15.25 \text{ \AA}$, $b = 11.88 \text{ \AA}$, $c = 13.49 \text{ \AA}$, $\beta = 116^\circ$, and $Z = 48$ which corresponds to $(\text{Cu}_2\text{S})_{48}$ units.

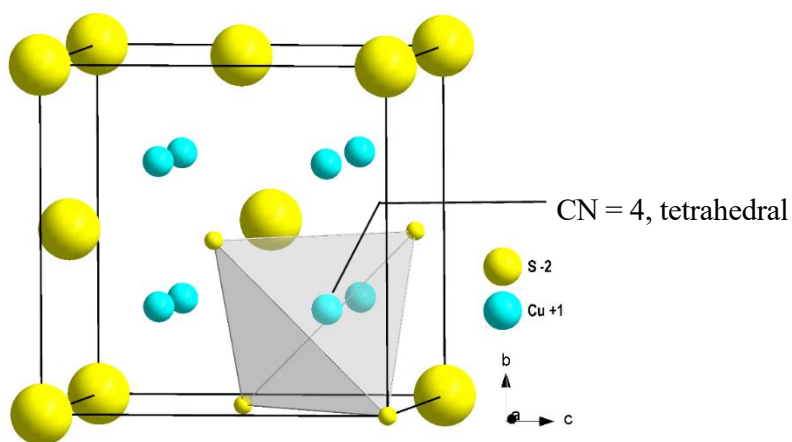


Figure A. 5.3: Unit cell of cubic high digenite γ -Cu₂S ($Fm\bar{3}m$) with exclusive tetrahedral coordination of the Cu atoms.

A.6 Appendix chapter 6

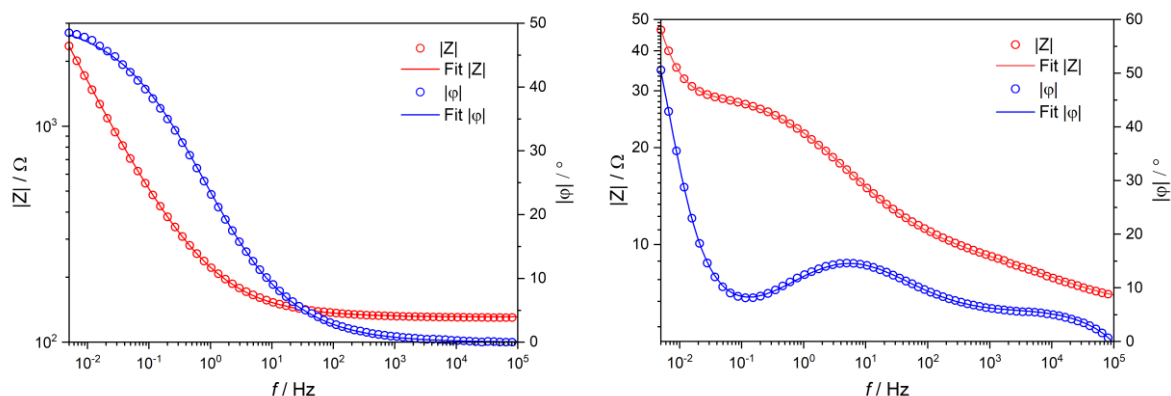


Figure A. 6.1: Left: Fitted Bode plot of the EIS measurement on the galvanic cell $\text{Cu}|\text{Cu}^+|\text{Cu}_2\text{S}$ at 40 °C. Right: Respective Bode plot for the EIS measurement at 190 °C.

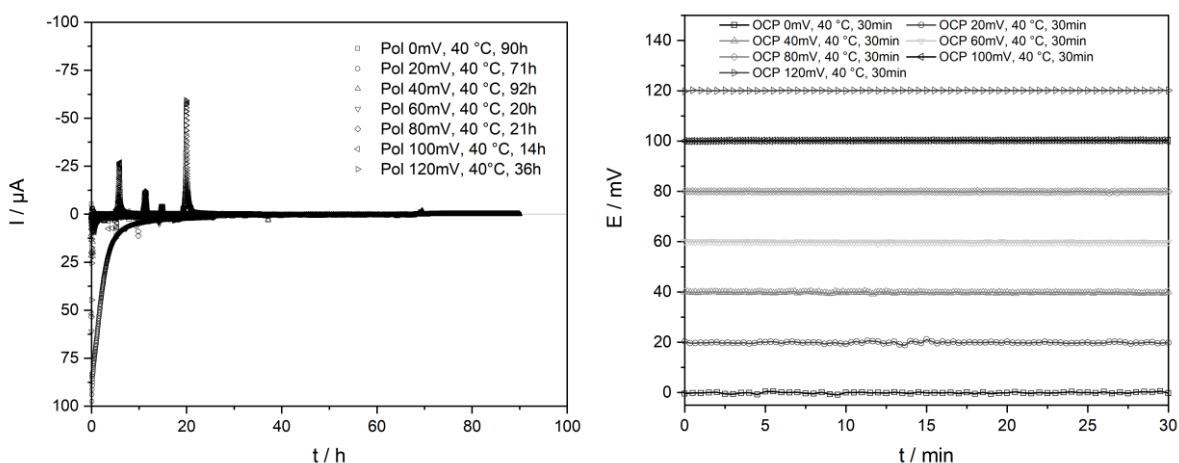


Figure A. 6.2: Left: Polarization towards the respective cell potentials (0 – 120 mV) prior to the EIS measurements. Here shown as a function of the cell current vs time. The cell current reaches a minimum towards the end, indicating a steady state. Right: Respective OCP for 30 mins after the cell polarization and prior to the EIS measurements. The OCP stays constant for 30 min which indicates a steady state of the galvanic cell.

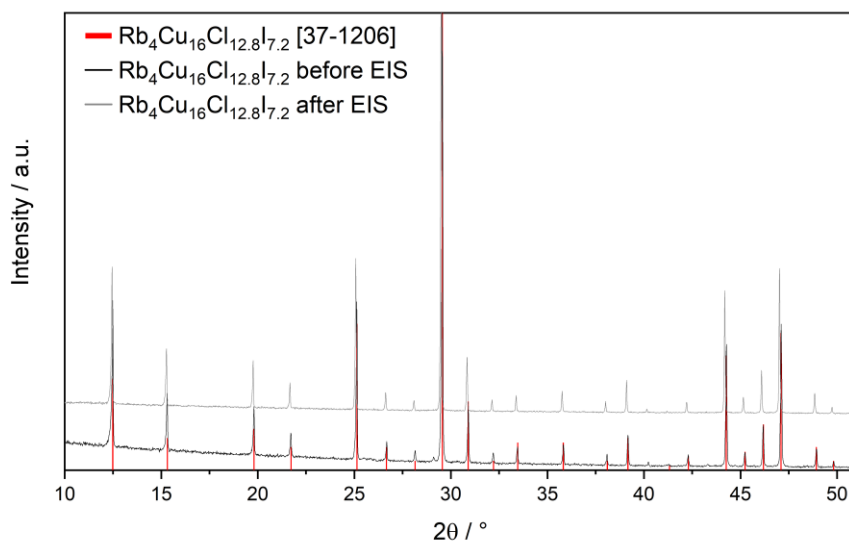


Figure A. 6.3: PXRD measurement of $\text{Rb}_4\text{Cu}_{16}\text{Cl}_{12.8}\text{I}_{7.2}$ before and after EIS. No change is observed

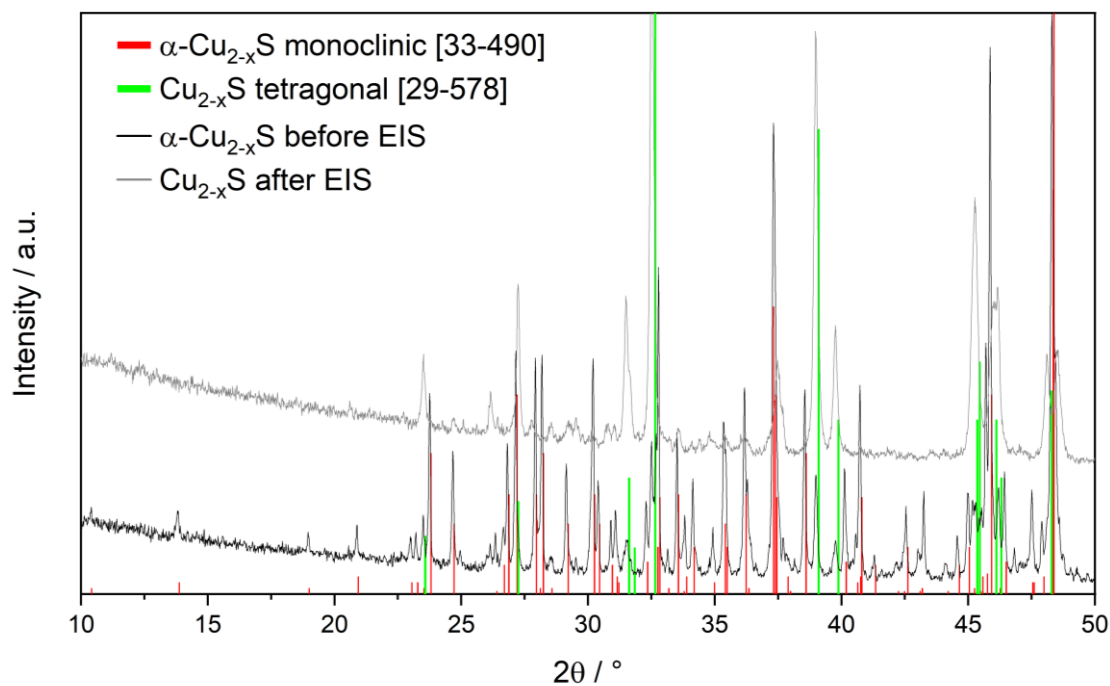


Figure A. 6.4: PXRD measurements of Cu_{2-x}S before series measurement from 0 mV to 120 mV in 20 mV increments and after EIS. Tetragonal Cu_{2-x}S is already present in minor amounts before the measurement. After the measurement, mostly tetragonal Cu_{2-x}S is present.

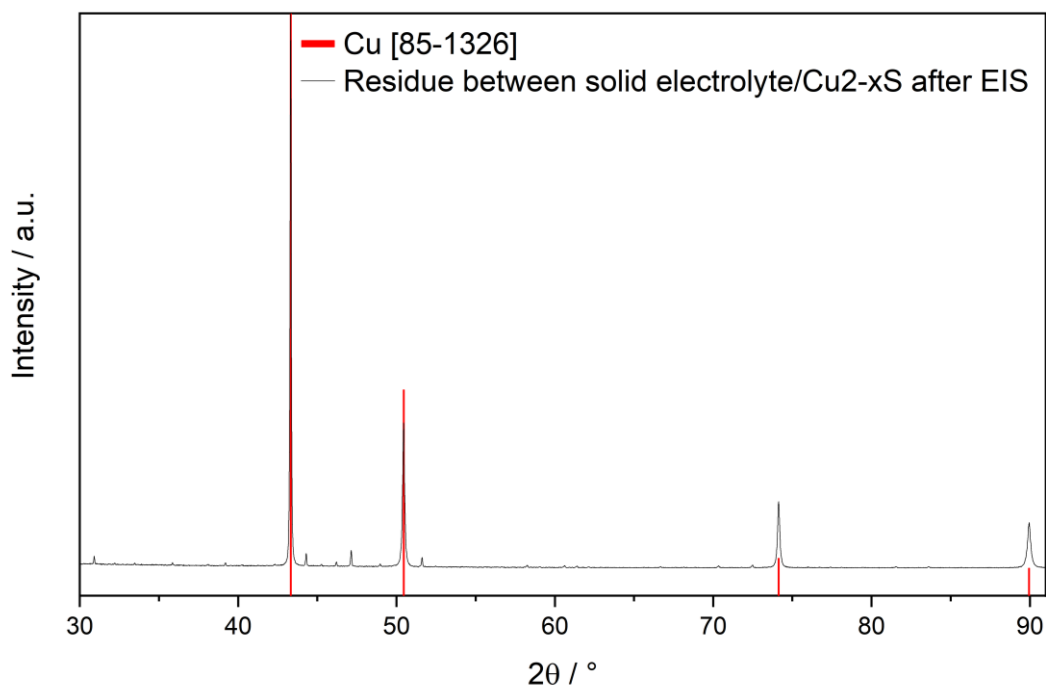


Figure A. 6.5: PXRD measurement of residue between solid electrolyte and Cu_{2-x}S after EIS. Pure Cu precipitated on the electrode surface of the Cu_{2-x}S electrode.

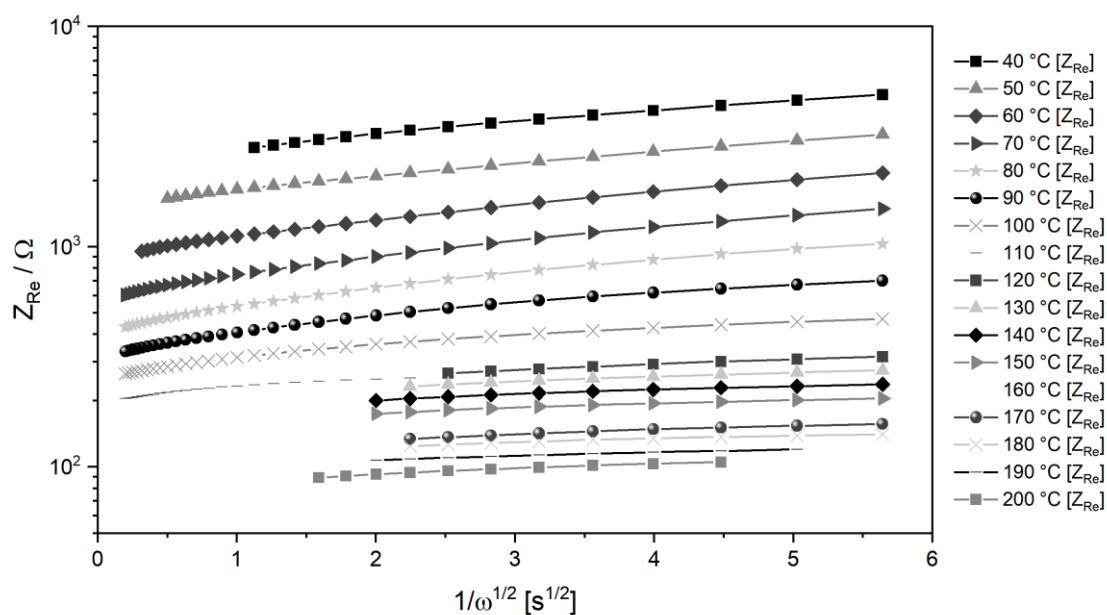


Figure A. 6.6: Randles plot of the diffusion curves with Z_{Re} plotted versus $1/\omega^{1/2}$ from 40 °C to 200 °C. All curves exhibit a straight line and are thus suitable for the subsequent calculation of the chemical diffusion coefficient \tilde{D}_{Chem} .

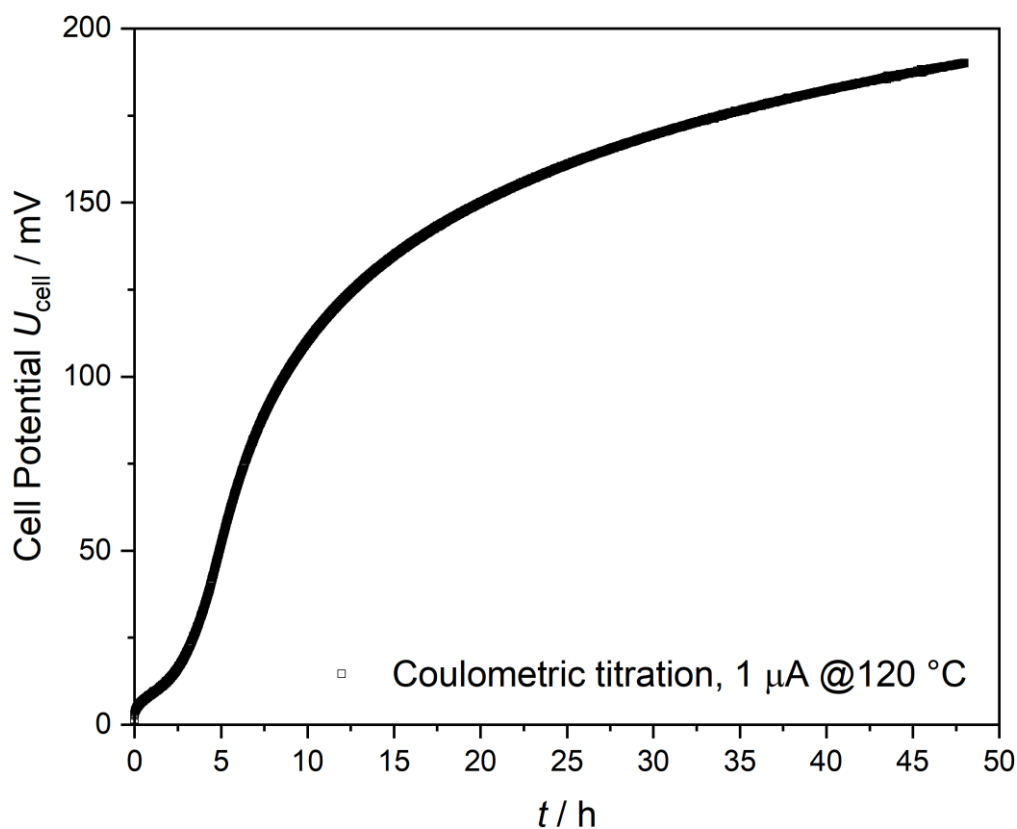


Figure A. 6.7: Coulometric titration curve at 120 °C with a constant current of 1 μA starting from a cell potential of 0 mV.

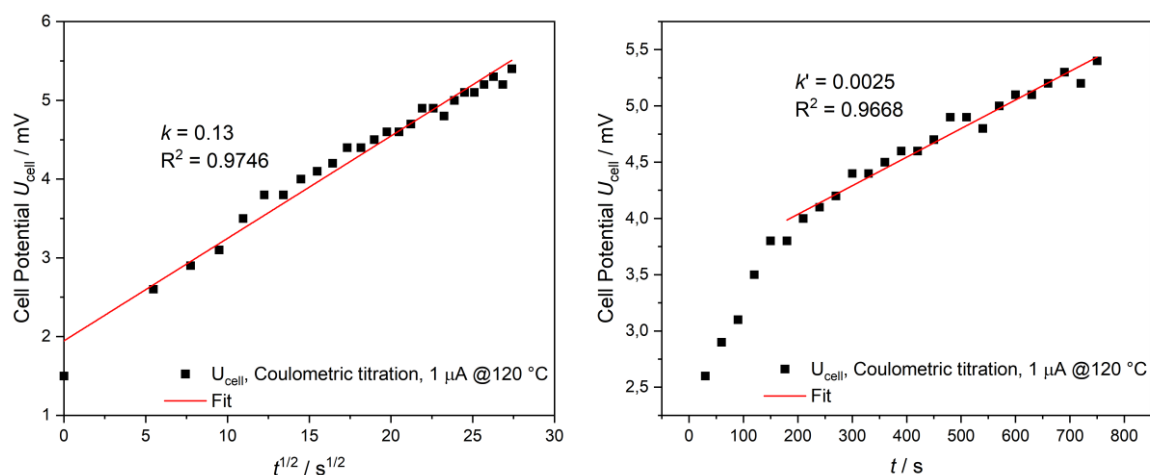


Figure A. 6.8: Left: Plot of U_{cell} versus $t^{1/2}$ at short titration times to determine the slope k from the coulometric titration at 120 °C. Right: Plot of U_{cell} versus t at longer titration times to determine the slope k' from the coulometric titration at 120 °C.

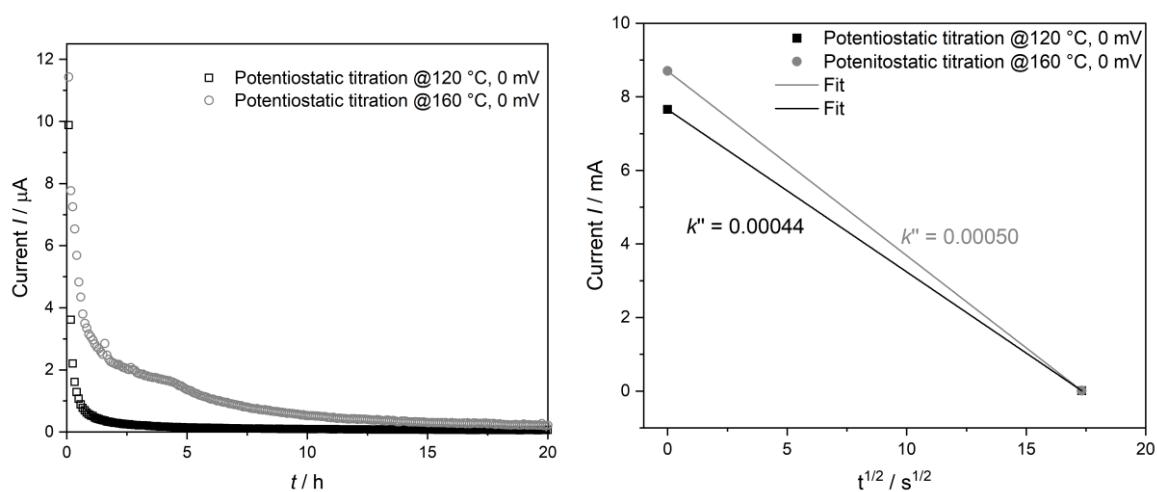


Figure A. 6.9: Left: Potentiostatic titration curves at 120 °C and 160 °C with a constant voltage applied of 0 mV starting from 200 mV. Right: Plot of I versus $t^{1/2}$ at short polarization times to determine the slope k'' from the potentiostatic titration at.

A.7 Appendix Chapter 7

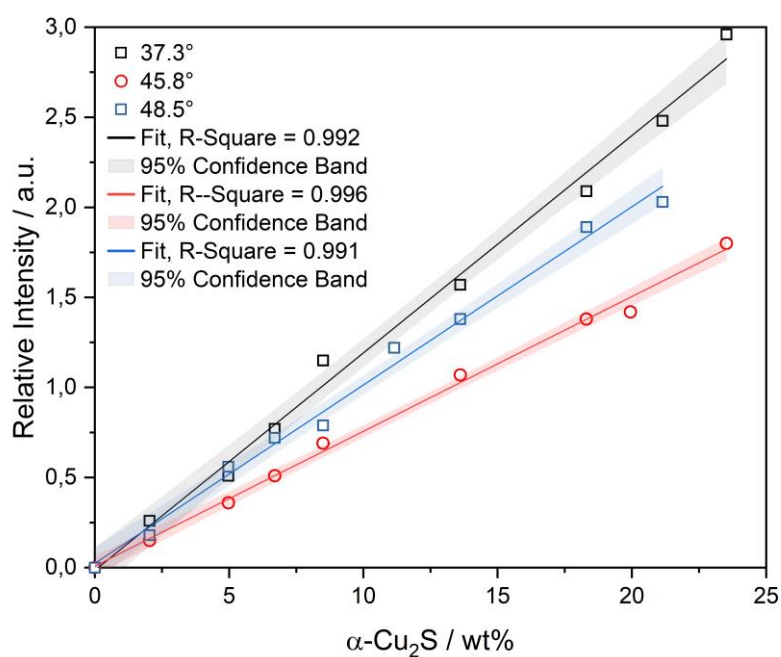


Figure A. 7.1: Calibration curve for copper sulfide generated with PXRD of the mixture Cu:TT: α -Cu₂S. This calibration curve is used for the stored Cu:TT mixture (molar ratio = 1:0.1).

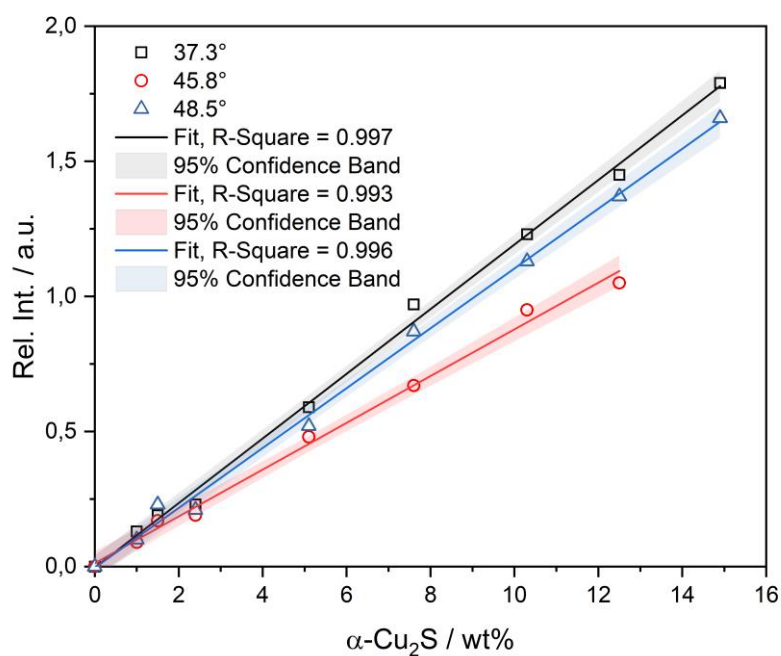


Figure A. 7.2: Calibration curve for copper sulfide generated with PXRD of the mixture Cu: α -Cu₂S. This calibration curve is used for the Cu:MS1 mixture (molar ratio = 1:0.1).

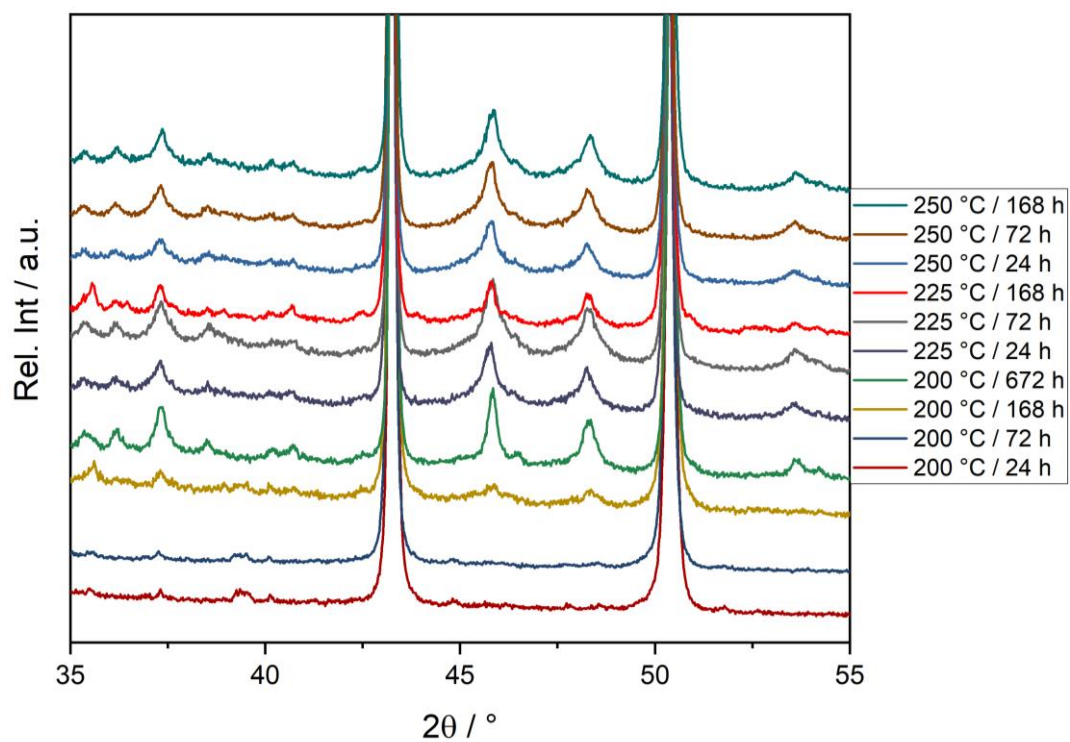


Figure A. 7.3: PXRD patterns of the mixture Cu:TT (molar ratio 1:0.1) after HTS at various times and temperatures. Starting from 200 °C and 24 h (bottom end) to 250 °C and 168 h (top end).

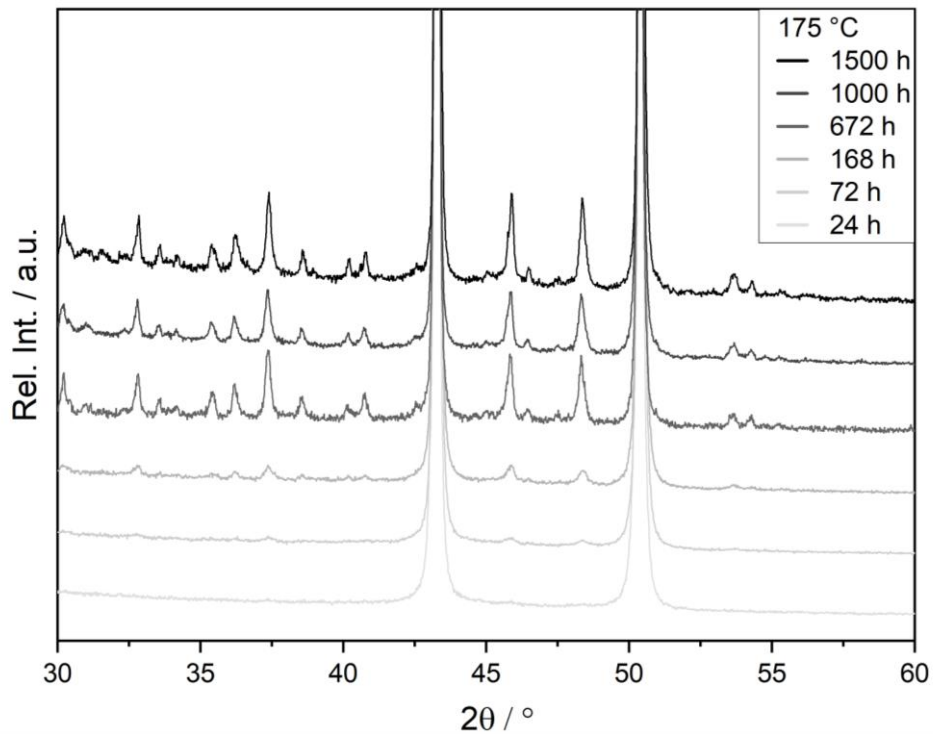


Figure A. 7.4: PXRD patterns of the mixture Cu:MS1 (molar ratio 1:0.1) after HTS at 175 °C for various times.

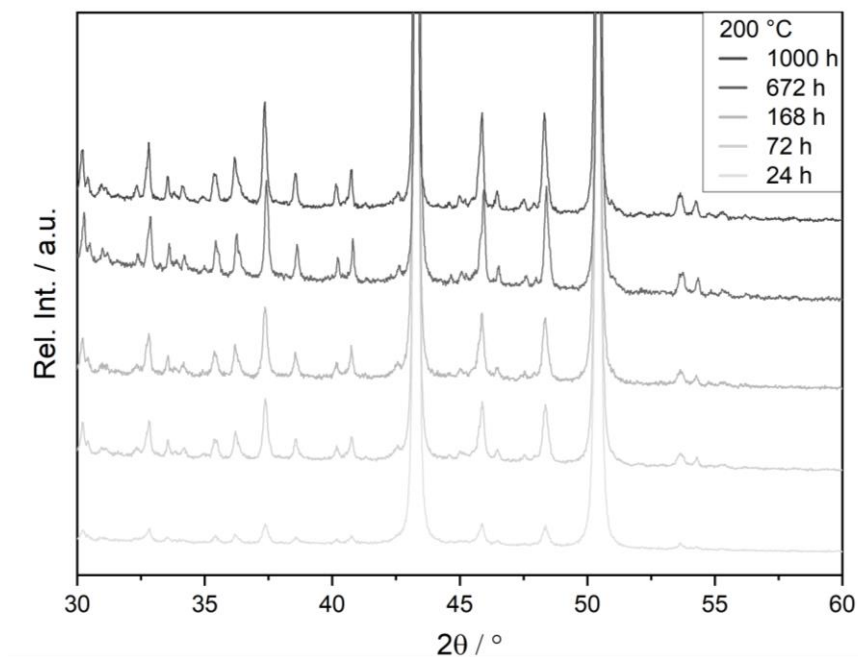


Figure A. 7.5: PXRD patterns of the mixture Cu:MS1 (molar ratio 1:0.1) after HTS at 175 °C for various times.

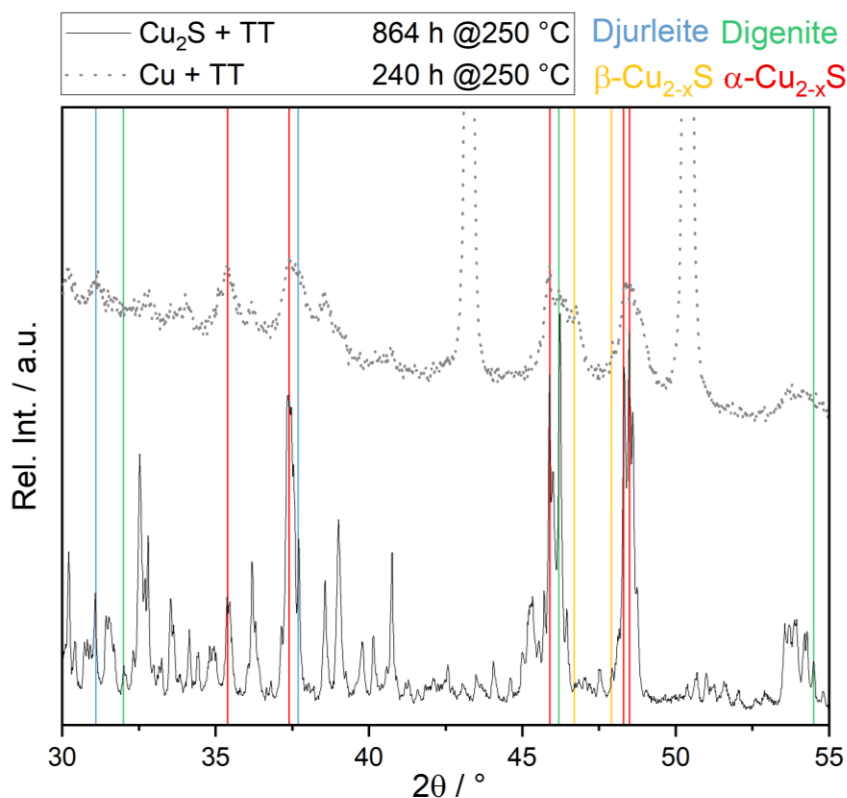


Figure A. 7.6: Conversion of α -Cu₂S: TT (molar ratio = 1:0.1) mixture to the copper-poorer phases digenite and djurleite. This is compared to a Cu:TT (molar ratio = 1:0.1) mixture which also changes towards copper-poor phases at 250 °C after longer reaction times. This explains the lower α -Cu₂S content in the 250 °C samples at longer reaction times. The most intense reflections are shown for the respective phases.

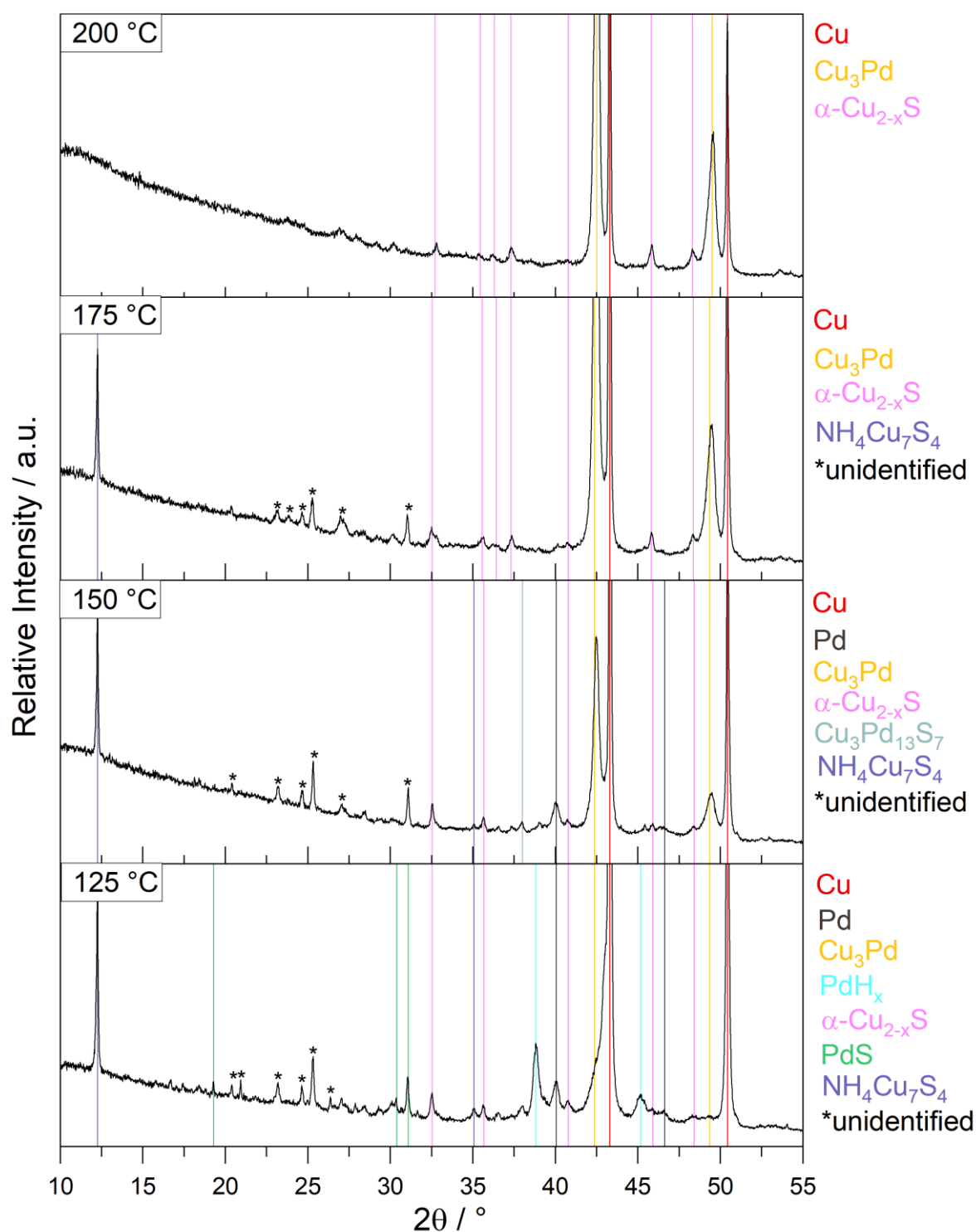


Figure A. 7.7: Powder patterns of the Cu:Pd:TT (molar ratio = 1:0.1:0.1) mixture after 672 h at different temperatures. At 125 °C palladium hydride, palladium sulfide and ammonium heptacopper sulfide are formed. As the temperature rises, the thermodynamic stable phases Cu_3Pd and $\alpha\text{-Cu}_2\text{S}$ remain. This is also observed for the mixture with MS1.

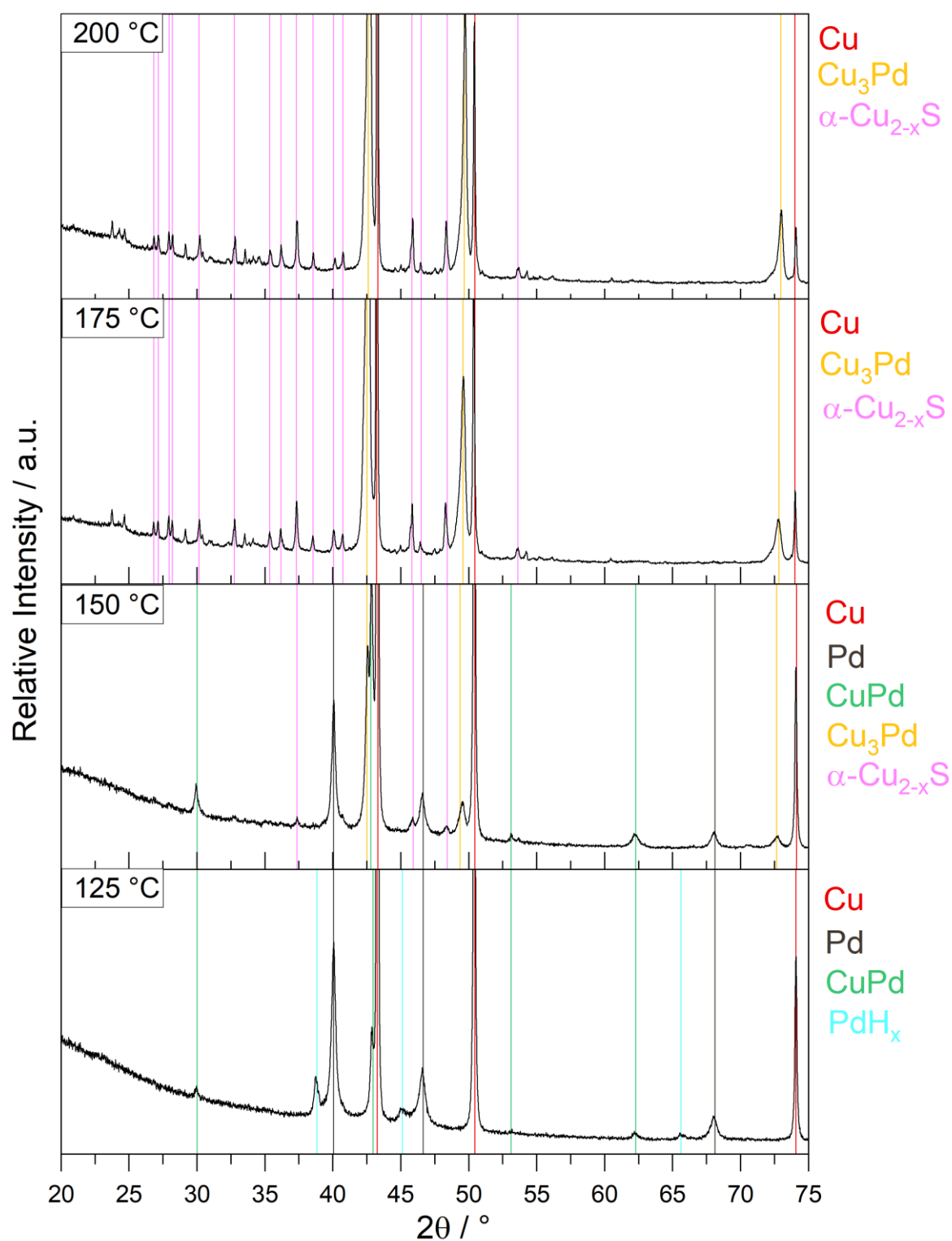


Figure A. 7.8: Powder patterns of the Cu:Pd:MS1 (molar ratio = 1:0.1:0.1) mixture after 672 h at different temperatures. At 125 °C palladium hydride forms. This is reversible and is not observed at higher temperatures. There the thermodynamic stable phases Cu_3Pd and $\alpha\text{-Cu}_2\text{S}$ remain. This is also observed for the mixture with **TT**.

Appendix

Table A 7.1 Phases in the XRD powder patterns and the corresponding Match! Entry # and the JCPDS file number.

Phase	Space group	Match! Entry #	COD #	JCPDS
Cu	$Fm\bar{3}m$ (225)	00-085-1326	96-500-0217	00-085-1326
α -Cu ₂ S	$P2_1/c$ (14)	96-900-8288	96-900-8288	00-083-1462
Cu _{1.96} S (djurleite)	$P2_1/n$ (14)	00-023-0959	-	00-023-0959
Cu _{1.8} S (digenite, cubic)	$Fm\bar{3}m$ (225)	00-072-1966	-	00-072-1966
Cu _{1.8} S (rhombohedral)	$R\bar{3}m$ (166)	00-047-1748	-	00-047-1748
Cu _{1.8} S (tetragonal)	$P4_32_12$ (96)	00-072-1071	-	00-072-1071
CuS (covellite)	$P6_3/mmc$ (194)	00-078-0876	-	00-078-0876
S ₈	$Fddd$ (70)	00-083-2285	-	00-083-2285
Pd	$Fm\bar{3}m$ (225)	96-900-9821	96-900-9821	00-005-0681
CuPd	$Pm\bar{3}m$ (221)	99-500-0028	99-500-0028	-
Cu ₃ Pd	$Pm\bar{3}m$ (221)	96-591-0110	96-591-0110	-
Cu ₃ Pd ₁₃ S ₇	$I\bar{4}3m$ (217)	99-500-0087	99-500-0087	00-030-0498
NH ₄ Cu ₇ S ₄	$I\bar{4}$ (82)	96-231-0583	96-231-0583	00-072-1211
PdH _x	$Fm\bar{3}m$ (225)	96-900-8698	96-900-8698	00-084-0300
PdS	$P4_2/m$ (84)	96-900-8964	96-900-8964	00-078-0206

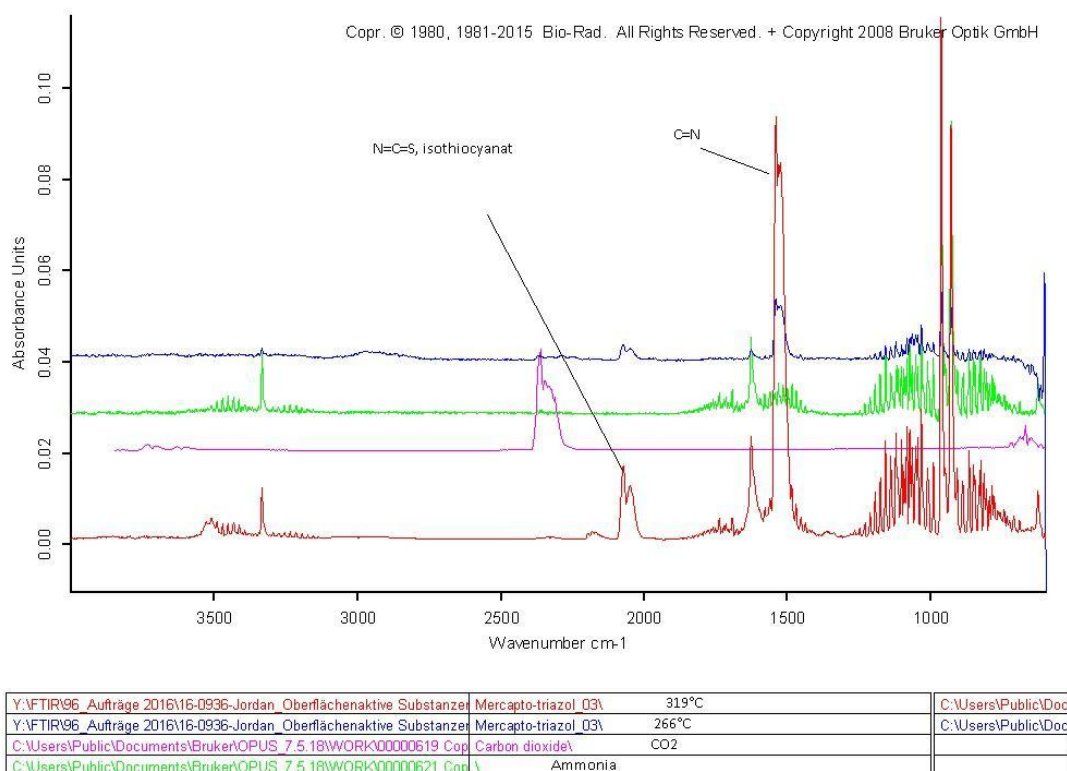


Figure A. 7.9: FT-IR spectra of the decomposing TT-molecule. The spectrum of decomposing TT matches with the spectra of NH₃. The formation of ammonia inside the silica ampoule leads to ammonium sulfide (NH₄)₂S which can react with copper sulfide towards the ammonium heptacopper sulfide NH₄Cu₇S₄. The FT-IR spectra was measured at Infineon Technologies AG.

A.8 Appendix Chapter 8

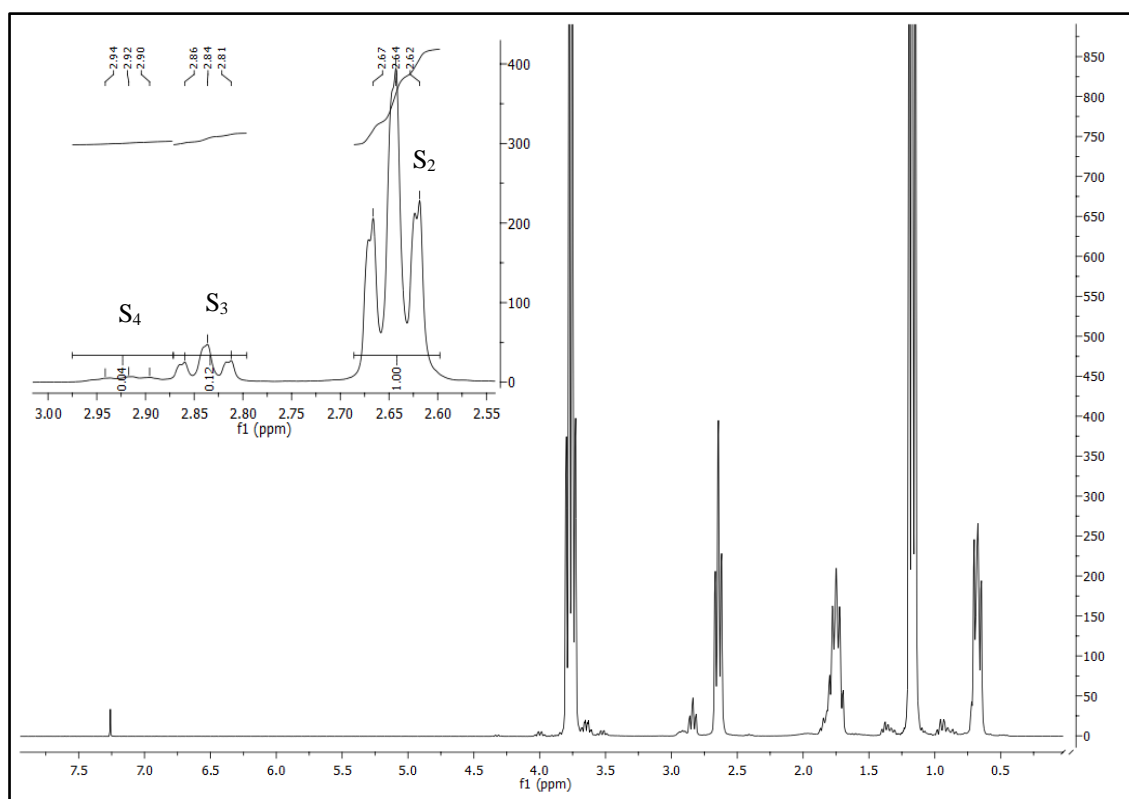


Figure A. 8.1: ^1H -NMR-Spectrum of the polysulfide mixture which consists of 84 % disulfide, 12 % trisulfide and 4 % tetrasulfide according to the integrals shown on the upper left side. The organic moieties are identical which results solely in a shift of the neighbouring ^1H -signals

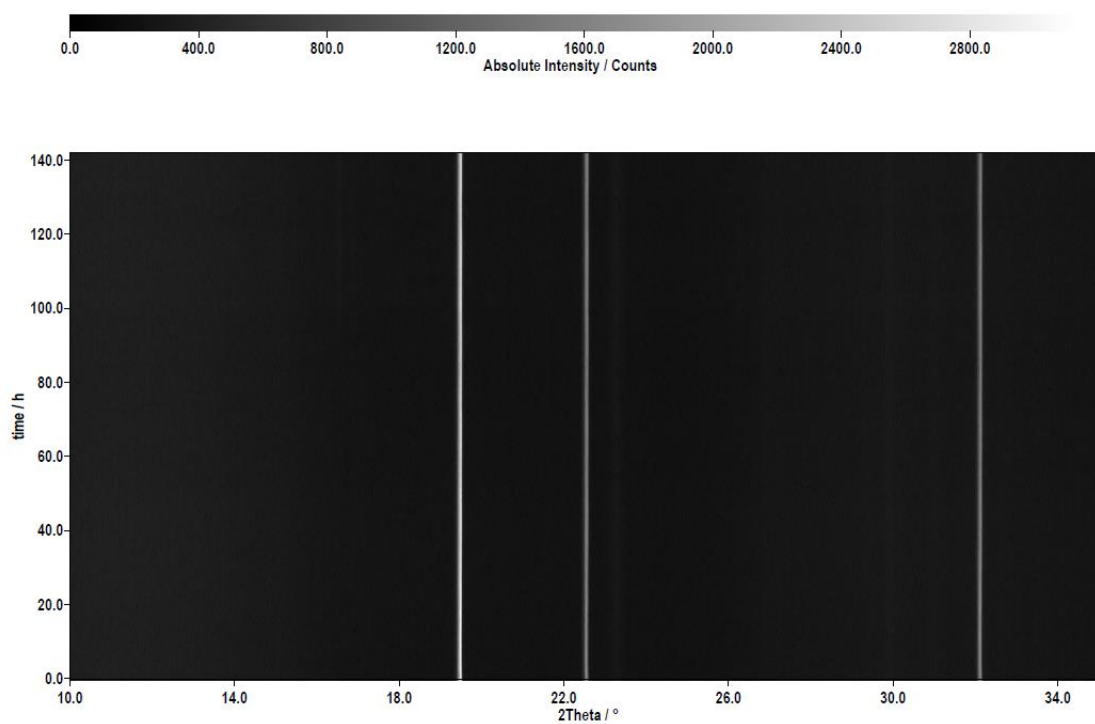


Figure A. 8.2: Isothermal HT-in situ-PXRD measurement of bare **Cu** bond wire with **TK** at 250 °C.

Appendix

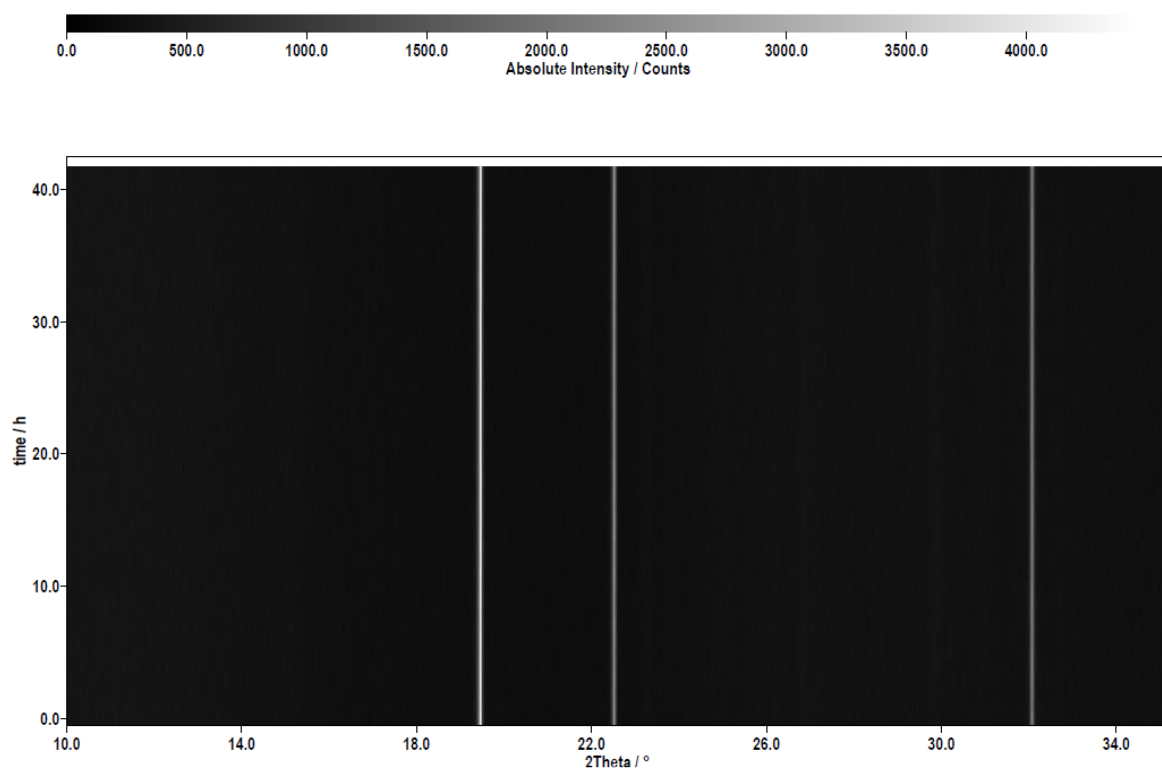


Figure A. 8.3: Isothermal HT-in situ-PXRD measurement of bare **Cu** bond wire with **SO** at 250 °C.

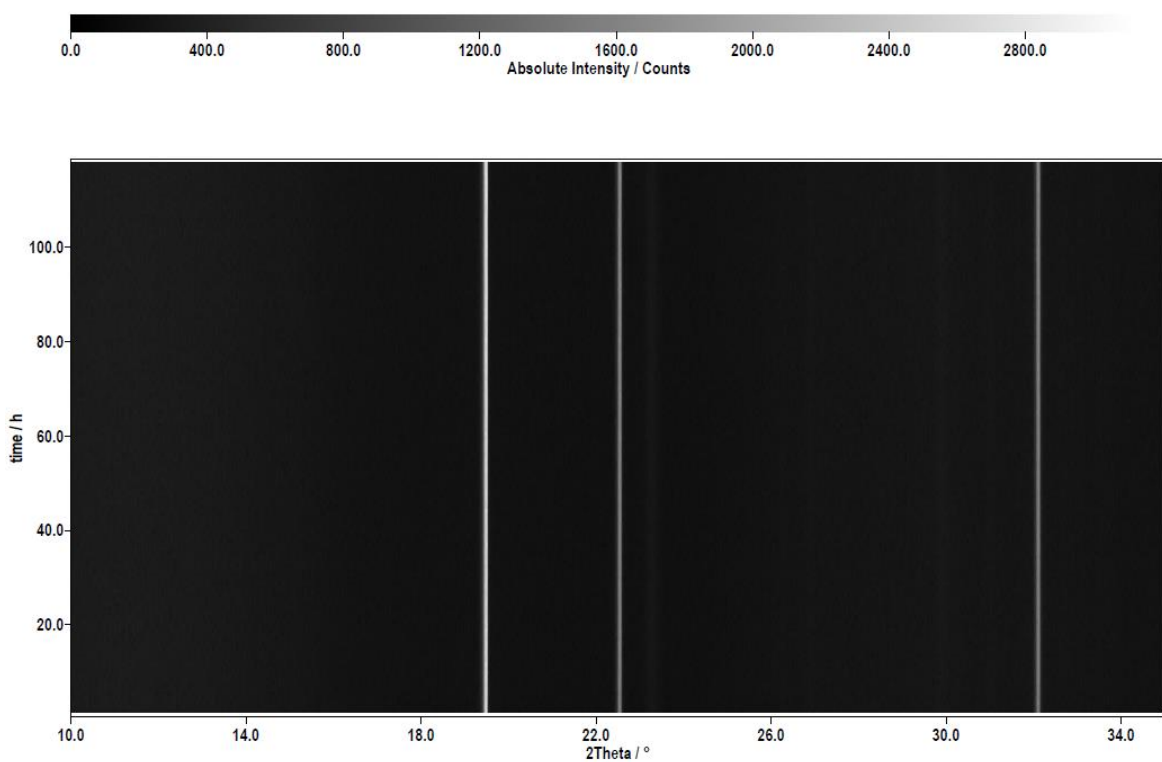


Figure A. 8.4: Isothermal HT-in situ-PXRD measurement of bare **Cu** bond wire with **TE1** at 250 °C.

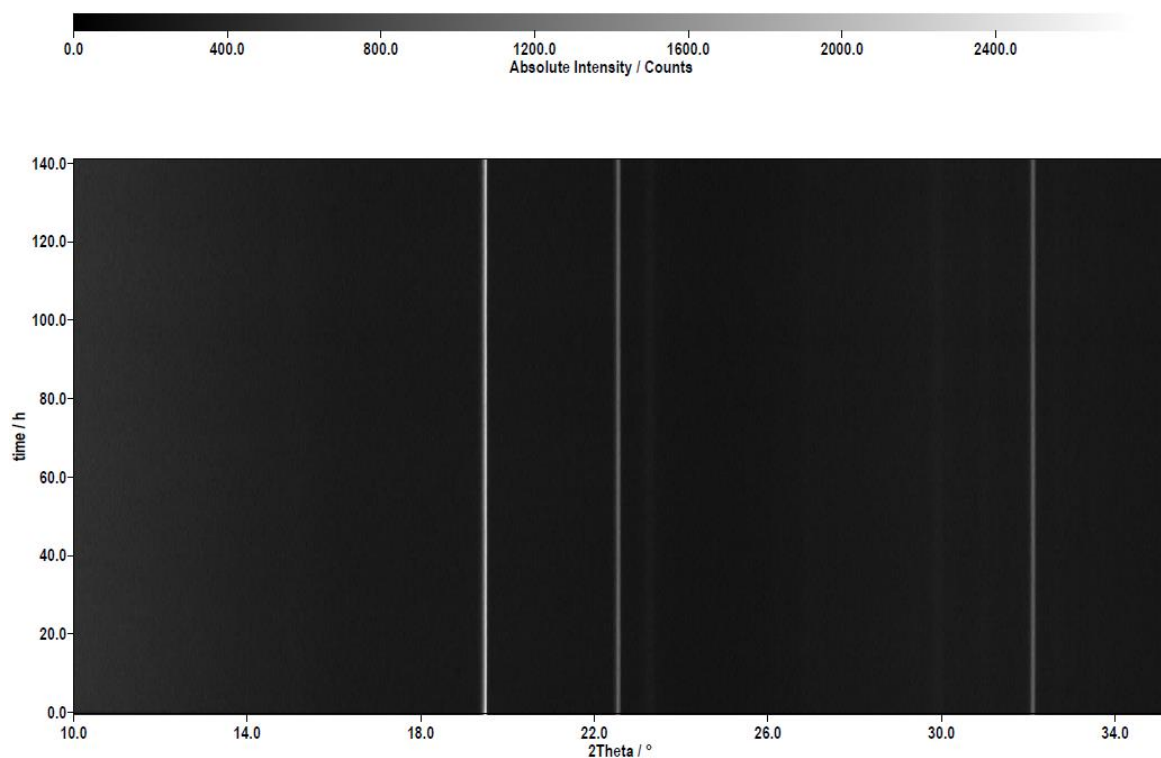


Figure A. 8.5: Isothermal HT-in situ-PXRD measurement of bare Cu bond wire with TE2 at 250 °C.

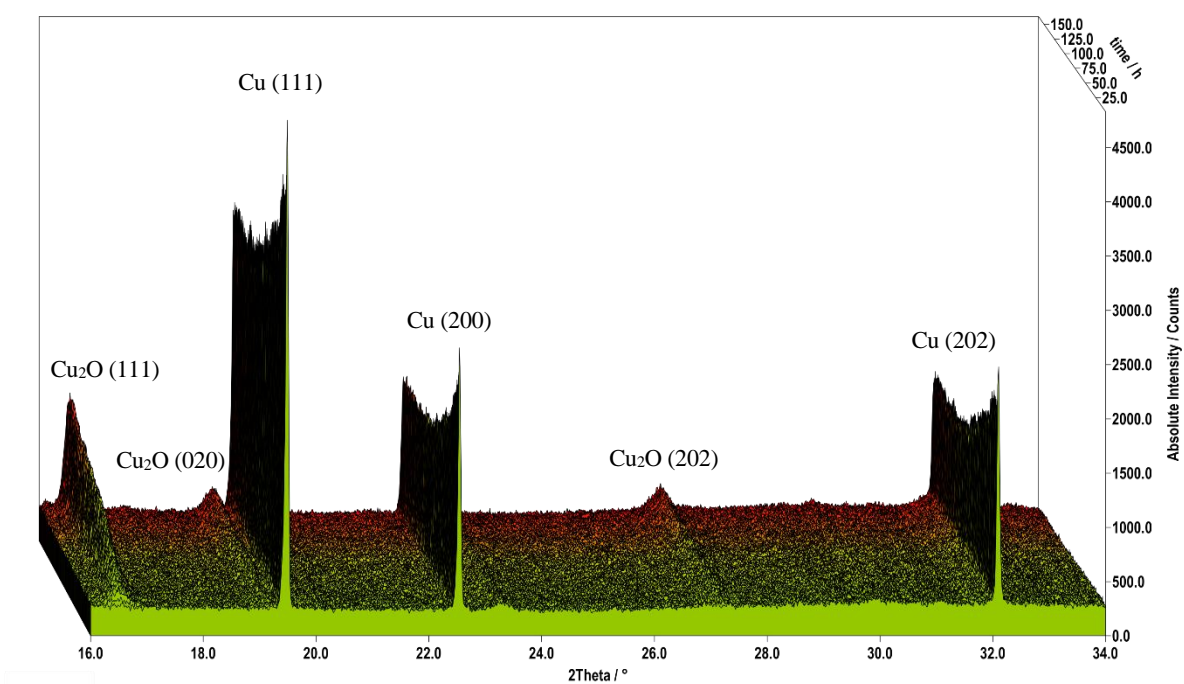


Figure A. 8.6: Isothermal HT-in situ-PXRD measurement of bare Cu bond wire at ambient air at 250 °C. The Cu reflections decrease and the Cu₂O (COD#: 99-500-0010) reflections increase over time.

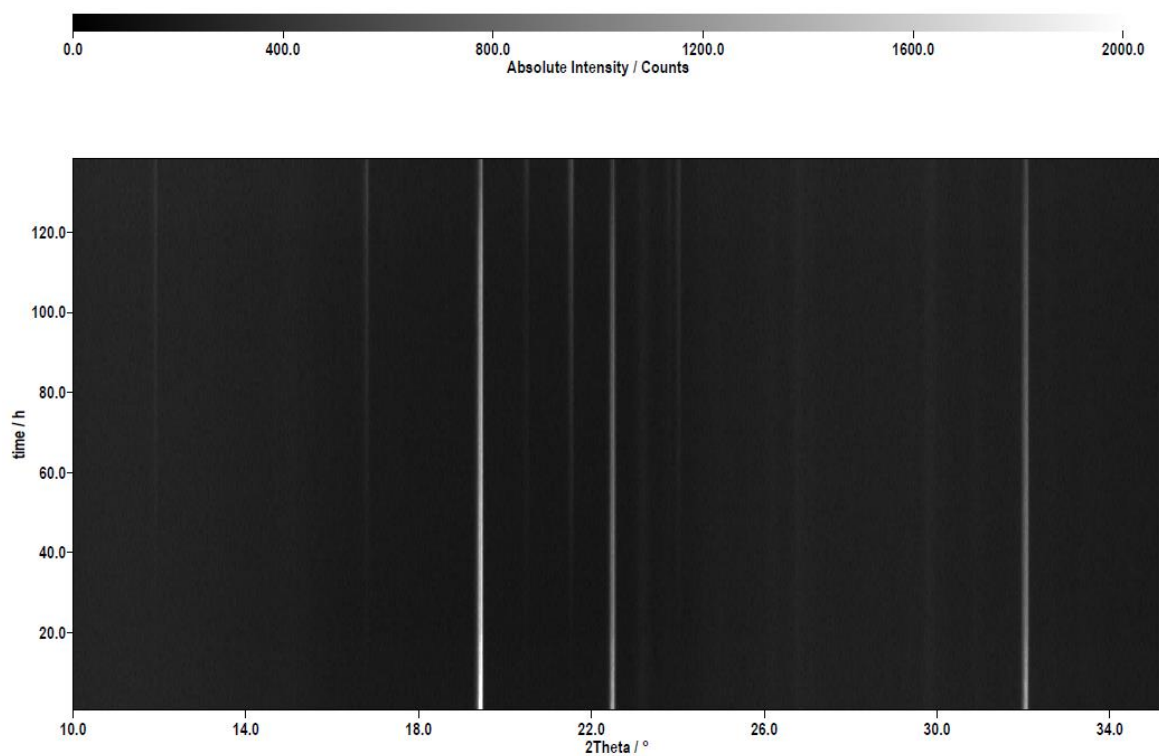


Figure A. 8.7: Isothermal HT-in situ-PXRD measurement of bare Cu bond wire with MS1 at 250 °C.

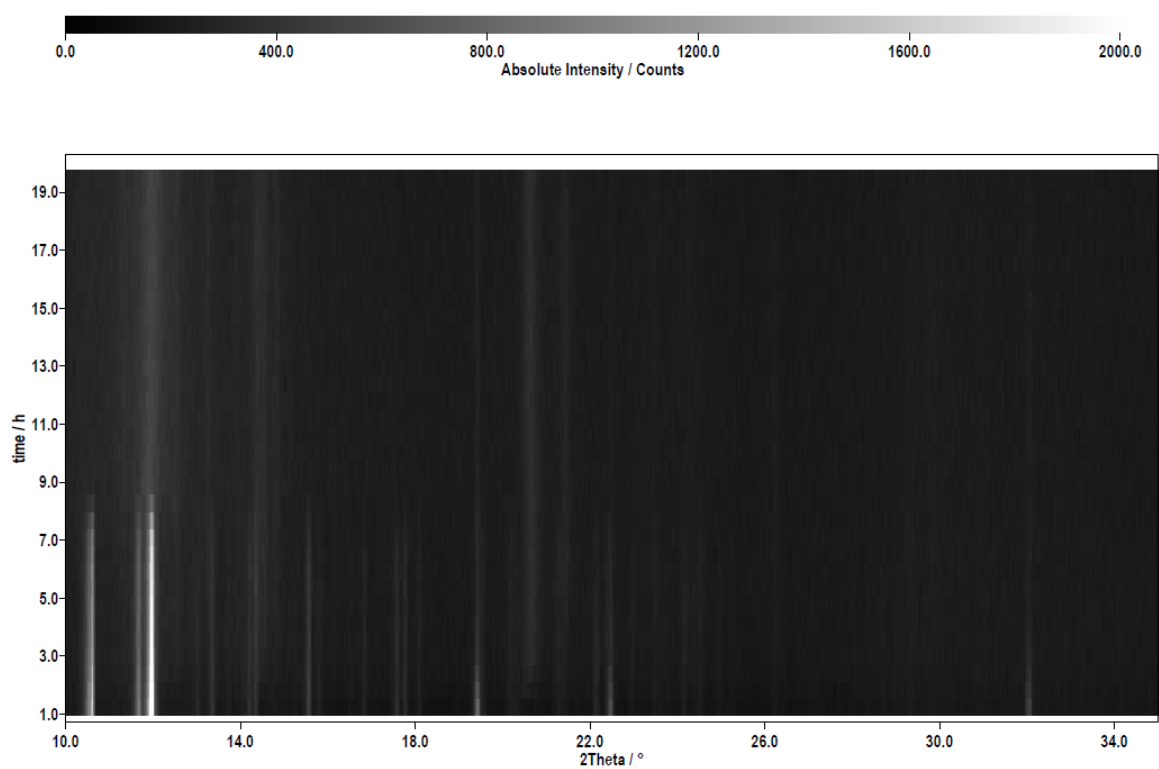


Figure A. 8.8: Isothermal HT-in situ-PXRD measurement of bare Cu bond wire with TT at 250 °C.

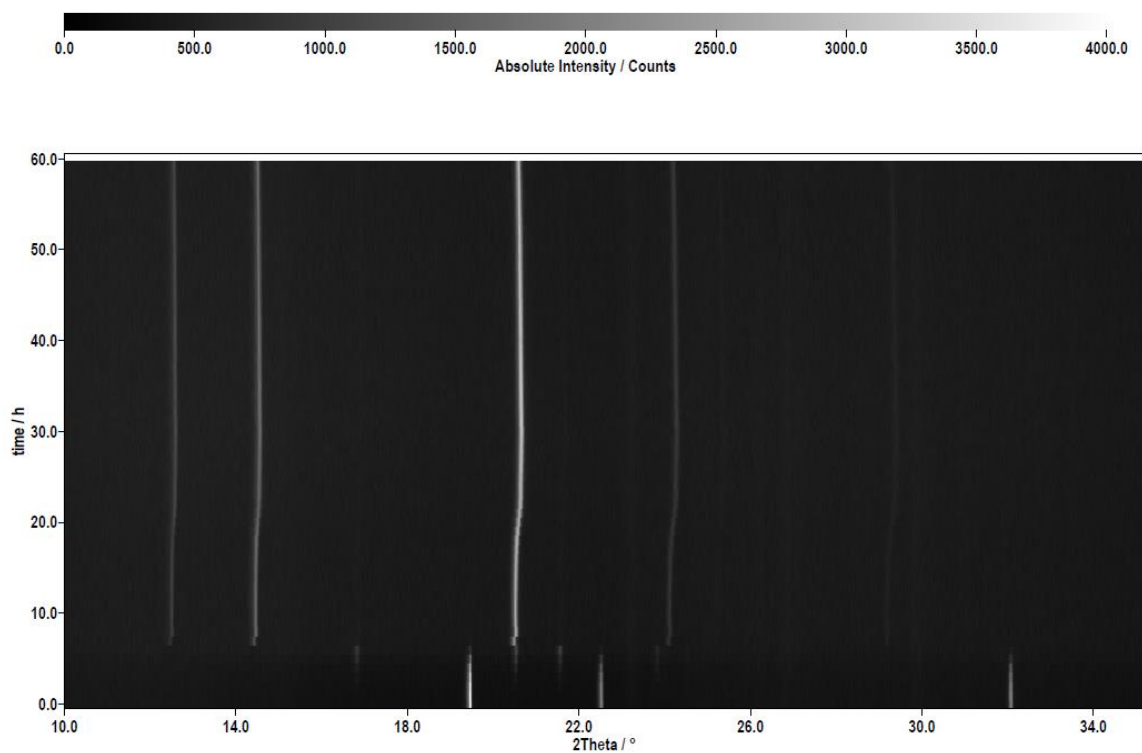


Figure A. 8.9: Isothermal HT-in situ-PXRD measurement of bare **Cu** bond wire with **DS** at 250 °C.

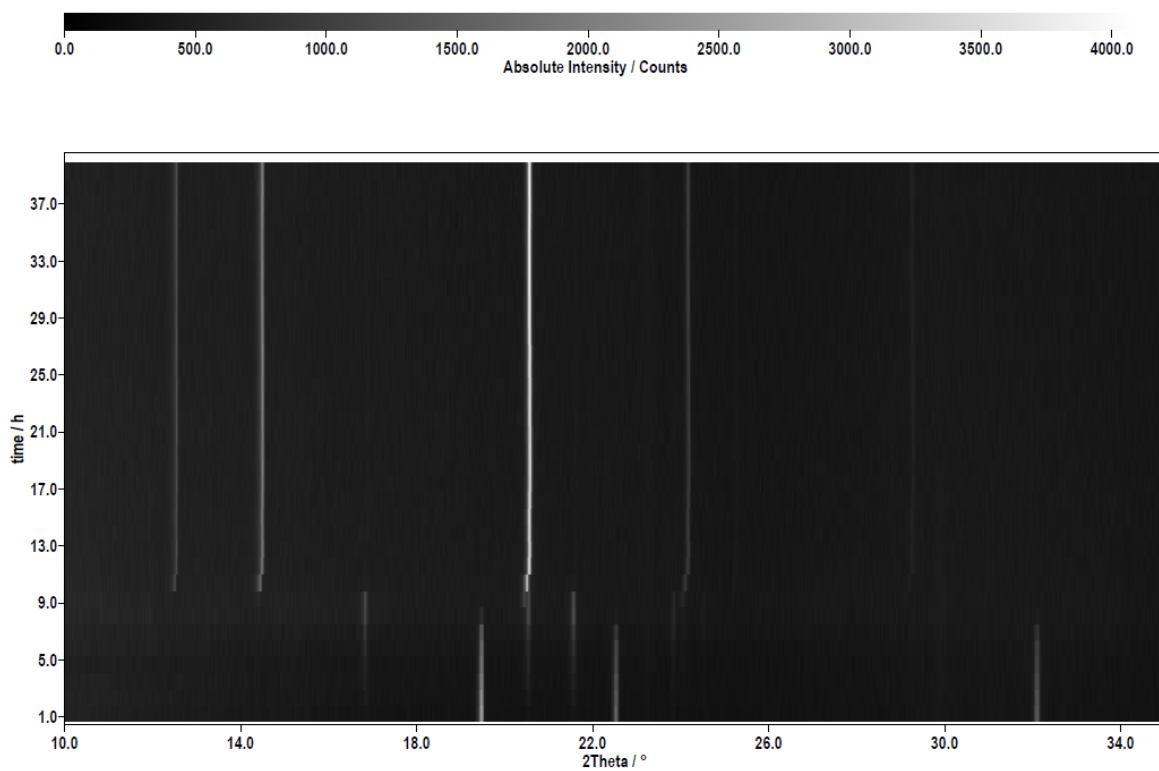


Figure A. 8.10: Isothermal HT-in situ-PXRD measurement of bare **Cu** bond wire with **DTTS** at 250 °C.

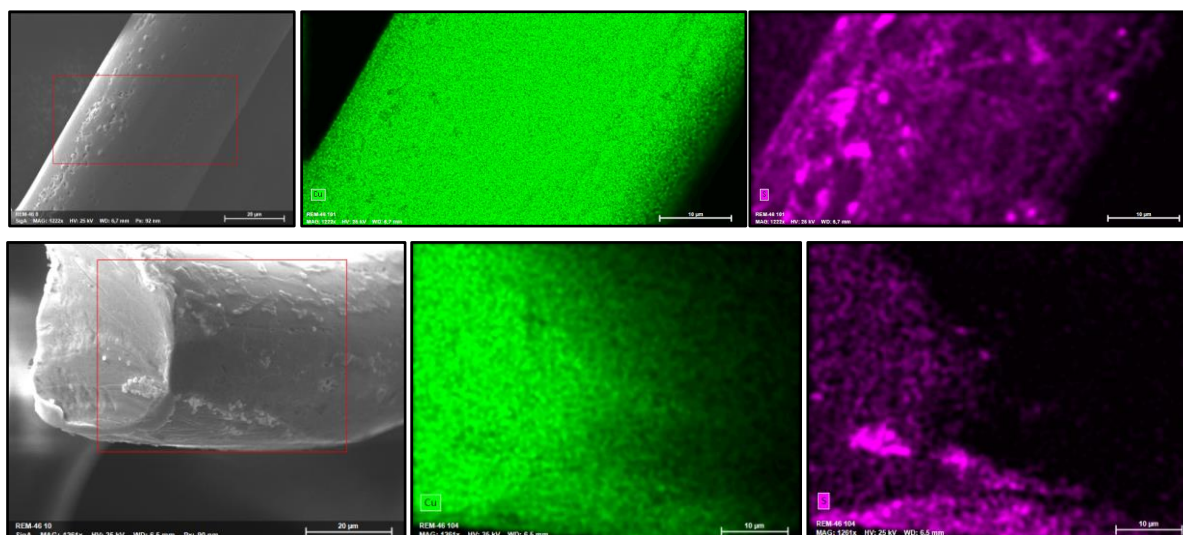


Figure A. 8.11: SEM and EDX analysis of the bare Cu wire after the HT-in situ-PXRD measurement (250 °C, 115 h) with **TE1**. The Cu wire shows minor signs of corrosion, which are small spheres on the surface of the bare Cu wire. These small spheres are comprised of S and Cu.

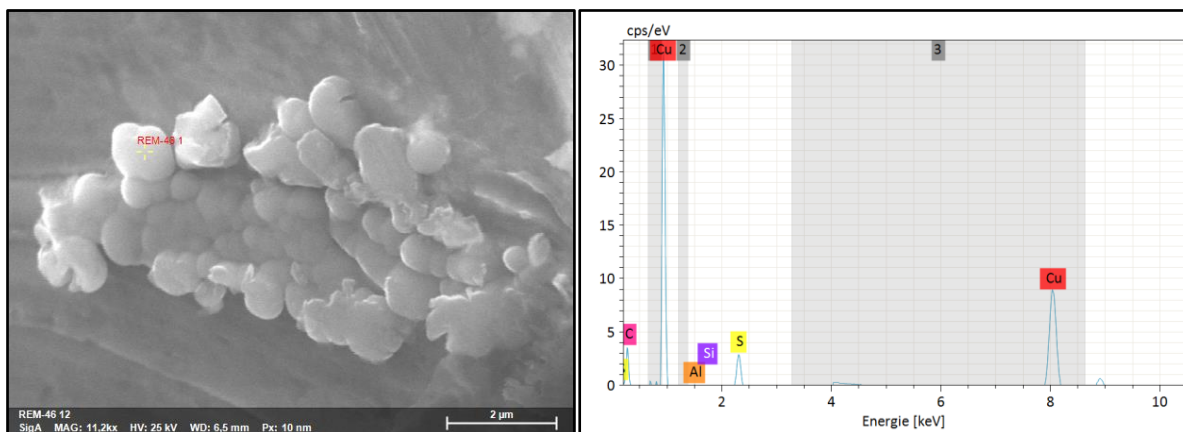


Figure A. 8.12: SEM and EDX analysis of the bare Cu wire after the HT-in situ-PXRD measurement (250 °C, 115 h) with **TE1**. Left: Magnification of Figure A 8.2, where small spheres are formed on the surface of the Cu wire. Right: EDX analysis of the marked spot on the formed sphere of the left picture. The analysis reveals that the sphere consists of Cu and S.

Table A 8.1: EDX analysis of the marked spot in Figure A 8.4. The EDX analysis reveals that the sphere is comprised of Cu and S in a ratio of $\approx 2:1$.

Element	Mass norm. / %	Atom-%	Abs. error / %	Rel. error / %
S	18.59	31.15	0.35	14.19
Cu	81.41	68.85	0.90	8.28

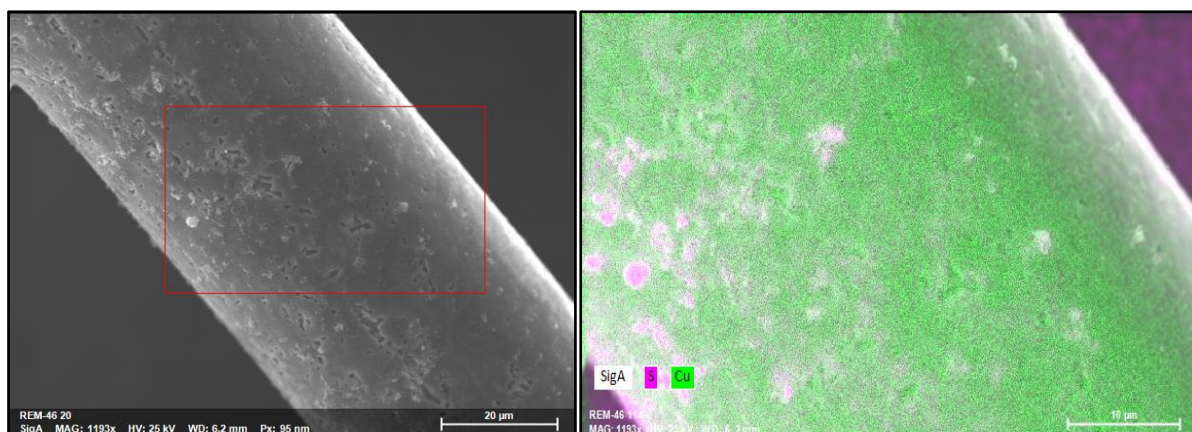


Figure A. 8.13: SEM and EDX analysis of the bare Cu wire after the HT-in situ-PXRD measurement (250 °C, 140 h) with **TE2**. The Cu wire shows minor signs of corrosion, which are small spheres and fragments on the surface of the bare Cu wire. These small spheres and fragments are comprised of S and Cu.

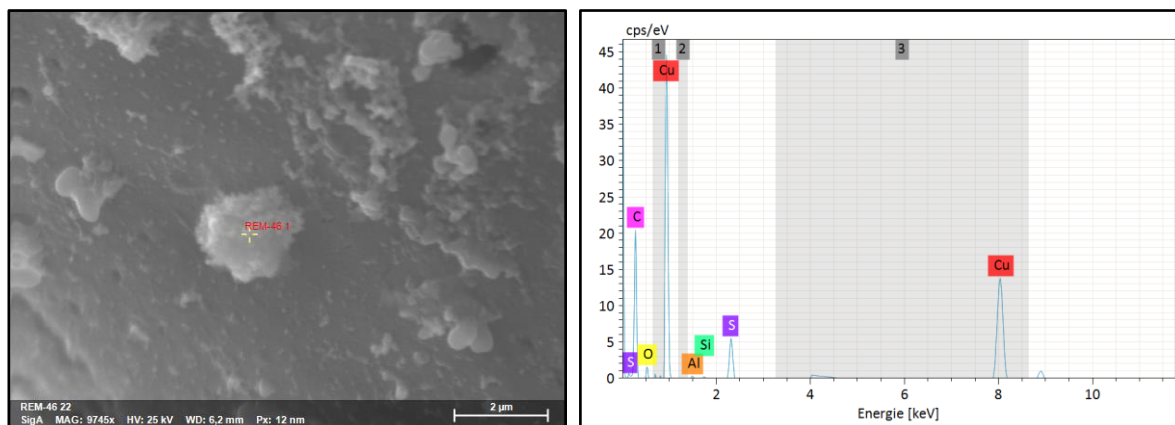


Figure A. 8.14: SEM and EDX analysis of the bare Cu wire after the HT-in situ-PXRD measurement (250 °C, 140 h) with **TE2**. Left: Magnification of Figure A 8.4, where small spheres are formed on the surface of the Cu wire. Right: EDX analysis of the marked spot on the formed sphere of the left picture. The analysis reveals that the sphere consists of Cu and S.

Table A 8.2: EDX analysis of the marked spot in Figure A 8.6. The EDX analysis reveals that the sphere is comprised of Cu and S in a ratio of $\approx 2:1$.

Element	Mass norm. / %	Atom-%	Abs. error / %	Rel. error / %
S	20.33	33.59	0.38	13.80
Cu	79.67	66.41	0.89	8.27

Appendix

Table A 8.3: Overview of the obtained kinetic parameters from SH-plot, JMAEK-fit, and master plots for bare Cu bond wire with O₂, MS1, and MS2 at 250 °C.

Wire	O ₂	MS1	MS2
T / °C	250	250	250
Sharp-Hancock Plot			
α -range / wt%	88-53	96-45 45-20	99-46
Avr. exp. n	0.39	1.15 3.26	1.22
k / h ⁻¹	$2.14 \cdot 10^{-3}$	$7.84 \cdot 10^{-3}$ $9.14 \cdot 10^{-3}$	$6.07 \cdot 10^{-3}$
Mechanism	D3	R3, Anti-R3 A3	R3, Anti-R3
JMAEK-Fit			
Avr. exp. n	0.38	1.68	1.40
k / h ⁻¹	$2.02 \cdot 10^{-3}$	$8.18 \cdot 10^{-3}$	$6.99 \cdot 10^{-3}$
Mechanism	D3	CD-D3, A2	Anti-R3, CD-D3
Master Plots			
Mechanism f(α)	D3	A2, R3, A3	A2, R2
Mechanism g(α)	D3	R1, A3	Anti-R3
Summary			
Assumed Mechanism	D3	R1 → A3	Anti-R3

Table A 8.4: Overview of the obtained kinetic parameters from SH-plot, JMAEK-fit, and master plots for bare Cu bond wire with TT, DS, and DTTS at 250 °C.

Wire	TT	DS	DTTS
T / °C	250	250	250
Sharp-Hancock Plot			
α -range / wt%	50-5	99-3	63-32 32-2
Avr. exp. n	0.59	3.10	0.56 3.68
k / h ⁻¹	$8.00 \cdot 10^{-1}$	$2.49 \cdot 10^{-1}$	$2.06 \cdot 10^{-1}$ $1.77 \cdot 10^{-1}$
Mechanism	D1, Anti-D3	A3	D3 A4
JMAEK-Fit			
Avr. exp. n	0.56	2.75	0.93
k / h ⁻¹	$8.03 \cdot 10^{-1}$	$2.47 \cdot 10^{-1}$	$2.62 \cdot 10^{-1}$
Mechanism	D3, Anti-D3	A3	D - R
Master Plots			
Mechanism f(α)	D3	A2	D3
Mechanism g(α)	D3	A3	D3, A2-A4
Summary			
Assumed Mechanism	D3	A3	D3 → A4

A.9 Appendix chapter 9

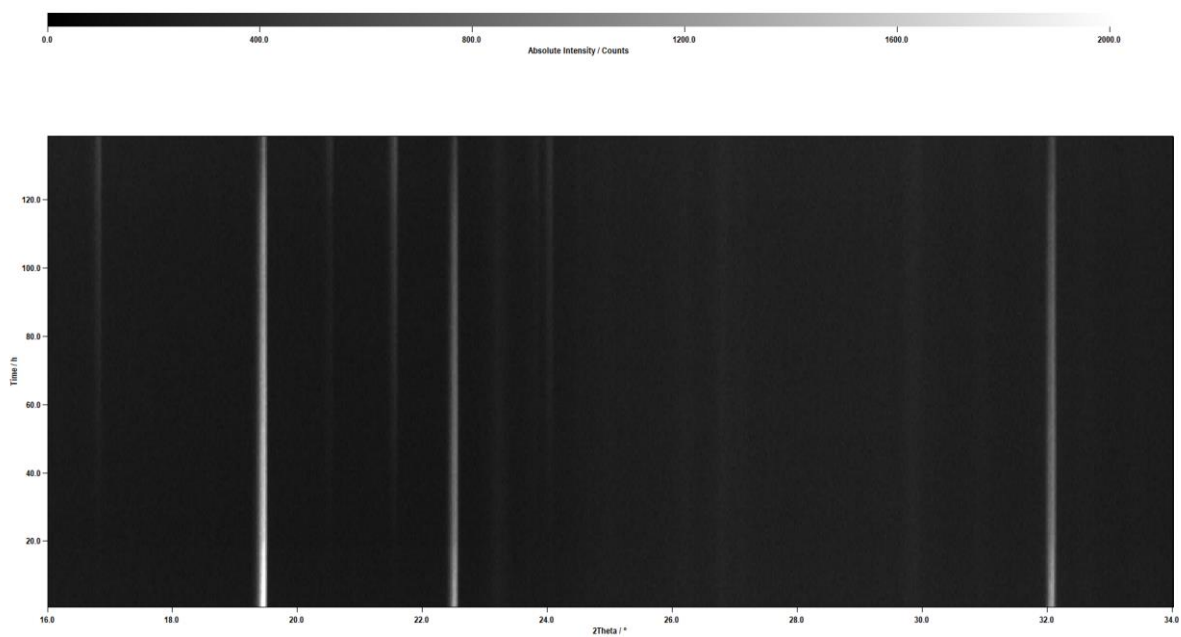


Figure A. 9.1: Isothermal HT-in situ-PXRD measurement of bare **Cu** bond wire with **MS1** at 250 °C.

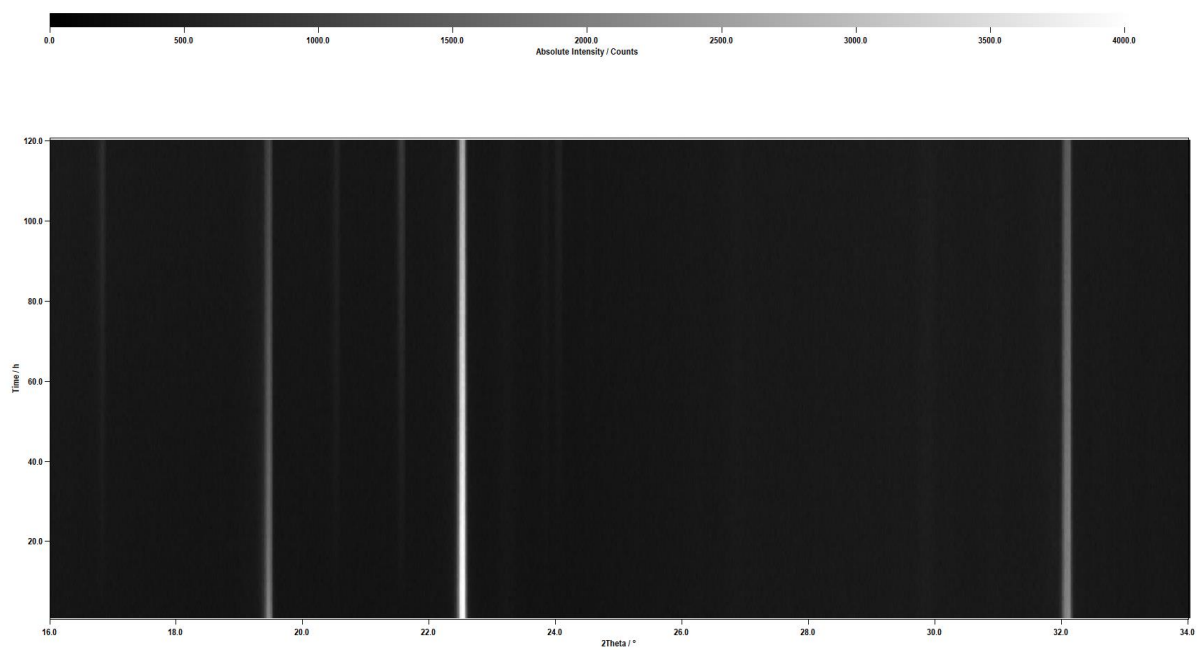


Figure A. 9.2: Isothermal HT-in situ-PXRD measurement of **PCC** bond wire with **MS1** at 250 °C.

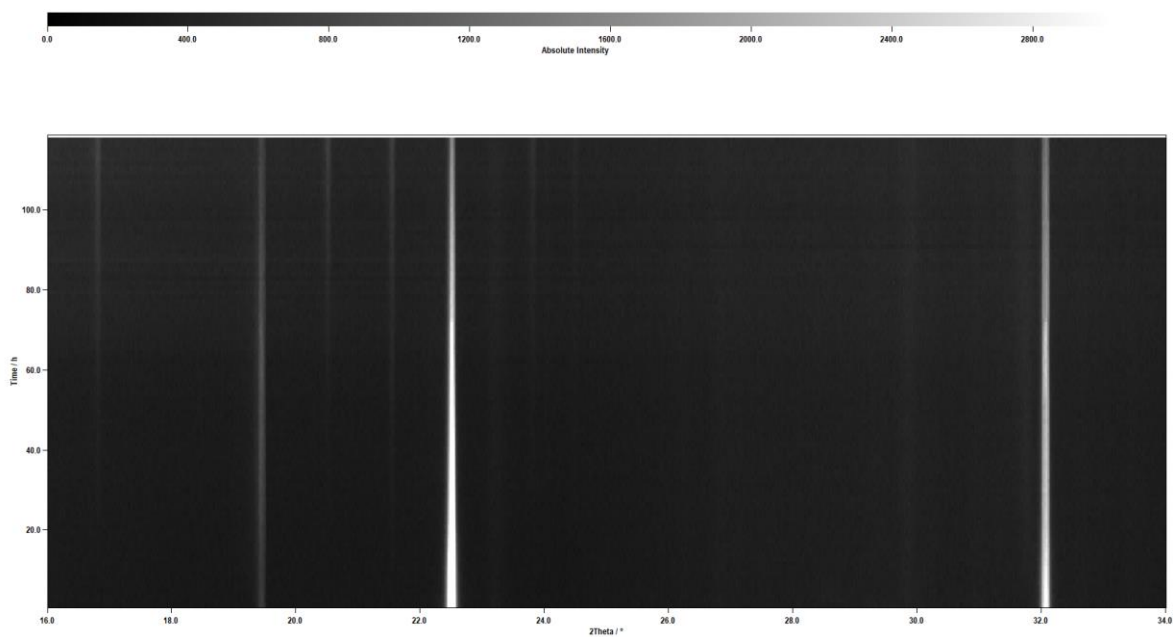


Figure A. 9.3: Isothermal HT-in situ-PXRD measurement of **APC** bond wire with **MS1** at 250 °C.

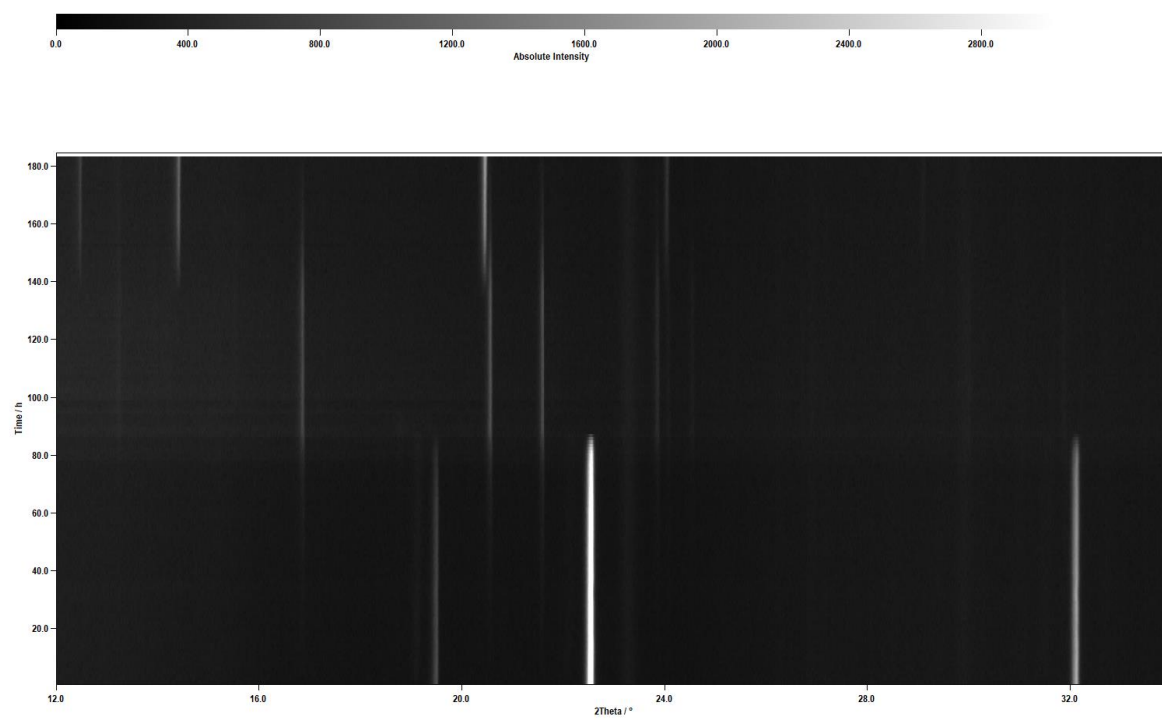


Figure A. 9.4: Isothermal HT-in situ-PXRD measurement of **APCX** bond wire with **MS1** at 250 °C.

Appendix

Table A 9.1: Overview of the obtained kinetic parameters from SH-plot, JMAEK-fit, and master plots for bare Cu, PCC, APC, and APCX bond wire with **MS1** at 250 °C.

Wire	Cu	PCC	APC	APCX
T / °C	250	250	250	250
Sharp-Hancock Plot				
α -range / wt%	96-45	97-45	99-78	100-48
	45-20		78-32	47-1
Avr. exp. n	1.15	1.02	1.00	0.75
	3.24		2.13	14.82
k / h ⁻¹	7.84·10 ⁻³	6.44·10 ⁻³	2.88·10 ⁻³	6.04·10 ⁻⁴
	9.14·10 ⁻³		8.43·10 ⁻³	1.45·10 ⁻²
Mechanism	Anti-R3	R3	R3	D - R
	A3		A2, P2	A4
JMAEK-Fit				
Avr. exp. n	1.68	1.12	2.13	-
k / h ⁻¹	8.48·10 ⁻³	6.94·10 ⁻³	8.47·10 ⁻³	-
Mechanism	CD-D3	R3, Anti-R3	A2, P2	-
Master Plots				
Mechanism f(α)	A2, Anti-D3	R3	A2	A2-A4, Anti-D3
Mechanism g(α)	Anti-R3, CD-D3	Anti-R3, Anti-D3	CD-D3, P2	Anti-D3, P4
Summary				
Assumed Mechanism	Anti-R3	R3, Anti-R3	R3	Anti-D3
	↓		↓	↓
	CD-D3		CD-D3, P2	P4

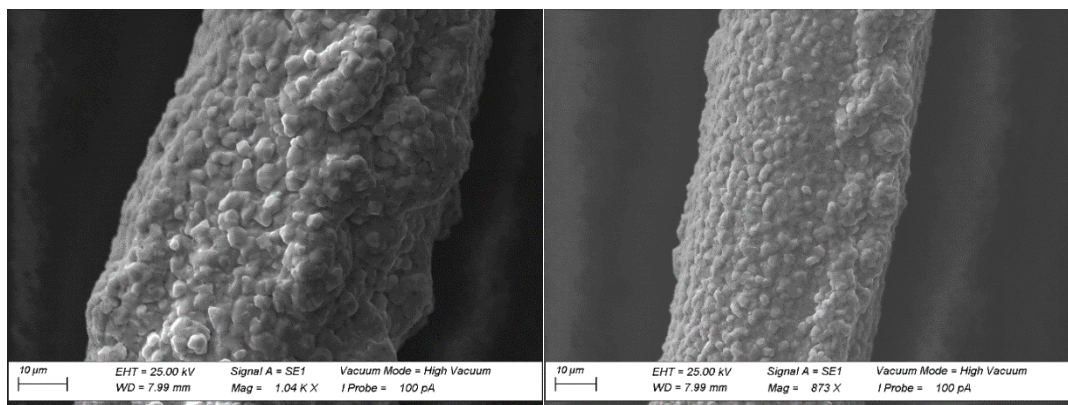


Figure A. 9.5: SEM analysis of the **PCC** wire surface with **MS1** after 120 h at 250 °C.

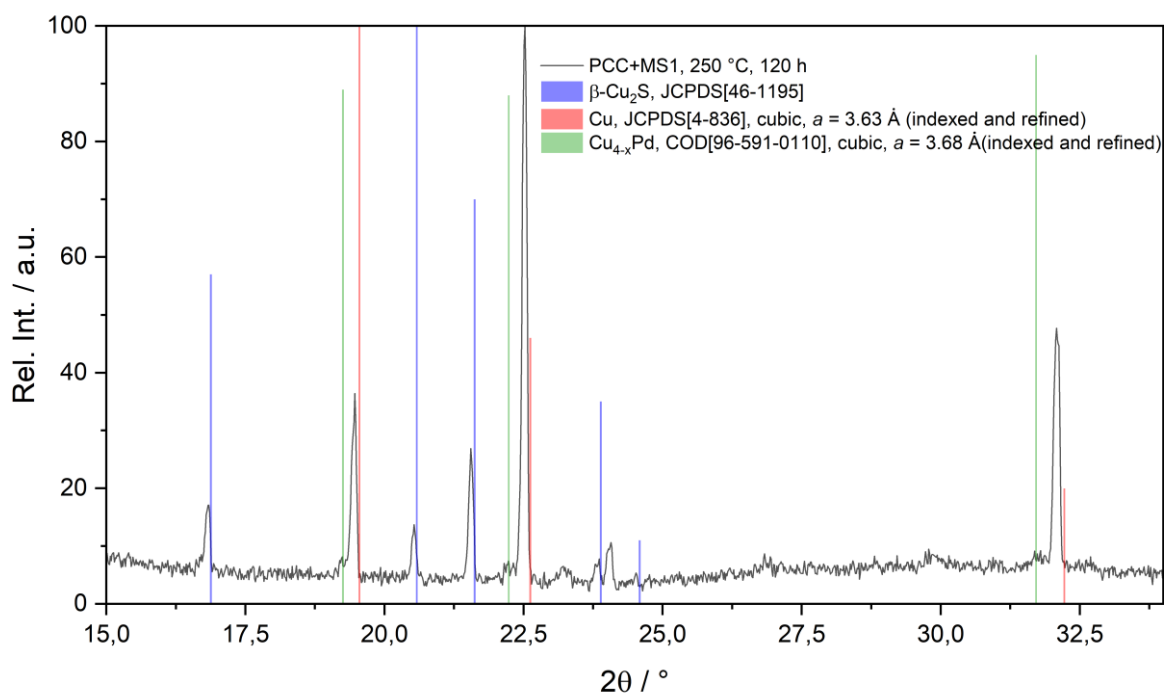


Figure A. 9.6: XRD powder pattern of the **PCC** wire after 120 h at 250 °C with **MS1**. The colored lines represent the reflections from β -Cu₂S, Cu, and Cu_{4-x}Pd, respectively. Note that the lattice parameter of Cu to Cu_{4-x}Pd increases from $a = 3.63$ to 3.68 Å. Simple extrapolation between pure Cu and Pd yields a Cu content of 74% for a cell parameter of $a = 3.68$ Å. This corresponds to a composition of Cu_{2.85}Pd (\approx Cu₃Pd).

Table A 9.2: ICP-OES measurement of the **APCX** wire. The wire is composed of a gold-palladium coating with a copper core. The copper core is doped with 3.1 ppm gallium and 1.6 ppm nickel. Measurement was performed at Infineon Technologies AG.

Element	ppm
Total	530 ppm
Cu	318.8 (signal saturated, lower values)
Pd	5.1
Au	1.7
Ga	3.1
Ni	1.6

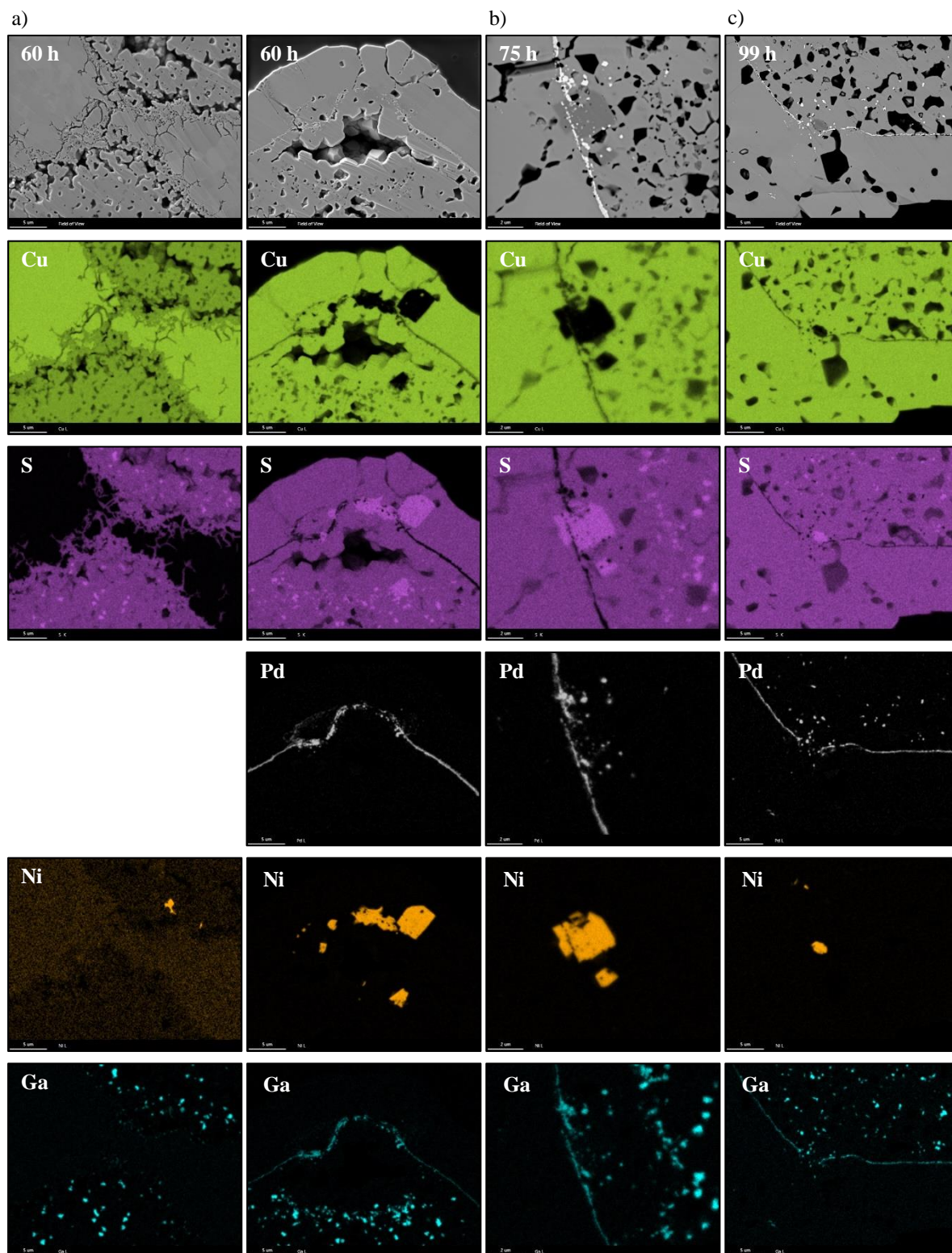


Figure A. 9.7: SEM and EDX micrographs of APCX wire cross-sections at 250 °C after a) 60 h, b) 75h, and c) 99h.

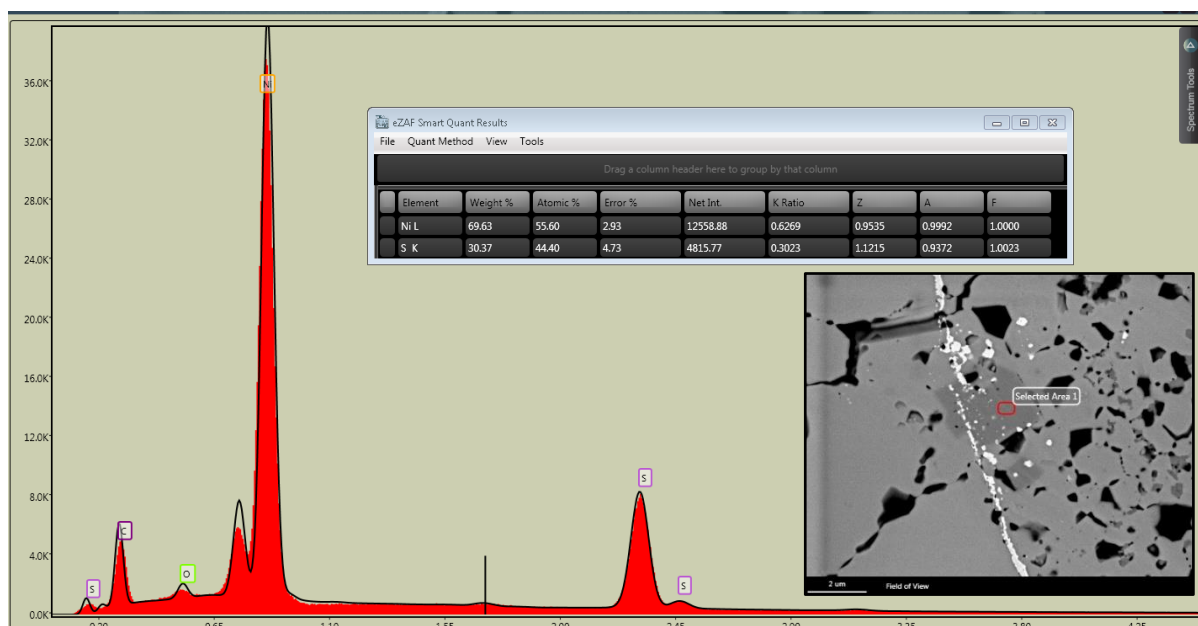


Figure A. 9.8: EDX spectrum of the APCX wire with MS1 after 75 h at 250 °C. Here, the dark spot reveals the existence of Ni_xS ($x = 1-1.5$). Measurement was performed at the Fraunhofer IMWS in Halle.

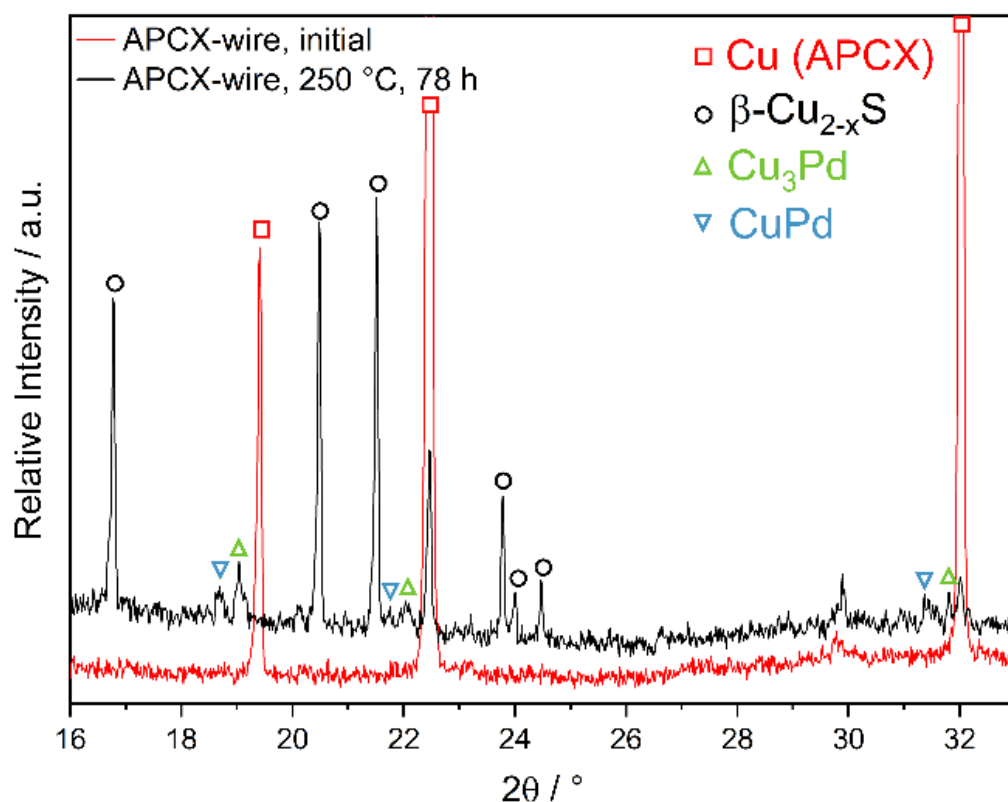


Figure A. 9.9: Powder pattern of APCX wire with MS1 at 250 °C after 78 h (black line) and initial (red line). After 78 h, presumably Cu_3Pd and CuPd is formed besides $\beta\text{-Cu}_2\text{S}$. Mixing of Cu with other alloying elements like Au is also feasible.

Table A 9.3: Overview of the obtained kinetic parameters from SH-plot, JMAEK-fit, and master plots for bare Cu, PCC, APC, and APCX bond wire with **TT** at 250 °C.

Wire	Cu	PCC	APC	APCX
T / °C	250	250	250	250
Sharp-Hancock Plot				
α -range / wt%	50-5	80-35	76-22	84-52
		35-17	20-15	52-22
Avr. exp. n	0.59	0.94	0.91	0.94
		0.18	0.24	0.26
k / h ⁻¹	8.00·10 ⁻¹	1.95·10 ⁻¹	9.91·10 ⁻¹	1.03
		3.13·10 ⁻¹	3.82	4.19·10 ⁻¹
Mechanism	D3, Anti-D3	R3	R3	R3
		D3	D3	D3
JMAEK-Fit				
Avr. exp. n	0.56	0.27	0.28	0.30
k / h ⁻¹	8.03·10 ⁻¹	1.25·10 ⁻¹	1.19	3.55·10 ⁻¹
Mechanism	D3, Anti-D3	D3	D3	D3
Master Plots				
Mechanism f(α)	F2	F2	F1, F2	F2, F3
Mechanism g(α)	D3	R3, D3	F1	D3
Summary				
Assumed Mechanism	D3	R3	R3	R3
		↓	↓	↓
		D3	D3	D3

A.10 Appendix chapter 10

Table A 10.1: Overview of the obtained kinetic parameters from SH-plot and JMAEK-fit for bare Cu, and APC bond wire with TT in combination with different solvents and as pure solid at 250 °C.

Wire	APC (DMSO)	APC (PC)	APC (Solid)	Cu (Solid)
T / °C	250	250	250	250
Sharp-Hancock Plot				
α -range / wt%	92-71 71-66	83-57 57-30	76-22 22-16	50-5
Avr. exp. n	1.13 0.15	0.25 0.63	0.91 0.38	0.59
k / h ⁻¹	1.09·10 ⁻¹ 1.43·10 ⁻⁴	1.05·10 ⁻² 6.46·10 ⁻²	9.91·10 ⁻¹ 1.89	8.00·10 ⁻¹
Mechanism	R1 D3	D3 D1, Anti-D3	D – R D3	D1, Anti-D3
JMAEK-Fit				
Avr. exp. n	0.32	0.56	0.28	0.56
k / h ⁻¹	3.84·10 ⁻³	6.35·10 ⁻²	1.19	8.03·10 ⁻¹
Mechanism	D3	D3, Anti-D3	D3	D3, Anti-D3
Summary				
Assumed Mechanism	R1 → D3	D3, Anti-D3	R1 → D3	D3, Anti-D3

Table A 10.2: Overview of the obtained kinetic parameters from SH-plot and JMAEK-fit for bare Cu, and APC bond wire with TT in combination with different solvents and as pure solid at 200 °C.

Wire	APC (DMSO)	APC (PC)	APC (Solid)	Cu (Solid)
T / °C	200	200	200	200
Sharp-Hancock Plot				
α -range / wt%	93-69	97-81	99-81	99-79
Avr. exp. n	0.53	0.48	0.59	0.71
k / h ⁻¹	1.34·10 ⁻²	5.22·10 ⁻⁴	2.71·10 ⁻⁴	1.34·10 ⁻³
Mechanism	D3	D3	D1, Anti-D3	D – R, F2
JMAEK-Fit				
Avr. exp. n	0.16	0.42	0.57	0.87
k / h ⁻¹	4.62·10 ⁻⁵	3.02·10 ⁻⁴	2.70·10 ⁻⁴	1.93·10 ⁻³
Mechanism	D3	D3	D2, Anti-D3	D – R, F2
Summary				
Assumed Mechanism	D3	D3	D1, Anti-D3	D – R, F2

Appendix

Table A 10.3: Overview of the obtained kinetic parameters from SH-plot and JMAEK-fit for APC bond wire with **TT** at 250-200 °C.

Wire	APC (Solid)	APC (Solid)	APC (Solid)
T / °C	250	225	200
Sharp-Hancock Plot			
α -range / wt%	76-22 22-16	96-58 58-13	99-81
Avr. exp. n	0.91 0.38	0.54 1.38	0.59
k / h^{-1}	$9.91 \cdot 10^{-1}$ 1.89	$6.28 \cdot 10^{-3}$ $1.53 \cdot 10^{-2}$	$2.71 \cdot 10^{-4}$
Mechanism	D – R D3	D3 R1, Anti-R3	D1, Anti-D3
JMAEK-Fit			
Avr. exp. n	0.28	1.09	0.57
k / h^{-1}	1.19	$1.56 \cdot 10^{-2}$	$2.70 \cdot 10^{-4}$
Mechanism	D3	R3	D2, Anti-D3
Summary			
Assumed Mechanism	R1 ↓ D3	D3 ↓ Anti-R3	D3

Table A 10.4: Overview of the obtained kinetic parameters from SH-plot and JMAEK-fit for APC bond wire with **TT** at 250-200 °C.

Wire	Cu (Solid)	Cu (Solid)	Cu (Solid)
T / °C	250	225	200
Sharp-Hancock Plot			
α -range / wt%	50-5	97-57	99-79
Avr. exp. n	0.59	1.00	0.71
k / h^{-1}	$8.00 \cdot 10^{-1}$	$1.34 \cdot 10^{-2}$	$1.34 \cdot 10^{-3}$
Mechanism	D1, Anti-D3	R3	D – R, F2
JMAEK-Fit			
Avr. exp. n	0.56	0.87	0.87
k / h^{-1}	$8.03 \cdot 10^{-1}$	$9.68 \cdot 10^{-3}$	$1.93 \cdot 10^{-3}$
Mechanism	D3, Anti-D3	D – R	D – R, F2
Summary			
Assumed Mechanism	D3, Anti-D3	D – R, F2	D – R, F2

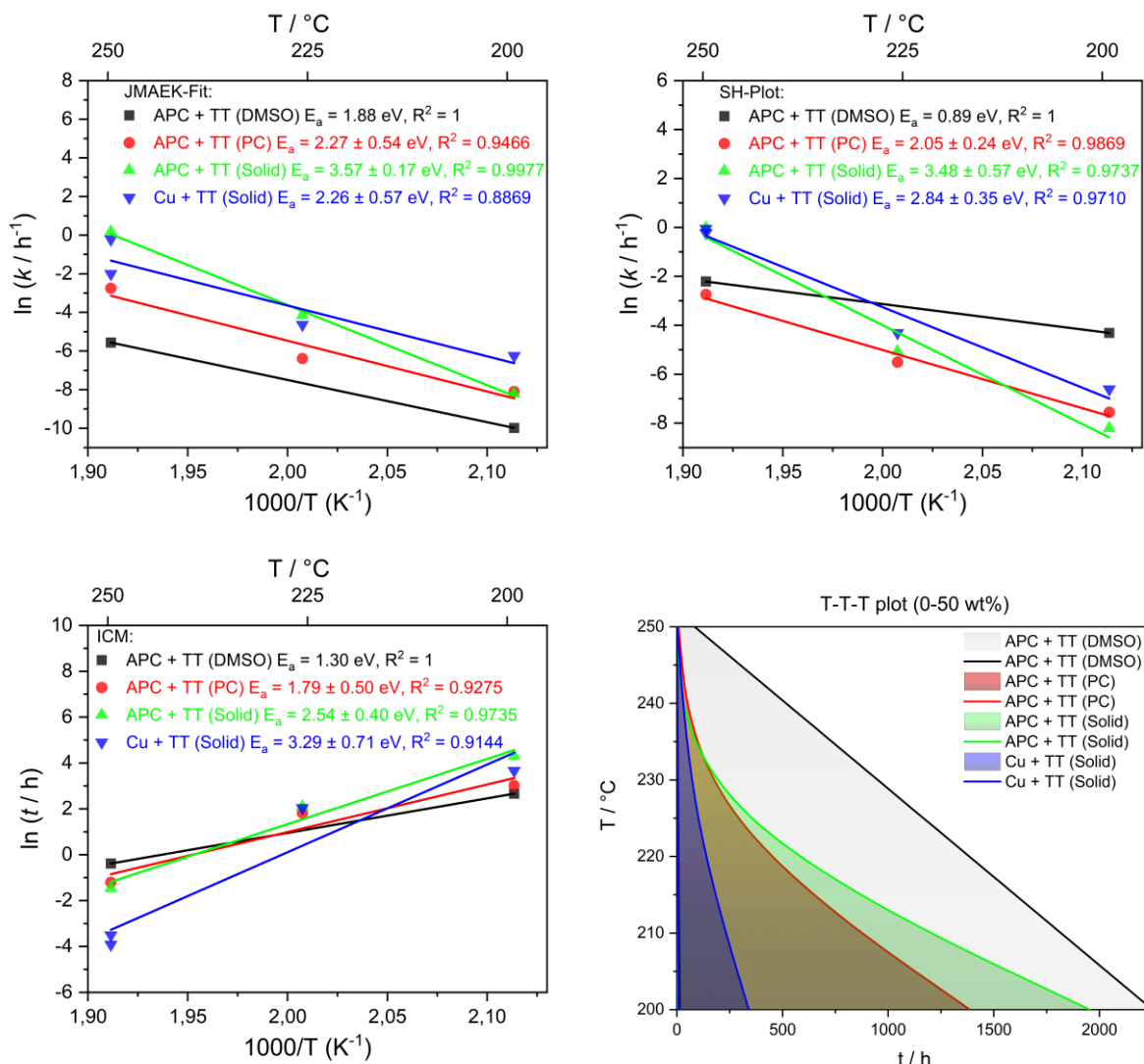


Figure A. 10.1: Arrhenius plots with the obtained rate constants from JMAEK-fit (top left), SH-plot (top right), and ICM (bottom left). On the bottom right, the T-T-T plot is shown from 0-50 wt% conversion.

Table A 10.5: Overview of the activation energies and preexponential factors obtained from SH-plot, JMAEK-fit, and ICM for bare Cu and APC bond wire with TT in combination with different solvents at 250-200 °C.

	APC (DMSO)	APC (PC)	APC (Solid)	Cu (Solid)
Activation energies E_a / eV				
E_a (SH-plot)	0.89	2.1(2)	3.5(6)	2.8(4)
E_a (JMAEK-fit)	1.88	2.3(5)	3.6(2)	2.3(6)
E_a (t_{10})	1.30	1.8(5)	2.5(4)	3.3(7)
Mean E_a	1.4(4)	2.0(2)	3.2(5)	2.8(4)
Preexponential factor A				
$\ln A$ (SH-plot)	17	43(6)	77(13)	63(8)
$\ln A$ (JMAEK-Fit)	36	47(13)	79(4)	49(13)
$\ln A$ (t_{10})	-29	-41(12)	-56(9)	-76(17)

A.12 Appendix chapter 12

Table A 12.1: Overview of the obtained kinetic parameters from SH-plot, JMAEK-fit, and master plots for bare **Cu** bond wire with **DS** at 250-175 °C.

Wire	Cu	Cu	Cu	Cu
T / °C	250	225	200	175
Sharp-Hancock Plot				
α-range / wt%	92-36	92-80	91-62	97-68
	36-1	80-23	62-22 22-8	68-7
Avr. exp. n	0.85	0.48	1.09	1.43
	3.48	2.00	0.89 5.75	0.94
k / h⁻¹	2.91·10 ⁻¹	1.02·10 ⁻²	1.19·10 ⁻¹	3.74·10 ⁻²
	3.42·10 ⁻¹	8.80·10 ⁻²	7.89·10 ⁻² 5.31·10 ⁻²	2.83·10 ⁻²
Mechanism	D - R	D3	R3	R1
	A3	A2	D - R A4	D - R
JMAEK-Fit				
Avr. exp. n	3.28	2.02	1.61	1.47
k / h⁻¹	2.08·10 ⁻¹	7.31·10 ⁻²	6.25·10 ⁻²	2.00·10 ⁻²
Mechanism	A3	A2	A2	A2
Master Plots				
Mechanism f(α)	A2 - A4	A2	Anti-R3, A2	R1, A2
Mechanism g(α)	R1	R1	Anti-D3	R1 - Anti-D3
Summary				
Assumed Mechanism	R1	D3	Anti-R3	R1
	↓ A3	↓ A2	↓ Anti-D3	↓ Anti-D3

Appendix

Table A 12.2: Overview of the obtained kinetic parameters from SH-plot, JMAEK-fit, and master plots for **PCC** bond wire with **DS** at 250-175 °C.

Wire	PCC	PCC	PCC	PCC
T / °C	250	225	200	175
Sharp-Hancock Plot				
α-range / wt%	93-80	91-23	99-15	96-77
	80-11	23-0	15-0	77-27
				27-0
Avr. exp. n	0.52	1.10	1.82	0.69
	1.93	4.32	4.52	1.31
				4.48
k / h⁻¹	1.71·10 ⁻¹	1.55·10 ⁻¹	8.62·10 ⁻²	5.42·10 ⁻³
	2.23·10 ⁻¹	1.36·10 ⁻¹	6.42·10 ⁻²	2.20·10 ⁻²
				1.97·10 ⁻²
Mechanism	D3	R2	A2	D3
	A2	A4	A4	R1
				A4
JMAEK-Fit				
Avr. exp. n	3.32	1.88	3.44	2.50
k / h⁻¹	1.45·10 ⁻¹	1.46·10 ⁻¹	4.78·10 ⁻²	1.71·10 ⁻²
Mechanism	A3	A2	A3	A3
Master Plots				
Mechanism f(α)	A2 – A4	A2 – A4	A2 – A4	A2 – A4
Mechanism g(α)	A2, Anti-R3	R2	A2, R2	R1
Summary				
Assumed Mechanism	A2		A2	A2, R1
	↓	A2, R2	↓	↓
	Anti-R3		A4	A4

Appendix

Table A 12.3: Overview of the obtained kinetic parameters from SH-plot, JMAEK-fit, and master plots for **APC** bond wire with **DS** at 250-175 °C.

Wire	APC	APC	APC	APC
T / °C	250	225	200	175
Sharp-Hancock Plot				
α-range / wt%	96-69	93-53	95-45	98-88
	69-0	53-2	45-0	80-34
				34-0
Avr. exp. n	1.72	0.87	1.24	0.60
	4.79	3.56	4.45	1.47
				4.04
k / h⁻¹	1.71·10 ⁻¹	1.19·10 ⁻¹	7.89·10 ⁻²	1.21·10 ⁻³
	2.23·10 ⁻¹	1.99·10 ⁻¹	7.49·10 ⁻²	2.22·10 ⁻²
				1.86·10 ⁻²
Mechanism	A2	D – R	R1, Anti-R3	D3
	A4	A4	A4	R1, A2
				A4
JMAEK-Fit				
Avr. exp. n	3.57	2.55	2.64	2.41
k / h⁻¹	1.42·10 ⁻¹	1.73·10 ⁻¹	5.97·10 ⁻²	1.74·10 ⁻²
Mechanism	A4	A3	A3	A2
Master Plots				
Mechanism f(α)	A2 – A4	A2 – A4	A2 – A4	A2 – A4
Mechanism g(α)	A2 – A4	R1, A3	R1, A3	A2
Summary				
Assumed Mechanism	A2	R1	R1	A2
	↓	↓	↓	↓
	A4	A3	A3	A4

Appendix

Table A 12.4: Overview of the obtained kinetic parameters from SH-plot, JMAEK-fit, and master plots for **APCX** bond wire with **DS** at 250-175 °C.

Wire	APCX	APCX	APCX	APCX
T / °C	250	225	200	175
Sharp-Hancock Plot				
α-range / wt%	90-63		95-67	99-27
	63-26	97-0	67-0	27-1
	26-1			
Avr. exp. n	2.07		2.95	2.88
	0.59	2.48	1.41	0.74
	3.75			
k / h⁻¹	1.57		1.76	2.33·10 ⁻¹
	1.84	1.19	1.26	3.35·10 ⁻¹
	4.84·10 ⁻¹			
Mechanism	A2		A3	A3
	D3	A3	R1, Anti-R3	D - R
	A4			
JMAEK-Fit				
Avr. exp. n	1.36	3.00	3.91	3.61
k / h⁻¹	5.85·10 ⁻¹	9.30·10 ⁻¹	5.93·10 ⁻¹	1.30·10 ⁻¹
Mechanism	R1, Anti-R3	A3	A4	A4
Master Plots				
Mechanism f(α)	R3, D2	A2	A2 – A4	A2 – A4
Mechanism g(α)	R1, D3	A2, A3	R1, A2	A3, A2
Summary				
Assumed Mechanism	A2, R1	A2	A2	A3
	↓	↓	↓	↓
	D3	A3	A4	A4

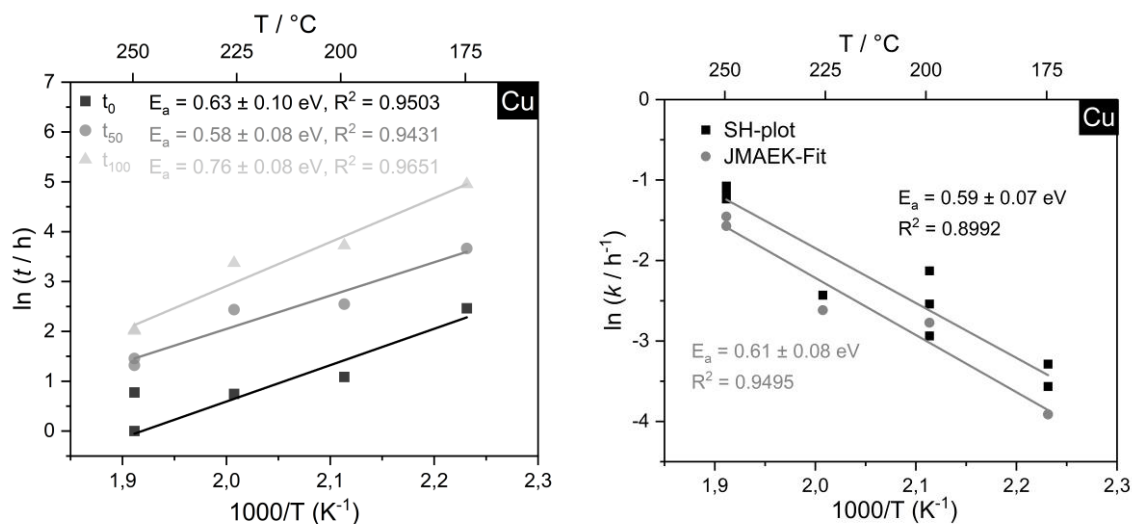


Figure A. 12.1: Arrhenius plots of Cu bond wire with DS from 175 °C to 250 °C. Left: Evaluation with the isoconversional method. Right: Evaluation with SH-plot and JMAEK-Fit.

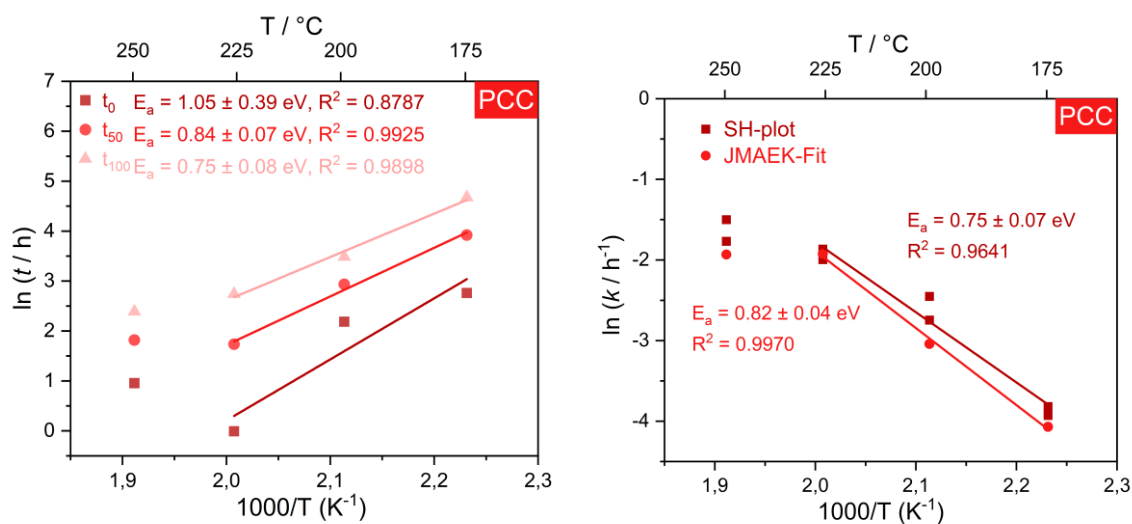


Figure A. 12.2: Arrhenius plots of PCC bond wire with DS from 175 °C to 250 °C. Left: Evaluation with the isoconversional method. Right: Evaluation with SH-plot and JMAEK-Fit.

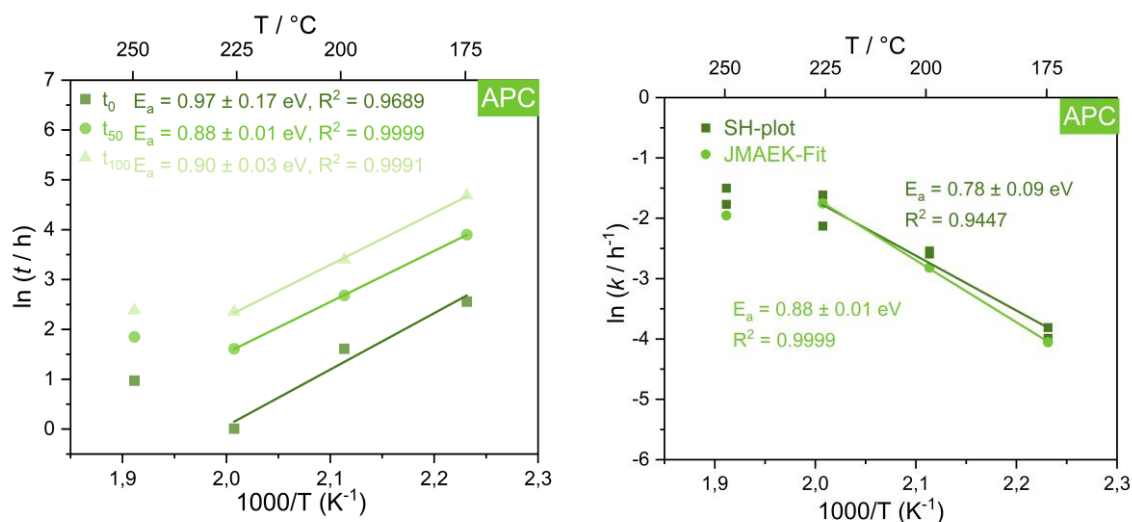


Figure A. 12.3: Arrhenius plots of APC bond wire with DS from 175 °C to 250 °C. Left: Evaluation with the isoconversional method. Right: Evaluation with SH-plot and JMAEK-Fit.

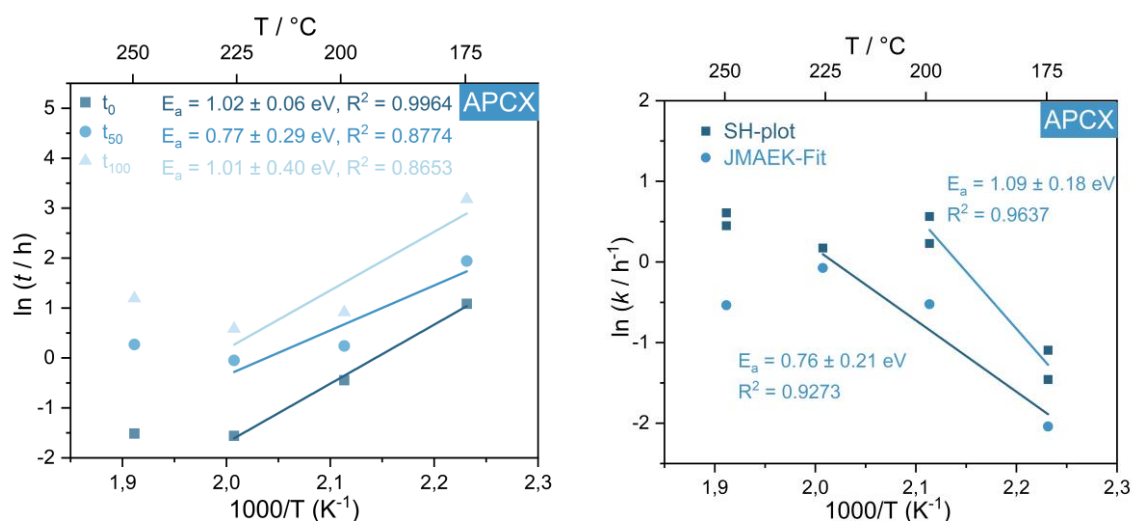


Figure A. 12.4: Arrhenius plots of APCX bond wire with DS from 175 °C to 250 °C. Left: Evaluation with the isoconversional method. Right: Evaluation with SH-plot and JMAEK-Fit.

Appendix

Table A 12.5: Overview of the activation energies and preexponential factors obtained from SH-plot, JMAEK-fit, and ICM for bare Cu, PCC, APC and APCX bond wire with **DS** at 250-175 °C.

	Cu	PCC	APC	APCX
Activation energies E_a / eV				
E_a (SH-plot)	0.59(7)	0.75(7)	0.78(9)	1.1(2)
E_a (JMAEK-fit)	0.61(8)	0.82(4)	0.88(1)	0.8(2)
E_a (t_0)	0.6(1)	1.1(4)	1.0(2)	1.02(6)
E_a (t_{50})	0.58(8)	0.84(7)	0.88(1)	0.8(3)
E_a (t_{100})	0.76(8)	0.75(8)	0.90(3)	1.0(4)
Mean E_a	0.63(7)	0.8(1)	0.88(7)	0.9(2)
Preexponential factor A				
ln A (SH-plot)	12(2)	16(2)	17(2)	18(5)
ln A (JMAEK-Fit)	12(2)	17(1)	19(1)	30(5)
ln A (t_0)	-14(2)	-24(9)	-23(4)	-25(2)
ln A (t_{50})	-11(2)	-18(2)	-19(1)	-18(7)
ln A (t_{100})	-15(2)	-15(2)	-19(1)	-23(9)

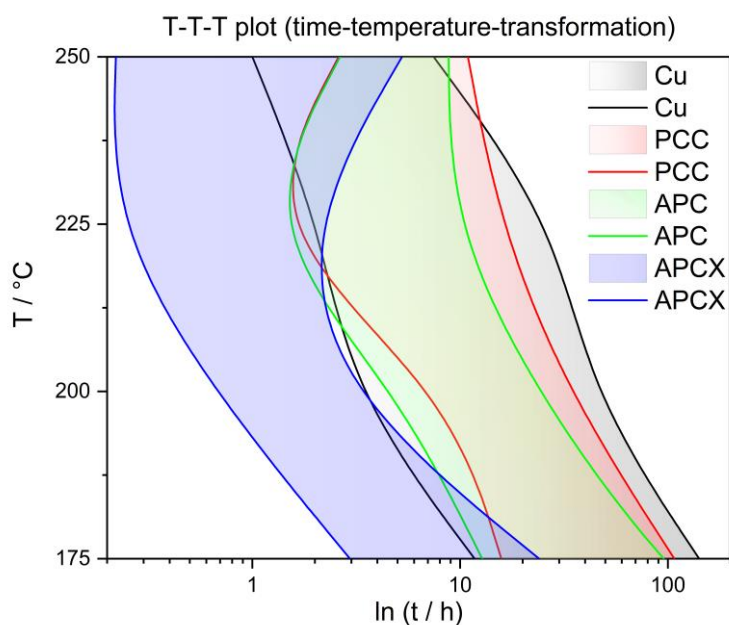


Figure A. 12.5: Logarithmic T-T-T-plot of Cu, PCC, APC, and APCX wire with DS from 250 °C to 175 °C. The left line represents the start of corrosion and the right line represents 100 wt% transformation.

Appendix

Table A 12.6: Overview of the obtained kinetic parameters from SH-plot, JMAEK-fit, and master plots for **Cu** bond wire with **MS1** at 250-175 °C.

Wire	Cu	Cu	Cu	Cu
T / °C	250	225	200	175
Sharp-Hancock Plot				
α -range / wt%	96-45 45-20	95-46	98-39	97-85
Avr. exp. n	1.15 3.26	1.17	0.91	0.84
k / h^{-1}	$7.84 \cdot 10^{-3}$ $9.14 \cdot 10^{-3}$	$3.34 \cdot 10^{-3}$	$1.78 \cdot 10^{-3}$	$2.41 \cdot 10^{-4}$
Mechanism	R3, Anti-R3 A3	R3, Anti-R3	D – R	D – R
JMAEK-Fit				
Avr. exp. n	1.68	1.25	0.93	0.96
k / h^{-1}	$8.18 \cdot 10^{-3}$	$3.52 \cdot 10^{-3}$	$1.82 \cdot 10^{-3}$	$4.03 \cdot 10^{-4}$
Mechanism	CD-D3, A2	R1	D - R	D - R
Master Plots				
Mechanism $f(\alpha)$	A2, R3, Anti-D3	A2, R3	R3, D2	R3, Anti-D3
Mechanism $g(\alpha)$	CD-D3, Anti-R3	Anti-R3	R3, Anti-D3	D3
Summary				
Assumed Mechanism	R3 ↓ Anti-D3	R3 ↓ Anti-R3	R3 ↓ Anti-D3	R3 ↓ D3

Appendix

Table A 12.7: Overview of the obtained kinetic parameters from SH-plot, JMAEK-fit, and master plots for **APC** bond wire with **MS1** at 250-200 °C.

Wire	APC	APC	APC
T / °C	250	225	200
Sharp-Hancock Plot			
α-range / wt%	99-78	99-97	97-94
	78-32	97-85	94-75
		85-18	75-60
			60-0
Avr. exp. n	1.00	0.26	0.26
	2.13	0.93	2.74
		2.19	1.52
			4.07
k / h⁻¹	2.88·10 ⁻³	8.30·10 ⁻⁸	1.47·10 ⁻⁷
	8.43·10 ⁻³	1.61·10 ⁻³	4.21·10 ⁻³
		5.23·10 ⁻³	2.88·10 ⁻³
			3.66·10 ⁻³
Mechanism		D3	D3
	R3	D – R	A3
	A2	A2	CD-D3
			A4
Avr. exp. n	2.13	2.12	3.88
k / h⁻¹	8.47·10 ⁻³	5.22·10 ⁻³	2.88·10 ⁻³
Mechanism	A2	A2	A4
Master Plots			
Mechanism f(α)	A2	A2	A4
Mechanism g(α)	A2, A3	A2	A2, A4
Summary			
Assumed Mechanism	R3	R3	A2
	↓	↓	↓
	A2	A2	A4

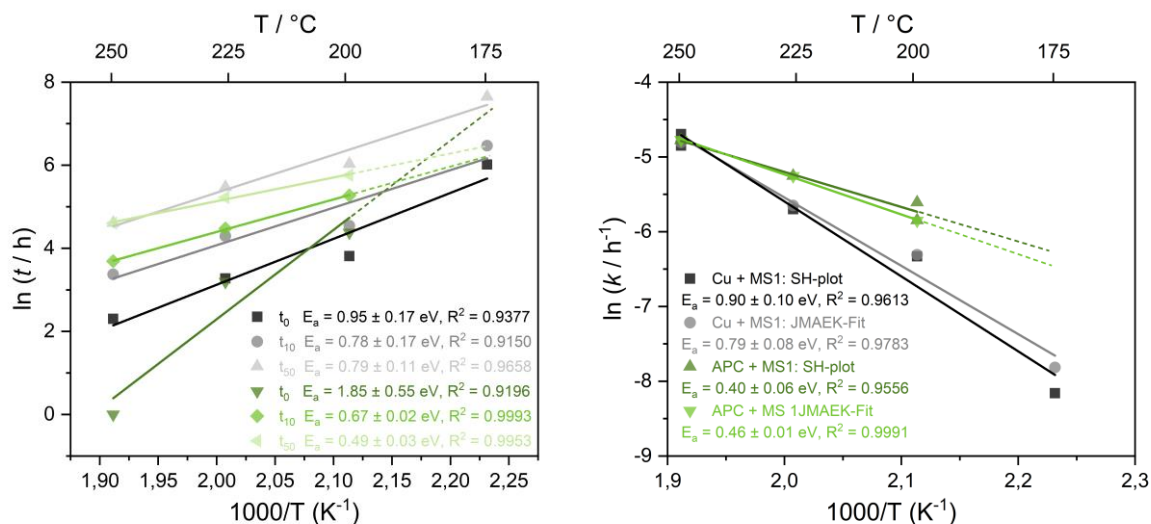


Figure A. 12.6: Arrhenius plots of Cu and APC bond wire with **MS1** from 175 °C (Cu) / 200 °C (APC) to 250 °C. Left: Evaluation with the isoconversional method. Right: Evaluation with SH-plot and JMAEK-Fit.

Table A 12.8: Overview of the activation energies and preexponential factors obtained from SH-plot, JMAEK-fit, and ICM for bare Cu, and APC bond wire with **MS1** from 175 °C (Cu) / 200 °C (APC) to 250 °C.

	Cu	APC
Activation energies E_a / eV		
E_a (SH-plot)	0.86(9)	0.40(6)
E_a (JMAEK-fit)	0.79(8)	0.46(1)
E_a (t_0)	1.0(2)	1.9(6)
E_a (t_{10})	0.8(2)	0.67(2)
E_a (t_{50})	0.8(1)	0.49(3)
Mean E_a	0.83(7)	0.8(6)
Preexponential factor A		
$\ln A$ (SH-plot)	15(2)	4(2)
$\ln A$ (JMAEK-Fit)	13(2)	5.5(3)
$\ln A$ (t_0)	-19(4)	-41(13)
$\ln A$ (t_{50})	-14(4)	-11.3(4)
$\ln A$ (t_{100})	-13(3)	-6.3(8)